OU-RM-DOE-17-F2

Geomechanics-Based Stochastic Analysis of Injection-Induced Seismicity
DE-FG36-08GO18194

Final Report Submitted by:

Ahmad Ghassemi

McCasland Chair Professor
Mewbourne School of Petroleum & Geological Engineering
The University of Oklahoma
Sarkeys Energy Center, Office 1314
100 East Boyd Street
Norman, OK
Tel. (405)-325-4347

A. Acknowledgements

The PI (A. Ghassemi) has benefited from the contributions of many individuals in completing this project, including the co-PI, Dr. Jafarpour, and graduate students whose efforts are also reflected in the publications listed at the end of this report. Alexander Verde, Sang-Hoon Lee, Reza Safari, Sonia Wang, Qinglu Cheng, Jianrong Lu, and Tarrahi worked on various aspects of the project as part of their Ph.D. studies.

This material is based upon work supported by the U.S. Department of Energy's Office of Energy Efficiency and Renewable Energy (EERE) Geothermal Technologies Office under Award Number DE-FG36-08GO1894.

B. Disclaimer

C. Introduction

The production of geothermal energy from dry and low permeability reservoirs is achieved by water circulation in natural and/or man-made fractures, and is referred to as enhanced or engineered geothermal systems (EGS). Often, the permeable zones have to be created by stimulation, a process which involves fracture initiation and/or activation of discontinuities such as faults and joints due to pore pressure and the in-situ stress perturbations. The stimulation of a rock mass is often accompanied by multiple microseismic events. Micro-seismic events associated with rock failure in shear, and shear slip on new or pre-existing fracture planes and possibly their propagations. The microseismic signals contain information about the sources of energy that can be used for understanding the hydraulic fracturing process and the created reservoir properties. Detection and interpretation of microseismic events is useful for estimating the stimulated zone, created reservoir permeability and fracture growth, and geometry of the geological structures and the in-situ stress state. The process commonly is referred to as seismicity-based reservoir characterization (SBRC). Although, progress has been made by scientific & geothermal communities for quantitative and qualitative analysis of reservoir stimulation using SBRC several key questions remain unresolved in the analysis of micro-seismicity namely, variation of seismic activity with injection rate, delayed micro-seismicity, and the relation of stimulated zone to the injected volume and its rate, and the resulting reservoir permeability. In addition, the current approach to SBRC does not consider the full range of relevant poroelastic and thermoelastic phenomena and neglects the uncertainty in rock properties and in-situ stress in the data inversion process.

The objective of this research and technology developments was to develop a 3D SBRC model that addresses these shortcomings by taking into account hydro-thermo-poro-mechanical mechanisms associated with injection and utilizing a state-of-the-art stochastic inversion procedure. The approach proposed herein is innovative and significantly improves the existing SBCR technology (e.g., Shapiro et al. 2003) for geothermal reservoirs in several ways. First, the current scope of the SBRC is limited with respect to the physical processes considered and the rock properties used. Usually, the geomechanics analyses within SBRC is limited to the pore pressure diffusion in the rock mass, which is modeled using a time-dependent parabolic equation and solved using a finite element algorithm with either a line or a point source. However, water injection induces both poroelastic and thermoelastic stresses in the rock mass which affect the stress state. In fact, it has been suggested that thermoelastic stresses can play a dominant role in reservoir seismicity (Ghassemi et al., 2007). We include these important effects by using a fully-coupled poro-thermoelastic constitutive equations for the rock mass which will be solved using a 3D finite element model with more realistic injection geometries such as multiple injection/extraction sources (and in fractures), uncertainty in the material parameters and the in-situ stress distribution to better reflect the pore pressure and stress distributions. In addition, we developed a 3D stochastic fracture network model to study MEQ generation in fracture rocks. The model was verified using laboratory experiments, and calibrated and applied to Newberry EGS stimulation.

In previous SBRC approaches, the triggering of micro-seismicity is modeled base on the assumption that the prior stochastic criticality model of the rock mass is a valid and adequate description. However, this assumption often does not hold in the field. Thus, we improved upon the current SBRC approach by using the micro-seismic responses to estimate the hydraulic diffusivity as well as the criticality distribution itself within the field. In this way, instead of relying on our a priori knowledge of criticality distribution,

we combine an initial probabilistic description of criticality with the information contained in micro-seismic measurements to arrive at criticality solutions that are conditioned on both field data and our prior knowledge. Previous SBRC have relied upon a deterministic inversion approach to estimate the permeability, and the extent of the stimulated zone, whereas a stochastic inversion algorithm that recognizes and quantifies the uncertainties in the prior model, the time evolution of pore pressure distributions (modeling errors), and the observed seismic events is developed and used herein to realistically assess the quality of the solution. Finally, we developed a technique for processing discrete MEQ data to estimate fracture network properties such as dip and dip directions. The approach was successfully applied to the Fenton Hill HRD experiment and the Newberry EGS with results in good agreement with field observations.

Chapter 1: Thermo-Poroelastic Modeling of Reservoir Stimulation and Microseismicity Using Finite Element Method with Damage Mechanics

1. Introduction

Stress analysis or rock mass failure in response to water injection is of much interest in oil and gas exploration and geothermal reservoir design. The process involves coupled rock deformation, fluid flow, heat transfer and chemical interactions in the porous rock. Interest in understanding rock deformation and failure during fluid injection has increased in enhanced geothermal systems, unconsolidated petroleum reservoirs, and unconventional resources such as gas shales.

From the geomechanical point of view, the impact of the variations of pore pressure, temperature and chemical interaction are key factors in reservoir engineering. These are of especially interesting around a wellbore, where their impact is particularly significant during injection and production, which may lead to problems such as borehole collapse, distortion, and buckling during injection or drilling (Yu et al., 2001). These problems are mainly caused where the rock's effective stress exceeds its strength. In addition, the far-field stresses are among the most important factors in geomechanical engineering since the stress regime impacts rock failure, its geometry, and the resulting fluid path. The stress distributions around a wellbore are influenced both by the injection-induced stress and far-field stress in the reservoir so they must be accounted for in determining the impact of fluid flow, temperature and chemical interaction with far-field stresses (Fig. 1.1).

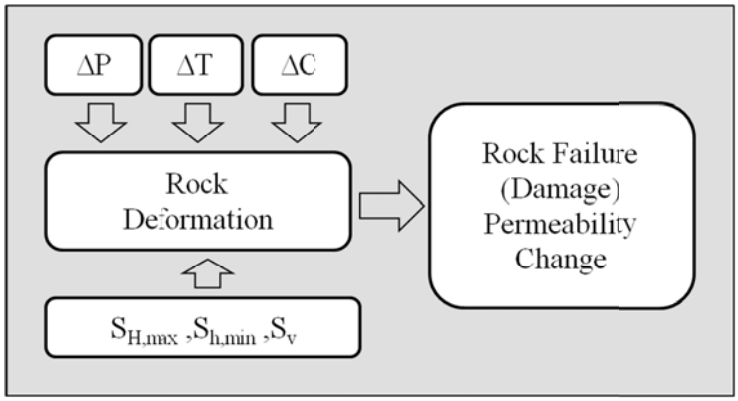

Fig. 1. The key factors in geomechanical engineering design.

Generally, the strain-stress behavior of rocks in experimental tests shows hardening and post-peak softening or directly reaches the softening regime, depending on the rock type and conditions such as pore pressure, stress conditions, and temperature (Jaeger et al., 2007). The continuum damage mechanics approach can capture the hardening and softening behavior of the rock (Yuan and Harrison, 2006), and permeability variation caused by the stress change and rock failure is critical in the analysis of wellbore stability and well stimulation. Induced microseismic events are among the promising approaches to estimate permeability changes and stress distributions since they measure the earthquake energy where geological formations have become imbalanced by fluid injection. The characteristics of microseismic events such as their locations, spatial patterns of distribution, and temporal relations between the occurrence of seismicity and reservoir activities are often studied for enhanced geothermal systems (EGS). Microseismic event detection and interpretation is used for estimating the stimulated volume and fracture growth, resulting reservoir permeability, and geometry of the geological structures and the in-situ stress state (Pine, 1984). Numerical modeling of the coupled processes in rock can help improve understanding of MEQ and will improve reservoir development activities.

1.1 Motivation and Objectives of the Study

The theory of thermo-poroelasticity can explain the coupling of fluid flow and temperature effects in rock deformation. It provides a robust framework for studying the rock deformation and stress redistributions after rock failure. However, its use and application could be improved by developing three-dimensional injection/extraction geomechanics models that not only consider induced rock failure and fracture propagation but also take into account rock damage and permeability variations. Continuum damage mechanics with fully coupled thermo-poroelasticity using finite element methods can be used for this purpose. The objectives of the research were to (i) develop a fully coupled thermo-chemo-poroelastic and three-dimensional finite element model that considers rock damage and stress-dependent permeability for simulating the influence of fluid flow and temperature with various injection schedules under anisotropic far-field stress conditions; (ii) observe the injection-induced stress variations, permeability change and rock failure; (iii) simulate and study the three-dimensional propagation of damage/fracture and microseismic events under different stress regimes, and better understand the key factors for temporal and spatial distributions of induced microseismic events.

1.2 Fluid Flow, Temperature, and Solute Transport in Porous Rock

Coupled hydromechanical process analysis was initially motivated by soil consolidation problems. Terzaghi (1923) presented the one-dimensional consolidation theory that takes into account pore pressure and the soil deformation. Biot (1941) developed a model for linear poroelasticity that considered the stress change under fluid loading and pore pressure variations under applied stress. This theory has been extended to include the influence of temperature, fluid flow, and rock deformation and is called thermo-poroelasticity (McTigue, 1986; Kurashige, 1989; Wang and Papamichos, 1994). Heidug and Wong (1996) proposed the constitutive equations for swelling shale based on nonequilibrium thermodyanamics. Ghassemi and Diek (2003) considered combined effects of chemical potential and thermal osmosis on water flow in and out of the mud and shale formation. They indicated that in addition to thermal osmosis, chemical osmosis also can be several times higher than hydraulic pressure in certain conditions. Also, a linear chemo-thermo-poroelasticity was developed to remedy the cumbersome solution of the original chemo-thermo-poroelasticity for practical applications. Details of these mathematical formulations will be illustrated in Section 2.

1.2.1 Biot's poroelasticity

Biot (1941) developed the coupled fluid and solids consolidation problem in porous media. He assumed that the material is homogeneous and fully saturated, and fluid flow follows Darcy's law in porous media. The problem domain that illustrated the influence of loading in excess pore pressure variation is shown in Fig. 1.2. Consider a fully saturated poroelastic layer from $z = 0$ to $z = h$, and normal traction P applied at the top surface. Initially the layer deforms as elasticity, and an excess pore pressure induces the change of displacement as results of the Skempton's effect. The fluid flow dries out gradually with time, and the layer continuously deforms vertically.

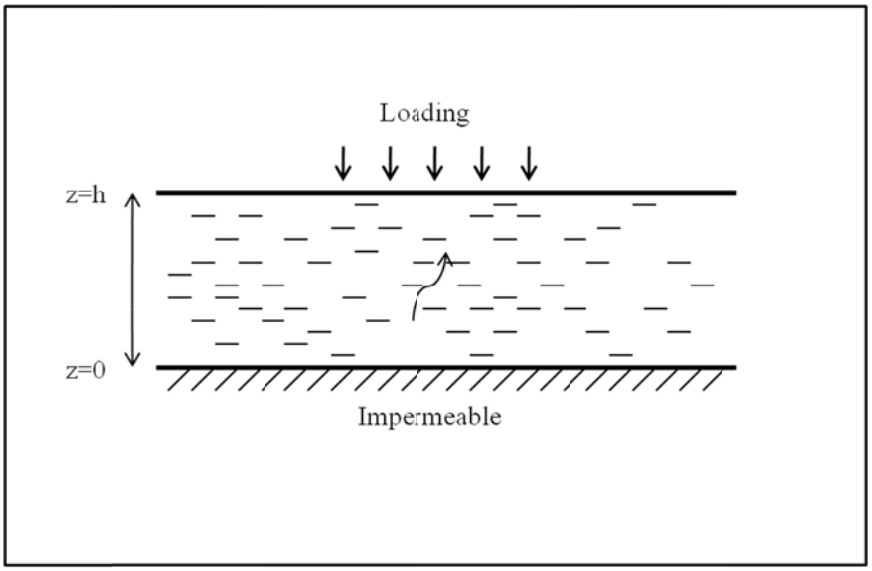

Fig. 1.2. Sketch of the Biot consolidation problem.

Assuming the fluid drains on the surface and the system is impermeable at the bottom, the governing equations for the transient phenomena of consolidation as follow,

$$\frac{1}{a}\frac{\partial^2 w}{\partial z^2} - \alpha \frac{\partial w}{\partial z} = 0 \qquad (1.1)$$

$$k\frac{\partial^2 p}{\partial z^2} = \alpha \frac{\partial^2 w}{\partial z \partial t} + \frac{1}{Q}\frac{\partial p}{\partial t} \qquad (1.2)$$

where $a = \dfrac{1-2\gamma}{2G(1-v)}$ is the compressibility, α is the Biot's constant, k is the coefficient of permeability of the soil including the viscosity, and Q is the volume of water which can be forced into the soil under pressure while the volume of the soil is kept constant.

Initial and boundary conditions for the consolidation problem can be described as no fluid flow at the bottom and zero pore pressure because of drainage on the surface.

$$\sigma = \frac{p_0}{\left(\dfrac{1}{\alpha a Q} + \alpha\right)} \quad for \quad t = 0 \qquad (1.3)$$

$$\frac{\partial p}{\partial z}(z = 0, t) = 0 \qquad (1.4)$$

$$p(z = h, t) = 0 \qquad (1.5)$$

The interesting solution for the consolidation problem is the change of displacement after loading (Biot, 1941).

$$w_s = \frac{8}{\pi} a h p_0 \sum_0^{\infty} \frac{1}{(2n+1)^2} \times \left\{1 - \exp\left[-\left(\frac{(2n+1)\pi}{2h}\right)^2 ct\right]\right\} \qquad (1.6)$$

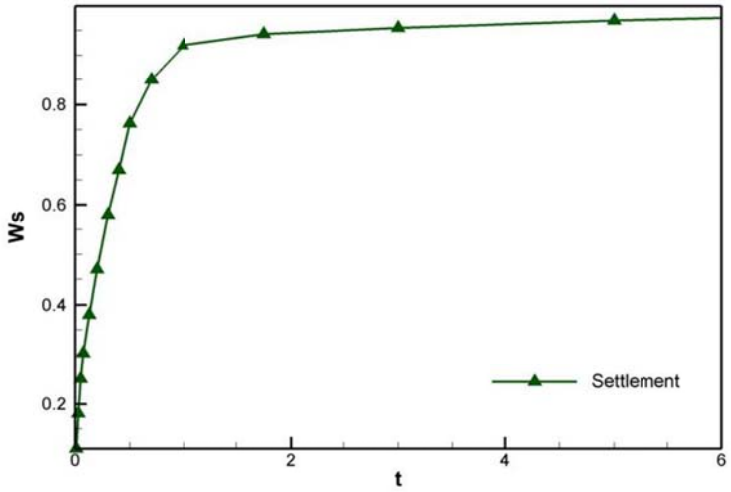

Fig. 1.3. Surface displacement with time.

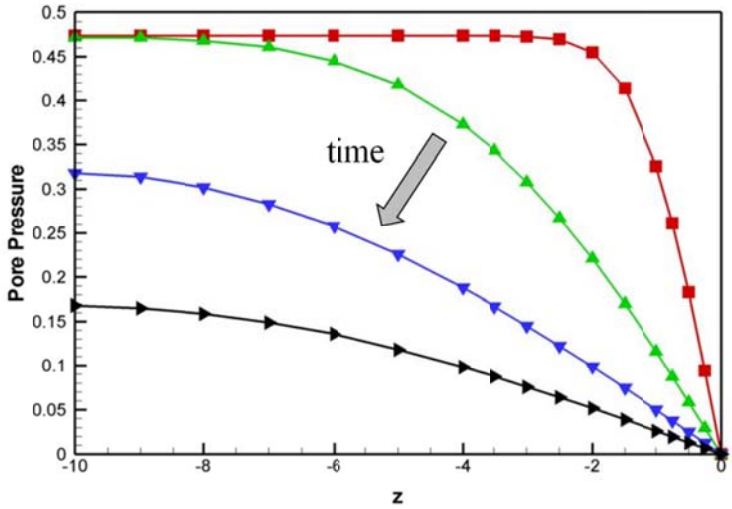

Fig. 1.4. Pore pressure change for various depths, as a function of time.

The analytical solution in Fig. 1.3 shows the displacement change on the top surface under loading with respect to time, and the corresponding pore pressure changes illustrate how (Fig. 1.4) the saturated water diffuses through the porous soil and out of its top surface as time increases. Note that maximum pore pressure in the middle (consolidation effect) can disappear in a very short time when the permeability (as is the case here) is relatively high (100 md). The consolidation effects will be discussed in more detail in Section 3, in the context of pore pressure distribution around a wellbore in ultralow-permeability rock.

The theory of Biot consolidation represents fully coupled interaction of fluid flow and solids. It provides general schemes of the interaction between fluid flow and mechanical loading. Similar phenomena are observed around a wellbore.

1.2.2 The concept of thermal stress

The change of temperature induces stress and displacement in a rock skeleton. The theory of thermoelasticity is analogous to the theory of poroelasticity, but instead of pore pressure, it includes the role of temperature change. Palciauskas and Domenico (1982) and McTigue (1986) studied the effects of temperature change on pore pressure and stress in rock. Considering linear elasticity, temperature decrease or rise causes a change of strain in the rock given by:

$$\varepsilon = -\beta \left(T - T_0\right) \qquad (1.7)$$

where β is the volumetric thermal expansion coefficient (at constant *t* and *p*) that indicates the change of strain by the difference of temperature in a rock. An increase in temperature will cause bulk volume increase, whereas a decrease of temperature will cause bulk volume decrease. Since the injection water in geothermal conditions is cold and reservoir temperature is hot, injection leads to tensile stress of rock in the injection well. For typical values such as K=10 GPa and β=10^{-5}/K, a temperature change of 10 K induces a thermal stress around 30 MPa.

The conductivity and thermal expansion coefficients do not vary widely because most rock-forming minerals have similar thermal expansion coefficients. The thermal conductivity of rock is in the range 1-10 W/m·K (Jaeger, Cook, and Zimmerman, 2007). An interesting phenomenon regarding the thermal effects in the rock is that the range of the thermal expansion coefficient does not vary significantly with rock type (Grimvall, 1986), in contrast to other rock properties such as porosity and permeability that may vary by many orders of magnitude. McTigue (1986) determined that the thermal expansion coefficient of a fluid-saturated rock is equal to that of the rock skeleton in drained conditions, whereas in undrained conditions, it is:

$$\beta_u = \alpha_s + \phi B\left(\beta_f - \beta_s\right) \qquad (1.8)$$

where ϕ and B are the porosity and the Skempton's coefficient. The subscripts *s* and *f* indicate the rock skeleton and fluid phase, respectively.

According to linear thermo-elasticity, the strain is the sum of stress-induced strain and thermally induced strain:

$$\varepsilon = \frac{1}{2G}\boldsymbol{\tau} - \frac{\nu}{2G\left(1+\nu\right)} trace(\tau)\mathbf{I} - \beta(T - T_0)\mathbf{I}\,, \qquad (1.9)$$

where $\boldsymbol{\tau}$ is the relationship of stress and strain in linear elasticity:

$$\boldsymbol{\tau} = \lambda\, trace(\tau)\mathbf{I} + 2G\varepsilon\,. \qquad (1.10)$$

The governing equation for thermoelasticity is obtained by combining Eq. 9 with the stress equilibrium equation, $\tau_{ij,j} = 0$ and the strain-displacement equations.

$$G\nabla^2\mathbf{u} + (\lambda + G)\nabla\left(\nabla\cdot\mathbf{u}\right) + 3\beta K\nabla T = 0 \qquad (1.11)$$

Fourier's law, $q_T = -k^T\nabla T$ and the energy balance equation for conductive heat transfer equation can be written as

$$\frac{\partial T}{\partial t} = \frac{k^T}{\rho c_p} \nabla^2 T \qquad (1.12)$$

The solutions of temperature distribution and displacement can be solved from Eq. 1.11 and Eq. 1.12. Thermo-elasticity has been extended to thermo-poroelasticity, which takes into account the influence of fluid flow and heat transfer.

1.2.3 The influence of chemical potential

The effect of chemical potential on water and solute transport is of interest in ultralow-permeability rock such as shale reservoirs. The general concept of chemical interaction in drilling fluid/shale has been studied by experiments (Chenevert, 1970; Hale et al., 1992; Mody and Hale, 1993). They showed that the in and out movement of water and solution between the drilling mud and the shale reservoir alters the pore pressure distribution, which in turns impacts the effective stresses. The fundamentals of fluid movement in shale can be explained by the difference of chemical potential between the water and shale as shown in Fig. 1.5.

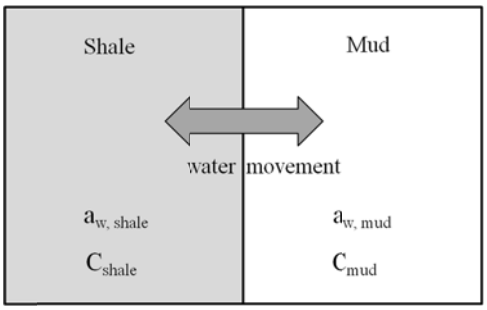

Fig. 1.5. Conceptual scheme of osmosis flow by chemical potential.

A model for chemo-poroelasticity that considers the osmosis, swelling, and solute transport between the drilling mud and pore fluid in the rock based on the Gibbs-Duhem equation in thermodynamics was presented by Heidug and Wong (1996). In this section, we only briefly introduce the general constitutive equations and transport equations for chemo-poroelasticity. Total stress and pore volume fraction has been introduced by Heidug and Wong (1996); that is (*tension positive*):

$$\dot{\sigma}_{ij} = L_{ijkl}\dot{\varepsilon}_{kl} - \alpha_{ij}\dot{p} + \sum_{\beta} \omega^{\beta}\dot{\mu}^{\beta}\delta_{ij} \qquad (1.13)$$

$$\dot{v} = \alpha\dot{\varepsilon}_{ij} + Q\dot{p} + \sum_{\beta} B^{\beta}\dot{\mu}^{\beta} \qquad (1.14)$$

where v is the pore volume fraction, and μ^{β} is the chemical potential of β^{th} chemical component. The elastic stiffness coefficients are the tensor in the case of isotropy, as

$$L_{ijkl} = G\left(\delta_{ik}\delta_{jl} + \delta_{il}\delta_{jk}\right) + \left(K - \frac{2G}{3}\right)\delta_{ij}\delta_{kl}, \qquad (1.15)$$

where K and G denote the bulk and shear modulus, respectively. The presence of hydraulic pressure and chemical potential cause the change of pore pressure and solute concentration with time. Fluid flux in shale can be written as:

$$J_f = -\frac{L^{11}}{\overline{\rho}_f}\nabla p - L^{12}\nabla\left(\mu^S - \mu^D\right), \qquad (1.16)$$

where *S* and *D* denote the solid and fluid, and the phenomenological coefficients are defined by:

$$L^{12} = -L^{11}\Re = -\frac{\overline{\rho}_f{}^2 k\Re}{\mu}, \qquad (1.17)$$

where k and μ are the permeability and viscosity, respectively. $\Re$ is the solute reflection coefficient which may range from 0 to 1.

1.3 Deformation and Failure of Rock

A number of cases in geothermal and petroleum reservoir operation involve rock deformation and failure caused by fluid flow change. Several different failure criteria are used for its applications (Jaeger, Cook, and Zimmerman, 2007). In this section, we briefly review the strain-stress behavior of rock under stress change, the Coulomb failure criterion, and the effect of pore pressure on rock failure.

1.3.1 Strain-stress curve

The most common tool for studying mechanical behavior of rocks is the uniaxial and triaxial test. It provides the rock properties such as modulus, rock strength, and hysteretic behavior during loading and unloading. In addition, it can estimate the brittle or ductile behavior of rock in a certain conditions of reservoir far-field stress and temperature. The general strain-stress curve for rock under compressive stress is illustrated in Fig. 1.6. In region A-B, the strain-stress behavior is almost elastic and hysteresis may be observed. The stress continues to rise in region B-C but nonlinear behavior, which is called the ductile state, begins at point B, which is the yield stress of the rock. The third region, C-D beginning with the maximum stress at point C leads to large permanent strain change caused by compressive stress, where deterioration of the rock causes a brittle state.

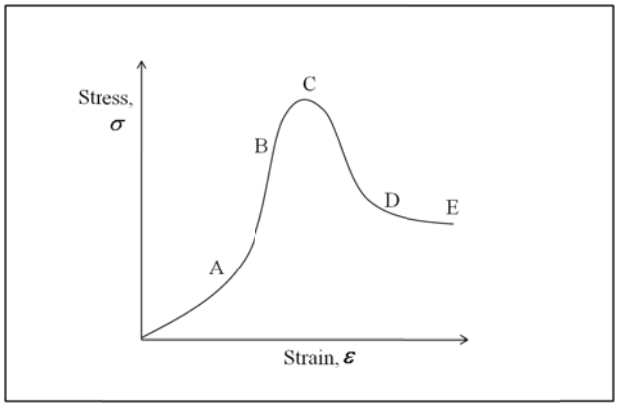

Fig. 1.6. General strain-stress curve for rock under compression.

1.3.2 Coulomb failure criterion

The mostly widely used model for the prediction of rock failure is the Mohr-Coulomb failure criterion. Coulomb (1773) developed the model through experimental investigation, assuming the shear stress along to the plane causes failure. This consideration can be mathematically expressed as:

$$|\tau| = S_1 + \mu_s \sigma \qquad (1.17)$$

where $|\tau|$ is shear stress, S_1 is finite shear stress, and μ_s and σ are the coefficients of internal friction and normal stress. Eq. 17 can be rearranged to the maximum and minimum principal stress as:

$$\frac{1}{2}(\sigma_1 - \sigma_3) = S_0 \cos\phi_c + \frac{1}{2}(\sigma_1 - \sigma_3)\sin\phi_c, \qquad (1.18)$$

where ϕ_c is the angle of internal friction and σ_1 and σ_3 are the minimum and maximum principal stress.

Understanding tensile failure requires the tension cut-off, $T_{0,}$ which can be measured from a tensile experiment since without a tension cut-off, the Coulomb failure criterion often overestimates the stress state for the failure criterion.

1.3.3 Effects of pore pressure in rock failure

Fluid injection causes rock failure because of the hydraulic pressure and chemical interactions between the rock and the fluid. The mechanical impact with pore pressure has been developed by Terzaghi (1936). He proposed that the failure of soil can be controlled by the effective principal stress σ'; that is,

$$\sigma = \sigma' - p \qquad (1.18)$$

where p is the pore pressure.

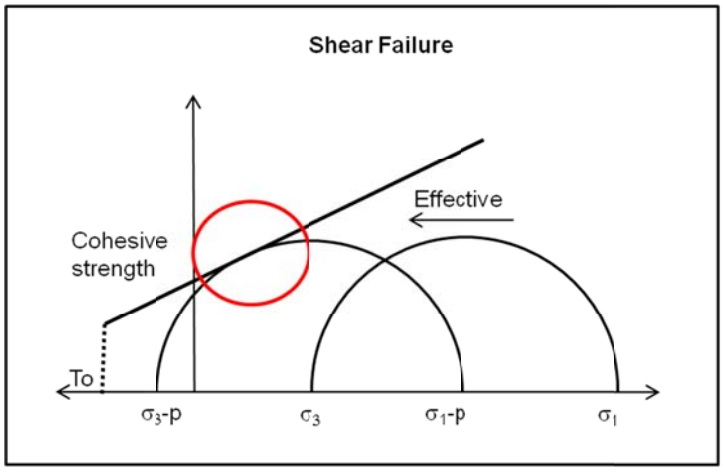

Fig. 1.7. Stress state that satisfies the shear failure curve.

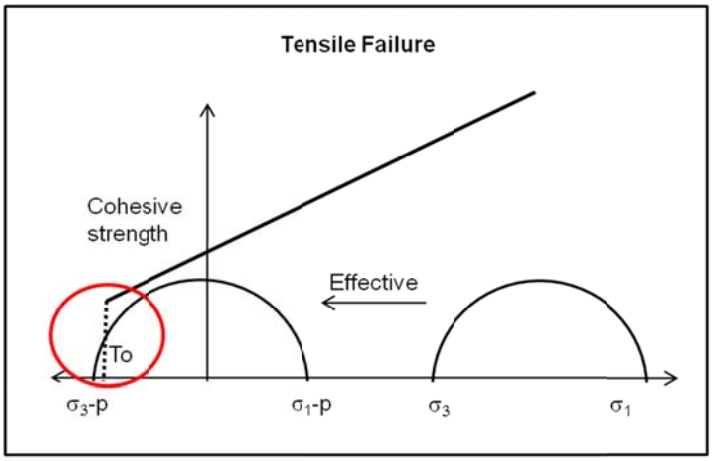

Fig. 1.8. Stress state that satisfies the tensile failure curve.

Fig. 1.7 and Fig. 1.8 illustrate the stress state in shear and caused tensile failure by pore fluid pressure. This fluid-induced failure is frequently observed around a borehole during the injection or production operation in geothermal and petroleum reservoirs since they experience significant change of pore pressure around a wellbore.

1.4 Fundamentals of Continuum Damage Mechanics

The nonlinear behavior of the rock is of much interest in well stimulation and hydraulic fracturing design in petroleum and enhanced geothermal reservoirs. Stress behavior in triaxial tests shows the hardening and softening process as the vertical compressive stress increases. This nonlinear behavior can also be observed frequently in oil and gas exploration in, for example, sanding problems in unconsolidated reservoirs, reservoir compaction during injection and production, and wellbore stability. More importantly, the process of hydraulic fracturing directly contributes to the nonlinearity of the rock by imposing fluid loading. Traditional poroelasticity cannot capture the hardening and softening behavior after the rock fails, so that it is necessary to consider the nonlinear behavior of rock under the effects of fluid flow, temperature change, and solute transport. In this section, we briefly review the continuum damage mechanics which illustrate microcracks, microcavities, nucleation, and coalescence. The continuum damage theory phenomenologically accounts for the initial evolution of defects such as nucleation of a certain amount of cracks and void growth during the deformation.

Various damage models have been proposed brittle and ductile materials. These include creep damage, cycle fatigue, and brittle damage (Kachanov, 1986; Lemaitre and Chaboche, 1990; Voyiadjis and Kattan, 1999). Kachanov (1958) first proposed a continuum damage model by introducing effective stress in a fictitious, undamaged configuration. Later researchers extended his theory for ductile material (Lemaitre, 1984, 1985; Murakami, 1988) and brittle material (Krajcinovic and Foneska, 1981; Krajcinovic, 1983, 1996). Ductile materials show a strong plastic deformation, which is the main contributor to the damage evolution and reverse process, so many models for ductile material consider the concepts of coupling between plasticity and damage mechanics (Gurson, 1977; Tvergaard, 1982; Rousselier, 1987; Mahnken, 2002).

The theory of damage in porous rock has been implemented by several researchers (Hamiel et al., 2004; Selvadurai, 2004; Tang et al., 2002). Bart et al. (2000) developed an anisotropic damage model in poroelastic brittle rock and Selvadurai (2004) presented the application of an isotropic damage model in a

poroelastic contact problem. Tang et al. (2002) illustrated brittle rock failure under compressive and tensile stress with triaxial tests. They described the sudden drop to the residual stress regime by assuming that strain-stress behavior follows the elasticity theory before the rock failure and the damage theory after the rock failure without considering the hardening process; instead, rock heterogeneity leads to distributed rock failure (different peak stress in each element), which defines the hardening process in the stress and strain behavior.

Chow and Wang (1987) and Zhao and Roegiers (1993) studied the influence of rock damage on the change in Poisson's ratio. Measurement of the change of compressibility in uniaxial tests of Berea sandstone and Cordoba cream limestone (Zhao and Roegiers, 1993) showed that Poisson's ratio is reduced as the damage variable increases during the rock fracturing progress. To understand the damage variable, we briefly introduce the physical meaning of damage variable d and its relations of stress change. We assume that the cross-sectional area of the cylindrical bar in the loading condition is A and the area of both cracks and voids (damage in the bar) is A^D. The removal of defects can be considered as a fictitious, undamaged configuration as shown in Fig. 1.9 to use continuum damage mechanics to remove both cracks and voids from the cylindrical bar.

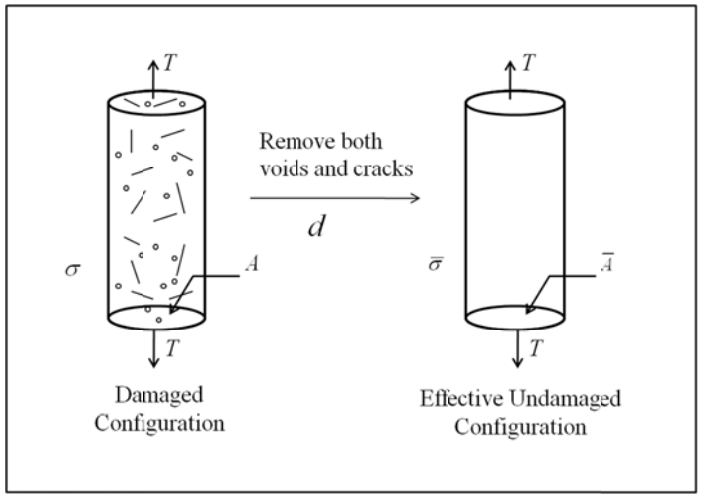

Fig. 1.9. Under uniaxial tension, both voids and cracks are removed in the effective undamaged configuration (Voyiadjis and Kattan, 1999).

The effective configurations of the cross-sectional area and the stress are denoted by $\overline{A}$ and $\overline{\sigma}$, respectively. The effective undamaged configuration of stress can be written as:

$$\overline{\sigma} = \frac{\sigma}{1-d} \qquad (1.18)$$

where the damage variable can be described from the continuum damage theory as:

$$d = \frac{A-\overline{A}}{A} = \frac{A^D}{A} \qquad (1.19)$$

where $\overline{A}$ is the effective configuration of the cross-sectional area, and A^D is the damaged area. We can formulate the effective configuration of the stress-strain relationship as:

$$\overline{\sigma}_{ij} = \overline{E}_{ijkl}\overline{\varepsilon}^{e}_{kl} \qquad (1.20)$$

where $\overline{E}_{ijkl}$ is the elastic moduli tensor for effective configuration of undamaged area and $\overline{\varepsilon}_{ij}^{e}$ is the similar effective strain.

The two theories in the transformation from the nominal to the effective configuration are the strain equivalence hypothesis and the strain energy equivalence hypothesis. Assuming that the strain in normal configuration is the same as in the effective configuration in strain equivalence hypothesis as:

$$\varepsilon_{ij} = \overline{\varepsilon}_{ij}, \qquad (1.21)$$

we can derive the expression for the relationship of the effective stress and strain configuration with the damage variable as follows:

$$\frac{\sigma}{1-d} = \overline{E}\varepsilon \qquad (1.22)$$

$$\frac{E\varepsilon}{1-d} = \overline{E}\varepsilon \qquad (1.23)$$

From the hypothesis of strain equivalence ($\varepsilon_{ij} = \overline{\varepsilon}_{ij}$), the relationship of damaged modulus with initial modulus can be written as:

$$E = (1-d)\overline{E} \qquad (1.24)$$

The other theory for the transformation relation between the damaged and fictitious undamaged state was proposed by Sidoroff (1981). The theory assumed that the elastic energy in terms of effective configuration and nominal stress are equal; therefore, the elastic strain energies for damage and undamaged configuration are the same:

$$\frac{1}{2}\sigma_{ij}\varepsilon_{ij} = \frac{1}{2}\overline{\sigma}_{ij}\overline{\varepsilon}_{ij} \qquad (1.25)$$

The relation of effective and nominal strain can be derived with Eq. 1.24 by substituting Eq. 1.18 such that

$$\overline{\varepsilon}_{ij} = (1-d)\varepsilon_{ij} \qquad (1.26)$$

Therefore, by rearranging of Eq. 1.26 and Eq. 1.18, we can obtain the relationship between the initial and damaged modulus,

$$E = (1-d)^2\overline{E} \qquad (1.27)$$

1.5 Stress-Dependent Permeability

One of the interesting physical properties in a rock is permeability. It varies by many orders of magnitude among the various rock types, and it influences the fluid transmissibility in porous rock, which in turns impacts the effective rock stress. Permeability appears to have a relationship with porosity, but that is still highly uncertain because of their complexity in rocks (Ingebritsen and Manning, 2010).

The permeability variations induced by altered stress and rock failure have been studied by many researchers (Shipping et al., 1994; Kiyama et al., 1996; Coste et al., 2001; Zoback and Byerlee, 1975). Zoback and Byerlee (1975) illustrated the relation between permeability change and the evolution of microcracks and voids. Their experimental tests on granite show permeability increases of up to a factor of four during rock deformation. Other studies present different magnitudes for the increase in

permeability depending on rock type and conditions (De Paola et al., 2009; Wang and Park, 2002). Stress-dependent permeability has been developed by Elsworth (1989) and Bai and Elsworth (1994, 1999) for fractured media and Bai and Elsworth (1994) for intact rock. They considered equivalent fracture networks and showed the sensitivity of permeability to effective stress with coupled poroelasticity.

The empirical models for the correlations relating the permeability increase to the porosity change have been proposed by several authors (Labrid, 1975; Lund and Fogler, 1976; Lambert, 1981). The Labrid permeability model based on porosity change can be supposed as:

$$\frac{k_0}{k} = M\left(\frac{\phi_0}{\phi}\right)^n, \qquad (1.28)$$

where k_0 and ϕ_0 are the initial permeability and porosity, respectively.

Labrid's permeability model based on porosity was extended by Thomas et al. (2003), who proposed that porosity has correlations with strain:

$$-\ln\left[\frac{(1-\phi)}{(1-\phi_0)}\right] = \varepsilon_v, \qquad (1.29)$$

where ε_v is the volumetric strain.

The other interesting permeability model considering the shear dilation was developed from Bai and Elsworth (1994):

$$\frac{k}{k_0} = \left\{1 \mp \frac{1}{2}\left[\frac{9(1-\nu^2)^2}{2}\left(\frac{\pi\Delta\sigma}{E}\right)^2\right]^{1/3}\right\}^2 \qquad (1.30)$$

where the alternate negative and positive sign denote compression and dilatational loading.

Tang et al. (2002) developed a stress-dependent permeability model based on effective stress that accounts for the permeability increase under shear and tensile failure. There model emerged from experimental observation in triaxial tests with fluid in and out through the core sample.
For undamaged rock:

$$k = k_0 \exp-\left[\beta_d\left(\sigma_{ii}/3 - \alpha p\right)\right] \qquad (1.31)$$

For damaged rock:

$$k = \xi_d k_0 \exp\left[-\beta_d\left(\sigma_{ii}/3 - \alpha p\right)\right] \qquad (1.32)$$

where ξ_d is the increasing factor after the rock failure and β_d represents the sensitivity of permeability in exponential decay by compression.

Permeability anisotropy is a key factor in the reservoir fluid path that can be caused by in-situ stress anisotropy. Experimental studies have shown that the permeability behaves isotropic under isotropic loading, whereas anisotropy becomes larger with anisotropic loading in core analysis (Bruno et al., 1991; Rhett et al., 1992; Ruistuen et al., 1996). From the experimental results of permeability behavior under stress variations, we can infer that reservoir permeability is dependent on the deviatoric far-field stress. Khan and Teufel (2000) illustrated the change of permeability anisotropy with respect to pore pressure variations and far-field stresses. They concluded that the maximum permeability direction is parallel to the maximum principal stress, and the permeability anisotropy increases as the deviatoric stress increases.

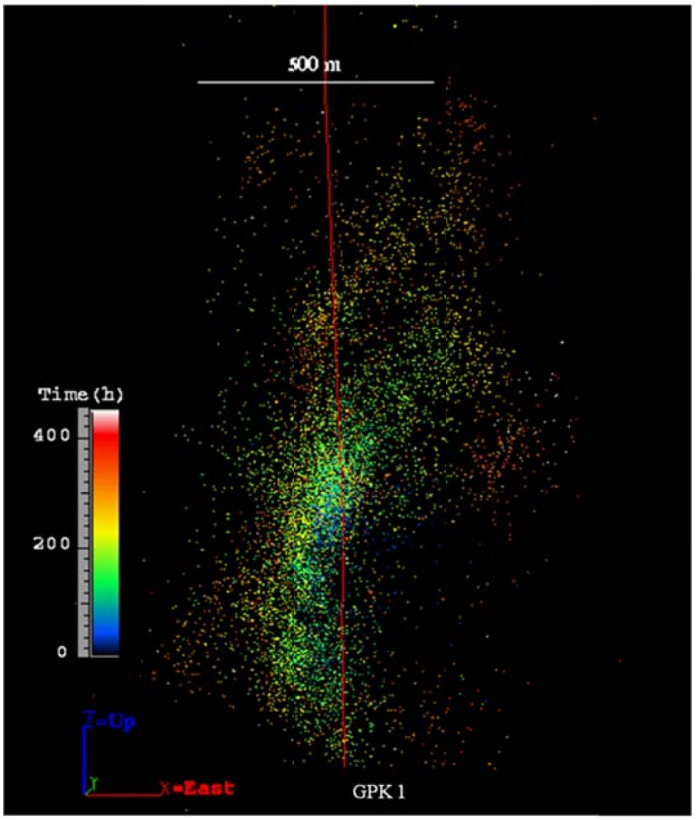

Fig. 1.10. Microseismic events induced during the injection experiments of the Soultz-Sous-Forets reservoir.

1.6 Injection-induced Microseismicity

In geological formations, earthquakes are occasionally caused by redistribution of the in-situ earth stresses in the rock mass. The interest in monitoring microseismic events during injection and production has increased over the past several years since it can be used as a tool to predict the natural fracture distribution and reservoir rock properties such as permeability and rock strength. Once injection and production begin in geothermal or oil and gas exploration, the pore pressures increase in the injection well and decrease in the production well. This change of pore pressure triggers earthquake activity by both shear and tensile failure as shown in Fig. 1.10.

Efforts to estimate reservoir properties during fluid injection and extraction have progressed by several researchers (Talwani and Acree, 1985; Shapiro et al., 1997; 1999; 2002; Adushkin et al., 2000; Fehler et al., 2001). Microseismic event detection and interpretation are used for estimating the stimulated volume; resulting fracture growth, reservoir permeability, and geometry of the geological structures; and the in-situ stress state (Pine, 1984). The process commonly is referred to as seismicity-based reservoir characterization. Progress has been made in quantitative and qualitative analysis of reservoir stimulation using microseismic events (Shapiro et al., 1997, 1999, 2002; Rothert and Shapiro, 2003). They demonstrated numerical simulations based on a fluid diffusion model with a permeability tensor, assuming microseismic events are triggered if the pore pressure exceeds certain threshold values. However, rock failure and permeability change were not considered. Also, in-situ stress and thermal effects on fluid-rock interaction have not been considered. Generally, induced seismicity occurs more

frequently by fluid injection if the cracks, natural fractures, and faults exist and are subjected to excess shear. Bruel (2002) and Baisch et al. (2003) considered shear failure by fluid injection in naturally fractured reservoirs, and Safari and Ghassemi (2011) showed thermo-poroelastic analysis of microseismicity, which considered the fluid flow and fracture deformation by injection/extraction in geothermal reservoirs. Hydraulic fracturing also induces microseismicity. Fracturing is accompanied by tensile failure, which contrasts with shear induced failure (although shear failure can also be present in the vicinity of the hydraulic fracturing). It creates high energy for monitoring tensile failure so that it can be a tool for predicting the intended fractured volume.

1.7 Heterogeneous Model

Rocks are heterogeneous, with natural weaknesses such as pre-existing cracks, voids, and grain boundaries. The variations of pore pressure and temperature during fluid injection can induce fractures at these defects, resulting in rock failure and fracture propagation. Muller et al. (2009) conducted stochastic borehole stability analysis using probability distribution functions for rock and reservoir properties such as bulk and shear modulus, far-field stress, initial pore pressure, and tension cutoff. They assumed the stochastic parameters follow lognormal and normal distributions which are widely used in heterogeneous reservoir simulations. The other probability function in geomechanics simulation is the Weibull distribution function (Weibull, 1951; Fang and Harrison, 2002; Tang et al., 2002; Gharahbagh and Fakhimi, 2010; Min et al., 2011), defined as: $\varphi = \frac{n}{s_0}\left(\frac{s}{s_0}\right)^{n-1} \exp\left[-\left(\frac{s}{s_0}\right)^{n}\right]$ where s in the variables s_0 represents the corresponding mean value. The shape parameter n determines the deviation from the mean value. The range of n is from 1 to infinity. If n increases, statistical deviations become narrow and the rock is homogeneous. Most rock properties, such as modulus and porosity, are heterogeneous because of the rock's components and origin, and numerical modeling needs to depict this initial heterogeneity. The Weibull distribution function can be used to generate an initial property distribution for numerical modeling. Also, the deviations of rock properties from the mean values are important. These deviations can be assumed as flaws in unit volume; therefore, homogeneous rock can be modeled with high value of n, and heterogeneity (flaws in unit volume) increase as n decreases.

1.7.1 Stochastic model

To approach realistic reservoir properties and conditions, many stochastic approaches have been developed to accommodate small and large-scale heterogeneities in reservoir simulations (Knutson, 1976; Smith and Morgan, 1986; Liu, 2006). The two main streams in stochastic approaches are the discrete and continuum models.

The discrete model considers discrete geological features such as naturally pre-existing fracture and faults in spatial distributions. Ezzedine (2010) presented stochastic discrete fracture network numerical model using Monte Carlo realizations and Cacas et al. (1990) proposed stochastic particle trajectories of flow patterns in fractured rock incorporating intersections with the network pipes model. Liu (2006) developed multiple-point simulations based on the Bayesian updating correction, and demonstrated the influence of geostatistical model parameters, number of replicates, and grid-scale.

The other stochastic approach is the continuum model. This model describes the mean level, deviations from the mean values, and how strongly typical properties are related with other neighboring points. Some key concepts are random distribution functions such as Gaussian, Weibull, and log-normal

distribution functions, and the model has been applied to the rock mechanics and reservoir simulations (Muller et al., 2009; Tang et al., 2002; Voss, 1985; Hewett, 1986).

The discrete models are better suited for modeling large-scale heterogeneous reservoirs to describe the discontinuities of rock mass. The continuous models are well-suited for geomechanical modeling of rock properties, assuming typical probability distributions with stationary change. The approach for describing the heterogeneity in this work is the continuum model which considers the deviation from the mean values based on Weibull distribution function.

1.7.2 Mesh size sensitivity for heterogeneous models

It is critical to consider the influence of mesh scale to model spatial distribution of geological media. Especially to describe the discontinuity of reservoir rocks, the mesh generation and size selection become more important problems. Liu (2006) tested geostatistical modeling with different scales and found good agreement between a finer-scale mesh and a training model that assumed a synthetic spatial distribution for channels in sinuous sand and shale. Similarly, for crack propagation modeling, mesh size is crucial to differentiate stress distribution during loading. Liang (2005) presented a strain-stress curve with different mesh sizes representing the heterogeneity of rock distributions. Fig. 1.11 shows the influence of mesh size for the numerical modeling of fracture propagation in heterogeneous media. The stress field in the coarse mesh can smear out the stress concentration near the crack tip, so it causes difficulty for geomechanical simulations. The finer mesh is suitable for describing the realistic spatial distribution; however, it requires extensive computational memory and CPU costs.

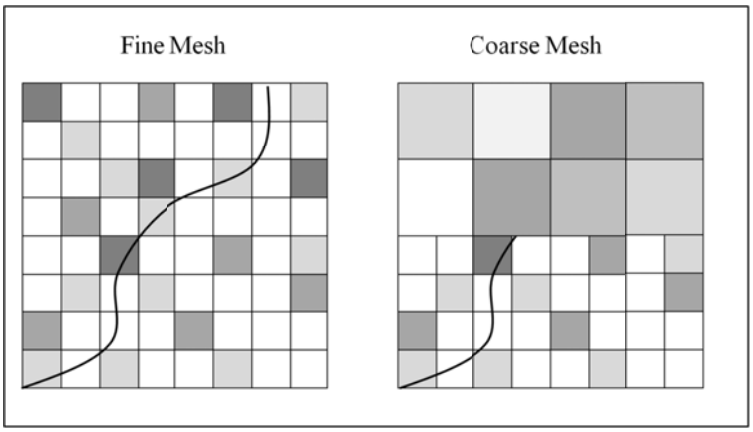

Fig. 1.11. The influence of mesh size on crack propagation in heterogeneous media (Liang, 2005).

A selection of optimum mesh size for geomechanical simulation is dependent on the local distribution of the reservoir properties and fluid injection conditions. Especially for the wellbore stability problem, the mud pressure is maintained in between the initial pore pressure and the fracture gradient to avoid well collapse and severe distortion. The mesh for numerical modeling for wellbore stability must be finer near the wellbore to capture the variations of stress, pore pressure, and temperature; however, the changes of pore pressure and temperature are small in the range far from the wellbore (~5m), so the large element size is suitable. The design of mesh size should be based on how significant the spatial variations of variables are. Also, loading conditions such as fluid injection and the difference of temperature between the injection fluid and reservoir are key factors in constructing the mesh size; too large mesh sizes and too high heat transfer rates can cause numerical oscillation for temperature distribution.

2. The Theory of Poroelasticity and its Extensions

The influence of fluid flow in a porous rock was initially recognized in the soil consolidation problem. The one-dimensional consolidation problem, which takes into account the pore pressure in soil, was developed by Terzaghi (1923), who demonstrated that the total stress concept consists of effective stress and pore pressure. Biot (1941) developed a coupled fluid/solid interaction model that assumed that the soil is homogeneous and water is incompressible, and used Darcy's law for fluid flow. The linear poroelasticity was extended to combined thermal and hydraulic stress (McTigue, 1986; Kurashige, 1989). Also the relation of chemical potential and rock deformation has been developed on the basis of the thermodynamic law and the Gibbs-Duhem equation (Mody and Hale, 1993; Heidug and Wong, 1996; Ghassemi and Diek, 2003; Ghassemi et al., 2009; Zhou and Ghassemi, 2009). The sign convention in this section follows positive tension.

2.1 Poroelasticity

The linear poroelasticity introduces the coupled interaction between the rock deformation and pore pressure variations. The change of pore pressure causes rock deformation and also rock could be deformed by fluid flow.

2.1.1 Constitutive equations

The relation between the solid (ε_{ij}) and fluid (ζ), the stress and pore pressure can be described as:

$$\varepsilon_{ij} = \frac{\sigma_{ij}}{2G} - \left(\frac{1}{6G} - \frac{1}{9K}\right)\delta_{ij}\sigma_{kk} + \frac{1}{3H'}\delta_{ij}p \quad (i = 1,2,3 \quad j = 1,2,3) \tag{2.1}$$

$$\zeta = \frac{\sigma_{kk}}{3H''} + \frac{p}{R'} \tag{2.2}$$

where the *K* and *G* are the bulk and shear modulus of the drained elastic solid. The constants H', H'' and R' denote the coupling between the solid and fluid stress and strain.

The change of strain by pore pressure is equal to the fluid contents change caused by the increase of volumetric stress:

$$\frac{\partial \varepsilon_{ij}}{\partial p} = \frac{\partial \zeta}{\partial \sigma_{ij}} \tag{2.3}$$

The poroelastic coupling parameters can be defined as (Rice and Cleary, 1976; Detournay and Cheng, 1993)

$$R' = \frac{2G(1+v)(v_u - v)}{\alpha^2(1-2v)^2(1+v_v)} \tag{2.4}$$

$$H' = H'' = \frac{2G(1+v)}{2\alpha(1-2v)} \tag{2.5}$$

Substituting Eq. 2.4 and Eq. 2.5 into Eqs. 2.1 and 2.2:

$$\varepsilon_{ij} = \frac{\sigma_{ij}}{2G} - \frac{v}{2G(1+v)}\delta_{ij}\sigma_{kk} + \frac{\alpha(1-2v)}{2G(1+v)}\delta_{ij}p \tag{2.6}$$

$$\zeta = \frac{\alpha(1-2v)}{2G(1+v)}\sigma_{kk} + \frac{\alpha^2(1-2v)^2(1+v_u)}{2G(1+v)(v_u-v)}p \qquad (2.7)$$

After rearranging Eq. 2.6 and Eq. 2.7 to include the stress σ_{ij} and pore pressure p, we obtain:

$$\sigma_{ij} = 2Ge_{ij} + \frac{2Gv}{1-2v}\delta_{ij}e - \alpha\delta_{ij}p \qquad (2.8)$$

$$p = -\frac{2GB(1+v_u)}{3(1-2v_u)}e + \frac{2GB^2(1-2v)(1+v_u)^2}{9(v_u-v)(1-2v_u)}\zeta \qquad (2.9)$$

where B is the Skempton pore pressure coefficient is defined by:

$$B = \frac{3(v_u - v)}{2(1-2v_u)(1+v_u)}.$$

2.1.2 Field equations

To solve the solutions for the stress and pore pressure, the balance equation for stress and fluid flow with Darcy's law are also necessary.

The equilibrium equations:

$$\sigma_{ij,j} = 0 \qquad (2.10)$$

The fluid mass balance equation can be written as:

$$\dot{\zeta} + q_{i,i} = 0 \qquad (2.11)$$

where q_i is the specific discharge vector which has a relation with Darcy's law:

$$q_i = -\frac{k}{\mu}p_{,i} \qquad (2.12)$$

The governing equation for solids is obtained from Eqs. 2.8 and 2.10 as

$$G\nabla^2 u_i + \frac{G}{1-2v_u}u_{k,ki} - \alpha p_{,i} = 0 \qquad (2.13)$$

After substituting Eq. 2.7 into Eq. 2.11 with Darcy's law (Eq. 2.11), the governing equation for fluid can be derived:

$$\dot{\zeta} - c_f\nabla^2\zeta = 0 \qquad (2.14)$$

where $c_f = \frac{2kB^2G(1-v)(1+v_u)^2}{9\mu(1-v_u)(v_u-v)}$ is the fluid diffusion coefficient. Substituting Eq. 2.7 into Eq. 2.9:

$$\dot{p} - kM\nabla^2 p = -M\alpha\dot{e} \qquad (2.15)$$

where $M = \frac{2G(v_u - v)}{\alpha(1-2v_u)(1-2v)}$ is the Biot modulus (similar to a storage coefficient) defined as the change of fluid contents per unit volume as a result of pore pressure variation under constant volumetric strain.

2.2 Thermo-poroelasticity

Nonisothermal conditions often arise when geothermal reservoir or steam assisted gravity drainage (SAGD) is used to enhance oil recovery. The difference of heat expansion coefficients between the rock and fluid cause rock deformation and pore pressure. The governing equations for thermo-poroelasticity were developed by McTigue (1986), assuming fully-saturated homogeneous rock.

2.2.1 Constitutive equations

The constitutive equations considering the relations of the strain, pore pressure, and temperature change were developed from the thermoelasticity and poroelsticity (McTigue, 1986):

$$\sigma_{ij} = 2Ge_{ij} + \frac{2Gv}{1-2v}\delta_{ij}e_{kk} - \alpha\delta_{ij}p - K\beta_s\delta_{ij}\Delta T \quad \text{..... (2.16)}$$

$$\zeta = \frac{\alpha(1-2v)}{2G(1+v)}\sigma_{kk} + \frac{\alpha^2(1-2v)^2(1+v_u)}{2G(1+v)(v_u-v)}p - \phi(\beta_f - \beta_S)\Delta T \quad \text{..... (2.17)}$$

where K is the bulk modulus, β_f and β_s are the volumetric thermal expansion coefficient for fluid and solid, respectively.

2.2.2 Field equations

Similarly from the poroelasticity derivations, the thermo-poroelastic governing equation can be derived from the constitutive equations and transport equations. We can obtain the governing equation for the solid from Eq. 2.16 and Eq. 2.10:

$$G\nabla^2 u_i + \frac{G}{1-2v_u}u_{k,ki} - \alpha p_{,i} + K\beta_S\delta_{ij}\Delta T = 0 \qquad (2.18)$$

The governing equation for the fluid can be derived by putting Eq. 2.17 into Eq. 2.11 with Darcy's law:

$$\dot{p} - kM\nabla^2 p = -M\alpha\dot{e} + (\alpha\beta_f + \beta_S)\Delta\dot{T} \qquad (2.19)$$

The heat transfer equation is obtained by combining the Fourier's law and energy balance equation:

$$Q_i = -k^T T_{,i} \qquad (2.20)$$

$$\rho_m c_p \dot{T} + Q_{i,i} = 0 \qquad (2.21)$$

where Q_i is the heat flux and k^T is the thermal conductivity. ρ_m and c_p are the total mass density and specific heat capacity.

Substituting Eq. 2.20 into Eq. 2.21 can obtain the heat transfer equation.

$$\dot{T} = c_T\nabla^2 T \qquad (2.22)$$

where $c_T = \frac{k^T}{\rho_m c_p}$ is the thermal diffusivity.

3. Finite Element Method for Coupled Problem and its Verifications

Section 2 described mathematical models for coupled fluid flow, temperature, and solute transport in rock deformation. This section describes the finite element method for coupled problems and its verification. The finite element method is one of the discretizing techniques for solving partial-differential equations. The method has been developed by many researchers (Zienkiewicz and Taylor, 1991; Strang and Fix, 1973; Cook et al., 2001). Finite element discretization for coupled problems for coupled solid-fluid interaction is described by several authors (Smith and Griffiths, 2004; Zienkiewicz and Taylor, 1991; Lewis and Schrefler, 1988).

3.1 Finite element formulations

3.1.1 Basics for discretization

In the finite element method, continuous variables such as displacement u, pore pressure p, temperature T, and solute concentration C^S can be approximated by $\widetilde{u}$, $\widetilde{p}$, $\widetilde{T}$, and, $\widetilde{C}^S$, in terms of their nodal values, interpolating the nodal to nodal values by shape functions. Considering a two-dimensional quadrilateral element or a three-dimensional hexahedron element (Fig. 3.1), the interpolation functions can be written as:

$$\widetilde{u} = \sum_{i=1}^{q} N_i u_i \qquad (3.1)$$

$$\widetilde{p} = \sum_{i=1}^{q} N_i p_i \qquad (3.2)$$

$$\widetilde{T} = \sum_{i=1}^{q} N_i T_i \qquad (3.3)$$

$$\widetilde{C}^S = \sum_{i=1}^{q} N_i C_i^S \qquad (3.4)$$

where $\widetilde{u}$, $\widetilde{p}$, $\widetilde{T}$ and $\widetilde{C}^S$ are approximated in terms of their nodal values u_i, p_i, T_i, and C_i^S in the system. N_i is the interpolation function and is generally referred to as a shape function where subscript "*i*" denotes the corresponding node.

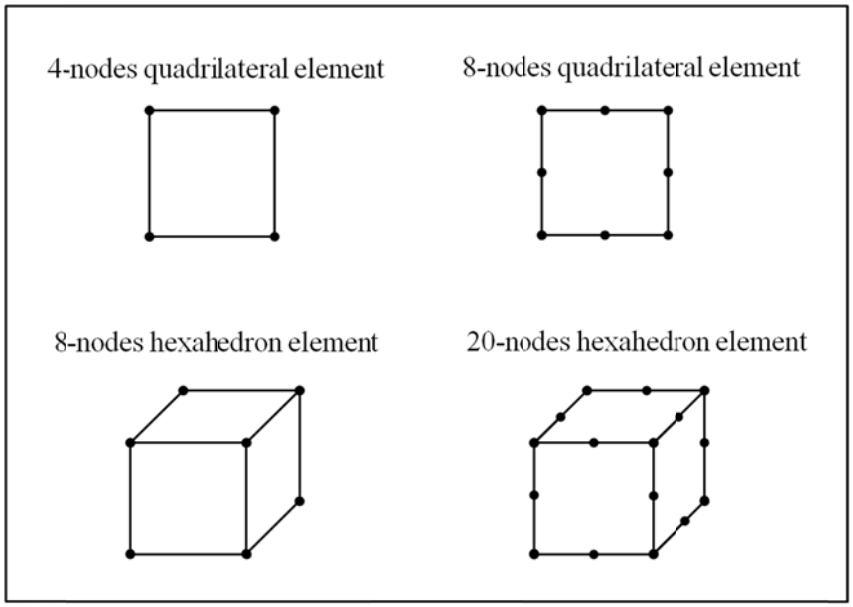

Fig. 3.1. Types of elements used for the finite element method.

The shape functions are often taken to be polynomials that depend on element type and the number of nodes in the element. Several types of shape functions for two-dimensional and three-dimensional elements are shown in Fig. 3.2 and Fig. 3.3.

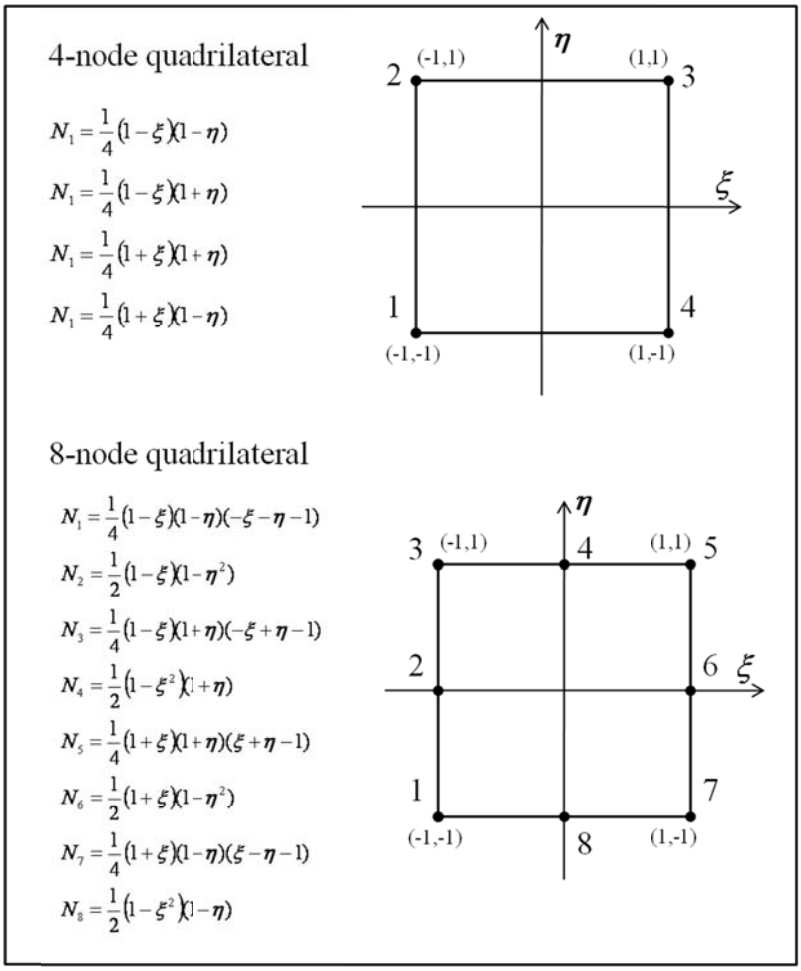

Fig. 3.2. Shape functions for two-dimensional 4-node and 8-node quadrilateral element.

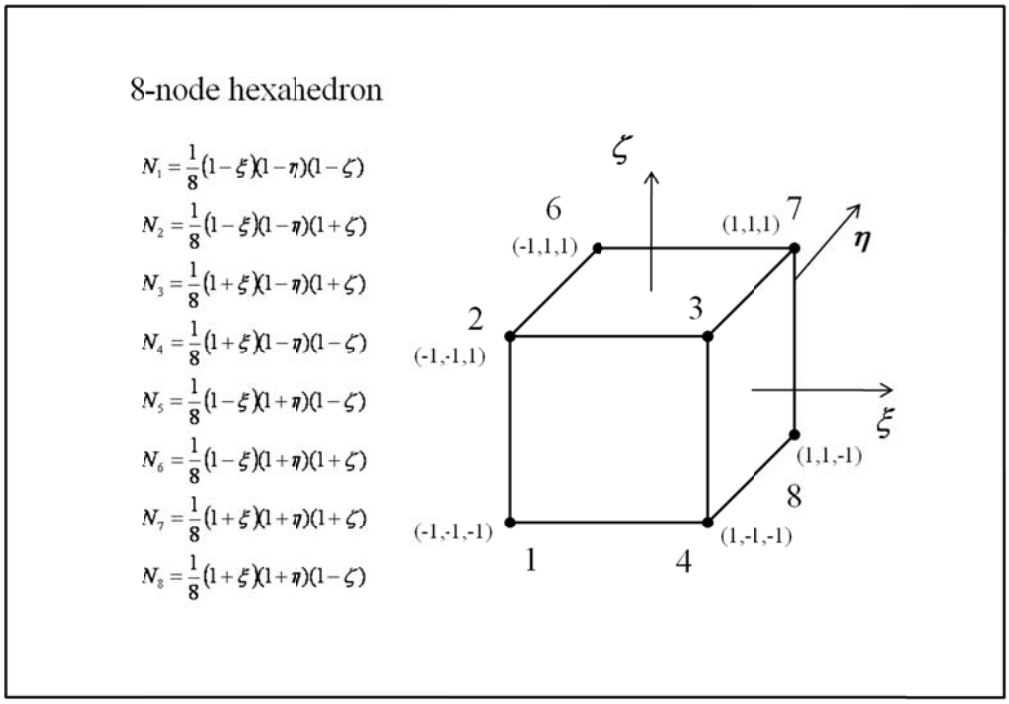

Fig. 3.3. Shape function for the case of three-dimensional 8-node hexahedron element.

The choice of shape function and element type varies depending on the purpose of the simulations. Especially for solving the mixed forms of finite element formulations, Zienkiewicz and Taylor (1991) presented a "patch test" to test the numerical stability of several types of element in two-dimensional coupled problems. They showed that finite element solutions are stable when the variable configurations are 8 nodes for displacement and 4 nodes for pore pressure in each element for a two-dimensional, quadrilateral element. For corresponding three-dimensional expansion, configurations for the variables are 20 nodes for displacement and 8 nodes for pore pressure in a hexahedron element. From a practical point of view, the numerical stability becomes critical around a wellbore because of significant gradients of pore pressure, temperature, and rock deformation by fluid injection. Lewis and Schrefler (1988) also suggested a degree of freedom in each element two times higher for displacement nodes than pore pressure and temperature to obtain more accurate finite element results. The limitations of element types for finite element approximations are related with ill-posed shape functions that cause the singularity problem which is divided by zero in numerical modeling, and the criterions of the stability is analyzed from Babuska (1971, 1973) and Brezzi (1974).

Since the shape functions are defined in a local coordinate system (ξ,η), it is necessary to describe the relation between the global (x,y) and local coordinate (ξ,η) system. For example, the coordinate transformation for the four-node quadrilateral element can be written as:

$$x = N_1 x_1 + N_2 x_2 + N_3 x_3 + N_4 x_4 = [\mathbf{N}]\{\mathbf{x}\}$$
$$y = N_1 y_1 + N_2 y_2 + N_3 y_3 + N_4 y_4 = [\mathbf{N}]\{\mathbf{y}\} \qquad (3.5)$$

where $[\mathbf{N}]$ denotes the shape function vector as described in (Fig. 3.2) and $\{\mathbf{x}\}$ and $\{\mathbf{y}\}$ are the nodal coordinates in the global coordinate system.

The other necessary coordinate transformation is the derivatives from the local to global coordinate, which can be described by the chain rule of the partial differentiation:

$$\begin{Bmatrix} \frac{\partial}{\partial \xi} \\ \frac{\partial}{\partial \eta} \end{Bmatrix} = \begin{bmatrix} \frac{\partial x}{\partial \xi} & \frac{\partial y}{\partial \xi} \\ \frac{\partial x}{\partial \eta} & \frac{\partial y}{\partial \eta} \end{bmatrix} \begin{Bmatrix} \frac{\partial}{\partial x} \\ \frac{\partial}{\partial y} \end{Bmatrix} = [\mathbf{J}] \begin{Bmatrix} \frac{\partial}{\partial x} \\ \frac{\partial}{\partial y} \end{Bmatrix} \tag{3.6}$$

or

$$\begin{Bmatrix} \frac{\partial}{\partial x} \\ \frac{\partial}{\partial y} \end{Bmatrix} = [\mathbf{J}]^{-1} \begin{Bmatrix} \frac{\partial}{\partial \xi} \\ \frac{\partial}{\partial \eta} \end{Bmatrix} \tag{3.7}$$

where $[\mathbf{J}]$ is the Jacobian matrix.

To solve a partial differential equation (Eqs. 3.10 to 3.13), it is necessary to understand the procedure for numerical integration (Eqs. 3.18 to 3.31) of the weighting residual by each shape function by integrating over the equations (Galerkin's method). The transformation between the local Jacobian coordinate and the global coordinate in integration should be evaluated as follow:

$$\iint dxdy = \int_{-1}^{1}\int_{-1}^{1} \det|\mathbf{J}| d\xi d\eta \tag{3.8}$$

The Gauss-Legendre quadrature for finite element numerical integration in two dimensions can be described as:

$$\begin{aligned} \int_{-1}^{1}\int_{-1}^{1} f(\xi,\eta)\det|\mathbf{J}| d\xi d\eta &\approx \sum_{i=1}^{n}\sum_{j=1}^{n} w_i w_j f(\xi_i,\eta_i) \\ &\approx \sum_{i=1}^{nip} W_i f(\xi,\eta)_i \end{aligned} \tag{3.9}$$

where *nip* is the total number of integration points (Gaussian point), w_i and w_j are the weighting coefficients, and (ξ_i,η_i) are sampling points in element.

3.1.2 Spatial discretization

For the case of chemo-thermo-poroelasticity, the combining the constitutive equations and the balance equations with transport equations yield the governing equations:

$$\left(K + \frac{G}{3}\right)\nabla(\nabla\cdot\mathbf{u}) + G\nabla^2\mathbf{u} + m\left(\alpha'\nabla p - \chi\nabla C^S + \gamma_1\nabla T\right) = 0 \tag{3.10}$$

$$\alpha(\nabla\cdot\dot{\mathbf{u}}) + \beta'\dot{p} + \chi'\dot{C}^S + \gamma_2\dot{T} - \frac{k}{\mu}\nabla^2 p + \frac{k}{\mu}L_D\nabla^2 C^2 = 0 \tag{3.11}$$

$$\phi\dot{C}^S - D^S\nabla^2 C^S - C^S D^T\nabla^2 T = 0 \tag{3.12}$$

$$\dot{T} - c^T\nabla^2 T = 0 \tag{3.13}$$

where *K* and *G* are bulk and shear modulus, respectively, α Biot's constant, μ viscosity. α' , χ , χ' , γ_1 , γ_2 , and β' are given by:

$$\alpha' = \alpha - \frac{M^S \omega_0}{\overline{\rho}_f RTC^D}$$

$$\beta' = \frac{\alpha - \phi}{K_s} + \frac{\phi}{K_f} + \frac{\omega_0(\alpha - 1)M^S}{\overline{\rho}_f KRC^D T}$$

$$\chi' = \frac{\alpha - 1}{K}\chi$$

$$\gamma_1 = K\alpha_s$$

$$\gamma_2 = \alpha\beta_s + (\beta_f - \beta_s)\phi$$

where M^S is molar mass of the solute, ω_0 the swelling coefficient, $\overline{\rho}_f$ the fluid mass density, R the universal gas constant, ϕ the porosity, C^S and C^D the solute and dilute concentrations, respectively, and β_f and β_s the thermal expansion coefficients of fluid and solid, respectively.

To discretize the field equations (Eqs. 3.10 to 3.13), we introduce an 8-node quadrilateral element and a 20-node hexahedron element for computing the displacement, pore pressure, solute mass concentration, and temperature. Substituting the shape functions for the factors (Eqs. 3.1 to 3.4) into the field equations (Eqs. 3.10 to 3.13), and then using Galerkin's method (Finlayson, 1972, see Appendix A), the finite element formulations for displacement, pore pressure, solute mass concentration, and temperature are obtained as:

$$\mathbf{K_m}\,\tilde{\mathbf{u}} + \mathbf{A}\,\tilde{\mathbf{p}} - \mathbf{W}\tilde{\mathbf{C}} + \mathbf{V}\,\tilde{\mathbf{T}} = \mathbf{0} \qquad (3.14)$$

$$\mathbf{A}^{\mathbf{T}}\dot{\tilde{\mathbf{u}}} + \mathbf{S}\,\dot{\tilde{\mathbf{p}}} + \hat{\mathbf{M}}\dot{\tilde{\mathbf{C}}} + \mathbf{N}\,\dot{\tilde{\mathbf{T}}} + \mathbf{H_H}\tilde{\mathbf{p}} + \mathbf{D_H}\tilde{\mathbf{C}}^{\mathbf{S}} = \mathbf{0} \qquad (3.15)$$

$$\mathbf{M}\dot{\tilde{\mathbf{C}}}^{\mathbf{S}} + \mathbf{D_D}\tilde{\mathbf{C}}^{\mathbf{S}} + \mathbf{Q_D}\,\tilde{\mathbf{T}} = \mathbf{f}^{\mathbf{u}} \qquad (3.16)$$

$$\mathbf{R}\,\dot{\tilde{\mathbf{T}}} + \mathbf{U}\,\tilde{\mathbf{T}} = 0 \qquad (3.17)$$

where

$$\mathbf{K_m} = \int_\Omega \mathbf{B}^{\mathbf{T}}\mathbf{D_u}\,\mathbf{B}\,d\Omega \qquad (3.18)$$

$$\mathbf{A} = \int_\Omega \mathbf{B}^{\mathbf{T}}\boldsymbol{\alpha}\,\mathbf{m}\,\mathbf{N_p}\,d\Omega \qquad (3.19)$$

$$\mathbf{W} = \int_\Omega \mathbf{B}^{\mathbf{T}}\,\chi\,\mathbf{m}\,\mathbf{N}_{\mathbf{C}^s}\,d\Omega \qquad (3.20)$$

$$\mathbf{V} = \int_\Omega \mathbf{B}^{\mathbf{T}}\,\gamma_1\,\mathbf{m}\,\mathbf{N_T}\,d\Omega \qquad (3.21)$$

$$\mathbf{S} = \int_\Omega \mathbf{N}_{\mathbf{p}}^{\mathbf{T}}\beta\,\mathbf{N_p}\,d\Omega \qquad (3.22)$$

$$\hat{\mathbf{M}} = \int_\Omega \mathbf{N}_{\mathbf{p}}^{\mathbf{T}}\chi'\mathbf{N}_{\mathbf{C}^s}\,d\Omega \qquad (3.23)$$

$$\mathbf{N} = \int_\Omega \mathbf{N}_{\mathbf{T}}^{\mathbf{T}}\gamma_2\,\mathbf{N_T}\,d\Omega \qquad (3.24)$$

$$\mathbf{M} = \int_{\Omega} \mathbf{N}_{\mathbf{C}^s}^{\mathbf{T}} \, \phi \mathbf{N}_{\mathbf{C}^s} \, d\Omega \qquad (3.25)$$

$$\mathbf{R} = \int_{\Omega} \mathbf{N}_{\mathbf{T}}^{\mathbf{T}} \mathbf{N}_{\mathbf{T}} \, d\Omega \qquad (3.26)$$

$$\mathbf{U} = \int_{\Omega} \left\{ (\nabla \mathbf{N}_{\mathbf{T}})^T \left(c^T \right) (\nabla \mathbf{N}_{\mathbf{T}}) + (\mathbf{N}_{\mathbf{T}})^T \mathbf{v}_{\mathbf{f}} (\nabla \mathbf{N}_{\mathbf{T}}) \right\} d\Omega \qquad (3.27)$$

$$\mathbf{H}_{\mathbf{H}} = \int_{\Omega} \left(\nabla \mathbf{N}_{\mathbf{p}} \right)^T (\mathbf{k} / \eta) \left(\nabla \mathbf{N}_{\mathbf{p}} \right) d\Omega \qquad (3.28)$$

$$\mathbf{D}_{\mathbf{H}} = \int_{\Omega} \left(\nabla \mathbf{N}_{\mathbf{p}} \right)^T L_D \left(\nabla \mathbf{N}_{\mathbf{p}} \right) d\Omega \qquad (3.29)$$

$$\mathbf{D}_{\mathbf{D}} = \int_{\Omega} \left(\nabla \mathbf{N}_{\mathbf{C}^s} \right)^T D^S \left(\nabla \mathbf{N}_{\mathbf{C}^s} \right) d\Omega \qquad (3.30)$$

$$\mathbf{Q}_{\mathbf{D}} = \int_{\Omega} \left(\nabla \mathbf{N}_{\mathbf{T}} \right)^T C^S D^S \left(\nabla \mathbf{N}_{\mathbf{T}} \right) d\Omega \qquad (3.31)$$

where the $[\mathbf{D_u}]$ is the stiffness property for stress-strain relations, and strain displacement can be described with $[\mathbf{B}]$. (See Appendix A for full explanation of the integrals in Eqs. 3.18 to 3.31.) For example, in the axisymmetric stress-strain problem, strain and displacement have a relation (Timoshenko and Goodier, 1982) as shown by Eq. 3.32:

$$\begin{Bmatrix} \varepsilon_r \\ \varepsilon_z \\ \gamma_{rz} \\ \varepsilon_\theta \end{Bmatrix} = \begin{bmatrix} \frac{\partial}{\partial r} & 0 \\ 0 & \frac{\partial}{\partial z} \\ \frac{\partial}{\partial z} & \frac{\partial}{\partial r} \\ \frac{1}{r} & 0 \end{bmatrix} \begin{Bmatrix} u \\ v \end{Bmatrix} \qquad (3.32)$$

Matrix $[\mathbf{B}]$ is the expression of the spatial derivative:

$$[\mathbf{B}] = \begin{bmatrix} \frac{\partial N_1}{\partial r} & 0 & \frac{\partial N_2}{\partial r} & 0 & \frac{\partial N_3}{\partial r} & 0 & \frac{\partial N_4}{\partial r} & 0 \\ 0 & \frac{\partial N_1}{\partial z} & 0 & \frac{\partial N_2}{\partial z} & 0 & \frac{\partial N_3}{\partial z} & 0 & \frac{\partial N_4}{\partial z} \\ \frac{\partial N_1}{\partial z} & \frac{\partial N_1}{\partial r} & \frac{\partial N_2}{\partial z} & \frac{\partial N_2}{\partial r} & \frac{\partial N_3}{\partial z} & \frac{\partial N_3}{\partial r} & \frac{\partial N_4}{\partial z} & \frac{\partial N_4}{\partial r} \\ \frac{N_1}{r} & 0 & \frac{N_2}{r} & 0 & \frac{N_3}{r} & 0 & \frac{N_4}{r} & 0 \end{bmatrix} \qquad (3.33)$$

3.1.3 Discretization in time

Among the methods to discretize the time steps for partial differential equations (Zienkiwicz and Taylor, 1989) are linear interpolations and fixed time step Δt (Smith and Griffiths, 2004). The finite element

formulations derived in Section 3.1.2 include the time-dependent variables for displacement, pore pressure, solute mass concentration, and temperature. The governing equations use the second order for the spatial domain and the first order for the time domain. These domains are categorized to a parabolic partial differential equation. A typical expression of a first-order time-dependent problem in a finite element formulation can be described by:

$$[\mathbf{K}]\{\boldsymbol{\varphi}\}+[\mathbf{m}]\left\{\frac{d\boldsymbol{\varphi}}{dt}\right\}=\{\mathbf{q}\} \tag{3.34}$$

Consider two consecutive time steps as follow:

$$[\mathbf{K}]\{\boldsymbol{\varphi}\}_0+[\mathbf{m}]\left\{\frac{d\boldsymbol{\varphi}}{dt}\right\}_0=\{\mathbf{q}\}_0 \tag{3.35}$$

$$[\mathbf{K}]\{\boldsymbol{\varphi}\}_1+[\mathbf{m}]\left\{\frac{d\boldsymbol{\varphi}}{dt}\right\}_1=\{\mathbf{q}\}_1 \tag{3.36}$$

where 0 and 1 indicate the previous and current time step, respectively. Then, variation of the variable φ over the two time steps can be expressed in terms of a linear interpolation between its values at the two time steps:

$$\frac{\{\boldsymbol{\varphi}\}_1-\{\boldsymbol{\varphi}\}_0}{\Delta t}\approx(1-\theta)\left\{\frac{d\boldsymbol{\varphi}}{dt}\right\}_0+\theta\left\{\frac{d\boldsymbol{\varphi}}{dt}\right\}_1 \tag{3.37}$$

Substituting Eq. 3.37 into Eq. 3.35 and Eq. 3.36, we obtain:

$$\{\boldsymbol{\varphi}\}_1=\{\boldsymbol{\varphi}\}_0+\Delta t\left((1-\theta)\left\{\frac{d\boldsymbol{\varphi}}{dt}\right\}_0+\theta\left\{\frac{d\boldsymbol{\varphi}}{dt}\right\}_1\right) \tag{3.38}$$

Using Eq. 3.35 and Eq. 3.36 and substituting them into Eq. 3.35 and Eq. 3.36, we arrive at the time discretization of finite element method:

$$\begin{aligned}([\mathbf{M}]+\theta\Delta t[\mathbf{K}])\{\boldsymbol{\varphi}\}_1 &= ([\mathbf{M}]-(1-\theta)\Delta t[\mathbf{K}])\{\boldsymbol{\varphi}\}_0 \\ &\quad +\theta\Delta t\{\boldsymbol{\varphi}\}_1+(1-\theta)\Delta t\{\boldsymbol{\varphi}\}_0\end{aligned} \tag{3.39}$$

If θ =1/2, it is called the "Crank-Nicolson" method,

$$\left\{[\mathbf{M}]+\frac{\Delta t}{2}[\mathbf{K}]\right\}\{\boldsymbol{\varphi}\}_1=\left\{[\mathbf{M}]-\left(\frac{\Delta t}{2}\right)[\mathbf{K}]\right\}\{\boldsymbol{\varphi}\}_0 \tag{3.40}$$

and if θ =1, is it the "fully implicit" method, which ignores any history since the past is unknown:

$$\{[\mathbf{M}]+\Delta t[\mathbf{K}]\}\{\boldsymbol{\varphi}\}_1=[\mathbf{M}]\{\boldsymbol{\varphi}\}_0$$

The discretization for the finite element method also has incremental version that results from rearranging the governing equations (Eq. 3.14 to Eq. 3.17) for solid, fluid, solute concentration, and temperature with linear interpolation for time:

$$\begin{bmatrix}\mathbf{K_m} & \mathbf{A} & -\mathbf{W} & \mathbf{V}\\ \mathbf{A}^{\mathbf{T}} & -(\mathbf{S}+\theta\Delta t\mathbf{H_H}) & -(\hat{\mathbf{M}}+\theta\Delta t\mathbf{D_H}) & -\hat{\mathbf{N}}\\ 0 & 0 & -(\mathbf{M}+\theta\Delta t\mathbf{D_D}) & -\theta\Delta t\mathbf{Q_D})\\ 0 & 0 & 0 & -(\mathbf{R}+\theta\Delta t\mathbf{U})\end{bmatrix}\begin{Bmatrix}\Delta\tilde{\mathbf{u}}\\ \Delta\tilde{\mathbf{p}}\\ \Delta\tilde{\mathbf{C}}^{\mathbf{S}}\\ \Delta\tilde{\mathbf{T}}\end{Bmatrix}$$
$$=\begin{Bmatrix}\Delta\mathbf{f}\\ \Delta t\mathbf{H_H}\tilde{\mathbf{p}}_{\mathbf{n-1}}+\Delta t\mathbf{D_H}\tilde{\mathbf{C}}^{\mathbf{S}}_{\mathbf{n-1}}\\ \Delta t\mathbf{D_D}\tilde{\mathbf{C}}^{\mathbf{S}}_{\mathbf{n-1}}+\Delta t\mathbf{Q_D}\tilde{\mathbf{T}}_{\mathbf{n-1}}\\ \Delta t\mathbf{U}\tilde{\mathbf{T}}_{\mathbf{n-1}}\end{Bmatrix} \tag{3.41}$$

The difference between these two methods is that absolute discretization obtains total values for displacement, pore pressure, solute mass concentration, and temperature, whereas incremental discretization computes the relative values. For example, if we have a constant pore pressure boundary condition at the wellbore, the corresponding traction and the values for pore pressure at the wellbore should be applied in each time step for the absolute version; but for the incremental version, we apply the traction and pore pressure values only for the first time step since there is no relative change with a constant boundary condition.

3.1.4 Boundary conditions

It is important to define the boundary conditions in geomechanics simulations; for example, hydraulic injection pressure p, injection rate Q, injection temperature T, mud solute concentration C^S are often used in geothermal and petroleum reservoir study. For the finite element formulation (Eq. 3.41), explicit variables such as displacement pore pressure, solute concentration, and temperature can define the boundary by the penalty method. This method operates by multiplying the corresponding prescribed boundary values on the left-hand side of the matrix and its corresponding coefficient on the right-hand side vector by a large value (Fig. 3.4). This in effect fixes the known value (boundary condition) on the nodes; that is, it prescribes the value we desired for the unknown variables.

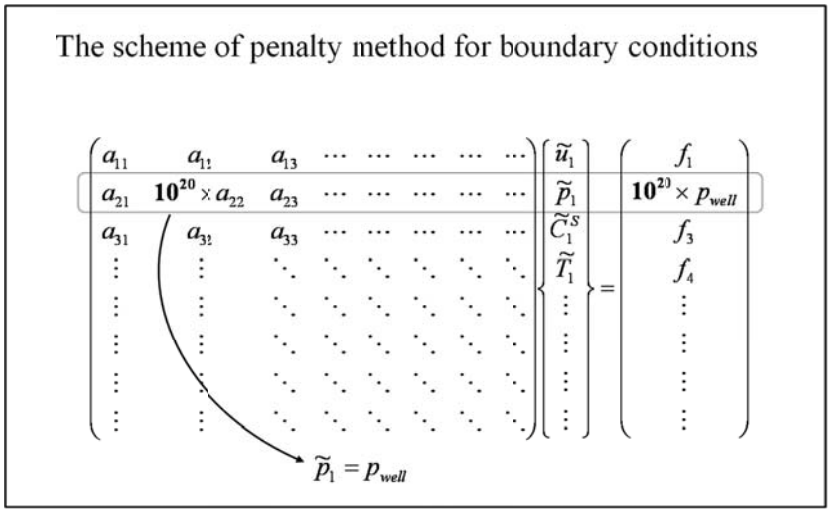

Fig. 3.4. Illustration of the penalty method in the finite element formulation for the boundary conditions of displacement, pore pressure, solute concentration, and temperature.

The other most-used boundary condition in geomechanics simulations is the injection rate boundary condition. Consider the finite element formulation for the fluid mass-balance equation (Eq. 3.11). The right-hand side matrix should be defined by injection rate Q at the boundary elements as,

$$\alpha\left(\nabla\cdot\dot{\mathbf{u}}\right)+\beta\,\dot{p}+\chi'\dot{C}^S+\gamma_2\dot{T}-\frac{k}{\mu}\nabla^2 p+\frac{k}{\mu}L_D\nabla^2 C^2=f_q \qquad (3.42)$$

where:

$$f_q=\sum_{i=1}^{nip}\left(N_i Q\right)d\Omega$$

where *nip* is the number of Gaussian points and N_i denotes the shape function.

A typical example of implementation of injection rate boundary conditions for the finite element method is illustrated in Fig. 3.5. The difference between the injection boundary condition and the pressure

boundary condition is that the pore pressure distribution is computed through the finite element for the given Q.

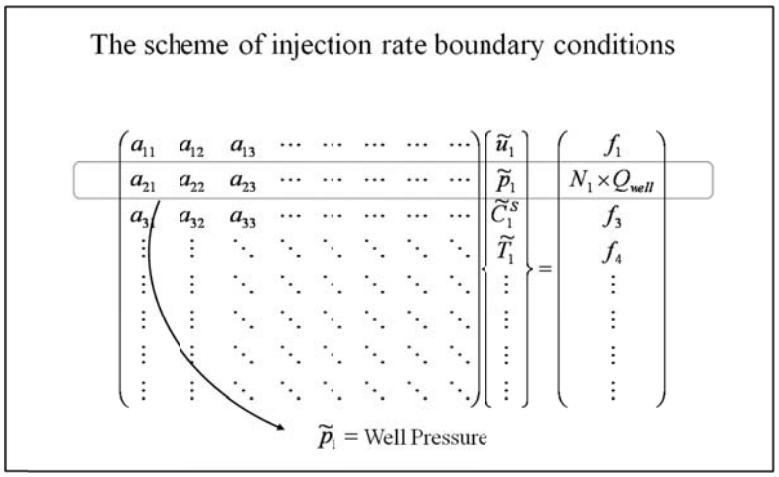

Fig. 3.5. Illustration of injection rate boundary conditions in the finite element method.

Another important boundary condition in coupled fluid flow and solid problems is mechanical loading. For describing the prescribed traction that results, for example, from pressurizing the wellbore, tractions must relate the acting wellbore with the far-field stress of the system. For example, if the pore pressure on the wall of the wellbore is 20 MPa and the far-field stress is 10 MPa, the applied traction is 20 MPa – 10 MPa = 10 MPa at the wellbore, which takes into account the relative force between the well pressure and natural in-situ stress. The mechanical loading term at the boundary for the solid in finite element formulations as is described by:

$$\mathbf{K_m}\,\tilde{\mathbf{u}} + \mathbf{A}\,\tilde{\mathbf{p}} - \mathbf{W}\tilde{\mathbf{C}} + \mathbf{V}\,\tilde{\mathbf{T}} = \mathbf{f} \qquad (3.43)$$

where:

$$f = \sum_{i=1}^{nip} \left(N_i f\right) d\Omega$$

The right-hand side of Eq. 3.43 is the mechanical load (traction on the boundary). Fig. 3.6 shows the matrix configuration for the mechanical loading at the boundary. For the poroelastic simulation without rock failure, it is not necessary to iterate to solve the variables. However, an iteration scheme should be introduced if we consider the rock failure and stress-dependent permeability since the results of stress and permeability conditions with certain loading are satisfied during the iterations. An illustration of the iteration procedure for the case of rock failure and permeability variations is presented in Section 4.

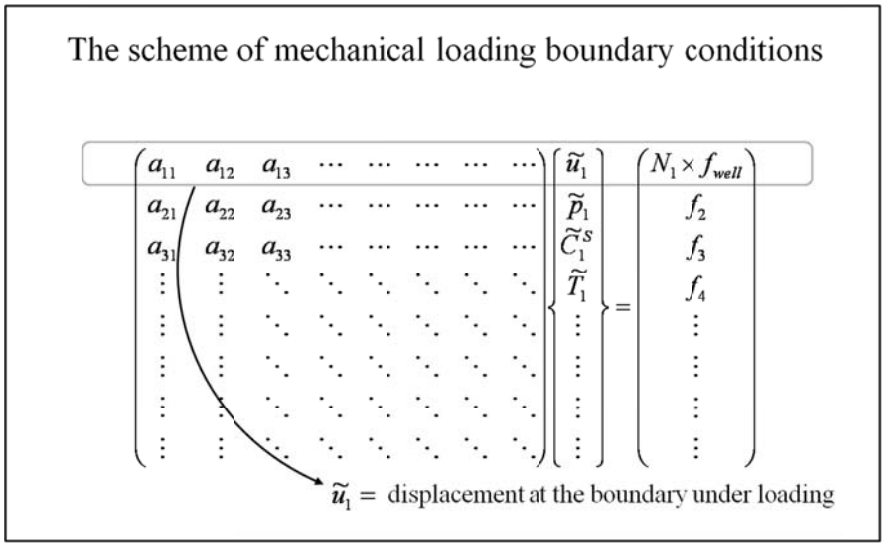

Fig. 3.6. Illustration of mechanical loading boundary condition in the finite element method.

3.2 Verifications of the Finite Element Method

In this section, finite element results for coupled problems are compared with analytical solutions. The reservoir conditions such as far-field stress, injection pressure, temperature, and initial pore pressure are critical in geomechanical simulations; therefore, it is necessary to validate the numerical modeling under various boundary conditions. We verified two-dimensional and three-dimensional finite element modeling using the analytical solutions for a wellbore in an poroelastic, thermo-poroelastic, and thermo-chemo-poroelastic formation. For the poroelastic case, Mode 1, Mode 2, and Mode 3 were considered (Detournay and Cheng (1988). The verifications of thermal and chemical loading were made possible by using the solution by McTigue (1986) and Ghassemi et al. (2009), respectively.

For better understanding of the wellbore response, the wellbore loading can be decomposed into three parts (Carter and Booker, 1982; Detournay and Cheng, 1988). We used three modes for decomposition of the poroelastic problem around a wellbore: Mode I is an isotropic stress loading of the wellbore; Mode II is the pore pressure loading or injection into the wellbore; and Mode III is the loading of the wellbore by a far-field deviatoric stress (deviatoric far-field). The complete solution is the sum of the solutions to the three modes. The verifications were performed with mesh consisting of 350 elements and 1141 nodes which have 8 quadrilateral nodes for displacements and 4 nodes for pore pressure, temperature, and solute concentration (Fig. 3.7). The maximum and minimum far-field stress components were applied to the x- and y-directions, respectively, and reservoir properties are described in Table 3.1.

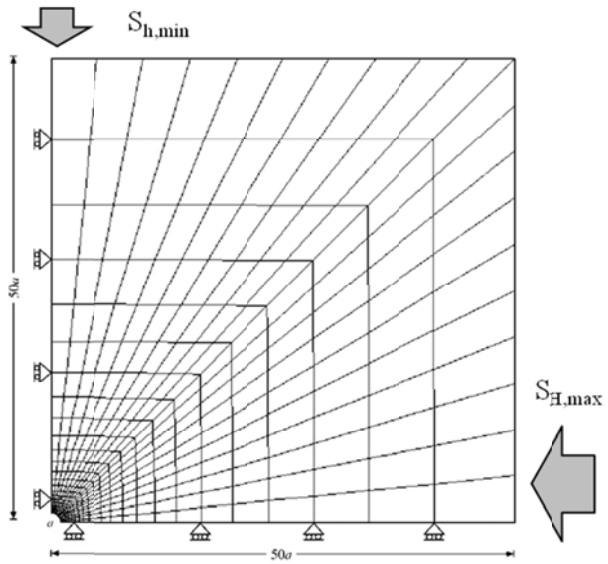

Fig. 3.7. Mesh used for the verifications, consisting of 350 elements and 1141 nodes.

Table 3.1. Rock properties of shale.

Young's modulus E (GPa)	1.85
Drained Possoin's ratio υ	0.219
Undrained Possoin's ratio υ_u	0.461
Skempton's coefficient, B	0.915
Permeability, k (md)	1×10^{-10}
Porosity, ϕ	0.299
Fluid mass density, ρ_f (kg/m^3)	1000
Fluid viscosity, □□(Pa·s)	0.3×10^{-3}

3.2.1 Isotropic far-field stress around a wellbore (Mode I)

Mode I represents the isotropic far-field stress distribution around a wellbore assuming no initial pore pressure; hence, Mode I results are the same as those for linear elasticity. We applied 10 MPa for isotropic far-field stress and compared finite element results with the analytical solution with a radius (Fig. 3.8; solid lines represent analytical solutions and numerical solutions are plotted as dotted symbols). The radial and tangential stresses are equally distributed around a wellbore by the isotropic far-field stress.

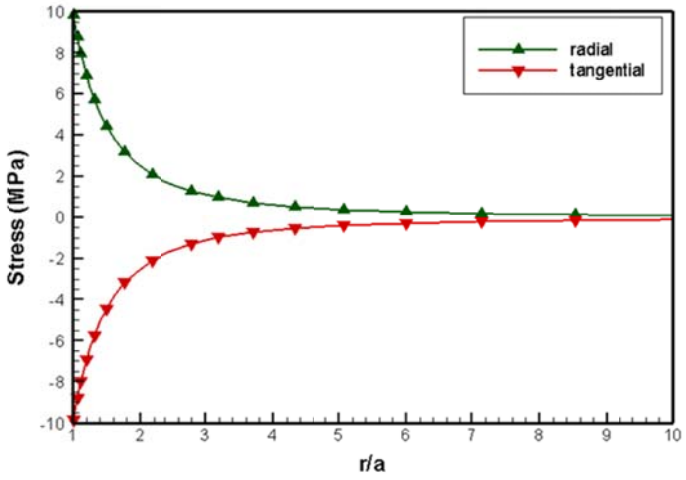

Fig. 3.8. Distributions of radial and tangential stress around a wellbore by isotropic far-field stress (Mode I). Finite element results are compared with the analytical solutions.

3.2.2 The influence of fluid flow around a wellbore (Mode II)

Initial reservoir pore pressure is maintained in equilibrium before we begin any exploration such as geothermal heat extraction, well stimulation, and oil and gas production. Once the change of pore pressure distribution occurs by fluid injection or production, fluid-induced stress variations should be considered. In this part, both production and injection-induced stress variations are presented.

In one example for stress variation induced by fluid production, we set boundary conditions so that the initial pore pressure was 10 MPa and wellbore pressure 0 MPa. Far-field stresses were assumed to be zero to study the induced stress variations. The comparison of finite element results and analytical solutions for pore pressure and total radial and tangential stresses are presented in Fig. 3.9 to Fig. 3.11 Note that fluid extraction causes significant changes of tangential stresses with time around a wellbore.

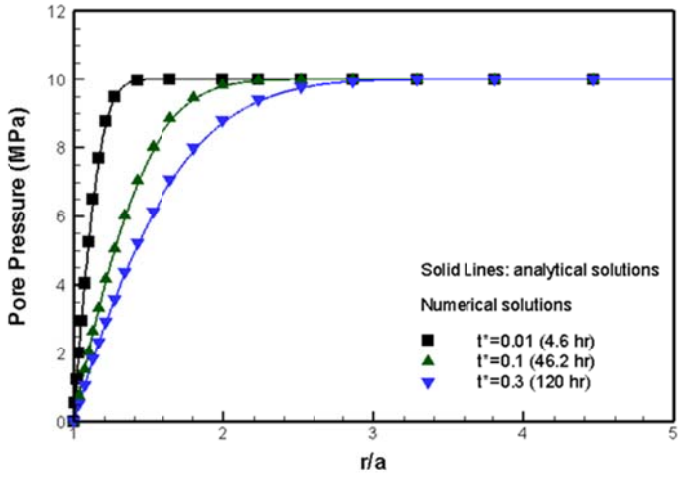

Fig. 3.9. Pore pressure distribution with respect to time when the pressure is zero at the wellbore (Mode II). Finite element results are compared with the analytical solutions.

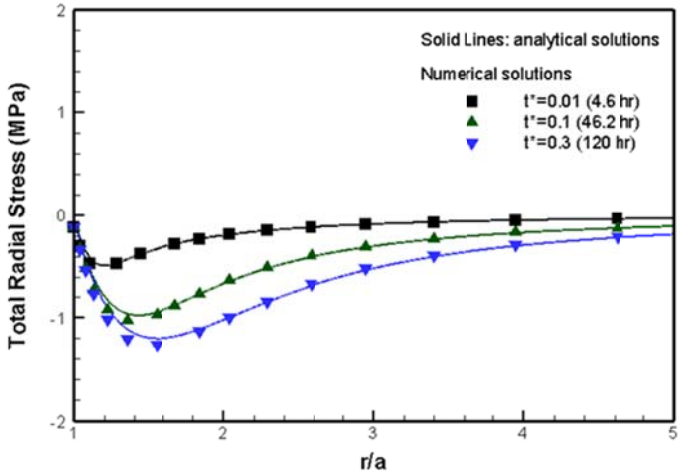

Fig. 3.10. The distribution of total radial stress with respect to time under production (Mode II). Finite element results are compared with analytical solutions.

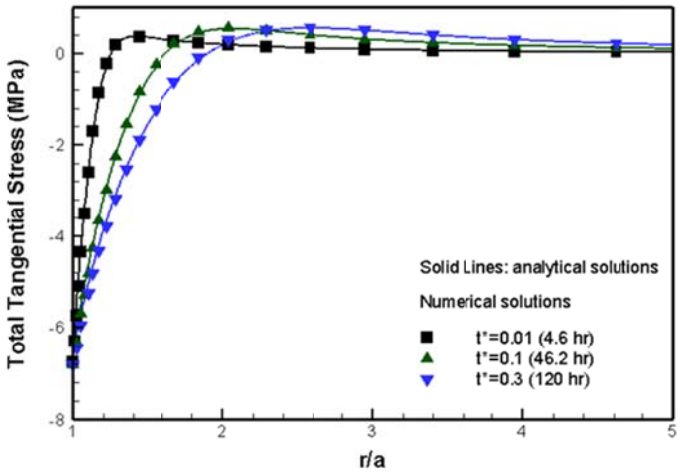

Fig. 3.11. Total tangential stress distribution with respect to time under production (Mode II). Finite element results are compared with the analytical solutions.

The other induced stress we are interested in is the injection case. The simplest condition for the injection sets pore pressure at the wall at 10 MPa, with no initial pore pressure and no far-field stresses. Results for numerical and analytical solutions are plotted in Fig. 3.12 to 3.14 for pore pressure and total radial and tangential stress distributions. In this case, the tangential stress distributions are significantly changed around a wellbore by fluid injection.

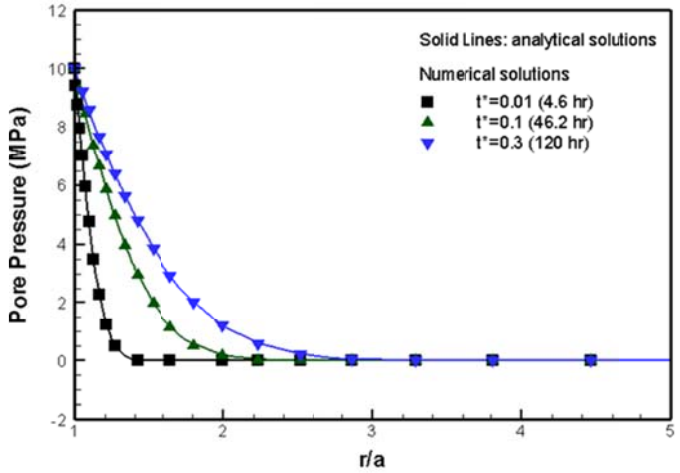

Fig. 3.12. Pore pressure distribution with respect to time when the pressure is 10 MPa at the wellbore (Mode II). Finite element results are compared with the analytical solutions.

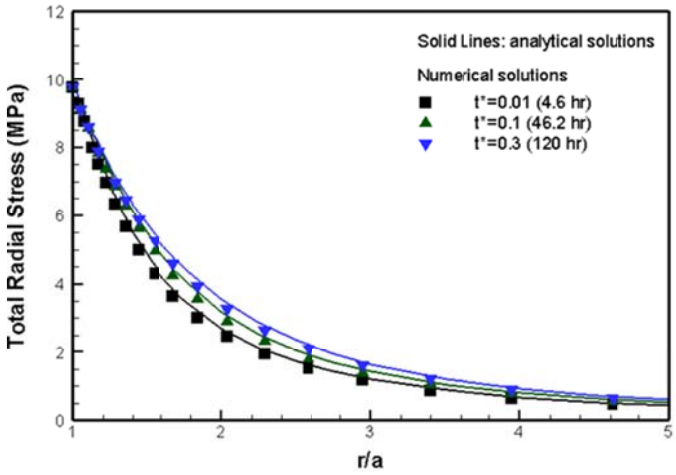

Fig. 3.13. The distribution of total radial stress with respect to time when the well is pressurized to 10 MPa (Mode II). Finite element results are compared with the analytical solutions.

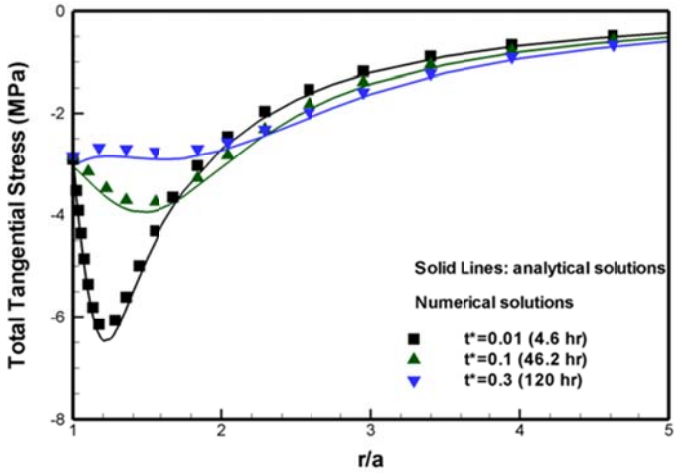

Fig. 3.14. Total tangential stress distribution with respect to time under pressurization (Mode II). Finite element results are compared with the analytical solutions.

3.2.3 The influence of deviatoric far-field stress (Mode III)

Deviatoric far-field stress plays an important role in stress distribution around a wellbore. It impacts tensile stress to the maximum far-field stress direction and compressive stress to the minimum far-field stress direction around a wellbore. This localized stresses often leads to shear and tensile failures around a wellbore. The boundary conditions on the well follow (Carter and Booker, 1982; Detrournay and Cheng, 1988):

$$\sigma_{rr} = -S_0 \cos 2\theta \qquad (3.44)$$

$$\sigma_{r\theta} = S_0 \sin 2\theta \qquad (3.45)$$

$$p = 0 \qquad (3.46)$$

where S_0 denotes the deviatoric components in far-field stress and θ is the horizontal rotational angle along to the wellbore.

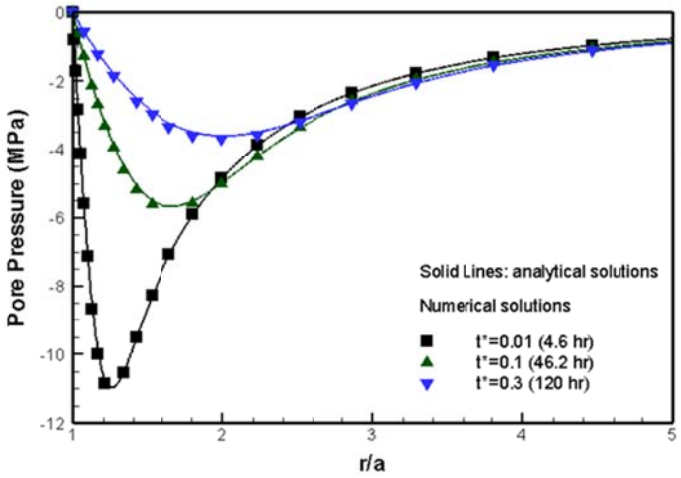

Fig. 3.15. Pore pressure distribution with respect to time along the maximum far-field stress direction when the deviatoric far-field (10 MPa) stress is applied (Mode III). Finite element results are compared with analytical solutions.

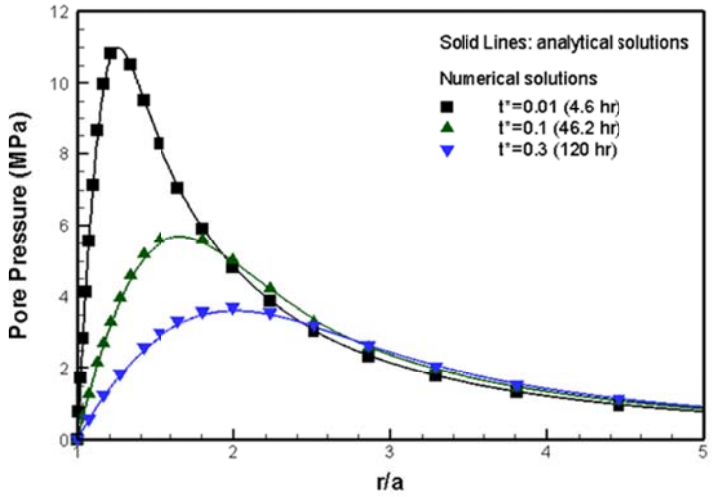

Fig. 3.16. Pore pressure distribution with respect to time along the minimum far-field stress direction when the deviatoric far-field (10 MPa) stress is applied (Mode II). Finite element results are compared with analytical solutions.

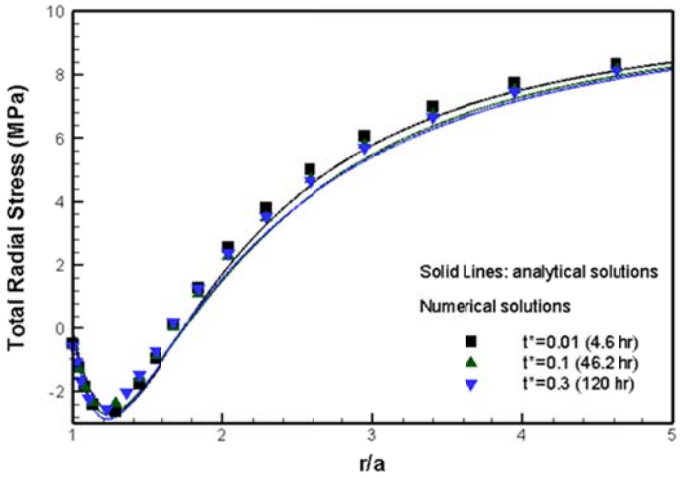

Fig. 3.17. The distribution of total radial stress along the maximum far-field stress direction when the deviatoric far-field (10 MPa) stress is applied (Mode III). Finite element results are compared with analytical solutions.

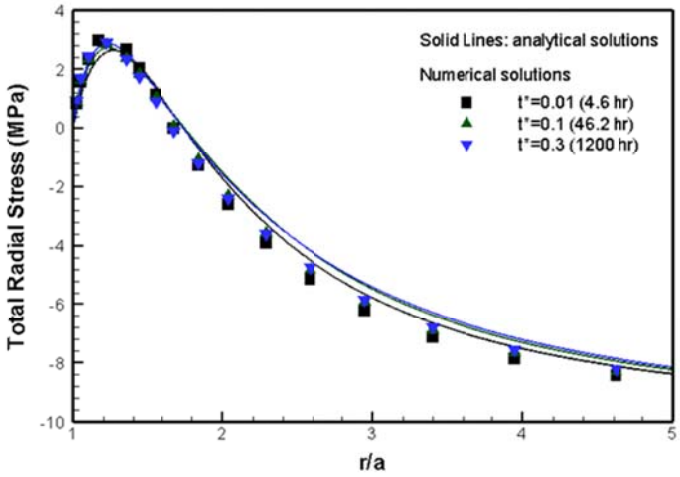

Fig. 3.18. The distribution of total radial stress along the minimum far-field stress direction when the deviatoric far-field (10 MPa) stress is applied (Mode III). Finite element results are compared with analytical solutions.

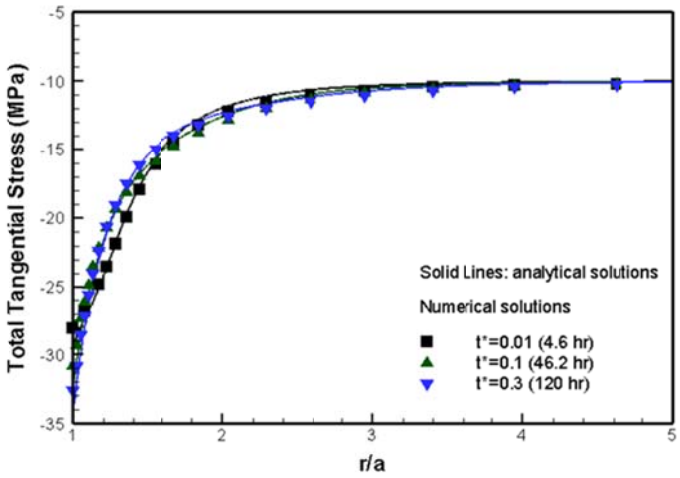

Fig. 3.19. The distribution of total tangential stress along the maximum far-field stress direction when the deviatoric far-field (10 MPa) stress is applied (Mode III). Finite element results are compared with analytical solutions.

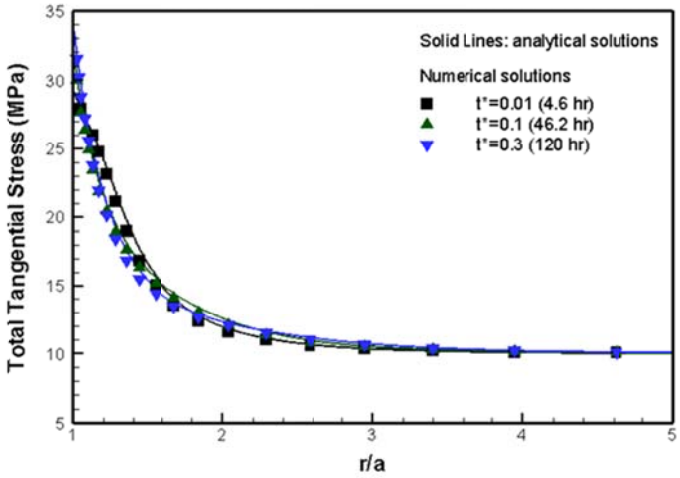

Fig. 3.20. The distribution of total tangential stress along the minimum far-field stress direction when the deviatoric far-field (10 MPa) stress is applied (Mode III). Finite element results are compared with analytical solutions.

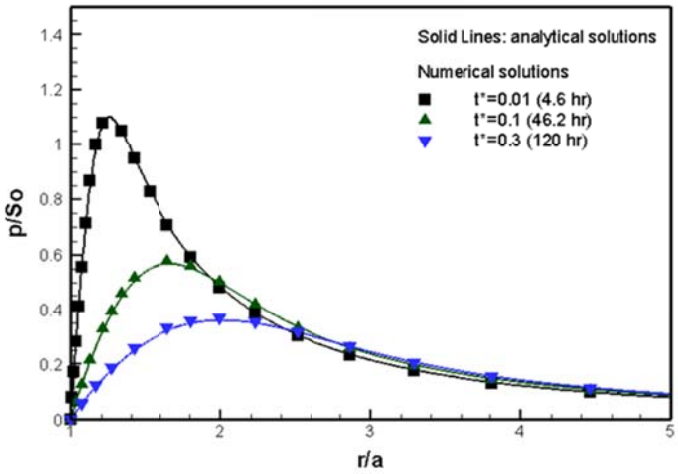

Fig. 3.21. Comparison of the finite element results with analytical solutions for the pore pressure variations with radius.

The influence of deviatoric stress is apparent where the deviatoric far-field stress is 10 MPa in the x-direction and -10 MPa in the y-direction. To clarify the influence of deviatoric stress effects, we assumed no initial pore pressure and no isotropic far-field stress. The distributions for pore pressure with time are presented in Fig. 3.15 and Fig. 3.16. The negative pore pressure distributions are localized to the maximum far-field stress direction and the positive pore pressure distributions to the minimum far-field stress direction, since the effects are coupled around a wellbore. From the physical point of view, tensile stress increases the pore volume, whereas compressive stress plays to decrease the pore volume. The finite element results for total radial and tangential stress distributions are compared with analytical solutions for both maximum and minimum far-field stress directions in Fig. 3.17 to Fig. 3.20. The influence of deviatoric stress on the fluid variations derived analytically by Detournay and Cheng (1988) are compared with finite element results in Fig. 3.21.

3.2.4 Combined influence (Mode I + Mode II + Mode III)

We considered the combined influence of isotropic far-field stress, deviatoric far-field stress, and fluid injection and production around a wellbore. Boundary conditions considering all factors are as follows:

$$\sigma_{rr} = P_0 - S_0 \cos 2\theta \qquad (3.47)$$

$$\sigma_{r\theta} = S_0 \sin 2\theta \qquad (3.48)$$

$$p = p_0 \qquad (3.49)$$

where P_0 denotes the isotropic far-field stress and p_0 is injection well pressure.

The given boundary conditions for the verifications are isotropic far-field stress 20 MPa, deviatoric far-field stress 5 MPa, and injection well pressure 10 MPa. The comparisons for pore pressure distributions are plotted in Fig. 3.22 (to the maximum far-field stress direction), and in Fig. 3.23 (to the minimum far-field stress direction). Total tangential stress distributions are also compared to the maximum and minimum far-field stress direction in Fig. 3.24 and Fig. 3.25.

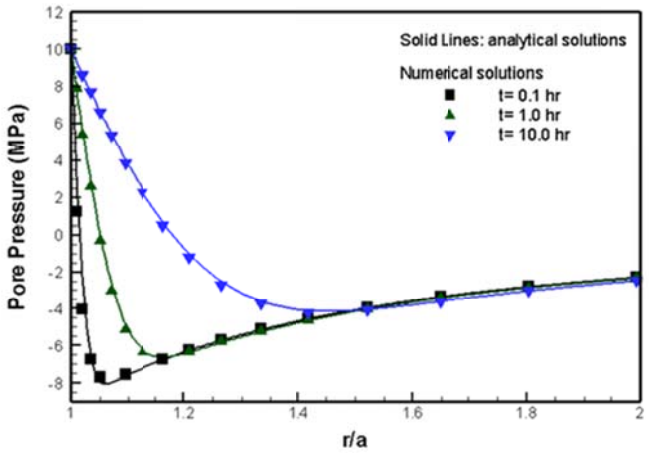

Fig. 3.22. Pore pressure distributions to the maximum far-field stress direction around a wellbore for an injection case under anisotropic far-field pressures. Finite element results are compared with analytical solutions.

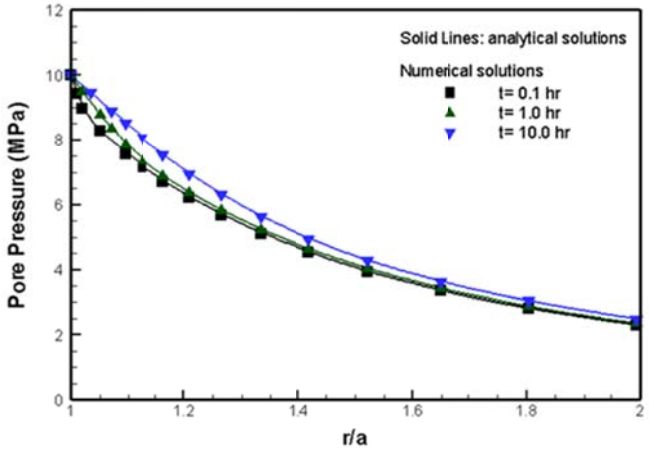

Fig. 3.23. Pore pressure distributions to the minimum far-field stress direction around a wellbore for injection case under anisotropic far-field. Finite element results are compared with the analytical solutions.

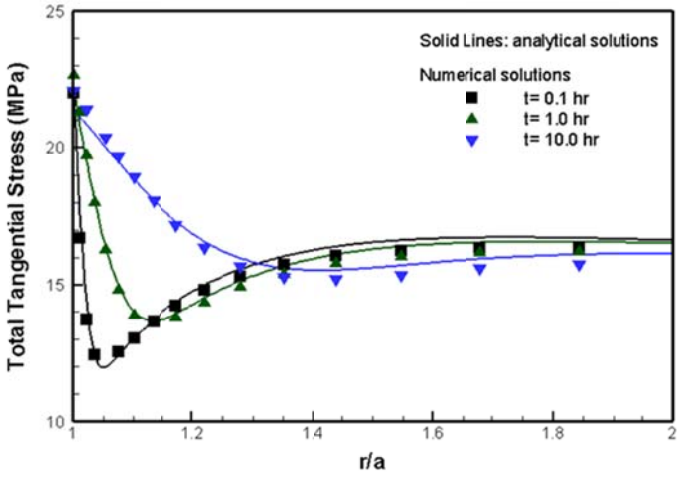

Fig. 3.24. Total tangential stress distributions to the maximum far-field stress direction around a wellbore for injection case under anisotropic far-field pressure. Finite element results are compared with the analytical solutions.

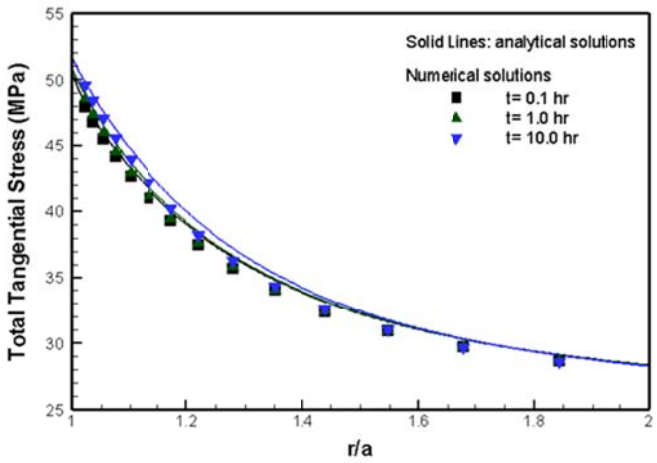

Fig. 3.25. Total tangential stress distributions to the minimum far-field stress direction around a wellbore for injection under the anisotropic far-field case. Finite element results are compared with analytical solutions.

3.2.5 Temperature and solute transport

The analytical solution for the impact of thermal loading has been developed by McTigue (1986), Kurashige (1989), Li et al. (1998), and Wang and Papamichos (1994). They found that the difference of thermal expansion coefficients between the rock and fluid flow cause the thermal stress to the rock in turn to impact the pore pressure distributions. Cold water injection to the hot reservoir causes rock shrinkage, and result in contributions to the tensile stress around the injection wellbore. The finite element results are compared with analytical solutions in Fig. 3.26 and Fig. 3.27. Initial reservoir temperature of 115°C and injection pressure of 65°C are applied in this comparison. Note that thermally-induced tensile stress leads the negative pore pressure distribution around a wellbore as described earlier in 3.2.3.

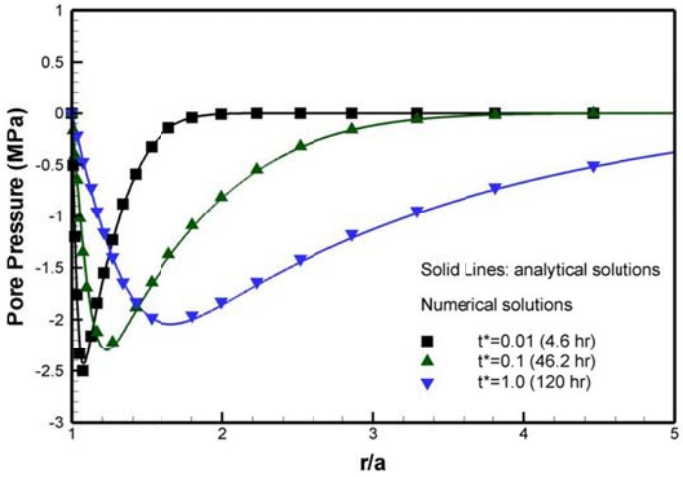

Fig. 3.26. Comparison of the pore pressure caused by temperature loading using variation with radial distance.

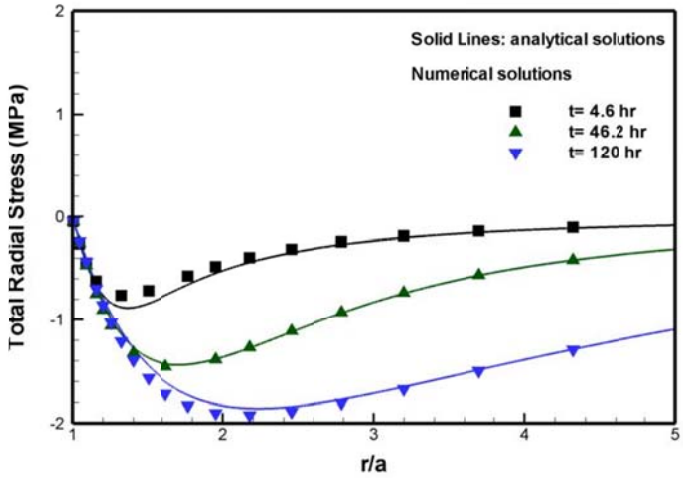

Fig. 3.27. Comparison of the total radial stress variations caused by temperature loading.

Sherwood and Baily (1994) proposed a constitutive model in the membrane system, assuming no solute transport consideration, and Heidug and Wong (1996) developed a fully coupled ion transport model. To accommodate the nonlinear relations between stress and solute concentration, Ghassemi and Diek (2003) proposed a linear chemo-thermo-poroelasticity model, and it has been shown both analytically and numerically that the resulting errors are negligible when the difference of solute concentration between the mud and the shale formation is not severe (Zhou and Ghassemi, 2009). Initial reservoir solute concentration is assumed to be 0.2 and mud concentration is 0.1 for the comparison. The pore pressure distributions and total tangential stress distributions during chemical loading are presented in Fig. 3.28 and Fig. 3.29. Results show that osmosis flow from the mud to the shale formation causes the increase of pore pressure around a wellbore (Fig. 3.28). The stress distributions are significantly affected by chemical loading (Fig. 3.29).

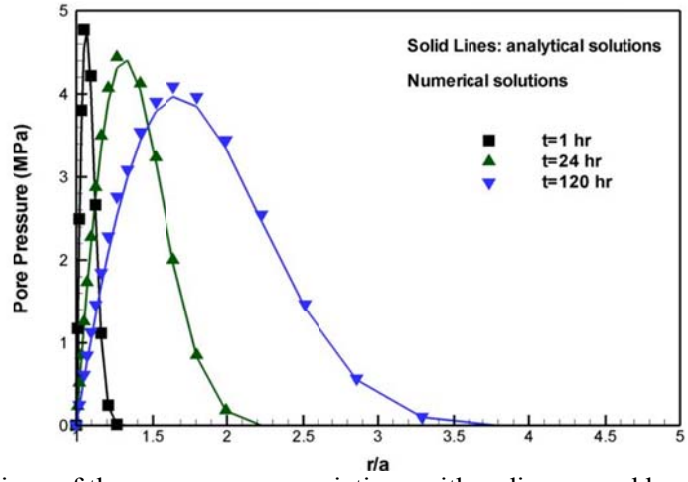

Fig. 3.28. Comparison of the pore pressure variations with radius caused by chemical loading, using numerical and analytical methods.

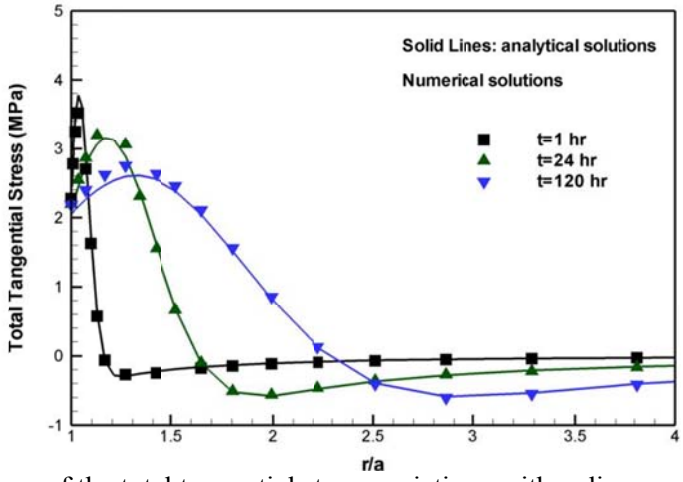

Fig. 3.29. Comparison of the total tangential stress variations with radius caused by chemical loading using numerical and analytical methods.

4. Implementation of Damage Mechanics and Stress-dependent Permeability

The previous section presented the numerical procedure for partial differential equations—especially for solving the displacement, pore pressure, solute concentration, and temperature problems—and also compared the finite element results with analytical solutions for various engineering problems such as hydraulic pressure under anisotropic far-field stress, the influence of thermal stress, and chemical loading around a wellbore.

A coupled chemo-thermo-poroelasticity is critical to understand the interaction of pore pressure, temperature, and chemical potential in rock deformation. However, the theory has limitations in that it assumes an elastic rock skeleton and constant permeability. It is often used to consider the nonlinear behavior of rock in field operations such as sanding management, fracturing jobs, and drilling operations

in unconsolidated reservoirs. Experimental core analysis for the strain-stress behavior of the rock in compressive loading shows the four stages of stress which are elastic, hardening, softening, and critical stress state (residual strength). Damage mechanics can describe the nonlinear behavior of rock under loading by considering the micro-crack, microvoid, and crackgrowth stresses (Kachanov, 1986; Lemaitre and Chaboche, 1990; Voyiadjis and Kattan, 1999). Kachanov (1986) proposed an effective configuration of undamaged material from the nominal state by introducing the damage variable, d .

Several researchers have shown that permeability is a stress-dependent property (Chin, 2000; Thomas et al., 2003; Bai and Elsworth, 1994; Tang et al., 2002). Tang et al. (2002) tested permeability variations under triaxial loading and indicated that permeability decays exponentially before the rock failure in compressive stress and it increases suddenly by a factor of 2 to 3 after the rock failure. Similar results have been reported by other researchers (Shipping et al., 1994; Kiyama et al. 1996; Coste et al., 2001; Zoback and Byerlee, 1975), with the increase in permeability depending on rock type and conditions (De Paola et al., 2009; Wang and Park, 2002). Zoback and Byerlee (1975) illustrated the relation between the permeability change and microcrack and void evolution.

In this section, we present a numerical approach for implementing damage theory and stress-dependent permeability models into a fully coupled thermo-hydro-mechanics model. Triaxial simulations with finite element methods have been carried out to find the material parameters which define the peak stress and residual strength. In addition, a stress-dependent permeability model has been applied to both elastic and inelastic rock states, and then we present the influence of localized rock damage and permeability change caused by fluid injection around a wellbore.

4.1 Damage Model

A damage and stress-dependent permeability model was proposed by Tang et al. (2002) from experiments for porous rock that measured the permeability and modulus change with respect to the change of strain (Yang et al., 2004). This model assumes that the strain-stress behavior before the rock failure follows the elasticity model without the hardening process and reaches the residual strength regime. From this damage model, there is no damage in the elastic phase, but the rock begins to fail by crack initiation and void growth when the stress conditions reach the failure state; that is, it satisfies the failure criterion. This model has an advantage for describing the behavior of brittle rock, which has a short range of hardening and directly reaches the softening regime in triaxial tests. An elastic-damage mechanics model represents the rock degradation by expressing the damage in terms of a reduction in the elastic modulus as the damage proceeds:

$$E = (1-d)E_0 \ , \qquad (4.1)$$

where d is the damage variable which describes the amount of degradation (crack initiation, microvoid growth, and crack propagation) and E and E_0 are altered modulus and initial modulus, respectively. The degree of damage level can be represented with damage variable from 0 to 1 with a relationship of strain variations. For example, d = 0 if the rock is in elastic phase, and d = 1 if the rock is perfectly damaged. The damage model from the rock failure can be considered as either of two types, compressive and tensile stresses.

In compressive rock failure, the damage variable for describing softening and the critical state can be described as:

$$d = 1 - \left\{ \left(\frac{f_{cr} - f_c}{\varepsilon_{cr} - \varepsilon_c} \right) (\bar{\varepsilon} - \varepsilon_c) + f_c \right\} \Big/ E_0 \bar{\varepsilon} \quad (\varepsilon_c < \bar{\varepsilon} < \varepsilon_{cr})$$

$$d = 1 - \frac{f_{cr}}{E_0 \bar{\varepsilon}} \tag{4.2}$$

where f_{cr} is the residual compressive strength and f_c is the maximum compressive stress. ε_{cr} and ε_c are the residual compressive strain and maximum compressive strain, respectively, and $\bar{\varepsilon}$ is the equivalent strain (Mazars, 1986):

$$\bar{\varepsilon} = \sqrt{\sum \langle \varepsilon \rangle_+^2} \tag{4.3}$$

where $\langle \varepsilon \rangle_+ = \varepsilon_i$ if $\varepsilon_i \le 0$ (tensile) and $\langle \varepsilon \rangle_+ = 0$ if $\varepsilon_i > 0$ (compressive).

This equivalent strain definition from Mazars (1986) represents a damage evolution that is dominated by tensile strain. These components of strain during damage evolution can be obtained as follows:

$$\sigma = \langle \sigma \rangle_t + \langle \sigma \rangle_c \tag{4.4}$$

where $\langle \sigma \rangle_t$ is built with the tensile components of the principal stress and $\langle \sigma \rangle_c$ is for compressive components of principal stress. In this way, we can obtain strain components for tensile and compressive stresses:

$$\varepsilon_t = \frac{1+v}{E_0(1-d)} \langle \sigma \rangle_t - \frac{v}{E_0(1-d)} tr\left(\langle \sigma \rangle_t \right) \tag{4.5}$$

$$\varepsilon_c = \frac{1+v}{E_0(1-d)} \langle \sigma \rangle_c - \frac{v}{E_0(1-d)} tr\left(\langle \sigma \rangle_c \right) \tag{4.6}$$

$$\sigma = \langle \sigma \rangle_t + \langle \sigma \rangle_c \tag{4.7}$$

If damage occurs in a tensile stress field, the damage variable is defined using the residual tensile strength of rock as:

$$d = 1 - \frac{f_{tr}}{E_0 \bar{\varepsilon}} \tag{4.8}$$

To trace the progress of damage under tensile stress, we introduced a tension cut-off, T_0, for tensile failure because the Mohr-Coulomb failure criterion was developed based on shear failure and it often overestimates the stress state for rock failure. The Mohr-Coulomb failure criterion for shear failure can be described as:

$$F = \frac{\sigma_1 + \sigma_3}{2} \sin \phi_f - \frac{\sigma_1 - \sigma_3}{2} - c_F \cos \phi_f \tag{4.9}$$

where σ_1 and σ_3 are the maximum and minimum principal stresses, respectively; ϕ_f and c_f represent the friction angle and cohesive strength, respectively.

4.2 Numerical Implementation of the Damage Model

The theory of damage mechanics has been implemented into the finite element code described above. For illustration purposes, we consider the numerical simulation of the stress-strain response of a rock obtained from a laboratory triaxial experiment. In particular, we simulated the experimental data of Wang and Park (2002) and Tang et al. (2002), which shows a rapid decrease from the peak stress. The simulation domain

for the axisymmetric triaxial test is shown in Fig. 4.1. The sample size is 1 cm×2 cm, which has axisymmetry so its actual ratio is 1:2. An axial load is applied in the z-directional in a step-wise manner by increasing the displacement of the top of the sample. Displacement step change in this simulation is 2×10^{-3}m per each step, and the total step number is 80. The procedure for implementation of damage mechanics and the stress-dependent permeability model is illustrated in Fig. 4.2. The state of stress is checked in each element by fluid and thermal loading. Once the stress condition is to be satisfied with the failure criterion, the damage variable for the element is computed using previously described damage equations (Eq. 4.2 to 4.8). It is important to consider the change of the poroelastic parameters such as bulk modulus, Biot's constant, and porosity. The change of porosity, □□ is equal to the damage variable, d (Shao, 2002), and other modulus-related parameters are also updated with the relation of $E = (1-d)E_0$. To obtain accurate numerical results, the convergence of damage variables under a certain loading is critical before moving to the next time step. For example, damage variables in each element in the first and second iterations are compared, and if the result does not satisfy the criterion, damage variables are updated with the same loading conditions. The tolerance criterion in this simulation is 0.1 %.

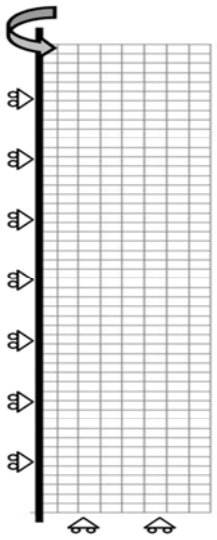

Fig. 4.1. Finite element mesh used for triaxial simulations.

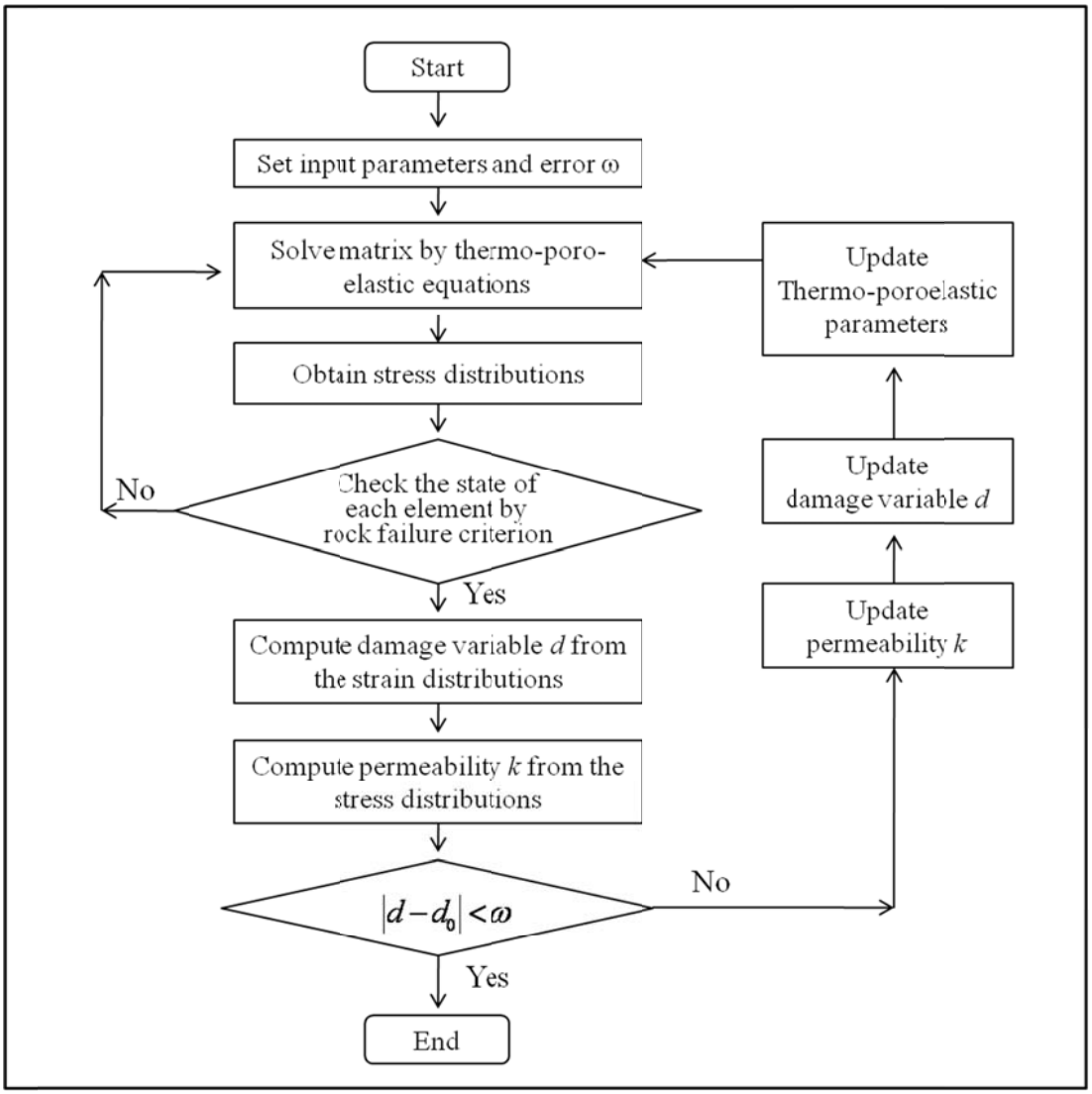

Fig. 4.2. Flow chart of the simulation procedures for the implementation of the damage and permeability model in thermo-poroelasticity with rock failure.

Simulated results in Fig. 4.3 show the peak stress variations by defining cohesive strength c_f and the residual strength change by defining f_{cr} in the damage model. Fig. 4.4 shows the simulated and actual curves for different pairs of c_f and f_{cr}. The best fits with experimental data are selected so that the residual strength, f_{cr}, in Eq. 4.4 and the cohesive strength, c_f, in the Mohr-Coulmb failure criterion are determined. The implementation of the damage model for the tensile failure case is illustrated in Fig. 4.5.

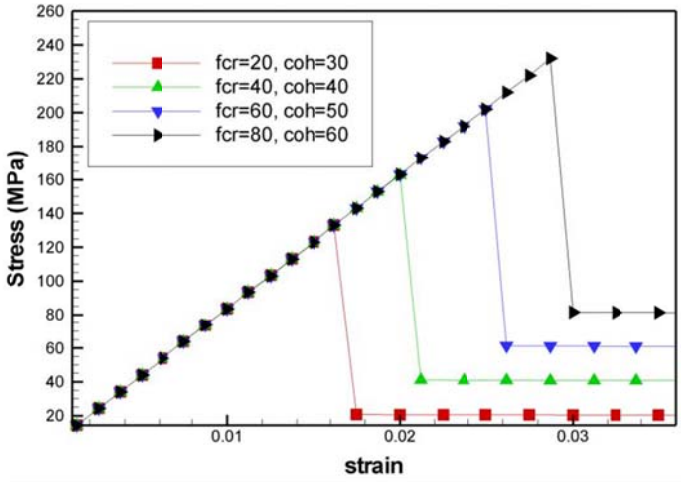

Fig. 4.3. Strain-stress curve variations with cohesive strength c_f and critical residual stress f_{cr}.

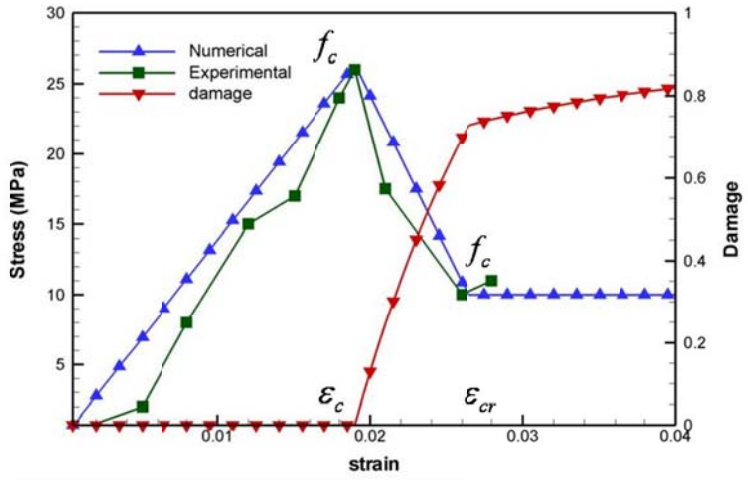

Fig. 4.4. Comparison of numerical implementation of the damage model and the experimental triaxial test. Triaxial test results are obtained from Tang et al. (2002).

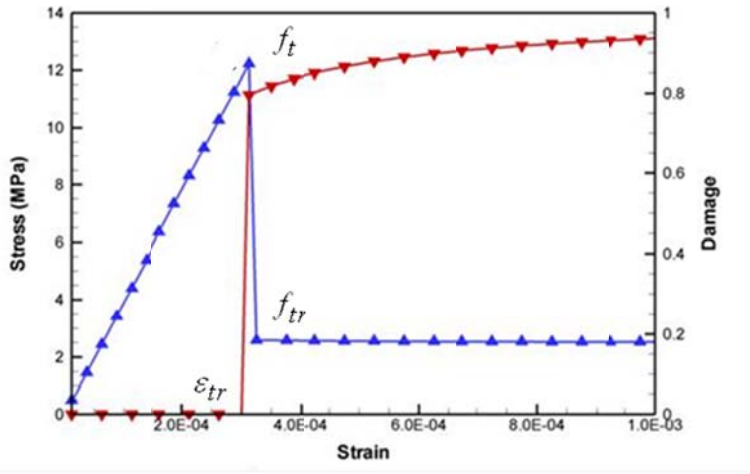

Fig. 4.5. Numerical implementation damage theory for the tensile failure case.

To simulate a more realistic triaxial test, we considered the heterogeneity of the modulus using the Weibull distribution function, which is widely used in a geomechanics simulation to depict the heterogeneity of rock. The heterogeneity of the modulus is introduced to the Gaussian points in each element. The Weibull distribution functions are defined as:

$$\varphi = \frac{n}{s_0}\left(\frac{s}{s_0}\right)^{n-1} \exp\left[-\left(\frac{s}{s_0}\right)^{n}\right] \qquad (4.10)$$

where s is the variables s_0 represents the corresponding mean value.

The parameter n is the control factor in Weibull distribution function. A large n indicates the distributions are narrow and more homogeneous, whereas lower n represents the more heterogeneous rock. This index influences the rock failure in triaxial tests so that average peak stresses are reduced if the rock is more heterogeneous because of the increase of the lower modulus in the distributions. The heterogeneous results are presented in Fig 4.6. Results show a reduction of peak stress and smooth variations in the heterogeneity case, which increase compared to homogeneous case. This is because of the earlier beginning of rock failure in low modulus elements.

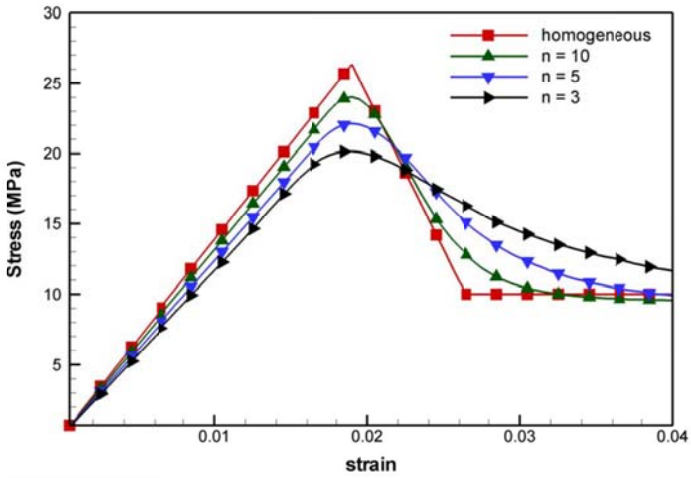

Fig. 4.6. Finite element results for triaxial stimulation with damage mechanics. The stress-strain curve varied with different levels of heterogeneity in Weibull distribution function.

4.3 Implementation of Stress-dependent Permeability Model

The rock permeability change is also considered in the elastic phase and the damage phase (Tang et al., 2002; Yang et al., 2004):

$$k = k_0 e^{-\beta_d (\sigma_{ii}/3 - \alpha p)} \qquad (d = 0) \qquad (4.11)$$

$$k = \zeta_d \, k_0 e^{-\beta_d (\sigma_{ii}/3 - \alpha p)} \qquad (d > 0) \qquad (4.12)$$

where k_0 is the initial permeability and ζ_d `and β_d are material constants determined empirically. Here ζ_d (ζ_d >1) indicates permeability increase caused by damage. Parameter β_d in the exponent term is the control parameter for the stress sensitivity of permeability in the porous rock. This permeability model has been developed from experimental results of triaxial compressive tests. The model describes a decay of permeability while compressive stress increases in the elastic phase. After the rock fails, there is a step increase of permeability that decreases again with continuous compressive stress. The numerical results for permeability variations during the triaxial loading are illustrated in Fig. 4.7.

The changes of poroelastic parameters after rock failure are also important to study injection-induced nonlinear behavior of rock since the poroelastic constants are applicable for the elastic phase. Major poroelastic parameters to be considered after the rock failure are bulk modulus K, shear modulus G, Biot's constant α, and porosity ϕ. We considered the change of poroelastic parameters with damage evolution; for example, Biot's constant is 1 and the modulus of bulk solids and fluid are also reduced with the change of damage variables. Porosity related parameters are recomputed assuming porosity, ϕ is equal to the damage variable, d (Shao, 2002).

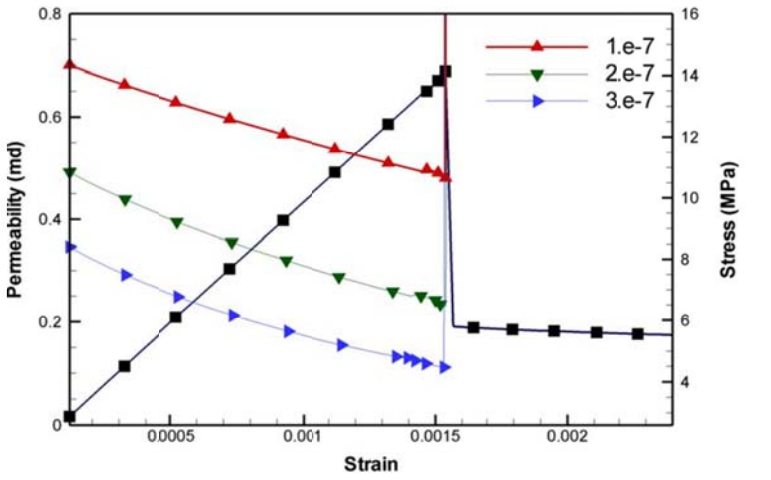

Fig. 4.7. Finite element results for permeability variation with triaxial simulation. Permeability varied with different material parameter, $\square_d$.

4.4 Numerical Analysis of the Thermo-poromechanical Process with Damage Evolution and Permeability Change

In this section, we present numerical examples for damage evolution and permeability alteration while considering poroelasticity and thermo-poroelasticity with convective heat transfer. First, we present poroelasticity and thermo-poroelasticity results without in-situ stresses to focus on the induced increments of damage and permeability around a wellbore.

4.4.1 The influence of damage evolution and permeability change in isothermal conditions

Consider the influence of fluid flow around a wellbore under isothermal reservoir conditions with pressure boundary conditions. We used 350 elements with 1141 nodes to simulate the domain of 5×5 m with a wellbore of radius 0.1 m (Fig. 4.8). No in-situ stress and no initial pore pressure are applied in initial reservoir conditions, and a wellbore pressure of 12 MPa is used in the simulation.

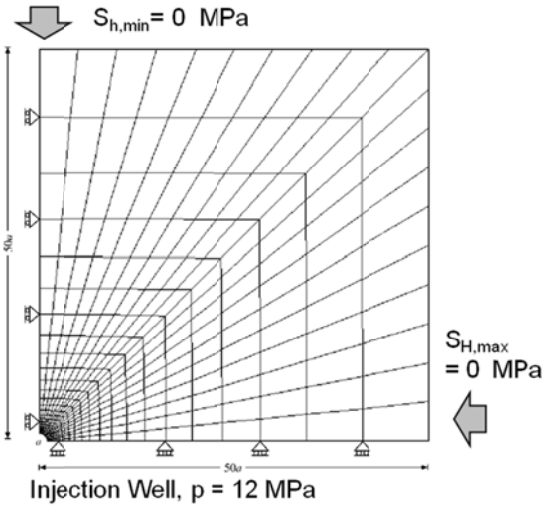

Fig. 4.8. Finite element mesh for coupled thermo-poroelasticity damage model consisting of 350 elements and 1141 nodes; zero in-situ stress pore pressure; wellbore pressure of 12 MPa.

Table 4.1. Rock properties of sandstone.

Young's modulus E (GPa)	7.92
Drained Possoin's ratio υ	0.14
Undrained Possoin's ratio υ_u	0.35
Skempton's coefficient, B	0.77
Permeability, k (md)	1
Porosity, ϕ	0.19
Fluid mass density, ρ_f (kg/m^3)	1000
Fluid viscosity, μ (Pa·s)	1×10^{-3}
Thermal expansion coefficient of solid, α_m (K^{-1})	1.8×10^{-5}
Thermal expansion coefficient of fluid, α_f (K^{-1})	3.0×10^{-4}
Thermal diffusivity, c^T (m^2/2)	1.6×10^{-6}

Damage evolution for this problem is presented in Fig. 4.9. The damage propagation in time is very slow for the pressure boundary condition. Rock failure around the wellbore is caused by tensile failure as the effective tensile stress dominates the failure around the wellbore. Fig 4.10 shows the distributions of permeability. A step increase is observed in the damage phase caused by microcrack and void growth in the rock. The resulting pore pressure distribution is discontinuous because of the high permeability in the damage phase (Fig. 4.11). The influence of damage and altered permeability is shown in comparison with the homogeneous poroelastic results in Fig. 4.11, where the solid lines represent the effect of damage and permeability change and dashed lines show the poroelastic results without damage and permeability increase (reference case). The distributions of total radial stress and tangential stress are plotted in Fig. 4.12 and Fig. 4.13; note that total radial stress distributions in the damage phase are relatively higher than in the reference case because the pore pressure is higher in the damage phase. From a stress analysis point of view, this small discontinuity of total radial stress between the damaged and elastic phase is caused by the lack of sufficient fluid movement at the interface between damaged and undamaged zones; that is, at

the boundary between the high permeability and low permeability zones. Different fluid pressures in these zones cause a discontinuity of total stress between the damaged and elastic phases.

Fig. 4.14 and Fig. 4.15 illustrate the effective radial and tangential stress around the wellbore. The solid lines in Fig. 4.14 and Fig. 4.15 represent the poroelastic case with damage evolutions and permeability alterations whereas the dashed lines are for the reference case. It is observed that the effective stresses in the damage phase are reduced in comparison to the reference case because of stress relaxation. However, stress concentration is observed between the damage and the elastic phase. This stress concentration effect between damage phase and intact rock drives damage propagation similar to the case of fracture propagation theory.

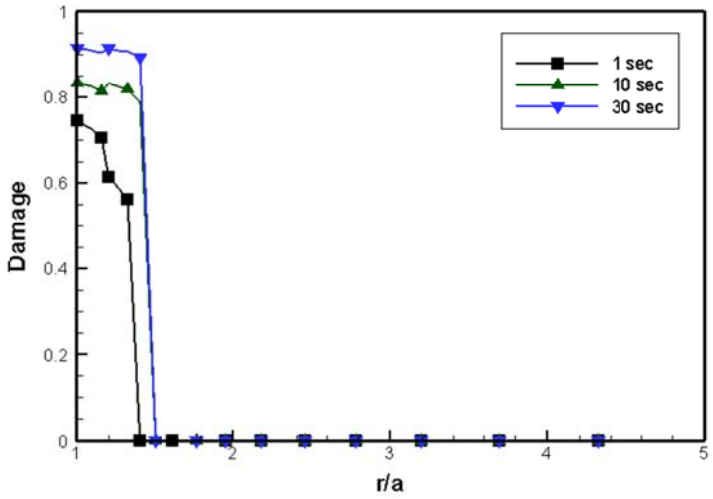

Fig. 4.9. Damage evolution around a wellbore.

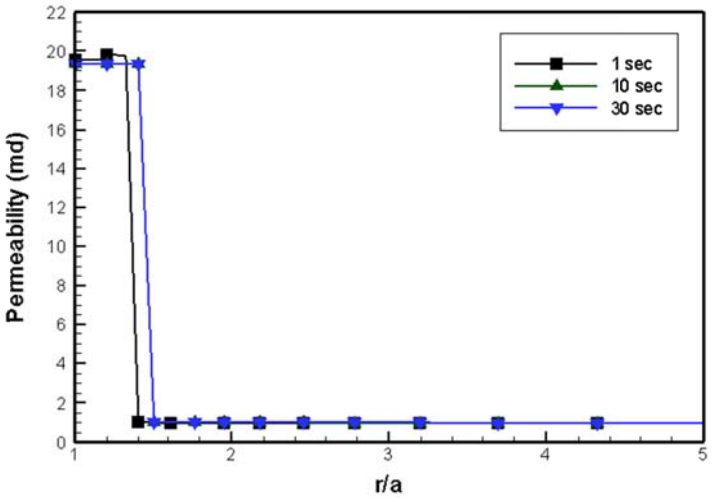

Fig. 4.10. Permeability distribution around the wellbore.

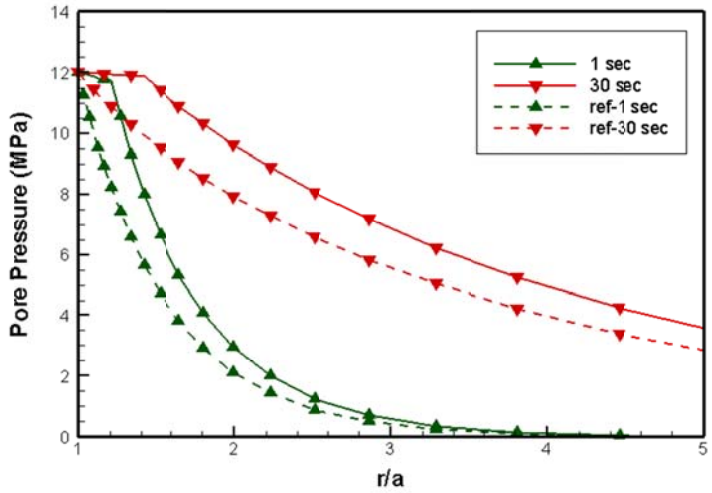

Fig. 4.11. Comparison of pore pressure distributions for simulations with and without damage. Solid lines: pore pressure distributions for damage evolutions and permeability change; dashed lines: the reference results from no damage and no step increase in permeability.

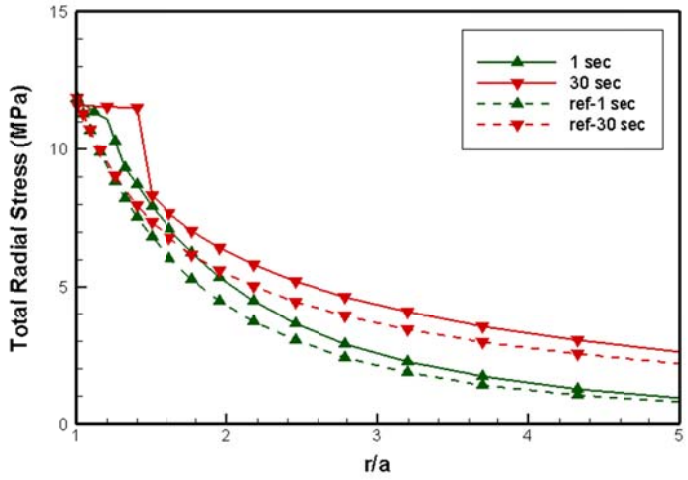

Fig. 4.12. Total radial stress distributions showing damage and altered permeability effects around a wellbore. Solid lines: stress distributions for damage case; dashed lines: the reference cases with no damage.

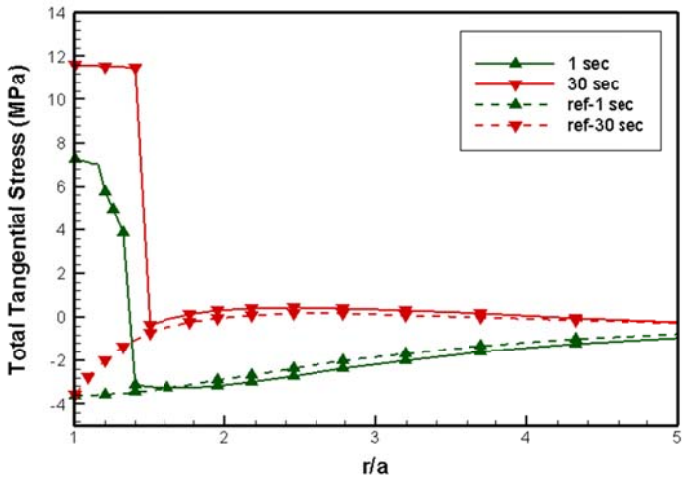

Fig. 4.13. Total tangential stress distributions showing damage and altered permeability effects around a wellbore. Solid lines: damage evolution and permeability change; dashed lines: reference case with no damage.

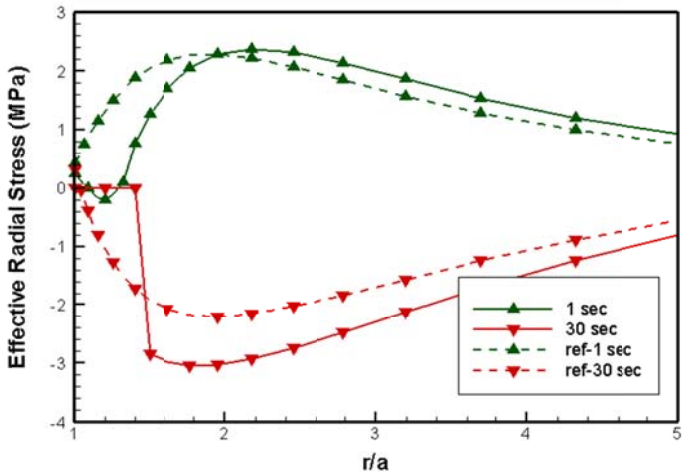

Fig. 4.14. Effective radial stress distributions around the wellbore. Solid lines: damage evolution included; dashed lines: no damage considered.

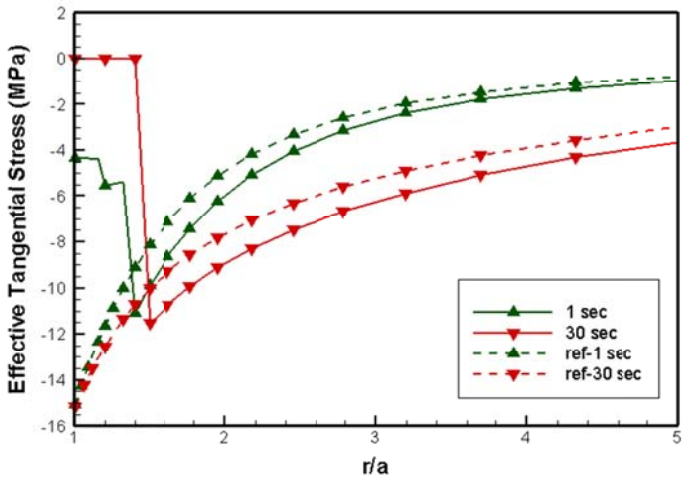

Fig. 4.15. Effective tangential stress distributions showing effects of damage and altered permeability around the wellbore. Solid lines: damage evolution; Dashed line: no damage.

4.4.2 The influence of damage evolution and permeability change in non-isothermal condition

Thermo-poroelastic simulations were performed while considering damage evolution and permeability alteration. Both conduction and convective heat transfer have been applied with fluid velocity computed using Darcy's law. We used the same 350 elements and 1141 nodes mesh in the thermo-poroelasticity case (Fig. 4.16). The penalty method is used for the pore pressure and temperature boundary conditions at the wellbore wall. Initial reservoir conditions of no in-situ stress and no pore pressure are first used to explain the pure effects of damage evolution in the fully coupled thermo-hydro-mechanical simulations.

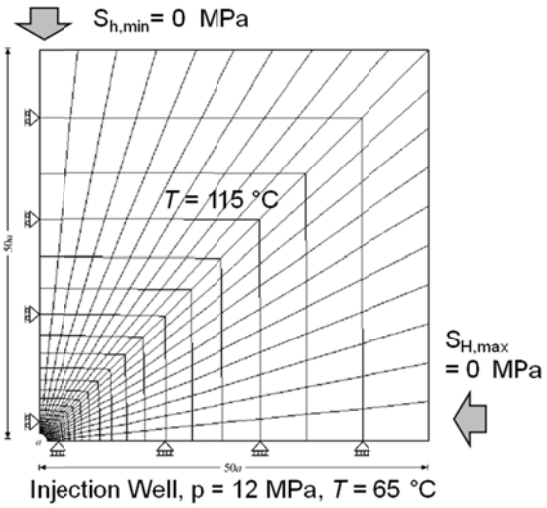

Fig. 4.16. Finite element mesh for the problem: 350 elements and 1141 nodes. Initial reservoir temperature is 115 °C, and wellbore pressure is 12 MPa.

The cooling associated with cold water injection in hot reservoir gives rise to tensile stresses associated with rock shrinkage. As a result, cooling influences the stress distributions differently from the isothermal conditions, as reflected in the distributions of damage variable as shown in Fig. 4.17; permeability distributions appear in Fig. 4.18. The effect of convective cooling around the wellbore is shown in Fig. 4.19. The solid lines represent the temperature profiles caused by both conduction and convection, whereas dashed lines are for the case of cooling by conduction only. We observe that the effect of convective cooling on temperature distribution can become significant, which in turn impacts the stress distributions around the wellbore caused by thermal stress. The pore pressure distributions are discontinuous at the interface due to the altered permeability in the damage phase as in Fig. 4.20. The total radial and tangential stress distributions are plotted in Fig. 4.21 and Fig 4.22, and effective stresses are plotted in Fig. 4.23 and Fig. 4.24. Again, we observe discontinuity in the total stress resulting from pore pressure discontinuity related to damage and relaxation of effective stress in the damage phase.

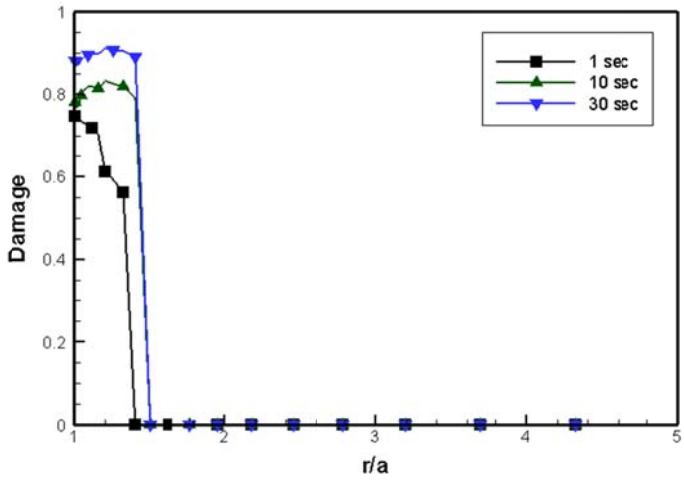

Fig. 4.17. Damage evolution around the wellbore.

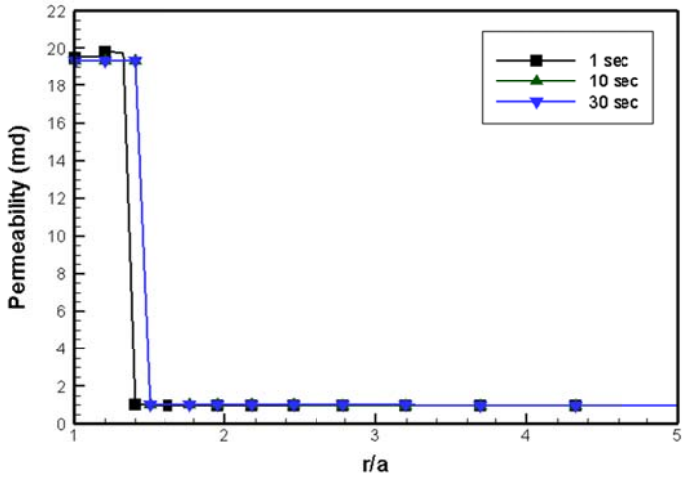

Fig. 4.18. Permeability distributions around the wellbore.

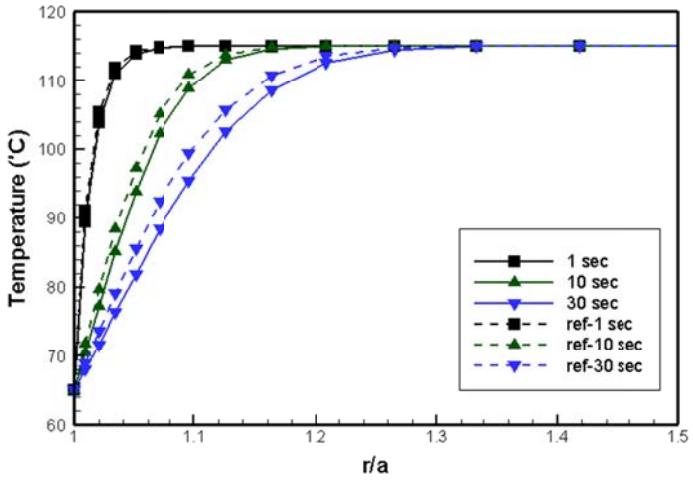

Fig. 4.19. Temperature distributions around the wellbore.

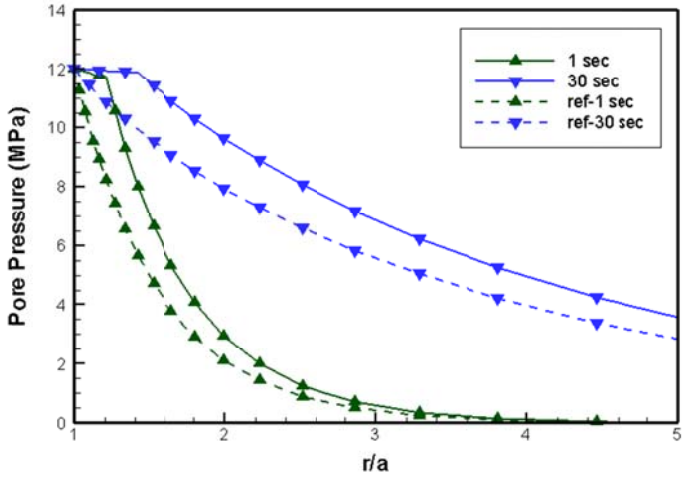

Fig. 4.20. Pore pressure distributions around the wellbore. Solid lines represent pore pressure distributions for damage; dashed lines give the results for the reference case with no damage.

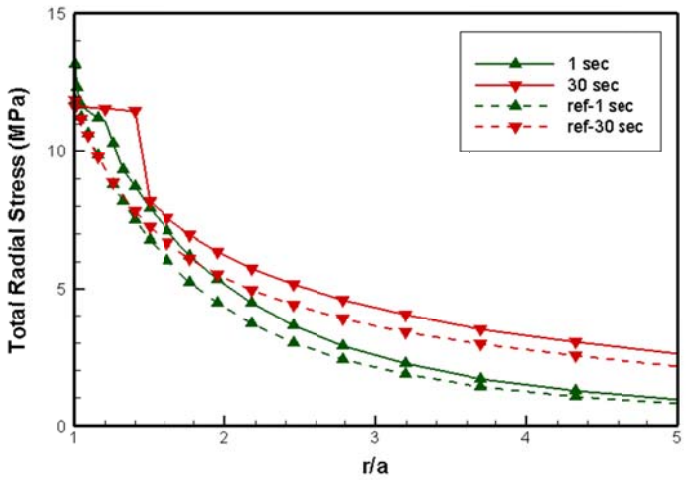

Fig. 4.21. Total radial stress distributions around the wellbore. Solid lines: with damage; dashed lines: no damage.

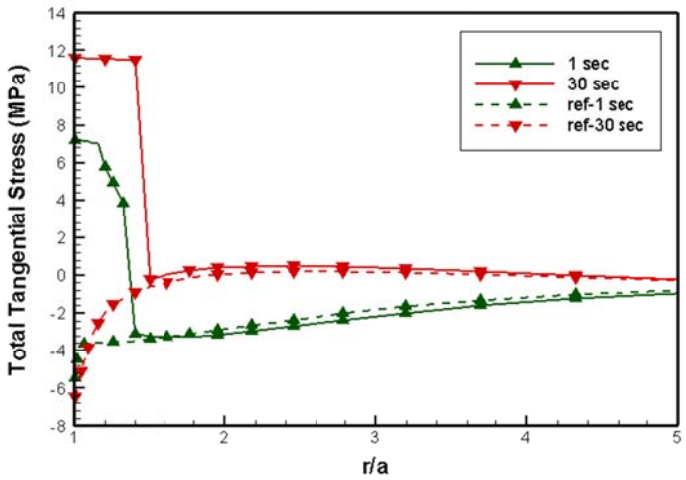

Fig. 4.22. Total tangential stress distributions comparing the damage and altered permeability effects around the wellbore. Solid lines: with damage evolutions and permeability change; dashed lines: reference case with no damage.

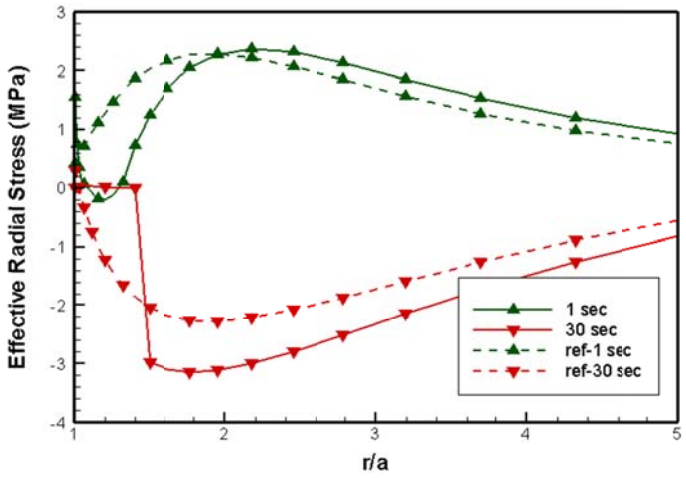

Fig. 4.23. Effective radial stress distributions around the wellbore showing the impact of damage and altered permeability. Solid lines: with damage evolution and permeability change; dashed lines: no damage and permeability increase.

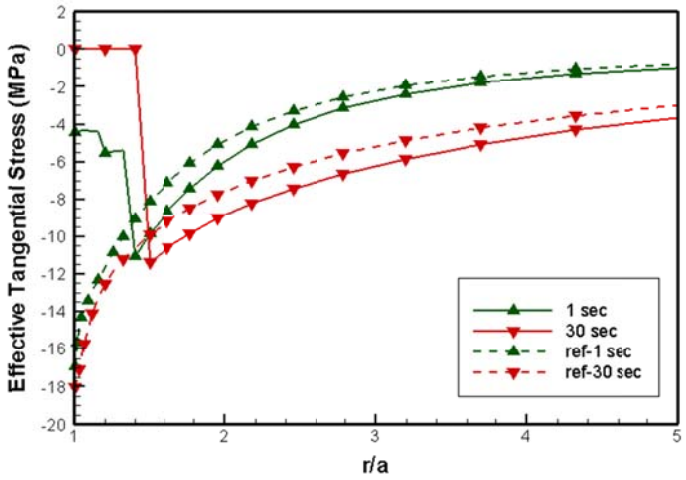

Fig. 4.24. Effective tangential stress distributions. Solid lines: damage evolutions and permeability change; dashed lines: no damage and no step increase of permeability.

4.5 Discussion

Damage and stress-dependent permeability models were applied to the theory of thermo-poroelasticity. Stress distributions with implementation of damage mechanics and the permeability model has been compared with a reference case (constant modulus and permeability). Stress relaxation occurred by modulus alteration and concentration of effective hoop stress at the interface between the damaged and undamaged rock. Also, pore pressure distribution shows the discontinuity at the interface due to the increase of permeability in the damaged area.

The damage model used in this section considered nonlinear behavior of strain-stress for the shear and tensile failure. This model can describe softening and residual strength regime with change the parameters f_{cr}, f_{tr}, and ε_{cr} better than other suggested damage models that include exponential terms in their equations (Mazars, 1986; Cheng and Dusseault, 1993; Selvadurai, 2004). These exponent-based damage models can depict the hardening and softening process smoothly; however, it is not convenient to control the desired softening regime and residual strength regime. For our applications, it is important to consider softening and residual strength since reservoir rocks (shale, sandstone, and granite) show brittle behavior with a short range of hardening regime.

5. Chemo-Thermo-poromechanical Finite Element Analysis with Damage Evolution around a Wellbore in Swelling Shale

Wellbore stability is important when drilling for oil and gas. Especially, well design must consider the influence of hydraulic pressure, temperature, and chemical osmosis in shale drilling in high pressure and high temperature. The interaction of solid and fluid in porous rock has been firstly developed by Biot's poroelastic theory (Biot, 1941; Cryer, 1963), and this theory has been extended with the influence of temperature, fluid flow, and rock deformation by thermo-poroelasticity (McTigue, 1986; Kurashige, 1989, Wang and Papamichos, 1994). These authors have shown the impact of thermal stress in wellbore stability: thermally induced pore pressure change can be significant in low permeability formations. The shale deterioration by chemical influence under isothermal condition around a wellbore has been studied extensively; the main driving mechanism of fluid flow is the chemical potential gradient in low permeability shale reservoirs. Heidug and Wong (1996) proposed constitutive equations for swelling shale based on nonequilibrium thermodynamics. Ghassemi and Diek (2003) considered combined effects of chemical potential and thermal osmosis on water flow in and out between the mud and shale formation. They indicated that thermal-osmosis flows are several times higher than hydraulic pressure in certain conditions. On the other hand, the chemo-poroelasticity model is not easy to implement because of its nonlinearity characteristics in physical parameters so that it can be simplified with linear chemo-thermo-poroelastic models if the difference of concentration is not severe (Ghassemi and Diek, 2003). The assumptions of elasticity and constant permeability in shale drilling have limitations in predicting the real behavior of shale around a wellbore. In addition, the strength of shale is weak, so that it is important to predict the stress changes precisely around a wellbore influenced by hydraulic pressure, mass solute concentration, and temperature. Generally, the stress and strain behavior for shale in triaxial tests shows the hardening and softening with compressive or tensile stress (Yuan and Harrison, 2006). The damage mechanics model is one of the methods to describe this hardening and softening behavior of rock. Continuum damage mechanics was first introduced by Kachanov and since has been developed by many researchers (Kachanov, 1958; Mazars, 1986; Simankin and Ghassemi, 2005; Tang et al., 2002; Li et al., 2005; Selvadurai, 2004) who have studied the inelastic rock behavior due to crack initiation, void growth, and crack growth. This damage mechanics model has been applied to poroelasticity by Selvadurai, who applied consolidation problems with altered moduli and permeability change. Also Hamiel et al. (2005) proposed a damage model in poroelastic rock and applied the model to the triaxial simulation, considering the time dependent degradation and healing process for a damage variable which is dependent on modulus, porosity, and Poisson's ratio. Tang et al. (2002) proposed an isotropic damage model based on Kachanov's (1959) effective stress hypothesis. Also he presented the permeability model which describes stress-dependent behavior in the elastic phase and altered permeability after the rock failure based on triaxial tests by measuring the permeability change with stress variation (Tang et al., 2002). This permeability change by rock failure has been studied by many researchers (Shipping et al., 1994; Kiyama et al.; 1996, Coste et al., 2001; Zoback and Byerlee, 1975). Their experimental results for tests on several rocks show permeability increase by a factor of two to four, and this increase of permeability by rock failure depends on the rock type and conditions (De Paola et al. 2009; Wang and Park, 2002).

This section presents the development of a finite element method to study the influence of chemo-thermo-poromechanical coupling on shale damage evolution and permeability alteration around a wellbore. The damage model describes the change of modulus with rock failure by water activity and thermal stress around a wellbore. A number of simulations are presented to verify the model and to illustrate the role of damage mechanics and stress-dependent permeability and resulting stress distribution by thermal stress and chemical osmosis. In addition, we present the different distributions of damage under different far-field stresses and compare the influence of temperature and chemical potential.

5.1 Finite element results for Chemo-thermo-poroelasticity

In this section, we briefly present two-dimensional finite element results around a wellbore to study the influence of fluid flow, solute transport, and temperature. The simulation domain is 12×12 m^2 (Fig. 5.1) and is divided into 8000 eight-noded quadrilateral elements. The individual shape functions in the mixed approximation will not yield meaningful results (Zienkiewicz and Taylor, 1991). Overcoming this numerical inaccuracy requires double degrees of freedom for displacements in the presence of large changes of stresses, pressure, concentration, and temperature around the wellbore. Details of shale properties in this simulation are illustrated in Table 5.1. Maximum and minimum far-field stress are 25 MPa and 15 MPa, respectively, and initial pore pressure and temperature are 10 MPa and 115°C. Mud pressure and temperature are set to 15 Pa and 65°C. Solute concentration in mud and shale formations are C_{mud}=0.1 C_{shale} = 0.2, respectively.

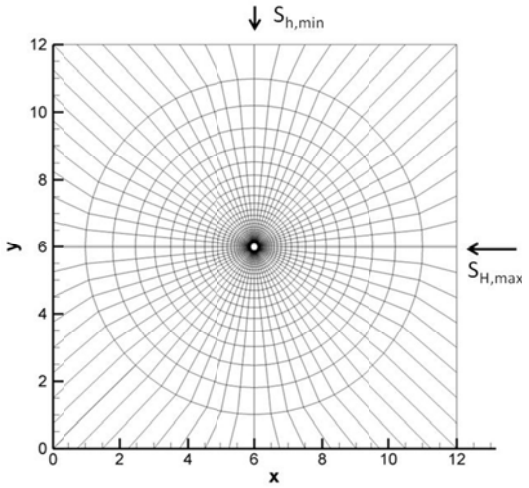

Fig. 5.1. Mesh used for finite element simulation.

Table 5.1. Input material properties for shale.

Young's modulus E (GPa)	1.853
Drained Poisson's ratio υ	0.219
Undrained Poisson's ratio υ_u	0.461
Biot's coefficient, α	0.966
Permeability, k (md)	1×10^{-6}
Porosity, ϕ	0.299
Fluid mass density, ρ_f (kg/m^3)	1111.11

Fluid viscosity, μ (Pa·s)	1×10^{-3}
Thermal expansion coefficient of solid, α_m (K^{-1})	1.8×10^{-5}
Thermal expansion coefficient of fluid, α_f (K^{-1})	3.0×10^{-4}
Thermal diffusivity, c^T ($m^2/2$)	1.6×10^{-6}
Reflection coefficient, $\Re$	0.2
Swelling coefficient, ω_0 (MPa)	1.5
Solute diffusivity, D^S ($m^2/2$)	2.0×10^{-9}

We compared the results which consider the influence of fluid flow, temperature, and solute transport based on poroelasticity, thermo-poroelasticity, and chemo-thermo-poroelasticity. Pore pressure distributions for isothermal and nonisothermal cases are plotted in Fig. 5.2 (a) and (b). The deviatoric far-field stress causes the lower pore pressure to the maximum far-field stress direction because of the tensile stress around a wellbore, and higher pore pressure to the minimum far-field stress direction because of the compressive stress. The influence of temperature is described in Fig. 5.2(b). Note that the difference of temperature between the mud and shale formation generates thermal stress as tensile around a wellbore because of rock shrinkage; therefore, the fluid disperses more easily than in the isothermal condition. Fig. 5.2(c) represents the influence of solute transport (C_m=0.1, C_{shale}=0.2) that the osmosis flow cause localized pore pressure inside the shale formation. The result for the fully coupled case has been described in Fig. 5.2(d). The effective radial and hoop stress distributions with different coupling schemes are plotted in Fig. 5.3 and Fig. 5.4. It is observed that the fluid flow, temperature, and solute transport are critical to rock stress; the variations in hoop stresses are especially significant. This localization of stress distribution often reaches the rock failure criterion, so it is necessary to consider the stress variations after the rock failure. The rock damage with altered modulus and permeability will be discussed in the next section.

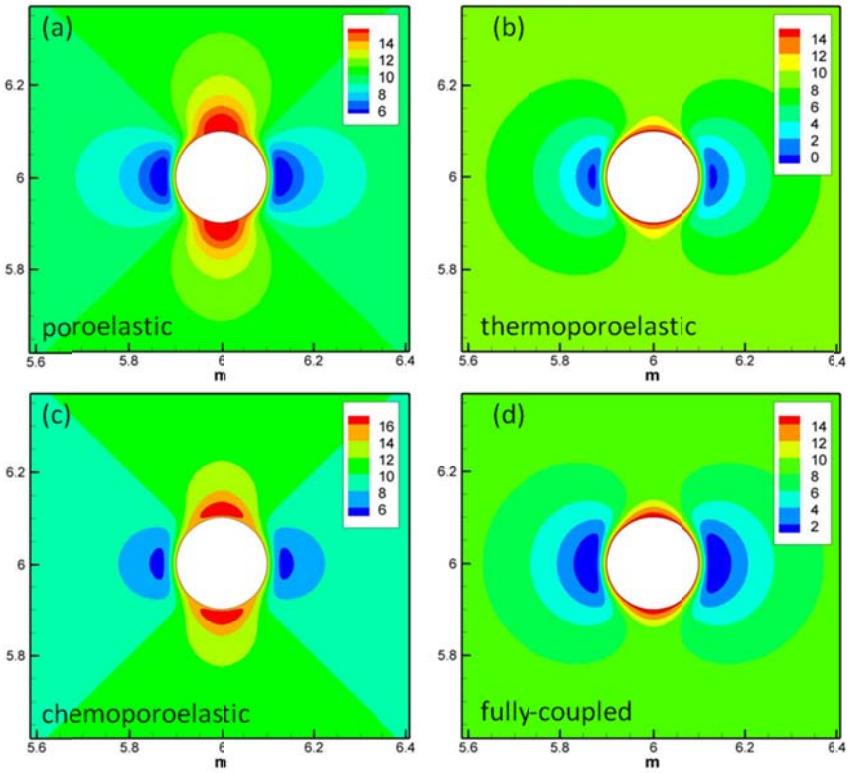

Fig. 5.2. Two-dimensional plots for pore pressure distribution. The solid-fluid interaction between the drilling mud and shale formation under anisotropic far-field stress is plotted in (a), the influence of thermal stress is in (b), chemical interaction with fluid is in (c), and fully coupled results are in (d).

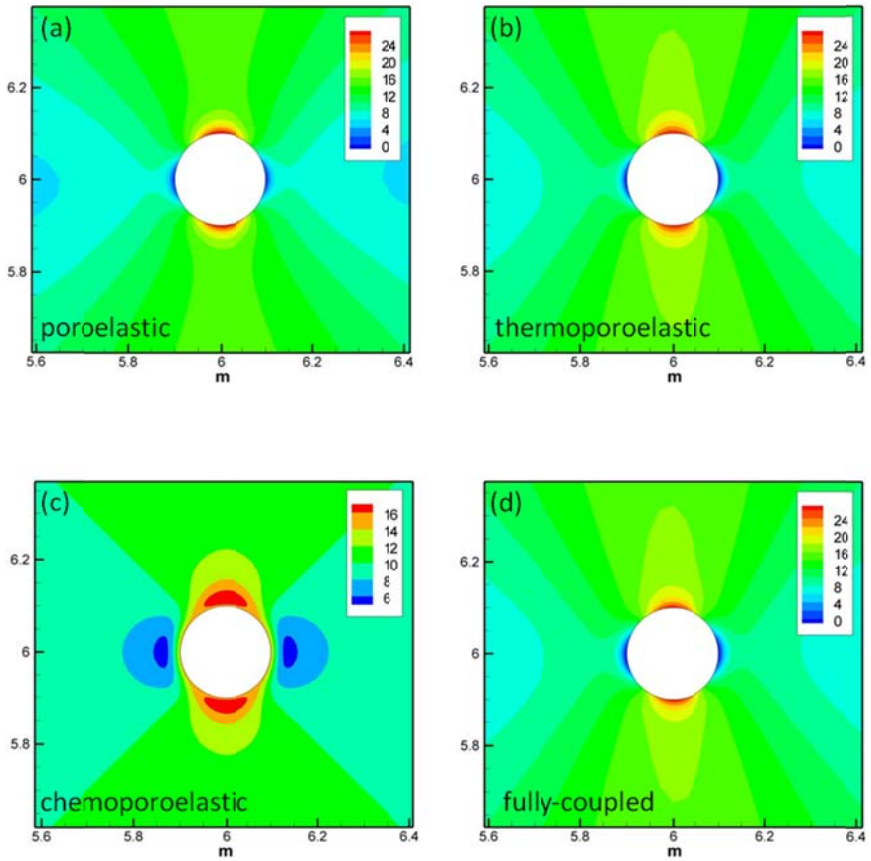

Fig. 5.3. Two-dimensional plots for effective radial stress distribution. The solid-fluid interaction between the drilling mud and shale formation under anisotropic far-field stress is plotted in (a), the influence of thermal stress is in (b), chemical interaction with fluid is in (c), and fully coupled results are in (d).

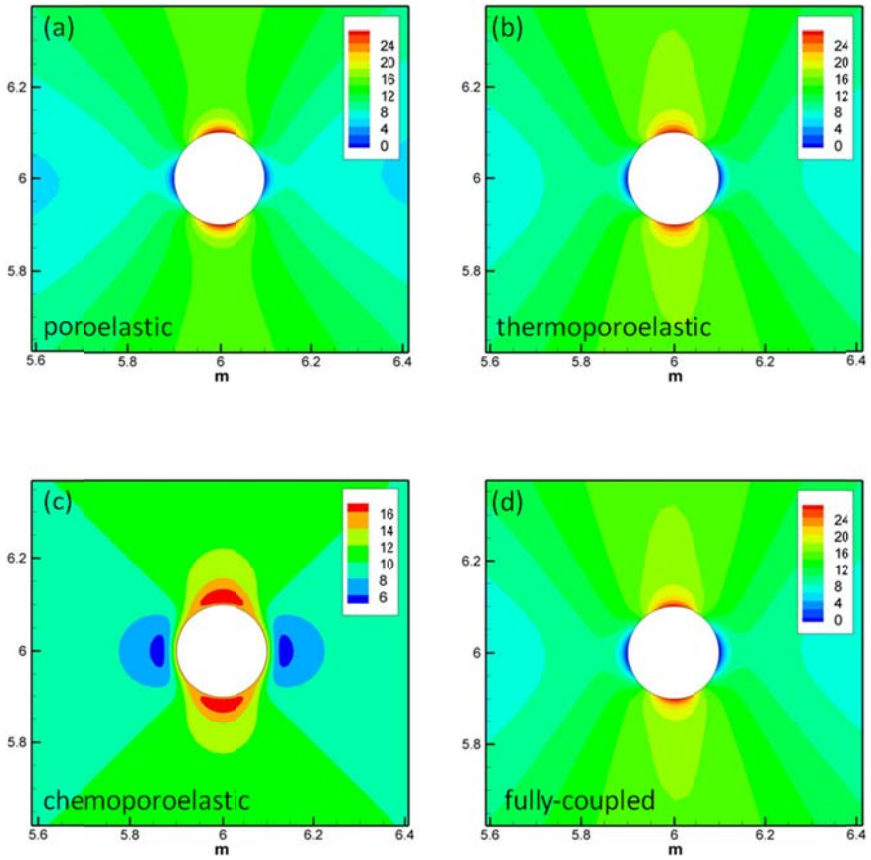

Fig. 5.4. Two-dimensional plots for effective tangential stress distribution. The solid-fluid interaction between the drilling mud and shale formation under anisotropic far-field stress is plotted in (a), the influence of thermal stress is in (b), chemical interaction with fluid is in (c), and fully coupled results are in (d).

5.2 Influence of Temperature and Salinity in Shale Damage

To illustrate the role of various mechanisms on wellbore damage, we considered the example of nonisothermal drilling in shale subjected to a stress field given by the maximum component of 25 MPa parallel to the x-axis and a minimum far-field component of 15 MPa in the y-direction. We assumed that initial pore pressure is 10 MPa and the mud pressure is 15 MPa. The initial shale formation temperature is 115°C and mud temperature assumed to be 65°C. Two different mud salinities of 0.3 and 0.1 are considered, and the wellbore integrity is analyzed after 12 hours of drilling.

The roles of temperature, salinity, and stress have been considered (Ghassemi et al., 2009; Zhou and Ghassemi, 2009), and it is known that for conventional rock response, cooling tends to reduce the shear failure potential while enhancing tensile failure. Also, high mud salinity reduces induced pore pressure and increases the effective radial stress at the wellbore wall. A lower mud salinity enhances flow into the rock and contributes to higher pressure distribution around a wellbore.

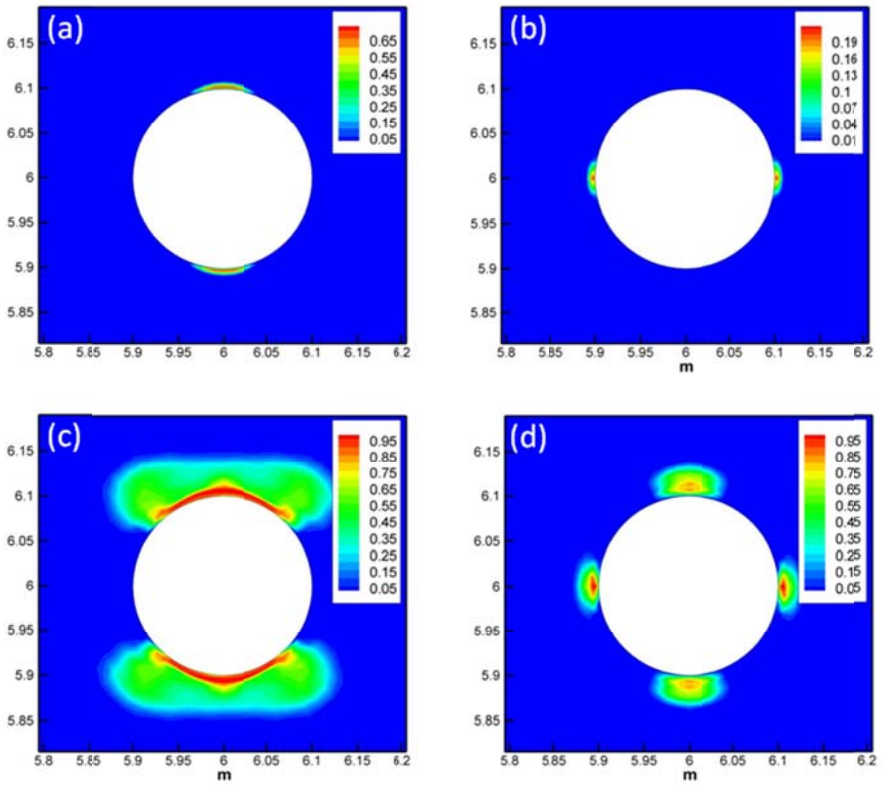

Fig. 5.5. The comparison of damage propagation at 12 hr with different coupling in numerical simulations. Results are compared with same conditions of mud salinity C_{mud} = 0.1, C_{shale} = 0.2, $S_{H,max}$ = 25 MPa, and $S_{h,min}$ = 15 MPa. Poroelastic damage I plotted in (a), cooling effects are present with thermo-poroelastic damage in (b), (c) shows the influence of osmosis flow with chemo-poroelastic behavior, (d) is fully-coupled chemo-thermo-poroelastic damage distribution.

Fig. 5.5 shows the comparison of damage propagation with respect to the degree of coupling and different chemical gradients. Note that Fig. 5.5 (a)-(d) show different rock failure distributions for different levels of coupling between thermal, poroelastic, and chemical processes. As shown in Fig. 5.5 (a), the poroelastic analysis shows that a small zone of rock damage develops in the direction of minimum stress. If cooling is taken into account, the shear failure is circumvented and no shear damage is observed. However, a small zone of tensile failure occurs in the direction of maximum in-situ stress response to cooling [Fig. 5.5 (b)]. This is because the tendency of rock to shrink reduces the compressive hoop stress and amplifies the tensile stress.

The impact of chemo-poroelastic effect is shown in Fig. 5.5 (c), where it is assumed that the drilling mud has lower salinity than shale. In this case, osmosis and chemically-induced stresses affect damage evolution around the wellbore. Fluid movement from the mud to the shale contributes to the higher pore pressure around a wellbore, leading to a large damaged area in the direction of minimum in-situ stress. The extent of failure zone is substantially reduced in this case, when the role of cooling is taken into account. Fig. 5.5 (d) shows that a fully-coupled simulation (hydraulic, thermal, and chemical osmosis) shows a much smaller shear failure zone but with a small tensile failure zone.

The distributions of pore pressure for the different coupling levels (Fig. 5.6) is the lowest in the thermo-poroelasticity case and the highest in the chemo-poroelasticity case of a lower salinity mud.

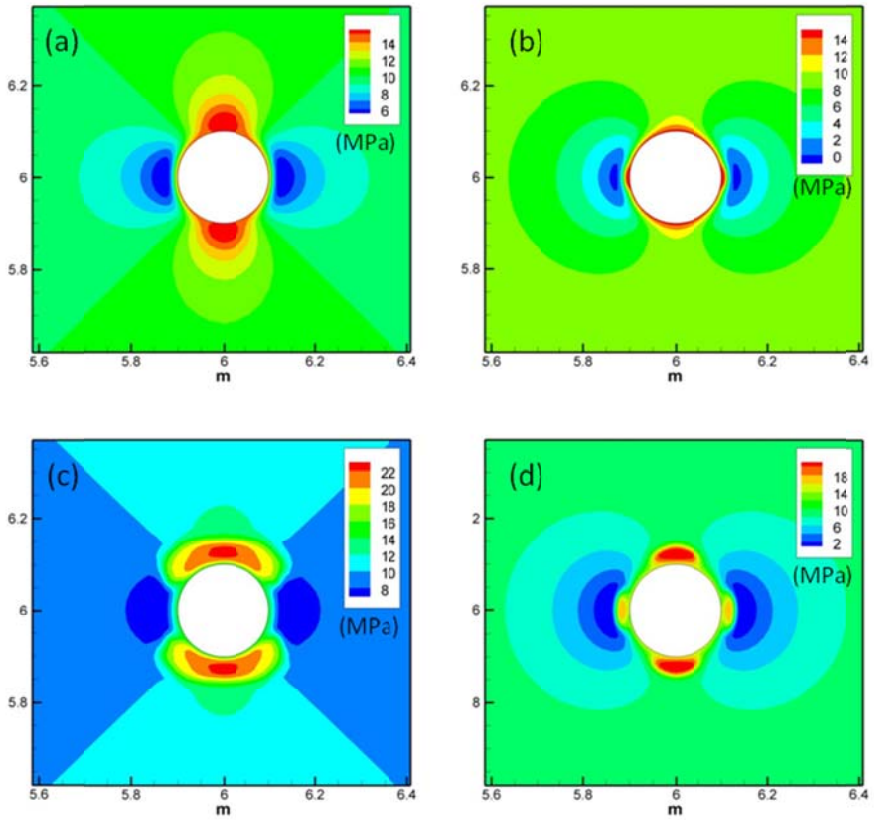

Fig. 5.6. The comparison of pore pressure distributions at 12 hr with different coupling in numerical simulations. Results are compared with same conditions of C_{mud} = 0.1 and C_{shale} = 0.2, $S_{H,max}$ = 25 MPa, and $S_{h,min}$ = 15 MPa. (a) poroelastic, (b) thermo-poroelastic, (c) chemo-poroelastic, (d) chemo-thermo-poroelastic pore pressure distribution.

The impact of stress-dependent modulus and permeability is easily captured with the model. Referring to Fig. 5.7, it is observed that the failed-zone is larger when we consider the variation of modulus and permeability. This effect can be explained by stress redistribution and the permeability effect. In constant modulus and permeability conditions, the stress distributions are same with rock failure. However, once the modulus reduced and permeability increased in the failed area, effective stresses reduced and pore pressure increased. These discontinuities in stress and pore pressure in the damage phase perform as barriers between the damaged and undamaged areas so that effective stresses are increased at the interface. This amplification of effective stresses in altered modulus and permeability resulted in larger damage distributions than constant modulus and permeability.

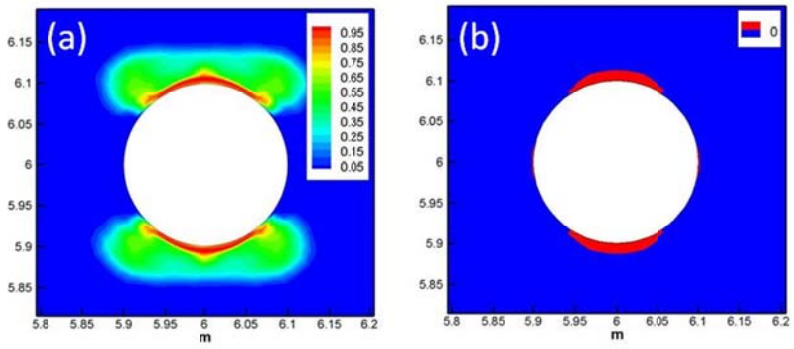

Fig. 5.7. The influence of modulus and permeability change for rock failure distributions. Results are compared with same conditions of lower mud salinity and $S_{H,\max}$ = 25 MPa, $S_{h,\min}$ = 15 MPa. (a) chemo-poroelastic rock failure with altered modulus and stress-dependent permeability (d) chemo-thermo-poroelastic rock failure with constant modulus and permeability model.

Another wellbore example to consider is the influence of mud salinity. The maximum far-field stress is 25 MPa and the minimum far-field stress is 15 MPa. We assumed that the initial pore pressure is 10 MPa and the mud pressure is 15 MPa. The initial shale formation temperature is 115 °C and the mud temperature is assumed to be 65°C. As before, two different mud salinities of 0.3 and 0.1 were considered, and the wellbore integrity was analyzed after 12 hrs of drilling.

Fig. 5.8 shows that slight damage observed to the maximum far-field stress direction when the mud salinity is higher than shale formation. When the mud salinity is lower than the formation, there are high damage by shear and tensile to the both maximum and minimum far-field stress directions. It is widely known that pore pressure increase in porous rock causes shear or tensile failure because of the effective stress reduction by fluid movement. The influence of osmosis flow from the mud to the shale causes higher pore pressure around a wellbore, and then it reached the shear and tensile failure to the maximum and minimum far-field stress direction. The comparison of pore pressure distributions around a wellbore has been presented in Fig. 5.9.

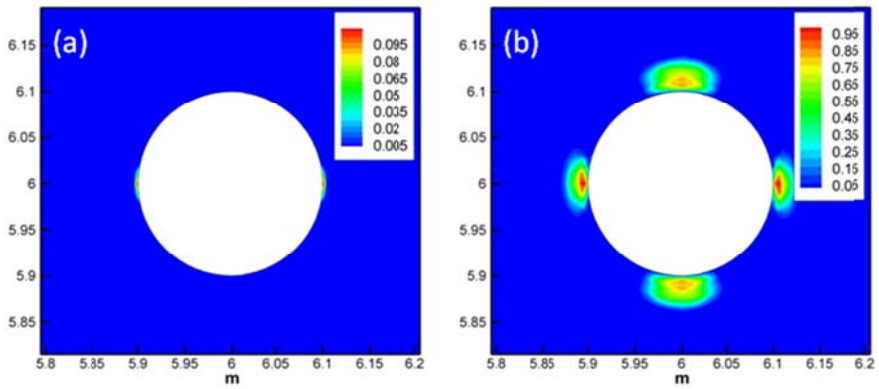

Fig. 5.8. Damage distributions at 12 hr with $S_{H,max}$ = 25 MPa, $S_{h,min}$ = 15 MPa. (a) higher mud salinity ($C_{mud} > C_{shale}$) (b) lower mud salinity ($C_{mud} < C_{shale}$)

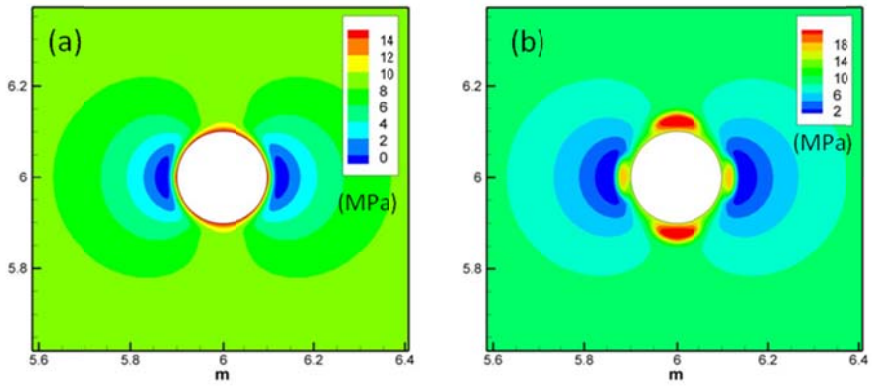

Fig. 5.9. Pore pressure distributions at 12 hr with $S_{H,max}$ = 25 MPa, $S_{h,min}$ = 15 MPa. (a) higher mud salinity ($C_{mud} > C_{shale}$) (b) lower mud salinity ($C_{mud} < C_{shale}$)

Fig. 5.10 shows the damage propagation with time. It is observed that shear failure occurred to the minimum far-field stress direction because of highly compressive effective hoop stress and then tensile failure to the maximum far-field stress direction begins as following the shear failure due to the osmosis flow invasion from the mud to the shale formation with respect to time. The distributions of temperature and solute concentration are plotted in Fig. 5.11 (a) and (b) for the case of lower mud salinity under given mud pressure, in-situ stress, initial pore pressure, and temperature. Note that the effective radial and hoop stress in Fig 5.11 (c) and (d) shows the stresses are relaxed in damage phase and redistributed around a wellbore by modulus reduction and permeability increase in failed zone.

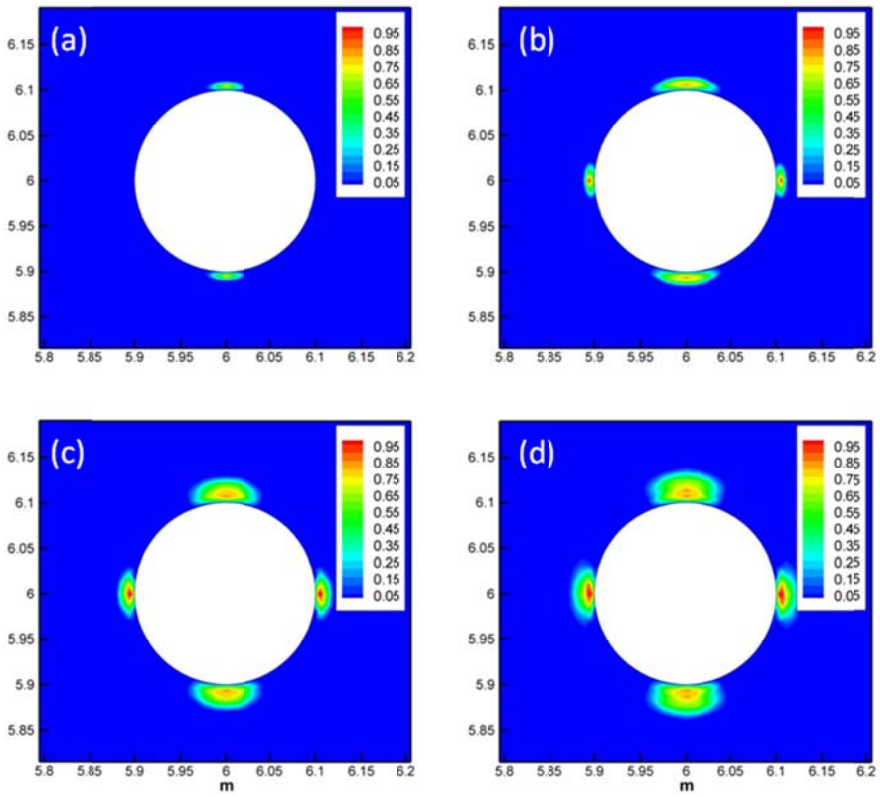

Fig. 5.10. Propagation of damage with respect to time with $S_{H,max}$ = 25 MPa, $S_{h,min}$ = 15 MPa. The case of lower mud salinity comparing shale formation (a) 0.5 hr (b) 1 hr (c) 3 hr (d) 6 hr.

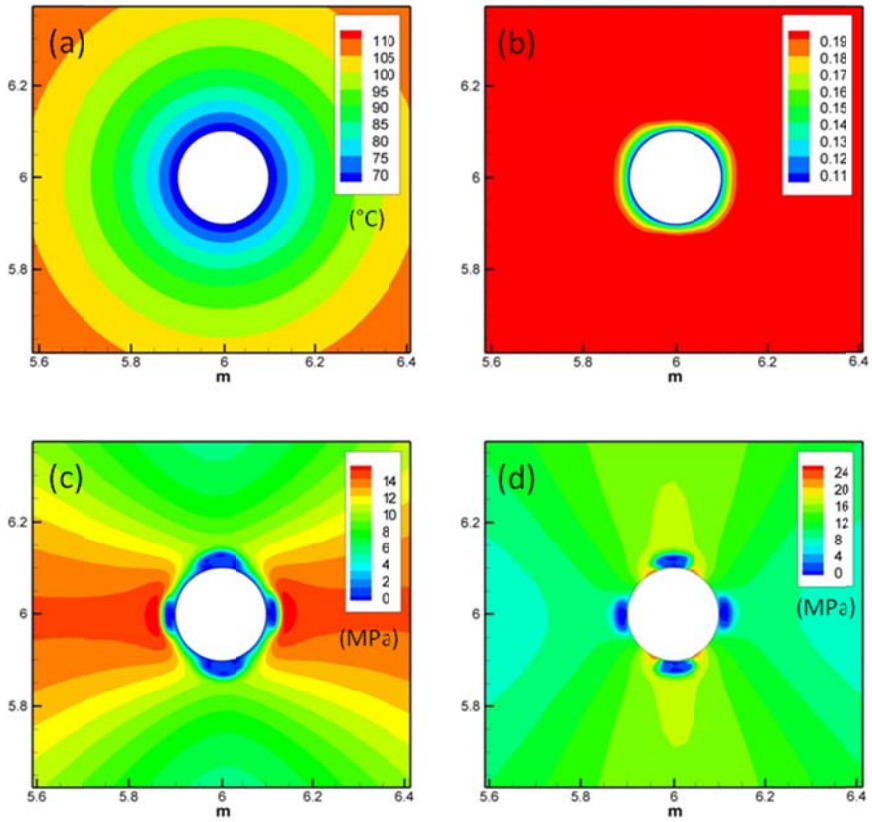

Fig. 5.11. The distributions of temperature (a), solute mass concentration (b) and effective radial and hoop stress distributions (c) and (d), respectively. All results are snap shots of 12 hr and the mud salinity C_{mud} = 0.1 and C_{shale} = 0.2 and $S_{H,max}$ = 25 MPa, $S_{h,min}$ = 15 MPa.

5.3 Conclusions

Two-dimensional fully coupled finite element methods have been developed for modeling damage-induced stress variations and permeability change around a wellbore. Results show the influence of chemical potential and thermal stress around a wellbore. It is clearly presented that the shale is unstable when the mud salinity is lower that formation by osmosis flow and cooling creates tensile stresses by the difference of thermal expansion coefficients of solid and fluid. Model can explain the different distributions of damage and pore pressure with different mud salinity. Far-field stresses are also important in wellbore stability, it tends to be reached failure condition in lower mud salinity where the far-field stress is low, although the mud pressure is set to the range of initial pore pressure and fracture gradient. In addition, the coupling of hydraulic pressure, solute transport and temperature has been compared under same conditions. Results show the impact of the osmosis and temperature in the analysis of stress distributions. This study indicates that the finite element method with damage mechanics and stress-dependent permeability model can be used to model the swelling shale.

6. Two-Dimensional Thermo-poromechanical Modeling of Well Stimulation and Induced Microseismicity

Stress analysis or rock mass failure in response to water injection is of much interest in geothermal reservoir design. The process involves coupled rock deformation and fluid flow as described in Biot's

poroelastic theory (Biot, 1941; Cryer, 1963), and its thermo-poroelastic (McTigue, 1986) and thermo-chemo-poroelastic extension (Ghassemi et al. 2009). Chemical effects can be significant with respect to the clay swelling and solute transport and reactivity. Thermo-poroelasticity can be used to assess the influence of fluid flow and temperature change on the stress variations in the reservoir. This influence is often computed assuming a linear elasticity with constant mechanical and transport rock properties. The assumption of elastic rock skeleton and fluid flow and heat transport in porous media under constant permeability conditions has limitations in predicting the real behavior of the reservoir rock. Generally, the strain-stress behavior of rocks in triaxial tests shows hardening and post-peak softening. This behavior depends on the rock type, pore pressure, stress conditions, and temperature (Jaeger, Cook, and Zimmerman, 2007). The continuum damage mechanics approach is one of the methods that can capture the hardening and softening behavior of the rock (Yuan and Harrison, 2006). Continuum damage mechanics was first introduced by Kachanov and since has been developed and applied by many researchers (Kachanov, 1958; Mazars, 1986; Simankin and Ghassemi, 2005; Tang et al., 2002; Yang et al., 2004; Selvadurai, 2004) who have investigated inelastic behavior caused by crack initiation, microvoid growth, and fracture propagation. Also, the evolution of rock damage in the presence of poroelastic and thermo-poroelastic effects has been considered. Selvadurai (2004) studied damage in poroelastic brittle rock. His results showed a significant permeability alteration caused by damage evolution in consolidation problems. Hamiel et al. (2005) developed a model with a time dependent damage variable, porosity, and material properties. They proposed different rock behavior with degradation and healing within the framework of the poroelastic theory. Tang et al. (2002) proposed a damage and permeability model based on experimental strain-stress observations and permeability measurements (Tang et al., 2002, Yang et al., 2004). The model was implemented in a finite element model and was used to simulate a uniaxial compression test and also hydraulic fracture propagation.

The permeability variations induced by altered stress and rock failure has been studied by many researchers (Shipping et al., 1994; Kiyama et al.; 1996, Coste et al., 2001; Zoback and Byerlee, 1975). Zoback and Byerlee illustrated the relation between permeability change and microcrack and void evolution. Their experimental results for tests conducted on granite show permeability increasing by a factor of four. Other studies present different magnitudes for the increase in permeability depending on rock type and conditions (De Paola et al. 2009; Wang and Park, 2002).

The stimulation of the reservoir rock mass is often accompanied by multiple microseismic events. Microseismic event characteristics such as their locations, spatial patterns of distribution, and temporal relations between the occurrence of seismicity and reservoir activities are often studied for enhanced geothermal systems (EGS). Microseismic event detection and interpretation is used for estimating the stimulated volume and fracture growth, resulting reservoir permeability, and geometry of the geological structures and the in-situ stress state (Pine, 1984). The process commonly is referred to as seismicity-based reservoir characterization. Although progress has been made in quantitative and qualitative analysis of reservoir stimulation using micro earthquakes (Shapiro et al., 1997; 1999; 2002; Rothert and Shapiro, 2003), the process of rock failure and permeability change is not considered. Also, in-situ stress and thermal effects on fluid-rock interaction have not been considered.

In this work, we present the development of a finite element model to study the influence of thermo-poro-mechanical coupling on rock damage evolution and permeability variation with reference to reservoir stimulation and induced seismicity. The damage model we used corresponds to the brittle rock failure behavior with post peak softening and permanent deformation prior to the fracture. To capture the full effects of rock cooling by injection in the presence of higher fluid fluxes caused by rock failure and permeability enhancement, the model considers both the conductive and convective heat transfer in porous media. Two types of injection schemes are considered in this work: explicit wellbore geometry for small scale simulations and a point source approach for large scale simulations. A number of numerical

simulations are presented to verify the model and to illustrate the role of various mechanisms in rock fracture.

6.1 Well Stimulation and Injection-induced Microseismicity

Two-dimensional fully-coupled thermo-poromechanical simulations have been conducted with an altered modulus and permeability model. Mesh information for these simulations is as follows: 12,000 quadrilateral elements for a 200×200 m^2 simulation domain which has a wellbore geometry with 0.1 m radius (Fig. 6.1). The reservoir rock is granite with properties listed in Table 6.1. The in-situ stress state is given by 30 MPa maximum horizontal stress in the x-direction and 20 MPa in the y-direction for minimum horizontal stress. Heterogeneous simulation was carried out using Weibull distribution functions for elastic modulus and permeability distributions. We assumed that the rock properties follow the Weibull distribution function in which the shape of the heterogeneities are n=2.0 for modulus and permeability, respectively. The same values are used for the tensile and cohesive strength distributions. The initial pore pressure is 10 MPa and wellbore pressure increased 5 MPa every 0.5 hr until it reached 30 MPa.

The simulation results are shown in Figs. 6.2 and 6.3. Injection-induced rock failure occurred around the wellbore and propagated out into the rock as shown in Fig. 6.2. In this simulation, we considered an initially anisotropic permeability distribution in the rock, and so the fluid flow in the damaged area is mostly focused in the direction of maximum permeability. Note that the far-field stress influences damage propagation significantly in this coupled fluid injection analysis. The far-field stress anisotropy around a wellbore contributes to tensile stress in the maximum far-field stress direction and causes compressive stress in the minimum far-field stress direction. Also, fluid injection causes tensile hoop stresses. Therefore, both anisotropic far-field stress and fluid-induced stress lead to tensile failure propagation in the maximum far-field stress direction. The simulated micro-seismic events are plotted in Fig. 6.3. We assumed that seismic events are checked in each Gaussian point and events occurred when the rock failed. These widely scatted events are observed in an early time step because of the initial failure. The injection-induced localized seismic events propagate into the rock with the passage of time.

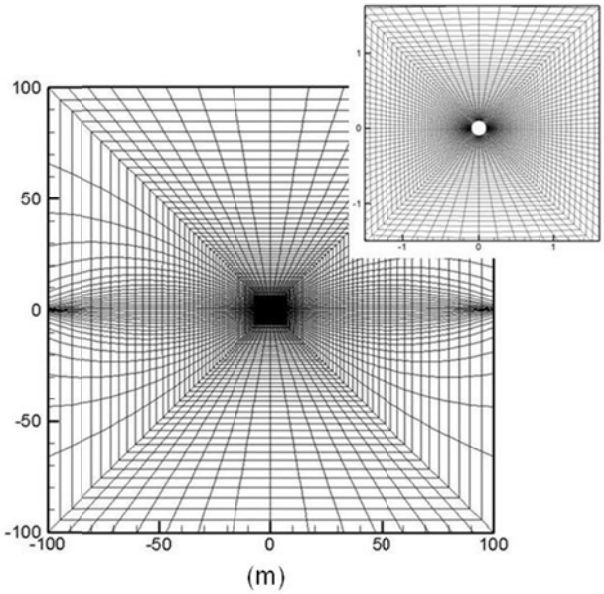

Fig. 6.1. Mesh used in damage evolution test with thermo-poro-mechanical simulations.

Table 6.1. Input material properties for granite.

Young's modulus E (GPa)	10
Drained Possoin's ratio υ	0.25
Undrained Possoin's ratio υ_u	0.33
Biot's coefficient, α	0.44
Permeability, $k_{H,\max}$ (md)	0.01
Permeability, $k_{H,\min}$ (md)	0.001
Fluid mass density, ρ_f (kg/m^3)	1111.11
Fluid viscosity, μ (Pa·s)	1×10^{-3}
Thermal expansion coefficient of solid, α_m (K^{-1})	2.4×10^{-5}
Thermal expansion coefficient of fluid, α_f (K^{-1})	2.1×10^{-5}
Thermal diffusivity, c^T (m^2/s)	2.0×10^{-6}
Porosity, ϕ	0.01

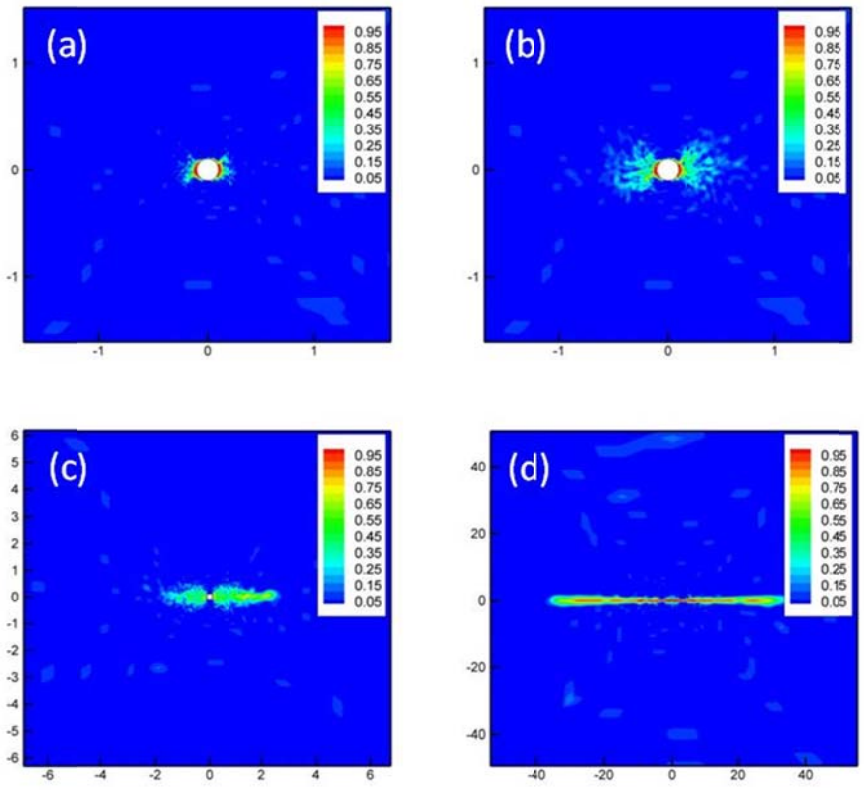

Fig. 6.2. Damage propagation with time; (a): 1 hr, (b): 3 hr, (c): 6 hr, and (d): 12 hr.

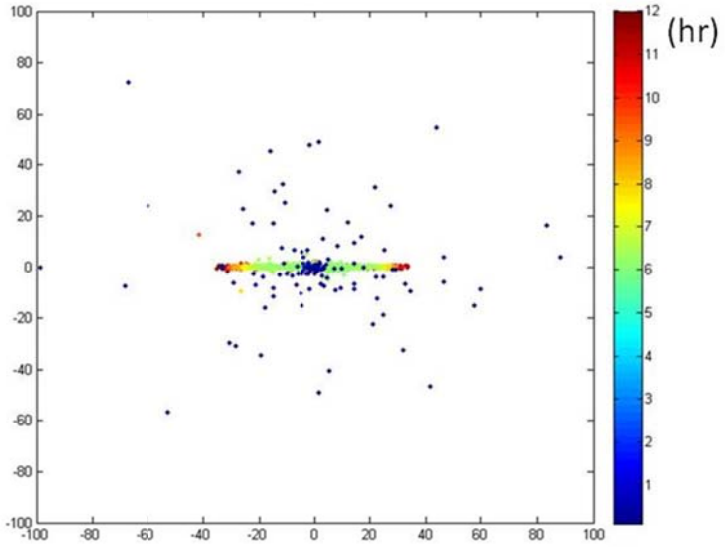

Fig. 6.3. Results of two-dimensional seismic events plot with time.

6.2 Point Source Injection and Microseismicity

We next applied two-dimensional point source injection for large reservoir simulation using quadrilateral regular mesh and anisotropic far-field stress distributions with 10,000 elements and reservoir size of 1 km × 1 km. Injection rate boundary conditions were applied to the point source element while injecting with step increases from 0.1 $m^3/m^3 \cdot s$ to 0.15 $m^3/m^3 \cdot s$. Maximum and minimum far-field stresses are 30 MPa and 20 MPa, and initial pore pressure is 15 MPa. Physical parameters for the granite reservoir we used in this simulation are described in Table 6.1. Fig. 6.4 represents the failure propagation in the homogeneous modulus and permeability to the maximum far-field stress direction with respect to time when fluid is moving from the point source to the reservoir. Results show that fluid injection induces the effective stress change where fluid contacts the area and causes tensile failure propagation in the maximum far-field stress direction. Injection-induced effective stress variations (σ_{xx}, σ_{yy}) are plotted in Fig. 6.5. In this study, rock failure propagated horizontally to tensile failure, which is similar to the previous well stimulation simulation. This horizontal propagation can be explained by the interaction of fluid with the rock skeleton that altered the modulus, and increased permeability created the stress relaxation in the damage area and amplification of stress distributions at the interface.

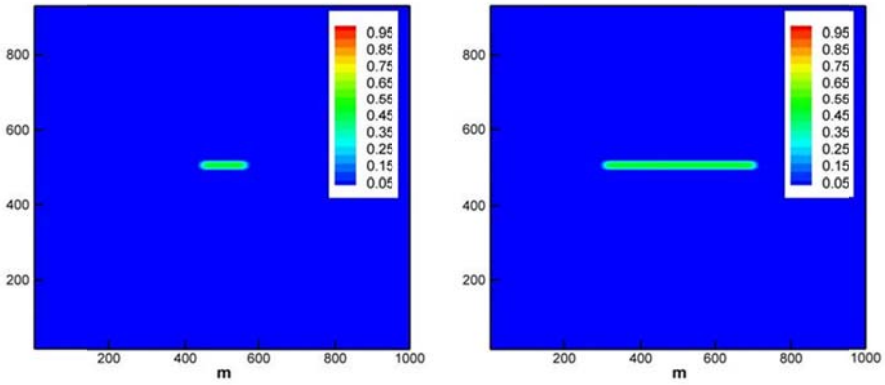

Fig. 6.4. Fluid induced damage (rock failure) distributions at 3 hrs and 12 hrs.

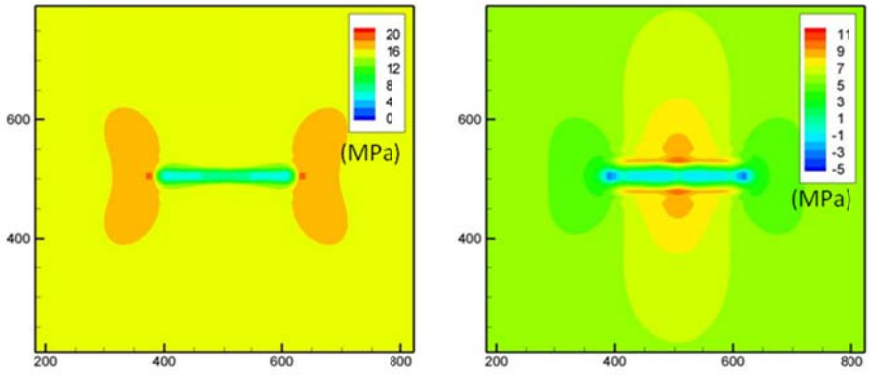

Fig. 6.5. Effective stress distribution of x (σ_{xx}) and y-direction (σ_{yy}).

Heterogeneous properties for modulus and permeability have been applied to depict more realistic simulations. We assumed that physical properties have Weibull distribution functions and seismic events are triggered when the rock stress reaches the Mohr-Coulomb failure criterion with fluid injection. Initial modulus and permeability distributions are illustrated in Fig. 6.6. We used n=2 for controlling the degree of heterogeneity in Weibull distribution functions. Initial modulus distributions varied from 2 GPa to 18 GPa with mean values of 10 GPa and the average of initial permeability was 0.01 md with a range of 0.002 ~ 0.02 md as shown in Fig. 6.6.

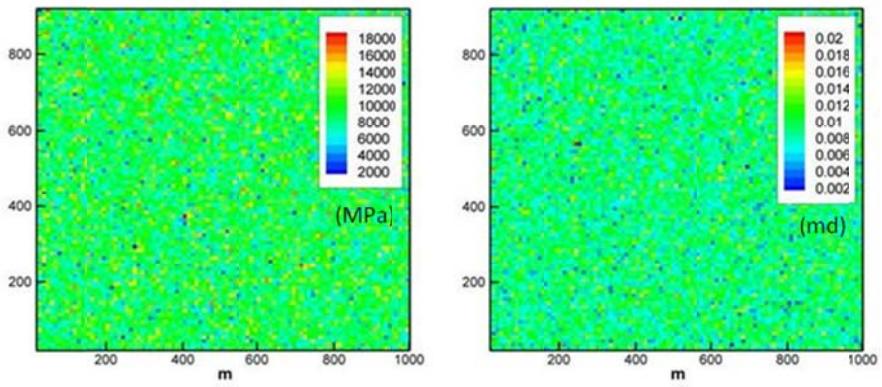

Fig. 6.6. Initial modulus and permeability distribution. The range of modulus is 2 GPa ~ 18 GPa and permeability is 0.002 ~ 0.02 md.

Results show that the damage by injection-induced rock failure propagates to the maximum far-field stress distribution; however, heterogeneity creates deviations of damage propagation caused by shear and tensile failure (Fig. 6.7). Pore pressure distributions are localized because of the permeability increase in the damaged area (Fig. 6.8). One of the features in the thermo-hydro-mechanical process of injection simulation is the localization of pore pressure caused by the localized propagation of rock failure and permeability increase. The result in Fig. 6.9 shows the seismicity plots with respect to time. Small circles are initial rock failure caused by far-field stress and large circles represent fluid injection-induced shear and tensile failure with time.

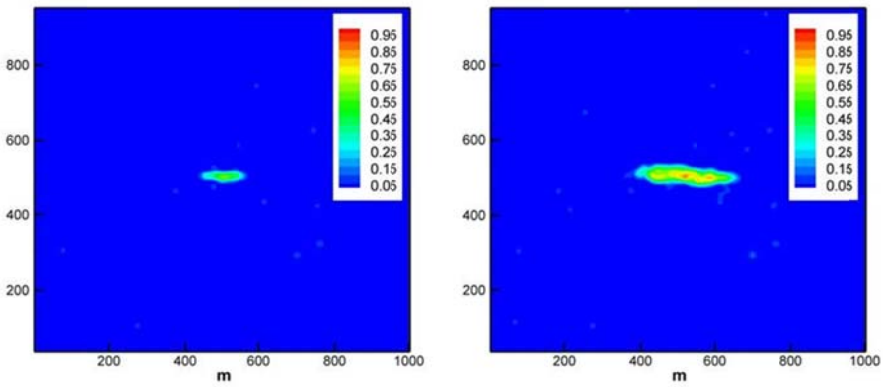

Fig. 6.7. Damage distributions at 3 hrs and 12 hrs in the heterogeneous case.

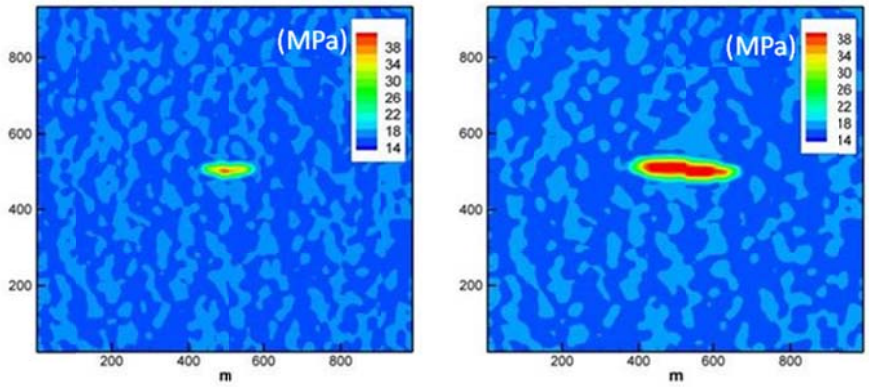

Fig. 6.8. Pore pressure distributions at 3 hrs and 12 hrs in the heterogeneous case.

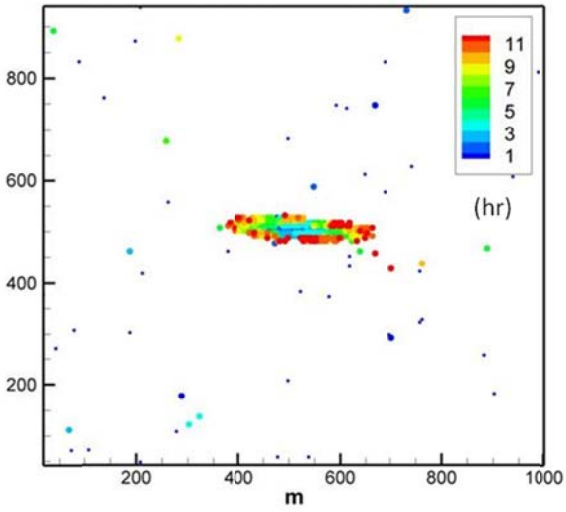

Fig. 6.9. Results for microseismic event propagation by fluid injection with time. The small circle is the initial rock failure by far-field stress and the large circle represents injection-induced triggering of microseismic events.

6.3 Discussion

Thermo-poroelastic modeling for microseismic event propagations with damage mechanics and the stress-dependent permeability model are presented in this section. Previous work from Shapiro (1997; 1999; 2002) for microseismicity modeling was developed from the fluid flow equation and criticality. He introduced concept of criticality values for pore pressure, assuming that microseismic events occurred if the pore pressure exceeded a certain value of criticality. This approach is reasonable from a certain point of view, because usually high pore pressure is needed to trigger rock failure. Shapiro's approach also has limitations in that it takes no consideration of permeability change, localization of stress distribution, or temperature effects in microseismic event modeling. Fig. 6.10 illustrates the simulation results for induced microseismicity with critical pressure and rock failure criteria. We applied the same heterogeneity and injection schedule. Maximum far-field stress is to the x-direction and minimum far-field stress is to the y-direction. Results show that microseismic events propagate in an isotropic manner

in critical pressure conditions, as opposed to the rock failure criterion. From the comparison, we conclude that the rock failure criterion can more effectively describe the ellipsoidal patterns from observation data. The main differences in this numerical simulation from Shapiro's model are the coupled impact of fluid flow, temperature, and stress change for the analysis of microseismic event propagation. The other improvement in this simulation is that permeability increases in the event locations, leading to the discontinuity of pore pressure and stress relaxations. In turn, it can explain the propagation of localized microseismic events in certain conditions. The influence of convective heat transfer is plotted in Fig. 6.11. Results show a larger region of cooling by permeability increase when we consider the convective heat transfer. The impact of convective heat transfer becomes important when the model considers fluid flow in fractures.

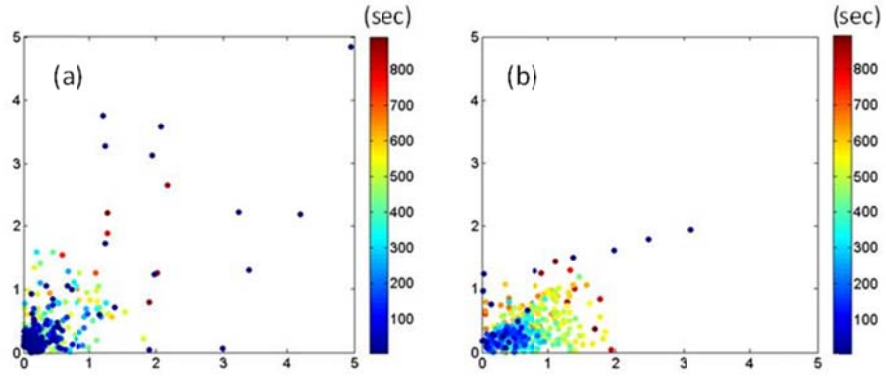

Fig. 6.10. Comparison of injection-induced microseimic event propagation under the same initial heterogeneity and injection schedule. Microseismic events based on critical pressure are plotted in (a), and rock failure criteria are plotted in (b).

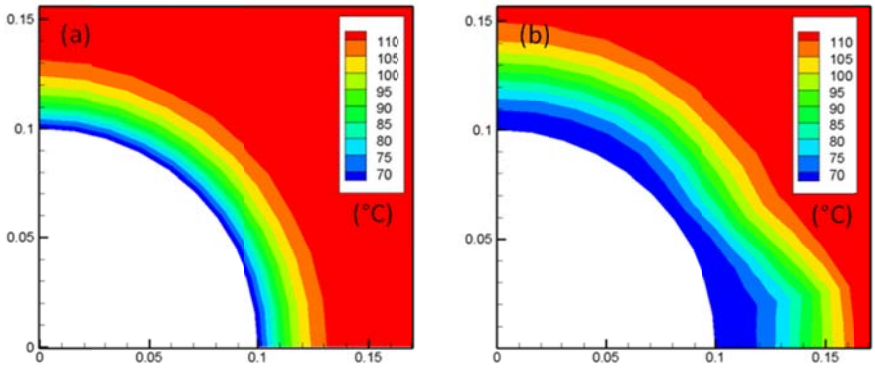

Fig. 6.11. Comparison of temperature distributions between conductive cooling and convective heat transfer in simulation of a sandstone reservoir which has 10 md for initial permeability and 100 md after rock failure. Only the conductive heat transfer case is plotted in (a) and convective with conductive heat transfer is plotted in (b). Both results are the snap shots at 180 sec.

6.4 Conclusions

Damage mechanics and the stress-dependent permeability model have been applied to fully-coupled thermo-poroelasticity. It is observed that effective stresses are relaxed in the damaged area and increased at the interface of the damaged and intact rock by the change of modulus and permeability with injection-induced rock failure. The model has been applied to the microseismic event simulation. Two types of injection schemes are used for geometrical well injection in small scale simulations and point source injection in large scale simulations. Results show distributed shear and tensile failure in the reservoir. The resulting rock failure and permeability enhancement is a function of the in-situ stress. Realistic patterns of micro-seismicity have been generated. Results show the significant roles of stress state and initial rock permeability in the resulting pattern. The results of this study indicate that the finite element method with damage can be used to model reservoir stimulation and induced seismicity.

7. Three-Dimensional Finite Element Modeling of Thermo-poromechanical Well Stimulation and Injection-induced Microseismicity

The study of stress variations by fluid injection is important in enhanced geothermal reservoir (EGS). Especially near the wellbore, there is a significant change of stresses by temperature, fluid flow and far-field stresses. The influence of fluid flow and porous rock has been developed by Biot (Biot, 1941; Cryer, 1963), and its extension version of thermo-poroelasticity has been proposed (McTigue, 1986; Kurashige, 1995; Wang and Papamichos, 1994). They showed that the impact of thermo-poroelasticity around a wellbore that thermally-induced pore pressure distribution is significant if the rock permeability is low. The influence of chemical potential also has been developed that considered the influence of chemical potential, temperature and fluid flow in shale (Heidug and Wong, 1996; Ghassemi and Diek, 2003; Ghassemi et al., 2009). Most of the geothermal reservoir rock is granite so that we should consider the low permeable and brittle rock with cold water injection. Thermo-poroelasticity can be used to assess the influence of temperature and fluid flow change on the stress variations; however, there are some limitations that the rock skeleton is assumed to be elastic and constant permeability in fluid flow. Generally, the modulus and permeability are changed if the rock reaches the failure criterion. The strain-stress behavior in triaxial test shows hardening and softening after post-peak stress. This behavior depends on the rock type, pore pressure, stress condition and temperature (Jaeger, Cook, and Zimmerman, 2007). Experimental results for permeability variation with stress also have been studied by many researchers (Shipping et al., 1994; Kiyama et al.; 1996, Coste et al., 2001; Zoback and Byerlee, 1975). Their experimental results for tests conducted on granite show permeability increase by a factor of four. Other studies present different magnitudes for the increase in permeability depending on rock type and conditions (De Paola et al. 2009; Wang and Park, 2002).

Continuum damage mechanics is used to consider the crack initiation, void growth, and crack propagation that can capture the hardening and softening behavior of a rock. Continuum damage mechanics was first introduced by Kachanov and since has been developed and applied by many researchers (Kachanov, 1958; Mazars, 1986; Simankin and Ghassemi, 2005; Tang et al., 2002; Li et al., 2005; Selvadurai, 2004). It can be contrasted with fracture mechanics in that damage mechanics describes crack initiation, microcracks, void growth, and crack propagation based on the failure criterion, whereas fracture mechanics assumes an initial crack for propagation. The impact of damage mechanics has been applied in the presence of poroelasticity. Selvadurai (2004) studied damage in poroelastic consolidation problems with a stress-dependent permeability model. His results showed a significant permeability alteration caused by damage evolution in consolidation problems. Hamiel et al. (2005) developed a model with time dependent damage

variable, porosity, and material properties. They proposed different rock behavior with degradation and healing within the framework of the poroelastic theory. Tang et al. (2002) proposed a brittle damage and permeability model based on experimental strain-stress observations and permeability measurements (Tang et al., 2002; Li et al., 2005). The model was implemented in a finite element model and was used to simulate a uniaxial compression test and hydraulic fracture propagation.

Damage mechanics has an advantage of considering the microfracture so that it can be one of the promising tools to predict injection-induced microseismic events. Microseismic event characteristics such as their locations, spatial patterns of distribution, and the temporal relation between seismicity and reservoir activities are often studied for enhanced geothermal systems (EGS). Microseismic event detection and interpretation is used for estimating the stimulated volume and fracture growth, resulting reservoir permeability, and geometry of the geological structures and the in-situ stress state (Pine, 1984). The process commonly is referred to as seismicity-based reservoir characterization. Although progress has been made in quantitative and qualitative analysis of reservoir stimulation using micro earthquakes (Shapiro et al., 1997; 1999; 2002; Rothert and Shapiro, 2003), the process of rock failure and permeability change has not been considered. In-situ stress and thermal effects on fluid-rock interaction have also not been considered.

In this work, we present the development of a three-dimensional (3D) finite element model to study the influence of thermo-poro-mechanical coupling on rock damage evolution and permeability variation with reference to reservoir stimulation and induced seismicity. The damage model we used corresponds to brittle rock failure with post-peak softening and permanent deformation prior to fracture. In order to capture the full effects of rock cooling by injection in the presence of higher fluid fluxes caused by rock failure and permeability enhancement, the model considers both the conductive and convective heat transfer in porous media. A number of numerical simulations are presented to verify the model and to illustrate the role of far-field stress and permeability change in rock fractures, distributed damage evolution, and induced seismicity.

7.1 Injection-induced Damage Propagation

In this section, we present numerical examples for hydraulic fracturing experiments under the influence of different far-field stresses while taking into account fluid and temperature variations around a wellbore. Before conducting large reservoir simulations, we tested a small simulation domain consisting of a 3D block of rock with dimensions of $10\times10\times5$ m^3 (Fig. 7.1) with a 0.2-m injection interval. We use an 8-noded hexahedron element for displacement and 8 nodes for pore pressure and temperature. All reservoir properties represented a granite reservoir (Table 6.1).

We compared the numerical solutions with analytical solutions for effective vertical stress distribution. We assumed zero far-field stress and pore pressure on the wall acting with 10 MPa along the vertical wellbore surface. The induced effective vertical stress component contributes to tensile stress since the pore pressure invasion to the reservoir leads the effective stress distribution from zero to the tensile stress as seen in Fig. 7.1. The plot in Fig. 7.2 compares the numerical solutions for effective vertical stress with analytical solutions with time. The comparison of pore pressure, total radial stress components, and total tangential stress components are presented in Figs. 7.3 to 7.5.

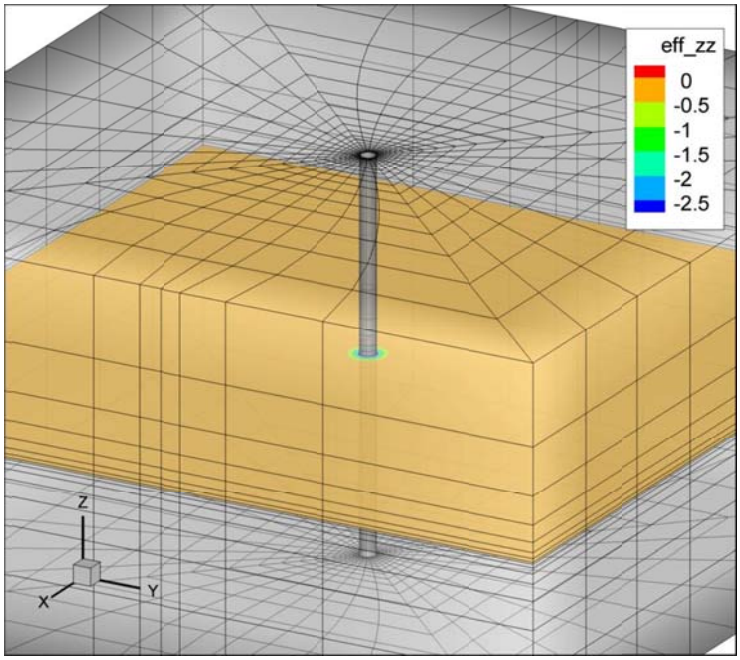

Fig. 7.1. Induced effective vertical stress variation by fluid injection.

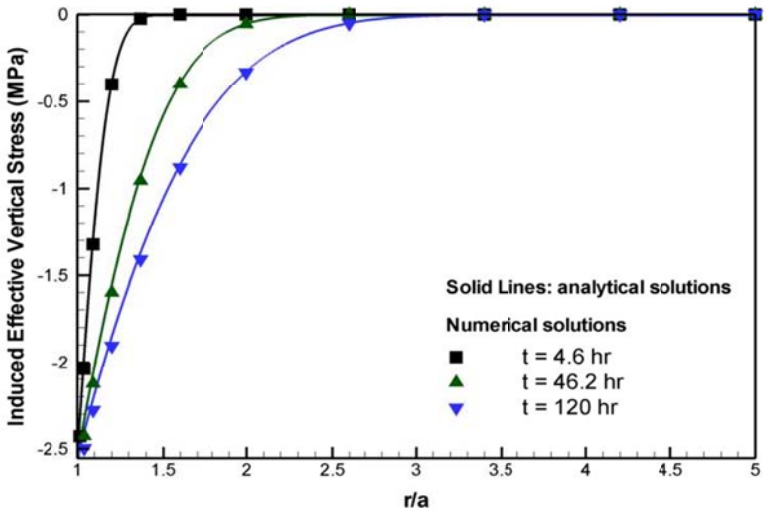

Fig. 7.2. Comparison of numerical solutions with analytical solutions for effective stress component, $S'_{zz,}$ distribution.

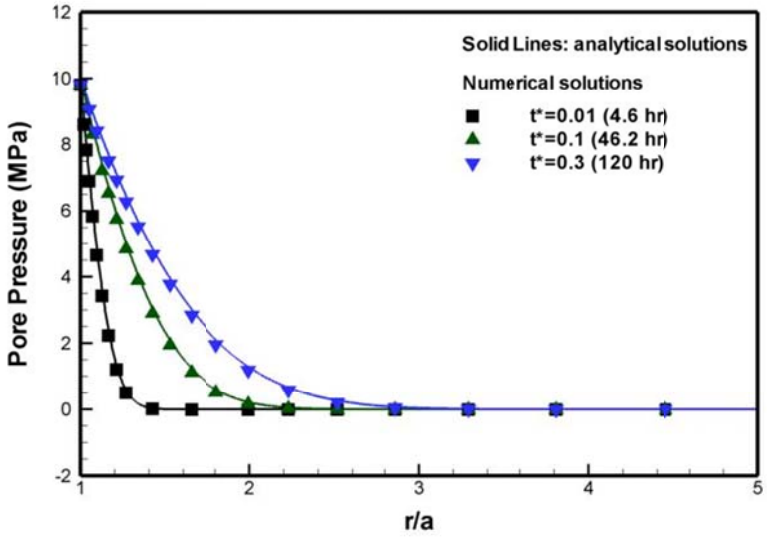

Fig. 7.3. Comparison of numerical solutions with analytical solutions for pore pressure distribution along to the radial direction.

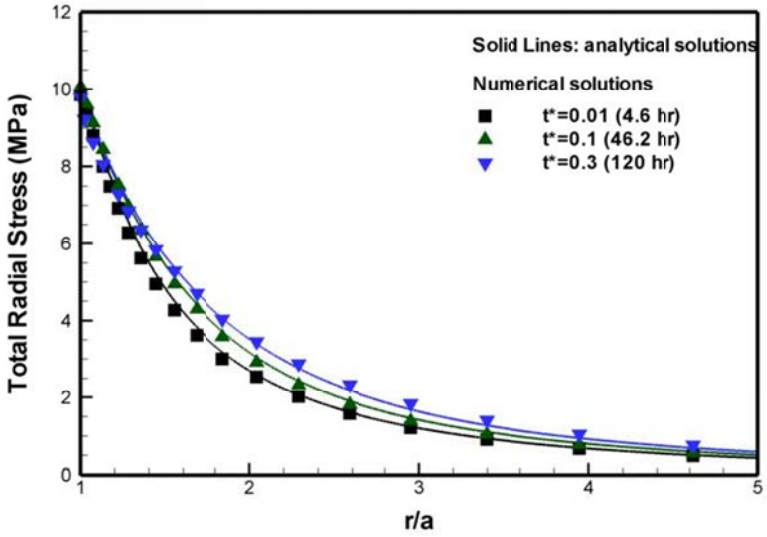

Fig. 7.4. Comparison of numerical solutions with analytical solutions for total radial stress, S_{rr}, distribution.

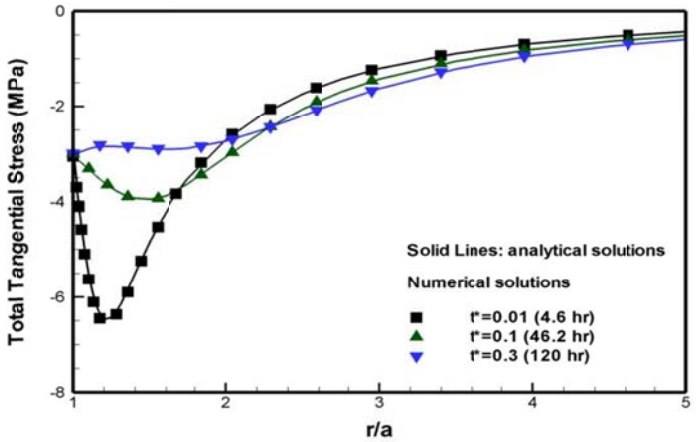

Fig. 7.5. Comparison of numerical solutions with analytical solutions for effective stress component, $S_{\theta\theta}$, distribution.

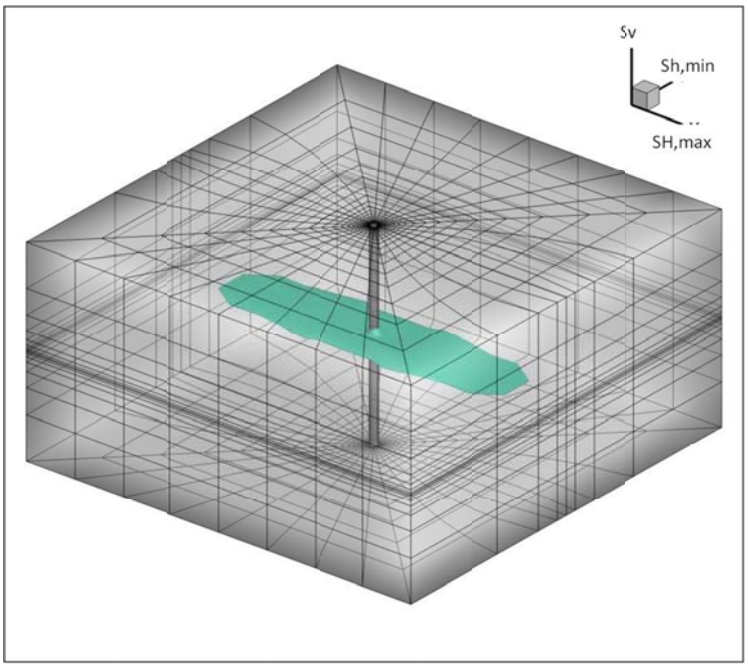

Fig. 7.6. Iso-surface (20%) of injection induced damage variable for the case when the minimum in-situ stress is S_v.

For the analysis of injection-induced rock failure and permeability change, we assumed that permeability in the maximum far-field stress direction (x-direction) is 5 times higher than that in the minimum far-field stress direction (y-direction). The vertical permeability value is assumed to be 10% of the permeability in the minimum far-field stress direction. The experimental results for the permeability anisotropy showed that the permeability path is higher in the maximum stress direction (Khan and Teufel, 2000). In this example, the maximum horizontal stress is 30 MPa (x-direction), minimum horizontal stress is 20 MPa (y-direction), and the vertical stress is 10 MPa (z-direction). The injection pressure starts at 13 MPa and is increased at 0.5-hr intervals until it reaches 20 MPa

The iso-surface of the area damaged 20% by 6-hr fluid injection is plotted in Fig. 7.6. The permeability and pore pressure distributions in the fracture zone are represented in Fig. 7.7. Note that axial stress (σ_{zz}) distribution and horizontal tangential stress contribute to failure around the wellbore. In our fracture simulation, the damaged area (microcrack and void-growth area) becomes sharper when damage variable convergences are satisfied. Also, the anisotropic permeability model under anisotropic far-field stress shows more realistic results since fluid injection plays an important role in this process and its simulation.

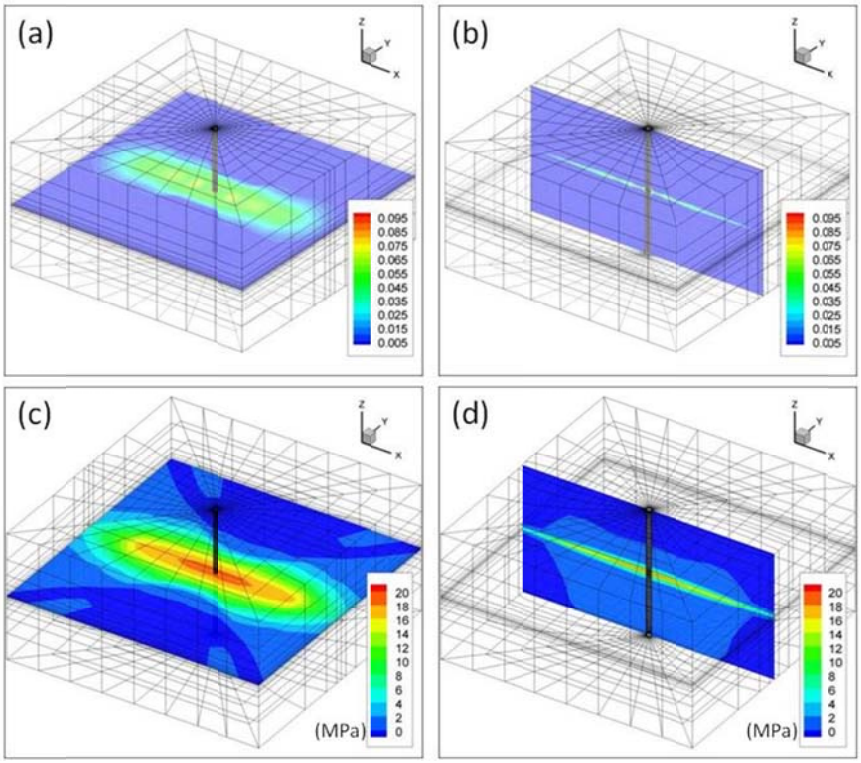

Fig. 7.7. Cross sectional view of permeability and pore pressure distributions. Results are for a time of 6 hrs. Permeability distributions: (a) and (b); pore pressure distributions: (c) and (d). See Table 7.1 for units. Unit for permeability is md.

7.2 Damage Propagation under Different Stress Regimes

After carrying out small reservoir geomechanical simulations, we conducted large scale reservoir simulations using a large mesh with 83,232 8-noded hexahedron elements for a reservoir size of 240×120 ×150 m^3 as shown in Fig. 7.8. We tested three different far-field stress regimes: strike-slip: ($S_{H,\max}$=30 MPa, $S_{h,\min}$=10 MPa, S_v=20 MPa), with horizontal far-field stresses as the maximum and minimum in-situ stresses; thrust ($S_{H,\max}$=30 MPa, $S_{h,\min}$=20 MPa, S_v=10 MPa), with vertical far-field stress as the minimum stress component; and normal faulting ($S_{H,\max}$=20 MPa, $S_{h,\min}$=10 MPa, S_v=30 MPa), with the vertical far-field stress as the maximum in-situ stress component. All reservoir properties are the same as the previous simulations, and permeability anisotropy is oriented according to the far-field stress direction; for example, $k_{h,\min}=0.1\times10^{-3}$ md, $k_{H,\max}=10\times10^{-3}$ md, and $k_v=0.1\times10^{-3}$ md are applied for the strike-slip regime, $k_{h,\min}=1\times10^{-3}$ md, $k_{H,\max}=10\times10^{-3}$ md, and $k_v=0.1\times10^{-3}$ md for the thrust regime, and $k_{h,\min}=0.1\times10^{-3}$ md, $k_{H,\max}=1.0\times10^{-3}$ md, and $k_v = 0.1\times10^{-3}$ md are applied for the normal fault regime.

Table 7.1. Reservoir properties used in the simulations.

	Case 1 (Strike-Slip)	Case 2 (Thrust)	Case 3 (Normal)
$S_{H,\,max}$	30 MPa	30 MPa	20 MPa
$S_{h,\,min}$	10 MPa	20 MPa	10 MPa
S_v	20 MPa	10 MPa	30 MPa
$k_{H,\,max}$ (md)	10×10^{-3}	10×10^{-3}	0.1×10^{-3}
$k_{h,\,min}$ (md)	1×10^{-3}	1×10^{-3}	1×10^{-3}
k_v (md)	0.1×10^{-3}	0.1×10^{-3}	0.1×10^{-3}

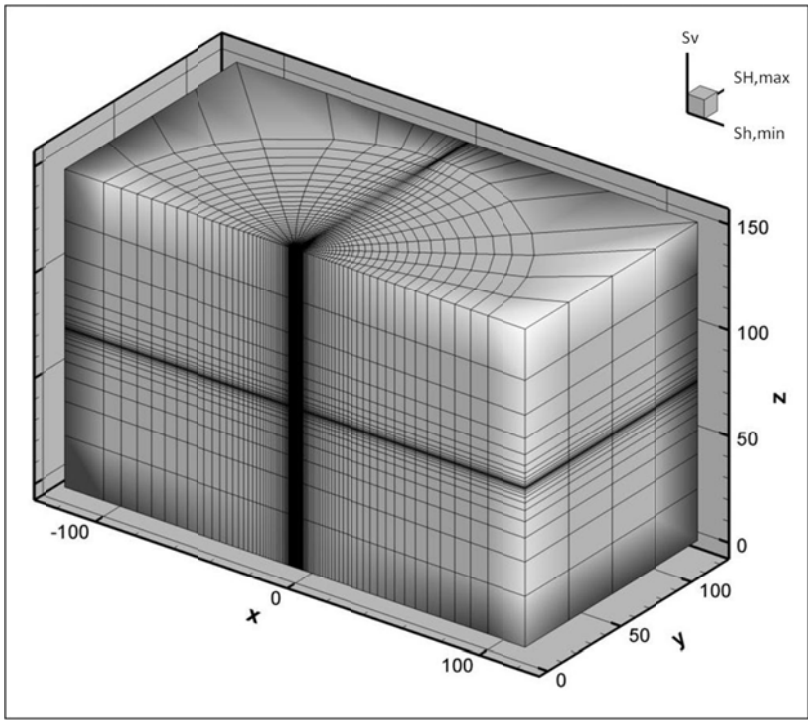

Fig. 7.8. Mesh used in simulation; $S_{H,\max}$ represents maximum horizontal stress, $S_{h,\min}$ is minimum horizontal stress, and S_v is vertical stress.

In these simulations, damage propagation caused by fluid injection was investigated in relation to the in-situ stress regime. The first case was when the minimum in-situ stress is horizontal (Case 1). The injection interval zone is 2 m and injection pressure begins at 8 MPa and is increased at 2.5 MPa increments every 0.5 hr until it reaches 32 MPa. Fluid injection causes both effective tangential and effective axial stresses to become tensile. These two stress components contribute to tensile principal

stress inside the rock. Fig. 7.9 shows the 20% damaged area. Note that damage and fractures propagate vertically and horizontally in this case where the minimum stress is horizontal. Height growth occurs rapidly near the wellbore where the axial stress effects dominate. Away from the wellbore, the in-situ stress controls the manner of damage zone propagation similar to a hydraulic fracture. The effective axial stress and pore pressure distributions are shown in Fig. 7.10.

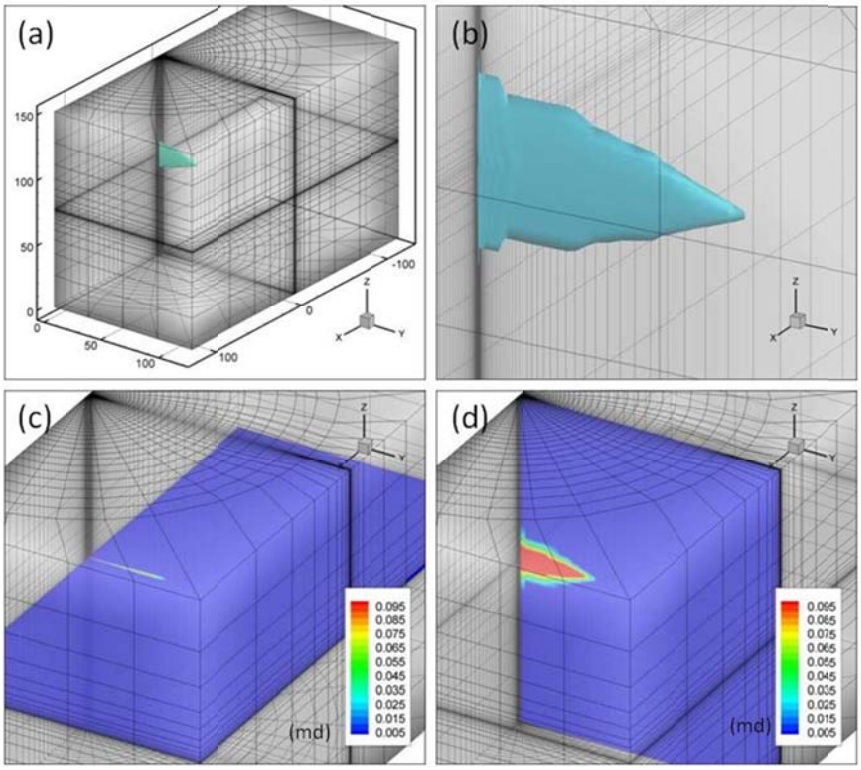

Fig. 7.9. Damage and permeability distributions for minimum horizontal far-field stress at 12 hrs. 20 % damage of iso-surface is plotted in (a), and (b) is a magnified image. Cross-sectional views of permeability distributions are illustrated in (c) and (d).

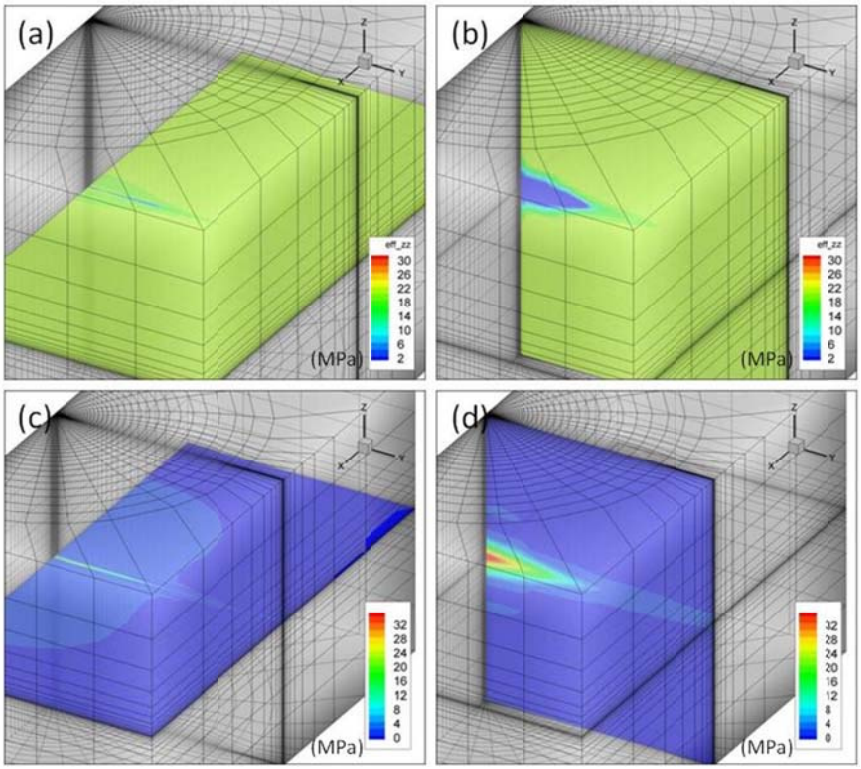

Fig. 7.10. Effective vertical stress and pore pressure distributions for minimum horizontal far-field stress at 12 hrs. Cross-sectional views of effective vertical stress are in (a) and (b), and pore pressure distributions are in (c) and (d), respectively.

For Case 2, the vertical minimum in-situ stress regime, the injection interval zone is 0.2 m and the pressure begins at 20 MPa and increases at 2.5 MPa at 0.5 hr until it reaches 42 MPa. Fig. 7.11 shows the fluid- induced 20% damaged area and the permeability distribution. Results show that injection-induced damage and the fractured area propagate horizontally. The propagation of damage is much larger in the maximum horizontal far-field stress direction than in the minimum horizontal far-field stress direction, which is influenced by permeability anisotropy.

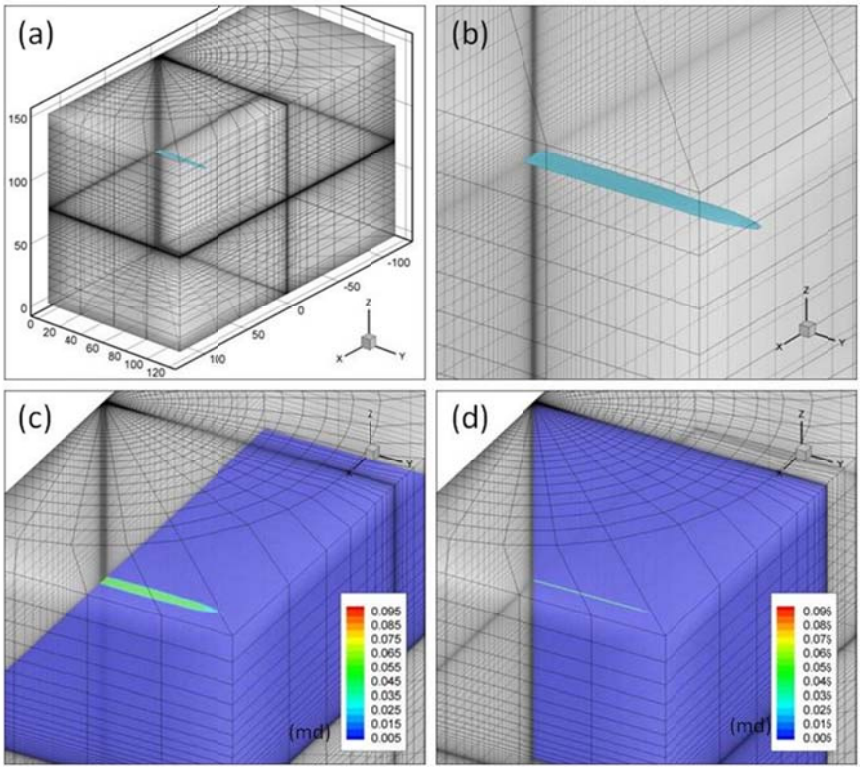

Fig. 7.11. Damage and permeability distributions for minimum vertical far-field stress at 6 hrs. 20 % damage of iso-surface is plotted in (a) and (b) is magnified image. Cross-sectional view of permeability distributions are illustrated in (c) and (d).

For the Case 3, vertical stress as the maximum far field stress, the same injection rate conditions of Case 1 are used for the comparison of the normal fault regime with the strike-slip regime (Case 1). The only different properties are far-field stress distribution and permeability anisotropy because maximum far-field stress directions are varied from the y-direction to the z-direction. Results show a stronger tendency for the induced damaged and fractured zone to propagate vertically; however, as shown in Fig 7.12, the damage area is smaller (for the same injection rate of Case 1) because of the influence of the large, vertical far-field stress.

The different geometry of the failure plane for the case of $S_{h,\min}$ and S_v as the minimum in-situ stress components can be attributed to different patterns of fluid and stress distribution in each case. In this simulation, the effective axial stress caused by fluid injection and deviatoric stress from the horizontal far-field stress are the main contributors to tensile failure across the wellbore for case 1 and case 3 ($S_{h,\min}$ as the minimum). However, in the case of S_v as the minimum stress, the effective axial stress is not significant compared to the minimum $S_{h,\min}$ and the wellbore hoop stress which serve to propagate the damage. We observe that a higher injection pressure is needed to generate the fracture plane in the homogeneous rock case, when *Sv* is the minimum in-situ stress rather than $S_{h,\min}$, because of the effective stress contributions for tensile failure. This is reasonable since there is additional hoop tensile stress (as opposed to only axial) when the fracture is initiated in a vertical plane.

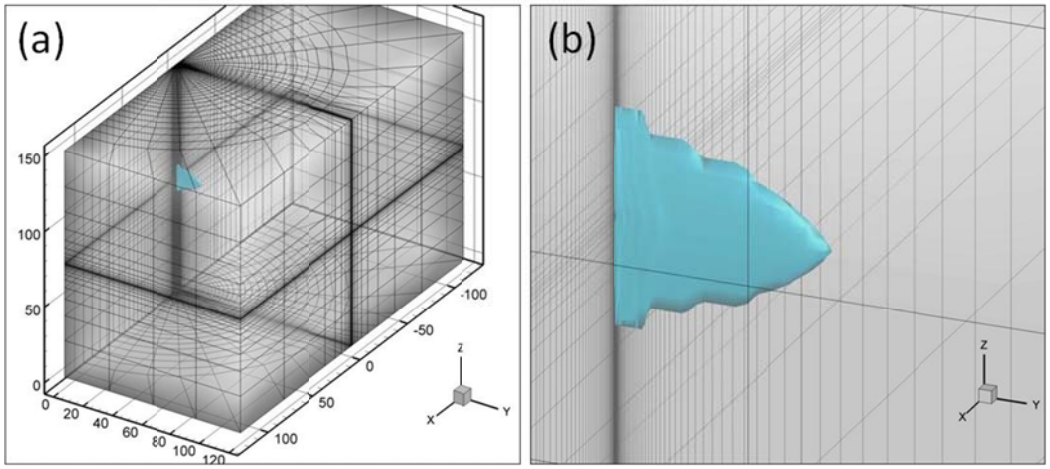

Fig. 7.12. Damage and permeability distributions for minimum vertical far-field stress at 6 hrs. 20 % damage of iso-surface

The variation of damage propagations with time for the strike-slip, thrust, and normal fault regimes are illustrated in Figs. 7.13 to 7.15 for comparison.

Hydraulic fracturing with cold water injection has been illustrated in Fig 7.16. Initial reservoir temperature is 200 °C and cold water temperature is 65 °C. Injection pressure is maintained 35 MPa for 6 hr, starting from 8 MPa. Both fluid injection and temperature difference contribute to fracture propagation. In this simulation, we assume the hydraulic fracture (macrocrack) as 90% damage. Results show that the 90% damage zone length is 24 m, height is 8 m, and average thickness near the well 10 cm. Note that temperature distribution is influenced by fluid flow, which is related with convective heat transfer, but the transfer rate is very slow. It is important to define the hydraulic fracturing in fluid injection. The main difference in the theory of fracture and damage mechanics is that the fracture considers macrocrack propagation, whereas damage mechanics considers the micro-fracture. Macrocrack propagation can be explained to be a sudden localization of microcracks (Mazars and Pijaudier-Cabor, 1996) so that the distributions of damage are generally broader than fracture propagations.

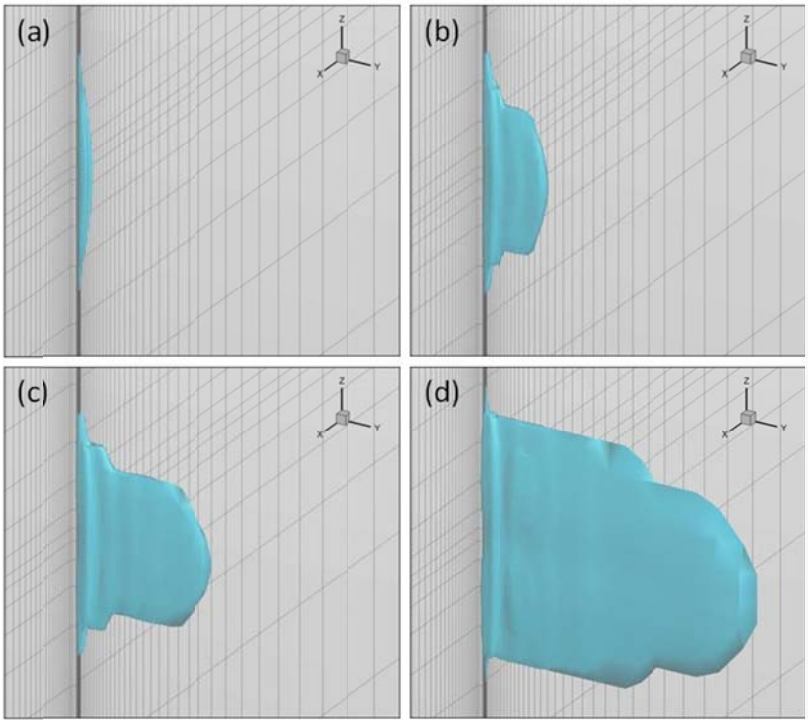

Fig. 7.13. Iso-surface 20% damage plot of 3D damage propagation with respect to time under horizontal far-field stress as the minimum: (a): 0.5hr, (b**)**: 1 hr, (c): 1.2 hr, (d): 1.5 hr.

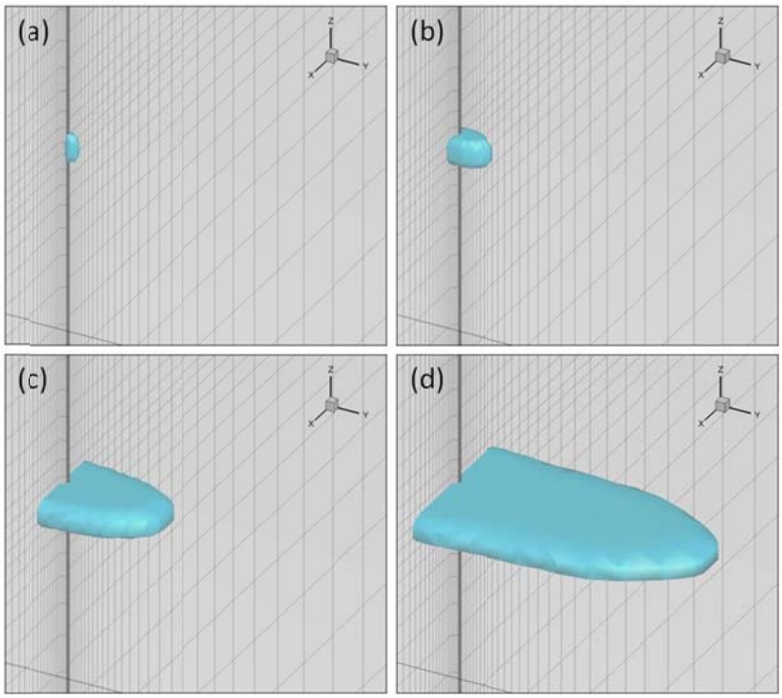

Fig. 7.14. Iso-surface 20% damage plot of 3D damage propagation with respect to time under vertical far-field stress as the minimum: (a): 1 hr, (b): 1.2 hr, (c): 1.5 hr, (d): 1.9 hr.

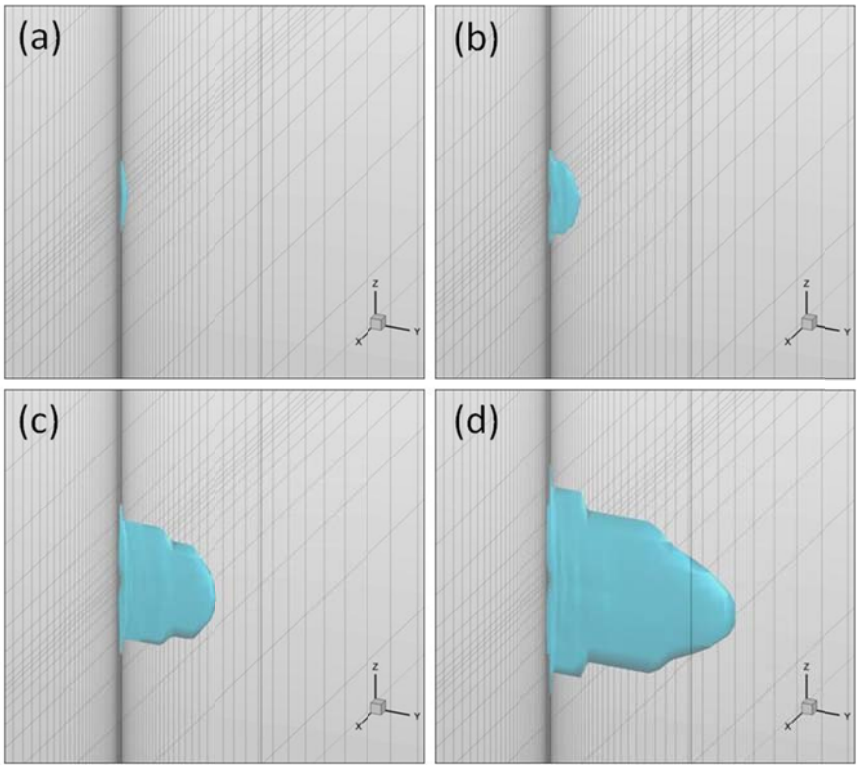

Fig. 7.15. Iso-surface 20% damage plot of 3D damage propagation with respect to time under vertical far-field stress as the maximum: (a): 1 hr, (b): 1.5 hr, (c): 2 hr, (d): 3 hr.

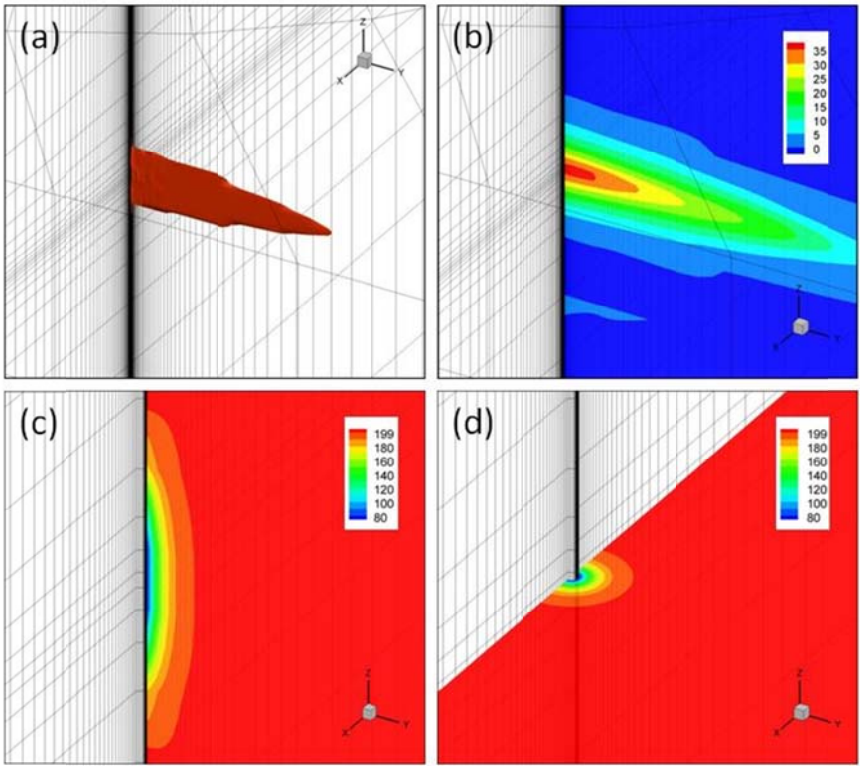

Fig. 7.16. Plot for hydraulic fracturing zone (90% damaged area) with minimum horizontal (a) and pore pressure distribution (b). Different plane views of temperature distributions in (c) and (d). All results have the same time step at 6 hr.

7.3 Injection Volume Analysis

The influence of injection volume under different stress regimes is reported in this section. Well pressure in this comparison is a step increase of 15 to about 44 MPa for normal regimes and 20 to about 48 MPa for thrust regimes. Initial well pressure is set to the pressure before the rock failure and damage evolution begins after the next step increase of wellbore pressure. Fig. 7.17 shows the comparison of a 40% damaged area with different far-field stresses when we inject 968 L for 3 days in the normal regime ($S_{H,\ max}$ = 20 MPa, $S_{h,\ min}$ = 10 MPa, S_v = 30 MPa, $k_{H,\ max} = 10\times10^{-3}$ md, $k_{h,\ min} = 1\times10^{-3}$ md, and $k_v = 0.1\times10^{-3}$) and 340 L for 3 days in the thrust regime ($S_{H,\ max}$ = 30 MPa, $S_{h,\ min}$ = 20 MPa, S_v = 10 MPa, $k_{H,\ max} = 1\times10^{-3}$ md, $k_{h,\ min} = 1\times10^{-3}$ md, and $k_v = 0.1\times10^{-3}$ md). The normal regime led to a larger damaged area and higher injection volume than the thrust regime. This is because of the influence of the horizontal deviatoric stress to increase damage distribution with similar injection pressure schedules. Injection pressure is similar to the case of thrust regime, but tangential stress creates larger failure in the maximum far-field stress direction around a wellbore in the normal regime. However, in the thrust regime the contribution of tangential stress is weak and induced vertical stress cause it to fail. Results indicate that larger damage and injection volume can be predicted with the same injection pressure where the minimum far-field stress is horizontal than in the thrust regime. The thrust regime needs a higher injection pressure schedule to create a fracture plane with given far-field stress condition.

Damage distribution and injection volume have been studied in the same injection pressure schedule with different far-field stress (Fig. 7.18). The conditions for far-field stress and permeability are $S_{H,\ max}$ = 20

MPa, $S_{h,\ \min}$ = 10 MPa, S_v = 30 MPa, $k_{H,\ \max}$ = 10×10^{-3} md, $k_{h,\ \min}$ = 1×10^{-3} md, k_v = 0.1×10^{-3} for the normal regime and $S_{H,\max}$ = 40 MPa, $S_{h,\min}$ = 20 MPa, S_v = 30 MPa, $k_{H,\max}$ = 10×10^{-3} md, $k_{h,\min}$ = 1×10^{-3} md, k_v = 0.1×10^{-3} for the strike-slip regime. The injection pressure is scheduled as step increases from 5 MPa to 32.5 MPa every 1 hr for both cases. Injection volume is 473 L with 3 day injection for the normal regime and 121 L also with 3 day injection for the strike-slip regime. Deviatoric stress for the strike-slip regime is 10 MPa, whereas it is 5 MPa for the normal regime. Larger damage and injection were observed in the normal-regime than in the strike-slip regime. Previous comparison shows the influence of deviatoric stress in damage distribution with the same initiation of rock failure. However, in this comparison, the failure beginning time is different in the normal and strike-slip regimes with same injection pressure schedule. Injection-induced damage propagation begins later in the strike-slip regime because of higher compressive horizontal stresses. This analysis shows that the roles of horizontal deviatoric stress and failure initiation pressure aare important to predict injection volume and fracture propagation. This analysis indicates that fracture propagation results from the complex interactions of the fluid injection pressure, far-field stress, permeability, and rock strength.

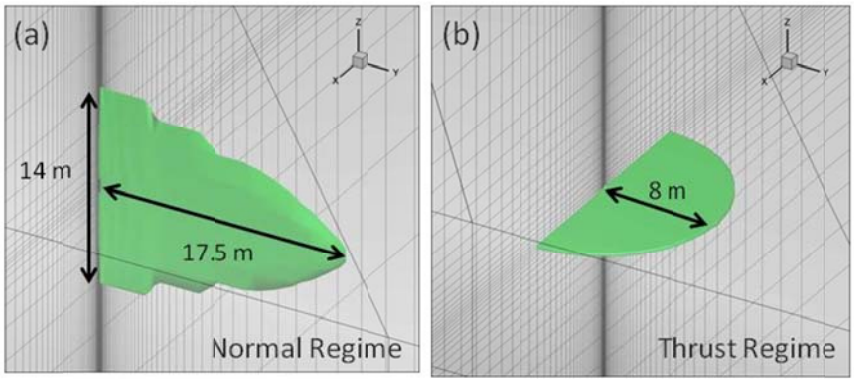

Fig. 7.17. The comparison of damage distribution under different stress regimes. (a) normal regime, 968 L for 3 days (b) thrust regime, 340 L for 3 days.

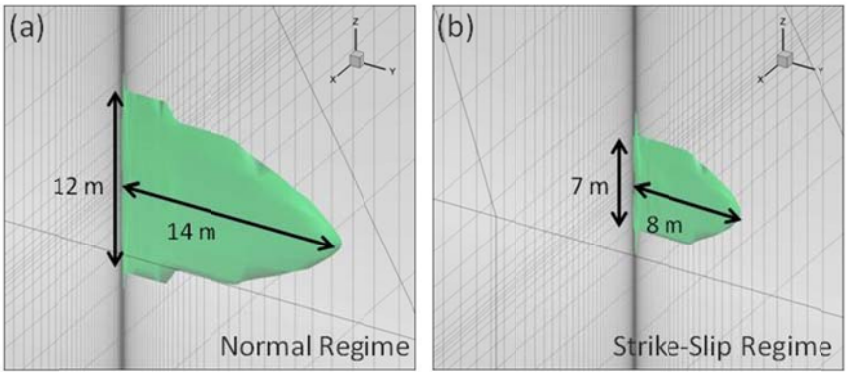

Fig. 7.18. The comparison of damage distribution under different stress regimes. (a) normal regime, 473 L for 3 days (b) strike-slip regime, 121 L for 3 days.

7.4 Heterogeneous Microseismicity Simulations

In this section, we consider induced microseismicity simulations with damage evolution. We assumed that seismic events are generated when the effective rock stress reaches the level prescribed by the failure criterion (Mohr-Coulomb) as fluid infiltrates the rock and stresses change. The simulation mesh is the same as in the previous homogeneous 3D simulations. However, heterogeneities of modulus and permeability are considered using Weibull distribution functions. The initial modulus and permeability distributions are illustrated in Fig. 7.19. As before, three different far-field stress regimes were tested: one with horizontal stress as the minimum, another with vertical stress as the minimum, and the other with vertical stress as the maximum. To investigate the permeability and far-field stress relationship, we also considered two different permeability models: (1) reservoir permeability properties are highly related to the far-field stress (anisotropic permeability), and (2) permeability is independent of the far-field stress (isotropic permeability). Details of reservoir properties are described in Table 7.2. In the case of anisotropic permeability, we simply assumed a permeability that is 10 times higher in the maximum in-situ stress direction and 10 times lower in minimum in-situ stress direction.

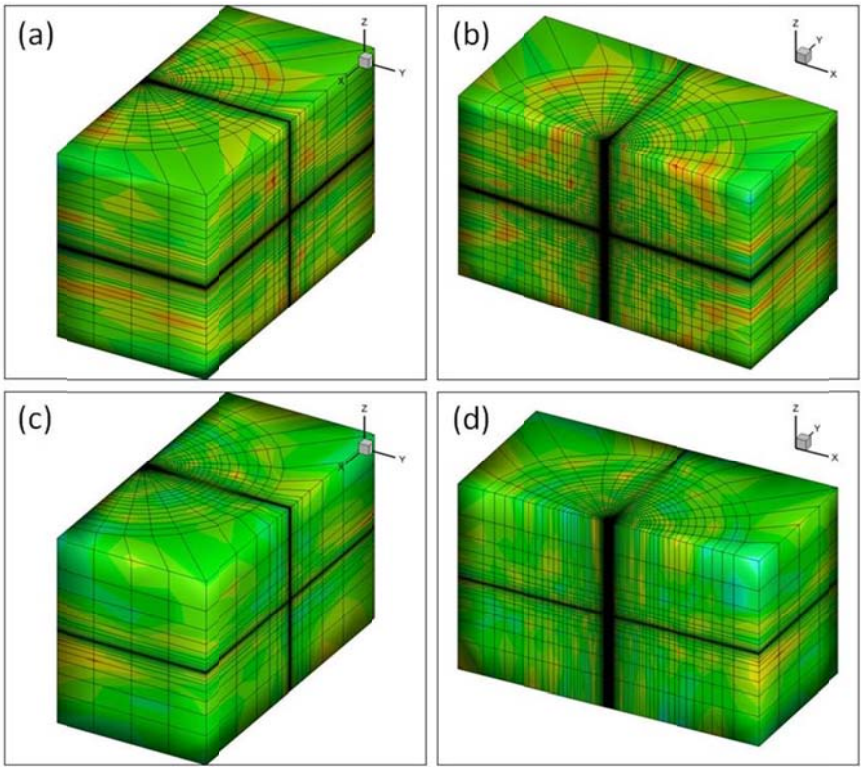

Fig. 7.19. Initial heterogeneous modulus which ranges from 4 GPa to 16 GPa in (a) and (b), and permeability distribution (0.004 to about 0.016 md) is presented in (c), (d).

Table 7.2. Reservoir properties used in 3D heterogeneous simulations.

	Case 1	Case 2	Case 3	Case 4	Case 5	Case 6
Stress regime	Strike-slip		Thrust		Normal	
E	10 GPa (n=1.5)		10 GPa (n=1.5)		10 GPa (n=1.5)	
k, [md] (n=1.5)	10^{-2}	$k_{max}=10\times10^{-2}$ $k_{min}=0.1\times10^{-2}$ $k_v=1.0\times10^{-2}$	10^{-2}	$k_{max}=10\times10^{-2}$ $k_{min}=1.0\times10^{-2}$ $k_v=0.1\times10^{-2}$	10^{-2}	$k_{max}=1\times10^{-2}$ $k_{min}=0.1\times10^{-2}$ $k_v=10\times10^{-2}$
C_0	100 MPa (n=2)		100 MPa (n=2)		100 MPa (n=2)	
T_0	5 MPa (n=2)		5 MPa (n=2)		5 MPa (n=2)	

The resulting seismic events distributions are plotted in Figs. 7.20 to 7.22 for different reservoir permeabilities in different in-situ stress regimes. Fig. 7.20(a) shows the seismic events in time for the conditions of isotropic permeability with minimum horizontal far-field stress. Fig. 7.20(b) shows a plot for the same far-field stress conditions and injection rate but with anisotropic permeability. The seismic events are scattered broadly when permeability is isotropic since there are no significant differences in fluid sweep velocities in the x-, y-, and z-directions. However, in the case of anisotropic permeability, seismic events are highly localized because fluid invasion is focused in the maximum far-field stress direction, and this leads to localized seismic events. Same conditions are simulated for the minimum vertical far-field stress case (Fig. 7.21). Similarly, broad distributed seismic events occur under isotropic permeability conditions, and scattered localized events are observed in the anisotropic permeability case. Vertical stress as the maximum has been plotted in Fig. 7.22. Note that same injection conditions are used for both stress regime simulations. Results show that for the normal faulting case, the induced seismicity does not propagate but stabilizes earlier because vertical stress is higher than the thrust regime, where a higher injection rate is needed to generate tensile failure for fracture propagation in the vertical direction. It is worth pointing out that the smaller gray points show the distribution of micro-seismic events as a result of the far-field stresses and might be interpreted as background values.

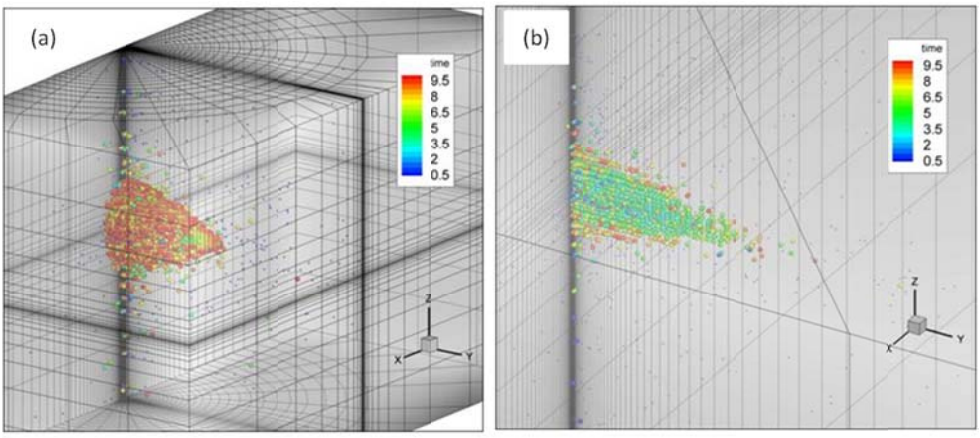

Fig. 7.20. Predicted micro-seismic events after 10 hrs of pumping for the case of horizontal stress as the minimum far-field stress: (a) isotropic permeability and (b) anisotropic permeability.

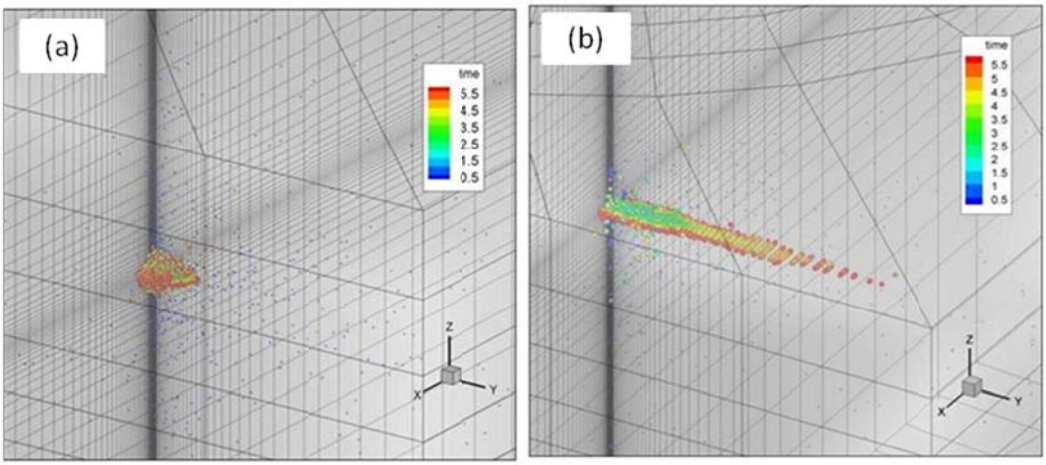

Fig. 7.21. Micro-seismic events after 6 hrs of pumping for the case that the vertical stress is the minimum far-field. (a) isotropic permeability and (b) anisotropic permeability.

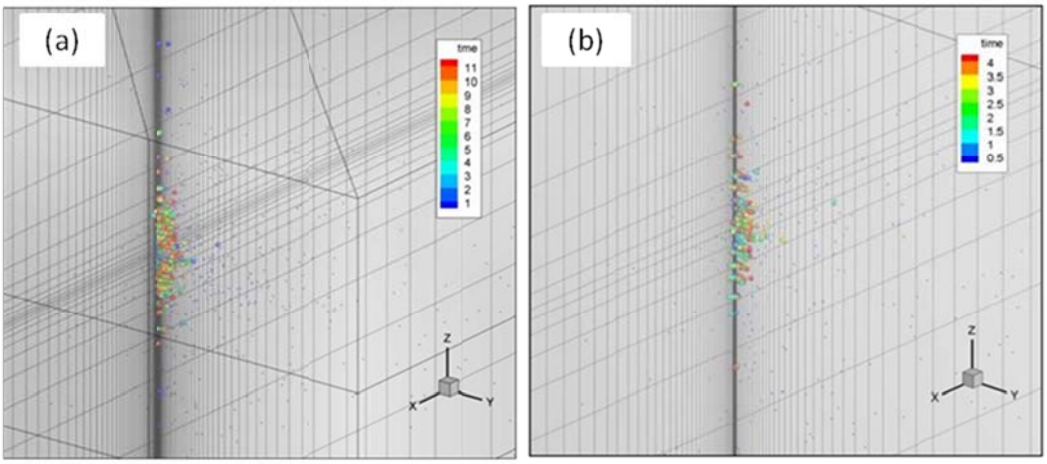

Fig. 7.22. Micro-seismic events after 6 hrs of pumping for the case that the vertical stress is the maximum far-field. (a) isotropic permeability and (b) anisotropic permeability.

The influence of cooling has been compared in Fig. 7.23. Initial reservoir temperature is assumed 200°C and injection cold water temperature is 50°C. The heat transfer by conduction and convection between the fluid flow and hot reservoir causes tensile stress, which creates larger induced microseismic events. For the cooling case, the fluid contact in an early time step contributes significantly to tensile stress, resulting in larger failure than in the isothermal case. Results show that larger initial microseismic events occurred for the case of cooling [Fig. 7.23(a)] than in the isothermal condition [Fig. 7.23(b)]. Since the heat transfer rate is slower than fluid transport, the effects of thermal stress are important for the long-term fluid injection (3 to 12 months). However, the thermal stress also plays an important role in short-term fluid injection (3 to 6 days) to estimate the microseismic event propagation since the cooling that creates more tensile stress in an early time step on the wall of the wellbore results in larger rock failure with the same fluid injection.

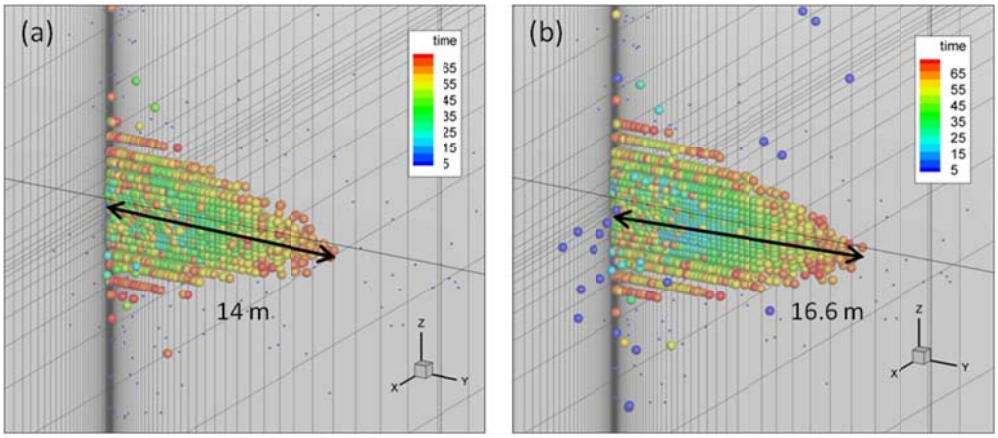

Fig. 7.23. Comparison of microseismic events after 65 hrs of pumping for the case of isothermal condition and cooling condition. (a) isothermal and (b) cold water (50°C) to the hot reservoir (200°C).

7.5 Conclusions

Damage mechanics and stress-dependent permeability models have been applied to injection induced stress variations in thermo-poroelasticity. The parameters for strain-stress and strain-permeability can be obtained by triaxial simulations comparing the experimental results. The modulus and permeability changes caused by rock failure influence the stress distributions, which in turn affect the impact of damage propagation. The results show that the failure plane is perpendicular to the minimum far-field stress distribution. Cold water injection in the normal or strike-slip regime shows penny-shape propagation which can capture the hydraulic fracturing. The study of injection volume indicates that the influence of far-field stress, injection pressure schedule, and fracture initiation pressure can be used to predict the drainage volume and fractured area related to fluid injection. We considered a heterogeneous modulus and permeability in microseismicity simulations and compared the effect of permeability anisotropy. The propagation of microseismic events is localized when the reservoir permeability is anisotropic because of fluid path localizations. The results of this study indicate that the finite element method with damage can be used to model reservoir stimulation and induced seismicity.

8. Three-Dimensional Thermo-poromechanical Analysis of Microseismicity

Three-dimensional injection induced damage/fracture propagation at well scalewas presented in the previous section. To simulate microseismic event propagation in larger space, it is efficient to consider the point source injection scheme because injection well radius (~0.1 m) is negligible compared to reservoir size. Point source is localized fluid and heat flux without geometry considerations for mathematical approximation to simplify the problem. The development of numerical implementation of the point source method was described in Section 3.1.3.

We performed three-dimensional (3D) simulation with point source fluid loading. We used an 8-node hexahedron element for displacement, pressure, and temperature, and the total element number used in this simulation is 32,000. Reservoir size is 1 km × 1 km × 0.5 km, and we assume that the depth of injection is 2.5 km and the injection interval is 25 m at the middle point of the reservoir (Fig. 8.1). We also considered gravitational force to the z-direction which has gradual change for vertical stress and maximum and minimum horizontal far-field stresses are constant to the vertical direction. Three different types of far-field stress regimes are studied with same injection rate to analyze the influence of far-field

stresses as shown in Table 8.1. Newberry geothermal reservoir stress regimes are used for strike-slip and normal regime. For thrust regime, we tested Cooper basin geothermal reservoir stress regime. Initial reservoir properties for modulus and permeability are generated using Weibull distribution functions.

To apply gravity in the simulations, we used the measured reservoir data as initial pore pressure and far-field stress for initial background stresses that increase with depth. The other method to apply gravity in the simulation is by applying the force to the z-direction in each element on a basis of rock density data. We performed the simulations based on reservoir stress data. The progress of reservoir stress distribution during fluid injection can be computed by summing the induced stress variation and the background far-field stress field in each Gaussian point of the element.

Fig. 8.2 shows initial heterogeneity with average modulus of 10 GPa and average permeability of 0.01 md. The injection schedule and pressure changes are plotted in caused by rock failure and the propagation of the damaged area.

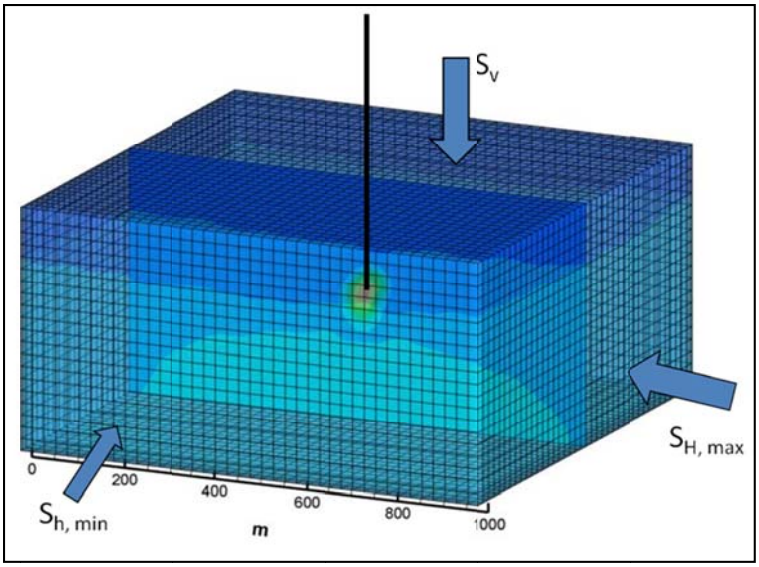

Fig. 8.1. Mesh used in three-dimensional simulation; $S_{H,\max}$ represents maximum horizontal stress, $S_{h,\min}$ is the minimum horizontal stress, and S_v is the vertical stress.

Table 8.1. Reservoir properties used in 3D simulations.

	Case 1 (Strike-slip)	Case 2 (Thrust)	Case 3 (Normal)
$S_{H,\max}$	70 MPa	95 MPa	48 MPa
$S_{h,\min}$	46 MPa	70 MPa	36 MP
S_v	60 MPa	60 MPa	60 MPa
$k_{H,\max}$	1×10^{-2} md	1×10^{-2} md	1×10^{-2} md
$k_{h,\min}$	1×10^{-2} md	1×10^{-2} md	1×10^{-2} md
k_v	0.1×10^{-2} md	0.1×10^{-2} md	0.1×10^{-2} md

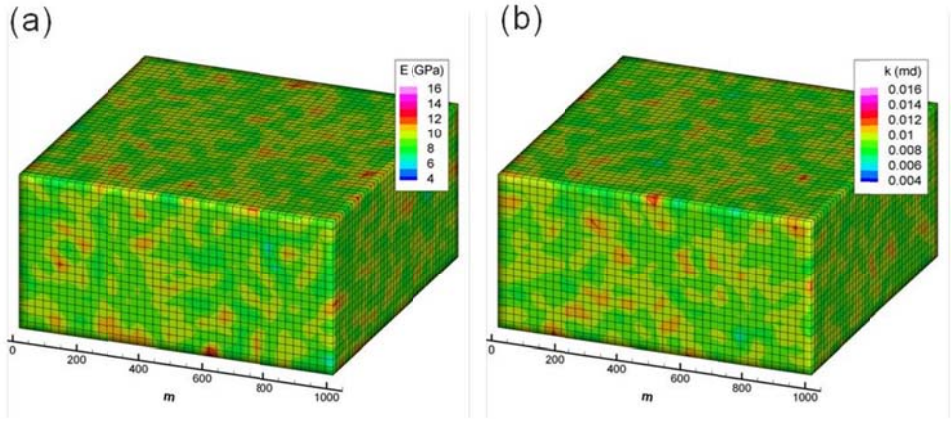

Fig. 8.2. Initial heterogeneous modulus (a) and permeability (b).

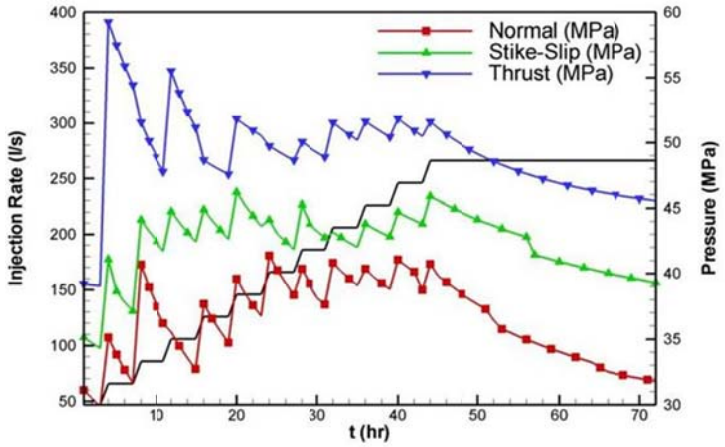

Fig. 8.3. Injection rate and injection pressure are plotted in normal, strike-slip, and thrust regime.

8.1 Microseismicity in Strike-Slip Regime

Three-dimensional injection-induced stress and permeability change were performed under a strike-slip regime (horizontal far-field stresses are the maximum and the minimum, and vertical stress is intermediate) for a Newberry geothermal reservoir. Fig. 8.4 describes the injection-induced microseismic events with respect to time. We assumed that microseismic events occurred if the effective rock stresses reached the shear or tensile failure criterion. Change of color represents the time scale from the initial time step to 72 hrs. Results show that seismic events are propagated irregularly because of the heterogeneity from fluid injection, but a cross-sectional view shows that the seismic event propagation follows the maximum horizontal stress direction as shown in Fig. 8.5. The different mode of rock failure is plotted in Fig. 8.6, where the red denotes the shear failure and the blue is tensile failure caused by the

stimulation. The distributions of S1-S3 (maximum principal stress – minimum principal stress) and minimum far-field stress distributions are plotted in Fig. 8.7 and Fig. 8.8. The stress distribution along the vertical direction increases as the depth increases because of the gravity in the far-field stress. The results of stress distribution show that fluid injection decreases the effective stress level, which results in shear and tensile failure and stress relaxation at the microseismic event location. Pore pressure distributions are plotted for 1-hr and 3-day stimulations in Fig. 8.9; it dispersed nonhomogeneously due to the heterogeneous permeability.

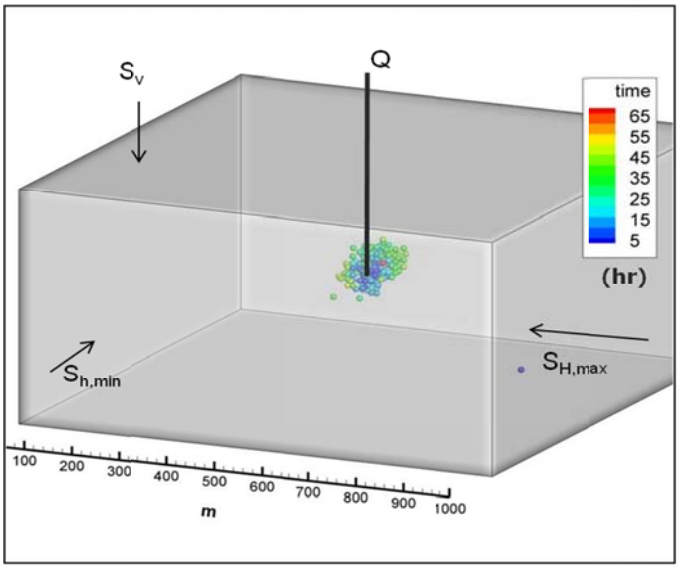

Fig. 8.4. Micro-seismic events after 3 days pumping for the case of strike-slip regime.

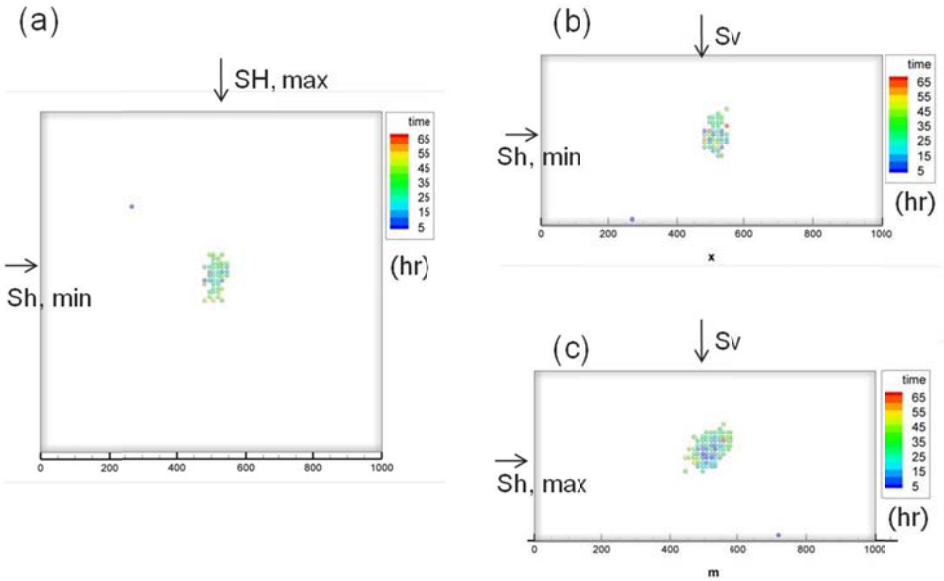

Fig. 8.5. Cross-sectional views for strike-slip regime. (a) represents top view, (b) is maximum directional side view, and (c) is minimum directional side view.

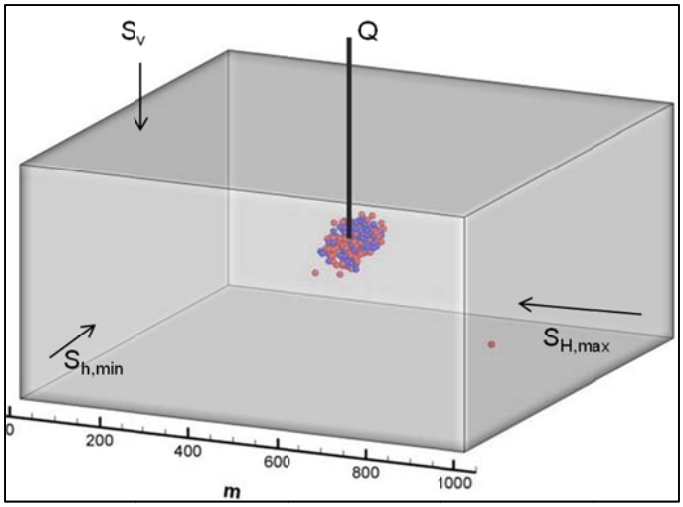

Fig. 8.6. Injection-induced failure analysis. Blue represents tensile failure and red shows shear failure.

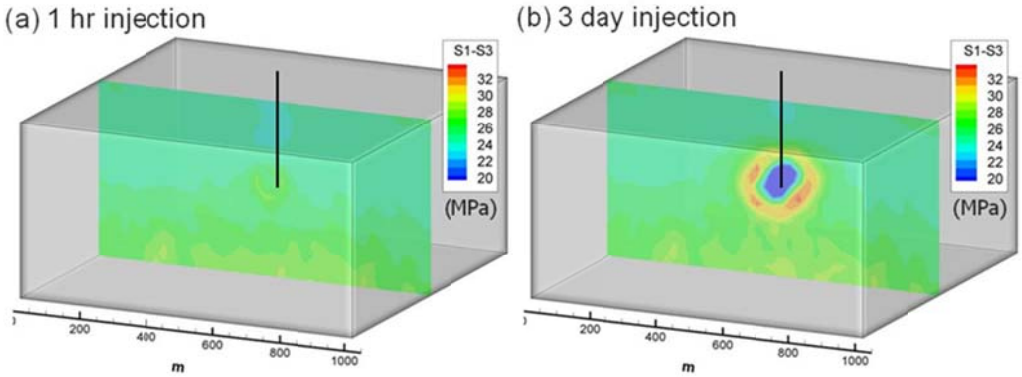

Fig. 8.7. The difference of maximum and minimum principal stress distribution for 1 hr injection (a) and after 3 days pumping (b).

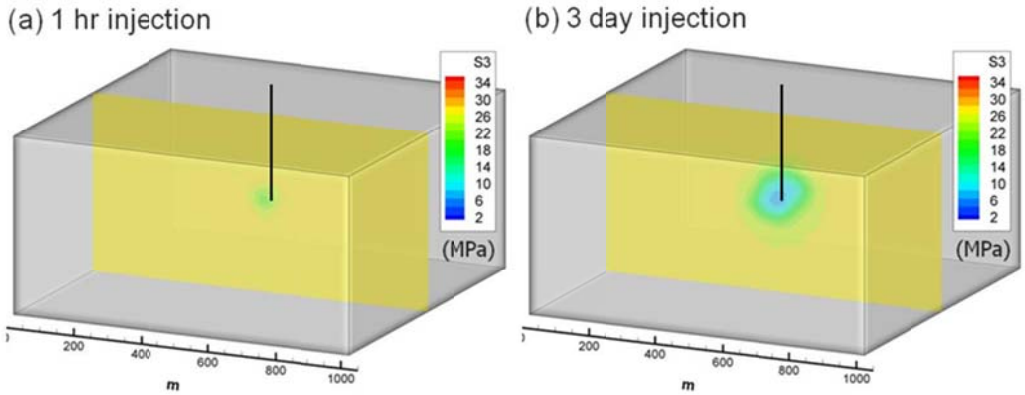

Fig. 8.8. Minimum principal stress distribution for 1 hr injection (a) and after 3 days pumping (b).

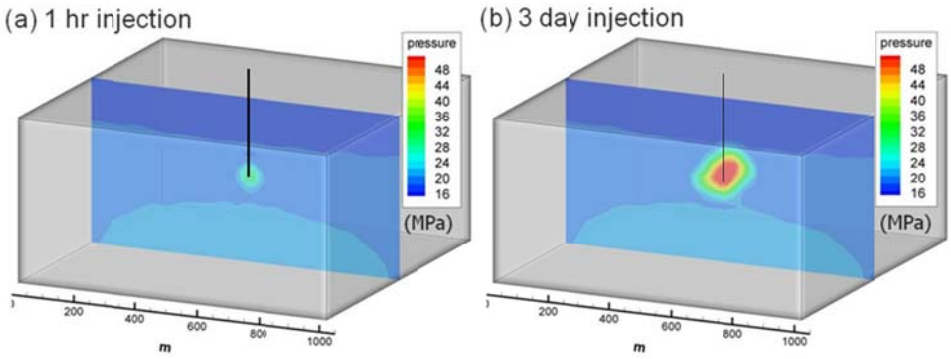

Fig. 8.9. Pore pressure distribution for 1 hr injection (a) and after 3 days pumping (b).

8.2 Microseismicity in Thrust Regime

In the Cooper Basin geothermal reservoir, the vertical far-field stress is the minimum (thrust regime). It has been tested with the same heterogeneity and injection rate schedule as performed in previous strike-slip regime. Injection-induced seismic events in a 3-day injection schedule are plotted in Fig. 8.10. Microsesimic events did not happen and the formation stabilized after 40 hrs because the rock failure did not occur with the given injection rate and far-field stress. The shape of the seismic-event clouds is spherical (Fig. 8.11) and the number of events is less than in the strike-slip regime case because the compressive far-field stress in the thrust regime case is higher; therefore, the possibility of rock failure was less with the same injection rate. Most seismic events were generated by shear failure in this simulation. Stress distributions for maximum and minimum principal are illustrated in Figs. 8.13 and 14.

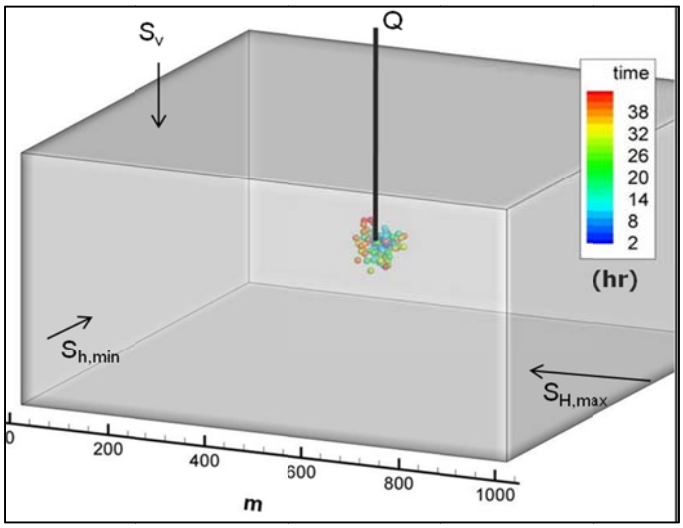

Fig. 8.10. Micro-seismic events after 3 days pumping for the thrust regime.

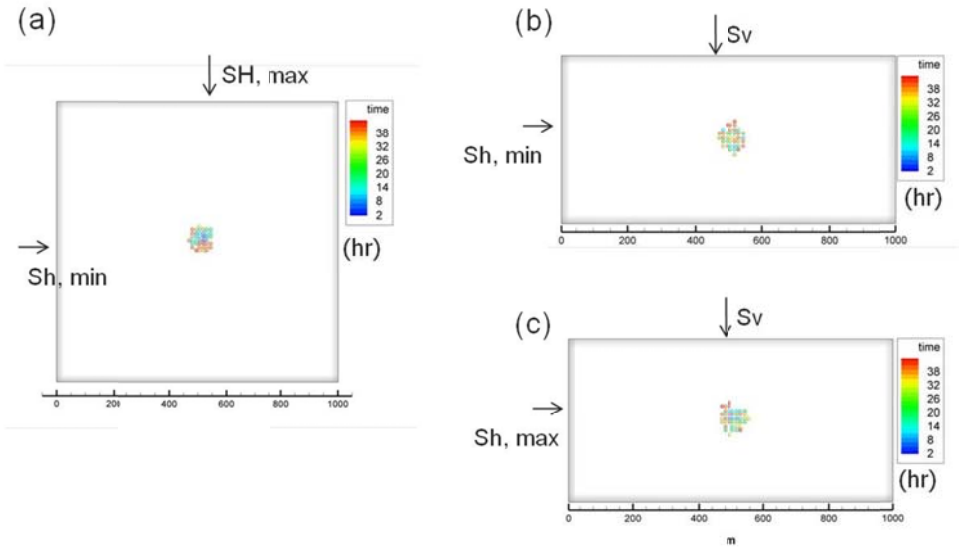

Fig. 8.11. Cross-sectional views for thrust regime. (a) represents top view, (b) is maximum directional side view, and (c) is minimum directional side view.

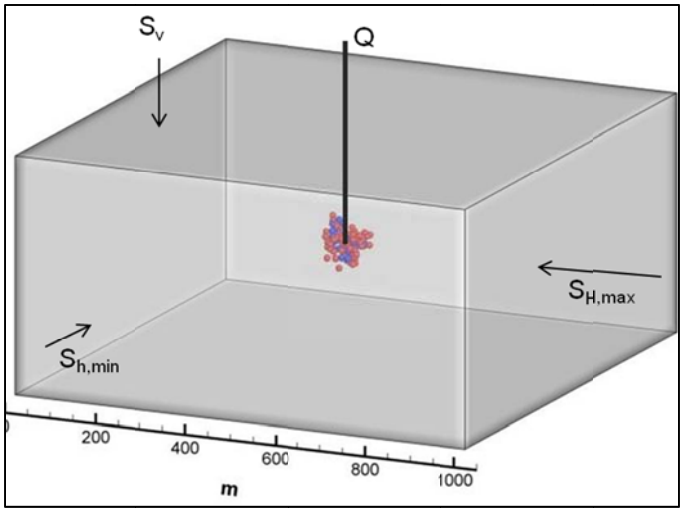

Fig. 8.12. Injection-induced failure analysis. Blue represents tensile failure and red shows shear failure.

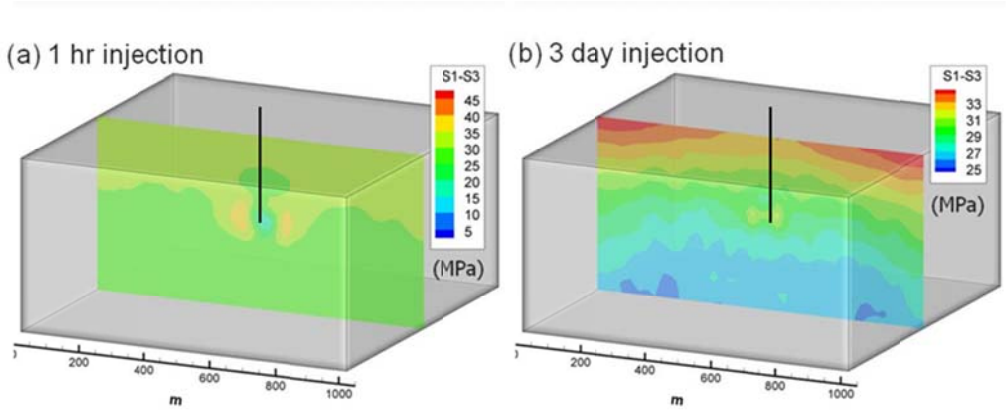

Fig. 8.13. The difference of maximum and minimum principal stress distribution for 1 hr injection (a) and after 3 days pumping (b).

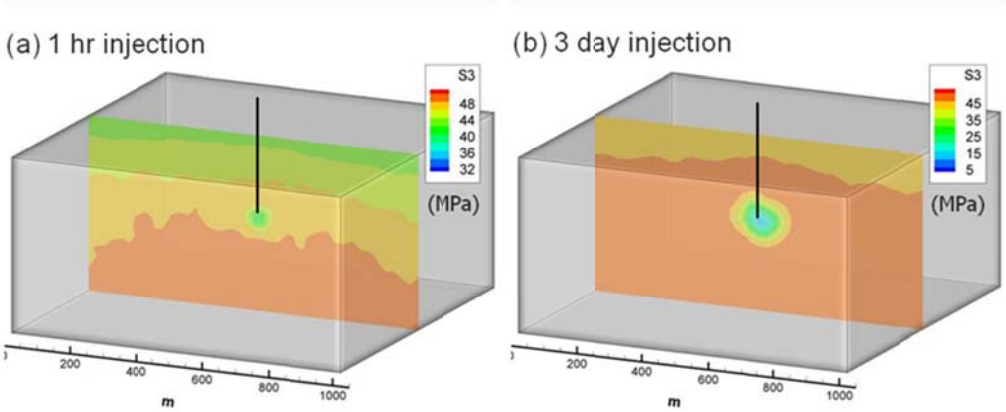

Fig. 8.14. Minimum principal stress distribution for 1 hr injection (a) and after 3 days pumping (b).

8.3 Microseismicity in Normal Regime

One of the most common stress regimes in reservoirs is the normal stress regime. In this stress regime, vertical fracturing is observed and the microseismic event shape is ellipsoidal because of the stress differences in horizontal far-field stress. Injection-induced seismic events are illustrated in Fig. 8.15. Small dots represent initial shear failure caused by natural compressive far-field stress. Cross-sectional views in Fig. 8.16 show that microseismic events are propagated to the maximum horizontal far-field stress direction and also to the vertical far-field stress direction. The pattern of events cloud is a penny shape, which is similar to hydraulic fracturing, but the events can be observed broadly since microseismic events include not only microcrack but also macrocrack generation by fluid injection. Shear and tensile failure modes are plotted in Fig. 8.17, which shows that shear failure is randomly observed at the bottom side because of the increase in vertical far-field stress due to gravity, and also induced shear and tensile failure are observed because of water injection. Changes in principal stress distributions and pore pressure distributions are plotted in Figs. 8.18 to 8.20.

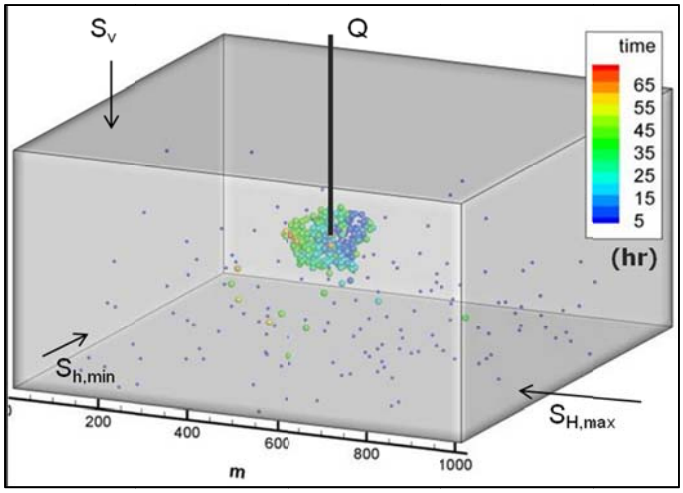

Fig. 8.15. Micro-seismic events after 3 days pumping for the normal regime.

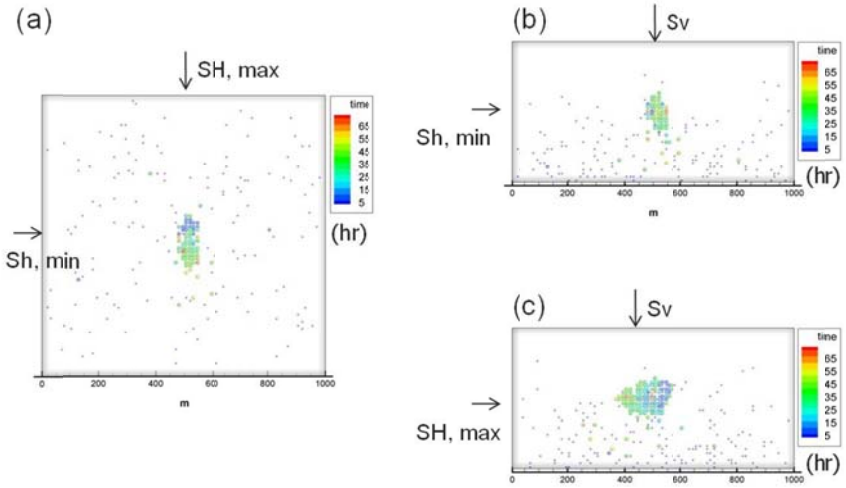

Fig. 8.16. Cross-sectional views for normal regime. (a) represents top view, (b) is maximum directional side view, and (c) is minimum directional side view.

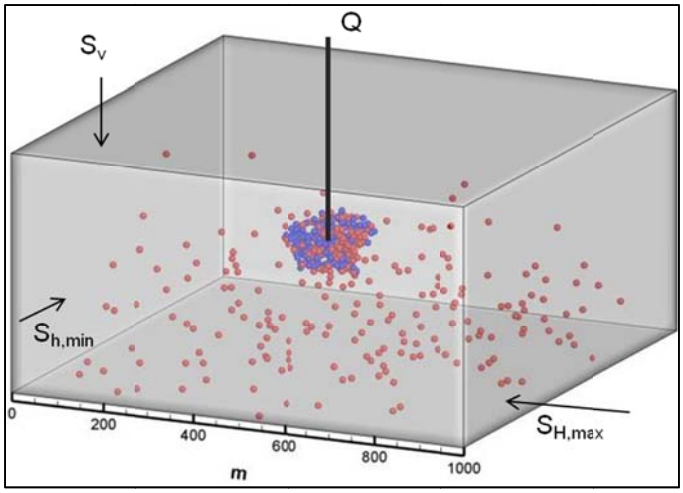

Fig. 8.17. Injection-induced failure analysis. Blue represents tensile failure and red shows shear failure.

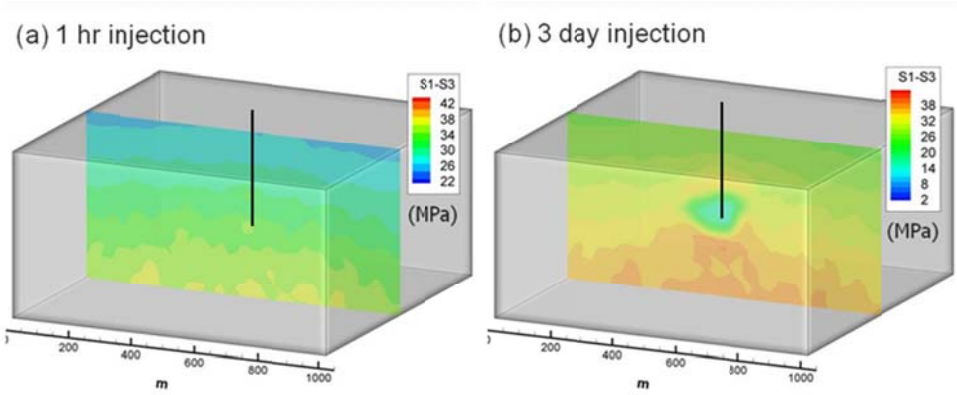

Fig. 8.18. The difference of maximum and minimum principal stress distribution for 1 hr injection (a) and after 3 days pumping (b).

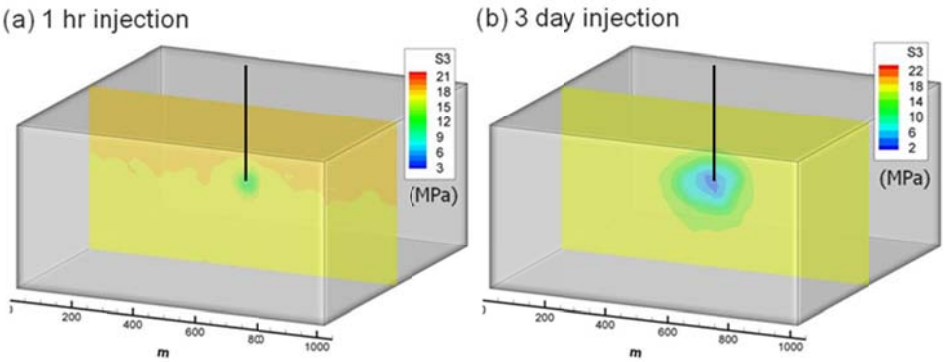

Fig. 8.19. Minimum principal stress distribution for 1 hr injection (a) and after 3 days pumping (b).

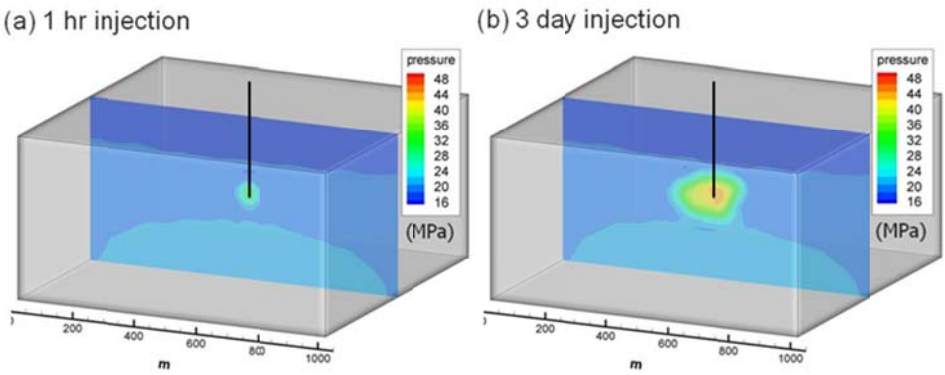

Fig. 8.20. Pore pressure distribution for 1 hr injection (a) and after 3 days pumping (b).

8.4 Discussion of Microseismicity in Three Different Stress Regimes

We presented microseismic event propagation under three different stress regimes (strike-slip, thrust, normal regime) with the same injection schedule and the same distribution of heterogeneity of modulus and permeability. Results show that the patterns of microseismic events are penny shaped for strike-slip and normal regimes. However, we observed differences in the event locations and times with changes in far-field stress conditions. Especially in the normal regime case, initial rock failure increased as the depth increased, and it also influenced the injection induced microseismic event propagation. The difference of seismic events with normal and strike-slip regimes is compared in Fig. 8.21. For the thrust regime in the simulation, it the distance of events from the injection source is relatively shorter than in the strike-slip and normal regimes because of the effective stress contributions toward shear and tensile failure. This is also observed in well-scale simulation (Section 7) for the thrust regime.

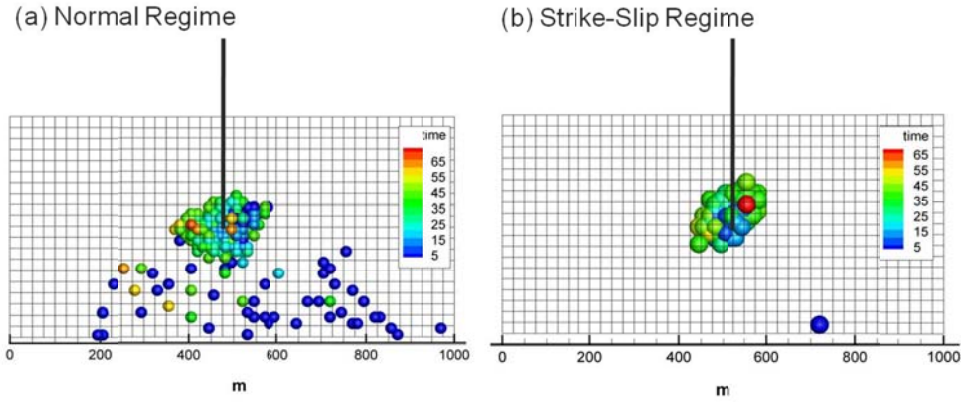

Fig. 8.21. Comparison of seismic events in normal and strike-slip regimes.

We tested the influence of permeability anisotropy in a thrust regime that had 10 times higher permeability in the horizontal directions and 10 times lower permeability in the vertical directions. This assumption is accompanied by the experimental results that the maximum fluid path increases

proportionally as the deviatoric stress increases in rock. Results in Fig. 8.22 show that injection-induced microseismic events are horizontally scattered. Note that small dots represent initial rock failure in the reservoir. Cross-sectional views in Fig. 8.23 show the microseismic events localized to the horizontal direction by fluid injection. This result indicates that the fluid flow path highly influences the stress distribution, and it causes the shape of the rock failure and microseismic events. Permeability distribution for the initial injection and after 3 days for the thrust regime is described in Fig. 8.24. The rock failure induced by injection increased permeability and triggered microseismicity.

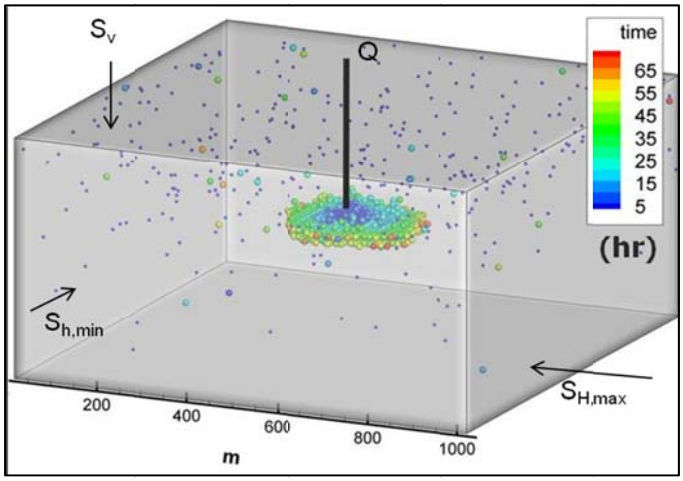

Fig. 8.22. Microseismic events after 3 days pumping in the highly anisotropic permeability case.

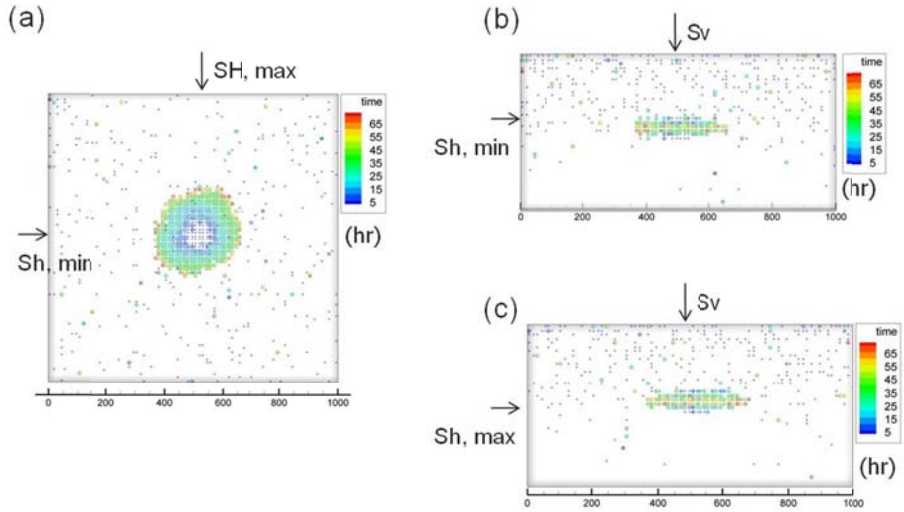

Fig. 8.23. Cross-sectional views for thrust regime. (a) represents top view, (b) is maximum directional side view, and (c) is minimum directional side view.

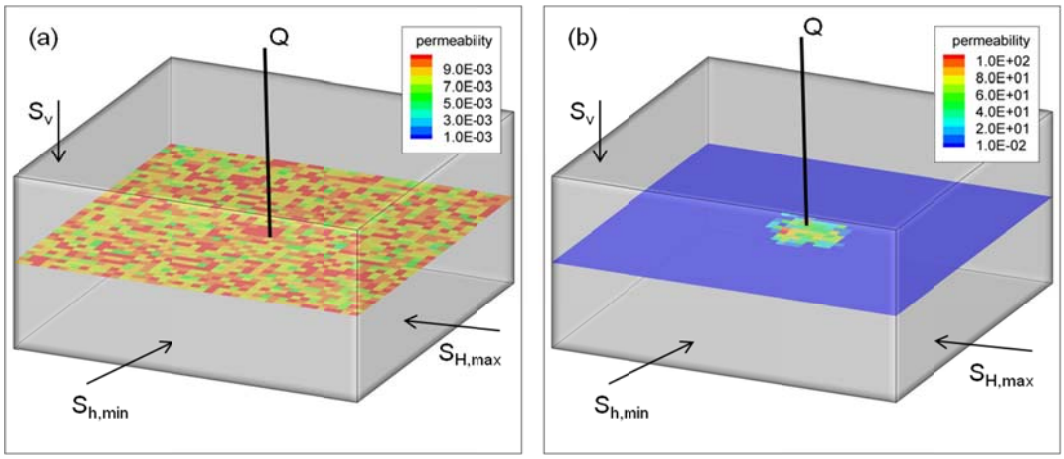

Fig. 8.24. Cross-sectional views for permeability distribution. (a) initial permeability distribution, (b) permeability distribution after 3 days injection.

8.5 Influence of Deviatoric Stress

In this section, we present the results of microseismic event propagation under three stress regimes that show different event propagation with the same injection schedule and the same distribution of heterogeneity. This indicates that the far-field stress plays an important role in induced seismicity. We studied the influence of deviatoric far-field stress in microseismic events propagations as changing horizontal deviatoric stresses. The simulation conditions for this study are presented in Table 8.2, in which horizontal far-field stress is changed with same vertical far-field stress (strike-slip regime). Permeability anisotropy is considered so that the vertical direction has 10 times lower permeability.

Table 8.2. Reservoir properties used in the simulations for stress regime and permeability anisotropy.

	Case 1	Case 2	Case 3
$S_{H,\,max}$	55 MPa	60 MPa	65 MPa
$S_{h,\,min}$	45 MPa	40 MPa	35 MPa
S_v	50 MPa	50 MPa	50 MPa
$k_{H,\,max}$	1×10^{-2} md	1×10^{-2} md	1×10^{-2} md
$k_{h,min}$	1×10^{-2} md	1×10^{-2} md	1×10^{-2} md
k_v	0.1×10^{-2} md	0.1×10^{-2} md	0.1×10^{-2} md

In contrast with the result for the thrust regime, the events cloud scattered horizontally. In the small deviatoric stress reservoir condition, the fluid path has the dominant effect in microseismic event propagation since permeability anisotropy in horizontal direction is 10 times higher than in the vertical direction. However, if the horizontal deviatoric stresses increase as in cases 2 and 3, the influence of horizontal deviatoric stresses becomes significant as the deviatoric stresses increase. Figs. 8.25 to 8.27 show that microseismic events propagate to the maximum far-field stress direction, and the cloud shape is sharper in the maximum horizontal far-field stress direction as the deviatoric stress increases. The results indicate that permeability anisotropy is critical for event propagation when the deviatoric stress is not severe, and also the far-field stress influences the microseismic pattern as the deviatoric stress increases.

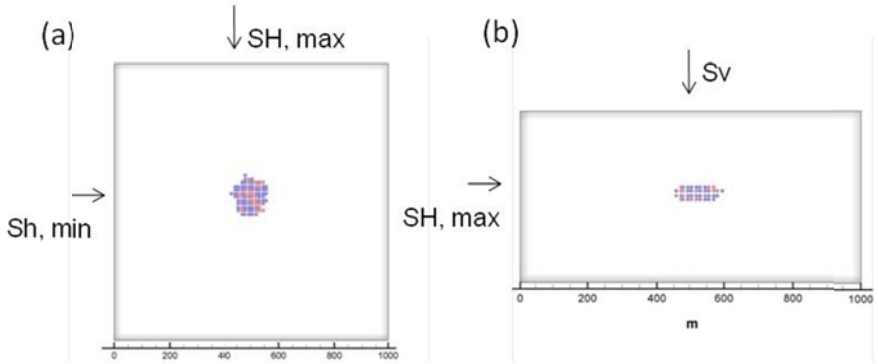

Fig. 8.25. Cross-sectional views for the case of 5 MPa as deviatoric stress after 3 day injection. (a) represents top view and (b) is minimum directional side view. Blue dots represent tensile failure and red dots are shear failure.

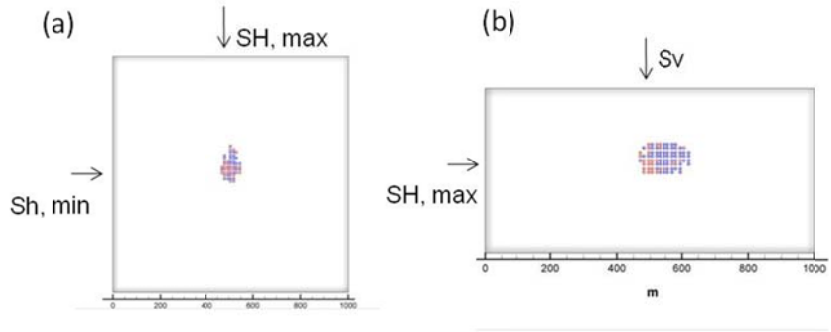

Fig. 8.26. Cross-sectional views for the case of 10 MPa as deviatoric stress after 3 day injection. (a) represents top view and (b) is minimum directional side view. Blue dots represent tensile failure and red dots are shear failure.

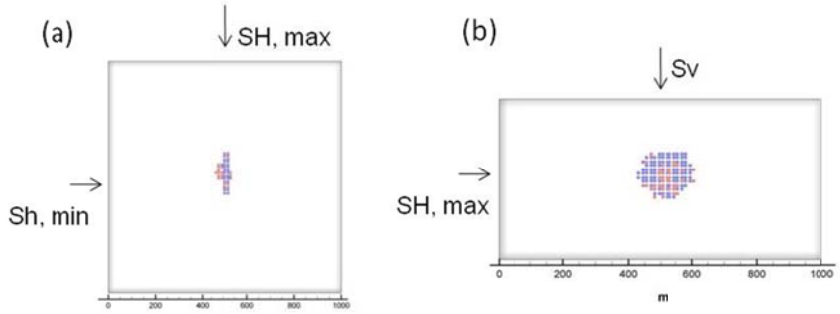

Fig. 8.27. Cross-sectional views for the case of 15 MPa as deviatoric stress after 3 day injection. (a) represents top view and (b) is minimum directional side view. Blue dots represent tensile failure and red dots are shear failure.

8.6 Anisotropic Permeability

As we have seen in previous results, fluid path is one of the key factors for microseismic event analysis. In this simulation, we studied the influence of permeability anisotropy. Table 8.3 shows different permeability anisotropy, which increases the permeability in the direction of the maximum horizontal far-field stress. Note that vertical permeability is lower than horizontal permeability and only the values of $k_{H,\,max}$ are changed and far-field stress conditions are the same.

Table 8.3. Input parameters for stress regime and permeability anisotropy.

	Case 1	Case 2	Case 3
$S_{H,\,max}$	60 MPa	60 MPa	60 MPa
$S_{h,\,min}$	40 MPa	40 MPa	40 MPa
S_v	50 MPa	50 MPa	50 MPa
$k_{H,\,max}$	2×10^{-2} md	5×10^{-2} md	10×10^{-2} md
$k_{h,min}$	1×10^{-2} md	1×10^{-2} md	1×10^{-2} md
k_v	0.1×10^{-2} md	0.1×10^{-2} md	0.1×10^{-2} md

Figs. 8.28 to 8.30 show clouds of seismic events for different permeability anisotropy after 3 day injection. The shape of the microseismic event clouds becomes narrow and sharper as the permeability anisotropy increases in the maximum direction because of the localization in the fluid path. Note that few events appear in the vertical direction because vertical permeability is 10 times lower than horizontal permeability.

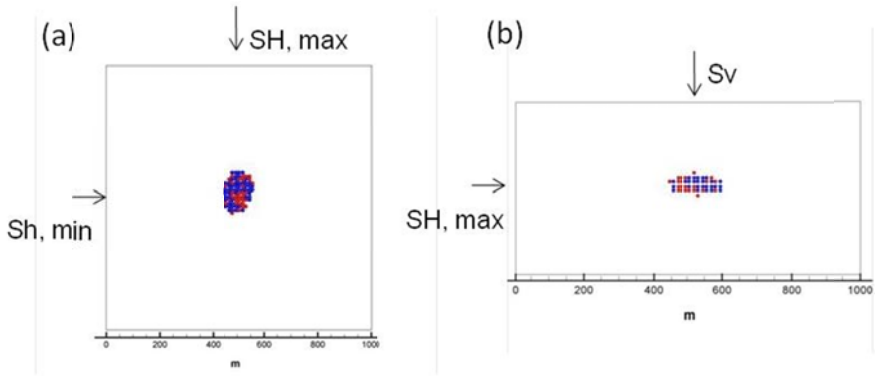

Fig. 8.28. Cross-sectional views for the case of $k_{H,\,max} = 2 \times k_{H,\,min}$ after 3 day injection. (a) represents top view and (b) is minimum directional side view. Blue dots represent tensile failure and red dots are shear failure.

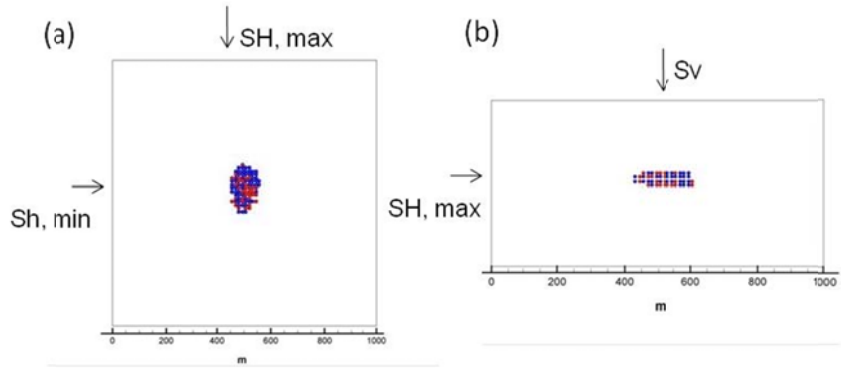

Fig. 8.29. Cross-sectional views for the case of $k_{H,\,max} = 5 \times k_{H,\,min}$ after 3 day injection. (a) represents top view and (b) is minimum directional side view. Blue dots represent tensile failure and red dots are shear failure.

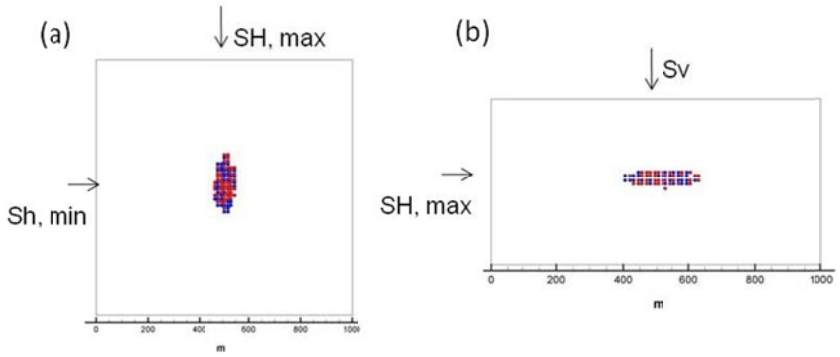

Fig. 8.30 Cross-sectional views for the case of $k_{H,\,max} = 10 \times k_{H,\,min}$ after 3 day injection. (a) represents top view and (b) is minimum directional side view. Blue dots represent tensile failure and red dots are shear failure.

8.7 Microseismic Simulations in Soultz-Sous-Forets Stress Regime

We performed microseismicity simulation with a Soultz-Souls-Forest stress regime. One of the most important characteristics in the GPK-1 and GPK-2 stress regime is a transition of stress regime from a normal regime to a strike-slip regime as the reservoir depth increases, as shown in Fig. 8.31. Three different stress regimes have been tested: the normal regime (1.25 km – 1. 75 km), the transition (2.75 km – 3.25 km), and the strike-slip regime (4.25 km – 4.75 km). We assumed that there are no natural fracture and fault in this simulation.

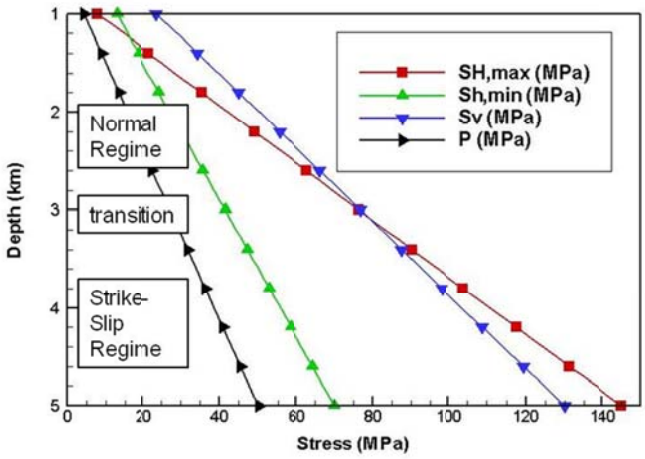

Fig. 8.31. Change of far-field stress with respect to depth in Soultz-Sous-Forets geothermal reservoir.

Microseismic events propagation with time and failure mode at 1.25 km–1.75 km are plotted in Fig. 8.32 and Fig. 8.33 (normal regime). Microseismicity propagated perpendicular to the minimum horizontal far-field stress direction. Transition and strike-slip regime cases are also plotted in Figs. 8.34 to 8.37. The minimum far-field stress does not change with depth variations as the minimum; therefore, microseismic events are propagated normal to the minimum far-field stress directions. Both shear and tensile failure from fluid injection were observed. The comparison of microseismic events propagation as the depth increase is illustrated in Fig. 8.38.

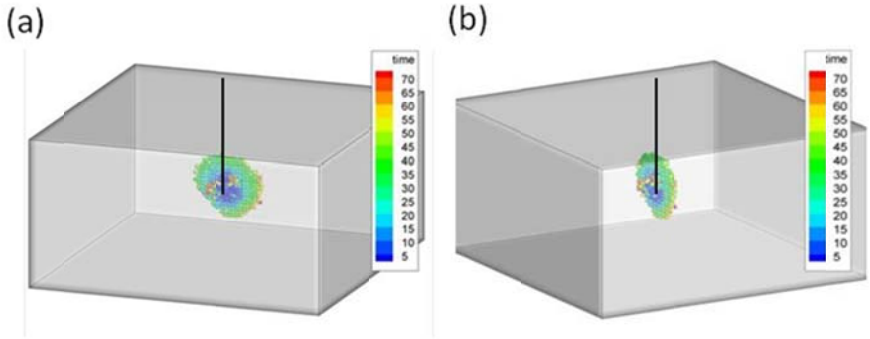

Fig. 8.32. Cross-sectional views for the normal regime (1.25km – 1.75km) after 3 day injection. (a) represents top view and (b) is minimum directional side view.

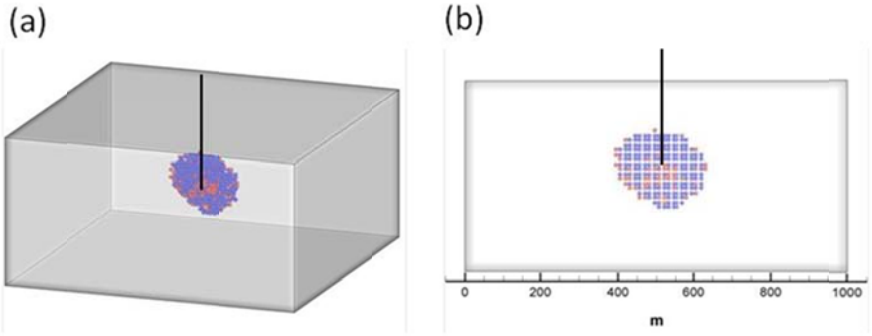

Fig. 8.33. Shear and tensile failure plot for the normal regime (1.25km – 1.75km) after 3 day injection. (a) represents top view and (b) is minimum directional side view. Blue dots represent tensile failure and red dots are shear failure.

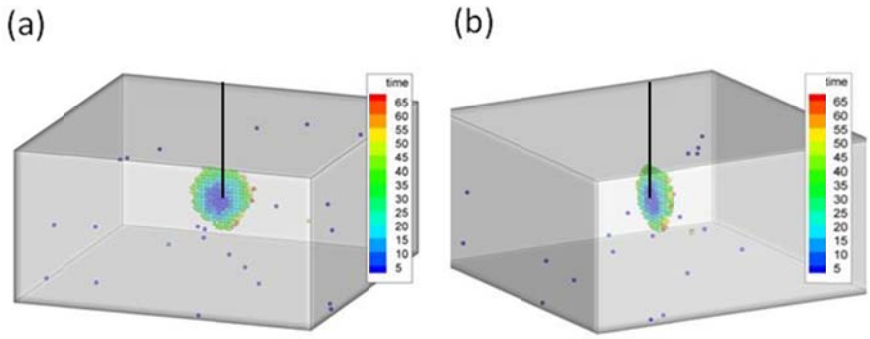

Fig. 8.34. Cross-sectional views for the transition regime (2.75km – 3.25km) after 3 day injection. (a) represents top view and (b) is minimum directional side view.

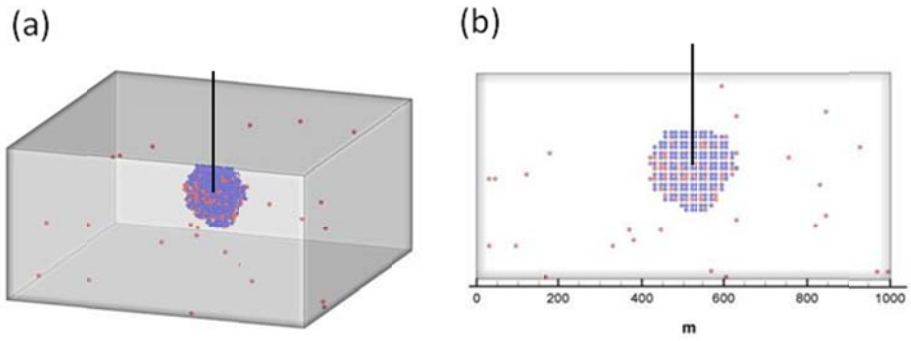

Fig. 8.35. Shear and tensile failure plot for the transition regime (2.75km – 3.25km) after 3 day injection. (a) represents top view and (b) is minimum directional side view. Blue dots represent tensile failure and red dots are shear failure.

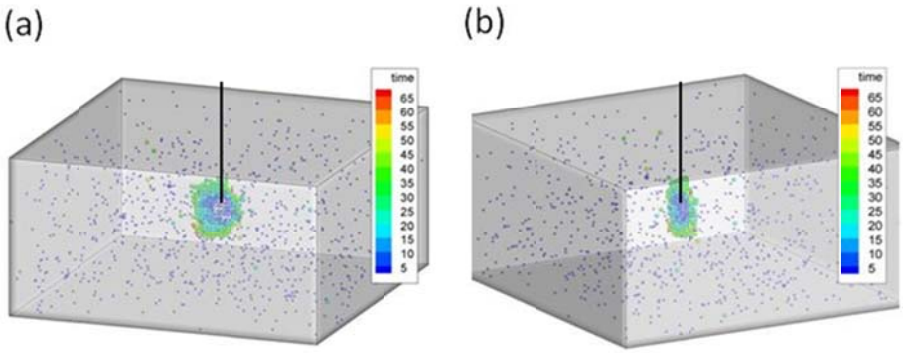

Fig. 8.36. Cross-sectional views for the strike-slip regime (4.25km – 4.75km) after 3 day injection. (a) represents top view and (b) is minimum directional side view.

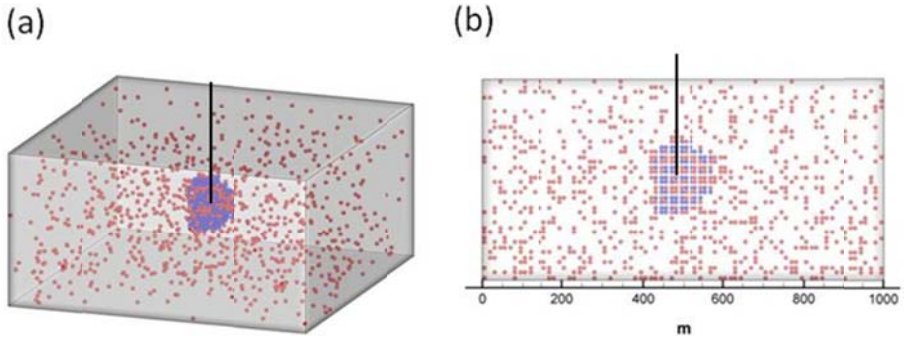

Fig. 8.37. Shear and tensile failure plot for the strike-slip regime (4.25km – 4.75km) after 3 day injection. (a) represents top view and (b) is minimum directional side view. Blue dots represent tensile failure and red dots are shear failure.

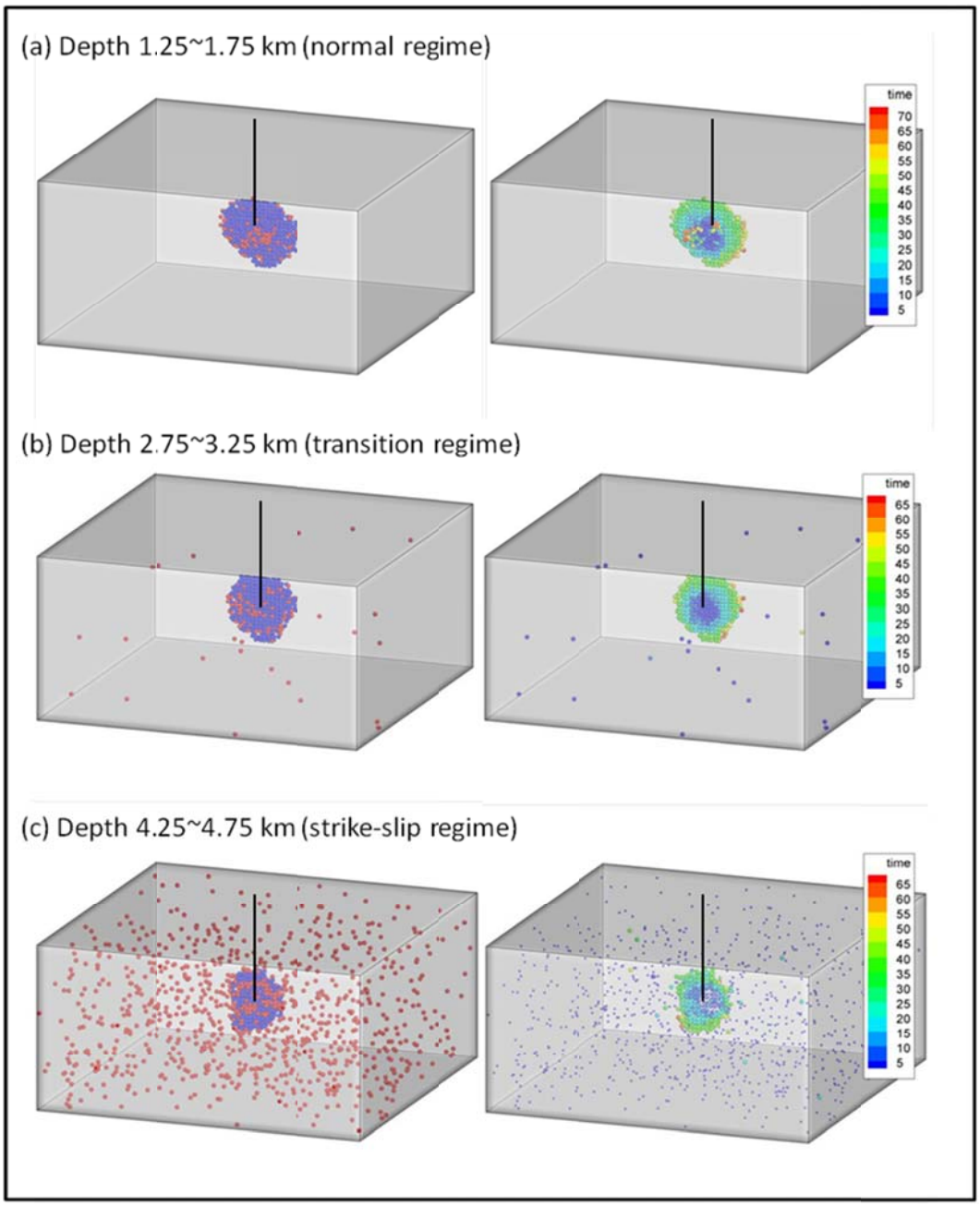

Fig. 8.38. Comparison of microseismic events propagation under different depth. (a) injection depth is 1.5 km in normal regime (b) 3 km in transition regime, and (c) 4.5 km in strike-slip regime.

We also performed injection-induced microseismic event propagations in existing natural fractures. The mesh used in this simulation is 250 m×250 m×250 m with an 8-node hexahedron element and one simplified, circular natural fracture (representing the conceptual model of a Soutz-Sous-Forets geothermal reservoir). The natural fracture is inclined by 20° from the vertical direction, and its fracture radius is 50 m (Bruel, 2002). To describe the natural fracture in finite element modeling, we assumed that is modulus is 10-5 times lower (~0.1 MPa) and permeability is 106 times higher (~103 md) than an intact granite

reservoir, and its cohesive strength is zero in the naturally fractured zone. The mesh for numerical modeling is presented in Fig. 8.39. Fig. 8.40 shows the initial natural fracture configuration and initial distribution of modulus. The stress regime in this simulation is a normal regime with SH,max = 50 MPa, Sh,min = 30 MPa, and Sv = 60 MPa; the injection rate is 24 L/sec.

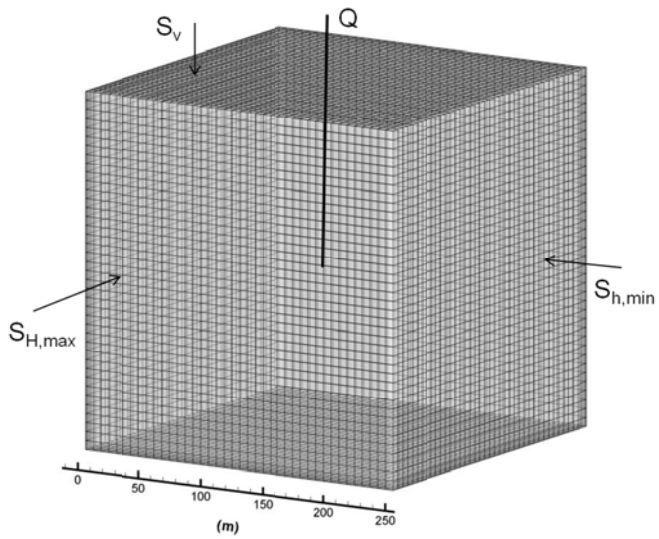

Fig. 8.39. Mesh used in naturally fractured reservoir simulation; 250×250×250 m^3 with 64,000 elements.

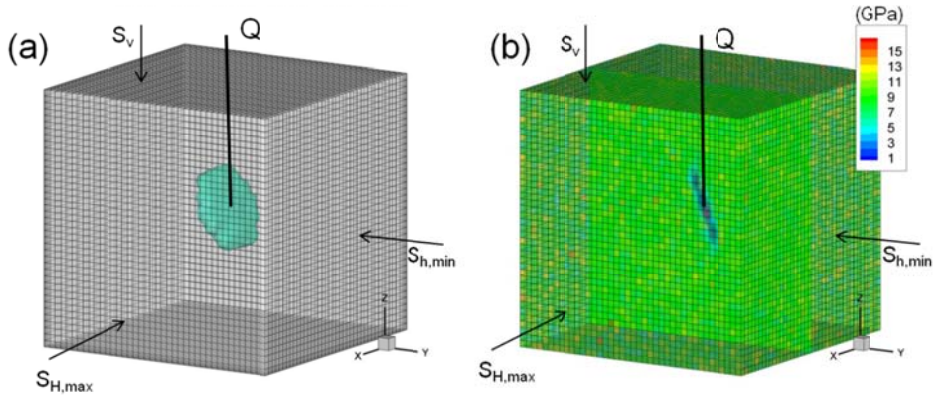

Fig. 8.40. Natural fracture configuration is illustrated in (a), and initial distribution of modulus properties are plotted in (b).

The results for microseismic event propagation with time and pore pressure distribution after a 3 day injection schedule are presented in Fig. 8.41. The microseismic event propagation in Fig 8.41(a) shows almost the same growth rate in the up and down direction because the influence of gravity in far-field stress, initial pore pressure, and fluid gravity is ignored in this simulation. Note that the microseismic event propagation is fast inside the natural fracture in early time steps because of quick fluid movement to the natural fracture, and then there is a small delay to generate propagation of new events. A possible reason is that it needs more pore pressure to propagate the rock failure in the intact rock since rock properties and permeability are discontinuous between the natural fracture and the intact rock. The

comparison of numerically obtained microseismicity with real field date is presented in Fig. 8.42. The numerical simulation that assumed a single large fracture can describe the main features of the experimental data in Soultz-Sous-Forets. However, the distribution of microseismicity between the simulation and field data is different. To improve the numerical modeling for microseismicity, it is necessary to consider not only large main fracture but also other factors that can influence microseismicity, such as localized permeability distribution, modulus, and rock strength in small natural fractures around the injection area.

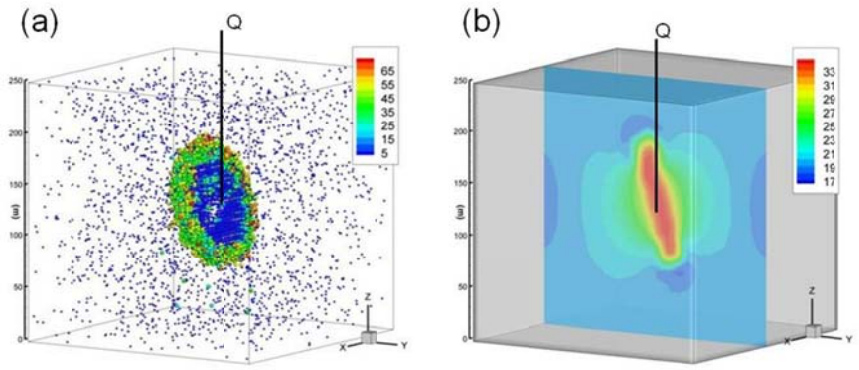

Fig. 8.41. Microseismic event propagation and pore pressure distribution with fluid injection to the natural fracture. (a) microseismic events propagation with time (b) pore pressure distribution after 3 days injection.

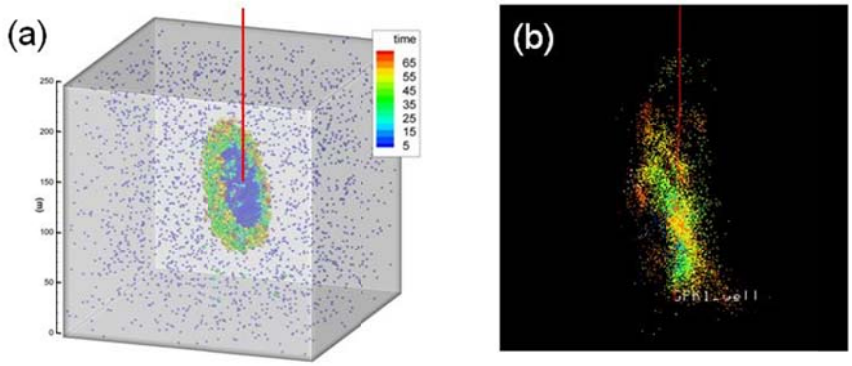

Fig. 8.42. Comparison of numerical results for injection-induced microseismicity with experimental data. (a) numerical results assuming the injection in single large fracture (b) experimental data at GPK1-well in Soultz-Sous-Forets geothermal reservoir.

8.8 Conclusions

The influence of far-field stress and permeability anisotropy has been studied through a thermo-hydro-mechanical model with damage evolution. Point source injection was applied to simulate a large reservoir efficiently. A fully-coupled finite element method with damage mechanics provided the tools to analyze injection induced microseismicity. Results show that the far-field stress and permeability anisotropy influence the stress distributions, which in turn impact microseismic event propagations. The event propagation is perpendicular to the minimum far-field stress distribution. Cold water injection in normal or strike-slip regime leads to vertical propagation, which can capture the effects of hydraulic fracturing,

but the event cloud shape is also related with permeability anisotropy when deviatoric stress is small. Thermal stress plays an important role for predicting the stress distribution by cold water injection and triggered microseismicity in early time steps. The pattern of microseismic events becomes elliptical and localized when the reservoir permeability anisotropy increases. Injection induced microseismicity in single large, fractured reservoirs also has been presented. Results show that event propagations are triggered quickly inside the fracture because of low modulus and higher permeability in natural the fracture. Comparing the simulated microseismicity with real data for Soultz-Sous-Forets qualitatively showed that numerical results with the assumption of a single large fracture can capture the main distribution of microseismicity in field experimental data.

9. Conclusions and Recommendations

9.1 Conclusions

Thermo-poro-mechanical and chemo-thermo-poro-mechanical models for the rock response to fluid injection and drilling mud infiltration were developed using the finite element method. The rock failure and damage propagation were modeled by considering the nonlinear strain-stress behavior of rock. Damage mechanics and stress-dependent permeability were also implemented into the finite element model. The model has been applied to plain-strain wellbore stability analysis in shale to study the effects of solute transport, heat transfer, and stress distribution around a wellbore. Also, a thermo-poro-mechanical process with damage mechanics and stress-dependent permeability was applied to two- and three-dimensional damage/fracture propagation and microseismicity. Especially for three-dimensional simulation, both well-scale and reservoir-scale numerical modeling was presented.

Finite element simulation of triaxial compression behavior of rock was carried out to find out optimum damage mechanics material parameters which can describe microvoid and microcrack growth and crack propagation. The hardening and softening behavior of rock and strain-permeability behavior under compression were compared with the experimental results. We described the influence of material parameters to determine the peak stress and residual strength regime.

The alteration of modulus and permeability with rock damage has been studied. The results show that the discontinuity of modulus and permeability causes retardation of fluid movement between the high permeability damaged and low permeability undamaged rock. Stress relaxation by modulus reduction in the damaged zone also plays an important role in propagation of damage and leads to the stress concentration between the interface of damaged and undamaged rock.

In shale instability analysis, if mud salinity is lower than the formation, it enhances rock damage by shear and tensile failure around a wellbore because of osmosis effects between the drilling mud and shale formation. Cooling of the rock causes more tensile hoop stress and reduces the pore pressure around a wellbore than in isothermal conditions. Results show that thermally induced tensile stress contributes to stabilize the shear failure in the minimum far-field stress direction; however, it enhances tensile failure potential in the maximum far-field stress direction.

We studied distribution of two- and three-dimensional injection-induced damage propagation microseismic events using the fully-coupled thermo-poroelastic finite element methods. To simulate the rock mass more realistically, heterogeneous modulus and permeability were implemented in the numerical modeling of microseismic events. We assumed that the rock properties follow a statistical distribution generated using the Weibull distribution function. Both well-scale and reservoir-scale simulation have been developed for the analysis of injection-induced rock damage and microseismic

event propagation. We found that deviatoric far-field stress and permeability anisotropy contribute to predict the localization of microseismic event propagation. The results show that the shape of injection-induced microseismic events becomes elliptical and sharper as the deviatoric far-field stress and permeability anisotropy increase. Also we illustrated that the microseismic events are localized when we use rock failure criteria for comparing the pore pressure criticality.

Results show that a finer mesh provides more accurate numerical solutions but there are limitations of computational speed and memory storage to solve large-scale, fully-coupled problems. To optimize the mesh size and element numbers, we used a finer mesh around the wellbore and saw significant changes of pore pressure, temperature, and solute mass concentration. For the wellbore stability problem, the system domain size is relatively small compared to the injection simulation, so we used a much finer mesh around a 2-meter radius zone around the wellbore. However, for the injection simulations, damage propagation in the maximum direction is longer than wellbore stability problem. So that a fine mesh is used not only around a wellbore but also in the areas parallel to the maximum far-field stress direction. There is a possibility of unrealistic large damage propagation if the mesh size is too large to accurately compute the stress localizations within elements.

9.2 Recommendations

In this work, we considered single-phase water injection and a mechanical damage model. The applications of heterogeneous reservoir modulus and permeability have been used to depict more realistic geomechanics simulations. In this work, a continuous stochastic model approach was used to simulate heterogeneous reservoirs. However, in reality geological media have a lot of discrete features such as fissures, faults, and natural fractures. To simulate these more realistically, we recommend introducing a combined approach of stochastic and discrete modeling. For example, we can model the natural fracture and faults by discrete modeling and other regions can be described with continuous stochastic modeling. Finer mesh will be better for near injection and production well, and coarse mesh is recommended for the regions where fluid injection and production do not cause much variation in stress, etc. The choice of finer and coarser mesh sizes is relative to the total reservoir size that needs be simulated, the numerical accuracy requirements for each case, and the variations of numerical variables by boundary conditions such as injection rate, well pressure, production rate, and far-field stress. The mesh dependency problem is more significant when we consider the nonlinear stress-strain behavior. Fig. 9.1 shows a typical example of damage/fracture trajectory with different scales of mesh size. We observed that damage distributions are localized as mesh density increases with the same loading conditions. Particularly for the simulation of damage propagation, the loading condition and post-peak response contributes to mesh density (Abu Al-Rub and Kim, 2010). As the mesh size decreases, average variation of displacement decreases during the damage propagation because of damage localization in finer mesh. Therefore, it is necessary to use finer mesh in finite element modeling for the nonlinear behavior of rock and stress dependent permeability.

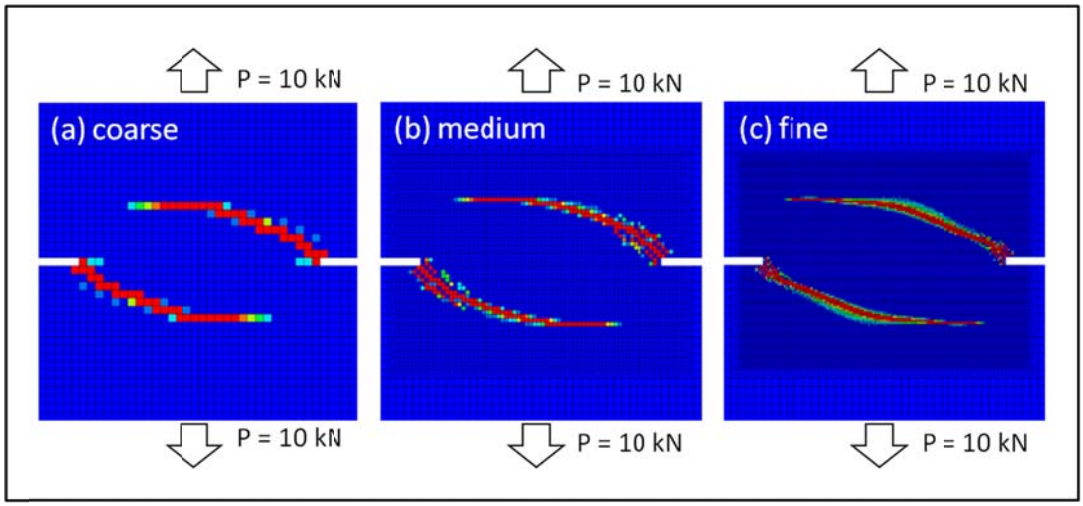

Fig. 9.1. Simulated crack propagation for three mesh densities: (a) coarse, (b) medium, and (c) fine (Abu Al-Rub and Kim, 2010).

10. Nomenclature

a	Compressibility
A	Cross-sectional area
A^D	Damaged cross-sectional area
B	Skempton's pore pressure coefficient
c_f	Fluid diffusion coefficient
c_F	Cohesive strength
c_p	Specific heat capacity
c_T	Thermal diffusivity
C^S	Solute concentration
d	Damage variable
D^S	Solute diffusivity
E	Elastic modulus
f	loading pressure
f_c	Maximum compressive strength
f_{cr}	Residual compressive strength
f_{tr}	Residual tensile strength
f_q	fluid injection rate
G	Shear modulus
h	Depth between bottom and surface
J^f	Fluid flux
J^S	Solute mass flux
k	Permeability
k_0	Initial permeability
$k_{H,max}$	Maximum horizontal anisotropic permeability
$k_{h,min}$	Minimum horizontal anisotropic permeability
k_v	Vertical anisotropic permeability
k^T	Thermal conductivity
$\boldsymbol{K}$	Elastic stiffness matrix
$\boldsymbol{J}$	Jacobian matrix
M	Biot's modulus
$\boldsymbol{N}$	Shape function vector
p	Pore pressure
p_0	Initial pore pressure
P_0	Isotropic far-field stress
s	The variables of s_0
s_0	Mean value of the corresponding of s
S_0	Finite shear stress
S_0	Deviatoric component in far-field stress
S_1	Finite shear stress

$S_{H,max}$	Maximum horizontal far-field stress
$S_{h,min}$	Minimum horizontal far-field stress
S_v	Vertical far-field stress
t	Time
T	Temperature
T_0	Initial temperature
u	Displacement of x-direction
v	Displacement of y-direction
w	Displacement of z-direction
w_s	Displacement of z-direction at the surface
α	Biot's constant
α_f	Volumetric thermal expansion coefficient of fluid
α_S	Volumetric thermal expansion coefficient of solid
β	Thermal expansion coefficients
β_d	Material parameter for stress-dependent permeability
ε	Strain
ε_c	Maximum compressive strain
ε_{cr}	Residual compressive strain
ε_{tr}	Residual tensile strain
ε_v	Volumetric strain
ϕ	Porosity
ϕ_f	Friction angle
μ	Fluid viscosity
θ	Parameter for time discretization
μ	Fluid viscosity
ρ_m	Total mass density
ν	Poisson ratio
ν_u	Undrained Poisson's ratio
σ	Total stress
σ'	Effective stress
σ_1	Maximum principal stress
σ_3	Minimum principal stress
τ	Stress which has the relationship with strain in linear elasticity
ω_0	Swelling coefficient
ξ	Fluid content

ξ_d	Increasing factor for permeability increase after failure
$\mathfrak{R}$	Reflection coefficient

11. References

Abu Al-Rub, R. K., Kim, S.M., 2010. Computational application of a coupled plasticity-damage constitutive model for simulating plain concrete fracture. Eng. Fracture Mech. 77, 1577-1603.

Adushkin, V., Rodionov, V.N., Turuntaev, S., 2000. Seismicity in the oil field. Oilfield Review 1, 2–17.

Babuska, I., 1971. Error bounds for finite element methods. Num. Math. 16, 322–333.

Babuska, I., 1973. The finite element method with Lagrange multipliers. Num. Math. 20, 179–192.

Bai, M., Elsworth, D., 1994. Modeling of subsidence and stress-dependent hydraulic conductivity for intact and fractured porous media. Rock Mech. Rock Eng. 27, 209–234.

Bai, M., Meng, F., Elsworth, D., Roegiers, J.C., 1999. Analysis of stress-dependent permeability in nonorthogonal flow and deformation fields. Rock Mech. Rock Eng. 32(3), 195–219.

Baisch, S., Voros, R., Rothert, E., Stang, H., Jung, R., Schellschmidt, R., 2009. A numerical model for fluid injection-induced seismicity at solutz-sous-forets. Int. J. Rock Mech. Min. Sci. 47(3), 405–413.

Bart, M., Shao, J.F., Lydzba, D., 2000. Poroelastic behavior of saturated brittle rock with anisotropic damage. Int. J. Num. and Anal. Meth. Geomech. 24, 1139–1154.

Biot, M.A., 1941. General theory of three-dimensional consolidation. J. Appl. Phys. 12, 155–164.

Brezzi, F., 1974. On the existence, uniqueness and approximations of saddle point problems arising from Lagrange multipliers. RAIRO Anal.Numer 8 (2), 129–51.

Bruel, D., 2002. Impact of induced thermal stress during circulation tests in an engineered fractured geothermal reservoir. Oil & Gas Sci. Tech. 57, 459–470.

Bruno, M.S., Bovberg, C.A., Nakagaw, F.M., 1991. Anisotropic stress influence on the permeability of weakly-cemented sandstones. In: Proceedings, 32nd U.S. Symposium on Rock Mechanics, Norman, OK, USA, 375–384.

Cacas, M.C., Ledoux, E., de Marsily G., 1990. Modeling fracture flow with a stochastic discrete fracture network: calibration and validation 2. The transport model. Water Resour. Res. 26, 491–500.

Carter, J.P., Booker, J.R., 1982. Elastic consolidation around a deep circular tunnel. Int. J. Solids Struct. 18, 1059–1074.

Chenevert, M.E., 1970. Shale control with balanced-activity oil-continuous muds. J. Petrol. Technol. 22 (10), 1309–1316.

Cheng, H., Dusseault, M.B., 1993. Deformation and diffusion behaviour in a solid experiencing damage: a continuous damage model and its numerical implementation. Int. J. Rock Mech. Min. Sci. Geomech. Abstr. 30, 1323–1331.

Chin, L.Y., Raghavan, R., Thomas, L.K., 2000. Fully coupled geomechanics and fluid-flow analysis of wells with stress-dependent permeability. Soc. Petrol. Eng. 5 (1), 32–45.

Chow, C.L., Wang, J. 1987. An anisotropic theory of continuum damage mechanics for ductile fracture. Eng. Fracture. Mech. 27, 547–558.

Cook R.D., Malkus D.S., Plesha, M.E., Witt, R.J., 2001. Concepts and application of finite element analysis, fourth ed. John Wiley, New York.

Coste, F., Bounenni, A., Chanchole, S., Su, K., 2001. A method for measuring hydraulic and hydromechanical properties during damage in materials with low permeability. Thermohydromechanical Behaviour of Deep Argillaceous Rock, in: Hoteit, N., Su, K., Tijani, M., Shao, J.-F. (Ed.), Swets & Zeitlinger Publisher, The Netherlands, pp. 109–116.

Coulomb, C.A., 1773. Application of the rules of maxima and minima to some problems of statics related to architecture. Aca. Roy. Sci. Mem. Math. Phys. 7, 343–382.

Cryer, C.W., 1963. A comparison of the three-dimensional compaction theories of Biot and Terzaghi. Q. J. Mech. Appl. Math. 16, 401–412.
Detournay, E., Cheng, A.H.D., 1988. Poroelastic response of a borehole in a non-hydrostatic stress field. Int. J. Rock Mech. Min. Sci. Geomech. Abstr. 25, 171–182.
Detournay, E., Cheng, A.H.D., 1993. Fundamentals of poroelasticity, Comprehensive Rock Engineering, in: Hudson, J. (Ed.), Pergamon Press, Oxford, UK, pp. 113–171.
De Paola, N., Faulkner, D. R., Collettini C., 2009. Brittle versus ductile deformation as the main control on the transport properties of low-porosity anhydrite rocks, J. Geophys. Res. 114 (B6), B06211.
Economides, M.J., Hill A.D., Ehlig-Economides, C., 1993. Petroleum production systems, Prentice Hall, Inc., Upper Saddle River, NJ, USA.
Elsworth, D., 1989. Thermal permeability enhancement of blocky rocks: one dimensional flows. Int. J. Rock Mech. Min. Sci. Geomech. Abst. 26, 329–339.
Ezzedine S.M., 2010. Impact of geological characterization uncertainties on subsurface flow using stochastic discrete fracture network models. In: Proceedings of the Thirty-fifth Workshop on Geothermal Reservoir Engineering. Stanford University, Stanford, CA, USA. pp. 1–7.
Fang Z., Harrison, J.P., 2002. Development of a local degradation approach to the modelling of brittle fracture in heterogeneous rocks. Int. J. Rock Mech. Min. Sci. 39, 443–457.
Fehler, M., Jupe, A., Asanuma, H., 2001. More than cloud: new techniques for characterizing reservoir structuring using induced seismicity. The Leading Edge 20(3), 324–328.
Finlayson, B.A., 1972. The method of weighted residuals and variational principles. Academic Press, New York, USA.
Gharahbagh, A.E., Fakhimi, A., 2010. Pore distribution and statistical size effect: a discrete element analysis. 44th US Rock Mechanics Symposium, Salt Lake City, Utah. 10–322.
Ghassemi, A., Diek, A., 2003. Linear chemo-poroelasticity for swelling shales: theory and application. J. Pet. Sci. Eng. 38, 199–212.
Ghassemi, A., Tao, Q., Diek, A., 2009. Influence of coupled chemo-poro-thermoelastic processes on pore pressure and stress distributions around a wellbore in swelling shale. J. Pet. Sci. Eng. 67, 57–64.
Grimvall, G., 1986. Thermophysical properties of Materials, North-Holland, Amsterdam, The Netherlands.
Gurson, A.L., 1977. Continuum theory of ductile rupture by void nucleation and growth. Part I: yield criteria and flow rules for porous ductile media. J. Eng. Mater. Tech. 99, 2–15.
Hale, A.H., Mody, F.K., Salisbury, D.P., 1992. Experimental investigation of the influence of chemical potential on wellbore stability. IADC/SPE–23885, pp. 18–21.
Hamiel, Y., Lyakhovshy, V., Agnon, A., 2005. Poroelastic damage rheology: dilation, compaction, and failure of rocks. Geochem. Geophy. Geosys. 6, 1–9.
Heidug, W.K., Wong S.W., 1996. Hydration swelling of water-absorbing rocks: a constitutive model. Int. J. Num. Anal. Methods in Geomech. 20, 403–430.
Hewett, T.A., 1986. Fractal distributions of reservoir heterogeneity and their influence on fluid transport. Paper presented at the SPE Annual Technical Conference and Exhibition, New Orleans, Louisiana. SPE–15386.
Ingebritsen, S.E., Manning, C.E., 2010. Permeability of the continental crust: dyanamic variations inferred from seismicity and metamorphism. Geofluids 10, 193–205.
Jaeger, J.C., Cook, N.G.W., Zimmerman, R.W., 2007. Fundamentals of rock mechanics, fourth ed. Blackwell Publishing, Malden, Massachusetts, USA.

Kachanov, L.M., 1958. On the creep fracture time, Izv Akad, Nauk USSR Otd. Tech. 8, 26–31.
Kachanov, L.M., 1986. Introduction to continuum damage mechanics. Martinus Nijhoff Publishers, The Netherlands.
Khan, M., Teufel, L.W., 2000. The effect of geological and geomechanical parameters on reservoir stress path and its importance in studying permeability anisotropy. SPE Reservoir Evaluation & Engineering (10), 66184
Krajcinovic, D.,1983. Constitutive equations for damage materials, J. App. Mech. 50, 355–360.
Krajcinovic, D., 1996. Damage mechanics, Elsevier, Amsterdam.
Krajcinovic, D., Foneska, G.U., 1981. The continuum damage theory of brittle materials. J. App. Mech. 48, 809–824.
Kurashige, M., 1989. A thermoelastic theory of fluid-filled porou materials. Int. J. Solids Struct. 25(9), 1039–1052.
Kiyama, T., Kita, H., Ishijima, Y., Yanagidani, T., Akoi, K., Sato, T., 1996. Permeability in anisotropic granite under hydrostatic compression and tri-axial compression including post-failure region. In: Proceedings of the second North American Rock Mechanics Symposium. Montreal, Quebec, Canada, pp. 383–391.
Knutson, C.F., 1976. Modeling of noncontinuous fort union and mesaverde sandstone reservoirs, Piceance Basin, Northwestern Colorado. SPE Journal, 16(4), 5024.
Labrid, J.C., 1975. Thermodynamic and kinetic aspects of argillaceous sandstone acidizing. Soc. Petrol. Eng. J. 117–128.
Lambert, M.E., 1981. A statistical study of reservoir heterogeneity. M.S. Thesis. The University of Texas, Austin, USA.
Lemaitre, J., 1984. How to use damage mechanics. Nuclear engineering and Design. 80, 233–245.
Lemaitre, J., 1985. A continuous damage mechanics model for ductile fracture. J. Eng. Mater. And Tech. 107, 83–89.
Lemaitre, J., Chaboche, J.L., 1990. Mechanics of solid materials, Cambridge University Press, London.
Lewis R.W., Schrefler, B.A., 1988. The finite element method in the static and dynamic deformation and consolidation of porous media, second ed. John Wiley, New York.
Li, X., Cui, L., and Roegiers, J.C., 1998. Thermoporoelastic modeling of wellbore stability in non-hydrostatic stress field. Int. J. Rock Mech. Min. Sci. 35, 4–5.
Liang Z.Z., 2005. Three-dimensional numerical modelling of rock failure process. PhD Thesis. Center for Rock Instability & Seismicity Research, Dallian University of Technology, Dallian, China.
Liu Y., 2006. Using the snesim program for multiple-point statistical simulation. Computers Geosiences. 32, 1544–1563.
Lund, K., Fogler, H.S., 1976. Acidization V. the prediction of the movement of acid and permeability fronts in sandstone. Chem. Eng. Sci. 31(5), 381–392.
Mahnken, R., 2002. Theoretical, numerical and identification aspect of a new model class for ductile damage. Int. J. Plasticity 18, 801–831.
Mazars, J., 1986. A description of micro- and macroscale damage of concrete structures. Eng. Fracture. Mech. 25, 729–737.
Mazars J., Pijaudier-Cabot, G., 1996, From damage to fracture mechanics and conversely: a combined approach. Int. J. Solids and Struct. 33, 3327–3342.

Min, K.S., Ghassemi, A., 2011. A study of numerical simulations of mixed-mode fracture propagation in rock. In: Proceedings, 36th Workshop on Geothermal Reservoir Engineering. Stanford University, Stanford, CA, USA SGP-TR-191.
McTigue, D.F., 1986. Thermoelastic response of fluid-saturated porous rock. J. Geophys. Res. 91(B9), 9533–9542.
Mody, F.K., Hale, A.H., 1993. Borehole-Stability model to couple the mechanics and chemistry of drilling-fluid/shale interactions. J. Petr. Tech. 45, 1093–1101.
Muller A.L., Vargas Jr, E.D.A., Vaz, L.E., Goncalves, C.J., 2008. Borehole stability analysis considering spatial variability and poroelastoplasticity. Int. J. Rock Mech. Min. 46, 90–96.
Murakami, 1988. Mechanical modeling of material damage. J. App. Mech. 55, 280–286.
Pine, R.J., Batchelor A.S., 1984. Downward migration of shearing in jointed rock during hydraulic injections. Int. J. Rock Mech. Min. Sci. 21(5), 249–263.
Palciauskas, W., Domenico, PA., 1982. Characterization of drained and undrained response of thermally loaded repository rocks. Water Res. Res. 18, 281–290.
Rhett, D.W., Teufel, L.W., 1992. Stress dependence of matrix permeability of North Sea sandstone reservoir rock. In: Proceedings, 33rd U.S. Symposium on Rock Mechanics. Santa Fe, New Mexico, 345–355.
Rice, J.R., Cleary, M.P., 1976. Some basic stress-diffusion solutions for fluid-saturated elastic porous media with compressible constituents. Rev. Geophys. Space Phys. 14, 227–241.
Rothert, E., Shapiro, S.A., 2003. Microseismic monitoring of borehole fluid injection: data modeling and inversion for hydraulic properties of rocks. Geophysics 68(2), 685–689.
Ruistuen, H., Teufel, L.W., Rhett, D.W., 1996. Influence of reservoir stress path on deformation and permeability of weakly cemented sandstone reservoirs. SPE–36535.
Safari, M.R., Ghassemi, A., 2011. A 3D analysis of enhanced geothermal reservoir: shear slip and micro-seismicity. 45th US Rock Mehcanics/Geomechanics Symposium. 11–480.
Selvadurai, A.P.S., 2004. Stationary damage modeling of poroelastic contact. Int. J. Solids Struct. 41, 2043–2064.
Shao, J.F. and Marchina, P., 2002. A damage mechanics approach for the modelling of sand production in heavy oil reservoirs. Paper presented at the SPE/ISRM Rock Mechanics Conference. SPE–78167.
Shapiro, S., Huenges, E., Borm, G., 1997. Estimating the crust permeability from fluid-injection-induced seismic emission at the KTB site. Geophys. J. Int. 131, F15–F18.
Shapiro, S., Audigane, P., Royer, J., 1999. Large-scale in situ permeability tensor of rocks from induced microseismicity. Geophys. J. Int. 137, 207–213.
Shapiro, S. A., Rothert, E., Rath, V., Rindschwentner, J., 2002. Characterization of fluid transport properties of reservoirs using induced microseismicity. Geophysics. 67, 212–220.
Sherwood, J.D., Bailey, L., 1994. Swelling of shale around a cylindrical well-bore. Proc. R. Soc. A 444, 161–184.
Shipping, L., Yushou, L., Yi, L., Zhenye, W., Gang, Z., 1994. Permeability-strain equations corresponding to the complete stress-strain path of Yinzhuang Sandstone. Int. J. Rock Mech. Min. Sci. Geomech. Abstr. 41, 2043–2064.
Sidoroff, F., 1981. Description of anisotropic damage application to elasticity. IUTAM Coloqium on Physical Nonlinearites in Structural Analysis. Springer-Verlag, Berlin.
Simakin, A., Ghassemi, A., 2005. Modelling deformation of partially melted rock using a poroviscoelastic rheology with dynamic power law viscosity. Tectonophysics 397, 195–209.

Smith I. M., Griffiths D. V., 2004. Programming the finite element method, fourth ed. John Wiley, New York.
Smith, P.J. and Morgan, D.T.K., 1986. Modelling faulted and fluvial reservoirs. Paper presented at the European Petroleum Conference, London, UK. SPE–15853-MS.
Strang G., Fix, G.J., 1973. An analysis of the finite element method. Wellesley Cambridge Press, Massachusetts.
Talwani, P., Acree, S., 1985. Pore pressure diffusion and the mechanism of reservoir-induced seismicity. Pure Appl. Geophys. 122, 947–965.
Tang, C.A., Tham, L.G., Lee, P.K.K., Yang, T.H., Li, L.C., 2002. Coupled analysis of flow, stress and damage (FSD) in rock failure. Int. J. Rock Mech. Min. 39, 477–489.
Tao, Q., 2000. Wellbore stability in water-sensitive shales. M.S. Thesis. University of North Dakota. Grand Forks, ND, USA.
Terzaghi, K., 1923. Die Berechnung des durchlassigkeitsziffer des tones aus dem verlauf der hydrodynamischen spannungserscheinungen, Sitz. Akad. Wiss. Wien, Abt. IIa. 132, 125– 38.
Terzaghi, K., 1936. The shearing resistance of saturated soils and the angle between planes of shear. Proc. Int. Conf. Soil Mech. Found. Eng. Vol. 1, Harvard University Press. Cambridge, MA, USA.
Thomas, L.K., Chin, L.Y., Pierson, R.G., Sylte, J.E., 2003. Coupled geomechanics and reservoir simulation. SPE–87339-PA.
Timoshenko, S.P., Goodier J.N., 1982. Theory of elasticity, international ed. McGraw-Hill, Singapore.
Tvergaard, V., 1982. Material failure by void coalescence in localized shear bands. Int. J. Solids Struct. 18, 659–672.
Voyiadjis, G.Z., Kattan, P.I., 1999. Advances in damage mechanics: metals and metals matrix composites. Elsevier Science, Oxford, UK.
Wang Y., Papamichos E., 1994. Conductive heat flow and thermally induced fluid flow around a wellbore in a poroelastic medium. Water Resour. Res. 30(12), 3375-3384.
Wang, J.A., Park H.D., 2002. Fluid permeability of sedimentary rock in a complete stress-strain process. Eng. Geol. 63, 291–300.
Weibull W., 1951. A statistical distribution function of wide applicability. J. Appl. Mech. 18, 293–297.
Yang, T.H., Tham, L.G., Tang, C.A., Liang, Z.Z., Tsui, Y., 2004. Influence of heterogeneity of mechanical properties on hydraulic fracturing in permeable rocks. Rock Mech. Rock Eng. 37, 251–275.
Yu, M., Chen, G., Chenevert, M.E., Sharma M.M., 2001. Chemical and thermal effects on wellbore stability of shale formations, Paper presented at the SPE Annual Technical Conference and Exhibition, New Orleans, Louisiana. SPE–71366.
Yuan, S.C., Harrison, J.P., 2006. A review of the state of the art in modeling progressive mechanical breakdown and associated fluid flow in intact heterogeneous rock, Int. J. Rock Mech. Min. 43, 1001–1022.
Voss, R.F., 1985. Random fractals: characterization and measurement, Plenum Press, New York.
Voyiadjis, G.Z., Kattan, P.I., 1999. Advances in damage mechanics: metals and metals matrix composites, Elsvier Science, Oxford.
Zhao, X.L., Ma, Q., Roegiers J.C., 1993. The measurement of compressibility of fractured rock. SCA–9318.
Zhou, X., Ghassemi, A., 2009. Finite element analysis of coupled chemo-poro-themo-mechanical effects around a wellbore in swelling shale. Int. J. Rock Mech. Min. 46, 769–778.
Zienkiewicz, O.C., Taylor, R., 1991. The finite element method. Mcgraw-Hill, New York.

Zoback, M.D., Byerlee, J.D. 1975. The effect of micro-crack dilatancy on the permeability of westerly granite. J. Geophys. Res. 80, 752–755.

12. Appendix A

Derivation of finite element discretization for fully coupled chemo-thermo-poroelasticity

1. Field equations for displacement, pore pressure, solute mass concentration, and temperature

$$\left(K+\frac{G}{3}\right)\nabla\left(\nabla\cdot\mathbf{u}\right)+G\nabla^2\mathbf{u}+m\left(\alpha'\nabla p-\chi\nabla C^S+\gamma_1\nabla T\right)=0 \qquad \text{(A.1)}$$

$$\alpha\left(\nabla\cdot\dot{\mathbf{u}}\right)+\beta'\dot{p}+\chi'\dot{C}^S+\gamma_2\dot{T}-\frac{k}{\mu}\nabla^2 p+\frac{k}{\mu}L_D\nabla^2 C^2=0 \qquad \text{(A.2)}$$

$$\phi\dot{C}^S-D^S\nabla^2 C^S-C^S D^T\nabla^2 T=0 \qquad \text{(A.3)}$$

$$\dot{T}-c^T\nabla^2 T=0 \qquad \text{(A.4)}$$

2. Weight residual method

The governing equation can be discretized from the following examples. A typical example for solving the differential equation is

$$L(u)=f \qquad \text{(A.5)}$$

where L is the differential equation as a function of u, and f is the known function of the independent variables.

The solution of u has weak formulations:

$$u(x)\approx U_N(x)=\sum_{j=1}^{N}c_j\phi_j(x)+\phi_0(x) \qquad \text{(A.6)}$$

If we substitute $U_N(x)$ in the left hand side of Eq. A.5, the residuals can be obtained by $L(U_N)-f$, which is called the residual of the approximation.

$$R\equiv U_N(x)-f=L\left(\sum_{j=1}^{N}c_j\phi_j(x)+\phi_0(x)\right)-f\neq 0 \qquad \text{(A.7)}$$

The parameter c_j is solved by setting residual R to vanish by integration in the weighted-residual method:

$$\int_\Omega \psi_i(x)R(x,C_j)\,d\Omega \qquad (i=1,2,3,...N) \qquad \text{(A.8)}$$

where $\psi_i(x)$ are the weight functions and the most widely used weighted-residual method can be summarized as

Galerkin's method: $\psi_i=\phi_i$

Petrov-Galerkin method: $\psi_i\neq\phi_i$

Least squares method: $\psi_i=\frac{\partial R}{\partial c_i}$

3. Application of Galerkin's method for the variables

The continuous variables *u, p,* C^S, and *T* are approximated by the nodal values through the shape functions as

$$\widetilde{u} = \sum_{i=1}^{q} N_i u_i \qquad \widetilde{p} = \sum_{i=1}^{q} N_i p_i \qquad \widetilde{T} = \sum_{i=1}^{q} N_i T_i \qquad \widetilde{C}^S = \sum_{i=1}^{q} N_i C_i^S$$

We can substitute the nodal variables to the field equations by applying Galerkin's residual method.

For solids,

$$\left(K + \frac{G}{3}\right) \int_{\Omega} [N_u]^T \frac{\partial^2}{\partial x^2} [N_u] \{\mathbf{u}\}\, d\Omega + G \int_{\Omega} [N_u]^T \frac{\partial^2}{\partial x^2} [N_u] \{\mathbf{u}\}\, d\Omega +$$

$$\left(K + \frac{G}{3}\right) \int_{\Omega} [N_u]^T \frac{\partial^2}{\partial x \partial y} [N_u] \{\mathbf{u}\}\, d\Omega + \alpha' \int_{\Omega} [N_p]^T \frac{\partial}{\partial x} [N_p] \{\mathbf{p}\}\, d\Omega -$$

$$\chi \int_{\Omega} [N_{C^s}]^T \frac{\partial}{\partial x} [N_{C^s}] \{\mathbf{C^S}\}\, d\Omega + \gamma_1 \int_{\Omega} [N_T]^T \frac{\partial}{\partial x} [N_T] \{\mathbf{T}\}\, d\Omega = 0$$

For fluids,

$$\alpha \int_{\Omega} [N_u]^T \frac{\partial}{\partial x} [N_u] \{\dot{\mathbf{u}}\}\, d\Omega + \beta' \int_{\Omega} [N_p]^T [N_p] \{\dot{\mathbf{p}}\}\, d\Omega +$$

$$\chi' \int_{\Omega} [N_{C^s}]^T [N_{C^s}] \{\dot{\mathbf{C}}^{\mathbf{S}}\}\, d\Omega + \gamma_2 \int_{\Omega} [N_T]^T [N_T] \{\dot{\mathbf{T}}\} -$$

$$\frac{k}{\mu} \int_{\Omega} [N_p]^T \frac{\partial^2}{\partial x^2} [N_p] \{\mathbf{p}\}\, d\Omega + \frac{k}{\mu} L_D \int_{\Omega} [N_{C^s}]^T \frac{\partial^2}{\partial x^2} [N_{C^s}] \{\mathbf{p}\}\, d\Omega = 0$$

For solute mass concentrations,

$$\phi \int_{\Omega} [N_{C^s}]^T [N_{C^s}] \{\dot{\mathbf{C}}^{\mathbf{S}}\}\, d\Omega - D^S \int_{\Omega} [N_{C^s}]^T \frac{\partial^2}{\partial x^2} [N_{C^s}] \{\mathbf{C^S}\}\, d\Omega$$

$$- \int_{\Omega} [N_T]^T \{\mathbf{C^S}\} \frac{\partial^2}{\partial x^2} [N_T] \{\mathbf{T}\}\, d\Omega = 0$$

For temperature,

$$\int_{\Omega} [N_T]^T [N_T] \{\dot{\mathbf{T}}\}\, d\Omega - c^T \int_{\Omega} [N_T]^T \frac{\partial^2}{\partial x^2} [N_T] \{\mathbf{T}\}\, d\Omega = 0$$

Integration by parts for the above three equations leads to

$$\mathbf{K_m}\, \widetilde{\mathbf{u}} + \mathbf{A}\, \widetilde{\mathbf{p}} - \mathbf{W} \widetilde{\mathbf{C}} + \mathbf{V}\, \widetilde{\mathbf{T}} = \mathbf{0}$$

$$\mathbf{A^T}\, \dot{\widetilde{\mathbf{u}}} + \mathbf{S}\, \dot{\widetilde{\mathbf{p}}} + \hat{\mathbf{M}} \dot{\widetilde{\mathbf{C}}} + \mathbf{N}\, \dot{\widetilde{\mathbf{T}}} + \mathbf{H_H} \widetilde{\mathbf{p}} + \mathbf{D_H} \widetilde{\mathbf{C}}^{\mathbf{S}} = \mathbf{0}$$

$$\mathbf{M}\dot{\widetilde{\mathbf{C}}}^{\mathbf{S}} + \mathbf{D_D}\widetilde{\mathbf{C}}^{\mathbf{S}} + \mathbf{Q_D}\,\widetilde{\mathbf{T}} = \mathbf{f}^{\mathbf{u}}$$

$$\mathbf{R}\dot{\widetilde{\mathbf{T}}} + \mathbf{U}\,\widetilde{\mathbf{T}} = 0$$

where :

$$\mathbf{K_m} = \int_{\Omega} \mathbf{B}^{\mathbf{T}}\mathbf{D_u}\,\mathbf{B}\; d\Omega$$

$$\mathbf{A} = \int_{\Omega} \mathbf{B}^{\mathbf{T}}\boldsymbol{\alpha}\,\mathbf{m}\,\mathbf{N_p}\; d\Omega$$

$$\mathbf{W} = \int_{\Omega} \mathbf{B}^{\mathbf{T}}\,\chi\,\mathbf{m}\,\mathbf{N}_{\mathbf{C}^{\mathbf{s}}}\; d\Omega$$

$$\mathbf{V} = \int_{\Omega} \mathbf{B}^{\mathbf{T}}\,\gamma_1\,\mathbf{m}\,\mathbf{N_T}\; d\Omega$$

$$\mathbf{S} = \int_{\Omega} \mathbf{N}_{\mathbf{p}}^{\mathbf{T}}\beta'\,\mathbf{N_p}\; d\Omega$$

$$\hat{\mathbf{M}} = \int_{\Omega} \mathbf{N}_{\mathbf{p}}^{\mathbf{T}}\chi'\mathbf{N}_{\mathbf{C}^{\mathbf{s}}}\; d\Omega$$

$$\mathbf{N} = \int_{\Omega} \mathbf{N}_{\mathbf{T}}^{\mathbf{T}}\,\gamma_2\,\mathbf{N_T}\; d\Omega$$

$$\mathbf{M} = \int_{\Omega} \mathbf{N}_{\mathbf{C}^{\mathbf{s}}}^{\mathbf{T}}\,\phi\,\mathbf{N}_{\mathbf{C}^{\mathbf{s}}}\; d\Omega$$

$$\mathbf{R} = \int_{\Omega} \mathbf{N}_{\mathbf{T}}^{\mathbf{T}}\,\mathbf{N_T}\; d\Omega$$

$$\mathbf{U} = \int_{\Omega} \left\{ (\nabla \mathbf{N_T})^T \left(c^T\right)(\nabla \mathbf{N_T}) + (\mathbf{N_T})^T\,\mathbf{v_f}\,(\nabla \mathbf{N_T}) \right\} d\Omega$$

$$\mathbf{H_H} = \int_{\Omega} \left(\nabla \mathbf{N_p}\right)^T (\mathbf{k}/\eta)\left(\nabla \mathbf{N_p}\right) d\Omega$$

$$\mathbf{D_H} = \int_{\Omega} \left(\nabla \mathbf{N_p}\right)^T L_D \left(\nabla \mathbf{N_p}\right) d\Omega$$

$$\mathbf{D_D} = \int_{\Omega} \left(\nabla \mathbf{N}_{\mathbf{C}^{\mathbf{s}}}\right)^T D^S \left(\nabla \mathbf{N}_{\mathbf{C}^{\mathbf{s}}}\right) d\Omega$$

$$\mathbf{Q_D} = \int_{\Omega} \left(\nabla \mathbf{N_T}\right)^T C^S D^S \left(\nabla \mathbf{N_T}\right) d\Omega$$

Chapter 2. Geomechanical Parameter Estimation and Uncertainty Quantification by Discrete Micro-Seismic Data Integration with Ensemble Kalman Filter

1. Introduction

The EnKF has been widely established as a practical data integration method for large-scale nonlinear dynamical systems and has been received favorably by the scientific community in a range of applications including hydrology, meteorology and oceanography (Evenson et al., 1996; Houtekamer and Mitchell, 1998; Madsen and Canizares, 1999), groundwater model calibration (Chen and Zhang, 2006; Franssen and Kinzelbach, 2008; Nowak, 2009; Schöniger et al., 2011), and oil reservoir characterization (Naevdal et al., 2006; Wen and Chen, 2005; Jafarpour and McLaughlin, 2009; Aanonsen et al., 2009; Jafarpour and Tarrahi, 2011). Evensen (2009) reviews the EnKF formulation and its wide range of applications. Ehrendorfer (2007) presents a review of important issues that are encountered in implementing the EnKF. Despite the existing limitations in operational implementation of the EnKF for more complex (non-Gaussian) and challenging large-scale problems, this approach has become popular as a promising approximate nonlinear estimation method in several applications. In this work, we propose SSBRC by applying the EnKF for MEQ data integration and evaluate its performance using several numerical experiments. Throughout this report, for pore-pressure-diffusion based forward model, all EnKF updates are applied to the natural logarithm of permeability. A parallel EnKF algorithm is also implemented to speed up the computations.

Generating seismicity density maps on the same grid system or mesh structure that is used for describing the geomechanical property distributions artificially increases the data resolution and, hence, the number of data that will be assimilated during the EnKF update step. Large scale datasets, such as 4D seismic data (Aanonsen et al., 2003; Skjervheim et al., 2007), and particularly in this study, high resolution seismicity density maps, can exhibit spurious spatial correlations in the observed data and create unrealistic correlations between rock properties and microseismic data, thereby can degrade the performance of the EnKF update and lead to underestimated solution uncertainty or ensemble collapse (Sakov and Oke, 2008; Myrseth, 2008). We first show the estimation results for the SSBRC approach using the standard EnKF algorithm to illustrate the underestimation of ensemble spread, and then propose three methods to resolve this issue and improve SSBRC uncertainty quantification. The first and simplest approach to overcome ensemble spread underestimation is to increase the observation error artificially by using a large variance for the observation noise. In the other two methods, we reduce the number of observations first by using a spectral projection (spectral dimension reduction) approach and second by coarsening the seismicity density map (spatial dimension reduction). In projection approach, the ensemble of perturbed observations are projected to a reduced subspace that is defined by the leading left singular vectors of the observation matrix. This step is aimed at de-correlating the original observations of the seismicity map. The EnKF update is then used to assimilate the resulting low-dimensional description of the data. In the second approach, we use a coarse grid system for interpretation of the seismic events. This approach is very similar to the original SSBRC implementation except that it uses a coarse grid system in KDE-based continuous seismicity interpretation to make lower resolution density maps. Then the reduced dimension or coarse seismicity density maps are used in the EnKF update equation. We present the

estimation results for these three methods following an introductory example to illustrate underestimation of uncertainty when the standard EnKF is used with large-scale seismicity density maps as observed data. In this work, we develop the practice of permeability inference from discrete MEQ data with EnKF and then extend it to geomechanical parameters by using a coupled geomechanical forward model and subsequently we improve the uncertainty quantification.

2. Modeling Methodology

The SSBRC method proposed in the project aims to infer spatially distributed reservoir properties by integrating MEQ monitoring data with EnKF. As mentioned earlier, we integrate microseismicity density maps as observed data. We use two forward modeling approaches for simulating the reservoir stimulation process. A complete forward model is required to relate the permeability distribution of the reservoir to seismicity density maps which includes pore-pressure diffusion reservoir model, criticality as failure criterion and KDE-based continuous seismicity interpretation. The main steps involved in the implementation of the pore-pressure diffusion overall forward model are schematically shown in Figure 1.

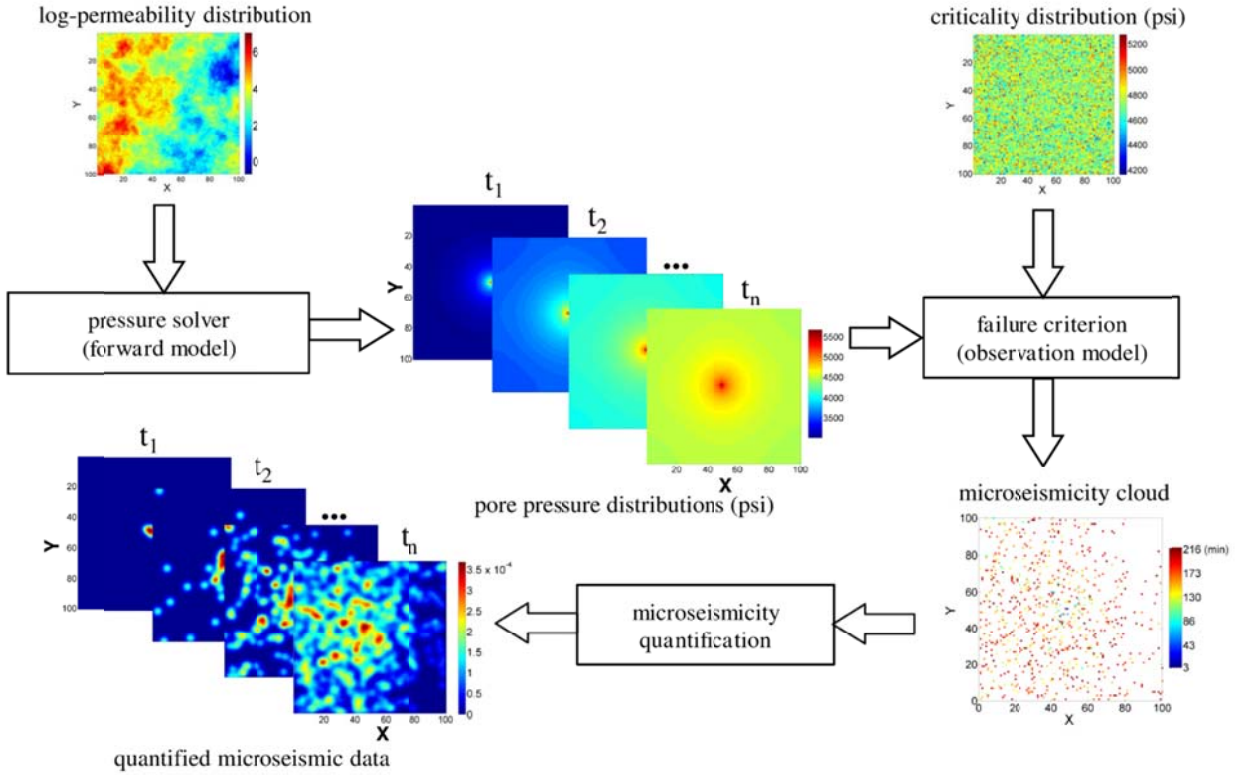

Figure 1. Overall workflow of the pore-pressure diffusion forward model that relates permeability distribution to microseismicity density observations.

Similarly, in the case of geomechanical reservoir model, a comprehensive forward model is needed to relate the reservoir hydraulic and geomechanical property distributions to seismicity density maps which includes FEM-based coupled geomechanical simulator, failure criteria, damage and permeability model and finally KDE-based continuous seismicity interpretation. The main steps involved in the

implementation of the geomechanical overall forward model are schematically shown in Figure 2. The reservoir property distributions such as permeability, Young's modulus, tensile strength and cohesion are used as input parameters to the coupled FEM simulator which involves the coupled process of rock deformation, fluid flow and heat transfer. The FEM simulator predicts the stress distributions in the reservoir and where the rock's effective stress exceeds its strength (prescribed by failure criteria) is used to establish the triggering mechanism and to predict microseismic events. These predictions are then converted into continuous seismicity densities, using the KDE method. Rock damage and permeability models are also used to update the elastic modulus and permeability values to model the rock degradation during hydraulic stimulation.

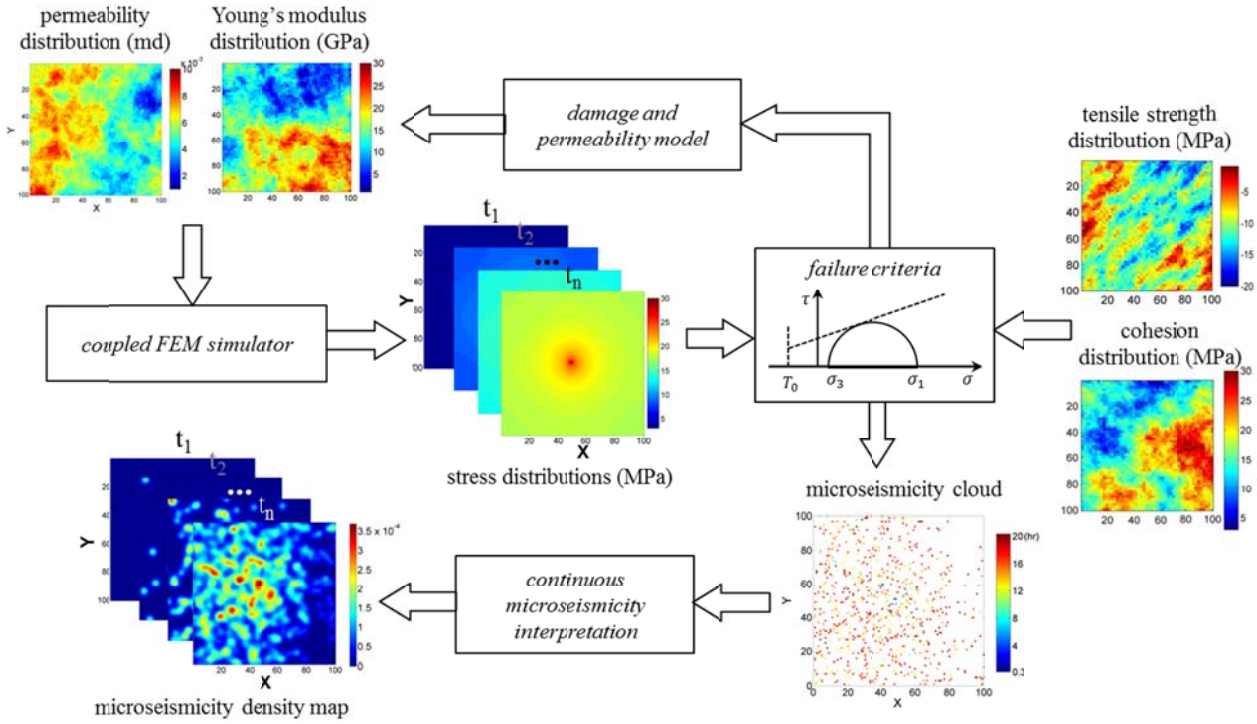

Figure 2. Overall workflow of the geomechanical forward model that relates hydraulic and geomechanical reservoir property distributions to microseismicity density observations.

The details of the geomechanics modeling were described in the previous chapter. In the following the implementation of the EnKf is described. with continuous seismicity interpretation method. Then the SSBRC inverse modeling approach based on EnKF is explained and proposed methods for improving uncertainty quantification are presented. Next, we present and discuss the results of applying the proposed approach to a series of experiments.

3. Continuous Microseismicity Interpretation with Kernel Density Estimation

An important property of the EnKF inversion is that the forward and observation models can be quite general with varying level of complexity. However, the update equation is designed for continuous

random variables (parameters and observations). As a result, the updates can be applied under various forms of event triggering mechanisms and failure criteria as long as the random variables representing the states, parameters and measurements are continuous.

As described before, for geomechanical forward model the MEQ events are determined by shear or tensile failures generated using the specified failure criterion (Mohr-Coulomb model with tension cut-off) at the nodes of the FEM mesh, consequently each MEQ event has its associated location $\mathbf{u}_e$ and occurrence time t_e ($\mathbf{u}$ and t denote general location and time respectively). Therefore at each time step t evaluating the failure criterion at different locations (nodes of the FEM mesh) in the reservoir identifies the distribution of seismicity clouds. Similarly for the pore pressure diffusion forward model, the location and occurrence time of the events are identified by comparing the pore pressure and criticality at each grid block of the reservoir model.

In practice, the discrete microseismic events identify the location of the passive seismic sources and are often generated through seismic source inversion methods. The raw seismic data (collected either from surface or borehole geophones) are inverted to map the location of seismic sources and characterize the associated uncertainty. In this work, however, we skip the seismic source inversion part and assume that, after seismic data analysis, the map of observed source (event) locations is available.

The available seismic observations, however, are of discrete nature since they only identify the seismic status (active or inactive) of a node in the FEM reservoir model. The discrete nature of MEQ events introduces a difficulty in implementing inversion methods that are designed for continuous problems. For gradient-based methods, the discrete form of MEQ observations complicates the calculation of their gradients with respect to unknown parameters. On the other hand, while the EnKF does not require gradient information explicitly, by construction it is formulated for estimation of continuous variables and observations. To address this issue, we interpret the MEQ events as continuous measurements using the kernel density estimation method. KDE is often used for nonparametric approximation of continuous probability density functions (PDFs). The general idea is to convert the discrete MEQ data (and their predictions) into a smooth and continuous seismicity density map. For this purpose, at each time step, we replace each MEQ event/source with a Gaussian kernel function centered at the event location. By adding up the kernels, we construct a continuous function over the model mesh that represents the spatial density of the MEQ events. The procedure for implementing the KDE method is illustrated in Figure 3 for a one-dimensional example. We note that the procedure in Figure 3 can be easily applied to two and three dimensional problems. Mathematically, the continuous seismicity density map can be written as:

$$s(\mathbf{u}) = \frac{1}{n_{MEQ}} \sum_{i=1}^{n_{MEQ}} K_i^{MEQ}(\mathbf{u}) \tag{1}$$

where $K_i^{MEQ}(\mathbf{u}) = N(\mathbf{u}_{MEQ}, \Sigma)$ is a Gaussian kernel, n_{MEQ} is the number of MEQ events at each time step, $\mathbf{u}_{MEQ}$ denotes the location coordinate of the MEQ events (center of the individual Gaussian kernels) and Σ is the covariance matrix of the Gaussian kernel. The continuous map $s(\mathbf{u})$ represents the seismicity

density at all locations (all nodes of the FEM mesh) in the reservoir and constitutes the observations for the EnKF update.

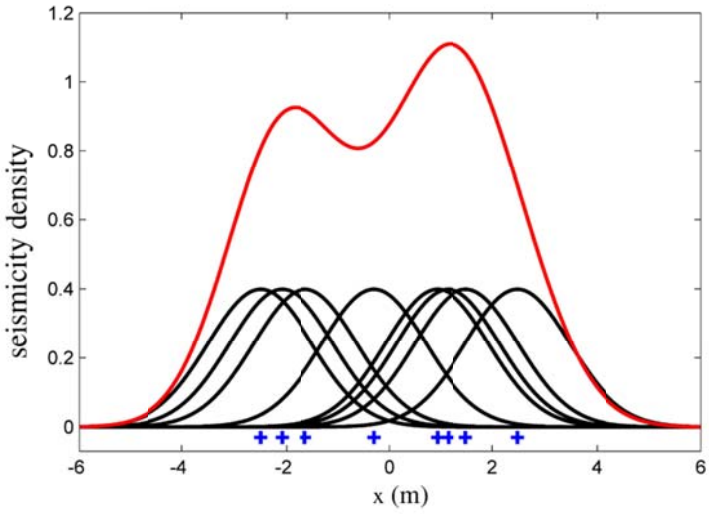

Figure 3. Schematic illustration of converting discrete microseismic event measurements to continuous seismicity density observations in one dimension using kernel density estimation method. The crosses on the x axis show the reconstruction of the discrete microseismic events, while the short symmetric curves display the corresponding Gaussian kernels used to represent each event as a density function with maximum value at the location of the discrete events. The red line shows the density of the microseismic events in space as a continuous observation to be used in the EnKF.

The Gaussian kernel has the form:

$$K^{MEQ}(\mathbf{u}) = N(\mathbf{u}_{MEQ}, \Sigma) = \frac{1}{2\pi|\Sigma|^{\frac{1}{2}}}\left(-\frac{1}{2}(\mathbf{u}-\mathbf{u}_{MEQ})^{T}\Sigma^{-1}(\mathbf{u}-\mathbf{u}_{MEQ})\right) \tag{2}$$

in which the covariance matrix can be specified either globally for all events or locally (or separately) for individual events. The covariance matrix for the kernel determines the shape, size and orientation of the Gaussian ellipsoid centered at the microseismic event location. In this work, we select an isotropic Gaussian kernel for quantification of the microseismic events and the uncertainty in the MEQ locations. Additionally the assigned kernels of all events are assumed exactly the same. Therefore the covariance matrix Σ, is diagonal and all diagonal members (two members for 2D and three members for 3D) are equal. Therefore, to specify the Gaussian kernel or the quantification specifications we only need to determine one single parameter which is the (isotropic) bandwidth h, of the smoothing kernel. The kernel covariance matrix is as follows:

$$\begin{aligned} &\text{In 2D case: } \Sigma = \begin{bmatrix} h^2 & 0 \\ 0 & h^2 \end{bmatrix} = h^2\mathbf{I}_{2\times 2} \\ &\text{In 3D case: } \Sigma = \begin{bmatrix} h^2 & 0 & 0 \\ 0 & h^2 & 0 \\ 0 & 0 & h^2 \end{bmatrix} = h^2\mathbf{I}_{3\times 3} \end{aligned} \tag{3}$$

where $\mathbf{I}_{2\times2}$ and $\mathbf{I}_{3\times3}$ are the identity matrices of the specified dimensions. We note that, in practice, the values of the bandwidth used for the kernel functions are identified from the uncertainty in locating the seismic sources from the raw surface or borehole seismic data. In this work, a simple sensitivity analysis revealed that selecting a bandwidth parameter as large as twice the dimension of each element in the FEM mesh leads to reasonable results. One advantage of the KDE is that it also provides a convenient procedure to account for the spatial uncertainty in the location of the events. For better illustration, the procedure for implementing the KDE method for a two-dimensional example is shown in Figure 4.

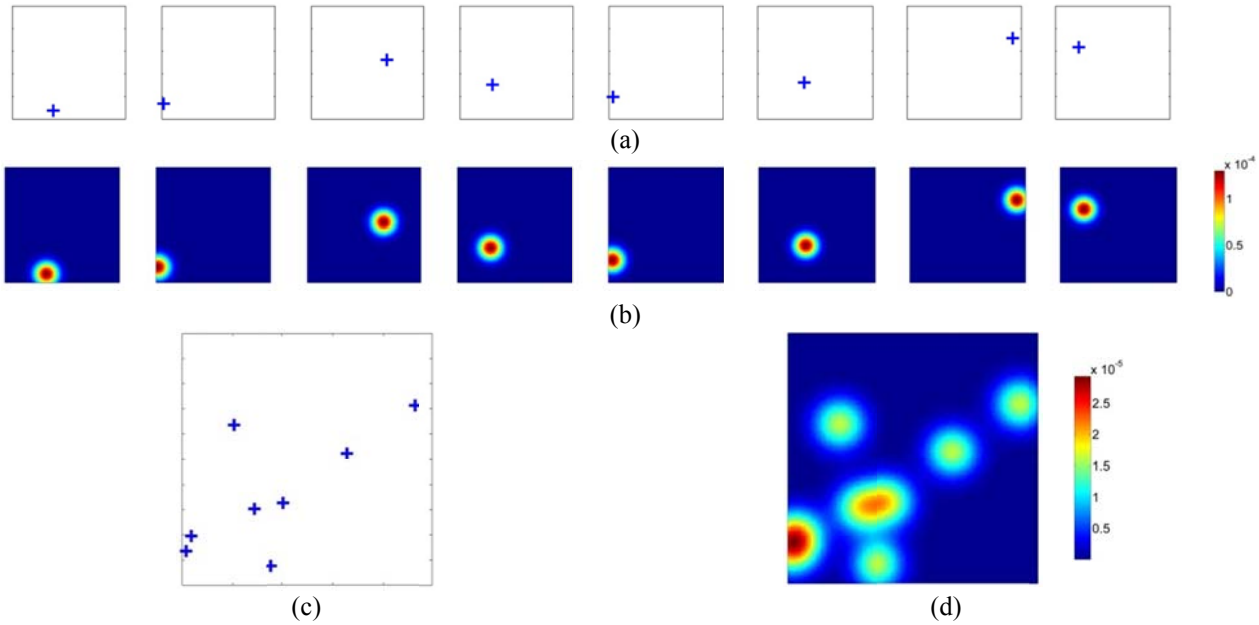

Figure 4. Illustrating the continuous seismicity interpretation in 2D. (a) the individual events in separate plots that make the seismicity cloud of (c). (b) corresponding density maps of single events of (a) that are made by putting 2D Gaussian kernel at the location of each events. (d) the seismicity density map corresponds to the cloud in (c) which is obtained by adding (averaging) all individual densities of (b).

Taken from a 2D geomechanical example (experiment 2 in section 0), Figure 5 shows the evolution of the MEQ cloud at 6 different time steps (called integration time steps) and Figure 6 illustrates the corresponding seismicity density maps created by KDE-based continuous interpretation through these time steps.

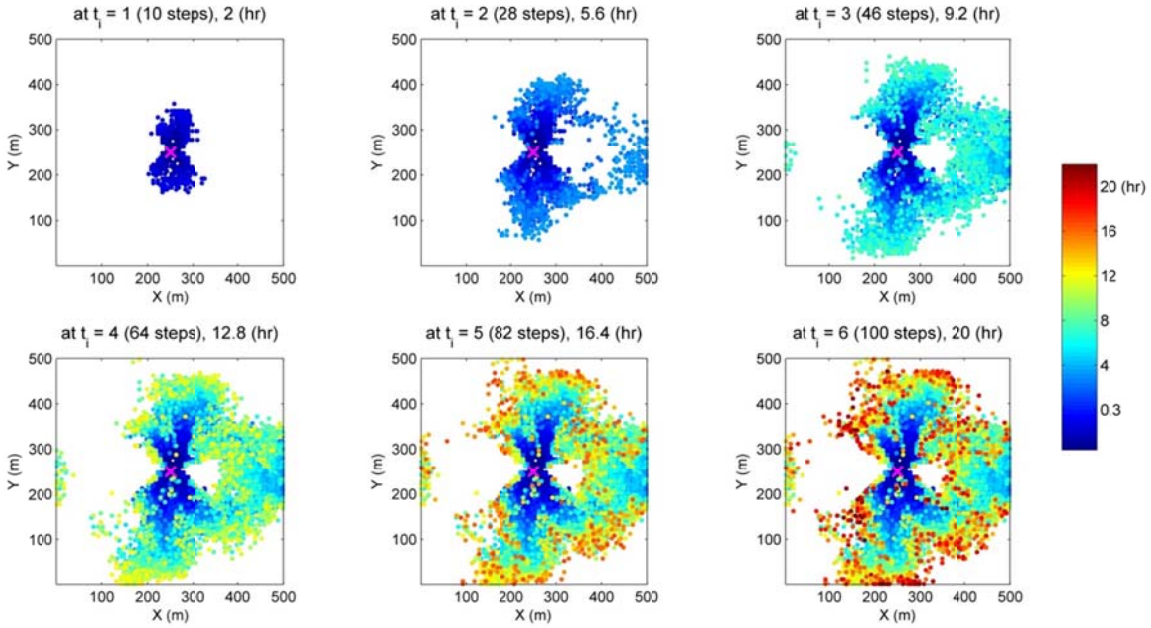

Figure 5. Seismicity cloud evolution in 6 different time steps.

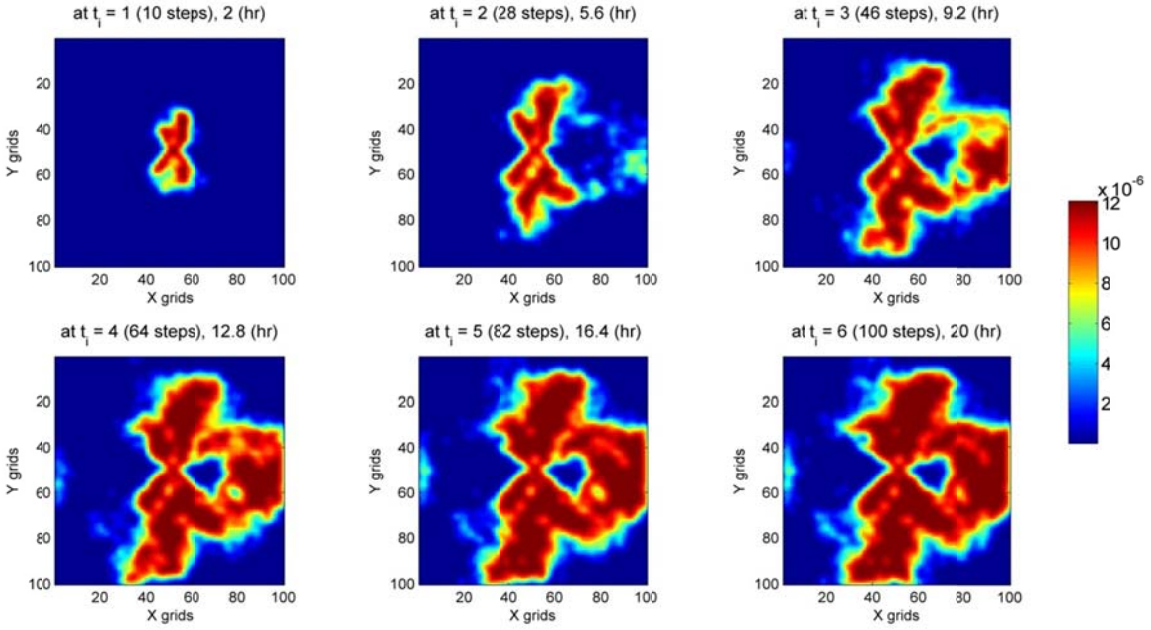

Figure 6. Seismicity density maps created by KDE method corresponding to seismicity clouds of Figure 5.

Quantification of microseismicity cloud on the original FEM mesh (or the original grid block configuration for pore pressure diffusion model) that the reservoir parameters are assigned to, results in a high resolution seismicity density and redundancy in observations. As we discuss in section 0, high dimensional observation or measurement in the EnKF update leads to uncertainty underestimation and bias in the estimation results. Therefore in section 0, we propose to quantify microseismicity on a coarse

mesh (with larger elements or grid blocks) which results in a coarse-scale seismicity density map that reduces the number of measurements.

4. Inverse Modeling Approach

We develop an inverse modeling approach called SSBRC method by adopting EnKF to integrate seismicity density observation for inference of hydraulic and geomechanical parameters. By applying SSBRC to the pore pressure diffusion forward model we infer permeability distribution and by employing SSBRC for the geomechanical forward model we are able to estimate permeability, Young's modulus, tensile strength and cohesion distribution. We also propose some methods to improve the uncertainty quantification and estimation performance of the SSBRC method. The proposed EnKF-based inversion framework begins by generating an ensemble of N_e prior realizations of the reservoir parameter model (e.g. permeability or Young's modulus) based on prior information (e.g., using geostatistical simulation methods). These realizations are used in the pore pressure diffusion forward model or the coupled FEM forward model to perform a Monte Carlo simulation to predict the pore pressure or stress distributions in the reservoir and then failure criterion is used to predict microseismic events. These MEQ cloud predictions are then converted into continuous seismicity densities, using the KDE method, and used in the EnKF update equation. The major computational cost of the method is related to the forecast or prediction step; however, EnKF can be conveniently parallelized to speed up the computations. The computations are implemented using the pore pressure diffusion forward model or the FEM geomechanical forward model and a parallel EnKF algorithm with MATLAB's Parallel Computing Toolbox (MATLAB, 2011). In addition, an ensemble of perturbed observations is generated using a zero-mean Gaussian error distribution with a variance value that is obtained through sensitivity study. The main steps involved in the implementation of the proposed SSBRC method are summarized as follows. (The details of SSBRC algorithm is also depicted in Table 1)

1. Convert discrete microseismic data (measurements) into quantified continuous seismicity density maps using KDE method (section 0).
2. Generate an ensemble of rock property models from available prior information (e.g., using geostatistical simulation techniques). Repeat steps 3–5 until all measurements are processed.
3. For the prediction step, using the developed FEM geomechanical numerical simulator (the pore pressure diffusion forward model), forecast the stress distribution (pore pressure distribution) for each member of the most recently updated ensemble realizations (section **Error! Reference source not found.** or **Error! Reference source not found.**). This step is implemented in parallel.
4. Predict the microseismic events for each realization by the failure criterion (section **Error! Reference source not found.**) and convert the results into seismicity density maps using the KDE approach (section 0).
5. Use the EnKF analysis equation with the seismicity density observations from (1) to update the ensemble of reservoir property models (section 0).

The details of each of these steps are discussed next.

4.1 Estimation with Ensemble Kalman Filter

The classical Kalman filter (Kalman,1960) is a sequential state estimation method for characterization of the first and second statistical moments of the states posterior distribution. Hence, the filter fully characterizes the posterior distribution of linear state-space systems that are characterized with jointly

Gaussian distributions (Kalman, 1960; Gelb, 1974). The implementation of the filter involves two steps: (1) a forecast step, in which a linear state propagation model is used to predict the mean and covariance of the states at the next time step; and, (2) an analysis step that updates the mean and covariance of the states using the dynamic observations and the forecast states mean and covariance. These two steps are repeated sequentially until all observations are assimilated.

For nonlinear dynamical systems, the EnKF provides a practical approximation of the Kalman filter that has been successfully applied to many applications ranging from hydrology, meteorology and oceanography to groundwater and oil reservoir model calibration (see e.g., Aanonsen et al., 2009; Evensen, 2009 and references therein). The sequential formulation of the EnKF distinguishes a forecast (or prior) PDF for the states (augmented vector of geomechanical reservoir parameter and continuous seismicity response $\mathbf{x}_t$) $p[\mathbf{x}_t|\mathbf{y}_{0:t-1}]$, conditioned on all measurements $\mathbf{y}_{0:t-1}$ taken through time $t-1$, and an updated (or posterior) density $p[\mathbf{x}_t|\mathbf{y}_{0:t}]$ conditioned on all measurements $\mathbf{y}_{0:t}$ (continuous seismicity response maps) taken through time t. To compute the cross covariance between predicted observations and parameters, the original state vector is augmented with uncertain model parameters (e.g. permeability, Young's modulus and tensile strength distribution) and predicted measurements. This state augmentation approach can be used to update states and parameters simultaneously. Alternatively, one can only update the uncertain parameters and derive the updated states by solving the flow equations (or coupled flow, heat and geomechanics equations) with the updated parameters. This is the approach taken in this work. The measurements $\mathbf{y}_t$ consist of seismicity density map $s_t(\mathbf{u})$, defined in equation (1) that represent microseismic measurements in space at time t.

Since the general multivariate PDFs and their statistical moments are difficult to characterize, the EnKF uses a Monte Carlo approximation approach by sampling an initial set of realizations from the high-dimensional prior PDF of the uncertain properties to form an ensemble of reservoir states (and/or parameters). These property maps are then used to generate an ensemble of state and measurement predictions that can be used to compute a sample (prior) covariance matrix for the EnKF update step as described below. The forecast step in the EnKF can be written as:

$$\mathbf{x}_{t|t-1}^{j} = f_t\left(\mathbf{x}_{t-1|t-1}^{j}, \mathbf{z}_{t-1}, \mathbf{w}_{t-1}^{j}\right) \qquad j = 1, \dots, N_e \tag{4}$$

where $.|t$ represents conditioning on observations up to time t; $\mathbf{z}_{t-1}$ is a vector of known (nonrandom) time-dependent boundary conditions and controls (such as injection rate); and $\mathbf{w}_{t-1}^{j}$ is a vector of random variables that accounts for modeling errors. The function $f_t(.,.,.)$ represents the state propagation equation from time $t-1$ to time t. The notations j and N_e are used to indicate the realization index and total number of realizations, respectively. In our application, equation (4) represents the solution of the coupled thermo-poroelastic equations (or pore pressure diffusion equation) that describes the time evolution of pore pressure, stress and temperature distributions for each individual realization j of the ensemble reservoir parameter. At time steps when MEQ data are available, the EnKF analysis equation is used to update the reservoir property realizations using the gain matrix and the misfit between predicted and observed seismicity density maps for each realization. At the update step we use an augmented state vector consisting of spatially distributed reservoir property (parameters to estimate) and realizations of the predicted continuous seismicity density map. After each update we apply a confirmation step (Wen and

Chen, 2005) by forecasting the future states and predictions from the initial time step with the updated parameters. We repeat the sequence of prediction and update steps until all measurements are integrated. For a model with N_b nodes (or grid blocks), each reservoir parameter realization $\mathbf{m}^j$ and its corresponding microseismicity density response $\mathbf{s}^j$ are vectors of size $N_b \times 1$. In this work, the reservoir property models are jointly Gaussian random fields that are generated using the sgsim (Geutsch and Journel, 1998) geostatistical simulation technique. The augmented state vector for this case is of the form

$$\mathbf{x}^j = \begin{bmatrix} \mathbf{m}^j \\ \mathbf{s}^j \end{bmatrix}; \qquad j = 1, \dots, N_e \;\Rightarrow \mathbf{X} = [\mathbf{x}^1 \;\; \mathbf{x}^2 \;\; \cdots \;\; \mathbf{x}^{N_e}] \tag{5}$$

The EnKF analysis equation that is used to update each reservoir property realization can be expressed as

$$\mathbf{x}_u^j = \mathbf{x}_f^j + \mathbf{K}\left(\mathbf{y}^j - \mathbf{H}\mathbf{x}_f^j\right), \quad \mathbf{K} = \mathbf{C}_\mathbf{x}^e \mathbf{H}^T (\mathbf{H}\mathbf{C}_\mathbf{x}^e \mathbf{H}^T + \mathbf{C}_\mathbf{d})^{-1} \tag{6}$$

where $\mathbf{K}$ is the Kalman gain matrix and the subscripts u and f denote updated and forecast quantities while the superscript e indicates ensemble calculated statistics. The notations $\mathbf{C}_\mathbf{x}^e$ and $\mathbf{C}_\mathbf{d}$ represent the states sample covariance and observation covariance matrices, respectively. The measurement matrix $\mathbf{H}_{N_b \times 2N_b} = \left[\mathbf{0}_{N_b \times N_b} | \mathbf{I}_{N_b \times N_b}\right]$, where $\mathbf{0}_{N_b \times N_b}$ and $\mathbf{I}_{N_b \times N_b}$ are zero and identity matrices of the specified dimensions, respectively, acts as a selection operator that extracts the predicted measurement components from the augmented state vector. The notation $\mathbf{y}^j$ is used to represent the jth realization of the perturbed observations. The states sample covariance $\mathbf{C}_\mathbf{x}^e$ can be computed from the ensemble of state vectors

$$\mathbf{C}_\mathbf{x}^e = \frac{1}{N_e - 1} \sum_{j=1}^{N_e} \left(\mathbf{x}_f^j - \bar{\mathbf{x}}_f^j\right)\left(\mathbf{x}_f^j - \bar{\mathbf{x}}_f^j\right)^T \;; \quad \bar{\mathbf{x}}_f^j = \frac{1}{N_e} \sum_{j=1}^{N_e} \mathbf{x}_f^j \tag{7}$$

where $\bar{\mathbf{x}}_f^j$ is used to denote the ensemble mean of the forecast states (that is, the reservoir property distribution from the previous step and the corresponding microseismic response forecasts). In the EnKF implementations, the covariance matrix in equation () need not be constructed explicitly and the update can be applied using its low-rank representation though a compact SVD implementation. The covariance matrix in equation () contains the covariance information about the reservoir parameter field as well as the cross covariance information between the reservoir parameter and (microseismic) measurements. It is the latter cross covariance that allows the estimation of uncertain geomechanical reservoir parameter distributions from microseismic observations. This relation bears similarity with the use of covariance and cross covariance in the kriging/simulation (Geutsch and Journel, 1998; Vargas-Guzman and Yeh, 1999) and cokriging/cosimulation (Kitanidis and Vomvoris, 1983; Yeh et al., 1995; Graham and McLaughlin 1989; Geutsch and Journel, 1998) methods, respectively. Note that in equation (), the term $\left(\mathbf{y}^j - \mathbf{H}\mathbf{x}_f^j\right)$ is the misfit between the jth perturbed observation and prediction, which in this case represents the observed

and predicted continuous map of seismicity density. Several remarks regarding the update equation for our problem will follow.

In addition to nonlinearity in the forward coupled geomechanics and flow model, a complexity of the measurement model in our application is the nonlinear failure criterion (i.e., hard truncation) that is used to convert the continuous stress distributions to discrete microseismic events. The Gaussian kernel that we apply to convert the MEQ predictions to continuous maps of seismic density makes the data more amenable to processing with the EnKF. However, the relationship between the magnitude of stress and the resulting seismicity map remains complex.

Considering the dynamic alteration of reservoir geomechanical parameters (Young's modulus and permeability) in our developed coupled FEM simulator based on the damage and permeability model (in section **Error! Reference source not found.**), in the SSBRC inverse modeling approach we estimate geomechanical properties of the intact (initial or undamaged) rock. It is also consistent with our EnKF data integration approach with confirmation step (Wen and Chen, 2005) that for each EnKF analysis step we run the forward model from the beginning (initial state) by updated or estimated intact rock properties. Therefore to obtain the properties of the final stimulated or damaged reservoir rock we just need to run the geomechanical simulator with the estimated intact rock properties.

In our EnKF implementation, to perturb the observations, we add an uncorrelated realization from a Gaussian random noise, with a specified observation covariance matrix $\mathbf{C_d}$, to the value of the observed quantities. We assume that the observation error standard deviation (Std) is proportional to the value of the observed quantity and compute the diagonal elements of the observation error matrix as:

$$\sigma_k^2 = \left(\sigma_{\min} + \frac{(\sigma_{\max} - \sigma_{\min})(y_k - y_{\min})}{(y_{\max} - y_{\min})}\right)^2 , \qquad k = 1,2,\dots,N_b \tag{8}$$

where σ_k^2 is the observation variance at the kth node or grid block (the kth diagonal entry for the observation covariance matrix), $\sigma_{\max}$ and $\sigma_{\min}$ are the minimum and maximum standard deviations specified for the observations, respectively. The notation y_k represents the observed seismicity density at location k while $y_{\min}$, $y_{\max}$ represent the minimum and maximum observed values of the seismicity density, respectively. The realization j of the perturbed observation at location k, can then be written as

$$\begin{gathered} y_k^j = y_k + \varepsilon_k^j , \qquad j = 1,2,\dots,N_e \\ \varepsilon_k^j \sim N\left(0, \sigma_k^2\right) \end{gathered} \tag{9}$$

In this work, we assume an uncorrelated Gaussian observation error with zero mean and standard deviation obtained from equation (). We note that other methods for generating the perturbed observations may also be considered. In particular in section 0 as one of the methods to improve uncertainty quantification of SSBRC, we first generate perturbed observations by perturbing the kernel bandwidth and given the large dimension and the spatial correlation that may exist between the observation errors, we then propose to assimilate the resulting observations in a low-rank subspace defined by the left singular vectors of the ensemble observations perturbations matrix in a similar way to Keepert (2004).

The given SSBRC formulations here are based on the assumption of estimating one of the reservoir properties distribution (assuming one property unknown and the rest known) which can be simply extended to simultaneously estimating more than one reservoir property distribution by only augmenting reservoir parameter vectors in the EnKF state vector.

To generate the ensemble of reservoir parameter realizations, we used a variogram-based geostatistical simulation method with specified variogram parameters. The sgsim algorithm (Geutsch and Journel, 1998) was used to implement the geostatistical simulations. In real applications, the number of realizations is typically determined through a trade-off between available computational resources and the desired statistical accuracy in computing the required sample statistics. For large-scale problems where the number of realizations is limited, practical considerations such as localization or local analysis (Hamill et al., 1995) have been proposed to avoid inaccurate updates due to spurious (nonphysical) correlations and to reduce the possibility of an ensemble collapse. As the results of the numerical experiment in section 0 and 0 show, the proposed SSBRC method with standard EnKF results in severe ensemble spread underestimation which will be resolved by proposed methods in section 0. In the examples that follow, we implement the EnKF algorithm with $N_e = 100$ and do not apply any localizations. The detailed steps of SSBRC method with parallel EnKF algorithm is shown in Table 1.

Table 1. Parallel EnKF algorithm for SSBRC

Parallel EnKF Pseudo Code
1: generate N_e initial parameter ($\mathbf{m}^j$) realizations
2: generate perturbed observations ($\mathbf{y}^j$) from true observation (based on $\mathbf{C_d}$)
3: **for** $t_i = 1$ **to** t_N **do** *(integration time steps)*
4: **par-for** $j = 1$ **to** N_e **do** *(run in parallel on different available cores)*
5: initialize the geomechanical simulator
6: write the j^{th} realization ($\mathbf{m}^j$) as the reservoir parameter
7: run the simulator from beginning until the current integration time (corresponds to t_i)
8: generate the corresponding seismicity cloud ($\mathbb{S}^j$)
9: use KDE to convert seismicity cloud ($\mathbb{S}^j$) to seismicity density ($\mathbf{s}^j$)
10: **end par-for**
11: calculate $\bar{\mathbf{x}}_f^j$, $\mathbf{C}_\mathbf{x}^e$, $\mathbf{K}$
12: update realizations by EnKF analysis equation
13: **end for**

t_i = integration time step index which corresponds to integration time
t_N = the total number of integration time steps (in this study = 6)
par-for = parallel **for** loop which executes its underlying commands in parallel
$\mathbb{S}^j$ = the simulated seismicity cloud corresponding to each $\mathbf{m}^j$

The full forward model simulator that relates the hydraulic or geomechanical parameter distribution to the microseismicity density map consists of geomechanical simulator (relating geomechanical parameter distribution to microseismicity cloud) and microseismicity continuous interpretation (relating microseismicity discrete cloud to microseismicity continuous density map). Figure 7 shows the schematic of the full forward model. In the propagation (Monte Carlo simulation) step of the EnKF procedure we run the full forward model for all ensemble members (geomechanical parameter samples). For the pore

pressure diffusion forward model that relates permeability distribution to MEQ cloud the same full forward model including MEQ continuous interpretation is constructed.

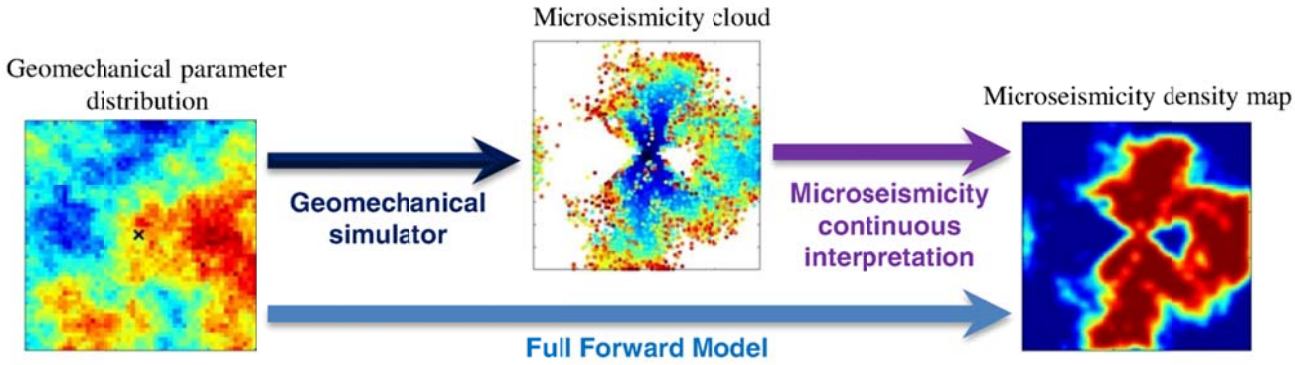

Figure 7. Full forward model relating geomechanical parameter distribution to microseismicity density map.

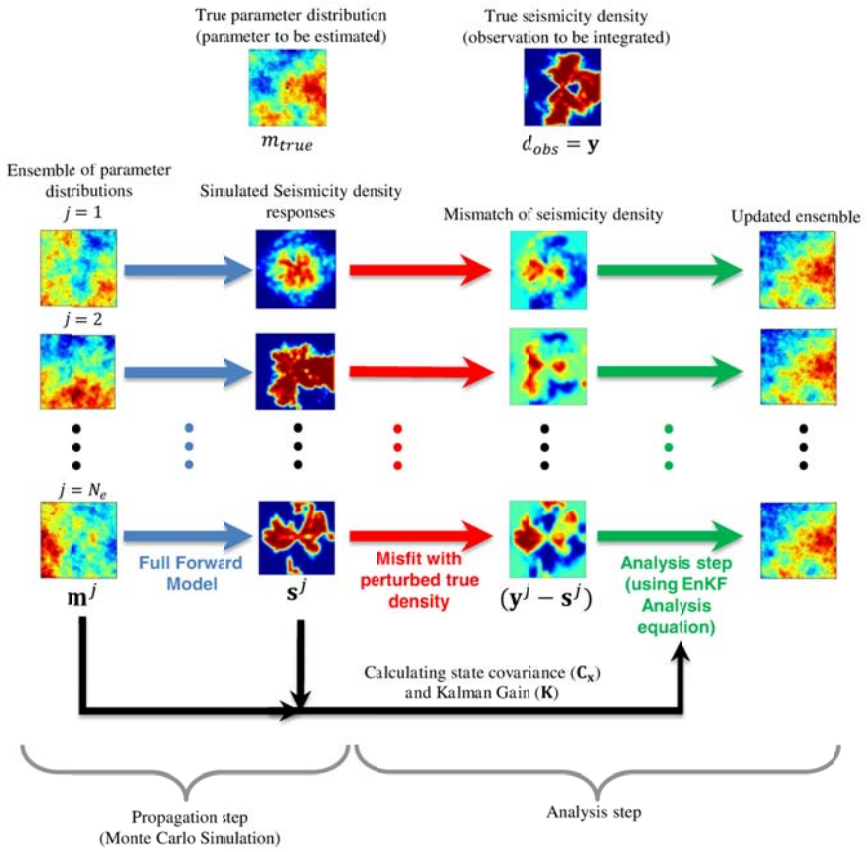

Figure 8. EnKF procedure (in each integration time step).

Figure 8 shows the schematic of the parallel EnKF pseudo code. We perform full forward model of the parameter ensemble (propagation step) in parallel. Since running the forward model is completely

independent for different parameter samples, we are able to run some samples simultaneously on the available cores of the machine. It should be noted that Figure 8 represents the estimation procedure in each integration step. For instance in the first integration step, the first column of Figure 8 is the initial ensemble of parameters and after integration of the first true seismicity density map, we will obtain the first updated ensemble (the last column of Figure 8) which will be the input ensemble (the first column of Figure 8) for the second (next) integration step.

4.2 Improved Uncertainty Quantification

In this section we focus on quantification of uncertainty that is a key concept of application of the EnKF data assimilation approach. It is well known that for large scale datasets, such as seismic data (Skjervheim et al., 2007) and high resolution spatial map of seismicity density, application of the standard EnKF without taking into account the spatial correlation in the observations can lead to underestimated solution uncertainty or ensemble spread. Underestimation of ensemble spread is not favorable as it can introduce unrealistic confidence in potentially inaccurate future predictions and decreases the likelihood of capturing the true behavior of the reservoir. High dimensional observation also leads to expensive computational load in updating scheme of EnKF. In this situation, severe underestimation of the prediction uncertainty can results in biased forecasts and an ensemble collapsing into a single realization.

The standard SSBRC implementation was based on generating seismicity density maps on the same grid system or mesh structure that was used for describing the hydraulic or geomechanical property distributions (section 0). A byproduct of this implementation is that it artificially increases the data resolution and, hence, the number of data that will be assimilated during the EnKF update step. As another significant byproduct of this preprocessing step, the resulting maps can exhibit spurious spatial correlations in the observed data and create unrealistic correlations between rock properties and microseismic data, thereby degrading the performance of the EnKF update.

We first show the estimation results for the SSBRC approach using the standard EnKF algorithm to illustrate the underestimation of ensemble spread (several numerical examples which are reported in section 0 and 0 confirm it), and then propose three methods to resolve this issue. The first and simplest approach to overcome ensemble spread underestimation is to increase the observation error artificially by using a large variance for the observation noise. In the other two methods, we reduce the number of observations first by using a spectral projection (spectral dimension reduction) approach and second by coarsening the seismicity density map (spatial dimension reduction). In projection approach, the ensemble of perturbed observations are projected to a reduced subspace that is defined by the leading left singular vectors of the observation matrix. This step is aimed at decorrelating the original observations of the seismicity map. The EnKF update is then used to assimilate the resulting low-dimensional description of the data. In the second approach, we use a coarse grid system for interpretation of the seismic events. This approach is very similar to the original SSBRC implementation except that it uses a coarse-scale grid system or mesh structure in KDE-based continuous seismicity interpretation in equations (),() to make lower resolution density maps. Then the reduced dimension or coarse seismicity density maps are used in the EnKF update equation. Additionally in general, observation space dimension reduction (either spectral or spatial) improves the computational efficiency of the analysis step of the EnKF.

We present the estimation results for these three methods following an introductory example to illustrate underestimation of uncertainty when the standard EnKF is used with large-scale seismicity density maps as observed data (in section 0 and 0).

4.2.1 Inflated observation error variance

The simple way to reduce the underestimation of ensemble variance is to increase observation error variance. The effect of this remedy is equivalent to damping the EnKF updates, the term $\mathbf{K}\left(\mathbf{y}^j - \mathbf{H}\mathbf{x}_f^j\right)$ in equation () or reducing the weight of observations (or Kalman gain, **K**). To do so, we increase $\sigma_{\min}$ and $\sigma_{\max}$ in equation () which leads to diminishing the effect of seismicity density observation in the EnKF update and finally results in preserving the ensemble spread during data assimilation. While the level of noise considered goes beyond most practical situations, this provides a simple way to improve the underestimation effect as shown in section 0 and 0. We also summarize the results from several experiments with increasing level of observation error variance. From the performed experiment results it is clear increasing the observation error variance can improve the underestimation effect observed in the standard EnKF. However, a main drawback of this approach is that it is not clear how the introduction of significant noise to the observed quantities will generally impact the quality of the EnKF update beside the damping effect. Hence, we consider two other alternative methods that do not corrupt the observations.

4.2.2 Reduced-order projection

The EnKF updating scheme particularly with high-dimensional observation can suffer from the problem known as filter divergence (Jazwinski, 1970), resulting from rank issues (Evensen, 2004) and estimation uncertainty (Houtekamer and Mitchell, 1998). To reduce these problems, (Evensen, 2004) introduced dimension reduction techniques in an EnKF setting. *Skjervheim et al*. (2007) also suggested an alternative EnKF updating using well-known dimension reduction techniques.

In this section we first propose a new method for generating an ensemble of perturbed observations then we use a dimension reduction method to reduce the number of observations integrated in EnKF update equation. The proposed method of perturbing seismicity observation is completely different than the typical procedure of adding Gaussian random noise to the observation (in section 0). To exhibit and finally capture the spatial correlation or redundancy of observation in more efficient fashion, we propose to generate each perturbed observation realization by perturbing the bandwidth of Gaussian kernel. In the standard observation perturbation method explained in section 0, we perturb the observed seismicity density map however here we use the observed seismicity cloud and generate perturbed observations by perturbing the kernel bandwidth in KDE based quantification.

After converting the discrete microseismic measurements to continuous seismicity density maps using Gaussian kernels, the resulting observations exhibit strong spatial correlations. Hence, this correlation (or redundancy) should either be taken into account during the update or should be removed from the data. To remove the correlations in the observations, we project the ensemble of perturbed observations onto a low-dimensional subspace defined by the leading left singular vectors of the observation matrix (Keepert, 2004). During the EnKF update, we use the transformed observations (after projection to the mentioned subspace) for data assimilation. To implement the update, the predicted observations must also be projected onto the same subspace. The procedure is described below.

In the projection approach, at each integration step we first choose a kernel bandwidth h, and its standard deviation σ_h, and then to make each perturbed observation realization, we individually perturb kernel bandwidth h, for each MEQ event of the true observation using a Gaussian distribution as below:

$$h_i^j \sim N\left(h, \sigma_h^2\right); \quad j = 1,2, \dots, N_e; \quad i = 1,2, \dots, n_{MEQ} \tag{1}$$

where N_e and n_{MEQ} are the number of realizations and the number of MEQ events at the specified integration step, respectively. Superscript j, and subscript i, indicate realization index and MEQ event index, respectively. Therefore, the jth perturbed observation realization $\mathbf{y}^j$ is made of a set of perturbed bandwidths h_i^j $(i = 1,2, \dots, n_{MEQ})$ as follows:

$$\mathbf{y}^j = \frac{1}{n_{MEQ}} \sum_{i=1}^{n_{MEQ}} K_i^{MEQ}(\mathbf{u}; h_i^j) \tag{11}$$

Equation (11) is the same as equation (1) but for the Gaussian kernels $K_i^{MEQ}(\mathbf{u}; h_i^j)$, which have different bandwidths. Afterwards we make the perturbed observation ensemble as:

$$\mathbf{Y} = [\mathbf{y}^1 \ \mathbf{y}^2 \ \dots \ \mathbf{y}^{N_e}] \tag{12}$$

To project the observation to a lower dimension space we take the SVD of $\mathbf{Y}$ to obtain the matrix of eigenvectors which is the projection matrix $\mathbf{U}$. Columns of $\mathbf{U}$ are eigenvectors spanning the space made by $\mathbf{Y}$. A finite number of the leading left singular vectors of $\mathbf{Y}$ form a low-dimensional subspace defined by columns of the matrix $\mathbf{U}$ that accurately approximate each observation realization. Since $\mathbf{Y}$ has a maximum rank of N_e, the maximum dimension of the transformed observations is N_e. To reduce the dimension of the observation space, non-leading columns of $\mathbf{U}$ can be truncated. The truncation number n_{trunc} varies in the range 1 to N_e. The projected perturbed observation ensemble $\mathbf{Y}_p$ is calculated as

$$\begin{gathered} \mathbf{Y}_p = \mathbf{U}_{\text{trunc}}^T \mathbf{Y} \\ \mathbf{U}_{\text{trunc}} = [\mathbf{u}^1 \ \mathbf{u}^2 \ \dots \ \mathbf{u}^{n_{\text{trunc}}}] \\ \mathbf{U} = [\mathbf{u}^1 \ \mathbf{u}^2 \ \dots \ \mathbf{u}^{N_e}] \end{gathered} \tag{13}$$

where $\mathbf{u}^j$ is the jth eigenvector. We also apply the same projection to the predicted seismicity density maps. The ensemble of predicted seismicity density is made by the same kernel band h.

$$\mathbf{S} = [\mathbf{s}^1 \ \mathbf{s}^2 \ \dots \ \mathbf{s}^{N_e}] \tag{14}$$

where $\mathbf{s}^j$ is the jth simulated seismicity density map which is made of jth simulated seismicity cloud $\mathbb{S}^j$. The projected ensemble of predicted seismicity density maps is then calculated as:

$$\mathbf{S}_p = \mathbf{U}_{\mathrm{trunc}}^T \mathbf{S} \tag{2}$$

The resulting observed and predicted data for the EnKF update step are $\mathbf{Y}_p$ and $\mathbf{S}_p$. It should be noted that projection method has two tuning parameters; kernel bandwidth standard deviation σ_h, and truncation number n_{trunc}, and the observation error standard deviation parameters $\sigma_{\min}$ and $\sigma_{\max}$ are no longer needed.

Application of this method to improve uncertainty quantification performance of SSBRC is shown in section 0 and 0 by numerical examples. As we will see, reduced-order projection of seismicity density observation both preserves the ensemble spread and improves the computational efficiency.

4.2.3 Coarse-scale microseismicity density map

Another approach to reduce the dimension of the seismicity map is to use a coarse scale description. This approach uses a coarser scale grid system or mesh structure to quantify the seismicity observations. The number of observations is equal to the dimension of seismicity density map. To reduce the dimension of the seismicity density map (number of observations to integrate) which is the major reason of the ensemble spread underestimation, we can build the continuous function of seismicity density on a coarser mesh or grid system $\mathbf{u}_{\mathrm{red}}$, instead of the original FEM fine mesh (or original fine grid block configuration for pore pressure diffusion forward model) $\mathbf{u}$, in equations (1),(2). So we only need to evaluate continuous seismicity density map on a new coarser grid system. In this work (in 2D experiments) the original mesh configuration of model is square with 100 nodes (or grid blocks) at each side N_{X}, that results in 10000 nodes (or grid blocks) or seismicity density observation values at $\mathbf{u}$. The coarse-scale mesh (or grid system) is assumed to have $N_{\mathrm{X,red}}$ nodes (or grid blocks) at each side which leads to $N_{\mathrm{X,red}}^2$ total nodes (grid blocks) or seismicity density observations at $\mathbf{u}_{\mathrm{red}}$. In SSBRC with coarse-scale seismicity density, we use a typical range of 5% to 10% for observation error standard deviation.

The result of sensitivity analysis of SSBRC performance with respect to different grid sizes (different number of observation) is presented in section 0 and 0. The results demonstrate that while the estimation quality in terms of reservoir parameter map is not affected, the estimation variance is severely underestimated when a large number of correlated observations in a high resolution map is used. The results suggest that the information content of the high resolution map does not provide significant additional details in estimating the reservoir geomechanical parameter.

4.3 Numerical Experiments

In this section we present several numerical examples to show that the distribution of the MEQ events (their source locations) can be used to infer the spatial distribution of the reservoir parameter field. In this work, we have assumed that an interpretation of the microseismic data (through seismic source inversion) in some preprocessing step provides a spatial map of the seismic event locations and then we use the proposed KDE-based continuous interpretation to generate the seismicity density map. Therefore for a

reservoir model with N_b nodes (or grid blocks), at each update step, a vector of N_b observations of seismicity density values is assimilated. The dimension of reservoir parameter vector is also N_b.
In this section we present the results of applying SSBRC to both pore pressure diffusion forward model and geomechanical forward model. The estimation results of homogeneous and heterogeneous 2D and 3D reservoir models in different settings are presented. We first present the application of standard SSBRC and its estimation performance and how it leads to ensemble spread underestimation and then we apply the proposed methods of improved uncertainty quantification along with SSBRC to resolve the issue of spread underestimation.

4.3.1 Description of experimental setup: Pore pressure diffusion

In this section we present the results of SSBRC application to single phase pore-pressure diffusion forward model (finite difference numerical modeling with Eclipse (2010)) and we also demonstrate the results of applying improved uncertainty quantifications methods for resolving ensemble spread underestimation. We present three sets of experiments covering a two-dimensional (2D) homogeneous and heterogeneous reservoir model, and a three-dimensional (3D) heterogeneous reservoir model. For the 2D example, we consider the estimation of a homogeneous and a heterogeneous permeability model and show that the distribution of the MEQ events can be used to infer the uniform permeability value and the spatial distribution of the permeability field. Our second experiment is based on a 3D reservoir configuration with a heterogeneous permeability model. In these experiments, one water injection well is located at the center of the field and the boundaries are closed to flow (noflow boundary conditions). The injection-induced MEQ events for this injection well are used to estimate the permeability in the reservoir. The 2D examples consist of 100×100 discretized models, leading to N_b=10000 grid blocks. In this work, we have assumed that an interpretation of the microseismic data (through seismic source inversion) in some preprocessing step provides a spatial map of the seismic event locations. Therefore, at each update step, a vector of 10000 observations of seismicity density values is assimilated. In homogeneous 2D model we estimate one single parameter (the value of uniform permeability) from 10000 seismicity observations and in heterogeneous 2D model we estimate 10000 parameters (spatial permeability distribution) from 10000 seismicity density observations. In the 3D example, the reservoir is discretized into a 50×50×30 (N_b=75000) grid configuration. Also in this case, one injection well is located at the center of the domain, which is perforated throughout the entire thickness of the formation. The source locations of the MEQ events throughout the 3D domain are used to estimate the heterogeneous permeability distribution.

4.4 Results and Discussion

We present and discuss the results of applying our methodology to the experiments described above. We present the results in terms of the estimated property maps and the ensemble statistics prior to and after data integration. As is common in ensemble data assimilation, we use the evolution of reservoir parameter estimation root-mean-square error (RMSE) and the ensemble spread (Sp) as performance measures. These measures are computed in each integration step using the following equations:

$$\mathrm{RMSE}(\mathbf{m}) = \frac{1}{N_b}\sum_{i=1}^{N_b}\sqrt{\frac{1}{N_e}\sum_{j=1}^{N_e}\left(m^{i,j} - m^{i}_{true}\right)^2} \tag{16}$$

$$\mathrm{Sp}(\mathbf{m}) = \frac{1}{N_b}\sum_{i=1}^{N_b}\sqrt{\frac{1}{N_e}\sum_{j=1}^{N_e}\left(m^{i,j} - m^{i}_{mean}\right)^2} \quad ; \quad m^{i}_{mean} = \frac{1}{N_e}\sum_{j=1}^{N_e} m^{i,j} \tag{17}$$

where N_b is the number of parameters (same as number of nodes or grid blocks here), N_e is the number of realizations and $m^{i,j}$ is the ith parameter of realization j. We plot the ensemble spread as a percentage of the initial ensemble spread. We also use the other measure of ensemble spread which is called the auxiliary ensemble spread $\mathrm{Sp}(B)$. To investigate and evaluate the effect of spurious correlation and spread underestimation, it is proposed to use an additional or auxiliary ensemble $B \in \mathcal{R}^{n_{rand}\times N_e}$ where each row contains zero mean, unit variance and uncorrelated Gaussian random samples (n_{rand} is the dimension of random sample which is assumed 100 in this study) (Evensen, 2009). In each analysis time step we perform updates as follows:

$$\begin{pmatrix}\mathbf{X}_u \\ B_u\end{pmatrix} = \begin{pmatrix}\mathbf{X}_f \\ B_f\end{pmatrix} Z \tag{18}$$

And B_f is equal B_u at previous update time (superscript 'f' for forecast ensemble and superscript 'u' for update ensemble). $\mathbf{X}$ is the original state ensemble matrix that is defined in equation (). By defining the matrix $Z \in \mathcal{R}^{N_e\times N_e}$, the EnKF analysis equation becomes a combination of the forecast ensemble members and searches for the updated ensemble state in the space spanned by the forecast ensemble. By rearranging the analysis equation, we can explicitly find the matrix Z,

$$\begin{gathered}\mathbf{Y} = [\mathbf{y}^1 \;\; \mathbf{y}^2 \;\; \cdots \;\; \mathbf{y}^{N_e}] \\ \mathbf{Y}' = \mathbf{Y} - \mathbf{H}\mathbf{X} \\ \mathbf{X}' = \mathbf{X} - \bar{\mathbf{X}} \\ S = \mathbf{H}\mathbf{X}' \\ C = SS^T + (N_e - 1)\mathbf{C_d} \\ Z = I + S^T C^{-1}\mathbf{Y}' \\ \mathbf{X}_u = \mathbf{X}_f Z\end{gathered} \tag{19}$$

where $\mathbf{X}$ and $\mathbf{Y}$ are the matrix of state ensemble members and the perturbed observation ensemble matrix, respectively. This kind of representation of EnKF analysis based on coefficient matrix Z gives us a very evident prospect of the procedure which is being done by updating the ensemble. $\mathrm{Sp}(B)$ is the mean of standard deviation (Std) of each realization of auxiliary ensemble B (columns of B).

$$B = [b^1 \quad b^2 \quad \cdots \quad b^{N_e}]$$

$$\mathrm{Sp}(B) = \frac{1}{N_e}\sum_{i=1}^{N_e} Std(b^i) \tag{20}$$

By analyzing $\mathrm{Sp}(B)$ through update steps we can find out the amount of variance reduction of the procedure. By the way, this measure is very sensitive to the spread of the perturbed observations $\mathbf{C_d}$, and can help us to choose the best spread of perturbed observation (perturbed observation Std) to obtain the appropriate result. Therefore the other measure of ensemble spread is the auxiliary ensemble spread $\mathrm{Sp}(B)$ that its inverse is called inflation factor ρ_{inf}. Auxiliary ensemble spread $\mathrm{Sp}(B)$ clearly shows what percentage of the original ensemble spread is lost only because of erroneous or spurious correlation of observation and parameter.

Experiment 1: 2D Homogeneous

In this experiment we present the result of SSBRC application to a 2D homogeneous reservoir model. This experiment is performed by the standard SSBRC with no improved uncertainty quantification methods applied. The 2D reservoir consists of 100×100 grid system (10000 grid blocks) and there is one water injection well at the center. The permeability of all grid blocks are assumed equal (homogeneous permeability distribution). The uniform initial reservoir pressure is equal 3000 (psi) and the injection pressure is 6000 (psi). We use Eclipse to numerically solve the single phase pore pressure diffusion equation by finite difference method. The criticality distribution is assumed spatially random distributed. Here by SSBRC we infer the value of homogeneous permeability (only one parameter to estimate) from 10000 seismicity density observations. The true homogeneous permeability value (the unknown parameter to estimate) is assumed 20 (md) and the criticality distribution (assumed known) is spatially random (uncorrelated) distributed and its values come from a Gaussian probability density function (PDF). Figure 9 shows the true reservoir model specifications including the pore pressure evolution through time, criticality distribution and the resulting MEQ cloud that will be used as observed data in EnKF. The stimulation period is 216 (min) and we specify 6 integration steps to assimilate MEQ observations. The MEQ density map is constructed on the original fine grid system and the observation error Std range ($\sigma_{\min}$ and $\sigma_{\max}$) is the typical range of 5 % to 10 %.

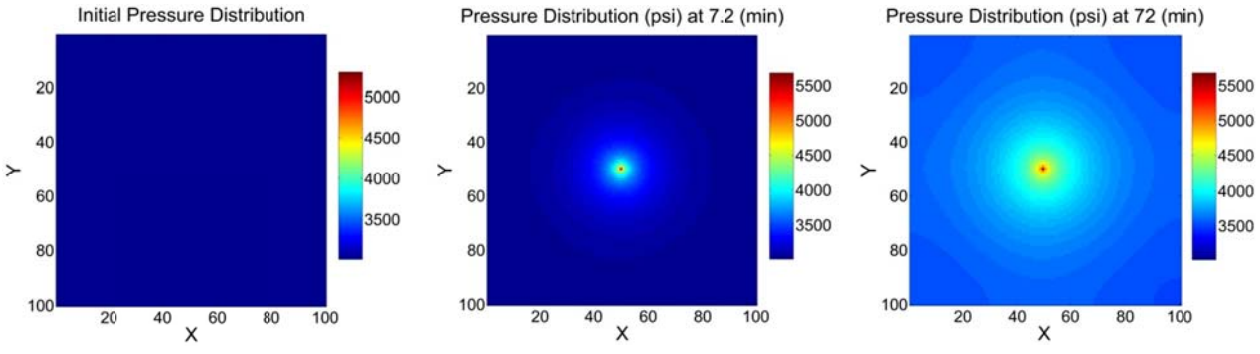

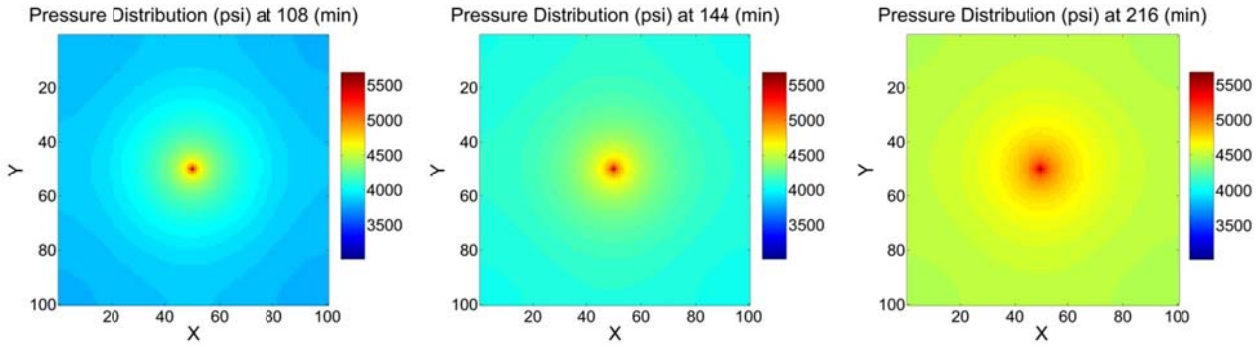

(a) pore-pressure distribution

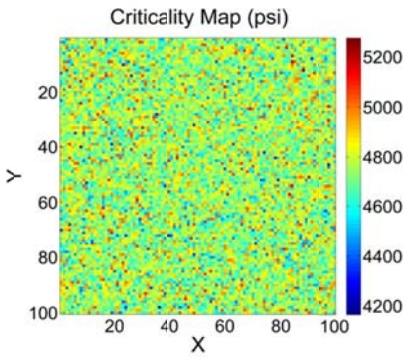

(b) criticality distribution

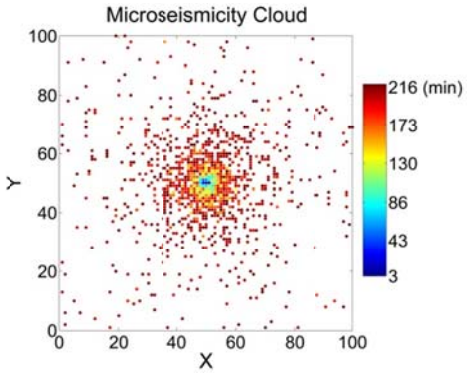

(c) MEQ cloud

Figure 9. Microseismicity cloud generation in a two-dimensional model with homogeneous permeability (20 mD): (a) snapshots of diffusive pore pressure distributions at different time steps $p(\mathbf{u}, t)$, (b) spatially uncorrelated Gaussian (white noise) rock criticality $C(\mathbf{u})$, and (c) the cloud of microseismic events generated by comparing rock criticality with pore pressure distributions at different times steps.

In this example, SSBRC with its standard setup (seismicity density map on the fine original mesh) and the typical range of observation error Std is used. The initial ensemble (100 realizations) is randomly generated from a Uniform PDF in the range of 1 (md) to 200 (md). The estimation results are shown in Figure 10.

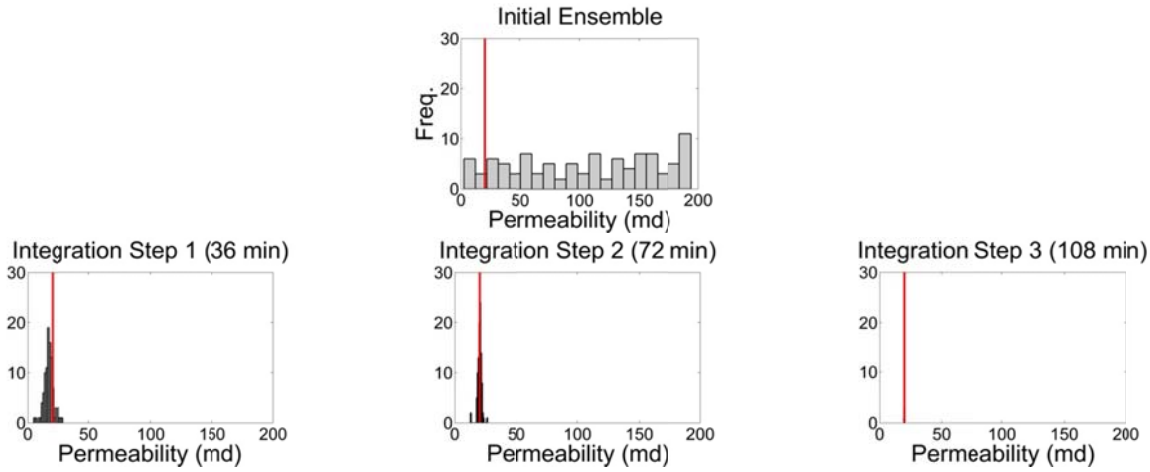

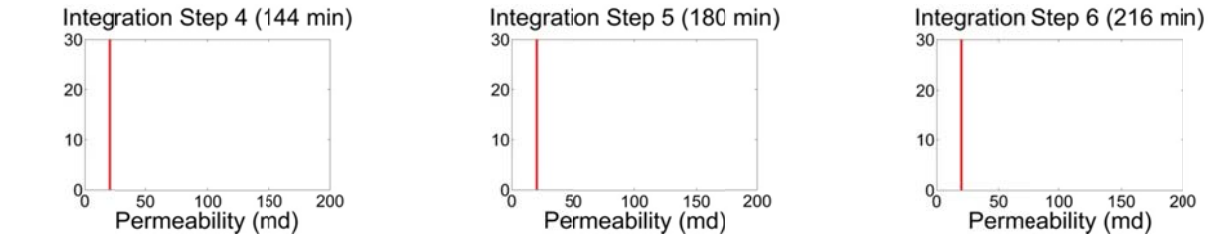

(a) evolution of the permeability ensemble histogram in integration steps

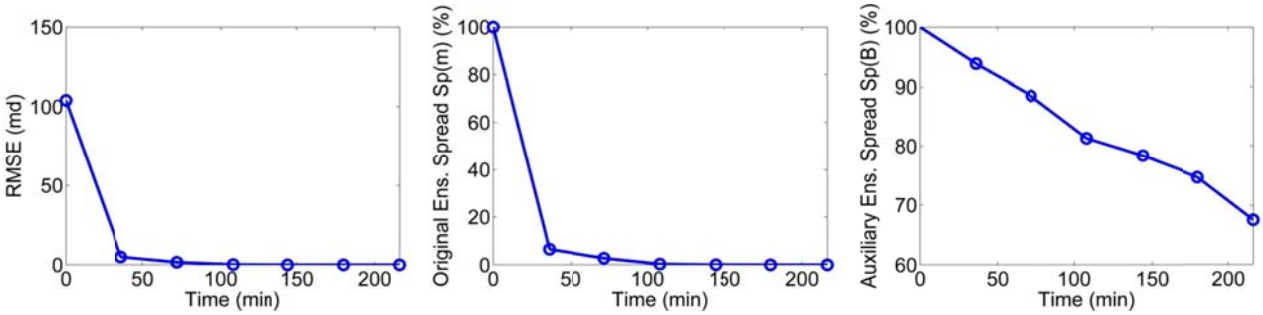

(b) estimation RMSE (c) original ensemble spread (d) auxiliary ensemble spread

Figure 10. Estimation results of the 2D homogenous permeability model with SSBRC. The vertical red line in (a) indicates the true value of homogeneous permeability.

Figure 10.a shows the evolution of permeability ensemble histogram throughout integration steps while the vertical red line indicates the true value of permeability. The first plot in Figure 10.a is the histogram of initial ensemble which comes from a Uniform PDF. As the histogram evolution shows the estimated permeability values are becoming closer to true permeability through integration steps and after the third update all the estimated realizations almost fall on true permeability. As the final estimated ensemble histogram illustrates, the estimation result is very precise which is also shown by the RMSE plot of Figure 10.b. Therefore the SSBRC is successful in inferring permeability from MEQ observations. As we can see in Figure 10.a, the parameter estimation is almost perfect while we are just losing at most 40 % of ensemble spread due to spurious correlation (represented by $\mathrm{Sp}(B)$ in Figure 10.d). In estimating one value, we already know that the final estimated ensemble ideally should not have any spread or variance which is happening here. Actually there is no spread in final ensemble as it is shown in the last histogram and the original ensemble spread in Figure 10.c, while from auxiliary ensemble spread $\mathrm{Sp}(B)$ plot, Figure 10.d, we still have most of the ensemble spread left which is a good sign that the spurious correlation just caused minor spread reduction. Again it should be noted that auxiliary ensemble spread $\mathrm{Sp}(B)$ is the spread of an auxiliary ensemble (each realization is a normal random uncorrelated vector) which is completely irrelevant to the original ensemble of parameters. In homogeneous case as the results show since we already expect almost perfect estimation (almost zero final spread for original ensemble), spread underestimation is not the target problem to solve. In this experiment the appropriate measure of spread is auxiliary ensemble spread $\mathrm{Sp}(B)$ which is acceptable (more than 60 %).

While as discussed this experiment does not seem to need resolving ensemble spread underestimation, we will apply three proposed improved uncertainty quantification methods to this experiment in later in the report and investigate their effects on SSBRC performance.

Experiment 2: 2D Heterogeneous

In this section, we apply SSBRC to a 2D pore pressure diffusion reservoir model with heterogeneous permeability distribution. The 2D model has a 100x100 grid block structure (10000 grid blocks) and the permeability field is a heterogeneous parameter. There is only on water injection well at the center of the field. The true log-permeability distribution is shown in Figure 11.b. In this experiment the dimension of the parameter to estimate and seismicity density observation are both equal to 10000. An uncorrelated Gaussian random distribution is also assumed for criticality map shown in Figure 11.c.

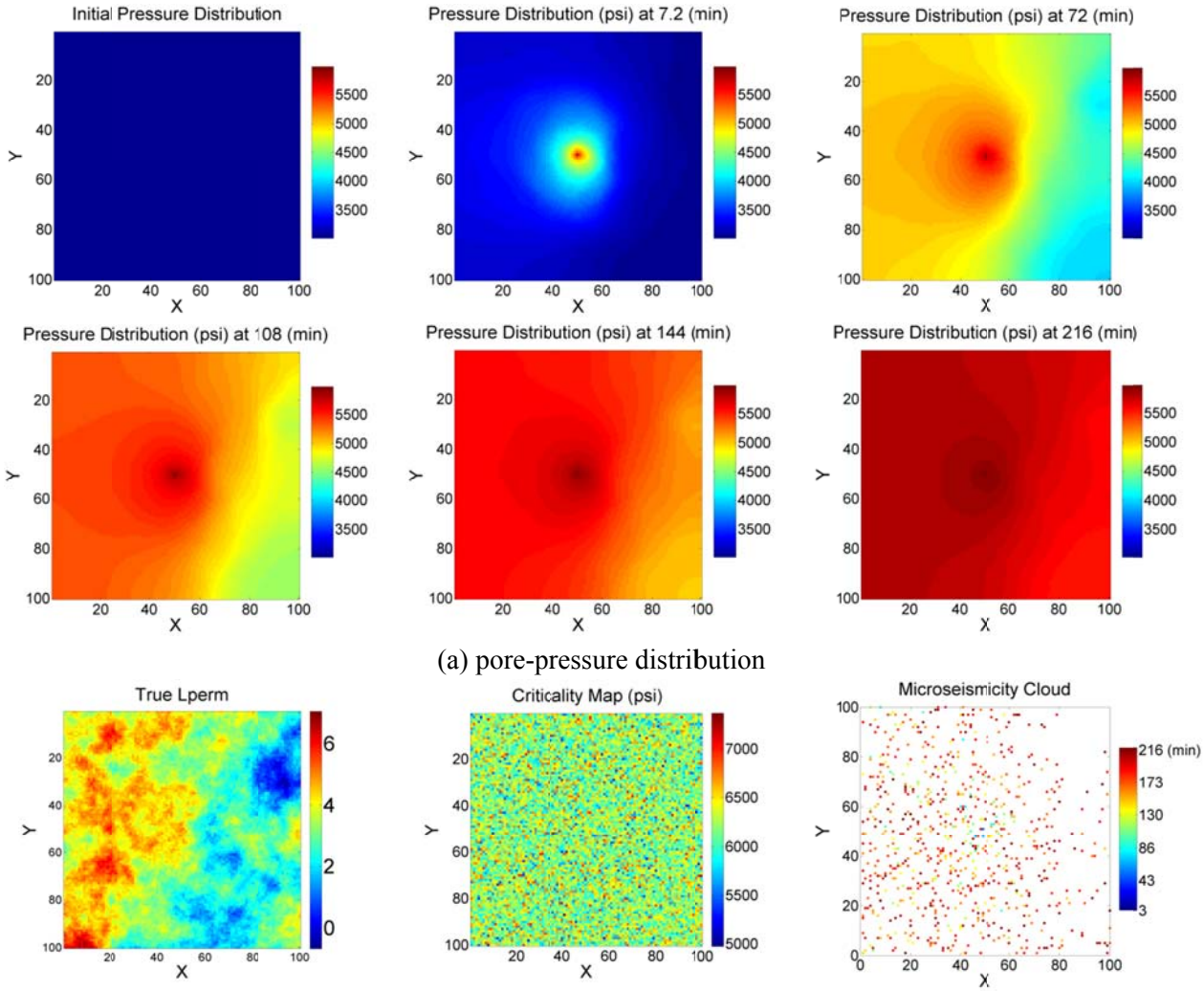

(a) pore-pressure distribution

(b) true log-permeability map (c) criticality map (d) MEQ cloud

Figure 11. Microseismicity cloud generation in a two-dimensional model with heterogeneous permeability: (a) snapshots of diffusive pore pressure distributions at different time steps $p(\mathbf{u}, t)$, (b) the true log-permeability distribution, (c) spatially uncorrelated Gaussian (white noise) rock criticality $C(\mathbf{u})$, and (d) the cloud of microseismic events generated by comparing rock criticality with pore pressure distributions at different time steps.

Other specifications of the true model are illustrated in Figure 11 including the pore pressure distribution in the field through stimulation period and the MEQ cloud observation which is generated by comparing pore pressure distributions and the criticality map. Using SSBRC we assimilate MEQ cloud observation, Figure 11.d, (after quantifying by KDE method) by EnKF update equation to infer heterogeneous log-permeability field, Figure 11.b. The stimulation period is 216 (min) and we specify 6 integration steps to assimilate MEQ observations. The MEQ density map is constructed on the original fine grid system and the observation error Std range is the typical range of 5 % to 10 %.

In the following figures in this section, the extensive estimation results of SSBRC are presented. Figure 12 shows the result of updating the permeability ensemble in terms of ensemble mean throughout 6 integration steps. It is seen that the estimated ensemble mean is becoming more similar to the true permeability map in Figure 12.a by assimilating MEQ observations in time. The initial ensemble (almost uniform initial ensemble mean in Figure 12.b) is completely uninformative about true permeability map, Figure 12.a, however after MEQ data assimilation the final ensemble mean, Figure 12.h, is very similar to the true map. Therefore SSBRC proves its suitability for heterogeneous permeability estimation from MEQ data.

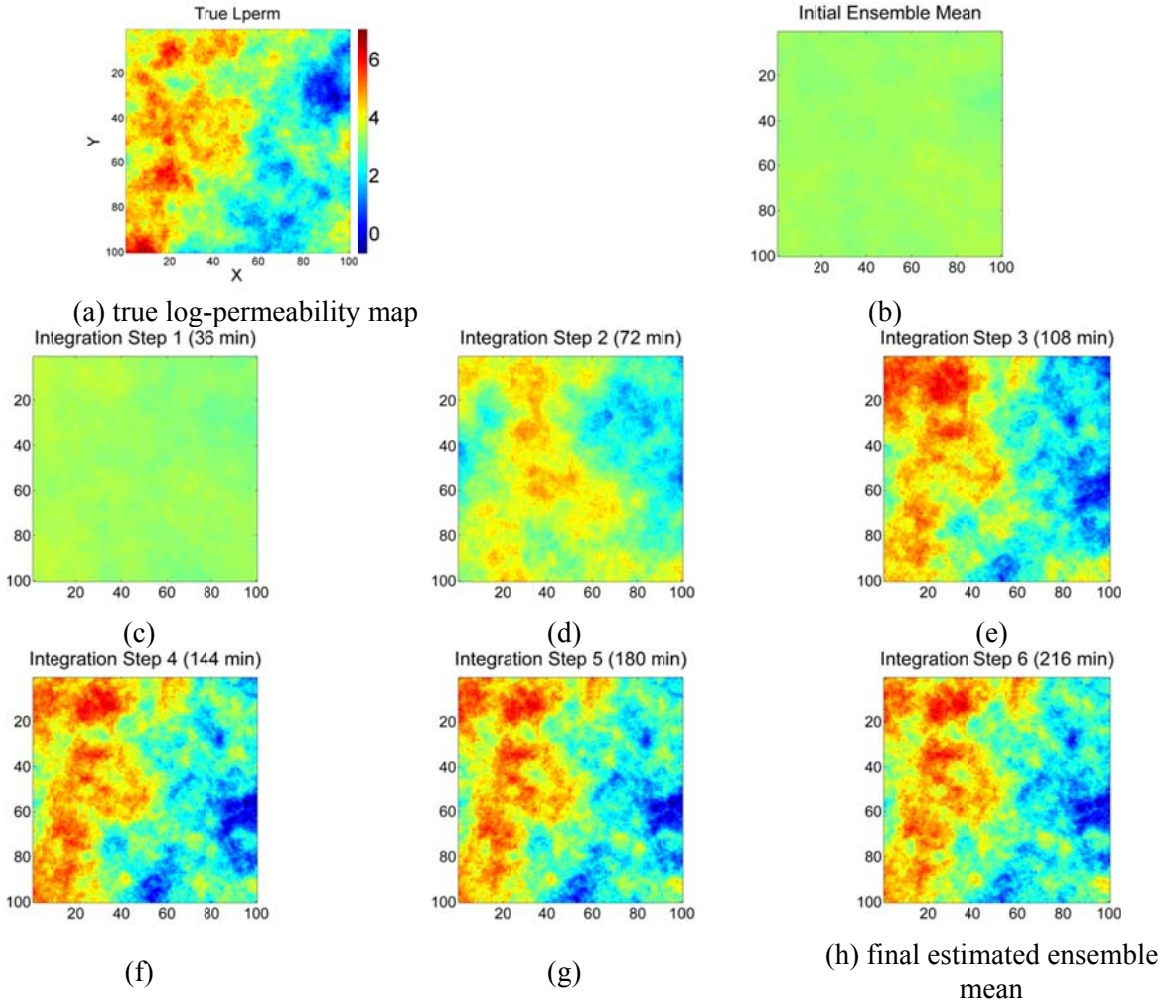

(a) true log-permeability map (b)

(c) (d) (e)

(f) (g) (h) final estimated ensemble mean

Figure 12. Estimating heterogeneous permeability by SSBRC. The evolution of the estimated ensemble mean through integration steps.

Figure 13 shows the estimation result in terms of one realization. The evolution of an individual permeability realization or sample is shown in this figure. As we can see again, SSBRC is able to update a dissimilar initial permeability realization, Figure 13.b, to a final estimated realization, Figure 13.h, which is quite comparable to the true permeability map, Figure 13.a.

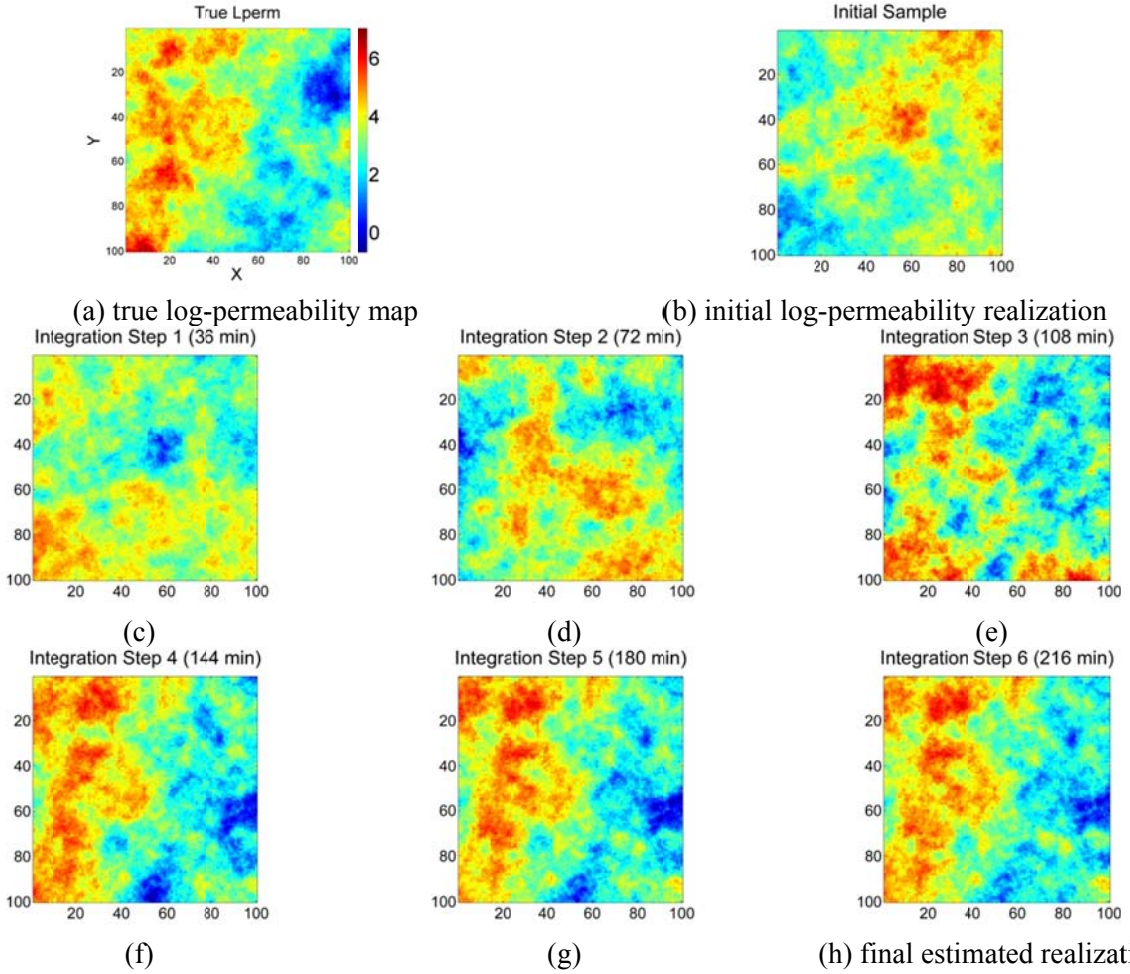

(a) true log-permeability map (b) initial log-permeability realization

(c) (d) (e)

(f) (g) (h) final estimated realization

Figure 13. Estimating heterogeneous permeability by SSBRC. The evolution of an individual realization through integration steps.

The performance measures of SSBRC estimation procedure are also shown in Figure 14. The continuous reduction of estimation RMSE, Figure 14.a, shows the success of SSBRC in estimating permeability distribution. The final RMSE value is almost half of initial RMSE. The ensemble spread is plotted in Figure 14.b which shows that almost 90 % of the initial ensemble spread is lost through estimation procedure. This very low final ensemble spread (10 %) shows severe ensemble spread underestimation. This uncertainty quantification issue will be resolved by applying the proposed methods of this section and the new estimation results will be presented in experiment 5.

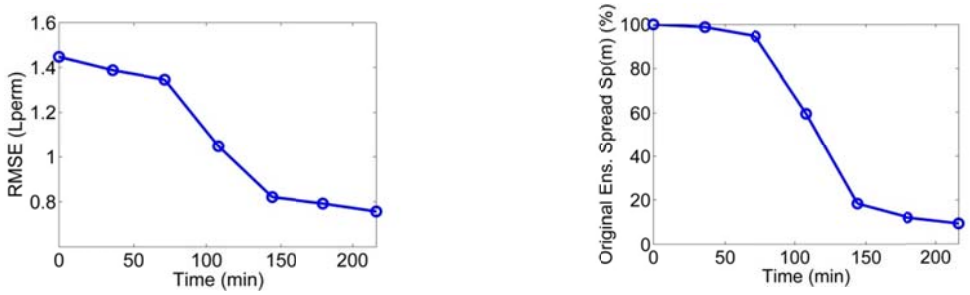

(a) estimation RMSE (b) ensemble spread

Figure 14. SSBRC performance measures in estimating 2D heterogeneous permeability field.

The other representation of ensemble spread is the standard deviation (Std) map of the ensemble which its evolution in integration steps is shown in Figure 15. By assimilating the MEQ data, the spread of the permeability ensemble decreases that results in lowering the ensemble Std map. Figure 15 shows constant reduction of ensemble spread. As Figure 15.g represents the final estimated ensemble Std is very low that again demonstrates the ensemble spread underestimation of SSBRC with high dimensional observations (MEQ density map on original fine grid system).

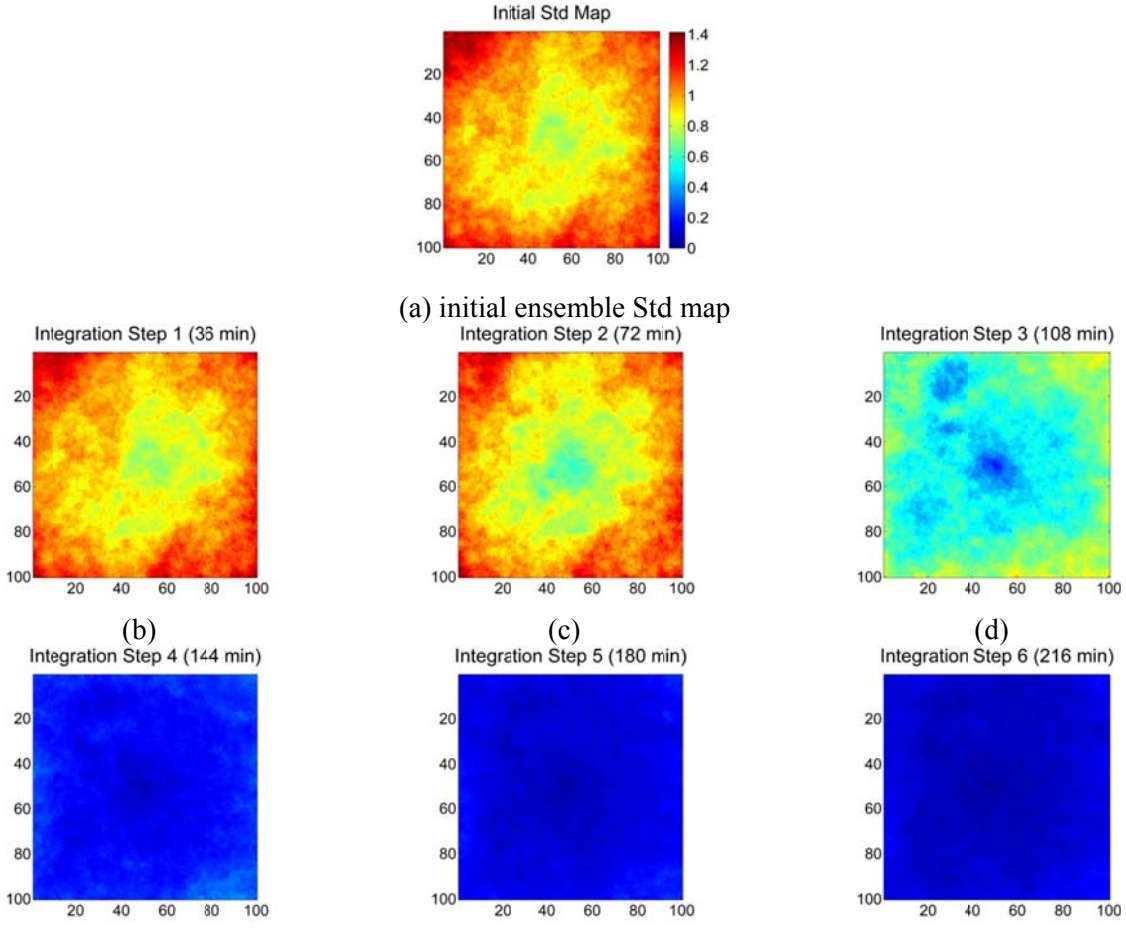

(a) initial ensemble Std map

(b) (c) (d)

(e) (f) (g) final estimated ensemble Std map

Figure 15. Evolution of the standard deviation (Std) map of permeability ensemble through integration steps.

Experiment 3: 3D Heterogeneous

In this section we apply SSBRC to a 3D pore pressure diffusion reservoir model with heterogeneous permeability distribution. The 3D model has a 50x50x30 grid block structure (75000 grid blocks) and the permeability field is a heterogeneous parameter. There is only on water injection well at the center of the field which is perforated throughout the entire thickness of the formation. The true log-permeability distribution is shown in Figure 16.b. In this experiment the dimension of the parameter to estimate and seismicity density observation are both equal to 75000. An uncorrelated Gaussian random distribution is also assumed for criticality map shown in Figure 16.c.

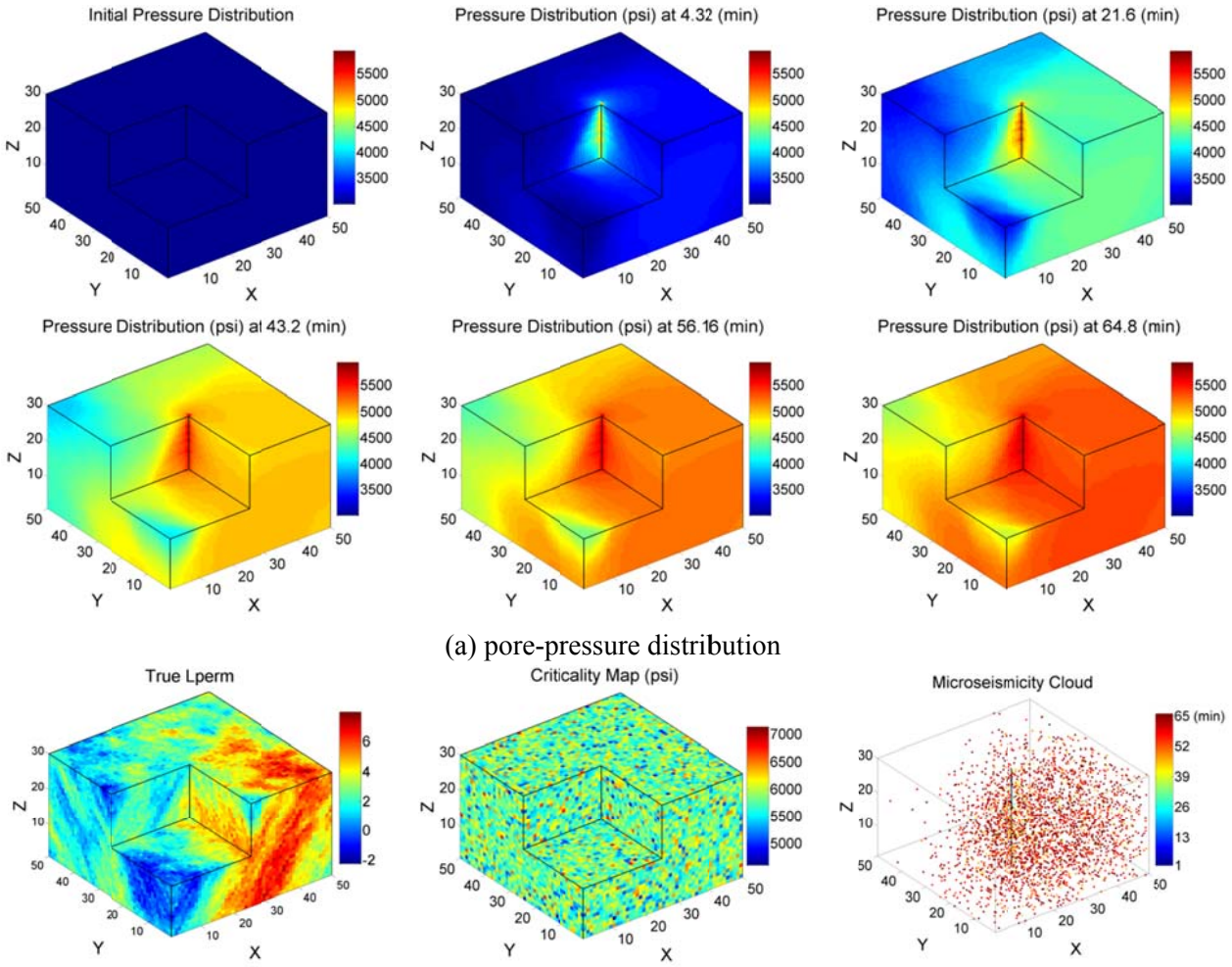

(a) pore-pressure distribution

(b) true log-permeability map (c) criticality map (d) MEQ cloud

Figure 16. Microseismicity cloud generation in a three-dimensional model with heterogeneous permeability: (a) snapshots of diffusive pore pressure distributions at different time steps, (b) the true log-permeability distribution, (c) spatially uncorrelated Gaussian (white noise) rock criticality, and (d) the cloud of microseismic events generated by comparing rock criticality with pore pressure distributions at different time steps.

Other specifications of the true model are illustrated in Figure 16 including the pore pressure distribution in the field throughout stimulation period, Figure 16.a, and the MEQ cloud observation, Figure 16.d,

which is generated by comparing pore pressure distributions and the criticality map. Using SSBRC we assimilate MEQ cloud observation, Figure 16.d, (after quantifying by KDE method) by EnKF update equation to infer 3D heterogeneous log-permeability field, Figure 16.b. The stimulation period is 65 (min) and we specify 6 integration steps to assimilate MEQ observations. The MEQ density map is constructed on the original fine grid system and the observation error Std range is the typical range of 5 % to 10 %.

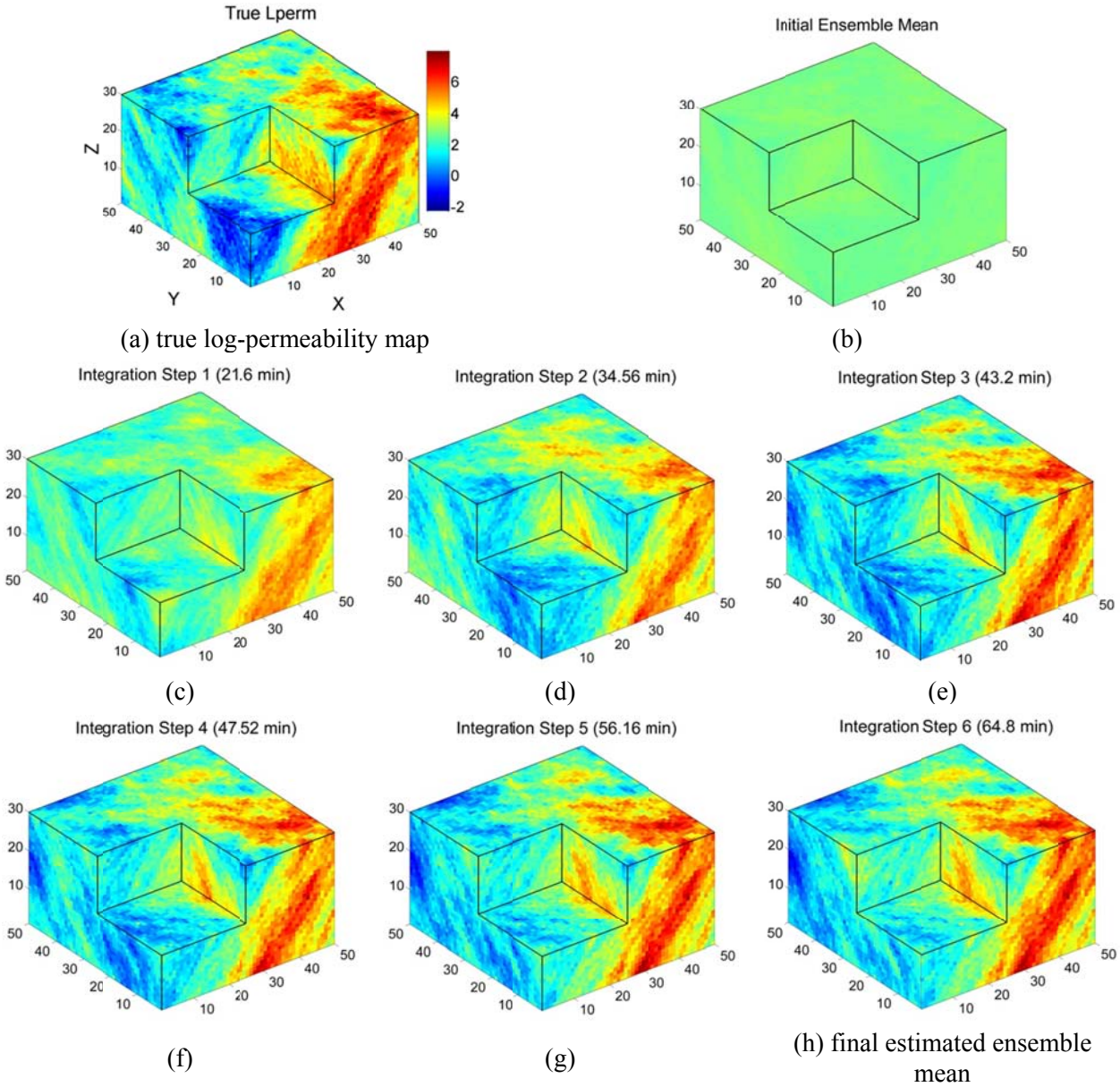

(a) true log-permeability map (b)

(c) (d) (e)

(f) (g) (h) final estimated ensemble mean

Figure 17. Estimating 3D heterogeneous permeability by SSBRC. The evolution of the estimated ensemble mean through integration steps.

In the following figures in this section the extensive estimation results of SSBRC are presented. Figure 17 shows the result of updating the permeability ensemble in terms of ensemble mean through 6 integration steps. It is seen that the estimated ensemble mean is becoming more similar to the true permeability map

in Figure 17.a by assimilating MEQ observations in time. The initial ensemble (almost uniform initial ensemble mean in Figure 17.b) is completely uninformative about true permeability map, Figure 17.a, however after MEQ data assimilation the final ensemble mean, Figure 17.h, is very similar to the true map. Therefore SSBRC proves its suitability for 3D heterogeneous permeability estimation from MEQ data.

Figure 18 shows the estimation result in terms of one individual realization. The evolution of an individual permeability realization or sample is shown in this figure. As we can see again, SSBRC is able to update a dissimilar initial permeability realization, Figure 18.b, to a final estimated realization, Figure 18.h, which is quite comparable to the true permeability map, Figure 18.a.

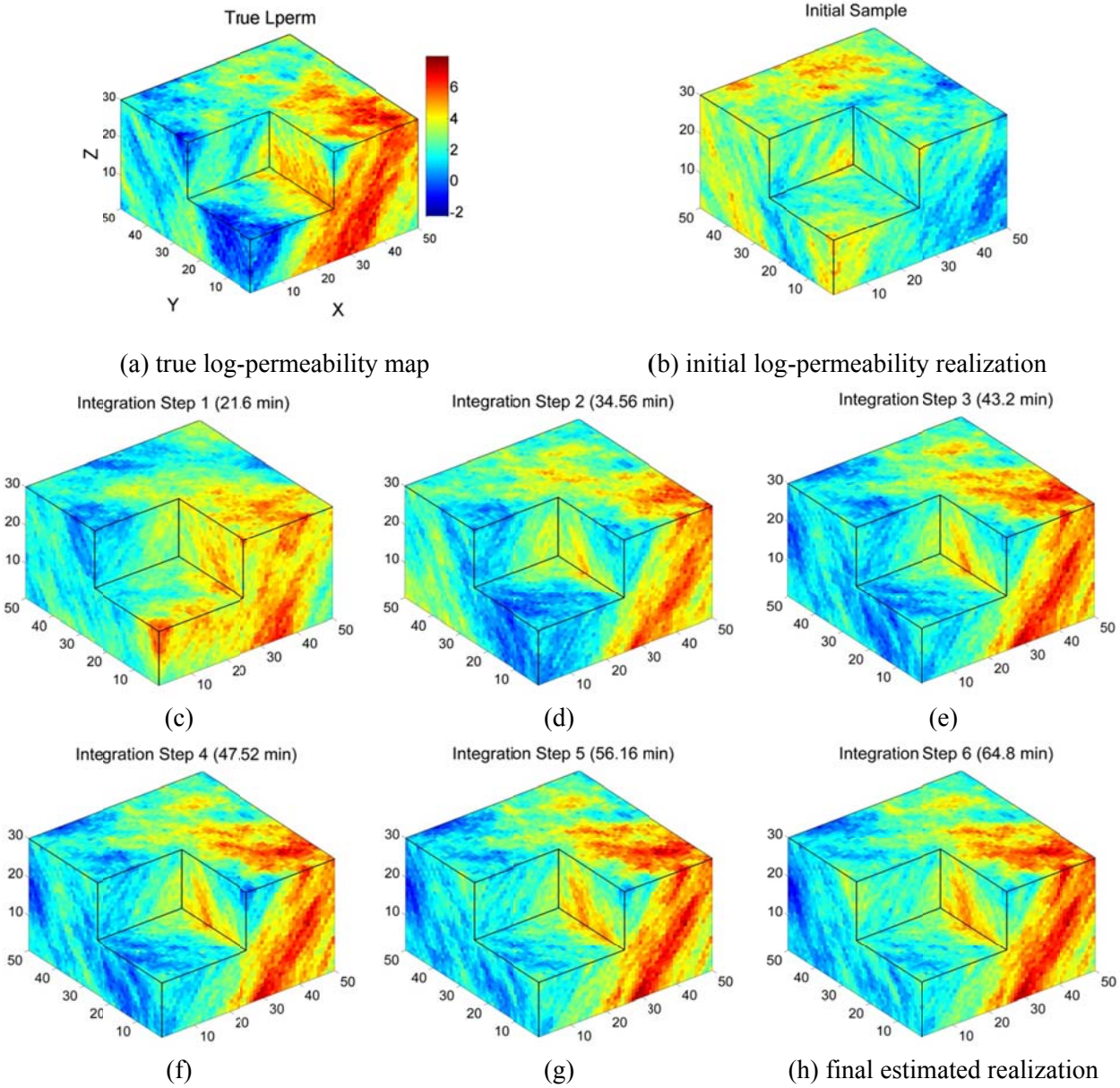

(a) true log-permeability map (b) initial log-permeability realization

(c) (d) (e)

(f) (g) (h) final estimated realization

Figure 18: Estimating 3D heterogeneous permeability by SSBRC. The evolution of an individual realization through integration steps.

The performance measures of SSBRC estimation procedure are also shown in Figure 19. The continuous reduction of estimation RMSE, Figure 19.a, shows the success of SSBRC in estimating 3D permeability distribution. The final RMSE value is less than half of initial RMSE. The ensemble spread is plotted in Figure 19.b which shows that 97 % of the initial ensemble spread is lost throughout the estimation procedure. This very low final ensemble spread (3 %) shows severe ensemble spread underestimation and ensemble collapse which is due to erroneous and spurious correlation of very high resolution seismicity density observation and permeability distribution. As discussed before, very high dimensional seismicity density observation (75000 seismicity observations) which is made on the original fine grid system introduces high amount of redundancy and spurious correlation to EnKF update and consequently results in ensemble collapse. This uncertainty quantification issue will be resolved by applying the proposed methods 0and the new estimation results will be presented in experiment 6.

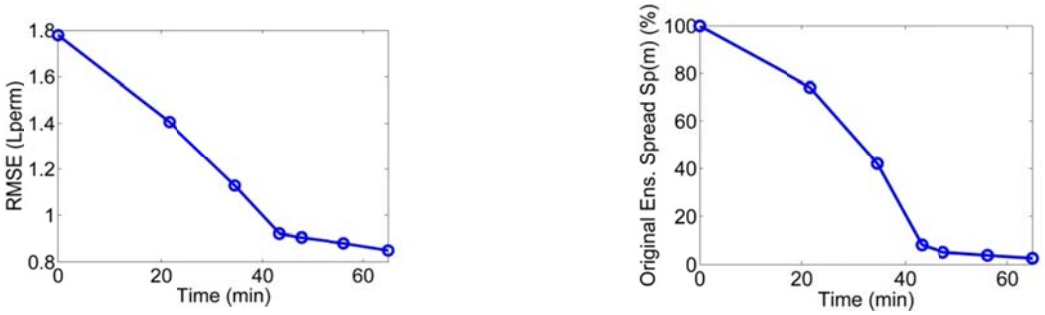

(a) estimation RMSE (b) ensemble spread

Figure 19. SSBRC performance measures in estimating 3D heterogeneous permeability field.

The other representation of ensemble spread is the standard deviation (Std) map of the ensemble which its evolution in integration steps is shown in Figure 20. By assimilating the MEQ data, the spread of the permeability ensemble decreases that results in lowering the ensemble Std map. Figure 20 shows continuous reduction of ensemble spread. As Figure 20.g shows the final estimated ensemble Std is extremely low that again demonstrates the ensemble spread underestimation of SSBRC with high dimensional observations (MEQ density map on original fine grid system).

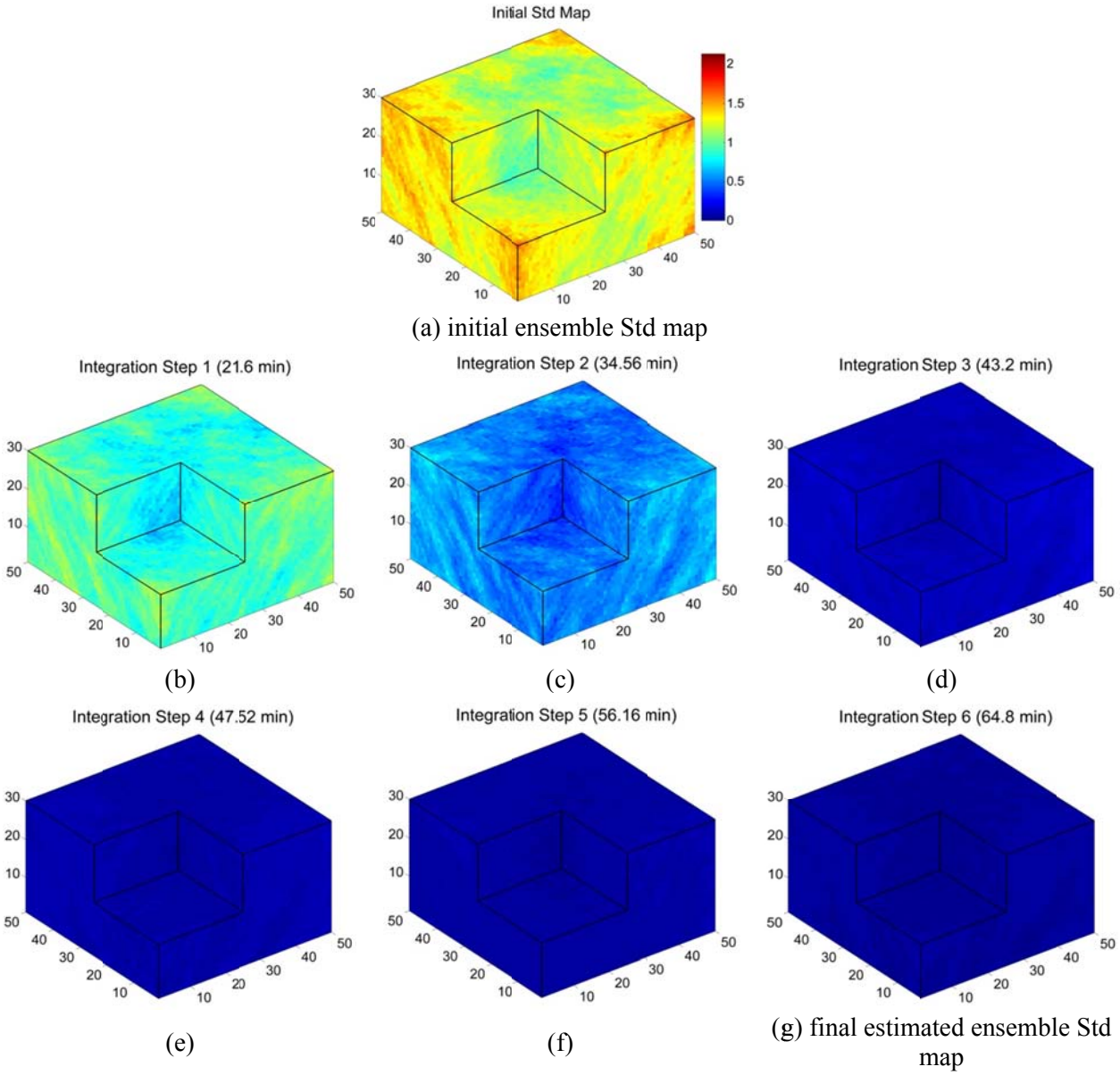

(a) initial ensemble Std map

(b) (c) (d)

(e) (f) (g) final estimated ensemble Std map

Figure 20. Evolution of the standard deviation (Std) map of permeability ensemble through integration steps.

Experiment 4: 2D Homogeneous, Resolving Spread Underestimation

In this set of experiments, we apply the three methods of improving uncertainty quantification in section 0 to the experiment 1 in section 0 (reference experiment) to resolve the issue of ensemble spread underestimation.

Inflated observation error variance

The simplest way of avoiding spread underestimation or ensemble collapse is adding large amount of noise to observation which can be done by specifying high observation standard deviation (Std) through increasing $\sigma_{\max}$ and $\sigma_{\min}$ in equation (8). To observe the effect of observation Std range, different Std intervals are tried in our experiment. The results of increasing the observation error Std range are given in

Table 2. The first row of Table 2, test # 1, shows the results of reference model that is experiment 1 in section 0. These results show improvement of final ensemble spread in terms of both Sp($\mathbf{m}$) and Sp(B) (preserving more ensemble spread) by increasing the observation error Std. However the increased Std range (e.g. test # 4 with observation Std of 100-200%) might seem unrealistic. It is also obvious from Table 2 that we can yet improve ensemble spread by further increasing the observation error Std. Figure 21 shows the estimation results of SSBRC with inflated observation error Std range (test # 4 from Table 2). In estimating one single parameter with SSBRC since we expect perfect estimation (zero spread) it does not seem necessary to apply improved uncertainty quantification methods however as the results of Table 2 show increasing observation Std helps in preserving the ensemble spread.

Table 2. Sensitivity of the SSBRC performance to different ranges of observation Std (standard SSBRC with seismicity density on the original fine grid) in estimating homogeneous permeability

test #	$\sigma_{\min}$ (%)	$\sigma_{\max}$ (%)	Final RMSE (md)	Final spread* (%) Sp($\mathbf{m}$)	Final Aux. Spread** (%) Sp(B)
1 (reference)	8	13	0.0021	0.0036	67.58
2	27	54	0.0030	0.0050	77.17
3	40	88	0.0036	0.0056	78.58
4	91	196	0.0115	0.0193	90.46

Initial RMSE = 104.0444 (md)

*Spread = spread of the original ensemble (permeability)

**Aux. Spread = spread of the random auxiliary ensemble (the inverse of inflation factor) used for the analysis of spurious correlation

The results of resolving ensemble spread underestimation by inflating observation error Std are shown in Figure 21. To briefly illustrate the estimation results, estimated ensemble histogram is only plotted in first, third and sixth (final) integration steps. As shown in Figure 21.a,b, the final estimated ensemble is almost equal to the true permeability which confirms the suitability of SSBRC for parameter estimation. In the experiments of Table 2 the appropriate measure of spread is auxiliary ensemble spread Sp(B) which is acceptable (more than 60 %) in all experiments. Different experiments and different setups do not have significant effect on the RMSE value in homogeneous case.

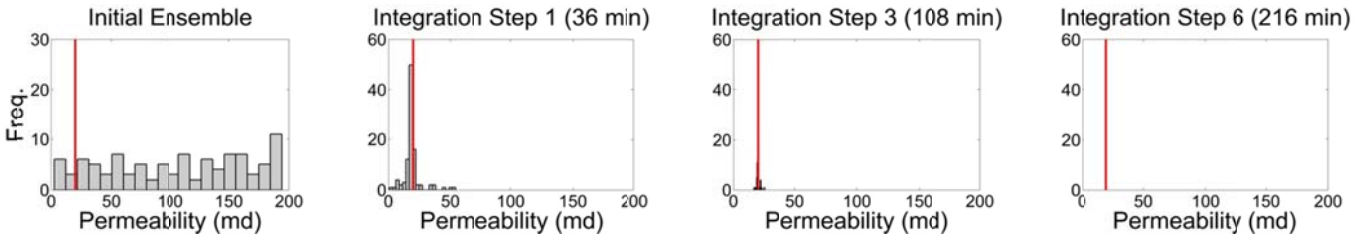

(a) permeability ensemble histogrm update through integration steps.

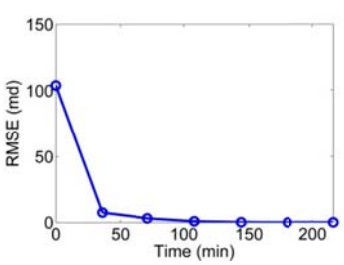

(b) permeability estimation RMSE

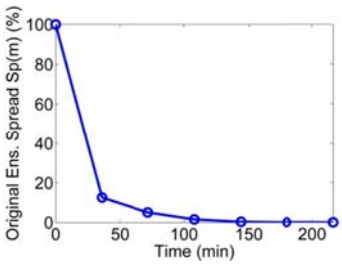

(c) original permeability ensemble spread

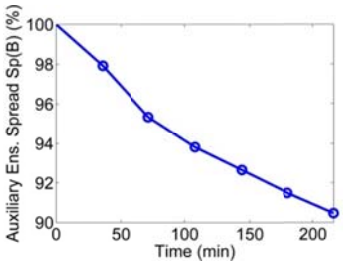

(d) auxiliary ensemble spread

Figure 21. Estimating homogeneous permeability from MEQ observation by SSBRC and improving uncertainty quantification by increased observation error Std.

Reduced-order projection

In this section we apply the projection method of section 0 to experiment 1 in section 0 to improve the final estimated ensemble spread. As mentioned earlier, projection method has two tuning parameters; kernel bandwidth standard deviation σ_h, and truncation number n_{trunc}. We investigate the performance of SSBRC with reduced-order projection with respect to four different sets of these parameters as shown in Table 3. As we can see from these tests, the estimation RMSE as we expect is almost zero and as the objective of the projection method, ensemble spread is greatly preserved (final ensemble spread is around 60% or more). It should be noted that the number of observations is decreased from 10000 to 25, 50 and 100 by projection method, as reported in Table 3, n_{trunc} column. Table 3 shows the sensitivity of the projection approach with respect to σ_h and n_{trunc}. The proposed observation projection approach is successful in preserving the ensemble spread and resolving ensemble spread underestimation of SSBRC through observation dimension reduction. Detailed estimation results of test # 1 from Table 3 are shown in Figure 22.

Table 3. SSBRC with observation projection approach. Sensitivity of the performance of projection approach with respect to kernel bandwidth Std (σ_h) and truncation number (n_{trunc}).

Test #	σ_h (%)	n_{trunc}	Final RMSE (md)	Final spread (%) Sp($\mathbf{m}$)	Final Aux. Spread (%) Sp(B)
1	25	100	0.0037	0.0063	59.73
2	25	50	0.0048	0.0080	66.93
3	25	25	0.0064	0.0103	84.61
4	10	50	0.0040	0.0067	69.64

Initial RMSE = 104.0444 (md)

Figure 22 shows homogeneous permeability estimation results by SSBRC with projection approach. As we can see from the plots in Figure 22 both estimation performance (RMSE) and ensemble spread are promising.

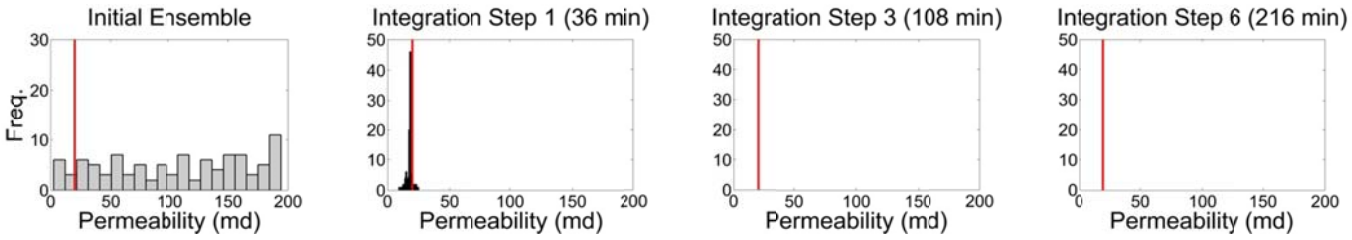

(a) permeability ensemble histogrm update through integration steps

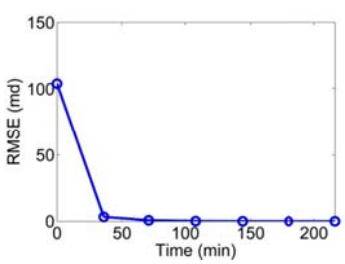

(b) permeability estimation RMSE

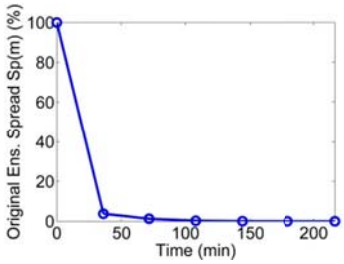

(c) original permeability ensemble spread

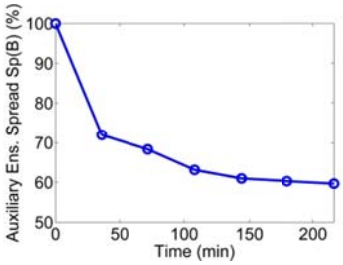

(d) auxiliary ensemble spread

Figure 22. Estimating homogeneous permeability from MEQ observation by SSBRC and improving uncertainty quantification by projection method.

Coarse-Scale microseismicity density map

The number of observations is equal to the dimension of seismicity density map. To reduce the dimension of the seismicity density map (number of observations to integrate) which is the major reason of the ensemble spread underestimation we can build the seismicity density map on a coarse grid system instead of the original fine grid system. So we only need to evaluate continuous seismicity density map on a new coarse grid system.

In this 2D case study where the grid block configuration is 100x100 (N_b = 10000, N_{X} = 100) we choose the coarse seismicity density mesh size e.g. equal to 10x10 (N_b = 100 seismicity observations, $N_{\mathrm{X,red}}$ = 10) which reduces the dimension of the observation vector by orders of magnitude. It should be noted that the range of the observation error Std in coarse seismicity density approach is the typical range of 5% to 10%. Different microseismicity density map sizes produces different number of observations and help in reducing the number of observations to resolve the observation space redundancy and ultimately ensemble spread underestimation in EnKF process. The dimension of microseismicity density map is considered in terms of number of grid blocks in x direction (the field configuration is square). For coarsening of the seismicity density map, we specify different sizes of $N_{\mathrm{X,red}}$ equal to 10, 15, 20, 30, 50, 70 and 90, that decrease the number of observations to 100, 225, 400, 900, 2500, 4900 and 8100, respectively where in the reference experiment by $N_{\mathrm{X,red}} = N_{\mathrm{X}} = 100$, there are 10000 observations.

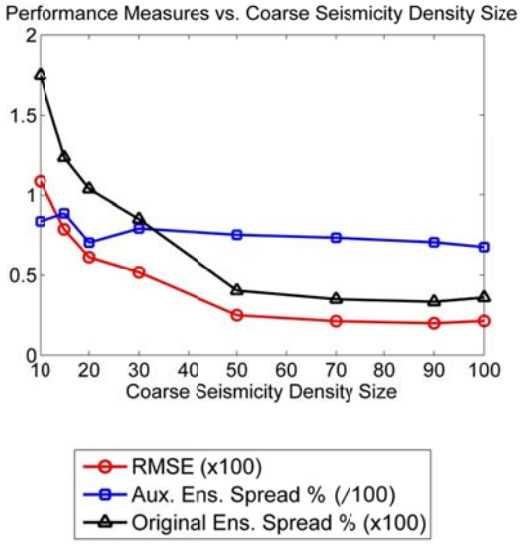

Figure 23. Effect of coarse microseismicity density dimension on the performance of SSBRC in homogeneous permeability estimation experiment, initial RMSE = 104.0444 (md).

The effect of different dimensions of microseismicity density map on the performance of SSBRC process is shown in Figure 23. In this experiment seven different sizes of seismicity density map ($N_{X,red} = 10,15,20,30,50,70,90$) are chosen and the reference case density map size is $N_X = 100$ (seismicity density map of 100×100 where the number of microseismicity observations is equal to 10000). Figure 23 shows both final estimation RMSE and final (original and auxiliary) ensemble spread of these eight experiments. Based on RMSE curve of Figure 23, it is seen that final RMSE is slightly decreasing by increasing the mesh dimension however in this case with homogeneous permeability final RMSE value is very insignificant and can be considered zero. It should be noted that we are looking for both low RMSE and high spread simultaneously while as mentioned before final RMSE value is acceptable in all experiments. Figure 23 shows the final ensemble spread (both original permeability ensemble and auxiliary ensemble) versus size of seismicity density map. As we already expected, by increasing the size of the density map there will be higher number of observations which consequently results in further underestimation of ensemble spread (lower ensemble spread value). As the result, the improvement of the ensemble spread is obviously seen in Figure 23 by decreasing the size of the seismicity density map (or using coarse seismicity density map) even though in homogeneous parameter estimation this improvement is not very significant. Based on the obtained results, the density size of 10 (10×10 coarse map in a 100×100 field) for coarse-scale mesh can be a suitable choice.

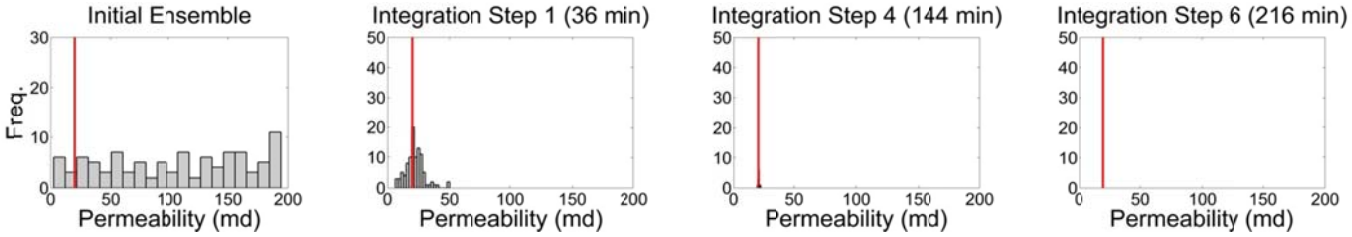

(a) permeability ensemble histogrm update through integration steps

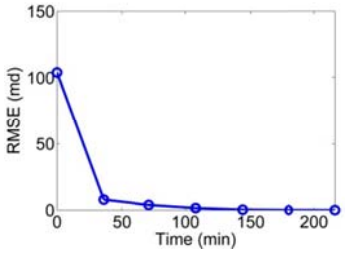

(b) permeability estimation RMSE

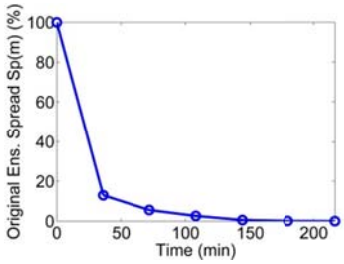

(c) original permeability ensemble spread

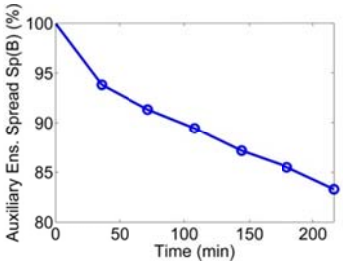

(d) auxiliary ensemble spread

Figure 24. Estimating homogeneous permeability from MEQ observation by SSBRC and improving uncertainty quantification by coarse seismicity density.

The estimation results of SSBRC with coarse seismicity density map $N_{\mathrm{X,red}} = 10$, are shown in Figure 24 which represents estimated ensemble histogram evolution, RMSE and spread curves. The histogram of final estimated permeability ensemble in Figure 24.a falls exactly on the true value of permeability which confirms the success of SSBRC in estimating permeability. Considering the performance of SSBRC with coarse density in terms of auxiliary ensemble spread, Figure 24.d clearly shows appropriate amount of ensemble spread (almost 85 %) at the final integration step. Continuous reduction of estimation error (RMSE) by integration step in Figure 24.b and very low final RMSE confirm the suitability of SSBRC for this estimation problem.

Experiment 5: 2D Heterogeneous, Resolving Spread Underestimation

In this set of experiments, we apply the three methods of improving uncertainty quantification in section 0 to the experiment 2 in section 0 (reference experiment) to resolve the issue of ensemble spread underestimation.

Inflated observation error variance

In this section to resolve the ensemble spread underestimation issue of SSBRC in experiment 2 section 0, we apply inflated observation error variance method. First we investigate the sensitivity of SSBRC performance to the range of the observation error Std. So we perform SSBRC with seismicity density on fine (original) grid system for different values of observation Std. In this experiment, we also show the sensitivity with respect to kernel band size, h. To resolve the ensemble spread underestimation, we find the optimal observation Std percent. As shown in Figure 25, SSBRC was performed at different kernel bandwidth sizes, h, and different observation Std percentages. To make the procedure of sensitivity analysis faster, only one integration step (integrating the whole seismicity cloud at once) is considered. Kernel bandwidth is changing from 0.1 to 5 (in terms of grid block size) which is color coded (50 different values) and $\sigma_{\min}$ is changing from 5 to 800 (100 different values) while $\sigma_{\max}$ equals twice $\sigma_{\min}$. We can find both optimal values of observation Std and Kernel bandwidth. For instance RMSE plot, Figure 25.a, shows that the minimum value of RMSE occurs around 100 % observation Std.

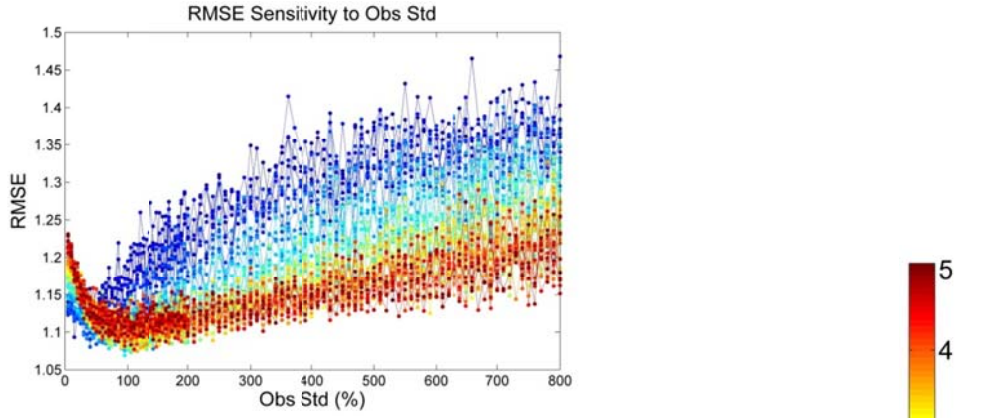

(a) Sensitivity of RMSE with respect to observation error Std % and kernel band

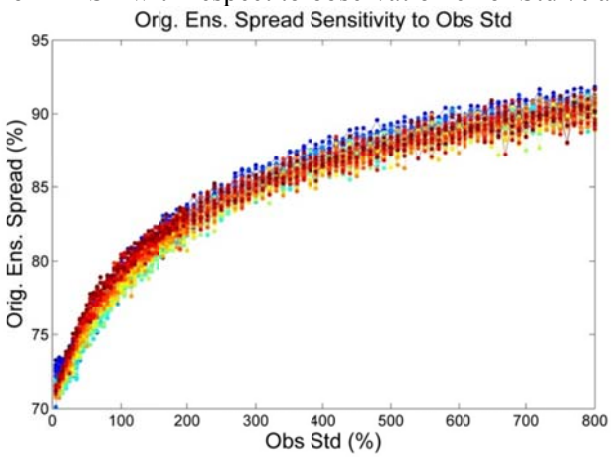

(b) sensitivity of original (Lperm) ensemble spread Sp(**m**)

Figure 25. Sensitivity of the performance of SSBRC with respect to observation error Std (%) and the size of the kernel band (the unit of kernel band is grid size).

To better investigate the effect of observation Std range, SSBRC results with different Std intervals are also shown in

Table 4. The first row of

Table 4, test # 1, shows the results of reference model that is experiment 2 in section 0. These results show improvement of final ensemble spread, characterized by Sp(**m**), (preserving more ensemble spread) by increasing the observation error Std. It can be seen in

Table 4 column Sp(**m**) that with increasing observation Std we can improve final ensemble spread from 10 % to 50 %. The test # 4 from

Table 4 (with 100 to 200 % observation Std range) is chosen as a representative experiment and its estimation results are shown in Figure 26. Comparing test # 1 (reference experiment with the typical range of observation Std) and test # 4 (improved uncertainty quantification) from

Table 4, we can see final ensemble spread increased from 10 % to almost 40 % and even estimation RMSE slightly decreased that means improvement both in parameter estimation (RMSE reduction) and uncertainty quantification (Sp($\mathbf{m}$) increase).

Table 4. Sensitivity of the SSBRC performance to different ranges of observation Std (standard SSBRC with seismicity density on the original fine grid) in estimating 2D heterogeneous permeability

test #	$\sigma_{\min}$ (%)	$\sigma_{\max}$ (%)	Final RMSE (Lperm)	Final spread (%) Sp($\mathbf{m}$)
1 (reference)	11	16	0.7576	9.39
2	34	90	0.7067	21.31
3	82	144	0.7078	32.03
4	100	203	0.7339	37.90
5	111	187	0.7394	41.09
6	143	227	0.7305	40.71
7	255	385	0.8075	51.42

Initial RMSE = 1.4478

In Figure 26 for concise illustration, only initial and final (at the sixth integration step) estimated maps are shown. Figure 26.b shows initial permeability ensemble mean, ensemble Std map and an individual permeability sample and Figure 26.c represents the final estimated ensemble mean, Std map and an individual sample after assimilating all MEQ observations. SSBRC is very successful in inferring the true permeability since the final estimated maps are very similar to the true permeability distribution. Additionally SSBRC along with inflated observation error Std results in preserving ensemble spread through estimation procedure which is shown by high Std map of Figure 26.c (middle plot). Estimation RMSE, Figure 26.d, and ensemble spread, Figure 26.e, prove successful estimation and ensemble spread improvement, respectively.

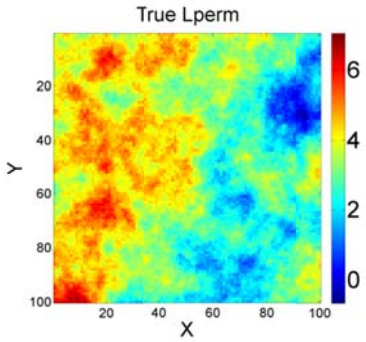

(a) true log-permeability map

(b)

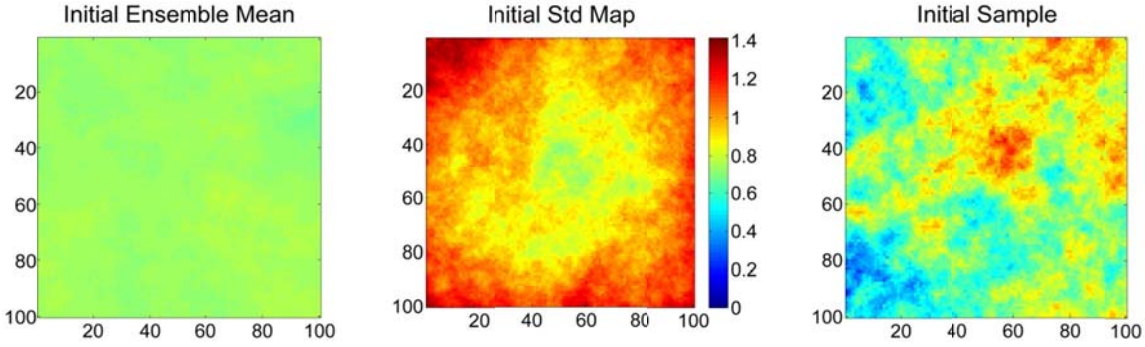

(c)

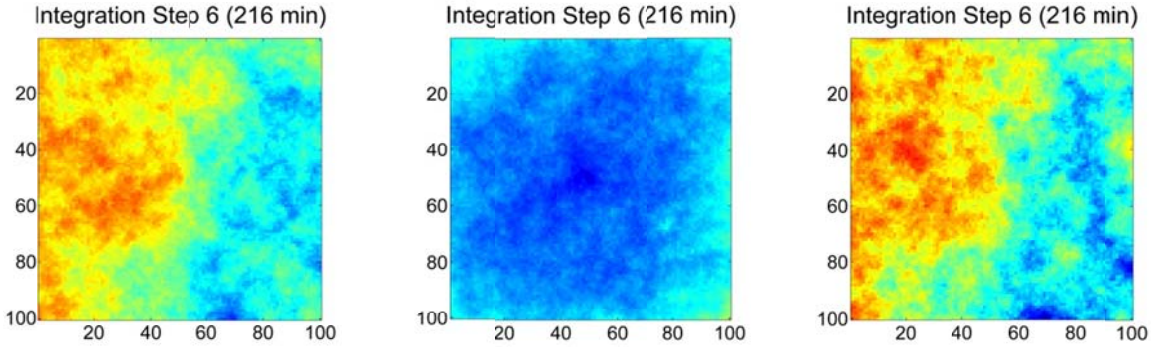

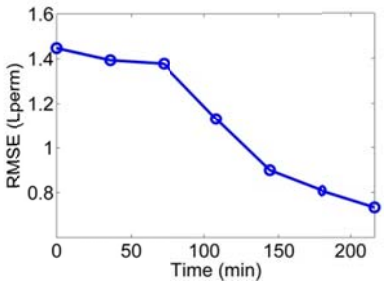

(d) estimation RMSE

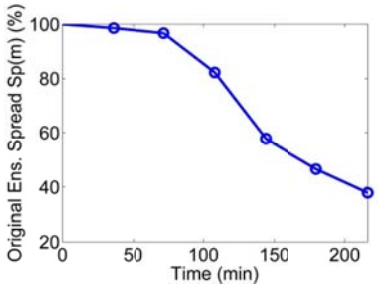

(e) ensemble spread

Figure 26. The SSBRC estimation results with inflated observation Std for a 2D heterogeneous permeability model: (a) the true log permeability model, (b) initial log-permeability ensemble mean (left), standard deviation map (middle), and an individual realization (right), (c) final log permeability ensemble mean (left), standard deviation (middle), and individual realization (right) after six update steps, and time evolution of (d) the log permeability RMSE and (e) normalized ensemble spread.

Reduced-order projection

The results of applying reduced-order projection along with SSBRC for different values of kernel bandwidth Std, σ_h, and truncation number, n_{trunc}, to experiment 2, section 0, are presented in
Table 5. The reference experiment (experiment 2, section 0) suffers from severe ensemble spread underestimation with only 10 % final spread however
Table 5 shows promising improvement of ensemble spread towards 40 to 80 %. The estimation RMSE of projection approach as shown in
Table 5 is not as low as reference experiment. It is clear from
Table 5 column n_{trunc} that reduced-order projection approach lowered the number of observations from 10000, in the reference experiment, to 25, 50 and 100, by spectral dimension reduction.

Table 5. SSBRC with observation projection approach. Sensitivity of the performance of projection approach with respect to kernel bandwidth Std (σ_h) and truncation number (n_{trunc}).

Test #	σ_h (%)	n_{trunc}	Final RMSE (Lperm)	Final spread (%) Sp($\mathbf{m}$)
1	25	100	1.02	50.61
2	25	50	0.9975	68.62
3	25	50	0.9682	64.84
4	25	100	0.9546	41.89
5	10	100	1.1382	28.41
6	25	25	1.1427	76.31

Initial RMSE = 1.4478

We choose test # 4 from
Table 5 as the representative experiment and its estimation results are shown in Figure 27. It should be noted that for this experiment five integration steps are considered. As it is seen in
Table 5 test # 4, the truncation number, n_{trunc}, is 100 which means by applying reduced-order projection we reduced the number of observations from 10000, in the reference experiment, to 100 in the improved experiment.

The final estimated ensemble mean and individual sample (left and right plots of Figure 27.c) demonstrate significant similarity with the true permeability map, Figure 27.a, and the estimation RMSE curve, Figure 27.d, is continuously decreasing. Therefore the estimation performance of SSBRC with projection approach is promising. As Figure 27.e shows the final ensemble spread is 40 %. The final Std map, Figure 27.c (middle plot), also demonstrates high values which confirms successful application of reduced-order projection for resolving ensemble spread underestimation.

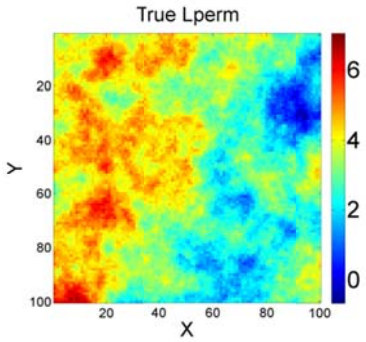

(a) true log-permeability map

(b)

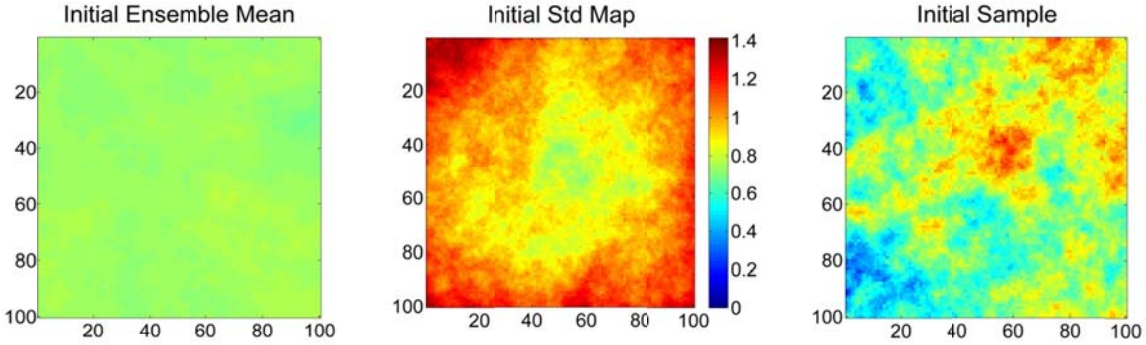

(c)

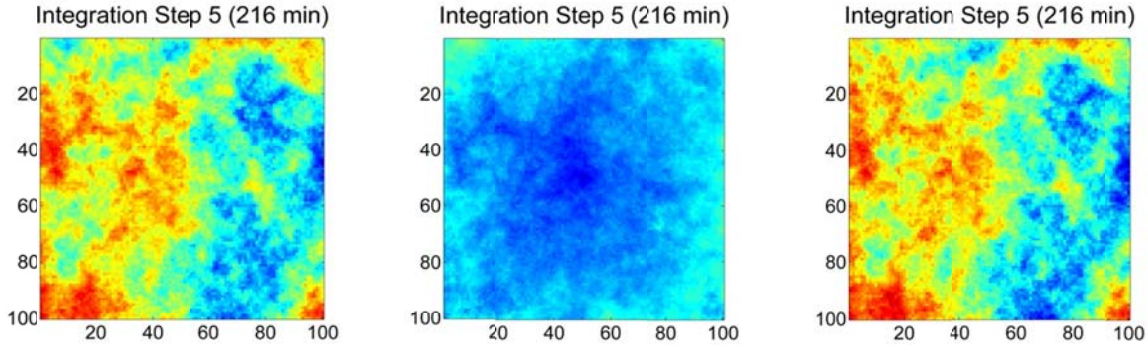

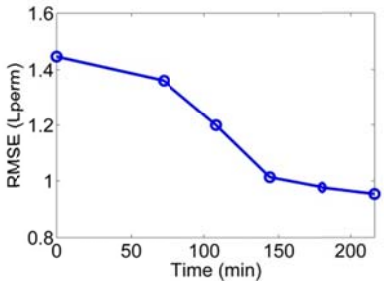

(d) estimation RMSE

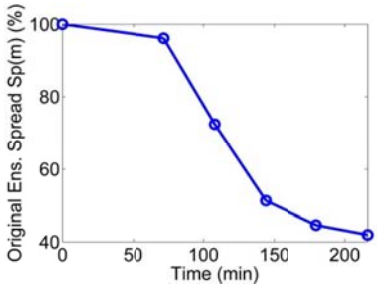

(e) ensemble spread

Figure 27. The SSBRC estimation results with observation projection approach for a 2D heterogeneous permeability model: (a) the true log permeability model, (b) initial log-permeability ensemble mean (left), standard deviation map (middle), and an individual realization (right), (c) final log permeability ensemble mean (left), standard deviation (middle), and individual realization (right) after six update steps, and time evolution of (d) the log permeability RMSE and (e) normalized ensemble spread.

Coarse-scale microseismicity density map

In this section preserving ensemble spread and improving uncertainty quantification is performed through reducing the number of observations by interpreting the discrete MEQ cloud on a coarse-scale grid system instead of original fine grid configuration. The reference experiment with ensemble spread underestimation in the one in section 0. The dimension of microseismicity density map is considered in terms of number of grid blocks in x direction (the field configuration is square). For coarsening of the seismicity density map, we specify different sizes of $N_{\mathrm{X,red}}$ equal to 10, 15, 20, 30, 50, 70 and 90, that decreases the number of observations to 100, 225, 400, 900, 2500, 4900 and 8100, respectively where in the reference experiment by $N_{\mathrm{X,red}} = N_{\mathrm{X}} = 100$, there are 10000 observations. In Figure 28, coarse-scale microseismicity density maps generated on different coarse grid configurations are shown. It is clear from Figure 28 that by coarsening the seismicity density map we are able to reduce the redundancy of MEQ density and consequently reduce the number of observations. In this experiment where permeability is heterogeneous the parameter dimension is also 10000.

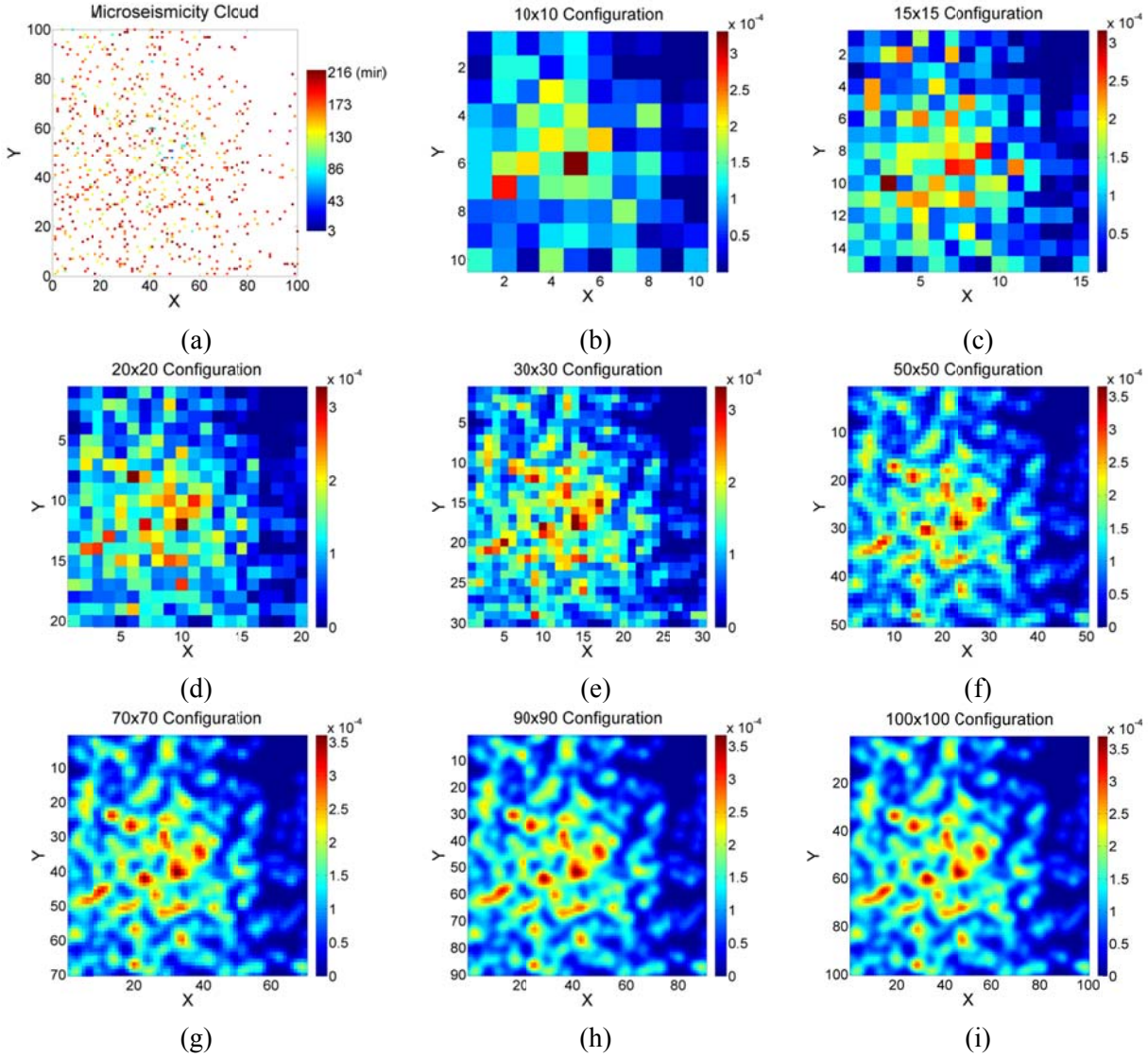

Figure 28. Continuous interpretation of MEQ cloud on different sizes of coarse-scale grid configuration. (a) discrete MEQ cloud, (b)-(i) coarse seismicity density maps on different coarse grid systems.

The results of sensitivity analysis of SSBRC performance with respect to coarse seismicity density size are given in Figure 29. All these experiments are performed with the typical range of observation error Std (5 % to 10 %). As we can see estimation RMSE is not very sensitive to size of the coarse grid system so the determining factor in choosing the appropriate size is ensemble spread. Figure 29 clearly shows that by increasing the dimension of the coarse grid system (rising the number of seismicity density observations) the ensemble spread will decrease. Therefore using coarse-scale grid system for generating seismicity density map greatly helps in preserving ensemble spread and avoiding ensemble collapse. As the representative experiment, we choose coarse grid system of 10×10 ($N_{\mathrm{X,red}}$=10) from Figure 29 and its estimation results are shown in Figure 30.

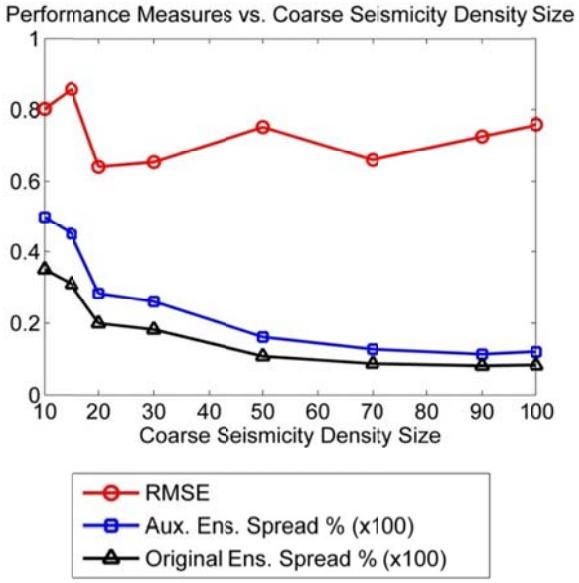

Figure 29. Effect of coarse microseismicity density dimension on the performance of SSBRC in heterogeneous permeability estimation experiment, initial RMSE = 1.4478.

Figure 30 presents the SSBRC estimation results with coarse-scale seismicity density map. The final estimated maps of permeability (Figure 30.c) are very similar to the true map (Figure 30.a) and the estimation RMSE curve is continuously decreasing which confirms promising estimation performance of SSBRC. Utilizing coarse-scale seismicity density resolves the ensemble spread underestimation issue and increases the final ensemble spread from 10 % in the reference experiment to 40 % in this improved experiment (Figure 30.e). Comparing the final ensemble Std map of Figure 30.c (middle) to the same map of reference experiment, Figure 15.g, indicates how effective coarse seismicity density approach is in improving uncertainty quantification of SSBRC.

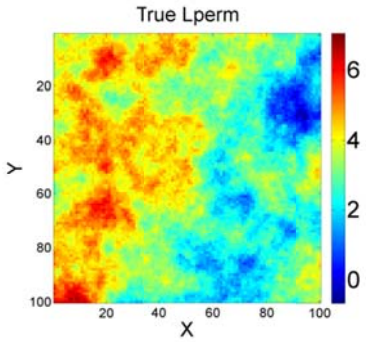

(a) true log-permeability map

(b)

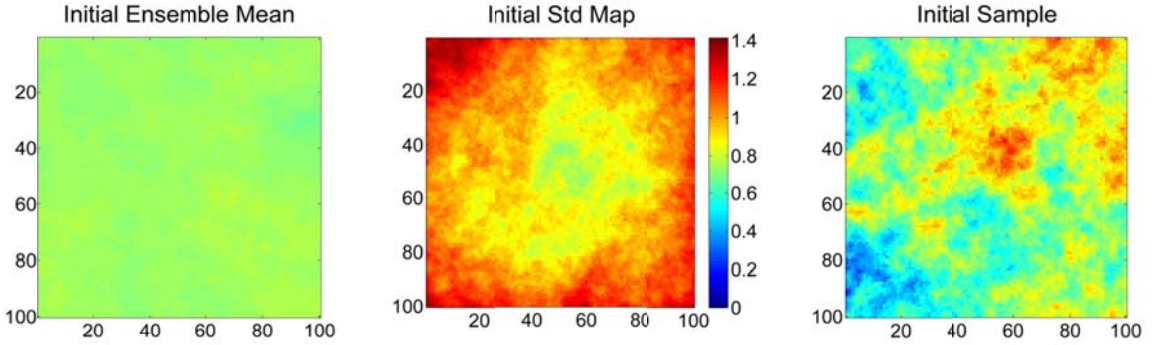

(c)

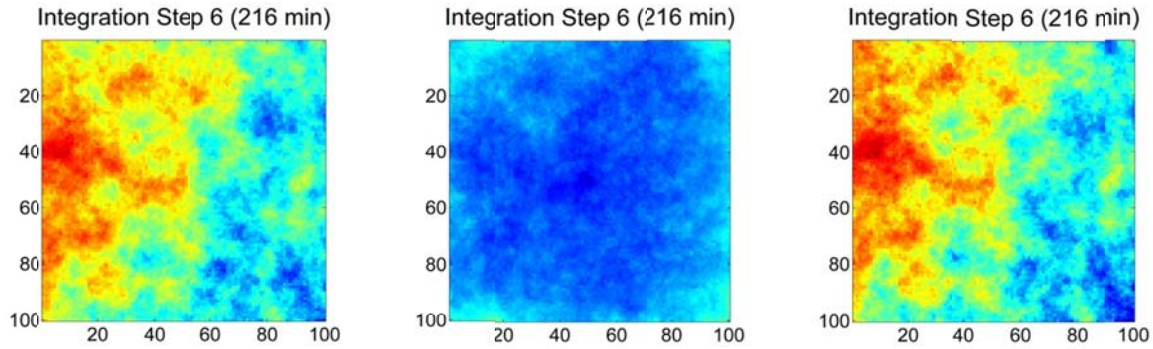

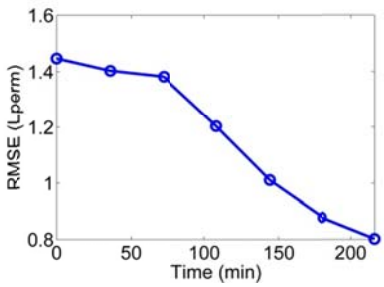

(d) estimation RMSE

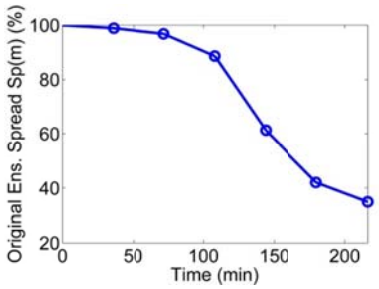

(e) ensemble spread

Figure 30. The SSBRC estimation results with coarse-scale seismicity density approach for a 2D heterogeneous permeability model: (a) the true log permeability model, (b) initial log-permeability ensemble mean (left), standard deviation map (middle), and an individual realization (right), (c) final log permeability ensemble mean (left), standard deviation (middle), and individual realization (right) after six update steps, and time evolution of (d) the log permeability RMSE and (e) normalized ensemble spread.

Experiment 6: 3D Heterogeneous, Resolving Spread Underestimation

In this set of experiments, we apply the three methods of improving uncertainty quantification in section 0 to the experiment 3 in section 0 (reference experiment) to resolve the issue of ensemble spread underestimation and ensemble collapse.

Inflated observation error variance

To resolve ensemble collapse problem with experiment 3 in section 0, in this section, we artificially increase observation error standard deviation range. To investigate the effect of observation Std range, SSBRC results with different Std intervals are shown in Table 6. The first row of Table 6, test # 1, shows the results of reference model that is experiment 3 in section 0. These results show improvement of final ensemble spread, characterized by $\mathrm{Sp}(\mathbf{m})$, (preserving more ensemble spread) by increasing the observation error Std. It can be seen in Table 6 column $\mathrm{Sp}(\mathbf{m})$ that with increasing observation Std we can improve final ensemble spread from 3 % to almost 20 %. The test # 3 from Table 6 (with 100 to 200 % observation Std range) is chosen as a representative experiment and its estimation results are shown in Figure 31. Comparing test # 1 (reference experiment with the typical range of observation Std) and test # 3 (improved uncertainty quantification) from Table 6, we can see final ensemble spread increased from 3 % to almost 20 % and even estimation RMSE slightly decreased that means improvement both in parameter estimation (RMSE reduction) and uncertainty quantification ($\mathrm{Sp}(\mathbf{m})$ increase). It is obvious from Table 6 that we can yet increase ensemble spread by further inflating observation error variance (increasing $\sigma_{\min}$ and $\sigma_{\max}$).

Table 6. Sensitivity of the SSBRC performance to different ranges of observation Std (standard SSBRC with seismicity density on the original fine grid) in estimating 3D heterogeneous permeability.

test #	$\sigma_{\min}$ (%)	$\sigma_{\max}$ (%)	Final RMSE (Lperm)	Final spread (%) $\mathrm{Sp}(\mathbf{m})$
1 (reference)	11	17	0.8504	2.58
2	25	59	0.8236	5.49
3	99	194	0.8151	18.65

Initial RMSE = 1.7793

In Figure 31 for concise illustration, only initial and final (at the sixth integration step) estimated maps are shown. Figure 31.b shows initial permeability ensemble mean, ensemble Std map and an individual permeability sample and Figure 31.c represents the final estimated ensemble mean, Std map and an individual sample after assimilating all MEQ observations. SSBRC is very successful in inferring the true permeability since the final estimated maps are very similar to the true permeability distribution. Additionally SSBRC along with inflated observation error Std results in preserving ensemble spread and avoiding ensemble collapse through estimation procedure which is shown by high Std map of Figure 31.c (middle plot). Estimation RMSE, Figure 31.d, and ensemble spread, Figure 31.e, prove successful estimation and ensemble spread improvement, respectively.

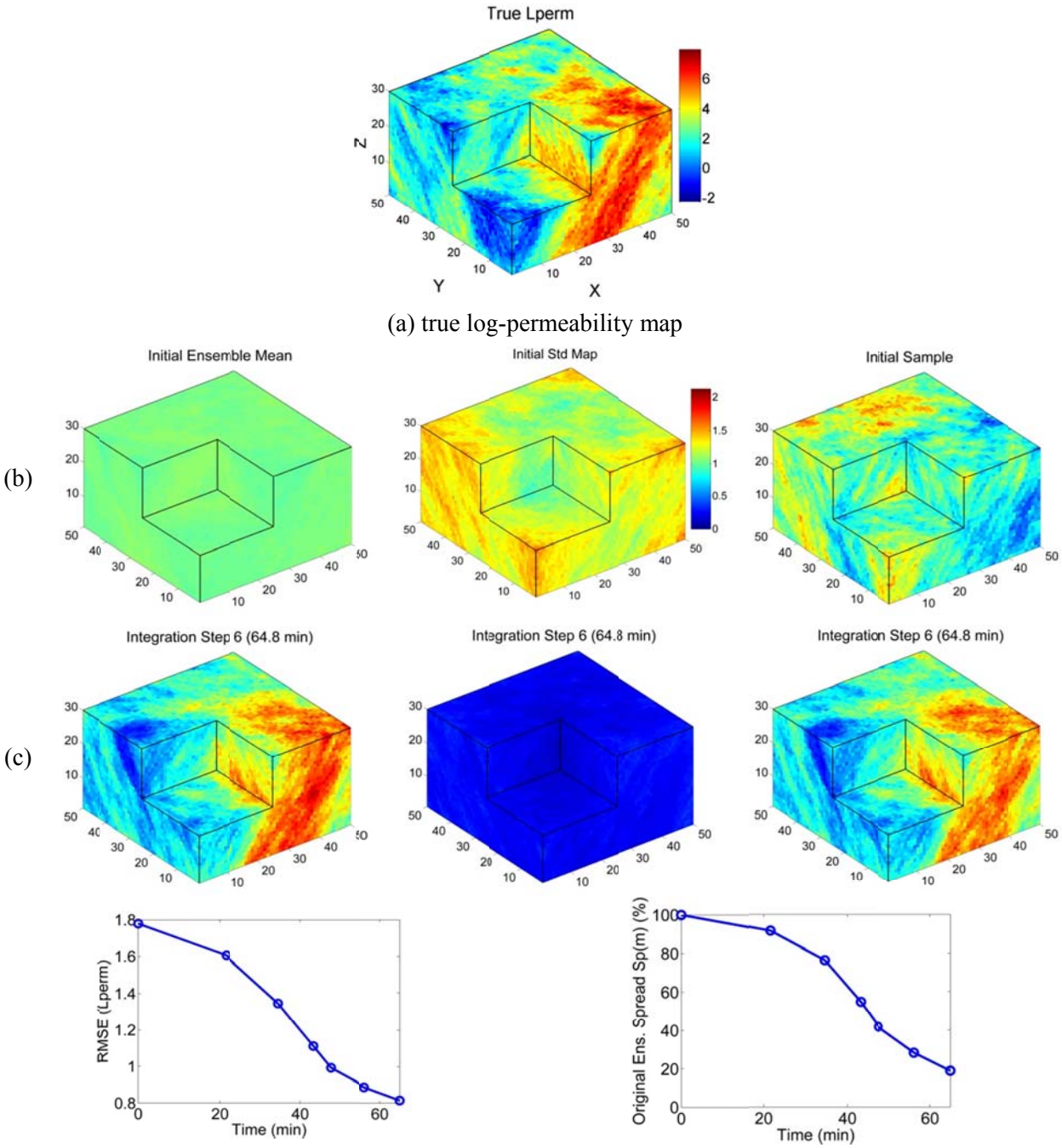

(a) true log-permeability map

(b)

(c)

(d) estimation RMSE

(e) ensemble spread

Figure 31. The SSBRC estimation results with inflated observation Std for a 3D heterogeneous permeability model: (a) the true log permeability model, (b) initial log-permeability ensemble mean (left), standard deviation map (middle), and an individual realization (right), (c) final log permeability ensemble mean (left), standard deviation (middle), and individual realization (right) after six update steps, and time evolution of (d) the log permeability RMSE and (e) normalized ensemble spread.

Reduced-order projection

The results of applying reduced-order projection along with SSBRC for different values of kernel bandwidth Std, σ_h, and truncation number, n_{trunc}, to experiment 3, section 0, are presented in Table 7.

The reference experiment (experiment 3, section 0) suffered from severe ensemble spread underestimation and ensemble collapse with only 3 % final spread however Table 7 shows promising improvement of ensemble spread towards 20 to 50 %. The estimation RMSE of projection approach as shown in Table 7 is not as low as reference experiment. We choose test # 1 from Table 7 as the representative experiment and its estimation results are shown in Figure 32. As it is seen in Table 7 test # 1, the truncation number, n_{trunc}, is 100 which means by applying reduced-order projection we reduced the number of observations from 75000, in the reference experiment, to 100 in the improved experiment.

Table 7. SSBRC with observation projection approach. Sensitivity of the performance of projection approach with respect to kernel bandwidth Std (σ_h) and truncation number (n_{trunc}).

Test #	σ_h (%)	n_{trunc}	Final RMSE (Lperm)	Final spread (%) Sp($\mathbf{m}$)
1	25	100	0.9785	19.52
2	25	40	1.0576	47.16

Initial RMSE = 1.7793

The final estimated ensemble mean and individual sample (left and right plots of Figure 32.c) demonstrate significant similarity with the true permeability map, Figure 32.a, and the estimation RMSE curve, Figure 32.d, is continuously decreasing. Therefore the estimation performance of SSBRC with projection approach is promising. As Figure 32.e shows the final ensemble spread is 20 %. The final Std map, Figure 32.c (middle plot), also demonstrates high values which confirms successful application of reduced-order projection for resolving ensemble spread underestimation and ensemble collapse.

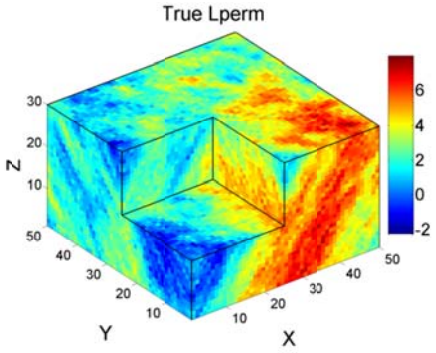

(a) true log-permeability map

(b)

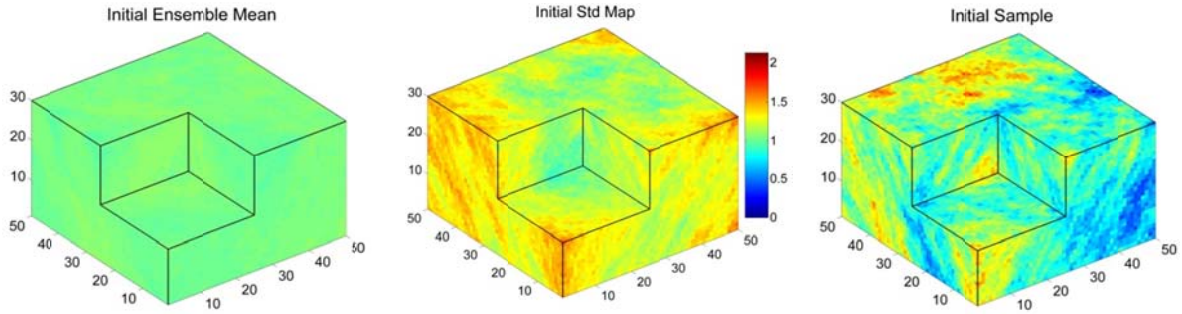

(c)

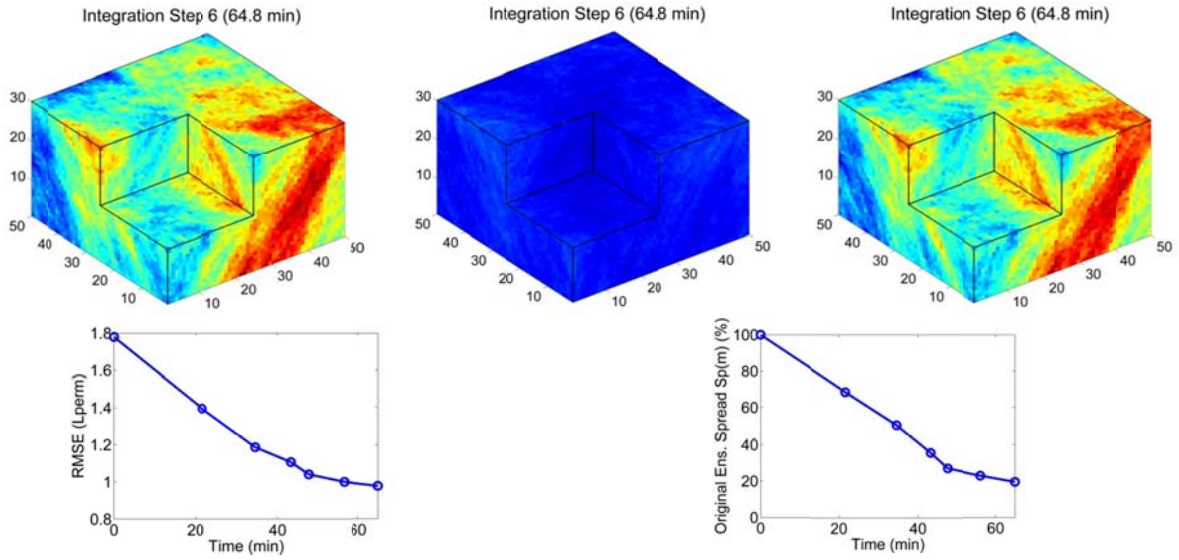

(d) estimation RMSE (e) ensemble spread

Figure 32. The SSBRC estimation results with observation projection approach for a 3D heterogeneous permeability model: (a) the true log permeability model, (b) initial log-permeability ensemble mean (left), standard deviation map (middle), and an individual realization (right), (c) final log permeability ensemble mean (left), standard deviation (middle), and individual realization (right) after six update steps, and time evolution of (d) the log permeability RMSE and (e) normalized ensemble spread.

Coarse-scale microseismicity density map

In this section preserving ensemble spread and improving uncertainty quantification is performed through reducing the number of observations by interpreting the discrete MEQ cloud on a coarse-scale grid system instead of original fine grid configuration. The reference experiment with ensemble spread underestimation in the one in section 0. We investigated two different coarse-scale grid configurations as reported in Table 8. These SSBRC experiments with coarse seismicity density are performed with the typical range of observation error Std (5 % to 10 %). The first coarse grid system (Table 8 test # 1) is 10x10x5 which results in the coarse seismicity density dimension of 500. In fact we discretize the original 3D field to 10x10x5 configuration to generate seismicity density instead of using the original fine grid system (50x50x30) which is used for numerical reservoir simulation. Therefore the number of observations is reduced from 75000 in the reference experiment to 500 in the improved experiment. In test # 2 of Table 8, the grid system is 15x15x10. In this case the number of seismicity density observations is 2250. The results of sensitivity analysis of SSBRC performance with respect to coarse seismicity density configuration are given in Table 8. Final ensemble spread values, $\mathrm{Sp}(\mathbf{m})$, in Table 8 clearly show that by coarsening the grid system the ensemble spread will increase. Therefore using coarse-scale grid system for generating seismicity density map greatly helps in preserving ensemble spread and avoiding ensemble collapse. As the representative experiment, we choose test # 1, coarse grid system of 10×10×5, from Table 8 and its estimation results are shown in Figure 33.

Table 8. SSBRC with coarse seismicity density. Sensitivity of SSBRC performance with respect to the size of coarse-scale grid system.

Test #	Coarse-scale grid	Final RMSE (Lperm)	Final spread (%) $\mathrm{Sp}(\mathbf{m})$

	configuration		
1	10x10x5	0.9171	25.72
2	15x15x10	0.8208	12.97

Initial RMSE = 1.7793

Figure 33 presents the SSBRC estimation results with coarse-scale seismicity density map. The final estimated maps of permeability (Figure 33.c) are very similar to the true map (Figure 33.a) and the estimation RMSE curve is continuously decreasing which confirms promising estimation performance of SSBRC. Utilizing coarse-scale seismicity density resolves the ensemble spread underestimation (ensemble collapse) issue and increases the final spread from 3 % in the reference experiment to 25 % in this improved experiment (Figure 33.e). Comparing the final ensemble Std map of Figure 33.c (middle) to the same map of reference experiment, Figure 20.g (where ensemble collapse happened), indicates how effective coarse seismicity density approach is in improving uncertainty quantification of SSBRC.

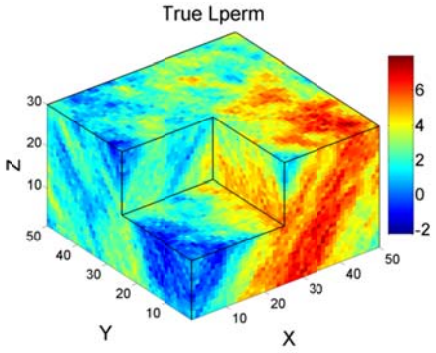

(a) true log-permeability map

(b)

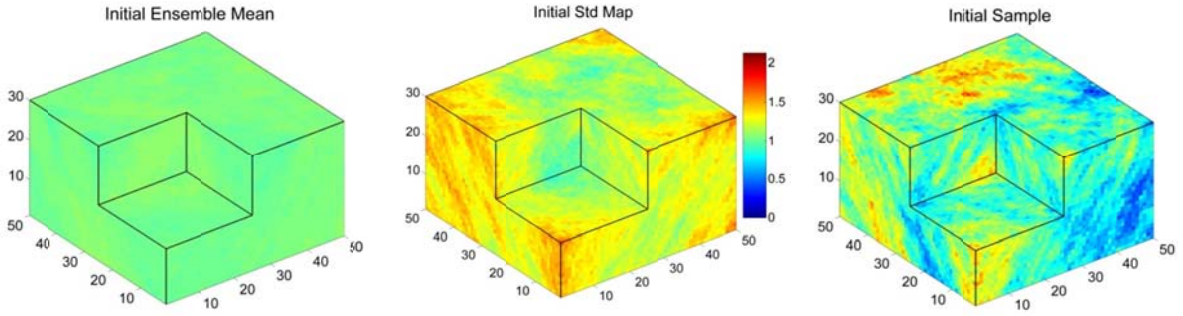

(c)

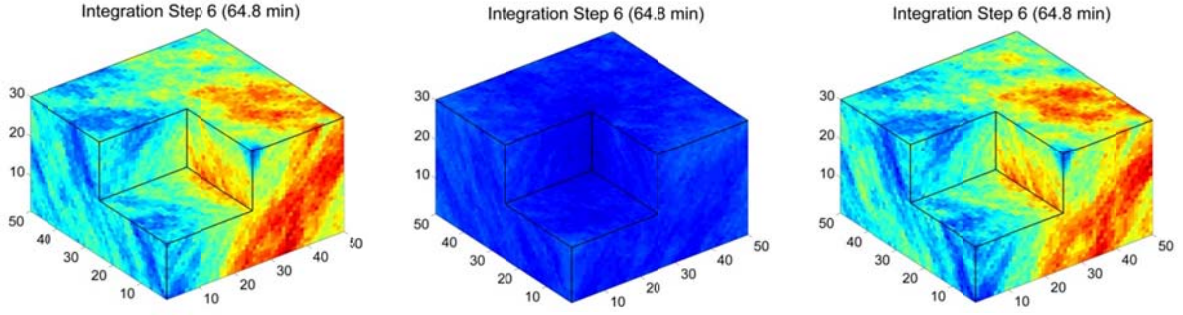

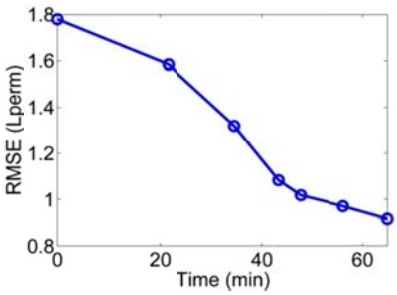

(d) estimation RMSE

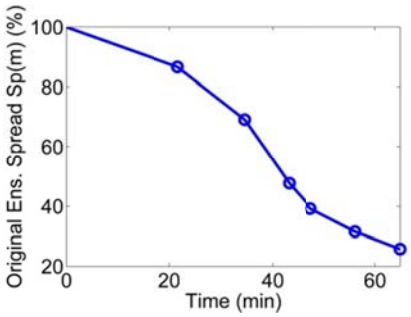

(e) ensemble spread

Figure 33. The SSBRC estimation results with coarse seismicity density for a 3D heterogeneous permeability model: (a) the true log permeability model, (b) initial log-permeability ensemble mean (left), standard deviation map (middle), and an individual realization (right), (c) final log permeability ensemble mean (left), standard deviation (middle), and individual realization (right) after six update steps, and time evolution of (d) the log permeability RMSE and (e) normalized ensemble spread.

4.5 Description of Experimental Setup: Geomechanical Model

In this section we apply the SSBRC method to the fully coupled geomechanical forward reservoir simulator. In these set of experiments we assimilate MEQ cloud (after converting it to continuous seismicity density map) in EnKF analysis equation to infer hydraulic (permeability) and geomechanical (Young's modulus or elastic modulus, tensile strength, Cohesion) parameters of the reservoir. The experiments in this section are performed on both homogeneous and heterogeneous 2D model and also on heterogeneous 3D model. We use a 2D FEM model with point source injection by quadrilateral regular mesh with 50×50 = 2500 elements (10000 nodes) and the reservoir size of 500 m × 500 m. The developed coupled FEM model is capable of handling spatially distributed parameters (heterogeneous distributions) such as permeability, Young's modulus, tensile strength, cohesion and friction angle. We assign the spatially distributed parameters to the nodes therefore 2D model parameter dimension is 10000. There is one water injection well with constant injection rate at the center of the field. The fluid is assumed single phase and the boundaries are closed to flow (No flow boundary condition). In 2D model, the stress boundary condition or far-field stress regime is specified by maximum horizontal stress $S_{H,max}$, minimum horizontal stress $S_{h,min}$, and the initial field pressure P_{ini}. It should be noted that our simulations are performed in isothermal reservoir conditions however the forward model is capable of handling thermal effects. The rock and fluid properties are reported in Table 9. In the 2D forward simulation, time step length is 720 (s) and there are 100 time steps. We also consider this 2D geomechanical model with homogeneous parameter and perform estimation experiment with SSBRC to infer a single parameter (e.g. the homogeneous Young's modulus) from MEQ observations.

Table 9. Rock/fluid properties used in simulations.

Fluid density, ρ_f	1000 kg/m^3
Fluid viscosity, η	10^{-3} Pa.s

Drained Poisson's ratio, ν	0.22
Undrained Poisson's ratio, ν_u	0.46
Porosity, ϕ	0.30
Material constant, ζ_d	20
Material constant, β_d	10^{-7}

In this work, we also use a 3D fully coupled FEM model with point source injection by hexahedron regular mesh with 30×30×15 = 13500 elements (108000 nodes) and the reservoir size of 750 m × 750 m × 370 m. The forward geomechanical model is very computationally expensive and in our case a single forward simulation takes almost 5 (hr) to run (on a machine with Intel Xeon CPU 3.07 GHz and 6 GB RAM). Consequently, SSBRC procedure which needs running multiple realizations in different integration steps, has extremely high run time. While as discussed earlier the SSBRC procedure is already implemented in parallel, the estimation process with 3D model is still very computationally intensive. Therefore, as we already know the original SSBRC leads to ensemble spread underestimation we choose to perform SSBRC with coarse seismicity density method. Here we only present the estimation results of a single 3D experiment which is estimating Young's modulus distribution from MEQ cloud using SSBRC with coarse-scale seismicity density method.
To do EnKF data integration, we consider six integration steps. In each SSBRC estimation experiment, we assume the spatial distribution of one reservoir property unknown (the parameter to estimate) and the rest of the properties are assumed known. We can also estimate more than one reservoir property distribution simultaneously from MEQ cloud.

4.5.1 *Results and discussion*
In this section we present the SSBRC estimation results with the geomechanical forward model. For the 2D model we first show the results of standard SSBRC that leads to ensemble spread underestimation and then the results of improved uncertainty quantification with SSBRC are presented. The estimation results of SSBRC with 3D geomechanical model are presented only by incorporating improved uncertainty quantification methods.

Experiment 1: 2D Homogeneous
To demonstrate the applicability of the SSBRC method for geomechanical model, we first apply it to a homogeneous parameter estimation problem. As the simplest experiment, we consider all parameters to be constant (homogeneous or uniform over the whole field, i.e., spatially invariable) and then we consider one of the parameters to be unknown and set out to estimate the unknown parameter (which is a scalar). When the unknown parameter is homogeneous, the initial random ensemble of realizations for EnKF consists of N_e real numbers while each number (or scalar) is a realization or candidate of the unknown parameter. Therefore, to show the ensemble we simply use a histogram. In this set of experiments we use the standard SSBRC with high resolution seismicity density which is generated on the original fine FEM mesh. The observation error Std range ($\sigma_{\min}$, $\sigma_{\max}$) is also chosen as 15 % to 50 % which is inflated to some extent comparing to typical range of observation Std (5 % to 10 %).
We consider integrating tensile microseismicity events to estimate the homogeneous reservoir parameters. We consider Young's modulus (E), permeability (k) and tensile strength (T_0) to be homogeneous (a single value for all nodes) and consider tensile failure distribution as monitoring data. A single true

geomechanical model is considered while in different estimation experiments different parameters are estimated. We consider three different settings for estimating three different parameters (Young's modulus, permeability and tensile strength). For instance in the first setting we assume k and T_0 known and E unknown then we integrate seismicity data to estimate homogeneous Young's modulus E. By the same procedure we setup the other two settings to estimate k and T_0. Figure 34 shows the true microseismicity cloud for the homogeneous parameter estimation experiment. The geomechanical model specifications are also indicated in Figure 34. The result resembles a conventional hydraulic fracture propagation.

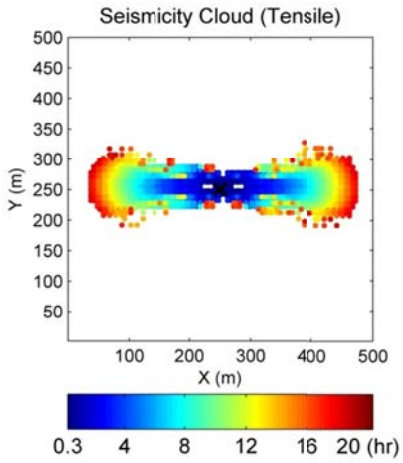

Figure 34. True seismicity cloud (tensile failures) of homogeneous parameter experiment; $\mathrm{P_{ini}} = 10\ (MPa), \mathrm{S_{H,max}} = 25\ (MPa), \mathrm{S_{h,min}} = 15\ (MPa)$, Inj. Rate $= 0.005\ (l/s), E = 10\ (GPa), k = 0.005\ (md), T_0 = -4\ (MPa)$. The black cross shows the injection well location.

First we consider estimating the homogeneous Young's modulus (E). To illustrate the ensemble of realizations in homogeneous parameter estimation we can simply use a histogram. To show the estimation procedure we plot the histogram of the ensemble at each integration step (six integration steps). Moreover, as a measure of estimation procedure performance we show the evolution of Root Mean Square Error (RMSE) of estimation through time (integration time steps). Figure 35 shows the estimation results of homogeneous E by integration of tensile events of Figure 34. The red vertical line in the histogram shows the true value of E ($10\ GPa$) which we are trying to estimate. In all experiments we use 100 realizations or samples of E i.e., the EnKF ensemble size is equal 100. Figure 35 shows the evolution of the ensemble histogram from (a) to (g) through integration time steps. It can be seen that the EnKF process is very effective in estimating the unknown parameter. The initial histogram (a) is very wide but by integration of seismicity data the histogram narrows around the true E value and from integration step 3 to the end all the realizations or samples of E almost coincide with the true value of E. Basically, we start with a random set of E samples (100 samples) between zero and 50 (GPa) as the initial ensemble, and after applying the EnKF and integrating true seismicity observations in time, all 100 samples converge to the true E value of 10 GPa. In plots (d) to (e) only the red vertical line is visible meaning that all the samples are equal true E value which shows the almost perfect estimation of E. The estimation error of E (RMSE), Figure 35.h, goes to almost zero which indicates a perfect estimation of the unknown parameter.

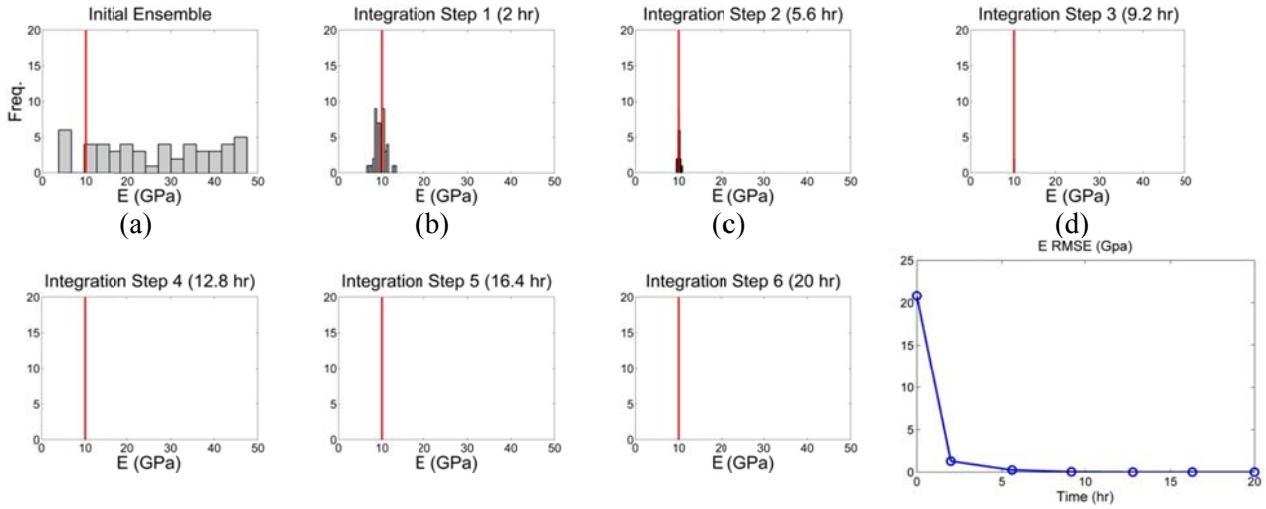

(a) (b) (c) (d)

(e) (f) (g) (h)

Figure 35. Results of homogeneous elastic modulus E, estimation; plots (a) to (g) show the evolution of ensemble histogram at each integration steps. Plot (h) shows the RMSE of estimation. (True $E = 10\ GPa$).

The uncertainty quantification performance of SSBRC is shown in Figure 36 in terms of ensemble spread throughout the integration steps. As we expect in a homogeneous parameter estimation problem the final original ensemble spread (Figure 36.a) is very insignificant (close to zero) since all the final estimated realizations are almost equal to the true value of Young's modulus. Figure 36.b still shows acceptable final auxiliary ensemble spread of 15 % which yet can be improved by further increasing observation Std.

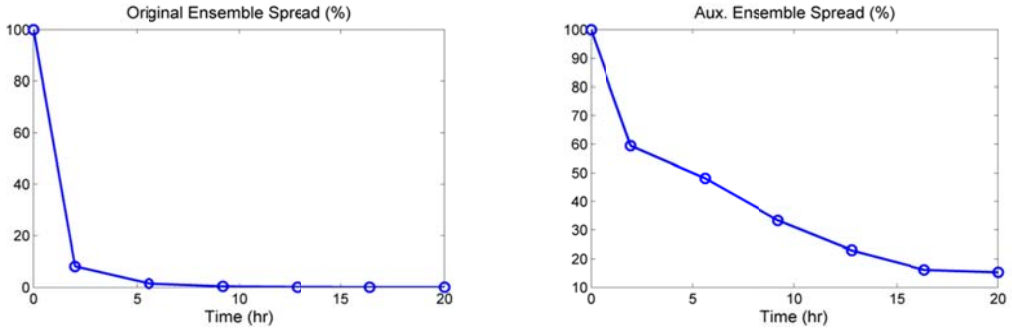

(a) Young's modulus ensemble spread (b)

Figure 36. Ensemble spreads in estimating homogeneous elastic modulus E, from MEQ events.

Figure 37 shows the estimation results of homogeneous permeability k, by integration of tensile events of Figure 34. The red vertical line in the histogram shows the true value of k (0.005 md) which we are trying to estimate. Figure 37 just represents the histogram of permeability ensemble in some specific integration steps to make the representation more concise. In this estimation example we again see at integration step 3 (Figure 37.d) the histogram fully narrows down to the true k value which means almost perfect estimation of unknown permeability value. Figure 37.a, the permeability RMSE, also shows the estimation error almost goes to zero.

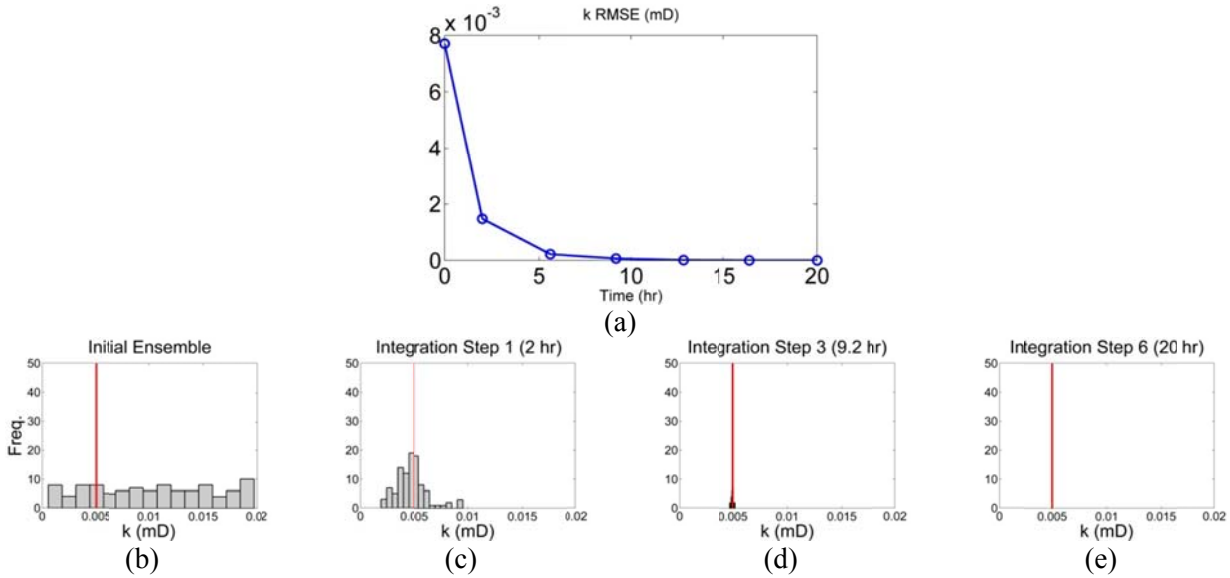

(a) (b) (c) (d) (e)

Figure 37. Results of homogeneous permeability k, estimation; Plot (a) shows the RMSE of estimation. Plots (b) to (e) show the evolution of ensemble histogram in integration steps. (true k = 0.005 md).

The uncertainty quantification performance of SSBRC is also shown in Figure 38 in terms of ensemble spread throughout the integration steps. As we expect in a homogeneous parameter estimation problem the final original ensemble spread (Figure 38.a) is very insignificant (close to zero) since all the final estimated permeability realizations are almost equal to the true permeability. Figure 38.b still shows fairly promising final auxiliary ensemble spread of 45 % which yet can be improved by further increasing observation Std or using other improved uncertainty quantification methods.

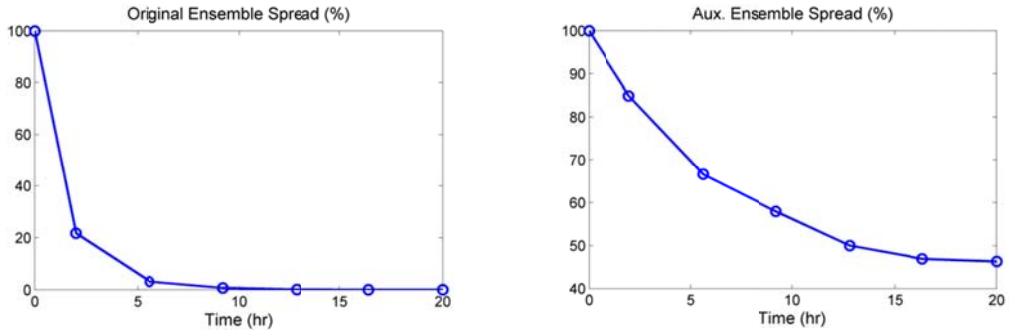

(a) permeability ensemble spread (b)

Figure 38. Ensemble spreads in estimating homogeneous permeability k, from MEQ events.

In the next example setting we assume tensile strength T_0, to be the unknown parameter and estimate it by seismicity data integration. Again the true model is shown in Figure 34 and we estimate homogeneous T_0 by integrating tensile events. The true tensile strength value is equal to -4 (MPa). Figure 39 illustrates the estimation results including both T_0 estimation error and T_0 ensemble histogram evolution. Confirming the previous homogeneous parameter estimation results, we can see the unknown homogeneous T_0 is estimated perfectly.

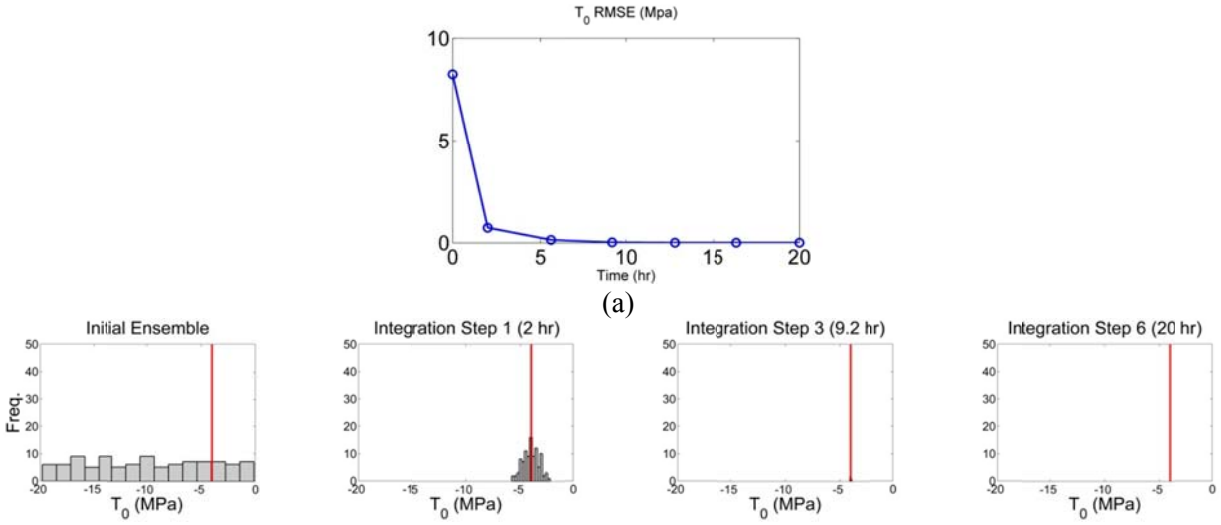

(a) (e) (f) (g) (h)

Figure 39. Results of homogeneous tensile strength T_0, estimation; Plot (a) shows the RMSE of estimation. Plots (b) to (e) show the evolution of ensemble histogram in integration steps. (true T_0 = -4 MPa).

Similar pattern is again seen in the ensemble spread results of Figure 40. The final T_0 ensemble spread (Figure 40.a) is almost zero which is expected in homogeneous parameter estimation and the final auxiliary ensemble spread (Figure 40.b) is equal to 30 % that indicates promising final spread value.

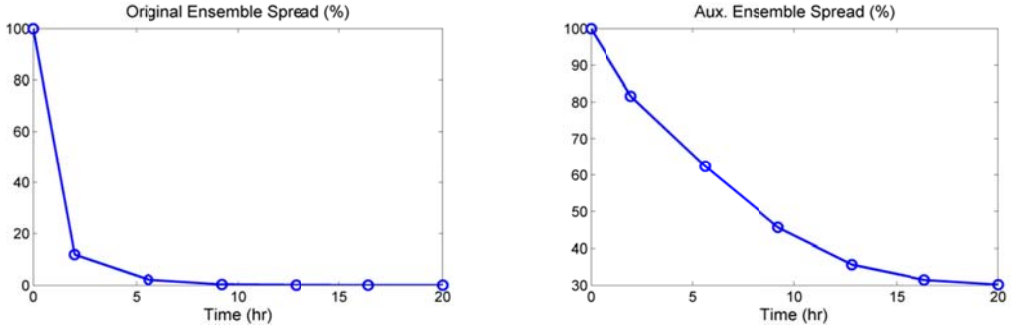

(a) tensile strength ensemble spread (b)

Figure 40. Ensemble spreads in estimating homogeneous tensile strength T_0, from MEQ events.

It should be noted again that we used a single true homogeneous model in three different estimation settings to estimate three different reservoir parameters (true model of Figure 34 and three estimation examples of Figure 35, Figure 37 and Figure 39). Based on these three examples for estimating homogeneous geomechanical reservoir parameters, we see the promise of using EnKF to effectively infer unknown reservoir parameters using MEQ data. In all these homogeneous parameter estimation experiments with SSBRC we might see the issue of ensemble spread underestimation or ensemble collapse that can be always handled with proposed improved uncertainty quantification methods of section 0. However in this of experiments, we only emphasize on estimation performance of SSBRC which is shown promising and we do not apply improved uncertainty quantification methods to preserve

the ensemble spread throughout integration steps. Although we applied SSBRC with slightly inflated observation error Std range (15 % to 50 %). It should be noted that in homogeneous parameter estimation with SSBRC, obtaining good estimation result means reaching very low ensemble spread or namely ensemble collapse.

Experiment 2: 2D Heterogeneous Tensile Strength

In this experiment we estimate heterogeneous tensile strength T_0, distribution from MEQ monitoring data. The true model specifications are shown in Figure 41. Figure 41.a shows the microseismicity cloud (due to only tensile failure) generated by the geomechanical forward model for a given distribution of tensile strength T_0, (Figure 41.b). In this setup, elastic modulus E, is assumed to be spatially random distributed and known. In this example the target parameter to estimate is tensile strength T_0, which is estimated by incorporating MEQ data. In this experiment permeability k, is constant in space. In the estimation process all the parameters except T_0 are assumed known and the unknown (assumed) T_0 is estimated. We generate Young's modulus E, distribution from a normal probability distribution by specific mean and standard deviation which is shown in Figure 41 (μ_E = mean of normal distribution = 50 GPa, σ_E = standard deviation of normal distribution = 15 GPa).

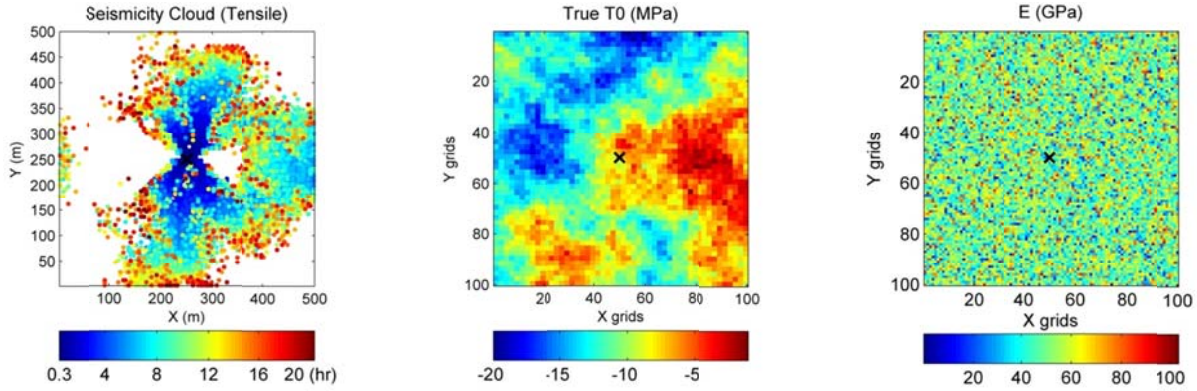

(a) true microseismicity observation

(b) true T_0 map

(c) E map

Figure 41. True model specification.
$S_{h,min} = 20$ (MPa), $S_{H,max} = 15$ (MPa), $P_{ini} = 10$ (MPa), Inj. Rate $= 0.006\ (l/s), k = 0.005\ (md)$, Young's modulus E, with Normal PDF (spatially random distribution) $\mu_E = 50\ (GPa), \sigma_E = 15\ (GPa)$. Black cross at the center shows the injection well location.

In this example the standard SSBRC method with MEQ density map on the original fine mesh is used for data integration. The observation error Std range ($\sigma_{\min}, \sigma_{\max}$) is also assumed 20 % to 55 % which is somewhat inflated comparing to the typical range of observation Std. Figure 42.a shows the estimation results by illustration of ensemble mean evolution throughout integration steps. In this EnKF procedure we use 100 random realizations of T_0 distributions as the initial ensemble. Before using any observation (seismicity data) the mean of the initial ensemble does not have any spatial trend or feature because it is made of 100 random realizations (as we can see in Figure 42.a, initial ensemble mean is almost uniform and non-informative). By subsequent integration of seismicity observations we can see that the ensemble mean is developing some special features in it, and finally the ensemble mean becomes very similar to the true tensile strength T_0, map. From Figure 42.a it is clear that the final estimated ensemble mean

(integration step 6) is very similar to the true map while the initial ensemble mean was completely non-informative. Because the ensemble mean is so close to the true parameter, each of final realizations is also very close to the true tensile strength. Figure 42.b shows the estimation error evolution in time which is RMSE of T_0 and is decreasing with time which means the estimation error is decreasing and the estimated map is becoming closer to true map. The tensile strength ensemble spread evolution throughout integration steps is shown in Figure 42.c and it clearly shows severe ensemble spread underestimation of standard SSBRC where the final spread in only 3 %.

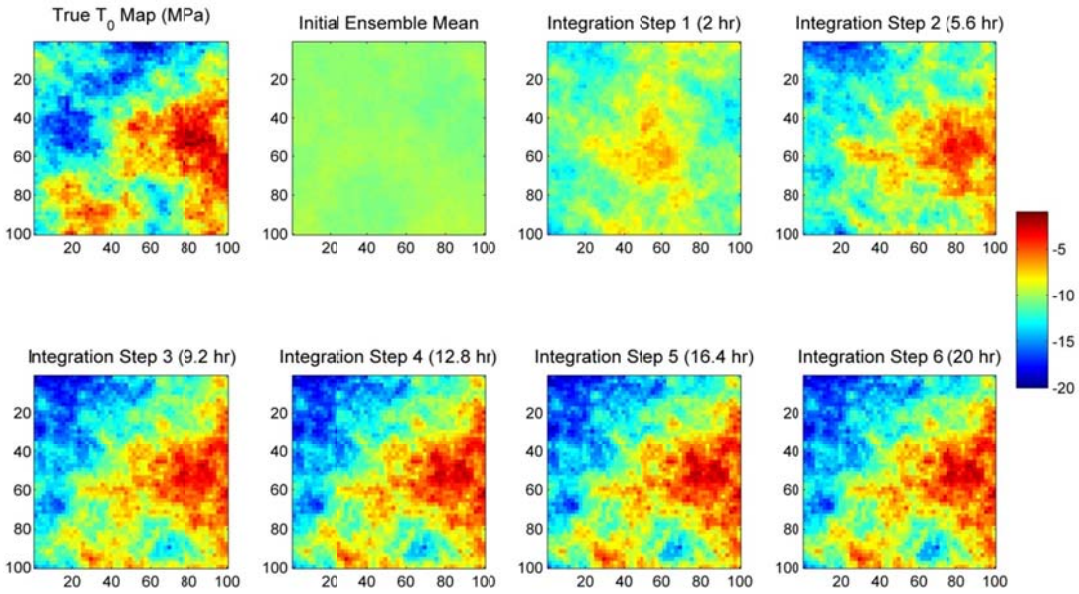

(a) estimated T_0 ensemble mean evolution through integration steps.

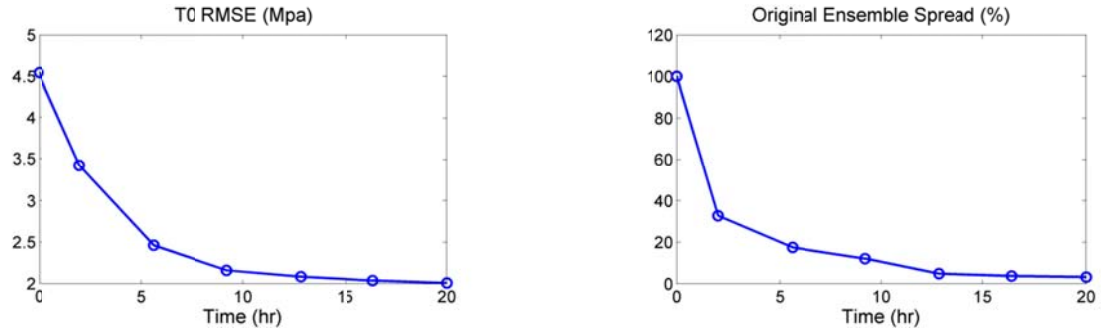

(b) T_0 RMSE evolution in time (c) T_0 ensemble spread

Figure 42. Tensile strength T_0, estimation results in terms of estimated ensemble mean map, RMSE and ensemble spread

Figure 43 shows the evolution of a single realization or sample through integration steps. From Figure 43 we can see the initial realization is completely different than the true map while after 6 seismicity data integration steps the differences become minor.

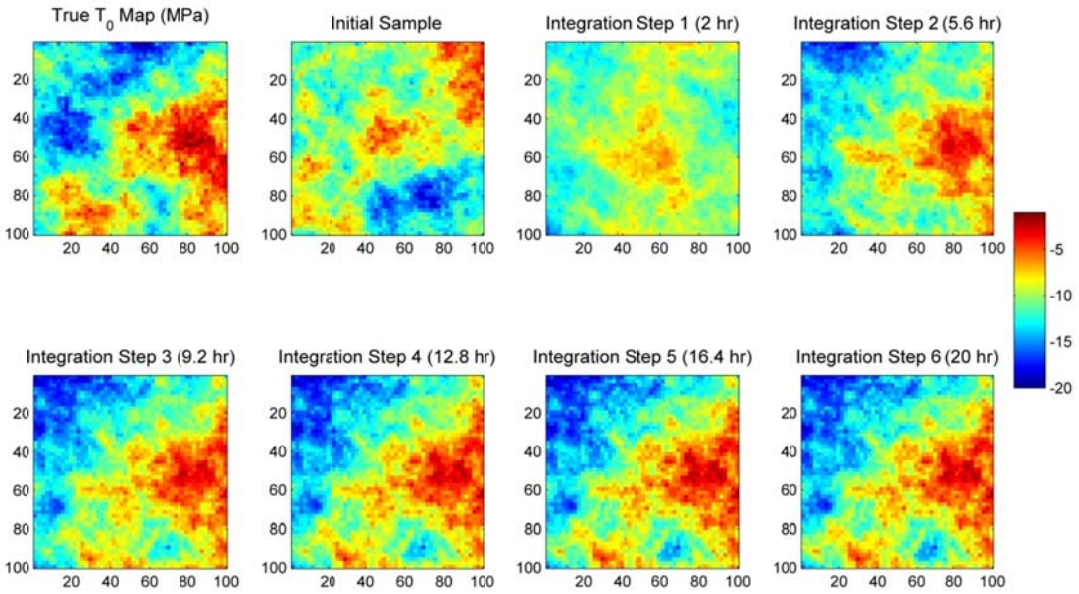

Figure 43. Evolution of one tensile strength T_0, realization throughout integration steps.

We start the estimation process with an initial ensemble of random samples. The initial ensemble represents the uncertainty in the parameter before integrating the seismicity observation. Having made of random samples the spread or uncertainty in initial ensemble is high. It means the standard deviation of initial ensemble is large. In the integration procedure by incorporating new data the samples are corrected and the new estimated ensemble will have smaller uncertainty or standard deviation (Std). So the ensemble spread changes by seismicity integration. As we integrate more data, the uncertainty in the ensemble decreases which results in reduction of the ensemble spread. To analyze the ensemble spread, the standard deviation (Std) of the ensemble is calculated. Figure 44 shows the evolution of the standard deviation of tensile strength T_0, ensemble and as it is seen, the uncertainty in the ensemble is reduced. Uncertainty reduction in the ensemble is what we expect from the EnKF method. However as we discussed before the standard SSBRC with high resolution seismicity density map leads to severe ensemble spread underestimation. The initial (guess) ensemble is very wide and non-informative (includes random samples) but after data integration, samples tend to develop a special shape or feature which is shape of the true parameter distribution.

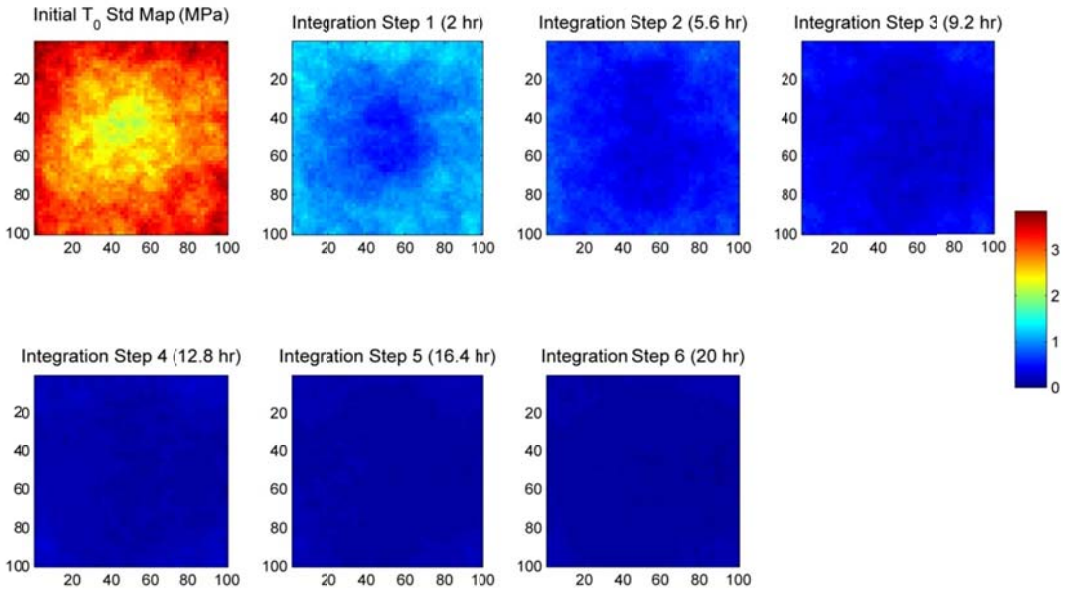

Figure 44. Evolution of tensile strength T_0, ensemble standard deviation map throughout integration steps.

Figure 45 shows the initial and final state of 6 realizations of tensile strength distributions (out of 100 realizations). As we can see all 6 realizations change from their initial state (which is completely dissimilar to true) to a final state which is very similar to true tensile strength T_0, map. Ensemble spread reduction is also obvious from Figure 45, where 6 completely different distributions of T_0 (wide variation or spread) converge to a specific distribution (narrow variation or spread). Since all of the final estimated samples are similar, the standard deviation of the final ensemble is extremely low (shown in Figure 44; integration step 6). It should be noted that we did not apply improved uncertainty quantification methods to this example.

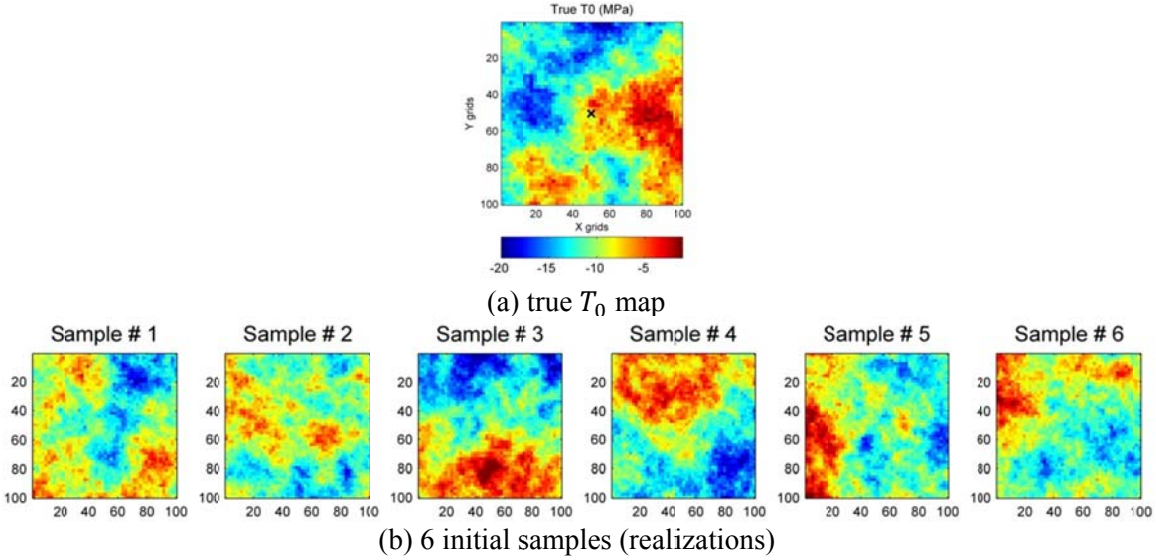

(a) true T_0 map

(b) 6 initial samples (realizations)

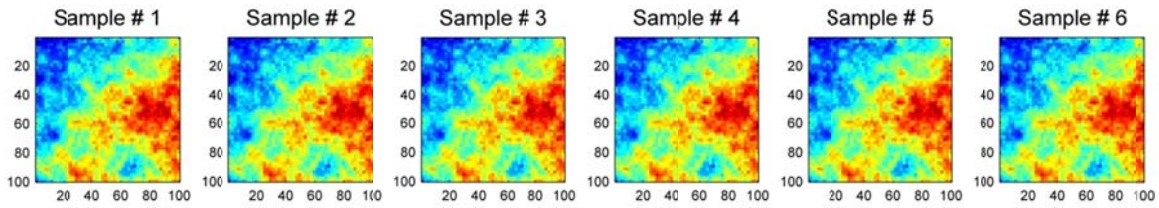

(c) final estimated samples (realizations)

Figure 45. Representation of 6 samples or realizations of T_0 in their initial and final estimated state.

Experiment 3: 2D Heterogeneous Cohesion

The other simulation is carried out for estimating rock mass cohesion c_f or C, from MEQ cloud when there are only shear failures. Figure 46 shows the true model setup and its specifications used to estimate cohesion C. In this experiment, tensile strength T_0, permeability k, elastic modulus E, and friction angle ϕ, distributions all are homogeneous and they are also assumed known parameters. The only heterogeneous reservoir property is cohesion C, which is assumed unknown. The standard SSBRC method with high resolution seismicity density map (on the original fine mesh) is used in this example. The observation error Std range ($\sigma_{\min}$, $\sigma_{\max}$) in this experiment is equal 23 % to 66 % which is slightly inflated.

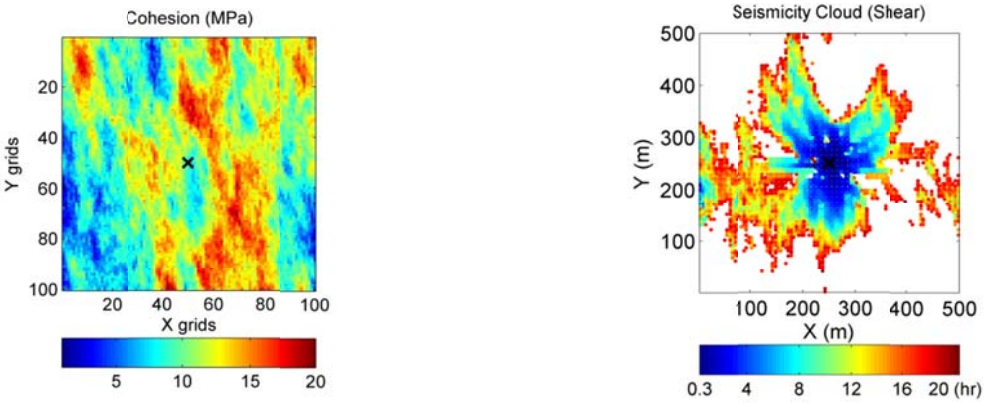

(a) true cohesion map (b) true seismicity cloud (shear events)

Figure 46. True model specification; $S_{h,min} = S_{H,max} = P_{ini} = 10$ (MPa), $R_{inj} = 0.006\ (l/s), T_0 = -5\ (MPa), k = 0.005\ (md), E = 20\ (GPa), \phi = 25^{\circ}$.

It should be noted that the value of tensile strength T_0, does not have any effect in the model response (shear-induced seismicity) in this experiment. The estimation results of Cohesion C, experiment are shown extensively in Figure 47. The true cohesion C, distribution is again presented in Figure 47.a. Cohesion estimation RMSE, Figure 47.b, shows continuous reduction and goes from 4.1 (MPa) (initial RMSE) to 2.1 (MPa) (final RMSE) which confirms the promising estimation performance of SSBRC. In Figure 47.c, the ensemble spread is presented which shows significant reduction and the final ensemble spread is only 2 % that indicates ensemble collapse. For this experiment we did not apply any improved uncertainty quantification methods to resolve ensemble spread underestimation. The evolution of estimated ensemble mean and two realizations throughout integration steps are shown in Figure 47.d,e,f, respectively. It is clear from the results that the final estimated maps (at integration step 6) are very similar to the true cohesion map which confirms the suitability of SSBRC for geomechanical parameter

estimation. The evolution of ensemble spread is shown in Figure 47.g, in terms of ensemble standard deviation. In Figure 47.g, the final ensemble Std map (at integration step 6) clearly shows severe ensemble spread underestimation.

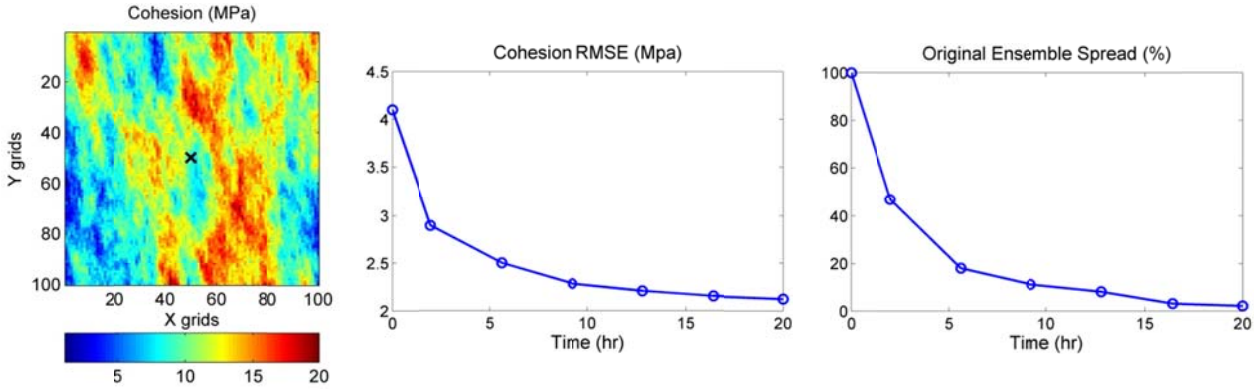

(a) true cohesion C, map (b) cohesion estimation RMSE (c) cohesion ensemble spread

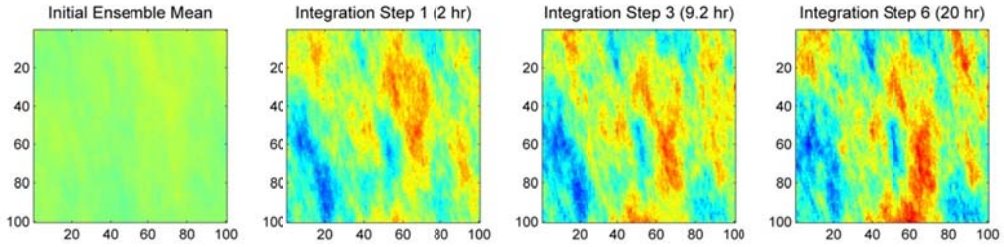

(d) ensemble mean evolution

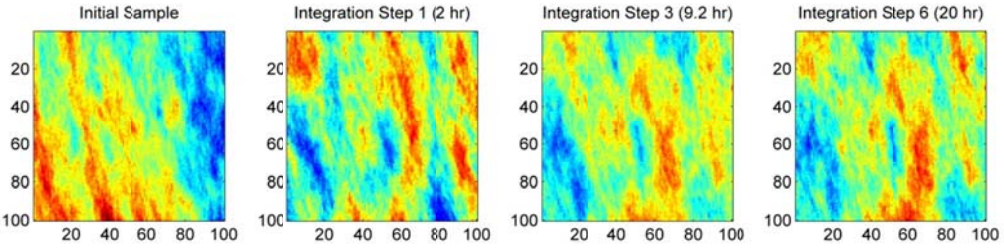

(e) sample or realization #1 evolution

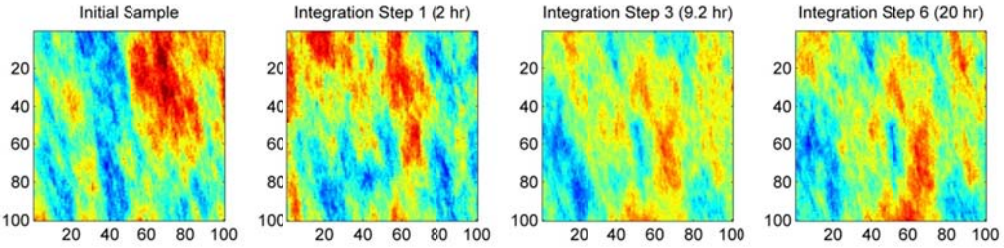

(f) sample or realization #2 evolution

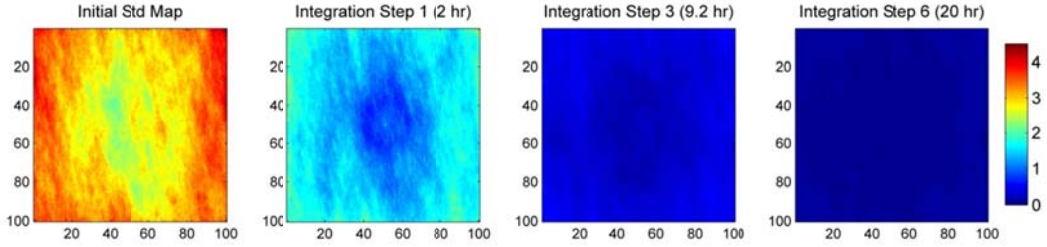

(g) ensemble standard deviation evolution
Figure 47: Cohesion C, estimation results.

Experiment 4: 2D Heterogeneous Elastic Modulus

In this experiment we present the application of standard SSBRC to estimate the heterogeneous distribution of Young's modulus E, from the MEQ cloud observation. To generate the seismicity density map, the original fine mesh is used in this experiment. The synthetic true Young's modulus distribution (parameter to estimate) and the corresponding seismicity cloud as the observed data are shown in Figure 48. The far-field stress boundary conditions $S_{H,max}$, $S_{h,min}$ and P_{ini}, are all assumed 10 (MPa) to investigate only the effect of hydraulic stimulation (injection-induced stress) in the reservoir. Fluid injection rate is equal 0.005 (Lit/s) and permeability is homogeneous in the field and is equal 0.005 (md). Tensile strength T_0, is assumed spatially random distributed and its values come from a Uniform PDF in the range of 5 (MPa) to 30 (MPa). In this experiment only tensile failures (as MEQ events) are considered.

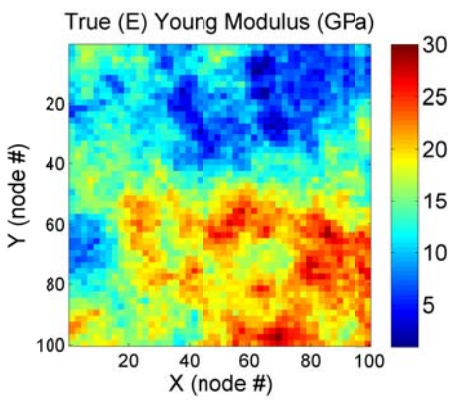

(a) True Young's modulus (E) map

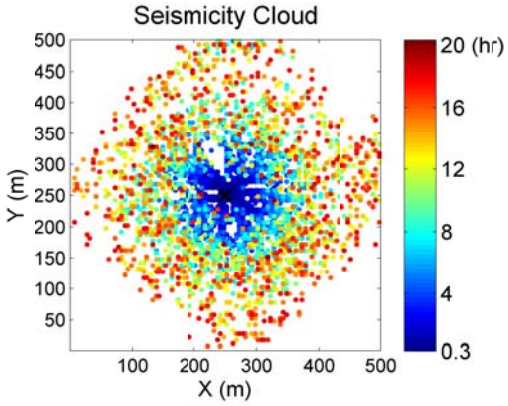

(b) True microseismicity cloud (tensile events)

Figure 48. True model setup; true Young's modulus distribution and the corresponding MEQ cloud.

This experiment was performed with the standard EnKF algorithm by a typical range of 5% to 10% for observation error standard deviation. The number of unknown parameters to estimate and observations are both equal to 10000 which is the number of nodes. Estimation results are shown in Figure 49. The evolution of the estimated ensemble mean of Young's modulus realizations, an estimated individual realization and the standard deviation of the ensemble in integration steps are shown in Figure 49.d, e, f, respectively. The estimated Young's modulus maps in Figure 49.d, e, tend to identify the major high- and low-value regions of elastic modulus in the reservoir. The final estimated maps (at 6^{th} integration step) of Figure 49.d, e., are very similar to the true Young's modulus map in Figure 49.a, which confirms the promising estimation performance of SSBRC. It is evident from these maps that the EnKF can infer information about the Young's modulus distribution by integrating the data about the distribution of the MEQ event locations. The decreasing trend of estimation RMSE in Figure 49.b, indicates increased confidence in the updated ensemble after integrating the MEQ data. However, the problem with these estimation results is a very low final ensemble spread and ultimately collapsing the ensemble to a single realization. It is seen in Figure 49.c, the final ensemble spread is only 1% which means the ensemble

loses 99% of its spread through data assimilation procedure. Figure 49.f (at integration step 6) also shows almost no spread in final ensemble based on the ensemble standard deviation map that means ensemble collapse (i.e. all final estimated realizations are almost the same). These estimation results point out the ensemble spread underestimation issue with the original setup of SSBRC. The experiment of Figure 49 is the reference experiment that we will improve its results (ensemble spread) by our proposed approaches.

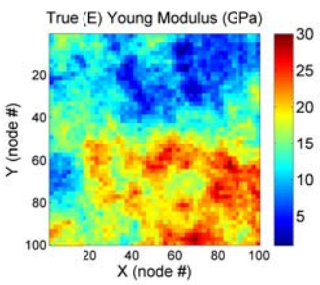

(a) true Young's modulus map

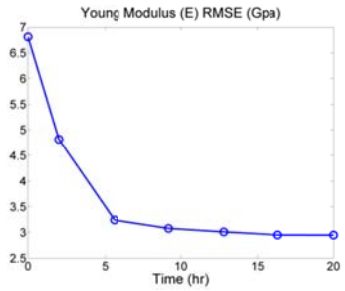

(b) estimation RMSE

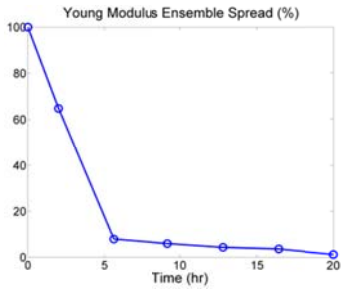

(c) ensemble spread

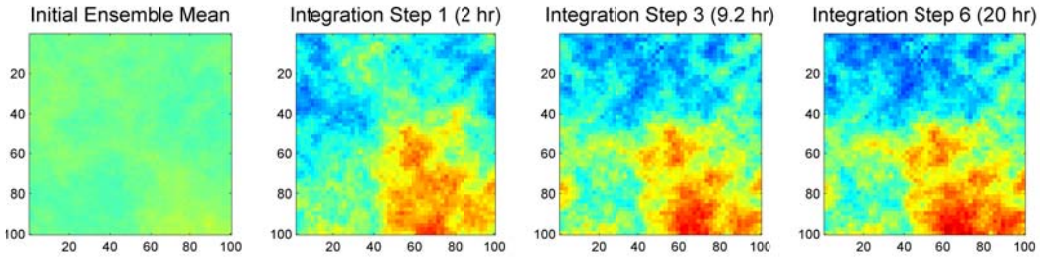

(d) evolution of ensemble mean

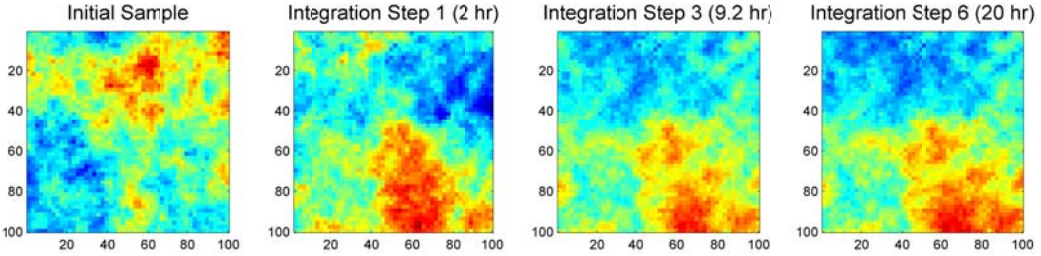

(e) evolution of an individual realization

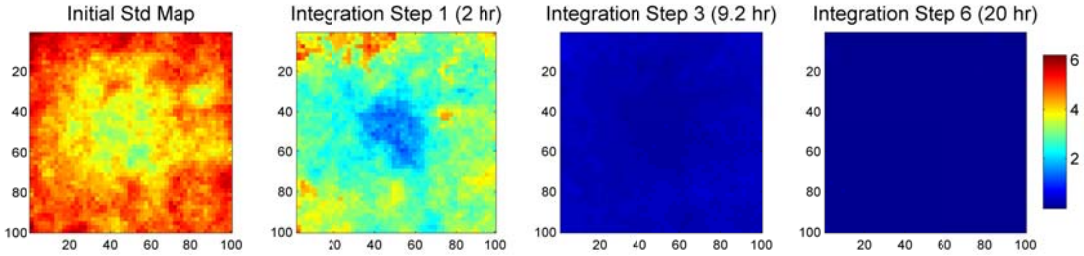

(f) standard deviation map evolution

Figure 49. Young's modulus E, estimation results of standard SSBRC with typical range of observation error Std (the reference experiment)

This experiment (and many others with the same setup but different reference reservoir property) shows promising estimation performance of the SSBRC however the problem of ensemble spread underestimation is evident. In the next set of experiments we apply the proposed methods for improving

uncertainty quantification to this example (as the reference experiment) to resolve ensemble spread underestimation issue.

Experiment 5: Improving Experiment 4

In this set of experiments, we apply the three methods of improving uncertainty quantification in section 0 to the experiment 4 in section 0 (reference experiment) to resolve the issue of ensemble spread underestimation.

Inflated observation error variance

The simplest way of avoiding spread underestimation or ensemble collapse is adding large amount of noise to observation which can be done by specifying high observation standard deviation (Std) through increasing $\sigma_{\max}$ and $\sigma_{\min}$ in equation (8). To observe the effect of observation Std range, different Std intervals are tried in our experiments. The results of increasing the observation error Std range are given in Table 10. The first row of Table 10, test # 1, shows the results of reference model that is experiment 4 in section 0. These results show improvement of final ensemble spread (preserving more ensemble spread) by increasing the observation error Std. However the increased Std range (e.g. test # 3 with observation Std of 100-200%) might seem unrealistic. It is also obvious from Table 10 that we can yet improve ensemble spread by further increasing the observation error Std. Figure 50 shows the estimation results of SSBRC with inflated observation error Std range (test # 3 from Table 10).

Table 10. Sensitivity of SSBRC performance to different ranges of observation error Std (in estimating Young's modulus E)

test #	$\sigma_{\min}$ (%)	$\sigma_{\max}$ (%)	Final RMSE (GPa)	Final ensemble spread (%)
1 (reference)	8	14	2.94	1.24
2	30	84	3.3	5.33
3	99	193	2.63	12.24

Initial RMSE = 6.8134 (GPa)

The decreasing trend of estimation RMSE in Figure 50.b shows promising estimation performance of SSBRC even with greatly increased Std range of observation. Figure 50.d,e,f, represent the evolution of ensemble mean, an individual realization and standard deviation map throughout integration steps. As shown by final estimated Young's modulus maps (at 6^{th} integration step) in Figure 50.d,e, SSBRC is successful in capturing the trends of true elastic modulus of Figure 50.a. More importantly ensemble spread underestimation problem of SSBRC is also resolved as can be seen in Figure 50.c that shows the ensemble spread of the estimated parameter. From the final standard deviation map of (at integration step 6) Figure 50.f, it is also evident that the ensemble spread is preserved during integration steps by the proposed method. (compare to the reference experiment results in Figure 49.c,f, where ensemble collapse happens).

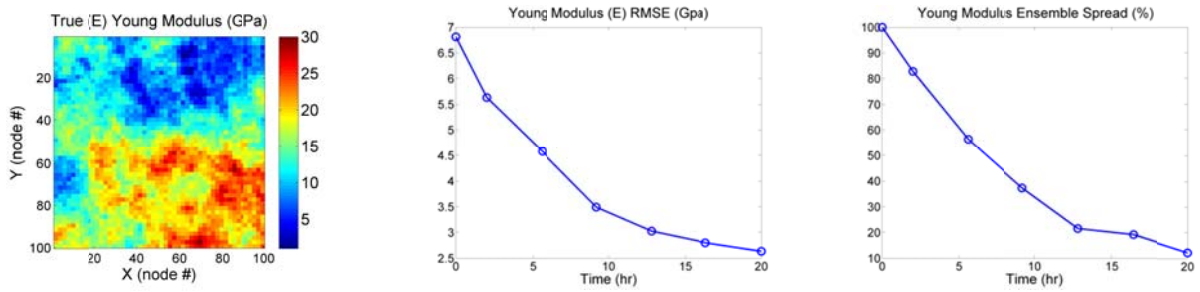

(a) true Young's modulus map (b) estimation RMSE (c) ensemble spread

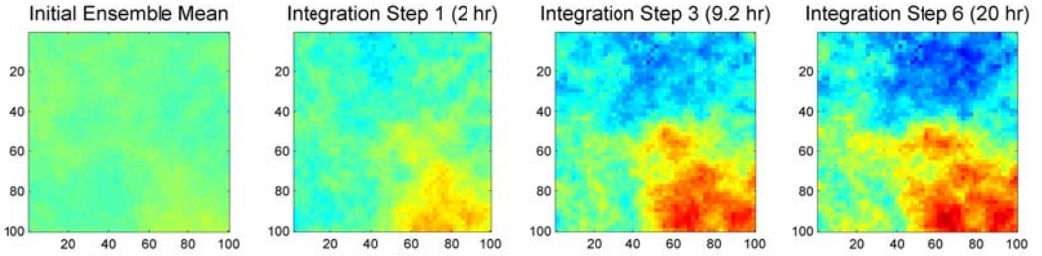

(d) evolution of ensemble mean

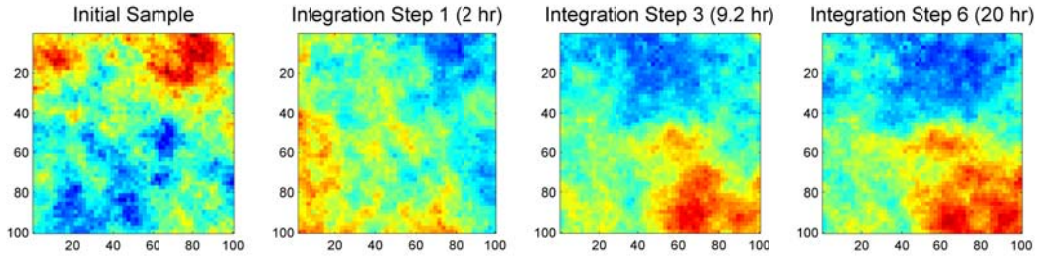

(e) evolution of an individual realization

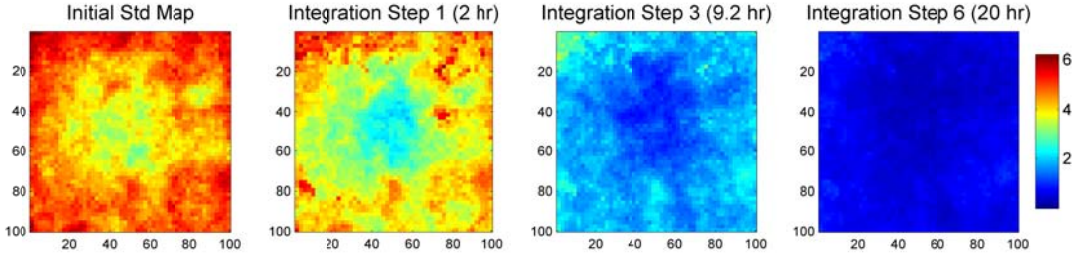

(f) standard deviation map evolution

Figure 50. Young's modulus E, estimation results of SSBRC with increased observation error Std (test # 3 from Table 10), its true model is shown in Figure 48.

In general in SSBRC, it is the correlation of MEQ events with the reservoir parameter (elastic modulus in this case) that is exploited by the EnKF update to reconstruct the trend in the reservoir property map.

Reduced-order projection

In this section we apply the projection method of section 0 to experiment 4 in section 0 to improve the final estimated ensemble spread. As mentioned earlier, projection method has two tuning parameters; kernel bandwidth standard deviation σ_h, and truncation number n_{trunc} that we investigate the performance of SSBRC with reduced-order projection with respect to three different sets of these parameters as shown in Table 11. As we can see from these three tests, the estimation RMSE is fairly low

(still not as low as RMSE of reference experiment in Figure 49.b or test #1 Table 10) and as the objective of the projection method, ensemble spread is greatly preserved (final ensemble spread is around 60%). It should be noted that the number of observations is decreased from 10000 to 25, 50 and 100, by projection method, as reported in Table 11, n_{trunc} column. Therefore the proposed observation projection approach is successful in preserving the ensemble spread and resolving ensemble spread underestimation of SSBRC through observation dimension reduction. However, the resulted estimation RMSE with projection approach is not as low as the standard SSBRC method. Detailed estimation results of test #3 from Table 11 is shown in Figure 51.

Table 11. Young's modulus E, estimation by SSBRC with projection method. Sensitivity of the performance of projection method with respect to kernel bandwidth Std σ_h, and truncation number n_{trunc} .

Test #	σ_h (%)	n_{trunc}	Final RMSE (GPa)	Final ensemble spread (%)
1	25	25	4.3	67.7
2	25	50	4.12	55.65
3	25	100	3.70	54.34

Initial RMSE = 6.8134 (GPa)

By choosing test #3 from Table 11, we reduced the number of observations from 10000 (in the reference experiment) to 100 (n_{trunc}) which resolves the observation redundancy issue of SSBRC. Figure 51 shows Young's modulus E, estimation results by SSBRC with projection approach. The final estimated Young's modulus distributions of Figure 51.d,e, (at integration step 6) are very similar to the true E distribution in Figure 51.a. The main advantage of projection approach in preserving ensemble spread and preventing ensemble collapse is shown by final ensemble Std map in Figure 51.f (at integration step 6). Figure 51.c shows that final ensemble spread is 54% which is significantly improved comparing to the reference experiment (Figure 49) by final ensemble spread of only 1% (Figure 49.c).

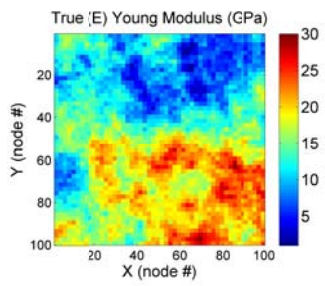

(a) true Young's modulus map

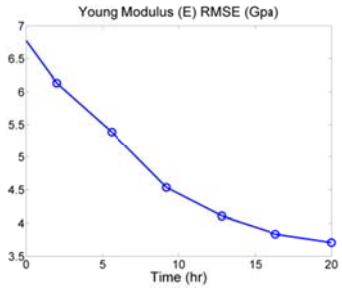

(b) estimation RMSE

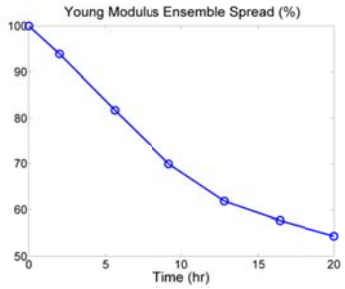

(c) ensemble spread

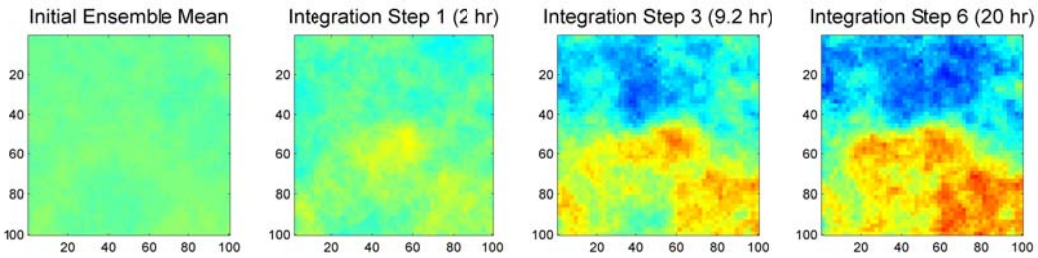

(d) evolution of ensemble mean

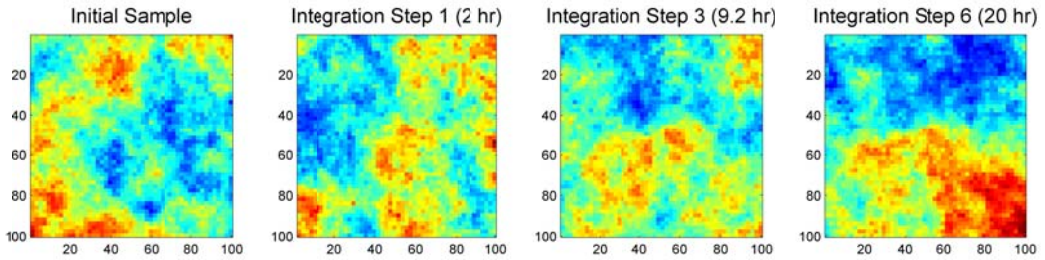

(e) evolution of an individual realization

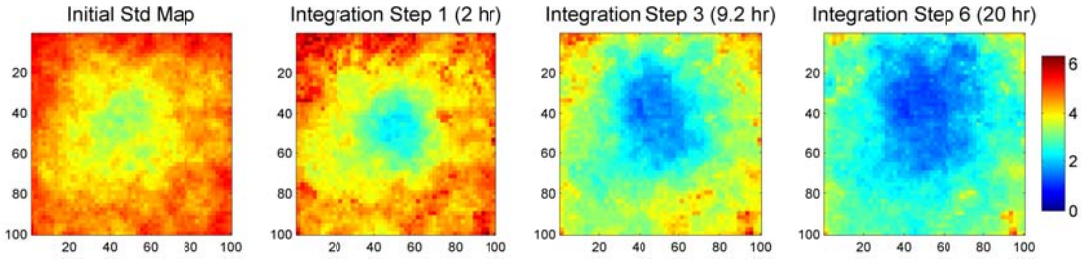

(f) standard deviation map evolution

Figure 51. Young's modulus E, estimation results of SSBRC with projection approach (test # 3 from Table 11), its true model is shown in Figure 48.

Coarse-scale microseismicity density map

The number of observations is equal to the dimension of seismicity density map. To reduce the dimension of the seismicity density map (number of observations to integrate) which is the major reason of the ensemble spread underestimation we build the seismicity density map on a coarse mesh or grid system instead of the original fine mesh. So we only need to evaluate continuous seismicity density map on a new coarse grid system. In 2D case studies where the node configuration size is 100x100 (N_b = 10000, N_{X} = 100) we choose the coarse seismicity density mesh size e.g. equal to 10x10 (N_b = 100 seismicity observations, $N_{\mathrm{X,red}}$ = 10) which reduces the dimension of the observation vector by orders of magnitude. It should be noted that the range of the observation error Std in coarse seismicity density approach is the typical range of 5% to 10% which leads to ensemble collapse in the regular approach i.e. reference experiment in Figure 49 (where the size of seismicity density mesh is equal to the size of parameter mesh).

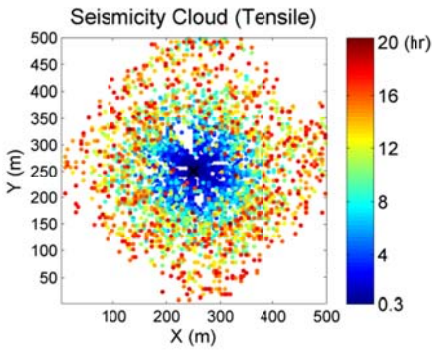

(a) final true seismicity cloud

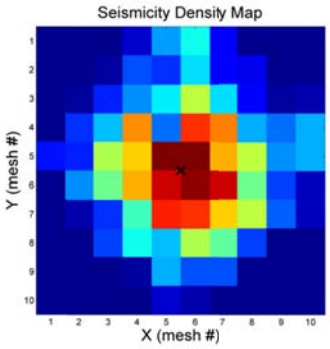

(b) $N_{\mathrm{X,red}} = 10$

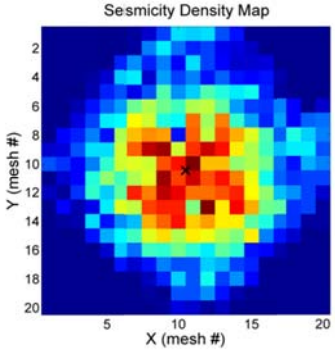

(c) $N_{\mathrm{X,red}} = 20$

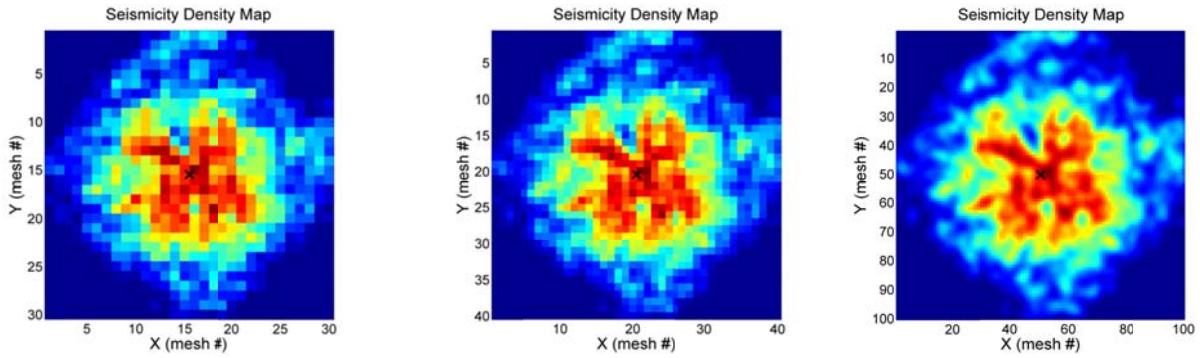

(d) $N_{\mathrm{X,red}} = 30$ (e) $N_{\mathrm{X,red}} = 40$ (f) $N_{\mathrm{X,red}} = N_{\mathrm{X}} = 100$

Figure 52. Microseismicity density maps (with different sizes) for final seismicity cloud. (b-e) show coarse seismicity density maps. (f) reference seismicity density map. (black cross at the center shows the injection well location)

Figure 52 shows the seismicity density maps with different sizes (based on final seismicity cloud of Young's modulus estimation problem from tensile seismicity events in section 0). Different microseismicity density map sizes produces different number of observations and help in reducing the number of observations to resolve the observation space redundancy and ultimately ensemble spread underestimation in EnKF process. The dimension of microseismicity density map is considered in terms of number of nodes in x direction (the field configuration is square). As explained before the number of parameters to estimate is equal to the number of nodes so in this 100×100 field, there are 10000 parameters to estimate (unknown Young's modulus at each node). For coarsening of the seismicity density map, we specify different sizes of $N_{\mathrm{X,red}}$ equal to 10, 20, 30, 40, that decreases the number of observations to 100, 400, 900, 1600, respectively where in the reference experiment by $N_{\mathrm{X,red}} = N_{\mathrm{X}} = 100$, there are 10000 observations.

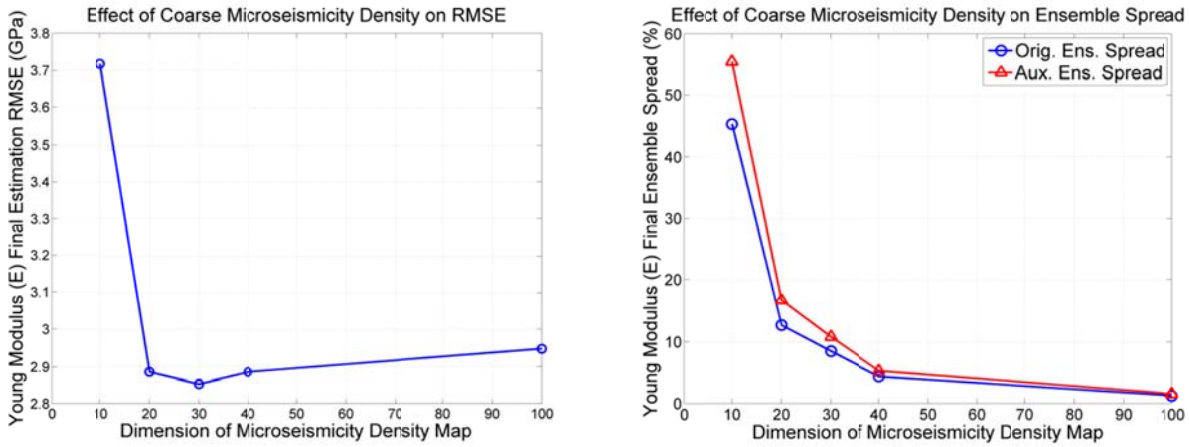

(a) (b)

Figure 53. Effect of coarse microseismicity density dimension on the performance of SSBRC in Young's modulus estimation experiment (initial Young's modulus RMSE = 6.8134 GPa)

The effect of different dimensions of microseismicity density map on the performance of SSBRC process is shown in Figure 53. In this experiment four different sizes of seismicity density map ($N_{\mathrm{X,red}} = 10,20,30,40$) are chosen and the reference case density map size is $N_X = 100$ (seismicity density map of 100×100 where the number of microseismicity observations is equal to the parameters). Figure 53 shows both final estimation RMSE and final (original and auxiliary) ensemble spread of these five experiments. Based on Figure 53.a, it is seen that there is an optimal size of the seismicity density map which results in the minimum RMSE (at $N_{\mathrm{X,red}} = 30$). It should be noted that this coarse seismicity density map size is optimal in RMSE sense however we are looking for both low RMSE and high spread simultaneously. Figure 53.b shows the final ensemble spread (both original Young's modulus ensemble and auxiliary ensemble) versus size of seismicity density map. As we already expected, by increasing the size of the density map there will be higher number of observations which consequently results in more underestimation of ensemble spread (lower ensemble spread value). In the reference experiment (Figure 49) with microseismicity density map size equal to the size of the field ($N_{\mathrm{X}} = 100$) as we see in Figure 49.c the final ensemble spread is only 1% which means ensemble collapse (losing almost all ensemble spread). As the result, the improvement of the ensemble spread is obviously seen in Figure 53.b by decreasing the size of the seismicity density map (or using coarse seismicity density map). To choose the appropriate size of the density map, we are looking for fairly low RMSE and high spread in Figure 53.a and Figure 53.b, respectively. Based on the obtained results, the density size of 10 to 30 (in a 100×100 field) for coarse-scale mesh can be a suitable choice.

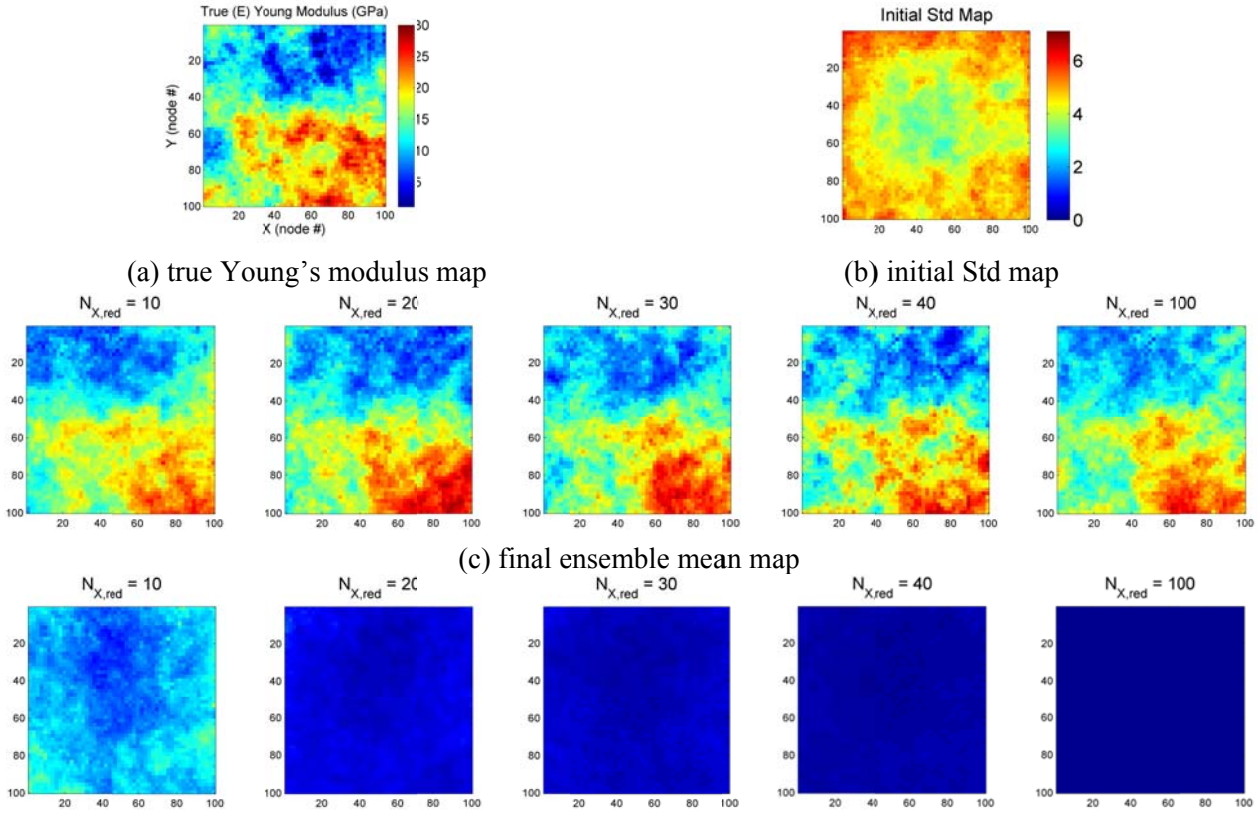

(a) true Young's modulus map

(b) initial Std map

(c) final ensemble mean map

(d) final Std map

Figure 54. Effect of coarse microseismicity density size on final estimated ensemble mean and Std map (Young's modulus estimation experiment)

The final estimated ensemble mean and standard deviation distributions are shown in Figure 54. It is clear from Figure 54.c that the final estimation results in all five experiments with different sizes of seismicity density map are almost the same and very similar to the true Young's modulus distribution (Figure 54.a). Therefore the determining factor to choose the appropriate size of the density map should be final standard deviation (Std) maps. Final Std maps of Figure 54.d show that the appropriate final ensemble spread occurs where $N_{X,red} = 10$.

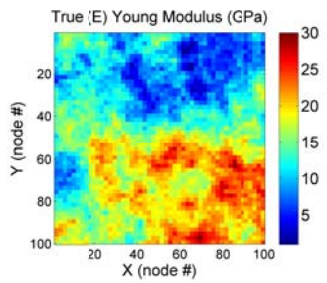

(a) true Young's modulus map

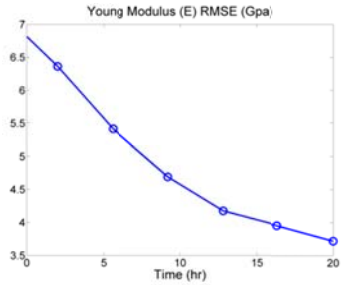

(b) estimation RMSE

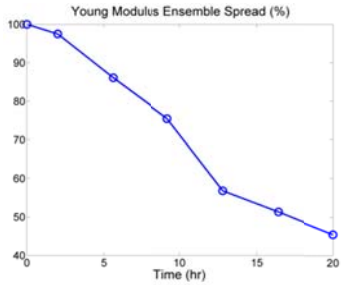

(c) ensemble spread

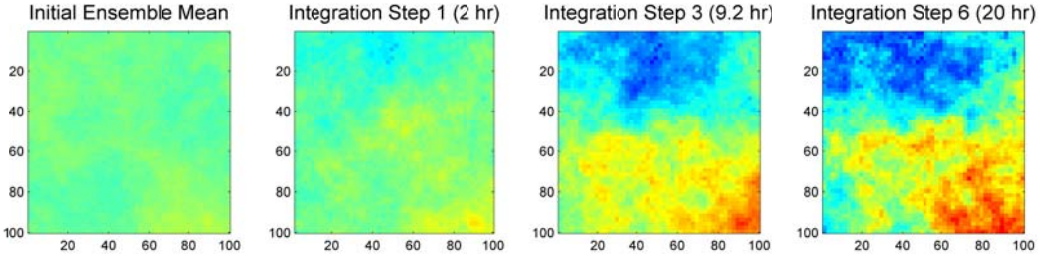

(d) evolution of ensemble mean

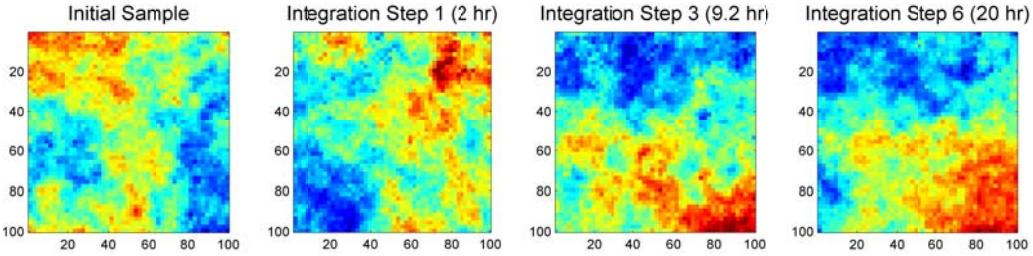

(e) evolution of an individual realization

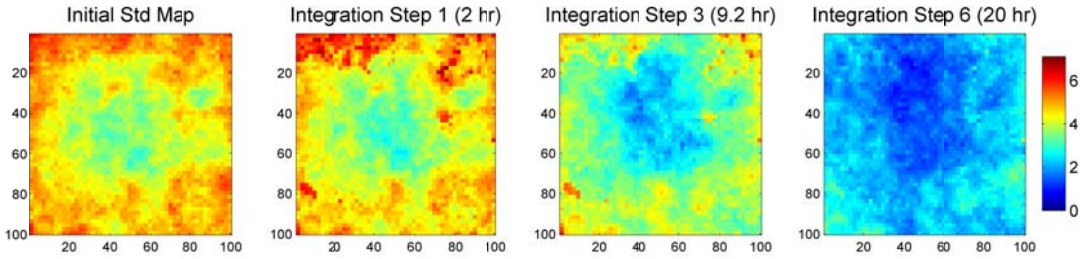

(f) standard deviation map evolution

Figure 55. Results of SSBRC with coarse seismicity density map $N_{\mathrm{X,red}} = 10$, for Young's modulus estimation. Its true model is shown in Figure 48.

The estimation results of SSBRC with coarse seismicity density map $N_{\mathrm{X,red}} = 10$, are shown in Figure 55 which represents the evolution of ensemble mean, an individual realization and standard deviation map throughout integration steps. The final estimated ensemble mean and an individual realization (at integration step 6), Figure 55.d,e, show appropriate performance of SSBRC in capturing the unknown true Young's modulus distribution in Figure 55.a. Considering the performance of SSBRC with coarse density in terms of ensemble spread, final standard deviation map of elastic modulus ensemble is seen in Figure 55.f (at integration step 6), which clearly shows appropriate amount of ensemble spread at the final integration step. The estimation performance of SSBRC is also shown in Figure 55.b,c by RMSE and spread. Continuous reduction of estimation error (RMSE) by integration step in Figure 55.b from 6.8 (GPa) to 3.7 (GPa) confirms the suitability of SSBRC for this estimation problem. From Figure 55.c, we also see that the final ensemble spread is 45% which shows promising performance of coarse seismicity density method in preserving the ensemble spread.

Experiment 6: 2D Heterogeneous Permeability (Shear Events)

In this experiment we estimate permeability distribution from MEQ cloud (shear failures). In this experiment we apply the standard SSBRC method with high resolution seismicity density map on the original fine mesh. The observation error Std range is also the typical interval of 5 % to 10 %. The true setup of the model is shown in Figure 56. The far field stress regime (boundary condition) is assumed $[S_{min}\ ,\ S_{max}\ ,\ P_{init}] = [20\ 15\ 10]$ (MPa). There is one injection well at the center of the model. Fluid injection rate is equal 0.005 (Lit/s) and Young's modulus E, is homogeneous in the field and equal 40 (GPa). Cohesion C, is assumed spatially random distributed with Normal PDF by 20 (MPa) and 7 (MPa) as its mean and Std, respectively. Friction angle ϕ, is assumed homogeneous and equal 25°.

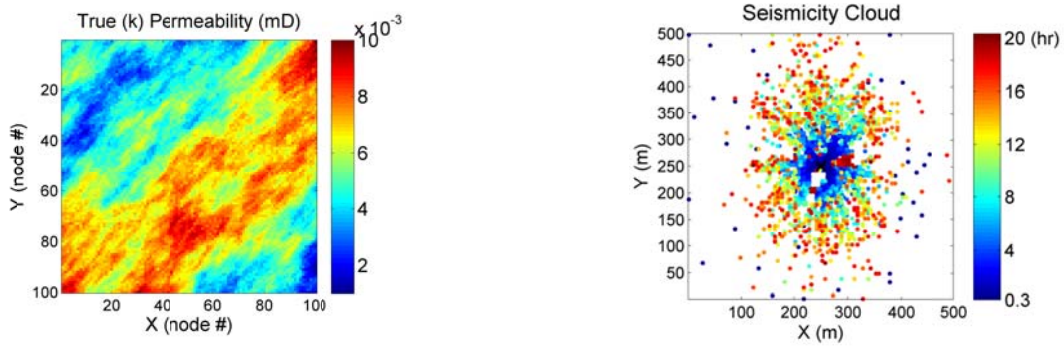

(a) True permeability (k) map (b) True microseismicity cloud

Figure 56. True model setup; true k distribution and the corresponding MEQ cloud.

Permeability estimation results are shown in Figure 57. The number of unknown parameters to estimate and observations are both equal to 10000 which is the number of nodes. The evolution of the estimated ensemble mean of permeability realizations, an estimated individual realization and the standard deviation of the ensemble in integration steps are shown in Figure 57.d,e,f, respectively. The estimated permeability maps in Figure 57.d,e, tend to identify the major high- and low-value regions of permeability in the reservoir. The final estimated maps (at 6th integration step) of Figure 57.d, e., are very similar to the true permeability map in Figure 57.a, which confirms the promising estimation performance of SSBRC. It is evident from these maps that the EnKF can infer information about the permeability distribution by integrating the data about the distribution of the MEQ event locations. The decreasing trend of estimation

RMSE in Figure 57.b, indicates increased confidence in the updated ensemble after integrating the MEQ data. However, the problem with these estimation results again is a very low final ensemble spread and ultimately collapsing the ensemble to a single realization. It is seen in Figure 57.c, the final ensemble spread is only 4% which means the ensemble loses 96% of its spread through data assimilation procedure. Figure 57.f (at integration step 6) also shows almost no spread in final ensemble based on the ensemble standard deviation map that means ensemble collapse (i.e. all final estimated realizations are almost the same). These estimation results point out the ensemble spread underestimation issue with the original setup of SSBRC. The experiment of Figure 57 is the reference experiment that we will improve its results (ensemble spread) by our proposed approaches.

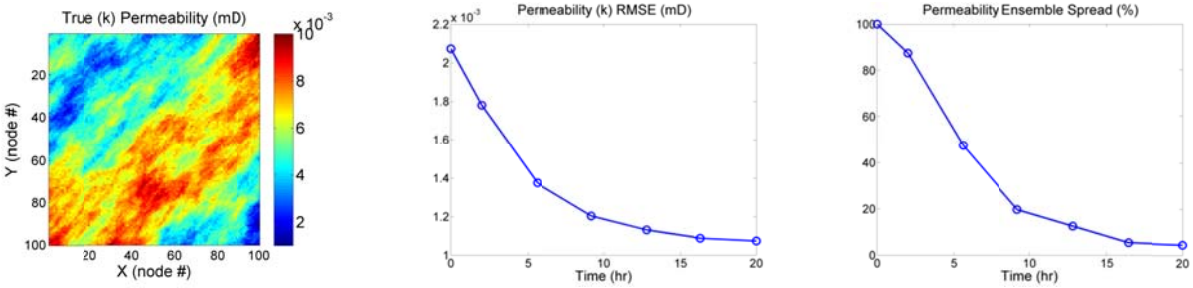

(a) true permeability map (b) estimation RMSE (c) ensemble spread

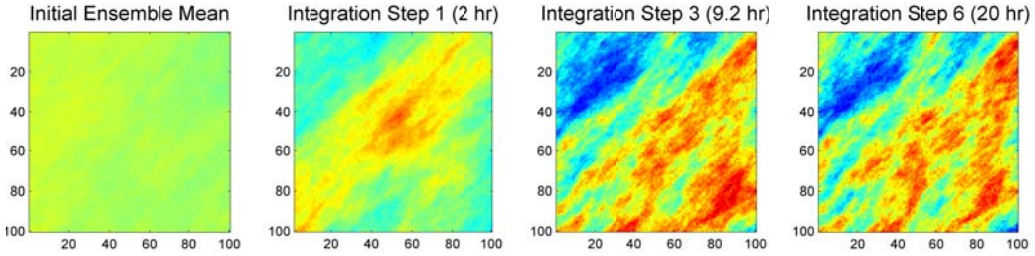

(d) evolution of ensemble mean

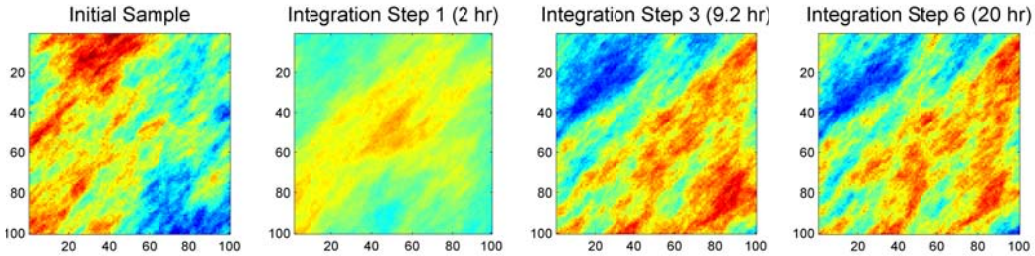

(e) evolution of an individual realization

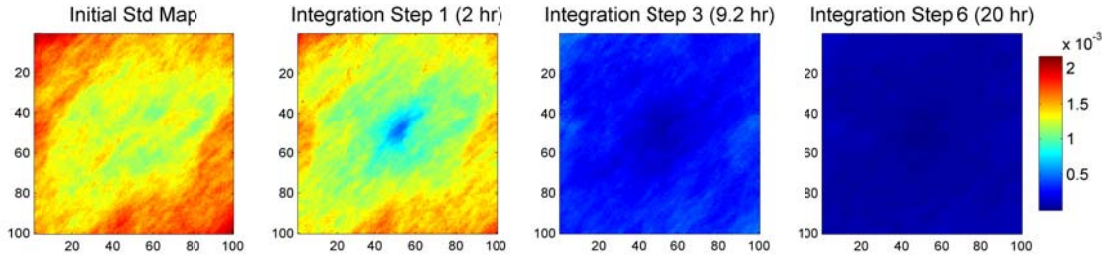

(f) standard deviation map evolution

Figure 57. Permeability k, estimation results of standard SSBRC with typical range of observation error Std (the reference experiment).

This experiment shows promising estimation performance of the SSBRC however the problem of ensemble spread underestimation is still evident. In the next set of experiments we apply the proposed methods for improving uncertainty quantification to this example (as the reference experiment) to resolve ensemble spread underestimation issue.

Experiment 7: Improving Experiment 6

In this set of experiments, we apply the three methods of improving uncertainty quantification in section 0 to the experiment 6 in section 0 (reference experiment) to resolve the issue of ensemble spread underestimation.

Inflated observation error variance

As discussed previously, artificially increasing observation error through specifying high observation standard deviation (Std) through increasing $\sigma_{\max}$ and $\sigma_{\min}$ in equation (8) helps in avoiding spread underestimation or ensemble collapse. To observe the effect of observation Std range, different Std intervals are tried in our experiment. The results of increasing the observation error Std range are given in Table 12. The first row of Table 12, test # 1, shows the results of reference model that is experiment 6 in section 0. These results show improvement of final ensemble spread (preserving more ensemble spread) by increasing the observation error Std. However the increased Std range (e.g. test # 3 with observation Std of 100-200%) might seem unrealistic. It is also obvious from Table 12 that we can yet improve ensemble spread by further increasing the observation error Std. Figure 58 shows the estimation results of SSBRC with inflated observation error Std range (test # 3 from Table 12).

Table 12. Sensitivity of SSBRC performance to different ranges of observation error Std (in estimating permeability k)

test #	$\sigma_{\min}$ (%)	$\sigma_{\max}$ (%)	Final RMSE (md)	Final ensemble spread (%)
1 (reference)	11	15	0.0011	4.44
2	22	81	0.0011	25.11
3	96	199	0.0010	36.97

Initial RMSE = 0.0021 (md)

The decreasing trend of estimation RMSE in Figure 58.b shows promising estimation performance of SSBRC even with greatly increased Std range of observation. Figure 58.d,e,f, represent the evolution of ensemble mean, an individual realization and standard deviation map throughout integration steps. As shown by final estimated permeability maps (at 6th integration step) in Figure 58.d,e, SSBRC is successful in capturing the trends of true permeability distribution of Figure 58.a. More importantly ensemble spread underestimation problem of SSBRC is also resolved as can be seen in Figure 58.c that shows the permeability ensemble spread. The final ensemble spread increased from 4 % in the reference experiment to 37 % in the improved case. From the final standard deviation map of (at integration step 6) Figure 58.f, it is also evident that the ensemble spread is preserved during integration steps by the proposed method. (compare to the reference experiment results in Figure 57.c,f, where ensemble collapse happens).

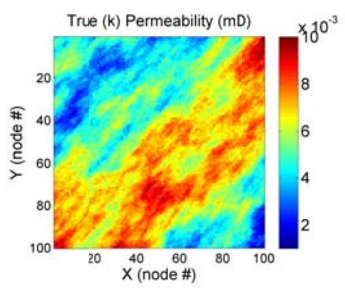

(a) true permeability map

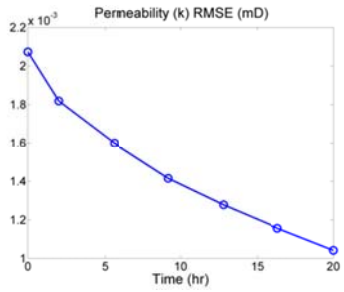

(b) estimation RMSE

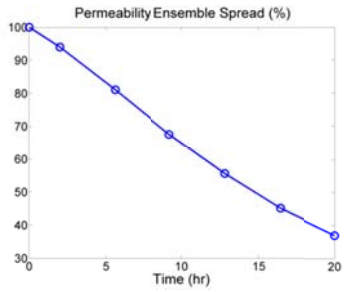

(c) ensemble spread

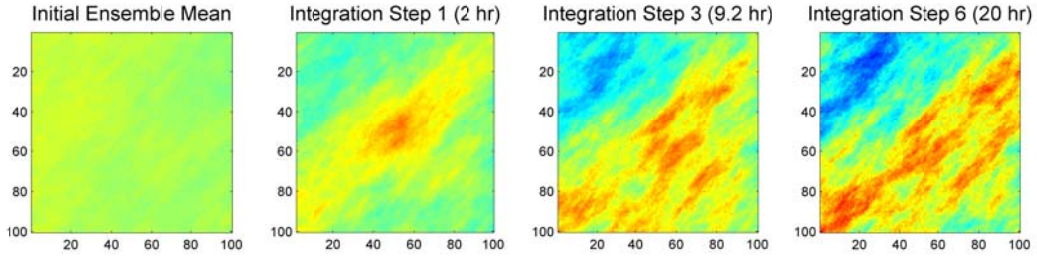

(d) evolution of ensemble mean

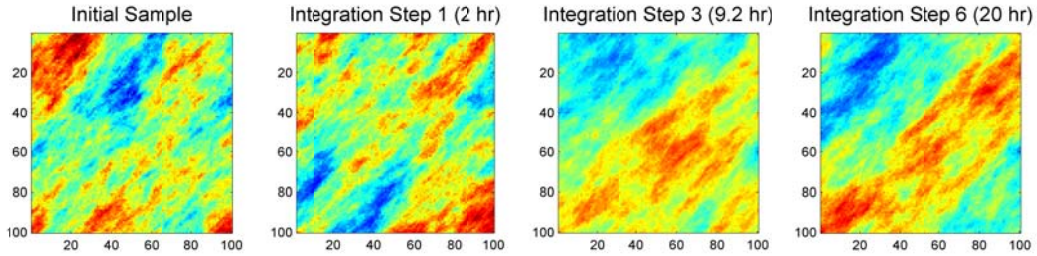

(e) evolution of an individual realization

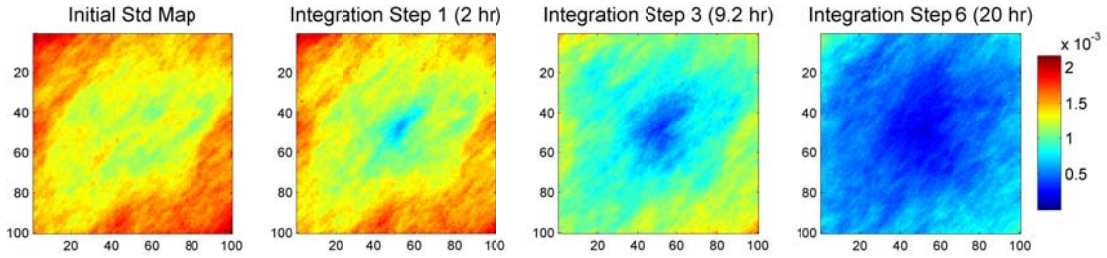

(f) standard deviation map evolution

Figure 58. Permeability k, estimation results of SSBRC with increased observation error Std (test # 3 from Table 12), its true model is shown in Figure 56.

Reduced-order projection

In this section we apply the projection method of section 0 to experiment 6 in section 0 to improve the final estimated ensemble spread. As mentioned earlier, projection method has two tuning parameters; kernel bandwidth standard deviation σ_h, and truncation number n_{trunc} that are set equal to 25 % and 100, respectively in Table 13. As we can see from this test, the permeability estimation RMSE is fairly low (still not as low as RMSE of reference experiment in Figure 57.b or test #1 Table 12) and as the objective of the projection method, ensemble spread is greatly preserved (final ensemble spread is 70 %). It should be noted that, in this experiment, the number of observations is decreased from 10000 to 100, by projection method, as reported in Table 13, n_{trunc} column. Therefore the proposed observation projection

approach is successful in preserving the ensemble spread and resolving ensemble spread underestimation of SSBRC through observation dimension reduction. However, the resulted estimation RMSE with projection approach is not as low as the standard SSBRC method. Detailed estimation results of this experiment, Table 13, is shown in Figure 59.

Table 13. Permeability k, estimation by SSBRC with projection method. performance measures of projection method and kernel bandwidth Std σ_h, and truncation number n_{trunc} .

σ_h (%)	n_{trunc}	Final RMSE (md)	Final ensemble spread (%)
25	100	0.0014	70.71

Initial RMSE = 0.0021 (md)

Figure 59 shows permeability k, estimation results by SSBRC with projection approach. The final estimated permeability distributions of Figure 59.d,e, (at integration step 6) are reasonably similar to the true k distribution in Figure 59.a, however they are not as good as the reference experiment's results, in Figure 57.d,e. The main advantage of projection approach in preserving ensemble spread and preventing ensemble collapse is shown by final ensemble Std map in Figure 59.f (at integration step 6). Figure 59.c shows that final ensemble spread is 70 % which is significantly improved comparing to the reference experiment (Figure 57) by final ensemble spread of only 4 % (Figure 57.c).

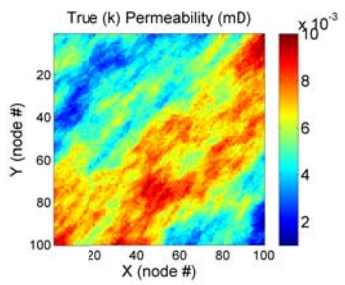

(a) true permeability map

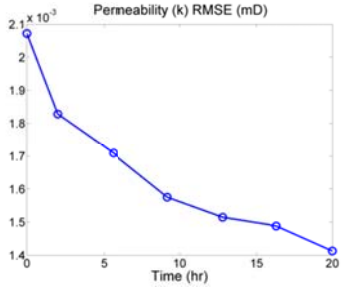

(b) estimation RMSE

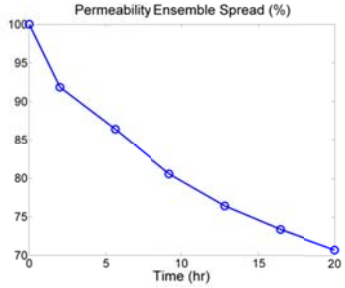

(c) ensemble spread

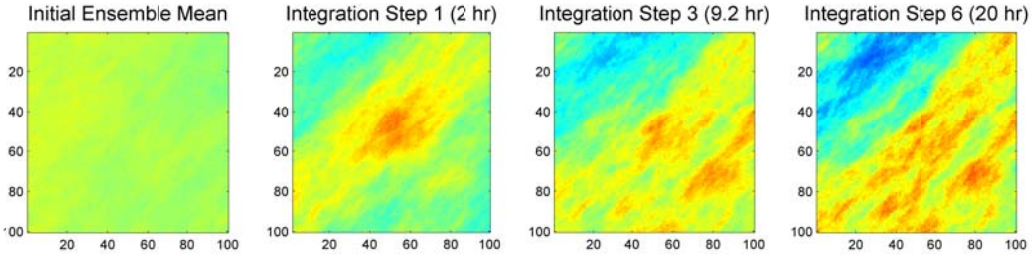

(d) evolution of ensemble mean

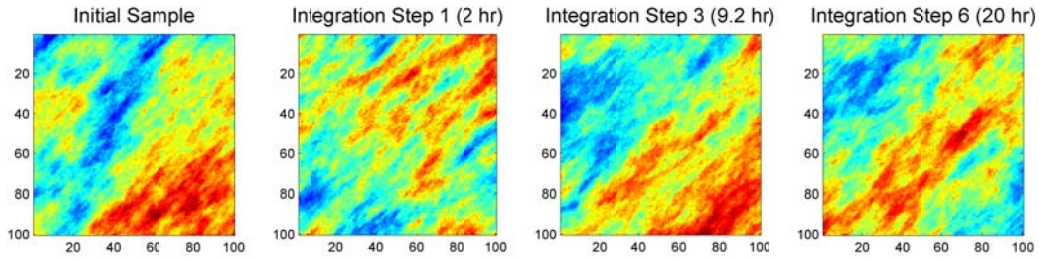

(e) evolution of an individual realization

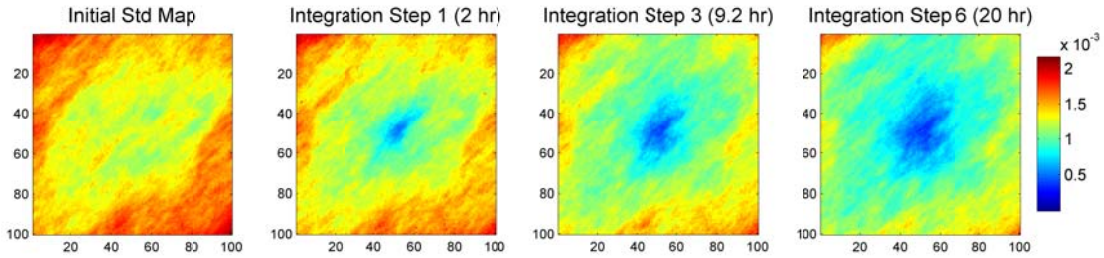

(f) standard deviation map evolution

Figure 59. Permeability k, estimation results of SSBRC with projection approach, its true model is shown in Figure 56.

Coarse-scale microseismicity density map

In standard SSBRC method, the number of observations is equal to the dimension of seismicity density map. To reduce the dimension of the seismicity density map (number of observations to integrate) which is the major reason of the ensemble spread underestimation we build the seismicity density map on a coarse mesh instead of the original fine mesh. So we only need to evaluate continuous seismicity density map on a new coarse grid system. In 2D case studies where the node configuration size is 100x100 (N_b = 10000, N_{X} = 100) we choose the coarse seismicity density mesh size e.g. equal to 15x15 (N_b = 225 seismicity observations, $N_{\mathrm{X,red}}$ = 15) which reduces the dimension of the observation vector by orders of magnitude. It should be noted that the range of the observation error Std in coarse seismicity density approach is the typical range of 5% to 10% which leads to ensemble collapse in the regular approach i.e. reference experiment in Figure 57 (where the size of seismicity density mesh is equal to the size of parameter mesh). The number of parameters to estimate is equal to the number of nodes so in this 100×100 field there are 10000 parameters to estimate (unknown permeability at each node). For coarsening of the seismicity density map, we specify different sizes of $N_{\mathrm{X,red}}$ equal to 15 and 30, that decreases the number of observations to 225 and 900, respectively where in the reference experiment by $N_{\mathrm{X,red}} = N_{\mathrm{X}} = 100$, there are 10000 observations.

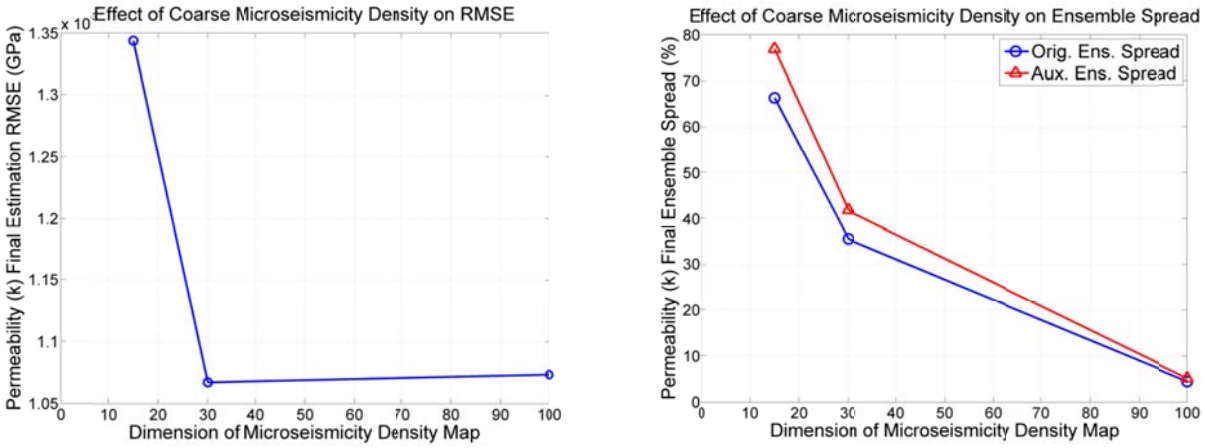

(a) (b)

Figure 60. Effect of coarse microseismicity density dimension on the performance of SSBRC in permeability estimation experiment (initial permeability RMSE = 0.0021 md).

The effect of different dimensions of microseismicity density map on the performance of SSBRC process is shown in Figure 60. In this experiment two different sizes of seismicity density map ($N_{\mathrm{X,red}} = 15,30$) are chosen and the reference case density map size is $N_X = 100$ (seismicity density map of 100×100 where the number of microseismicity observations is equal to the parameters). Figure 60 shows both final estimation RMSE and final (original and auxiliary) ensemble spread of these three experiments. Based on Figure 60.a, it is seen that there is an optimal size of the seismicity density map which results in the minimum RMSE (at $N_{\mathrm{X,red}} = 30$). It should be noted that this coarse seismicity density map size is optimal in RMSE sense however we are looking for both low RMSE and high spread simultaneously. Figure 60.b shows the final ensemble spread (both original permeability ensemble and auxiliary ensemble) versus size of seismicity density map. As we already expected, by increasing the size of the density map there will be higher number of observations which consequently results in more underestimation of ensemble spread (lower ensemble spread value). In the reference experiment (Figure 57) with microseismicity density map size equal to the size of the field ($N_{\mathrm{X}} = 100$) as we see in Figure 57.c the final ensemble spread is only 4 % which means ensemble collapse (losing almost all ensemble spread). The improvement of the ensemble spread is obviously seen in Figure 60.b by decreasing the size of the seismicity density map (or using coarse seismicity density map). To choose the appropriate size of the density map, we are looking for fairly low RMSE and high spread in Figure 60.a and Figure 60.b, respectively. As the representative experiment, we choose the coarse-scale seismicity density size equal to $N_{\mathrm{X,red}} = 30$, and show its estimation results in Figure 61.

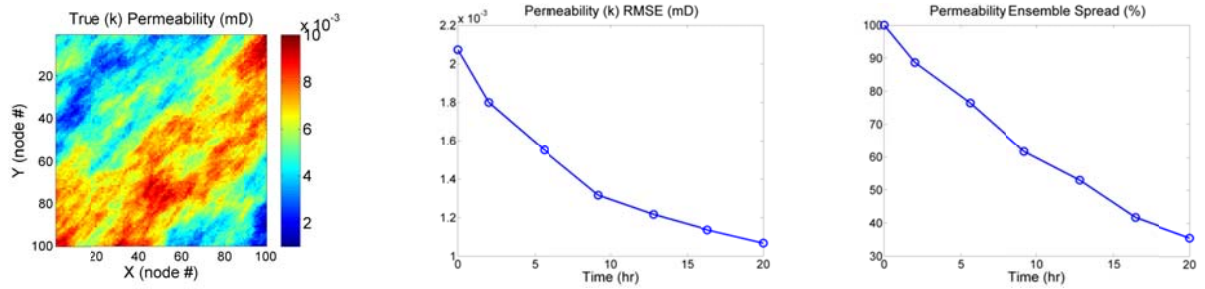

(a) true permeability map (b) estimation RMSE (c) ensemble spread

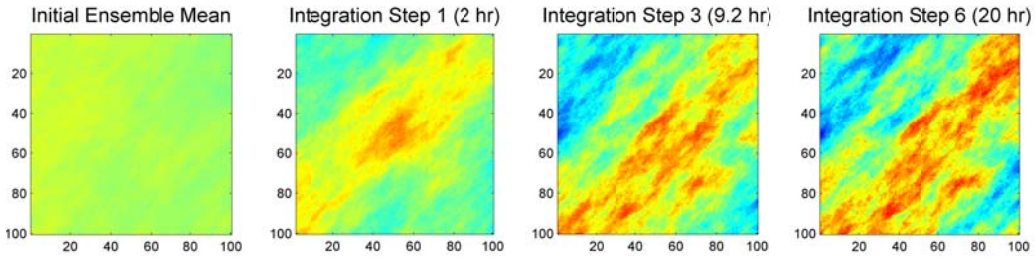

(d) evolution of ensemble mean

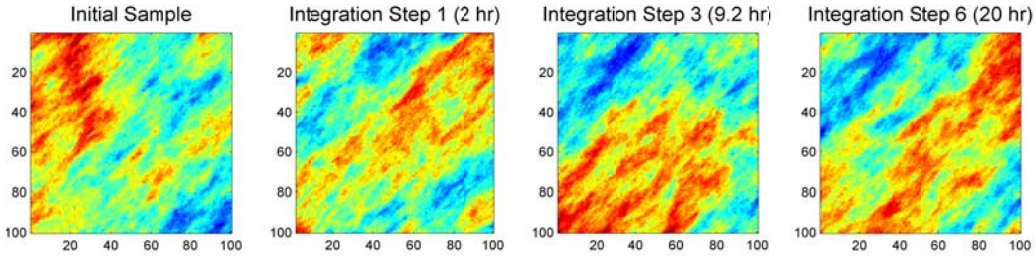

(e) evolution of an individual realization

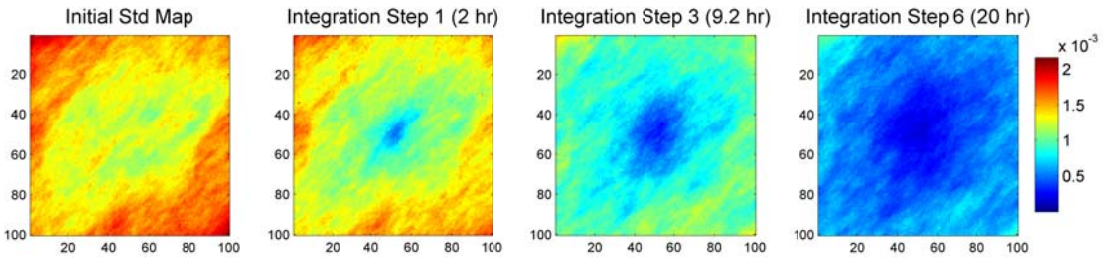

(f) standard deviation map evolution

Figure 61. Results of SSBRC with coarse seismicity density map $N_{\mathrm{X,red}} = 30$, permeability estimation experiment. Its true model is shown in Figure 56.

The estimation results of SSBRC with coarse seismicity density map $N_{\mathrm{X,red}} = 30$, are shown in Figure 61 which represents the evolution of ensemble mean, an individual realization and standard deviation map throughout integration steps. The final estimated ensemble mean and an individual realization (at integration step 6), Figure 61.d,e, show appropriate performance of SSBRC in capturing the unknown true permeability distribution in Figure 61.a. Considering the performance of SSBRC with coarse density in terms of ensemble spread, final standard deviation map of permeability ensemble is seen in Figure 61.f (at integration step 6), which clearly shows appropriate amount of ensemble spread at the final integration step. The estimation performance of SSBRC is also shown in Figure 61.b,c by RMSE and spread. Continuous reduction of estimation error (RMSE) by integration step in Figure 61.b from 0.0021 (md) to 0.0011 (md) confirms the suitability of SSBRC for this estimation problem. From Figure 61.c, we also see that the final ensemble spread is 35 % which shows promising performance of coarse seismicity density method in preserving the ensemble spread.

Experiment 8: 2D Heterogeneous Permeability (Tensile Events)

The other simulation is carried out for estimating rock permeability k, from MEQ cloud when there are only tensile failures. Figure 62 shows the true model setup and its specifications used to estimate permeability k. In this experiment, elastic modulus E, distribution is homogeneous. Tensile strength T_0,

distribution is assumed spatially random and its values come from a Normal PDF with $\mu_{T_0} = -15$ (MPa) and $\sigma_{T_0} = 5$ (MPa). We also consider tensile strength T_0, as a known parameter. The standard SSBRC method with high resolution seismicity density map (on the original fine mesh) is used in this example. The observation error Std range ($\sigma_{\min}, \sigma_{\max}$) in this experiment is equal 34 % to 81 % which is slightly inflated that helps in resolving ensemble spread underestimation.

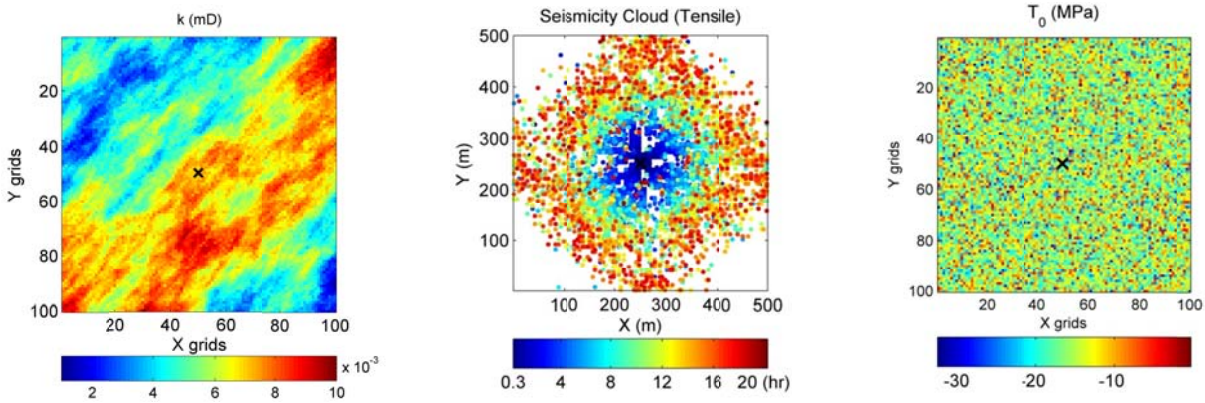

(a) true permeability (k) map (b) true seismicity cloud (c) T_0 map

Figure 62. True model specification; $S_{h,min} = S_{H,max} = P_{ini} = 10$ (MPa), Inj. Rate $= 0.005(l/s)$, $E = 20$ (GPa), T_0 with Normal PDF (spatially random distribution) $\mu_{T_0} = -15$ (MPa), $\sigma_{T_0} = 5$ (MPa).

The estimation results of permeability k, experiment are shown extensively in Figure 63. The true permeability k, distribution is again presented in Figure 63.a. Permeability estimation RMSE, Figure 63.b, shows continuous reduction and goes from 0.0021 (md) (initial RMSE) to 0.0009 (md) (final RMSE) which confirms the promising estimation performance of SSBRC. In Figure 63.c, the ensemble spread is presented which shows significant reduction and the final ensemble spread is 17 % which still is fairly acceptable. The evolution of estimated ensemble mean and two realizations throughout integration steps are shown in Figure 63.d,e,f, respectively. It is clear from the results that the final estimated maps (at integration step 6) are very similar to the true permeability map which confirms the suitability of SSBRC for hydraulic reservoir parameter estimation. The evolution of ensemble spread is shown in Figure 63.g, in terms of ensemble standard deviation map.

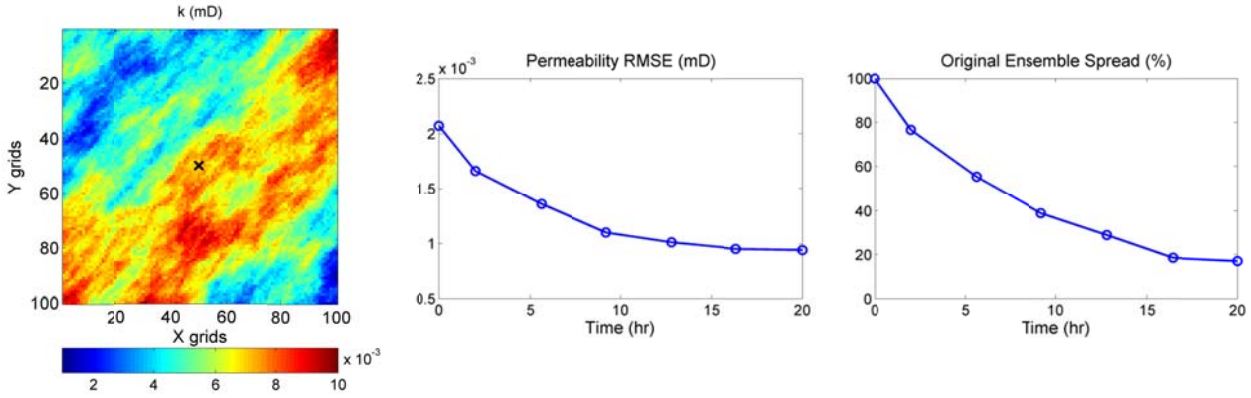

(a) true permeability k, map (b) permeability estimation RMSE (c) permeability ensemble spread

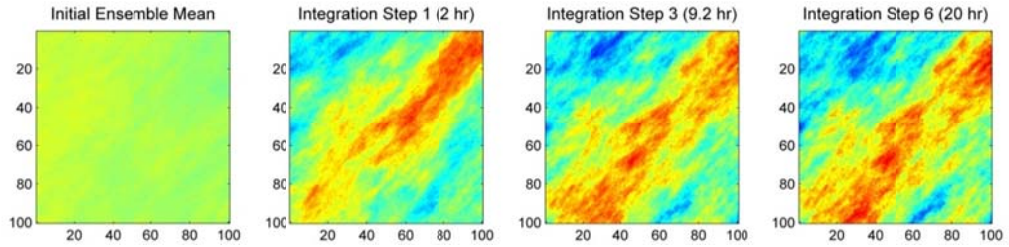

(d) ensemble mean evolution

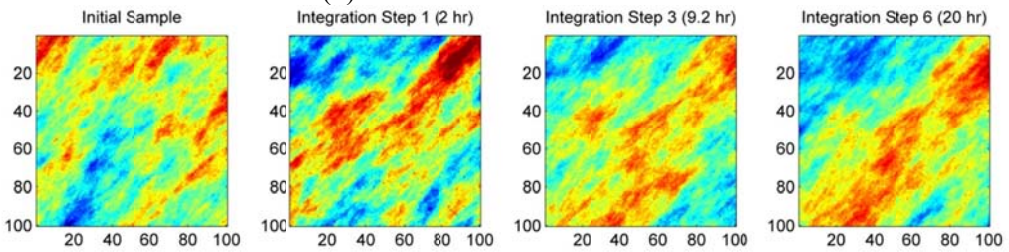

(e) sample or realization #1 evolution

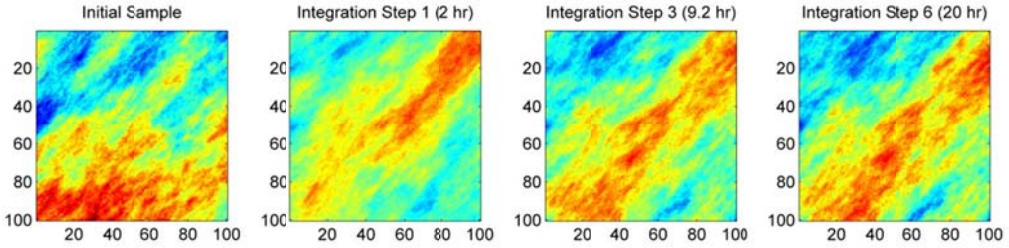

(f) sample or realization #2 evolution

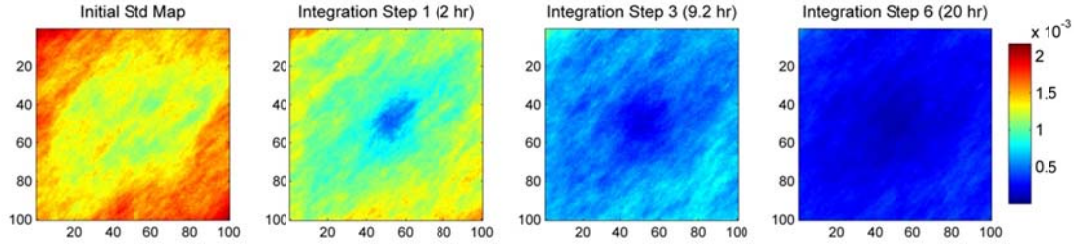

(g) ensemble standard deviation evolution

Figure 63. Permeability k, estimation results.

Experiment 9: 3D Heterogeneous Elastic Modulus

In this section, we apply SSBRC to the developed 3D fully coupled thermo-poroelastic finite element method (FEM) model. We present the results of estimating 3D Young's modulus distribution from MEQ cloud using SSBRC. In this experiment we use coarse-scale seismicity density method to preserve the ensemble spread through update steps.

In the 3D model the injection well as a point source is at the center of the field. Permeability distribution is homogeneous in the field and equal to 0.5 (md). We suppose there are only tensile failures, so in order to avoid any shear failures, the cohesion as a homogeneous property in the field is assumed a very high value of 1000 (MPa). In this experiment, the far-field stress boundary conditions including initial reservoir pressure P_{ini}, minimum horizontal stress $S_{h,min}$, maximum horizontal stress $S_{H,max}$ and vertical stress S_v, are equal 10 (MPa), 13 (MPa), 15 (MPa) and 18 (MPa), respectively. In each forward

simulation, time step length is 3600 (s) and there are 72 time steps so the stimulation period is 72 (hr). The injection rate scenario is shown in Figure 64.

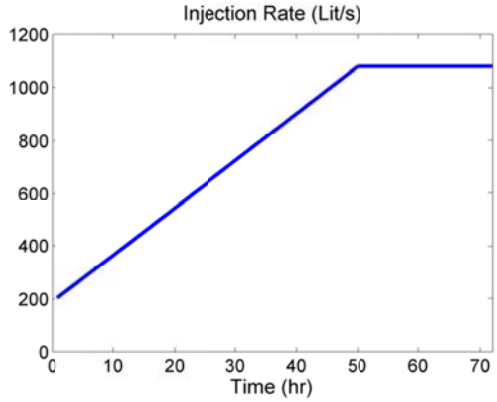

Figure 64. Injection rate scenario

The true Young's modulus distribution (as the parameter to estimate), the assumed tensile strength (failure criteria) and the MEQ cloud response (the true monitoring MEQ data to be integrated in EnKF) are shown in Figure 65. In Figure 65.c, the microseismic events are tensile failures as mentioned previously. By SSBRC stochastic estimation algorithm, we estimate the 3D Young's modulus distribution (Figure 65.a) which is assumed unknown from discrete MEQ cloud observation (Figure 65.c).

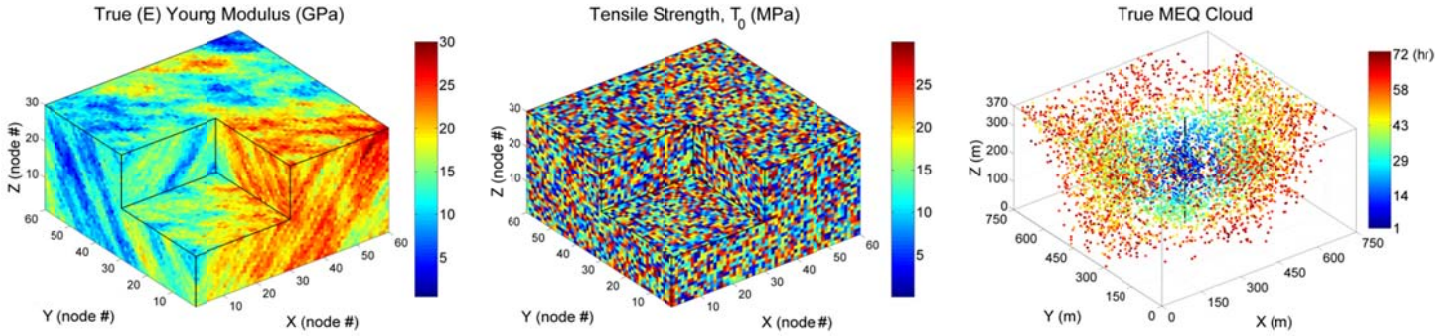

(a) true Young's modulus distribution (b) T_0 distribution (c) true microseismicity cloud

Figure 65. True model setup; true Young's modulus and T_0 distribution and the corresponding MEQ cloud.

The vertical black line in MEQ cloud plots (e.g. Figure 65.c) indicates the location of the injection well and the injection point (point source) is at the center of the model (at the middle of the black line). To better illustrate true MEQ data, Figure 66 represents it in 4 different views.

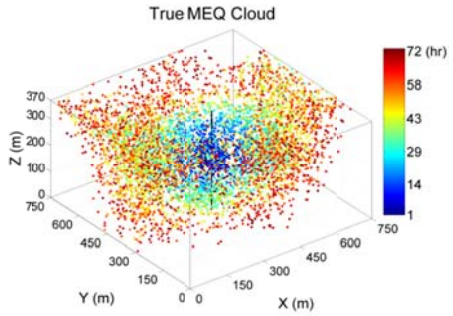

(a) original view

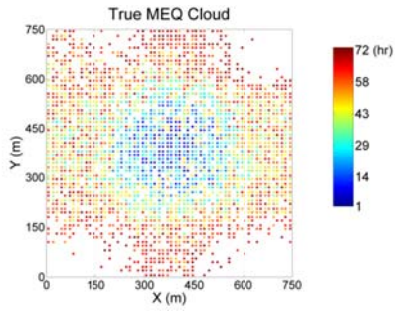

(b) XY view

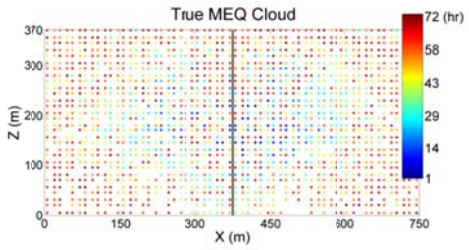

(c) XZ view

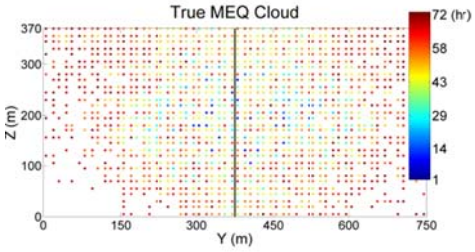

(d) YZ view

Figure 66. True MEQ cloud in different views.

In SSBRC estimation procedure we consider 6 integration time steps. The true MEQ cloud is shown throughout these 6 integration steps in Figure 67. We sequentially integrate the monitoring MEQ data at each integration step by EnKF to estimate the Young's modulus distribution.

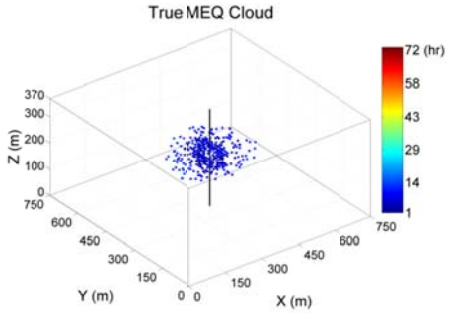

(a) integration step 1 (12 hr)

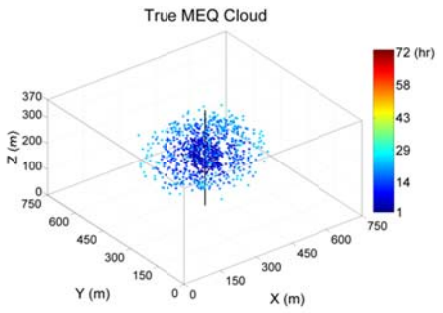

(b) integration step 2 (24 hr)

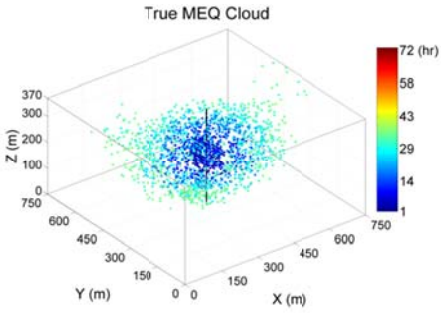

(c) integration step 3 (36 hr)

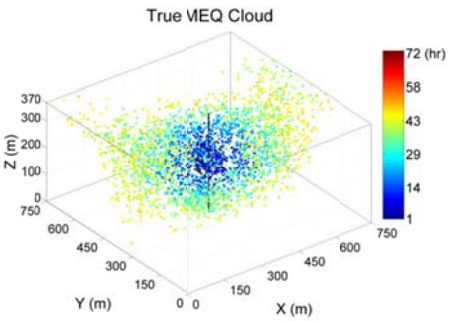

(d) integration step 4 (48 hr)

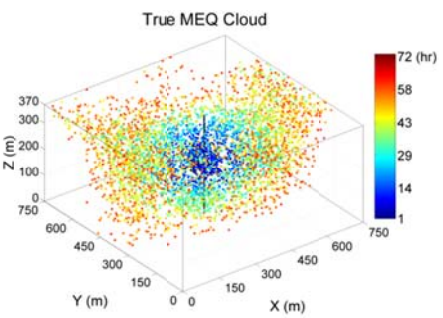

(e) integration step 5 (60 hr)

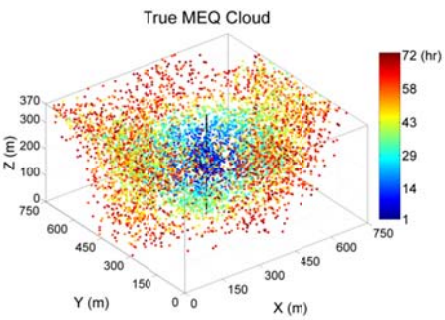

(f) integration step 6 (72 hr)

Figure 67. True MEQ cloud through integration steps

As already mentioned discrete MEQ data are not directly amenable to be used in EnKF algorithm so we use a KDE-based continuous interpretation method to convert discrete MEQ cloud to MEQ density maps. The corresponding seismicity density maps of true MEQ cloud of Figure 67 are shown in Figure 68 on the original fine mesh. In fact, 6 seismicity density maps of Figure 68 are the continuous observation data that can be used in EnKF to estimate unknown reservoir parameter (108000 parameters) which in this case is Young's modulus. The continuous interpreted MEQ density on the original fine mesh has a very high resolution (108000 observations) and will result in redundant data which causes ensemble spread underestimation and biased estimation in SSBRC. Therefore we consider using coarse-scale seismicity density method to reduce the number of observations.

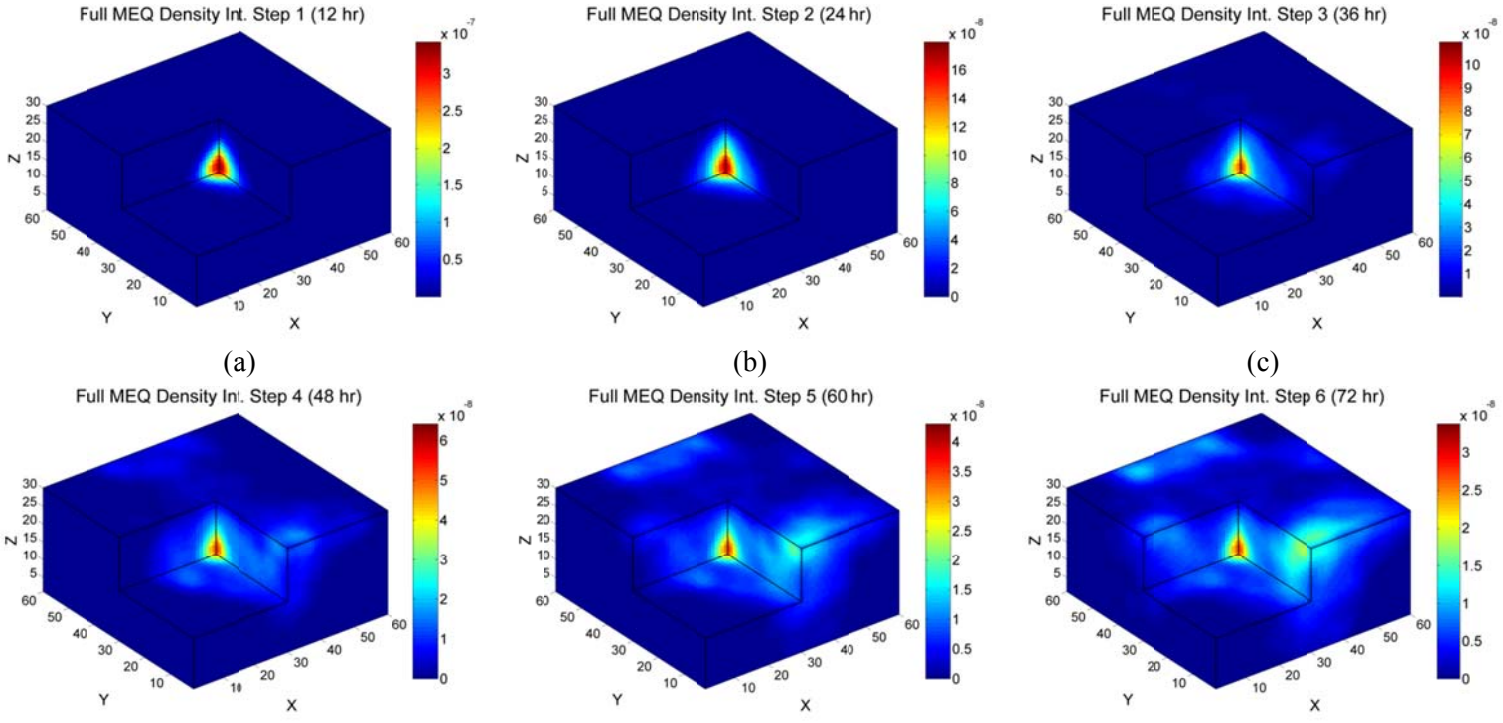

(a) (b) (c)

(d) (e) (f)

Figure 68. True MEQ density maps through integration steps (on full size mesh).

The final true MEQ cloud is converted to MEQ density map with different sizes of coarse-scale mesh and the resulted density maps are shown in Figure 69. From the investigation of Figure 69 and performing the EnKF analysis equation after one integration step with different sizes of coarse scale mesh we chose 20×20×10 mesh as the appropriate size for coarse-scale continuous MEQ interpretation.

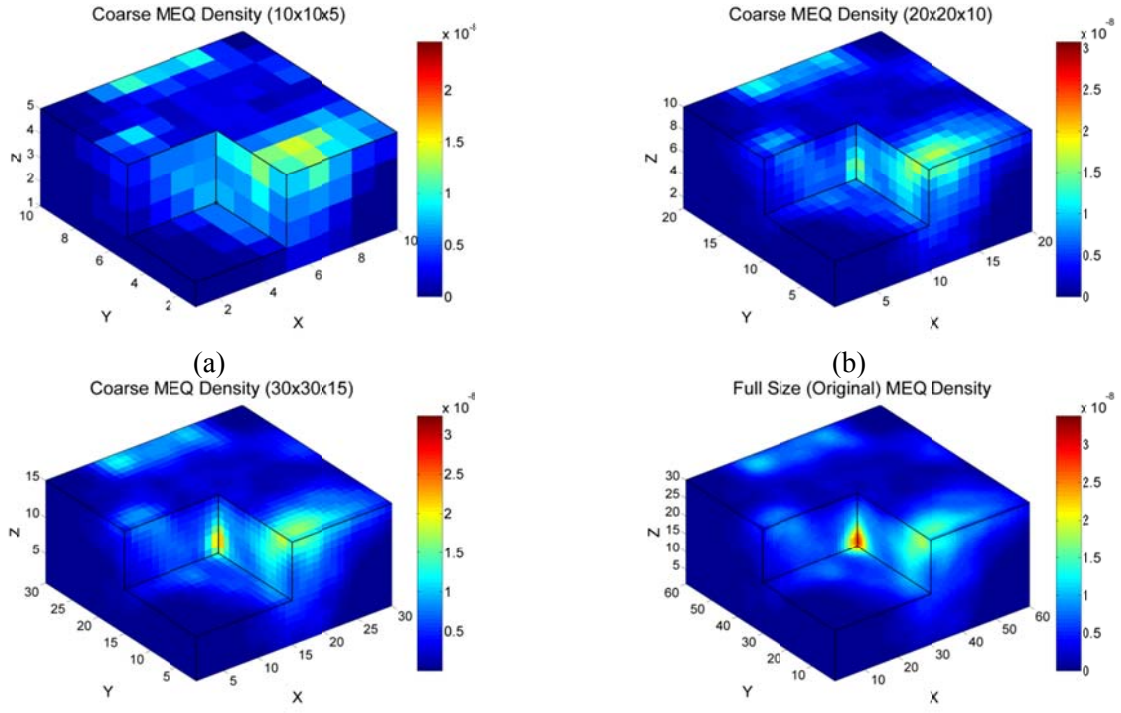

(a) (b) (c) (d)

Figure 69. Final (at 6th integration step) true MEQ density maps on different coarse size meshes.

As seen in Figure 69, it is clear how the resolution of the seismicity density map reduces by coarsening the continuous interpretation mesh which consequently results in reducing the number of observations. As of Figure 69, the number of observations in plots (a), (b), (c) and (d) are 500, 4000, 13500 and 108000 respectively. The coarse-scale seismicity density map on 20×20×10 mesh is shown in Figure 70 throughout integration steps. By using 20×20×10 coarse scale mesh, we reduce the dimension of the observation from 108000 to 4000 which results in preserving the ensemble spread through data integration using EnKF. In our SSBRC estimation experiment the seismicity density plots of Figure 70 are observation data.

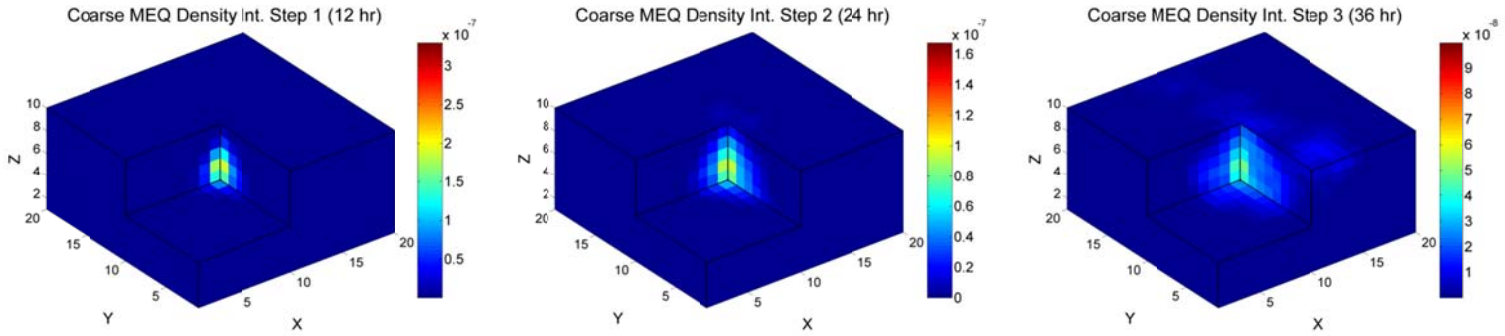

(a) (b) (c)

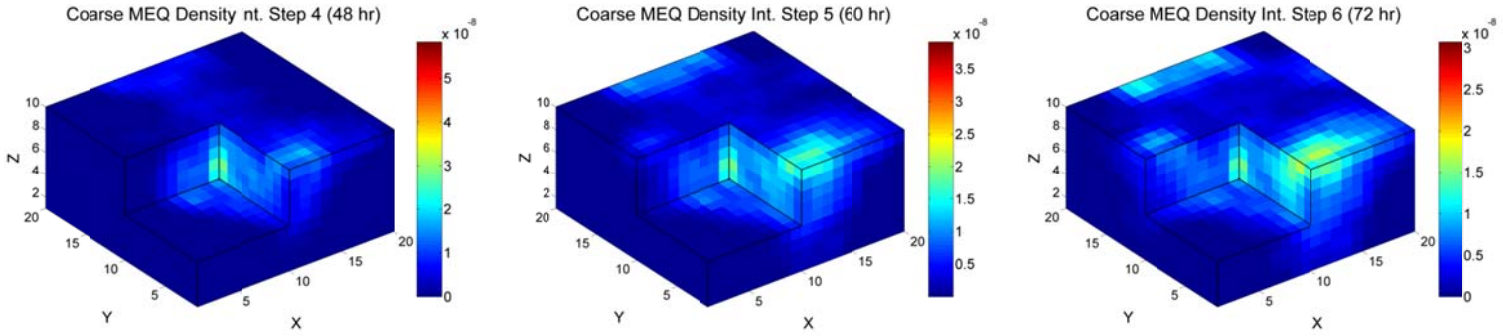

(d) (e) (f)

Figure 70. True MEQ coarse-scale density maps through integration steps (on 20x20x10 mesh).

For the EnKF algorithm, the ensemble size (number of realizations) is assumed 100. We also considered 6 integration steps regularly specified in 72 (hr) of total forward run simulation. As we mentioned, each 3D geomechanical model forward run takes almost 5 (hr) to run therefore our SSBRC experiment with 100 realizations and 6 integration time steps (utilizing parallel EnKF algorithm with confirmation step) and assuming 4 available CPUs, takes almost 20 (days). Because of the extremely high computational load of SSBRC with 3D model, we managed to split the job and run it on multiple machines and finally we reduced the run time to almost one week. Initially to make sure we will resolve ensemble spread underestimation of SSBRC we utilize coarse-scale seismicity density method. Since the forward 3D model is very computationally expensive to run, it was not convenient to run SSBRC with coarse-scale density for different sizes of coarse mesh. Therefore to find the appropriate size of coarse mesh, we investigated different sizes of coarse-scale seismicity density map after one integration step only. So we propagated the initial ensemble till the first integration step and performed the first EnKF analysis equation with different coarse mesh configuration then we decided about the optimal size based on the best values of RMSE and Spread. By applying coarse-scale seismicity density method in SSBRC for this experiment, we estimate or update 108000 parameters (Young's modulus value at each node) from 4000 observation values (coarse seismicity density map dimension for 20×20×10 mesh configuration) at each integration time step. In the estimation procedure we assume all the parameters of the true model are known but the Young's (elastic) modulus distribution. The true model setup is shown in Figure 65.

As the first estimation result we show the estimated mean of elastic modulus ensemble through integration steps in Figure 71. While the initial ensemble mean (Figure 71.b) is almost homogeneous and completely uninformative about the true elastic modulus (Figure 71.a), as we can see in Figure 71.b-h by marching through integration steps and integrating MEQ data the estimated ensemble mean becomes more similar to the true Young's modulus distribution (Figure 71.a) and ultimately the final estimated ensemble mean (Figure 71.h) captures the trends and features of the true parameter distribution.

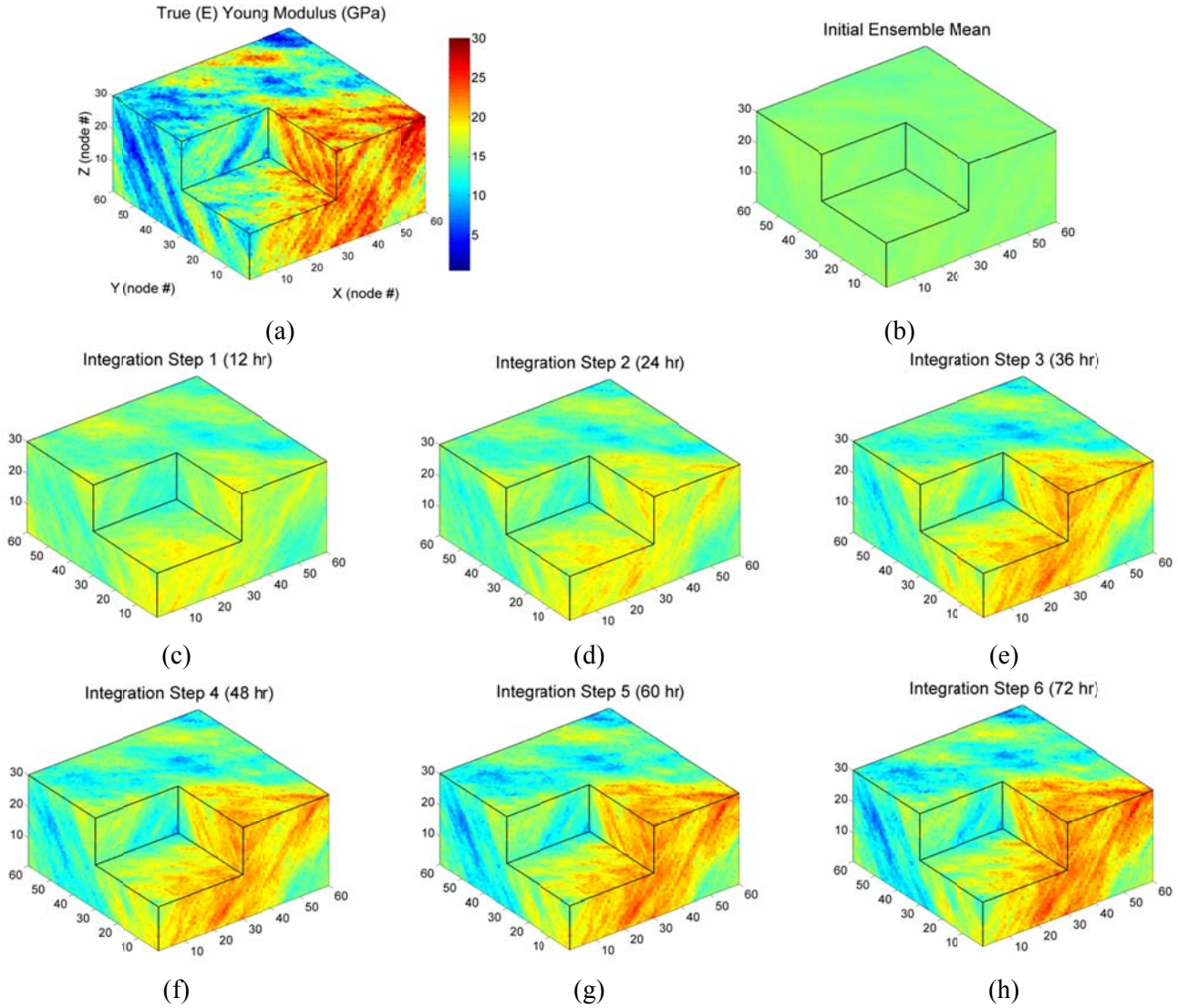

Figure 71. Young's modulus estimation results: evolution of estimated ensemble mean through integration steps.

The estimation performance of SSBRC is also represented by the root mean squared error (RMSE) of estimated elastic modulus ensemble through time (Figure 72.a). Continuous reduction of estimation RMSE from 5.5 (GPa) to 2 (GPa) through integration steps confirms successful application of SSBRC in characterization of 3D geomechanical models by MEQ data. Uncertainty quantification performance of SSBRC estimation procedure is shown by the ensemble spread which should not reduce to a very low value. Both the original Young's modulus ensemble spread and auxiliary ensemble spread are shown in Figure 72.b,c, respectively. The ensemble spread percentage is defined as the ratio of the ensemble spread at each integration step to the initial ensemble spread. As can be seen the final ensemble spread is 30 % which is a promising in EnKF estimation procedure and it confirms that ensemble collapse did not happen and the ensemble spread underestimation issue is resolved.

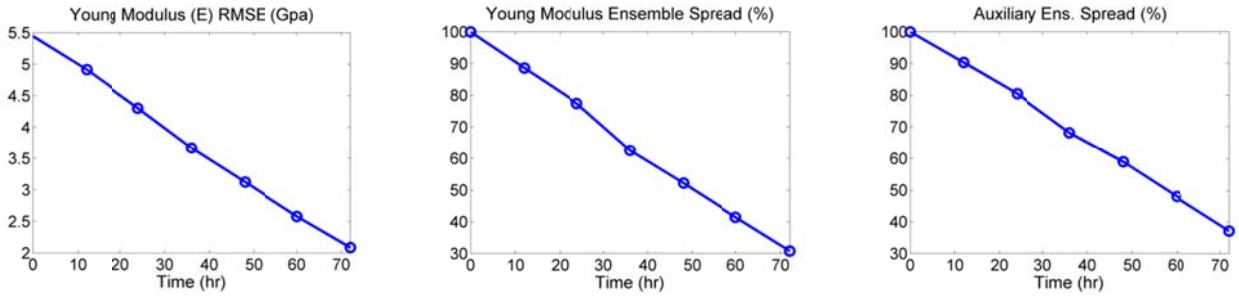

(a) (b) (c)

Figure 72. Estimation performance measures.

To better represent promising estimation performance of SSBRC, evolution of a single sample (realization) through integration steps is shown in Figure 73. Again we start with an initial elastic modulus sample (Figure 73.b) that is completely different than true modulus distribution (Figure 73.a) and through integration steps the estimated sample captures the features of the true elastic modulus distribution and the final estimated realization (Figure 73.h) is very close to the true model.

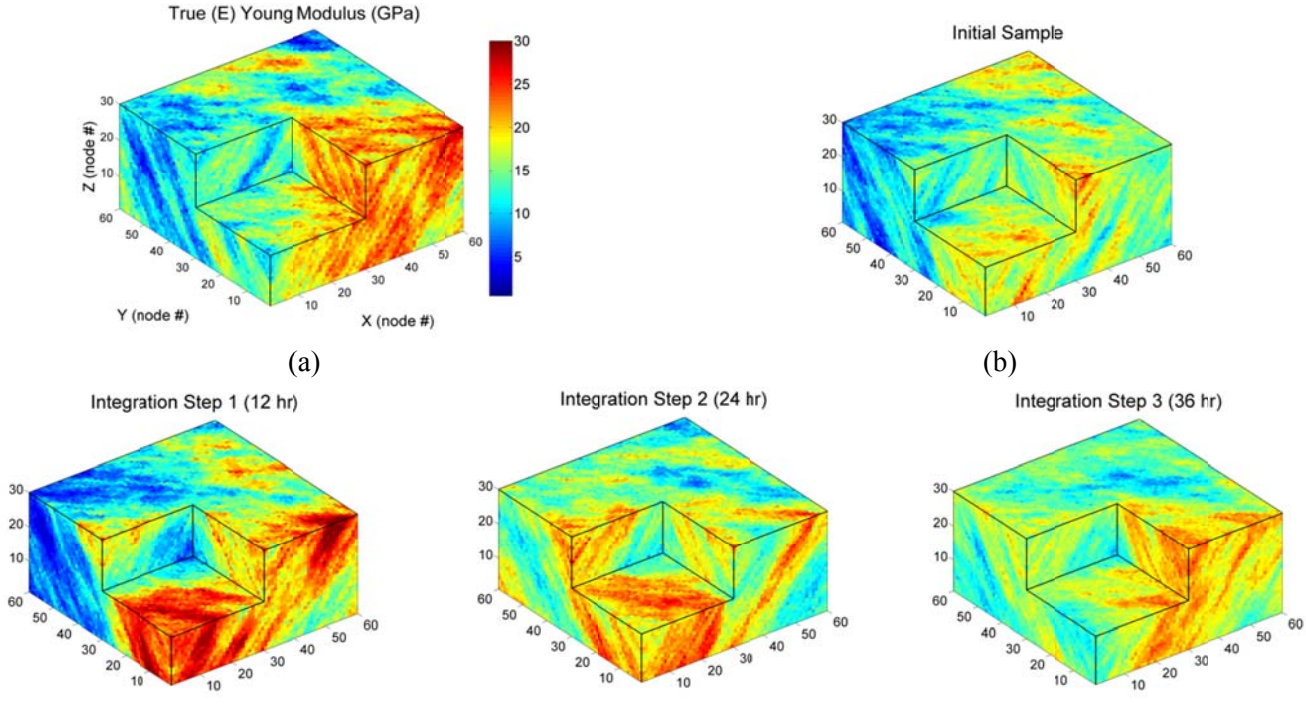

(a) (b)

(c) (d) (e)

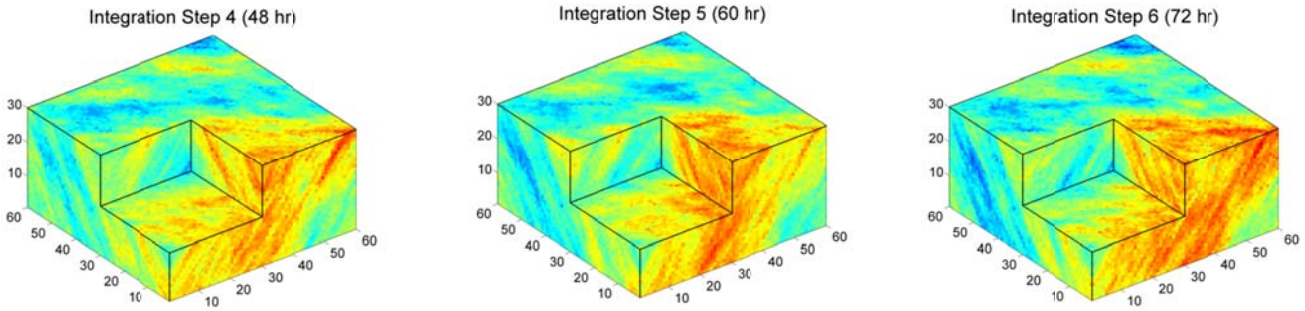

(f) (g) (h)

Figure 73. Young's modulus estimation results: evolution of a Young's modulus realization (sample) through integration steps.

In Figure 74, the corresponding MEQ responses of the estimated sample of Figure 73 in different integration steps are shown. The MEQ forecasts of Figure 74 becomes more and more similar to true MEQ cloud (Figure 74.a) as we advance in integration steps because the estimated elastic modulus distribution gets closer to the true elastic modulus distribution.

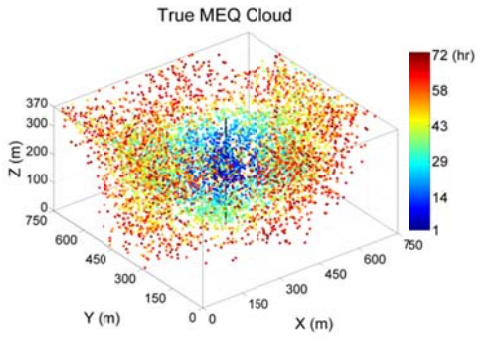

(a) true microseismicity cloud

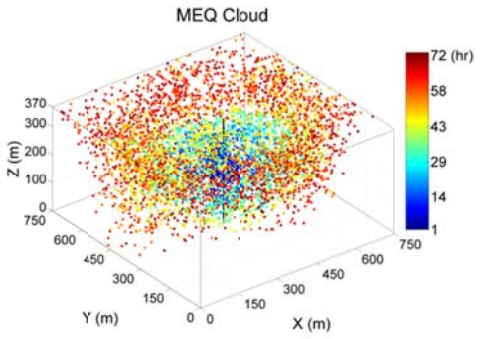

(b) initial sample

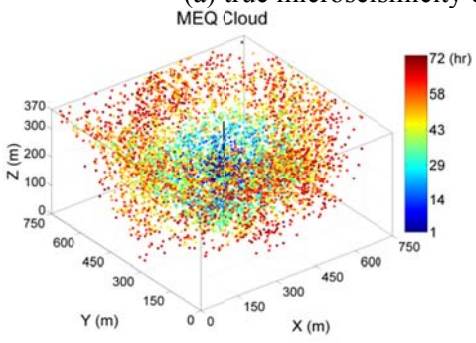

(c) updated till integration step 1

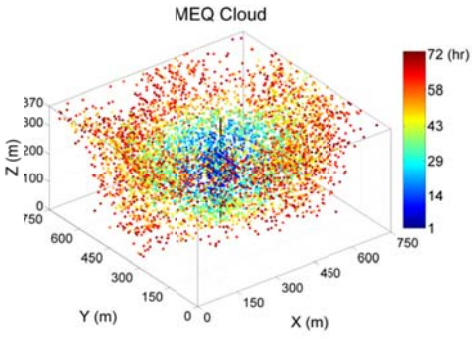

(d) updated till integration step 2

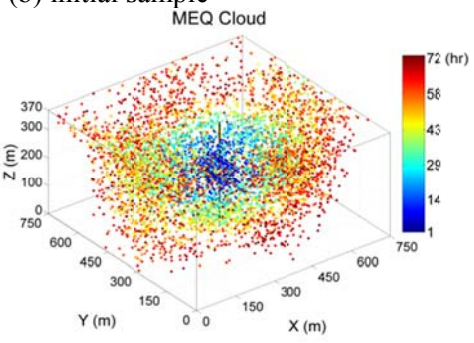

(e) updated till integration step 3

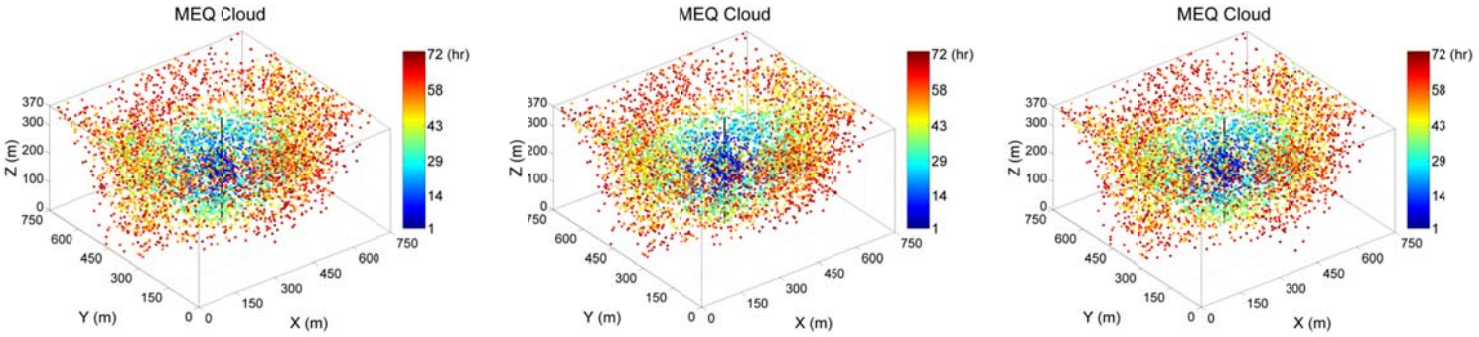

(f) updated till integration step 4 (g) updated till integration step 5 (h) updated till integration step 6

Figure 74. Corresponding MEQ cloud response of the estimated sample in different integration or update steps.

Another estimated sample evolution through integration steps is shown in Figure 75. Once more we can see how a dissimilar initial sample (Figure 75.b) changes to become close to the true elastic modulus distribution (Figure 75.a) throughout the sequential data integration procedure.

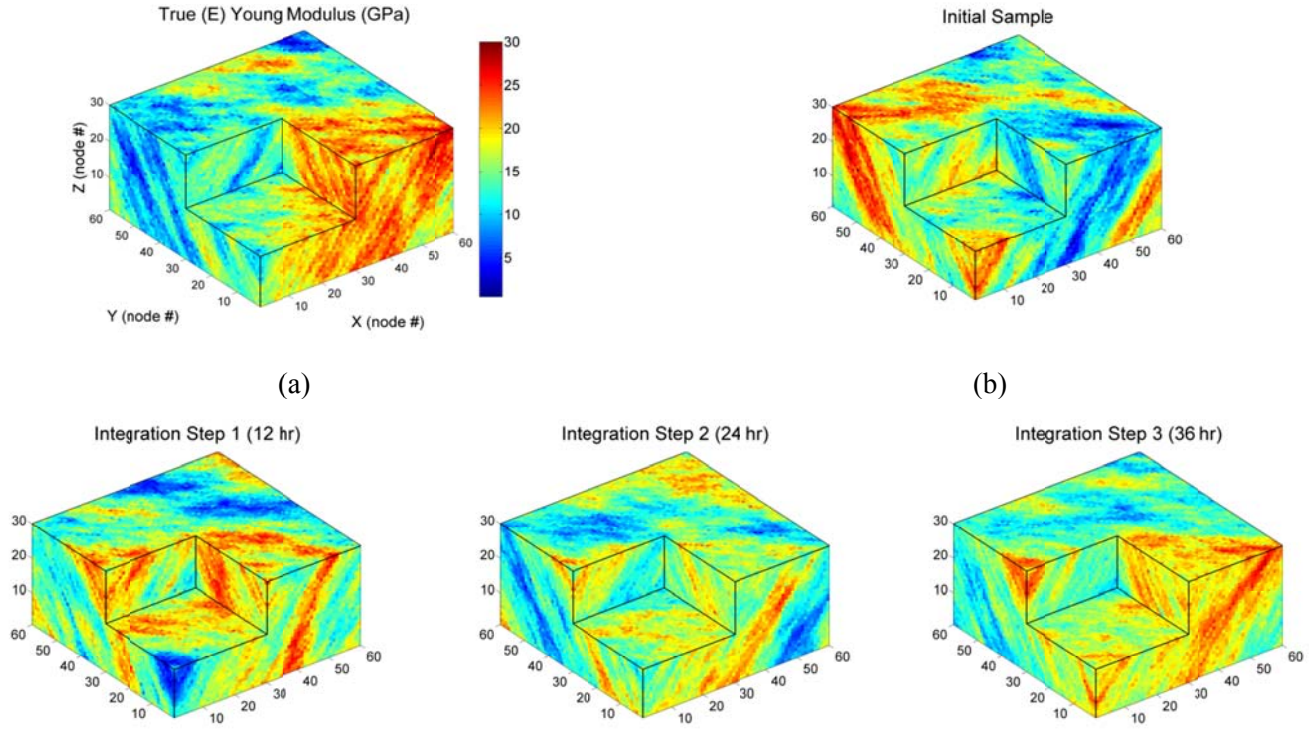

(a) (b)

(c) (d) (e)

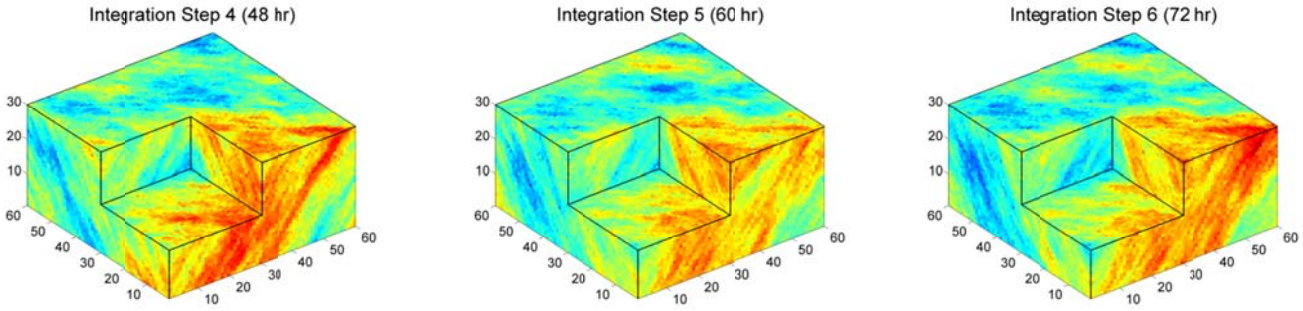

(f) (g) (h)

Figure 75. Young's modulus estimation results: evolution of another Young's modulus realization (sample) through integration steps.

As mentioned before the uncertainty quantification performance of SSBRC is evaluated by ensemble spread or ensemble standard deviation. Therefore the evolution of the ensemble standard deviation map is shown in Figure 76 which represents the reduction of the ensemble spread throughout the integration steps that means the realizations are becoming more and more similar and in the same time they are getting close to the true elastic modulus distribution. Reduction of ensemble spread or standard deviation shows that the initial guesses are becoming more similar to true value.

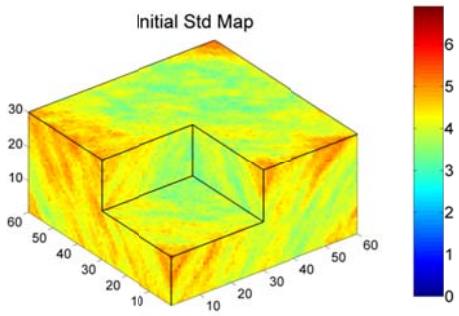

(a)

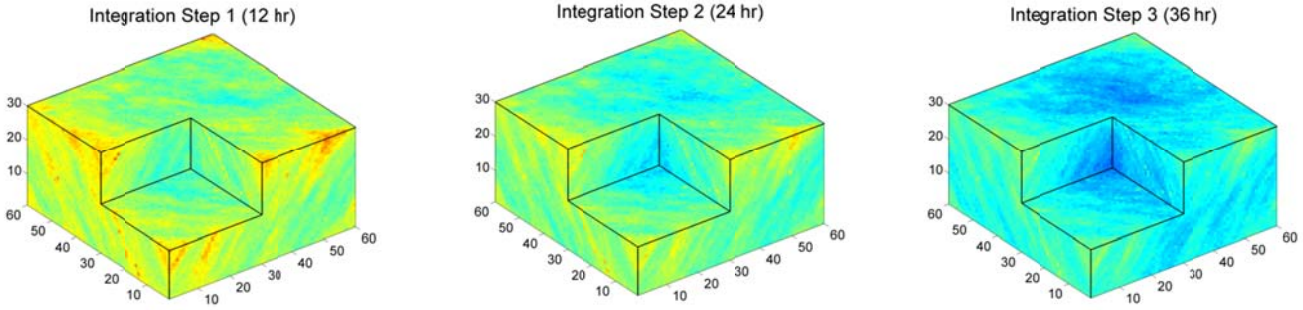

(b) (c) (d)

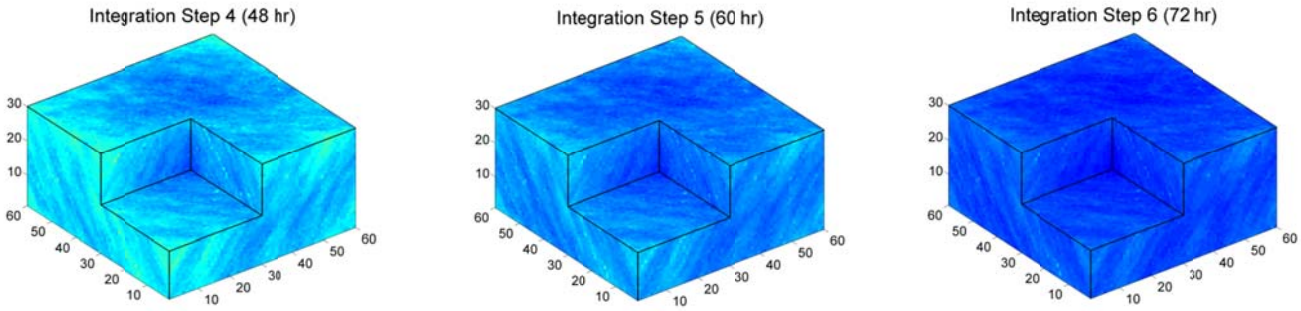

(e) (f) (g)

Figure 76. Evolution of the standard deviation map of Young's modulus ensemble.

The results of the above experiments (and many others with similar well setup but different reference reservoir property maps that were not included) indicate that the EnKF can be used to successfully infer hydraulic and geomechanical reservoir parameter distributions from continuous interpretations (through KDE) of the discrete MEQ monitoring measurements. This outcome has important implications for characterization of subsurface reservoirs from MEQ events as an emerging monitoring technology in several important energy and environmental applications. While simple and easy to implement, the EnKF proves to be an effective model calibration tool for nonlinear problems where the optimality requirements of the original Kalman filter update equation, namely jointly Gaussian states and measurements and linear state-space model assumptions, are not strictly met. While the examples illustrated in this report clearly show the feasibility of applying the EnKF to constrain different reservoir parameter distributions based on microseismic event locations, we did not consider the seismic analysis step that is required to provide the MEQ sources locations. In addition to event locations, other information about the seismic source may be extracted from the raw seismic data (e.g., the magnitude and confidence of events) and be used to further constrain rock property distributions. An important aspect that was not considered in this study is the presence, initiation and propagation of fractures in the rock during the hydraulic fracturing process. In general, microseismic events can carry important information about the location and geometrical attributes of the fractures, which can be exploited for fracture model calibration purposes.

5. Conclusions

Seismicity-based reservoir characterization is a promising approach for monitoring and improving reservoir performance in a number of important energy and environmental applications. We formulated an EnKF-based model calibration approach to integrate discrete MEQ events into the description of reservoir property distributions in both pore-pressure diffusion and fully coupled geomechanical forward model. Since the EnKF is a continuous estimation approach, we introduced a new interpretation of the MEQ event locations as a continuous seismicity density map that is amenable to assimilation with the EnKF. A main advantage of the EnKF to previously introduced SBRC methods is that it is a stochastic inversion that provides an ensemble of solutions to facilitate uncertainty assessment. Other important advantages of the EnKF are the ability to systematically incorporate uncertainty in models and observations, and its generality for application under any forward model, failure criteria, and MEQ event triggering mechanisms. In addition, the simple and versatile implementation of the EnKF allows for estimation of different types of parameters from various data types.

In this work, we developed a coupled geomechanical reservoir simulator with rock failure criteria and damage mechanics model, and focused on developing a framework called stochastic seismicity-based reservoir characterization (SSBRC) for automatic and robust integration of MEQ-type discrete data sets using the EnKF. We first developed 2D and 3D FEM fully coupled thermo-poro-elastic models with Mohr-Coulomb failure criterion (including tension cut-off) and, permeability and damage model to relate hydraulic and geomechanical reservoir parameters to discrete microseismicity cloud. An important property of the EnKF is that its sequential update scheme provides different representations of unknown parameters after each update. By construction, the EnKF is designed to update time-varying states of a system. In forward geomechanical model that rock damage is reflected in the alteration of elastic modulus and permeability, field stress disturbances change the rock physical properties (parameters) with time, the EnKF-type sequential filtering techniques prove quite useful for estimation of dynamically varying parameters. We also set up 2D and 3D pore-pressure diffusion forward models using a finite difference based commercial reservoir simulator that relates permeability distribution to MEQ cloud distribution.
In pore-pressure forward model, by applying SSBRC we can infer permeability distribution from MEQ data. Considering the coupled flow and geomechanics-based forward model, SSBRC method is capable of inferring permeability, elastic modulus, tensile strength, cohesion and friction angle from MEQ event cloud. Here, both tensile and shear failures are considered as microseismicity events.

Using KDE to generate seismicity density map on the same fine grid system of pore pressure diffusion model or fine mesh of FEM model leads to high-dimensional and redundant observation. EnKF update with large number of correlated observations results in severe ensemble spread underestimation. We proposed three methods to preserve the ensemble spread and improve uncertainty quantification of SSBRC. We resolved this issue by either artificially adding large random noise to observation or reducing the number of observations by spectral and spatial dimension reduction. As the simplest method of avoiding ensemble collapse, we proposed to inflate observation error variance. We also proposed projecting the microseismic data onto a low-dimensional subspace that is defined by left singular vectors of the perturbed observations matrix, and lastly using coarse-scale continuous representation of the microseismic data. The proposed KDE approach for transforming the discrete MEQ data in this work inevitably introduces some error into the estimation results. A more natural estimation approach for integration of MEQ data is one that does not convert the discrete events into continuous measurements. Developing discrete data integration algorithms can eliminate the discrete data quantification step and potentially lead to additional improvements in the estimation results.

Here, a continuum approach has been used and discrete fracture systems were not explicitly considered in the estimation. Further refinements of the workflow may also be possible by including seismic modeling as one of the components in the inversion framework that can help better characterize the MEQ events both in terms of their distribution and intensity. Analyses of the raw microseismic data can lead to additional information about the induced fractures and their properties.

6. References

Evensen, G., and P. J. van Leeuwen (1996), Assimilation of Geosat altimeter data for the Agulhas current using the ensemble Kalman filter with a quasigeostrophic model, *Mon. Weather Rev., 124*, 85–96.

Houtekamer, P. L., and H. L. Mitchell (1998), Data assimilation using an ensemble Kalman filter technique, *Mon. Weather Rev., 126,* 796–811.

Madsen, H., and R. Canizares (1999), Comparison of extended and ensemble Kalman filters for data assimilation in coastal area modeling, *Int. J. Numer. Methods Fluids, 31*, 961–981.

Chen, Y., and D. Zhang (2006), Data assimilation for transient flow in geologic formations via ensemble Kalman filter, *Adv. Water Resour., 29*, 1107–1122.

Franssen, H. H., and W. Kinzelbach (2008), Real-time groundwater flow modeling with the ensemble Kalman filter: Joint estimation of states and parameters and the filter inbreeding problem, *Water Resour. Res., 44*, W09408, doi:10.1029/2007WR006505.

Nowak, W. (2009), Best unbiased ensemble linearization and the quasilinear Kalman ensemble generator, *Water Resour. Res., 45*, W04431, doi:10.1029/2008WR007328.

Schöniger, A., W. Nowak, and H. J. Hendricks Franssen (2011), Parameter estimation by ensemble Kalman filters with transformed data: Approach and application to hydraulic tomography, *Water Resour. Res., 48*,W04502, doi:10.1029/2011WR010462.

Naevdal, G., L. Johnsen, S. Aanonsen, and E. H. Vefring (2005), Reservoir monitoring and continuous model updating using ensemble Kalman filter, *SPE J., 10*(1), 66–74.

Wen, X. H., and W. Chen (2005), Real-time reservoir model updating using ensemble Kalman filter, paper SPE 92991 presented at SPE Reservoir Simulation Symposium, Soc. of Pet. Eng., Richardson, Texas.

Jafarpour, B., and D. McLaughlin (2009), Estimating channelized reservoir permeabilities with the ensemble Kalman filter: The importance of the ensemble design, *SPE J., 14*(2), 374–388.

Aanonsen, S., G. Naevdal, D. Oliver, A. Reynolds, and B. Valles (2009), Reservoir monitoring and continuous model updating using ensemble Kalman filter, *SPE J., 14*(3), 393–412.

Jafarpour, B., and M. Tarrahi (2011), Assessing the performance of the ensemble Kalman filter for subsurface flow data integration under variogram uncertainty, *Water Resour. Res., 47,* W05537, doi :10.1029/2010WR009090.

Evensen, G. (2009), The ensemble Kalman filter for combined state and parameter estimation: Monte-Carlo techniques for data assimilation in large systems, *IEEE Control Syst. Mag., 29*(3) 83–104, doi:10.1109/MCS.2009.932223.

Ehrendorfer, M. (2007), A review of issues in ensemble-based Kalman filtering, *Meteorol. Z., 16*(6), 795–818.

Aanonsen, S. I., I. Aavatsmark, T. Barkve, A. Cominelli, R. Gonard, O. Gosselin, M. Kolasinski, and H. Reme (2003), Effect of scale dependent data correlations in an integrated history matching loop combining production data and 4D seismic data, SPE Reservoir Simulation Symposium.

Skjervheim, J. A., G. Evensen, S. Aanonsen, B. O. Ruud, and T. A. Johansen (2007), Incorporating 4D seismic data in reservoir simulation models using ensemble Kalman filter, *SPE J. 12*(3): 282-292, SPE-95789-PA.

Sakov, P., and P. R. Oke (2008), A deterministic formulation of the ensemble Kalman filter: an alternative to ensemble square root filters, *Tellus A*, *60*(2), 361-371.

Myrseth, I. (2008), Robust ensemble Kalman filter for high dimensional data, VIII International Geostatistics Congress, Santiago, Chile.

Eclipse (2010), Eclipse reference manual and technical description, Schlumberger-GeoQuest, Houston, Tex.

Cansi, Y. (1995), An automatic seismic event processing for detection and location: The P.M.C.C. Method, *Geophysical research letters, 22*(9), 1021-1024.

MATLAB version 7.12.0 (R2011a), Natick, Massachusetts: The MathWorks Inc., 2011.

Kalman, R. E. (1960), A new approach to linear filtering and prediction problems, *J. Basic Eng., 82*, 35–45.

Gelb, A. (1974), *Applied Optimal Estimation,* MIT Press, Cambridge, Mass.

Deutsch, C., and A. Journel (1998), *GSLIB: Geostatistical Software Library and User's Guide,* Oxford Univ. Press, New York.

Vargas-Guzman, J. A., and T.-C. J. Yeh (1999), Sequential kriging and cokriging: Two powerful geostatistical approaches, *Stochastic Environ. Res. Risk Assess., 13*(6), 416–435.

Kitanidis, P. K., and E. G. Vomvoris (1983), A geostatistical approach to the inverse problem in groundwater modeling (steady state) and one-dimensional simulations, *Water Resour. Res., 19*(3), 677–690, doi:10.1029/ WR019i003p00677.

Yeh, T.-C. J., A. L. Gutjahr, and M. H. Jin (1995), An iterative cokriging like technique for ground water flow modeling, *Ground Water, 33*(1), 33–41.

Graham, W., and D. McLaughlin (1989), Stochastic analysis of nonstationary subsurface solute transport: 2. Conditional moments, *Water Resour. Res., 25*(11), 2331–2355, doi:10.1029/WR025i011p02331.

Keepert, J. D. (2004), On ensemble representation of the observation error covariance in the ensemble Kalman filter, *Ocean Dyn., 6*, 539–560.

Hamill, T., J. S. Whitaker, and C. Snyder (2001), Distance-dependent filtering of background error covariance estimates in an ensemble Kalman filter, *Mon. Weather Rev., 129*, 2776–2790.

Evensen, G. (2004), Sampling strategies and square root analysis schemes for the EnKF. *Ocean Dynamics*, *54*(6), 539-560.

Jazwinski, A. H. (1970), *Stochastic processes and filtering theory* (Vol. 63). Academic press.

Furrer, R., and T. Bengtsson (2007), Estimation of high-dimensional prior and posterior covariance matrices in Kalman filter variants, *Journal of Multivariate Analysis, 98*(2), 227-255.

Chapter 3. Three-Dimensional Fully Coupled FEM Analysis of Geothermal Reservoirs with Stochastic Fracture Networks

1. Introduction

Simulation the response of an engineered geothermal reservoir (EGS) requires analyzing the THM response of the reservoir rock, which are generally fractured and with heterogeneous properties to some extent. The THM response of the reservoir rock includes the opening and propagation of natural fractures, and the failure process of intact rock. To assess the mechanical (deformation) and hydraulic (permeability enhancement) response of fractured rock during stimulation, three sub-models are required: a fracture network model, a rock heterogeneity model, and a coupled THM model. The rock heterogeneity model and the FEM THM model have been explained in detail previously (Chapter 1). The emphasis of this chapter is fracture network modeling and its implementation for seismicity generation.

2. Fracture Network Model Development

Fractures serve as hydraulic conductors, barriers, channels of chemical contaminants transport, and play important roles in the stability of engineered structures and excavations. The presence of natural fractures in the reservoir puts challenges for designing, exploration, evaluation, and modeling of the reservoir. Major challenges for numerical modeling from natural fractures include but are not limited to: 1) how to identify, locate, and characterize natural fractures? 2) How do flow and transport occur in fracture systems? 3) How can changes in fracture systems be predicted and controlled. In this work, countermeasures to above concerns are 1) developing a conceptual model to represent the fracture network geometry; 2) developing a mathematical model to represent fluid flow and solute transport in fractured media; 3) building a hydro-mechanical model which can analyze the coupled fluid and solid response, and simulate the fracture deformation and porous rock response simultaneously.

There are generally two classes of fracture models, stochastic fracture models and deterministic models. There are also works that utilize combined deterministic and stochastic fracture networks. In most reservoir stimulation and fracture modeling, the thermo-poroelastic coupling process has been either neglected or simplified to empirical correlations (Cladouhos et al. 2001; Willis-Richards et al., 1996; Bruel, 2002). Three-dimensional THM models have been developed and applied to reservoir stimulation, development, and well bore stability analyses (Zhou and Ghassemi, 2009; Lee and Ghassemi, 2011). However, the reservoir rock was modeled as continuous porous media with possibly a few major fractures.

In this work, a fracture network is introduced into a coupled poroelastic model with heat transport. Poroelastic stresses in the rock matrix are computed at each time step, and are interpolated onto the natural fracture faces when calculation the fracture apertures change. The overall permeability of fractured rock is estimated using the equivalent permeability (Tezuka and Watanabe, 2000). An iterative method is employed to retrieve the stress-dependent permeability at each time step. Considering the problem complexity and the computational cost, the rock strain and fracture geometry changes are

considered independent from the thermal response. The heat transport in the reservoir is assumed to occur via fluid flow within the fractures, and the heat conduction from rock matric to the fracture fluid. Compared to heat convection via fracture flow, heat convection within rock matrix is insignificant in early stage of injection and is neglect in this work. The heat conduction from rock matrix to the fracture fluid is assumed to be linear and governed by 1-D diffusive equation.

2.1 Natural Fracture Network Model

There are generally two classes of fracture models, stochastic fracture models (Cladhuous et al. 2011; Bruel et al. 1994; Willis-Richards et al. 1996; and Tezuka et al. 2005) and deterministic models (Kolditz and Clauser 1998, Ghassemi et al. 2007, and Safari and Ghassemi 2011). According to the treatment of fluid flow through fracture systems, fracture models can also be classified in to equivalent continuum models (Carrera et al. 1990) and discrete fracture models (Hudson and La Pointe, 1980; Long et al., 1982). This work develops a hybrid method using discrete stochastic networks in building a continuum approximation.

In a conventional equivalent continuum model, the induced rock heterogeneity by fractures is modeled using sub-regions with different local properties. Individual fractures are not explicitly present unless their scale is large enough to be considered separately as determined unit in the model. Each sub-region has uniform properties, such as poroelastic modulus and permeability, which are resulted from the volume-averaged behavior of many fractures inside the sub-domain. For example, flow through a sub-domain is calculated in every direction and is used to form the equivalent permeability tensor for the sub-domain. In this work, a sub-domain is viewed as one FEM (Finite Element Method) element. If the properties for the equivalent continuum are used as being known with certainty, the model is deterministic. If the coefficients are viewed as randomly distributed with a probability, the model is stochastic (Long et al. 1982, Robinson 1984, Dershowitz 1984, and Hudson and LaPointe 1980). In stochastic framework, fractures are reproduced only in a statistical sense to capture the overall connectivity of the entire region and not distinguished locally higher or lower than average zones. It is important to note that, in order to approximate the conductive fracture geometry (the inner connection of fractures), interference testing and tracer testing is critical to see how is the system interconnected (National Research Council, 1996).

2.2 Stochastic Fracture Network Model

In stochastic fracture network model, the fracture network consists of series of penny-shape fractures, the distributions of which is determined by the statistic descriptions of fracture density, size, and orientation. The stochastic distribution function of fracture network properties can be fitted from field survey data or experience. In this work, fracture network generation is inherited from Cacas et al. (1990). The fracture density, size, and orientation are described by Poisson distribution, log-normal distribution, and Fisher-von Mises distribution respectively. Parameters for these three distributions are from field data. However, slight modification can be made to the distribution function case by case. ALTAROCK (2011) suggested an elliptical Fisher distribution fits better for field data from Newberry site. In our numerical model, Poisson's parameter (λ) indicates the total number of fractures expected in the modeled volume. The variables from a Poisson random generator are the coordinates of fracture centers, which give the location of fractures in the modeled domain. There are two parameters in the log-normal distribution. μ is the

mean of log(radius), and σ is the standard deviation of the log(radius) with the radius in meters. The variables from a log-normal random number generator indicate the radius of the fractures. Fracture orientation can be defined by its altitude and azimuth. The two angles are generated according to Fisher von Mises distribution (Equation 2.1) independently. The parameter κ is from field data fitted curve.

$$f(\alpha) = \frac{k}{2\sinh(k)}\exp(k\cos(\alpha))\sin(\alpha) \quad (1)$$

where α is the angle variable and κ is the concentration parameter. A fracture network with five hundred penny shape fractures is shown in Figure 1. Geometry algorithms for visualization of 3D penny shape fractures network is presented in the Appendix.

The initial fracture aperture is related to the fracture size (r) with a coefficient β:

$$a = \beta r^n \quad (2)$$

where a is the initial aperture. β equals 0.004, estimated from average virgin permeability (Willis-Richards, 1996), . β is a field dependent factor and requires careful evaluation. We use n = 0.5, which adopted from Tezuka and Watanabe 2000.

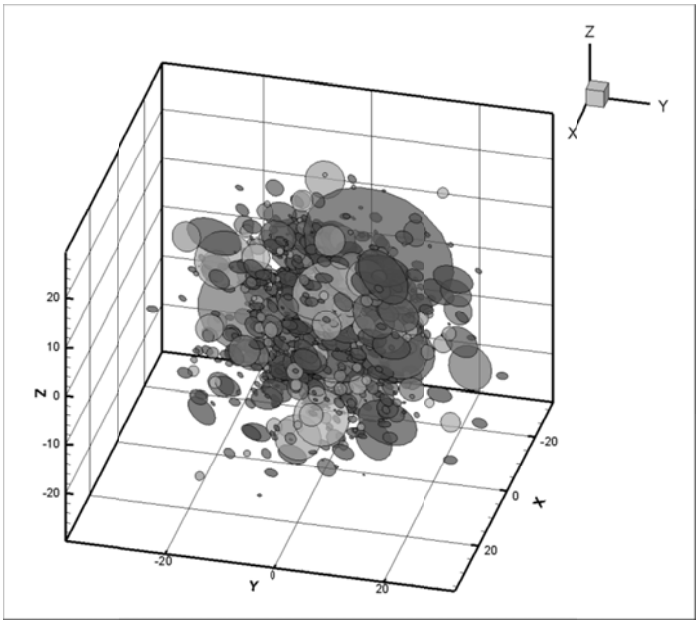

Figure 1. A stochastic fracture network with 500 penny shape fractures.

2.2.1 Fracture locations (density)

The distribution of fracture centers follows Poisson distribution (Equation 3) in this work. Poisson distribution is a discrete probability distribution that describes the probability of a given number of events occurring in a fixed domain (time or space). In this work, the expected value of x in Equation (3) is the expected number of fractures in our modeling domain, i.e. the fracture density.

$$f(x;\lambda) = \frac{\lambda^x e^{-\lambda}}{x!} \tag{3}$$

Fracture location can be obtained by randomly generating center coordinates following Equation (3). Figure 2 shows examples of fracture center distributions with different density parameters in a 500×500×500 m^3 volume.

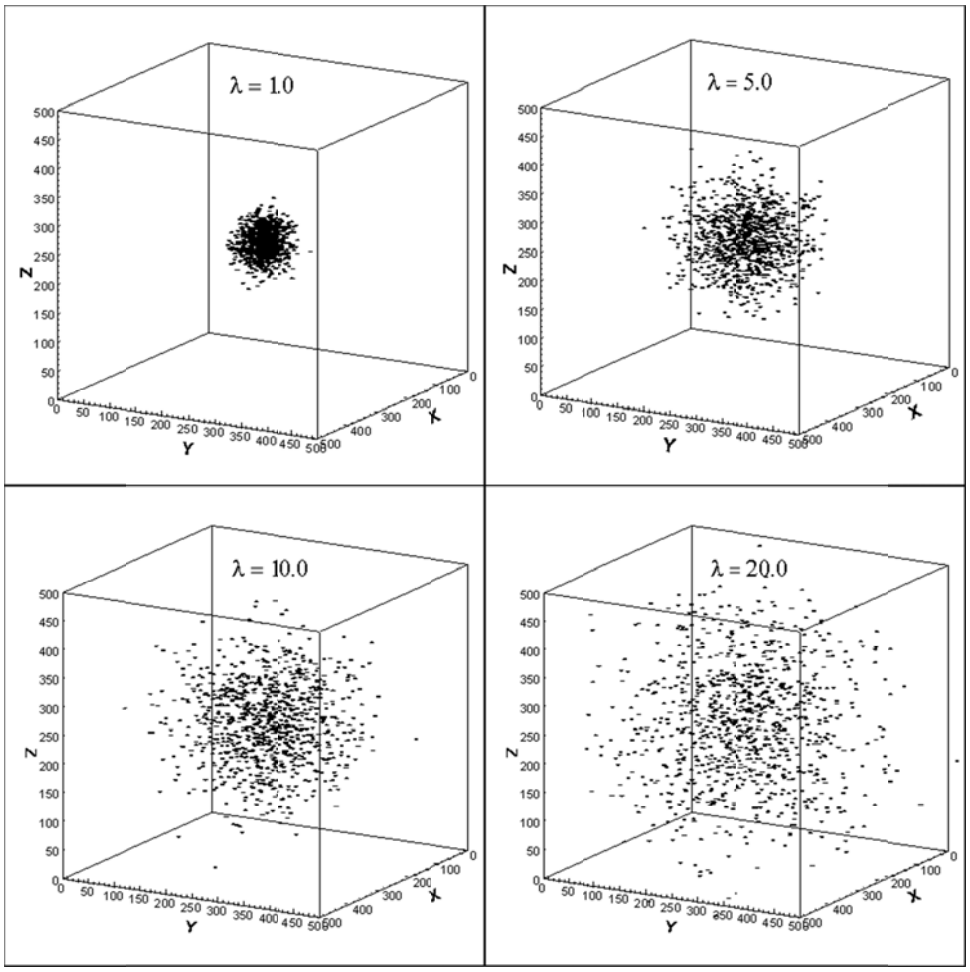

Figure 2. Fracture center distributions with different density parameters.

It should be noted that three random arrays, representing x-, y-, z- coordinates of centers, are generated independently. The density parameter (λ), from logging, well-imaging, or other methods, usually indicates one dimensional fracture density, i.e. number of fractures per length. More realistic three-dimensional distribution can be obtained by well correlation, which is outside the scope of this study. Here we assume the fracture distribution has the same density and is independent in x-, y-, and z-directions.

2.2.2 Fracture size

Fracture sizes are generated following log-normal distribution. In this work, the two parameters of the log-normal distribution are the mean and standard deviation of the fracture radius's natural logarithm. We

assume the sizes of all fractures in the simulated domain follow one single distribution with one set of parameters. However, sub-sets or different distributions can always be applied using similar algorithms, when suggested by field data. Figure 3 shows examples of penny shape fractures having same location and orientation but different size distribution.

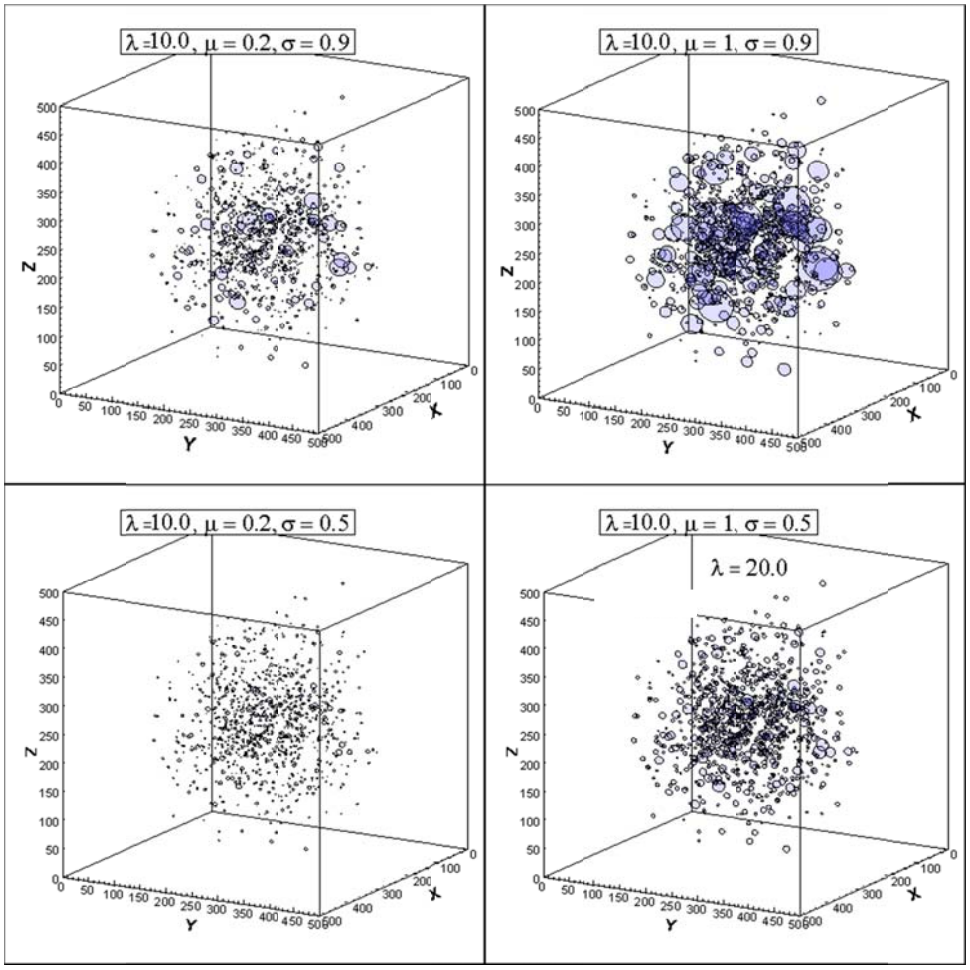

Figure 3. Fracture networks with different size parameters.

2.2.3 Fracture orientation

Fisher von Mises distribution is usually used in directional statistics to describe the distribution of directions on a sphere. Figure 4 shows examples of Fisher von Mises distribution with mean direction at (-1, 1, 1) and different ***k*** parameters. In this work, modified Fisher von Mises distribution (Equation 1) is used (Cacas et al. 1990). First, an array of direction angles is generated randomly. Then these values are substituted into Equation 1, generating the fracture orientations. Finally, direction angles that fall outside the range of fracture orientations are eliminated. Figure 5 shows comparisons of fracture networks with different orientation distribution parameters.

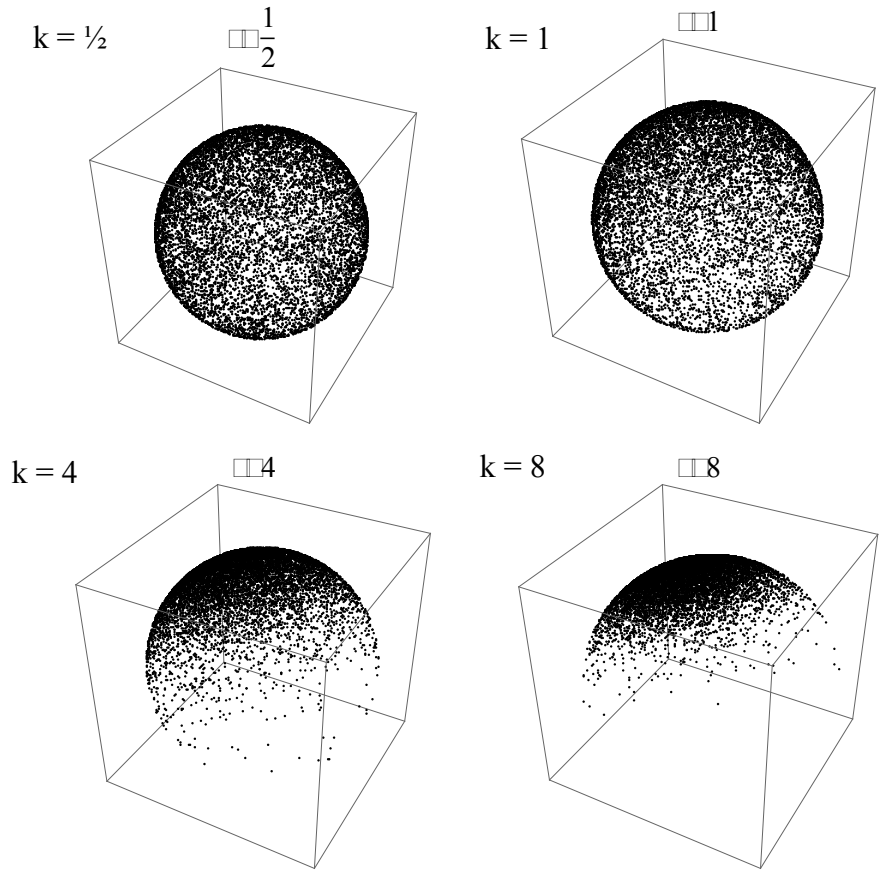

Figure 4. Fisher von Mises distributions with mean direction at (-1, 1, 1) and k = ½, 1, 4, and 8.

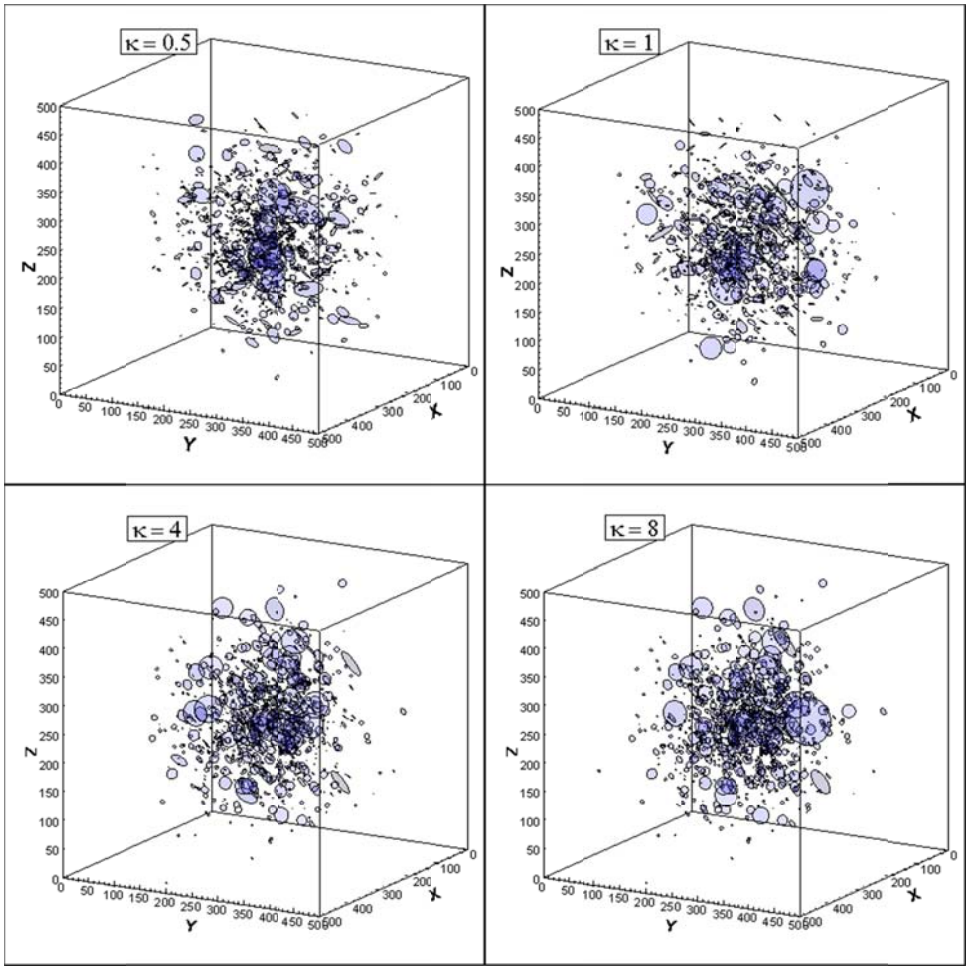

Figure 5. Fracture networks with different orientation distributions.

2.3 Conversion from Discrete Fracture Network to Continuum Media

The fracture flow model is based on the assumptions that fluid moves through the reservoir body within an interconnected fracture network, and that flow from the rock matrix to fractures is negligible in comparison with the flow in the fracture (Figure 6). Therefore, within one elemental volume, we consider fracture flow and matrix flow separately, and superpose these two parts together at the end of elemental evaluation using volume weighted averaging (Equation 4). We use Darcy's for matrix flow calculation.

$$\bar{k} = \frac{k_f V_f + k_m V_m}{V} \tag{4}$$

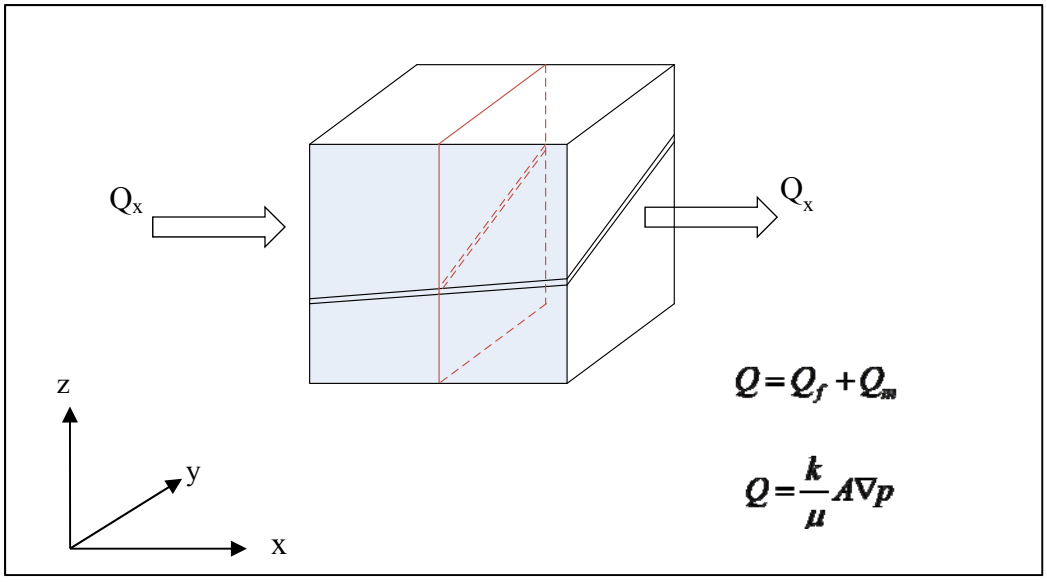

Figure 6. Illustration of x- directional flow through a fractured element.

The fluid flow in fracture is assumed to be governed by the cubic law shown by the following equation:

$$Q = \frac{wa^3}{12\mu}\frac{\Delta p}{\Delta L} \tag{5}$$

where Q is the volumetric flow rate in m^3/s, w is the length of intersection line between fracture and element interface in m; a is the aperture of the fracture in m; μ is the fluid viscosity; Δp is the pore pressure change in Pa after the flow travel through ΔL distance in m. In numerical simulations, the reservoir block is divided into small elements as shown in Figure 7. The fractures have apertures (a) and intersect the elements with an intersection length (l). The directional conductivity of the element can be expressed in the following way (e.g., Rahman et al. 2002):

$$k_i = \sum_{j=1}^{n_{fi}} \frac{a_j^3 l_{ij}}{12 A_i}, i = x, y, z \tag{6}$$

Where, n_{fi} is the total number of fractures in the element, which contributes to the flow in i^{th} directional. a_j and l_{ij} are the aperture and intersection line length of the j^{th} fracture on the intersected element surface. A_i is the cross section area of the corresponding direction, which is the interface of two elements in this model. The total permeability of the individual elements is obtained by the superposition of the rock mass permeability and the equivalent permeability of fractures using Equation (4). Geometry algorisms for calculation intersections between penny shape fractures and element faces can be found in the Appendix at the end of this dissertation.

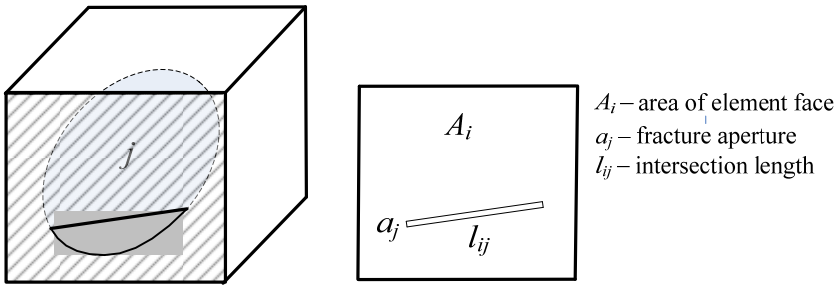

(a) Fracture *j* intersects elem (b) Notations used in Eqn. (2.6)

Figure 7. Conversion of fracture permeability into equivalent permeability of FEM element.

2.4 Mechanical and Hydraulic Properties of Fractured Rock

The simulation domain in this model is treated as continuum. It is essential to mapping fracture properties into rock matrix, and forming a continuum with equivalent mechanical and hydraulic properties. The parameter sensitivity and mesh sensitivity of this conversion is also evaluated.

2.4.1 Mechanical properties of fractured rock

Finite Element Method (FEM) is used in our numerical modeling. In simulations, the simulated domain is discretized into finite elements (meshing). In FEM simulation, each element is required to have its individual properties, such as Young's modulus, Poisson's ratio, and permeability, etc. In modeling of rock heterogeneity, we statistically distribute the local properties into individual elements. In some cases when rock mass with natural fractures are considered, it is necessary to calculate the equivalent elemental properties of elements that contain fracture(s) before conducting Finite Element analysis. In the following, Young's modulus is used as an example to explain the equivalent technique for modeling the properties of fractured sample. The basic concept is similar to the equivalent permeability method introduced previously. As conservation of flow rate is used in permeability conversion, the balance of displacement is used accordingly for the equivalent Young's modulus. The overall displacement of the fractured rock is equal to the displacement of converted continuum mass with equivalent Young's modulus under the same external loading. Rosso 1976 illustrated correlations among joint stiffness, axial and transverse strains of rock sample, and Young's modulus of intact rock during a triaxial test (Figure 8):

Coefficient of friction: $\mu = \tau / \sigma_n$

Average joint displacement: $d_s = \dfrac{(\varepsilon_3 - \varepsilon_2)D + d_n \cos\theta}{\sin\theta}$

Average joint closure: $d_n = \left[\left(\varepsilon_1 L - \dfrac{\sigma_1}{E} L\right) - (\varepsilon_3 - \varepsilon_2) D \cot\theta\right] \sin\theta$

Joint shear stiffness: $K_s = \dfrac{\tau}{d_s}$

Joint normal stiffness: $K_n = \dfrac{\sigma_n}{d_n}$

Shear stress: $\tau = (\sigma_1 - \sigma_3)\sin\theta\cos\theta$

Normal stress: $\sigma_n = \sigma_3 + (\sigma_1 - \sigma_3)\sin^2\theta$

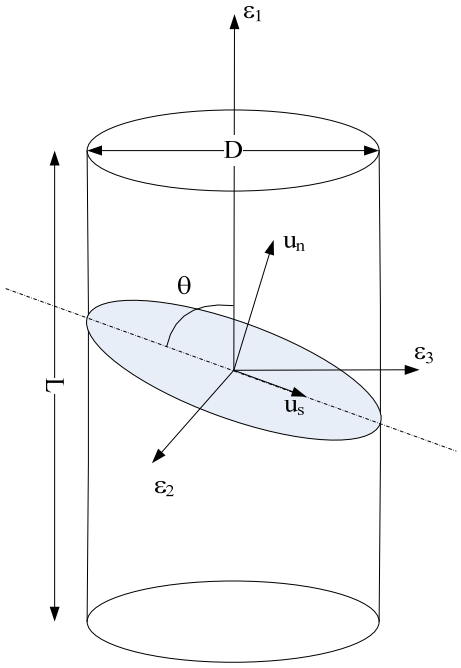

Figure 8. Illustration of relations between variables in triaxial test of a fractured specimen.

In above correlations and Figure 8, ε_1 is axial strain; ε_2 is small transverse strain; ε_3 is large transverse strain; D is sample diameter; θ is angle between the joint surface and the sample axis; L is sample length; E is elastic modulus determined from the competent specimen; σ_1 is axial stress; σ_3 is confining pressure.

From above relations, we can derive an expression of vertical equivalent Young's modulus in terms of properties of intact rock and fracture.

$$\frac{\sigma_d}{E'} = \frac{\sigma_d \sin^3\theta}{K_n L} + \frac{\sigma_3 \sin\theta}{K_n L} - \frac{\sigma_d}{K_s L}\sin\theta\cos^2\theta + \frac{\sigma_1}{E} \qquad (7)$$

where deviatory stress $\sigma_d = \sigma_1 - \sigma_3$; E' is equivalent Young's modulus of the fractured sample; and other parameters are same as defined above. Here we assume the fracture properties and intact rock properties are known. Figure 9 shows the comparison between lab test result and calculated result using Equation (7). We can see that that equation approximates the lab test result well in elastic part.

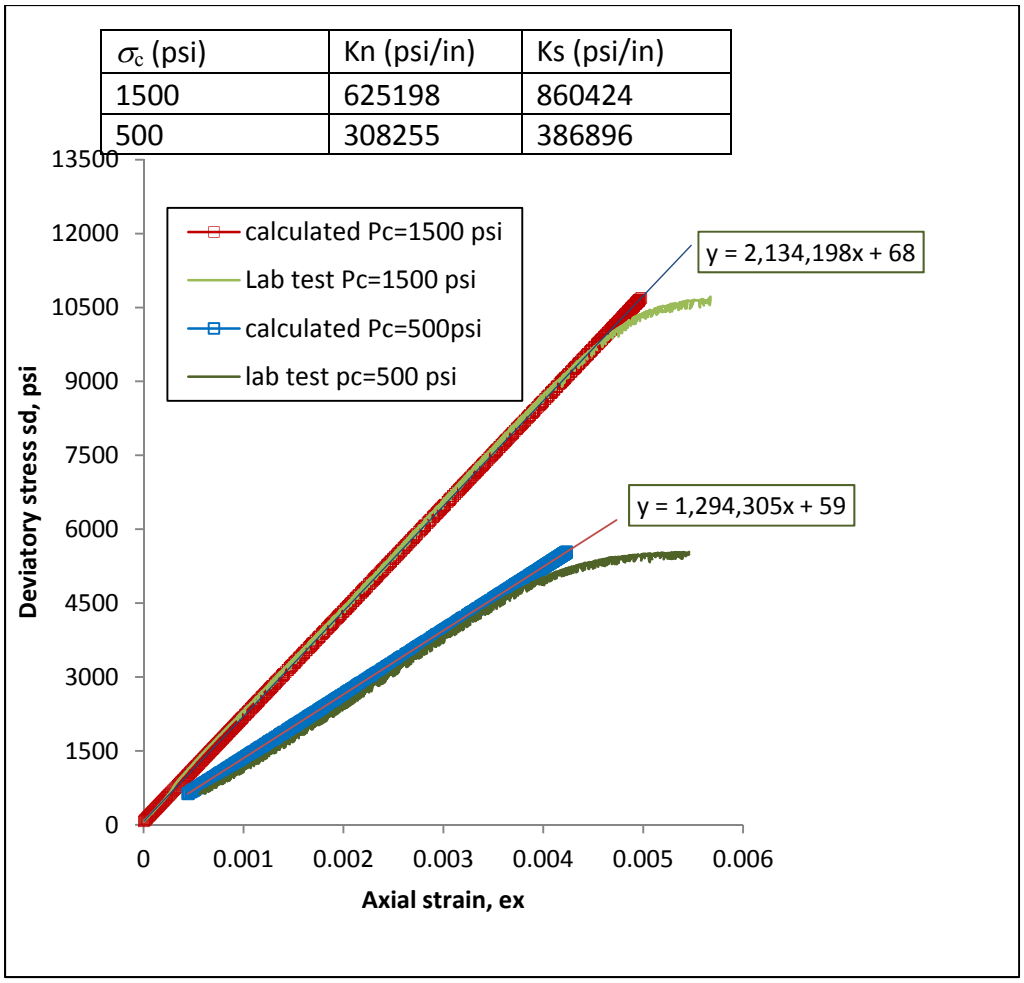

Figure 9. Comparison between Equation 7 results with lab test data.

When the scale gets bigger, or the mesh gets coarser depending on modeling requirements, a single element can contain several fractures. In practice, average local properties can be calculated using different averaging approaches depending on the definition of the problem. A single element can be divided into finite number of sub-elements such that one sub-element only includes one cut-through fracture. Then the averaging formula can be applied to find equivalent elemental properties. This method has been validated by comparing it to numerical simulations. Results show that the equivalent Young's modulus is less depended on fracture location in the element, but highly depended on the fractured level (number of fractures per volume). In the numerical model, Young's moduli of sub-elements are randomly distributed and five random samples have been selected. The results are sufficiently close to calculation using the averaging formula (Equation 8). Therefore, in later simulations related to fractured rock, the equivalent Young's modulus of an element will be calculated using averaging formula.

$$\overline{E} = \left(\frac{1}{nels}\sum_{i=1}^{nels} E_i^{1/3}\right)^3 \qquad (8)$$

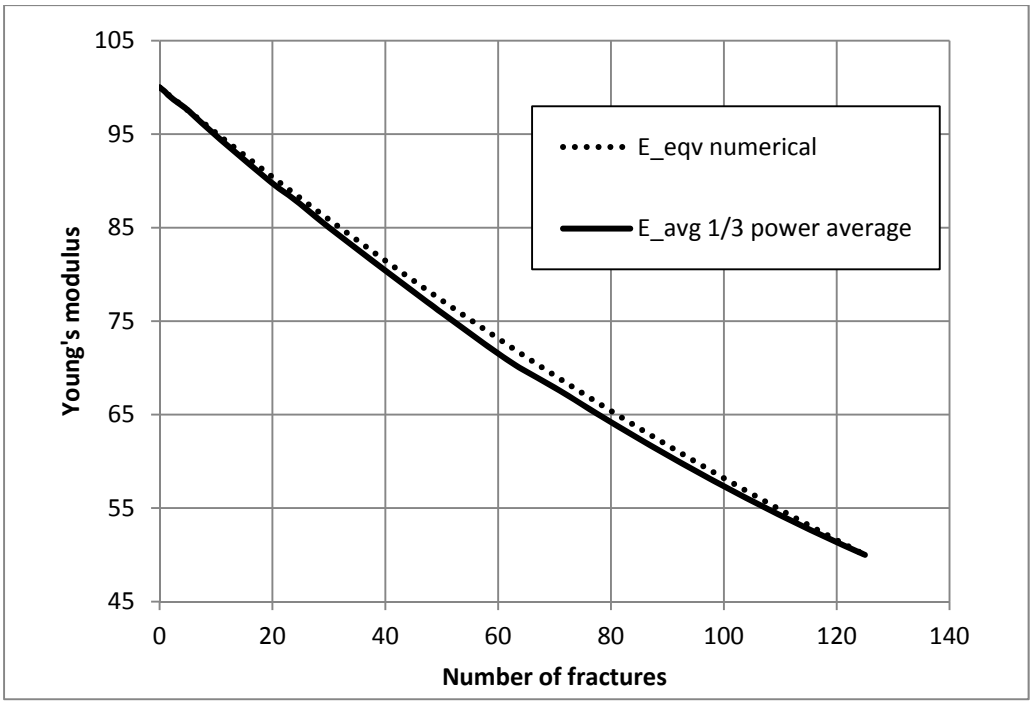

Figure 10. Comparison between Equation 2.8 results with numerical simulation results.

2.4.2 Hydraulic properties of fractured rock

The equivalent permeability technique converts fracture networks into a continuous media with equivalent permeability. The conductivity of the resulting continuous media is dramatically influenced by the connectivity of the fracture network, and is also affected by the finite element mesh selection. An example is shown in this part to analyze the parameter sensitivity of fractures connectivity and to test the mesh sensitivity of the equivalent permeability technique. In the following example, a network of 500 fractures is created within the domain matrix block using different fracture orientation and distribution parameters. Three different sizes of finite element mesh were used to investigate the impact of the mesh.

Figure 11A-D shows the influence of fracture orientations on the fracture network directional conductivities. The blue color shows the connectivity of fracture networks whose orientations are derived using the Fisher von Mises distribution (FVM) (group I) and the random distribution (group II). We can see that the fracture network with random orientations has higher conductivity in x- and y- directions and a lower conductivity in the z- direction when compared with Fisher von Mises distributed fracture networks. Considering the geometric average conductivity (Figure 11D), group (II) fractures also show higher values than group (I). These two groups have the same number of fractures, and the same size distributions. The finite element meshes are the same as well. By comparison, we can see the connectivity of fracture networks is significantly influenced by the fracture orientations.

II

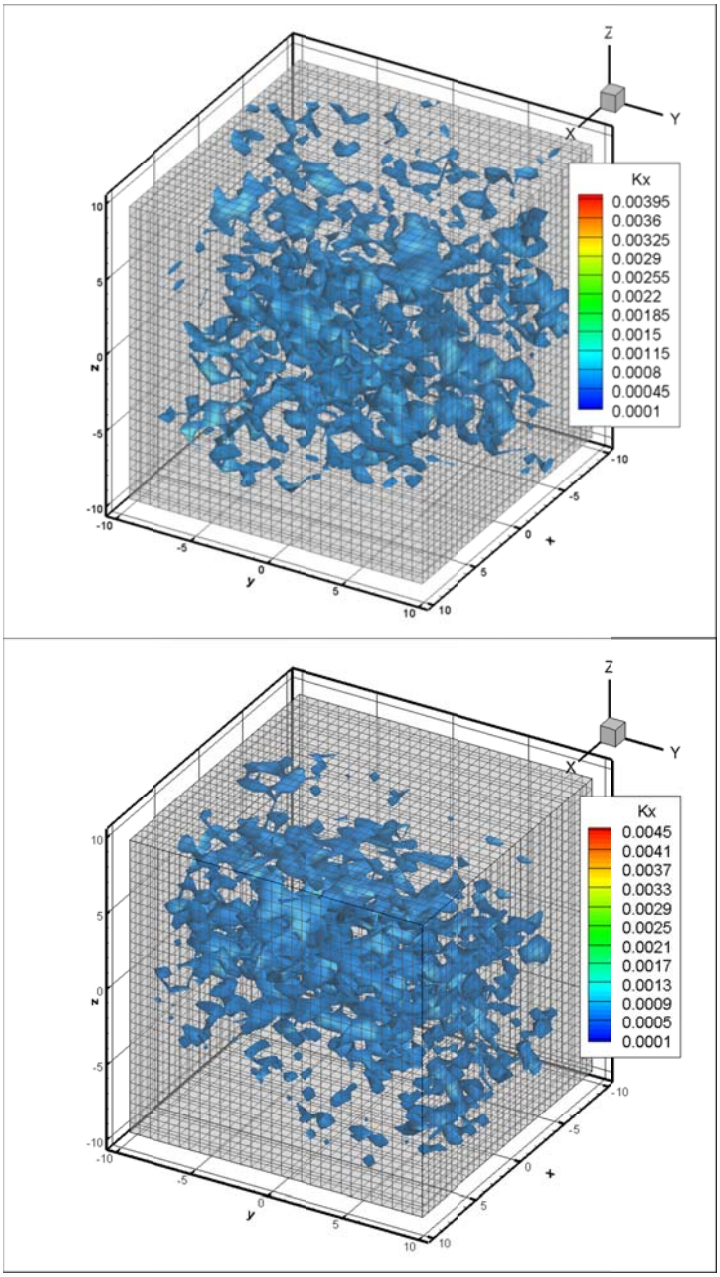

Figure 11A. The equivalent x- directional connectivity on FEM mesh of networks with Fisher von Mises (above, $\boldsymbol{k}$ = 2.8) and random orientation distribution (below).

I

II

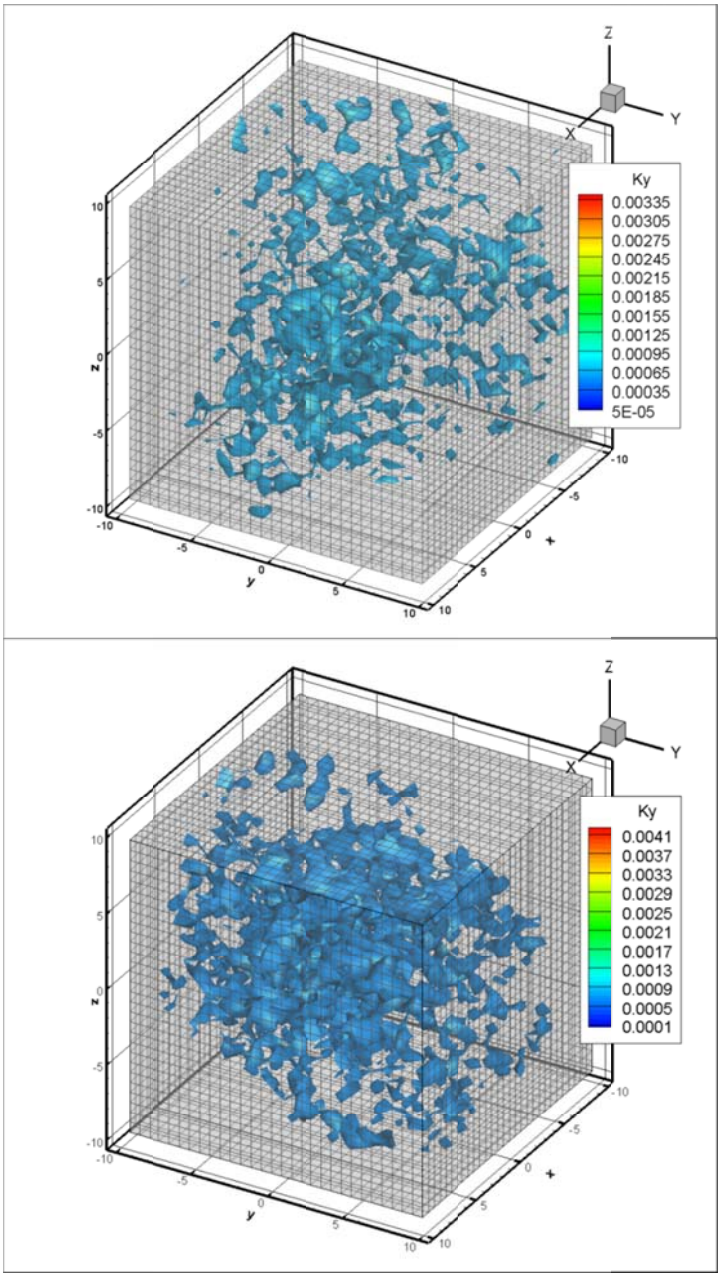

Figure 11B. The equivalent y- directional connectivity on FEM mesh of networks with Fisher von Mises (above, $\boldsymbol{k}$ = 2.8) and random orientation distribution (below).

I

II

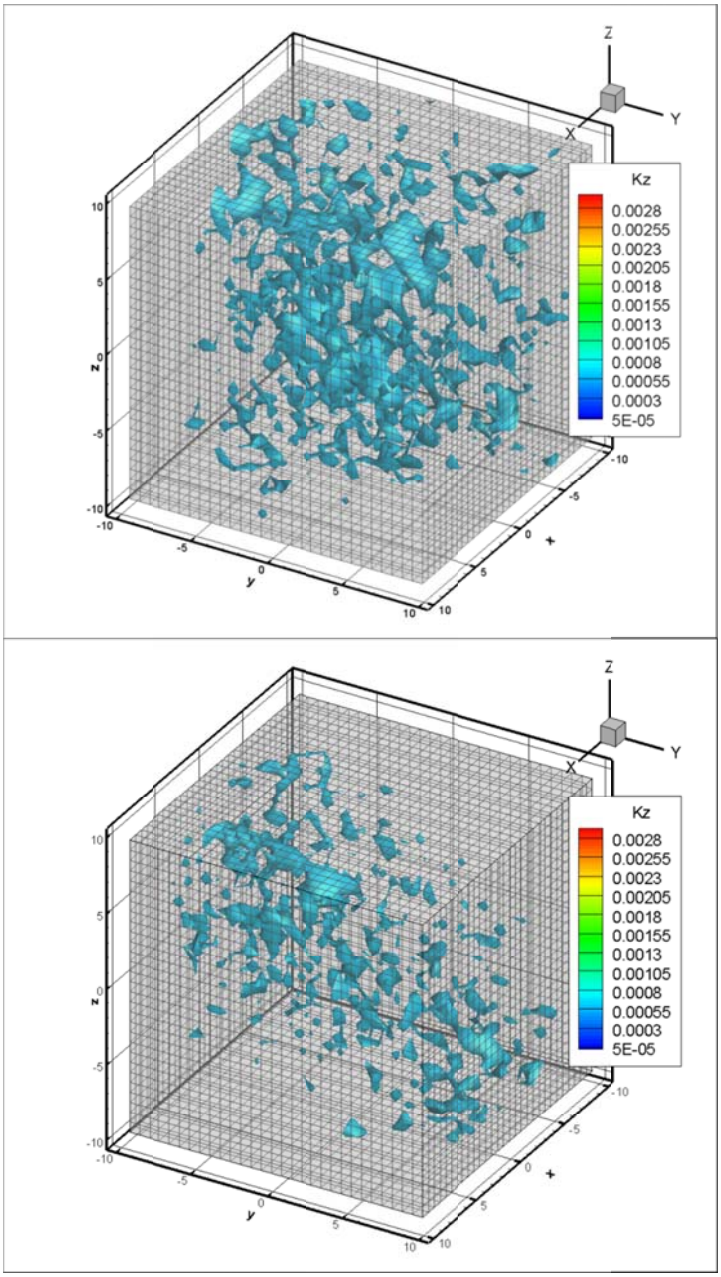

Figure 11C. The equivalent z- directional connectivity on FEM mesh of networks with Fisher von Mises (above, $\boldsymbol{k}$ = 2.8) and random orientation distribution (below).

I

II

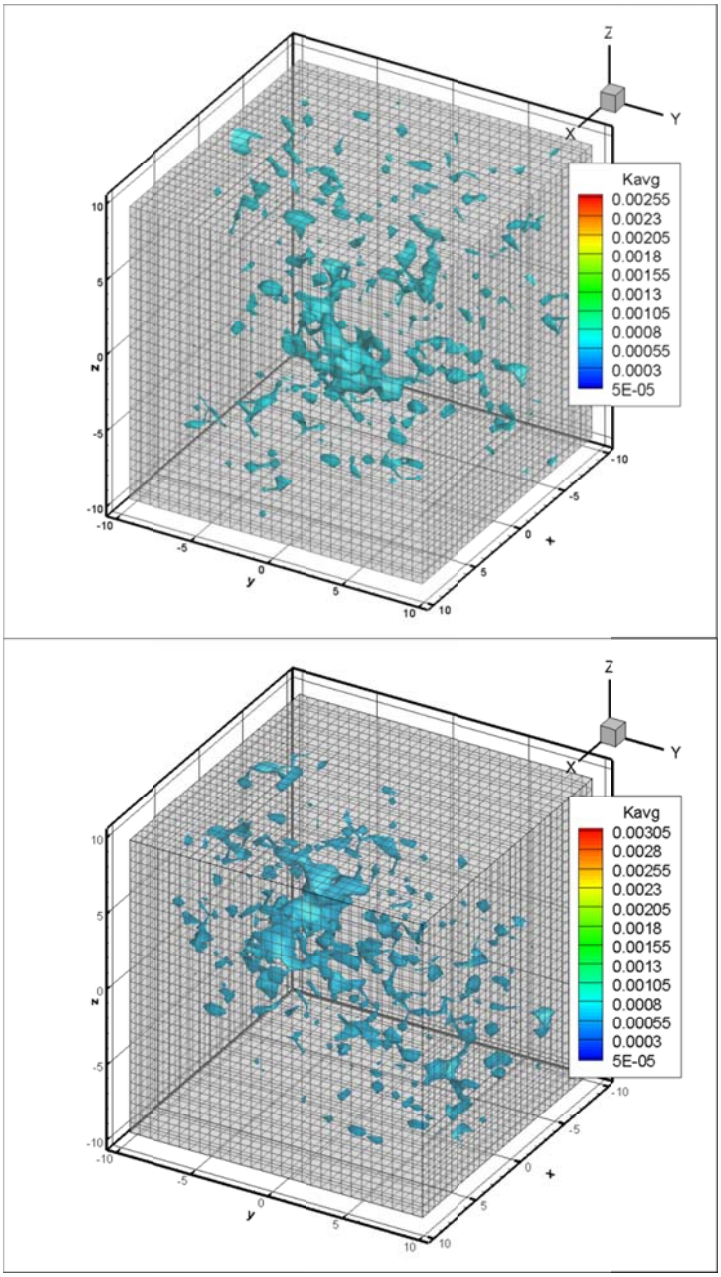

Figure 11D. The equivalent elemental average connectivity on FEM mesh of networks with Fisher von Mises (above, $\boldsymbol{k}$ = 2.8) and random orientation distribution (below).

The equivalent permeability is evaluated on each element's surfaces. Figure 12A-B shows the effect of mesh size on the permeability evaluation. The same two fracture groups -as above are used. The matrix block is discretized in to 1000, 8000, and 27000 elements for three test cases, respectively (I, II, III series in Figure 12A and B). We can see that after the fractures and the matrix elements are converted to a continuous media, the patterns of heterogeneity of the element conductivity are similar in all three cases (I, II, III) with different mesh sizes. However, as the mesh becomes finer, connectivity deteriorates. For the mesh with 27000 elements, most of the high conductivity zones are isolated. The isolated high conductivity zones will negatively impact fluid flow and heat transfer in the model. Comparing plots in

Figure 12A (Fisher von Mises distribution) with those in Figure 12B (random distribution), we can see that the randomly distributed cases have higher connectivity for all three mesh sizes.

I

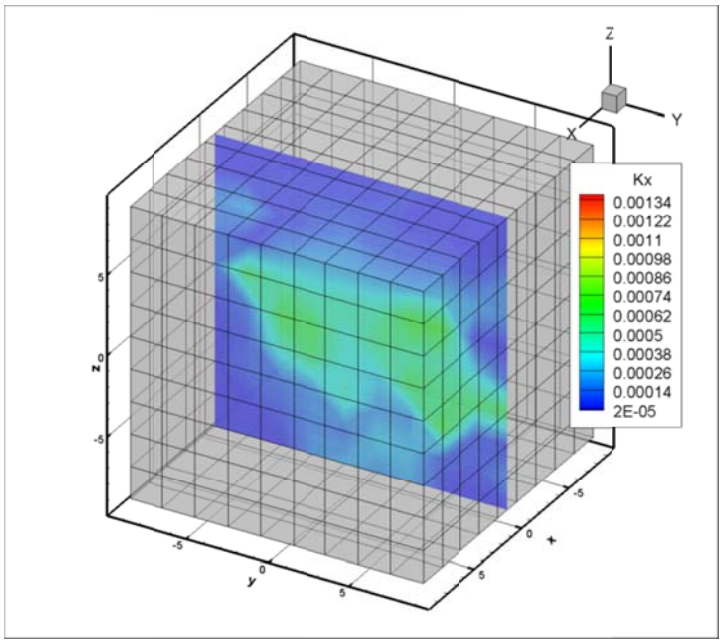

II

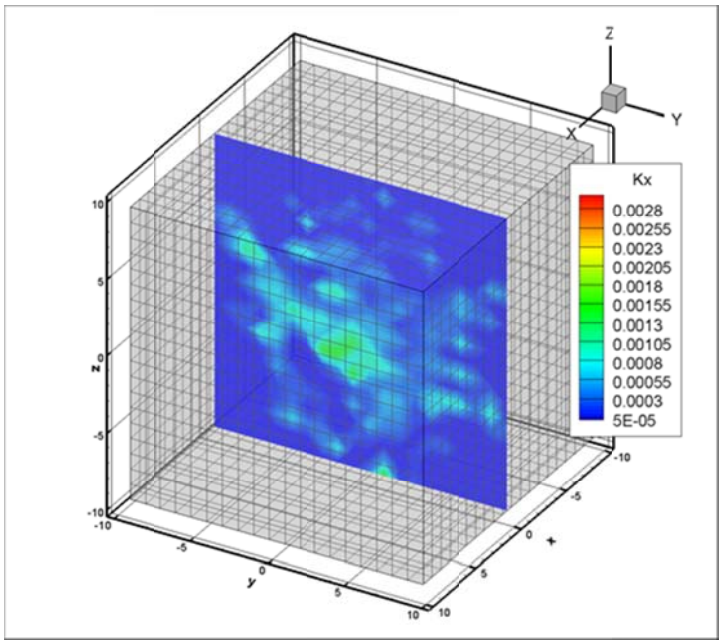

III

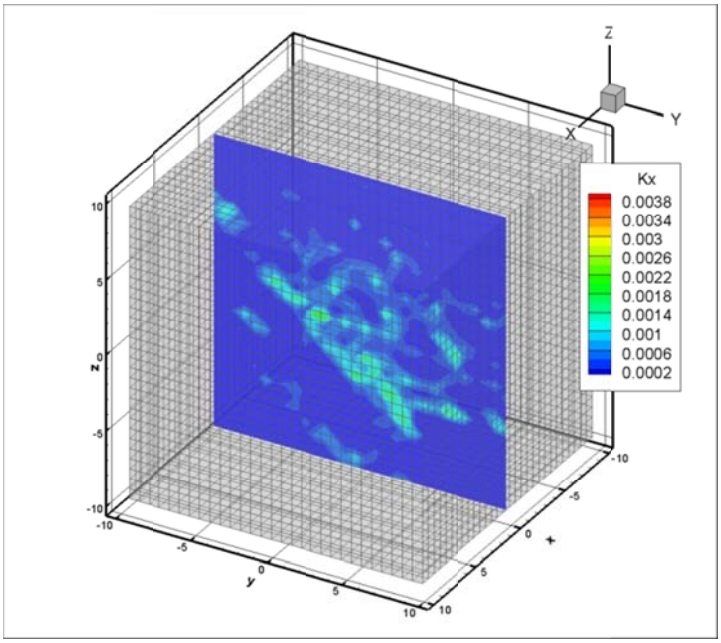

Figure 12A. The equivalent fracture connectivity on different mesh sized of networks with Fisher von Mises orientation distribution (***k*** = 2.8).

I

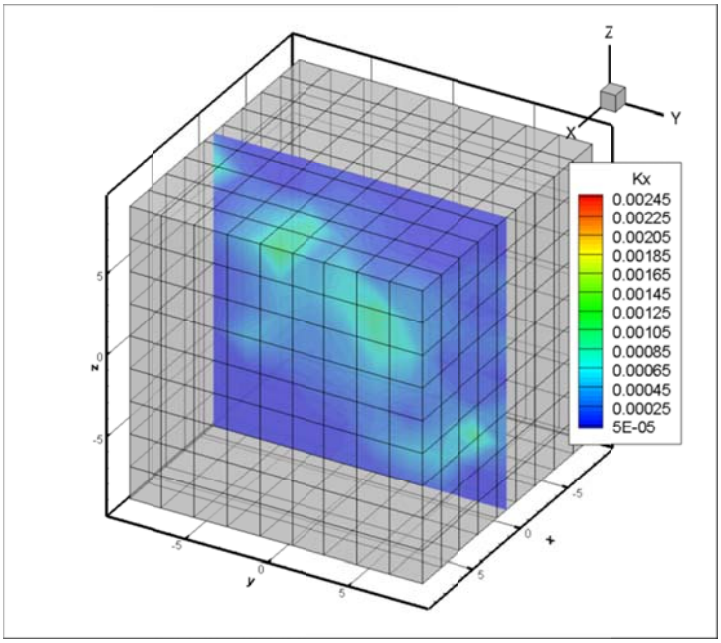

II

III

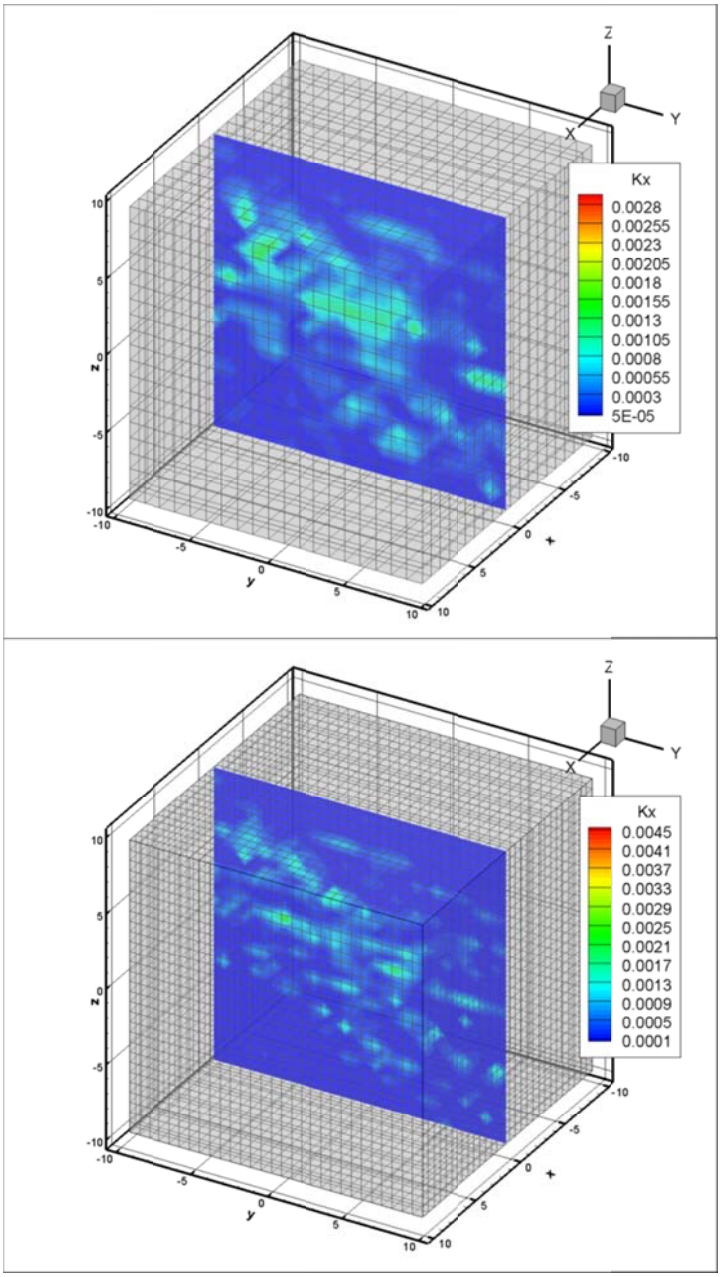

Figure 12B. The equivalent fracture connectivity on different mesh sized of networks with random orientation distribution.

Average permeability of the entire reservoir is used to evaluate the mesh size effect on fracture connectivity. Harmonic mean, geometric mean, and arithmetic mean are commonly used for permeability averaging of a heterogeneous reservoir. In practice, harmonic mean is used to get the effective permeability for layered-vertical flow. For a system with log-normal permeability distribution, the geometric mean approximation is better than harmonic or arithmetic averages (Warren and Price, 1961). However, some studies suggested that the effective permeability of 3D composite is a 1/3 power average (Equation 9) for log-normal system (Neotinger, 1994; Hristopulos and Christokos, 1999):

$$\overline{K} = (\frac{1}{n_{els}} \sum_{i=1}^{n_{els}} (K_i)^{1/3})^3 \quad (9)$$

where K_i is the variable of each elements, n_{els} is the total number of elements.

We use the 1/3 power average to approximate the average permeability of the entire block, and to quantify the mesh size effect on fracture connectivity. Figure 13 shows the correlation between mesh size and effective permeability of the entire reservoir. Two fracture networks with same stochastic parameters as in group (I) of Figure 11 are analyzed (fracture network with FVM orientation distribution). As the mesh becomes finer, the average permeability decreases and converges to some smaller value. Also, the curves for the two stochastic fracture networks in Figure 13 show that the horizontal permeability (x- and y- directions) is slightly higher than the vertical permeability (z- direction), which is consistent with the results from Figure 11.

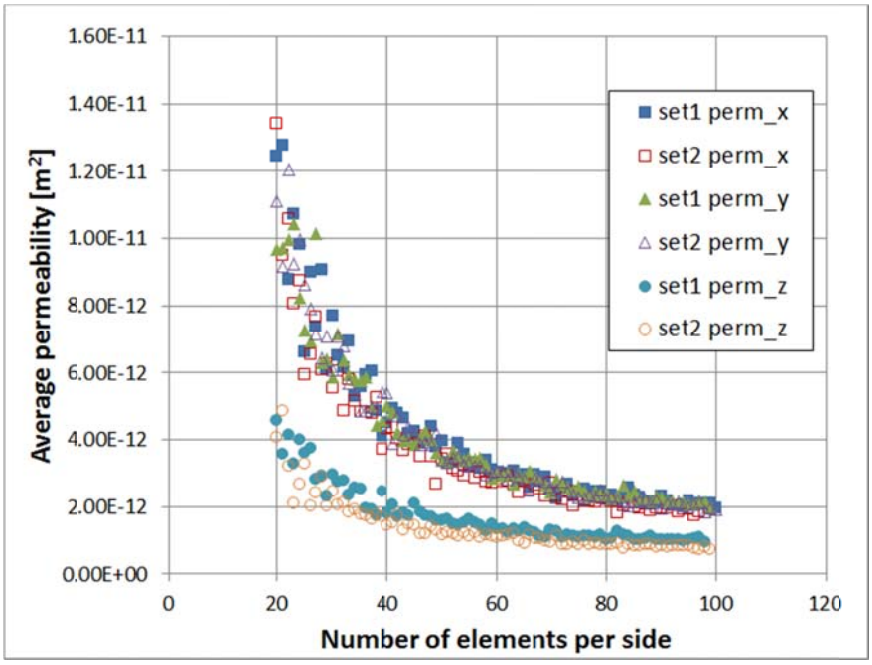

Figure 13. Change of overall average permeability with mesh size.

2.4.3 Heat transfer via fracture flow

In some cases, heat transfer can be de-coupled from mechanical response analysis. For example, heat flow (convection) in interconnected fracture network takes place so rapidly that the convection from adjacent rock to fracture can be ignored during the simulation time. Bi-linear heat transfer model include two parts: 1) 1D linear heat conduction from adjacent rock into fracture; and 2) 1D linear heat convection through channels formed by interconnected fractures (Figure 15, Equation 11). In this model, it is assumed that 1) fluid flow (heat convection) primarily occurs in channels within fractures; 2) heat conduction develops perpendicular to the fracture face; and 3) No heat is retained by the volume of fluid with in the fractures (Bruel 2002). In heat transfer calculations, the water flow through the rock matrix is ignored, therefore, the heat convection is confined within the interconnected fracture network. Assuming that no energy is retained by the fluid stored within the fracture, the energy conservation is obtained (Brue, 2002) at each

fracture center by balancing the heat convection (via fluid flow) and heat conduction between adjacent rock mass and the fluid in the fracture. It is assumed the temperature at fracture face is continuative (Brue, 2002):

$$T_f = T_m \text{ at y=0} \quad (10)$$

The energy balance equation can be expressed as:

$$\Delta E_i + \sum_j^{in} \rho_f C_f q_{ij} T_{fj} \Delta t = \sum_k^{out} \rho_f C_f q_{ik} T_{fk} \Delta t \quad (11)$$

Where $\Delta E_i = k_m S_i (\frac{dT_m}{dy})_{y=0} \Delta t$ denotes the energy from the heat flux at fracture walls which is governed by conduction (diffusive equation, Equation 12). q_{ij} and q_{ik} represents the fluxes flow in a given fracture *i*, from fracture *j* and flow out to fracture *k* with temperature T_{fj} and T_{fi}, respectively (Figure 14). The fluid exits to the fracture *k* having the same temperature as the current temperature in fracture *i*. Similarly, fluid flows from fracture *j* to fracture *i* having the same temperature as the current temperature in fracture *j*.

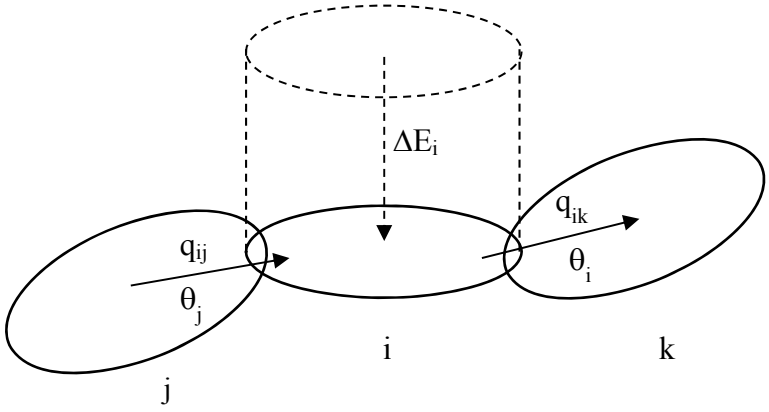

Figure 14. Energy conservation of fracture i.

The heat exchange across the fracture face can be described as (Brue, 2002):

$$dE_i = \Phi_i S_i dt$$

$$\Phi_i = k_m (dT_m / dy)_{y=0}$$

$$\alpha \Delta T_m = \frac{\partial T_m}{\partial t} \quad (12)$$

The above diffusive equation is solved using the finite difference method. Given the fracture temperature at time *t*, the solution will return the temperature distribution from the fracture face to the other end of the rock cylinder. After that, the heat flux Φ_i can be obtained and the energy exchanged (ΔE_i) calculated. At

each fracture center, one energy balance equation is set up, and the set of equations is solved for q_{fi} at each time step. Parameters that appear in the above equations are ρ_f and ρ_m are the fluid and rock density respectively, C_m is the solid heat capacity, α_m is the heat diffusivity of rock mass, S_i is the fracture face area, and k_m is the heat conductivity of rock mass.

The shape of the heat source rock block is assumed to be cylindrical with a radius equal to the fracture radius. The length of the cylinder is chosen so that the temperature on the other end of the cylinder remains unchanged during stimulation (Marin, 2010). The results show that the temperature changes will not develop at a long distance within test time period. Therefore, the cylinder to cylinder interaction and the thermal stress effects are ignored at this stage. According to characteristic length definition (Marin, 2010), the length of a cylinder of rock with a heat diffusivity of 1.15×10^{-6} m^2/s, is approximately 12 m. This length ensures the temperature on the opposite end of the matrix block is unchanged during one year of heat transfer. The 1D heat diffusive equation for heat conduction can be written as

$$\frac{k_m}{\rho_m C_m}\frac{\partial T_m^2}{\partial y^2} = \frac{\partial T_m}{\partial t} \tag{13}$$

Defining $\alpha_m = \dfrac{k_m}{\rho_m C_m}$, then equation (13) becomes:

$$\alpha_m \frac{\partial T_m^2}{\partial y^2} = \frac{\partial T_m}{\partial t} \tag{14}$$

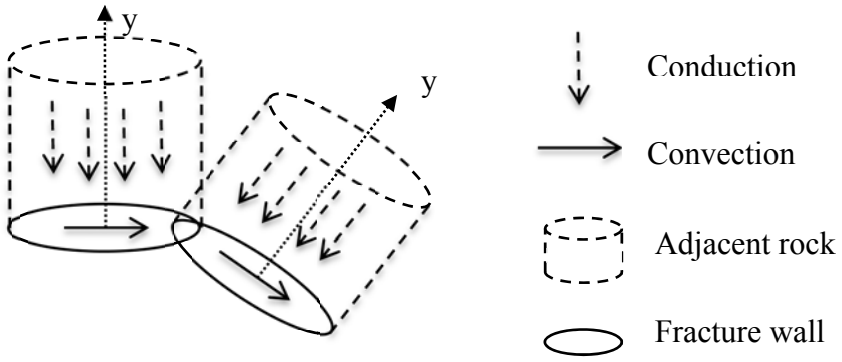

Figure 15. Bi-linear heat transfer in interconnected fracture network.

It is easier to solve above equation using Finite Difference Method (FDM) than using FEM. The right hand side can be discretized in y- coordinate direction as:

$$\frac{\partial T_m^2}{\partial y^2} = \frac{T_m(i+1) - 2T_m(i) + T_m(i-1)}{(\Delta y_i)^2} \tag{15}$$

The one dimensional heat conduction takes place in a cylinder which has a cross section area of $A = \pi r^2$. Therefore, the volume of each element (i) has a volume of $V_i = \pi r^2 \Delta y_i$. We can then write the discretized form of equation (14) as:

$$\frac{\alpha_m A}{\Delta y_i}\left[T_m(i+1) - T_m(i)\right] + \frac{\alpha_m A}{\Delta y_i}\left[T_m(i-1) - T_m(i)\right] = V_i \frac{T_m(t1) - T_m(t0)}{\Delta t} \qquad (16)$$

If we use uniform element size, i.e. $\Delta y = const.$, then according to central differentiation, we can denote the coefficients as

$$K_T(i+) = K_T(i-) = \frac{\alpha_m}{(\Delta y)^2} \qquad (17)$$

And finally the diffusion equation can be written in matrix form as

$$(1 - K_T \Delta t) T_m(t1) = T_m(t0) \qquad (18)$$

The temperature distribution ($T_m|_y$) in the rock cylinder at time t can then be calculated. The temperature gradient dT_m / dy at fracture wall is needed in the heat convection calculation as the heat gain of the fracture from adjacent rock. In this model it is approximated by $(T_{m1}\text{-}T_{m0})|_t / \Delta y$.

In the heat transfer part, the fluid flow is confined within the connected fracture networks. Therefore, it is necessary to find out the connected fractures. A search algorithm is used to determine the connectivity. Every fracture is checked whether or not it belongs to a connected flow path. Then, dead ends and isolated fractures are removed. An iterative analysis is employed to do the searching.

In order to solve the system of equation for heat transfer, the fluid flow in fracture network need to be solved first. As explained in the equivalent permeability section, fluid flow is confined within fracture networks. Fluid flow in fractures is assumed to be similar to that of parallel surfaces. Then the cubic law provides the volumetric flux (m^3/s) through a fracture with aperture a and length l:

$$Q = \frac{-a^3 l}{12\mu} \frac{dp}{dl} \qquad (19)$$

The flow network considers each connected fracture as a 1D pipe linking the centers of adjacent fractures (Figure 16). Let k_i and k_j represent the conductivity of fracture i and j, and let p_i and p_j be the pore pressure at each fracture center. L_i and L_j are the channel length in fracture i and j, respectively. The volumetric flow rate between fractures i and j can be write as:

$$Q_{ij} = k_{ij} \frac{p_i - p_j}{L_i + L_j};\ k_{ij} = \frac{L_i + L_j}{L_i / k_i + L_j / k_j} \qquad (20)$$

Conductivity of each fracture can be obtained from the modified cubic law:

$$k_i = \frac{-a_i^3 L_i}{12\mu} \tag{21}$$

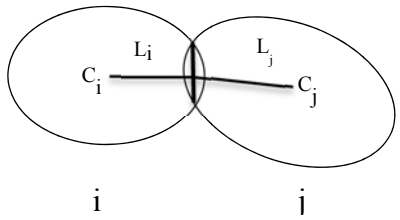

Figure 16. Flow channel between two connected fractures. C_i and C_j are centers of fractures i and j, L_i and L_j are the channel lengths in fractures i and j, respectively.

The system of equations for solving fluid flow between fractures can be generalized using flow-in equals to flow-out $\sum_i Q_{ij} + source = 0$ (22)

$$[K_T][[p] = [Q] \tag{23}$$

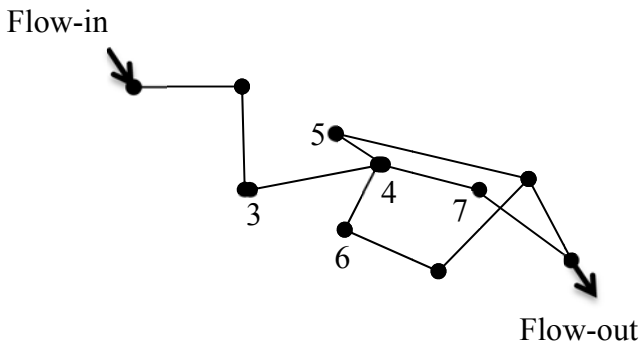

Figure 17. An example of pipe model for interconnected fracture network.

Taking node 4 in Figure 17 as an example, the above matrix equation can be expanded as

$$\begin{bmatrix} & & & & & & & & & \\ & & & & & & & & & \\ 0 & 0 & \frac{K_{34}}{L_{34}} & -\sum \frac{K_{ij}}{L_{ij}} & \frac{K_{45}}{L_{45}} & \frac{K_{46}}{L_{46}} & \frac{K_{47}}{L_{47}} & 0 & 0 & 0 \\ & & & & & & & & & \end{bmatrix} [p_i] = \begin{bmatrix} \vdots \\ \vdots \\ Q_4 \\ \vdots \\ \vdots \end{bmatrix} \tag{24}$$

where $\sum \frac{K_{ij}}{L_{ij}} = \frac{K_{34}}{L_{34}} + \frac{K_{45}}{L_{45}} + \frac{K_{46}}{L_{46}} + \frac{K_{47}}{L_{47}}$;

$[p_i] = [p_1, p_2, p_3, p_4, p_5, p_6, p_7, p_8, p_9, p_{10}]$;

$[Q_i] = [q_{in}, 0, 0, 0, 0, 0, 0, 0, 0, q_{out}]$.

After obtaining the nodal pore pressure, using Equation (20) we can find out the q_{ij} terms in Equation (11). And finally we can solve for the temperatures in each fracture. Figure 18 shows the result of a 2D pipe network example, and Figure 19 shows the result of a 3D pipe network example. All interconnected fractures are represented as pipes.

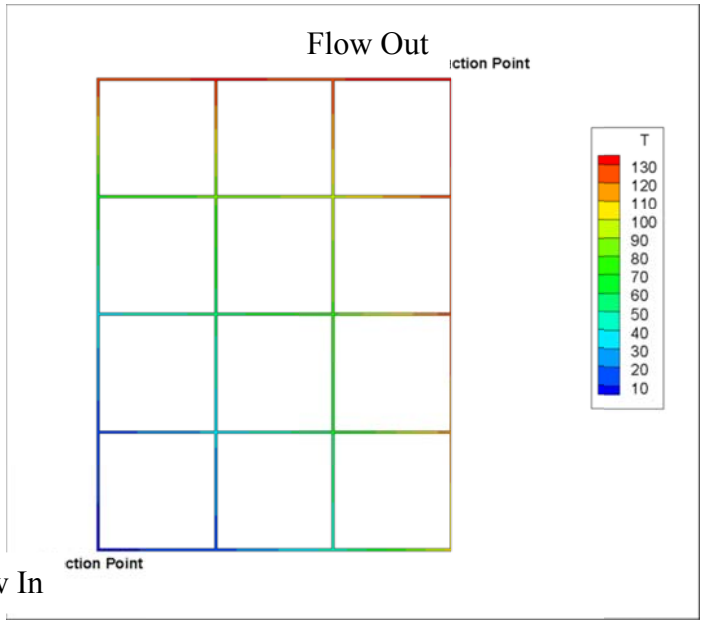

Figure 18. Temperature distribution in 2D channels formed by 1D pipes.

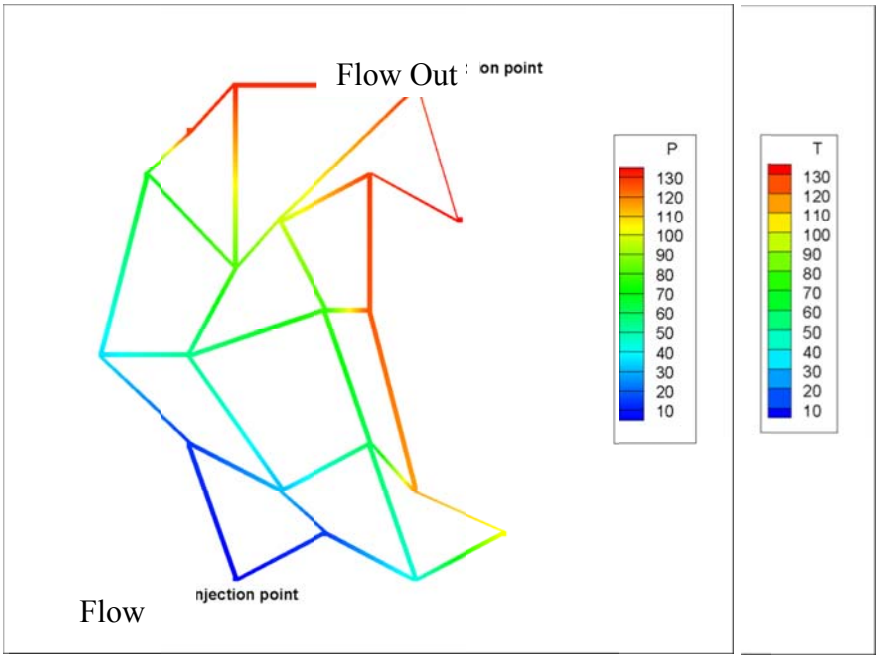

Figure 19. Temperature distribution of a 3D pipe network.

2.5 Fracture Slip, Seismicity, and Permeability Enhancement

Fracture dilates during shear slippage. As the shear stress acting on fracture surface exceeds fracture shear strength, shear failure occurs and induces rock deformation of the surface of rupture. This permanent displacement is referred as shear displacement which has significant influence on permeability improvement of natural fractures. Shear slippage criterion can be derived from the theory of shear failure using the linear Mohr-Coulomb criterion. Using Patton's method (Patton 1966), the shear strength of the fracture can be calculated as:

$$\tau_p = \sigma' \tan\left(\varphi_{basic} + \varphi_{dil}^{eff}\right) \tag{25}$$

where σ' is the effective normal stress acting on fracture surface. φ_{basic} is the basic friction angle which is a material property of the fracture surface, usually varies between 30˚ and 40˚ (Rahman et al. 2002). φ_{dil}^{eff} is the effective shear dilation angle which is related to the roughness of fractures, can be calculate from laboratory-measured dilation angle, φ_{dil} as:

$$\varphi_{dil}^{eff} = \frac{\varphi_{dil}}{1+9\sigma'/\sigma_{nref}} \tag{26}$$

σ_{nref} is the effective normal stress which causes 90% closure of the compliant aperture. When the shear stress on fracture surface exceeds the shear strength, shear slippage occurs. And the resulted shear displacement can be estimated by:

$$U_s = \frac{\tau_n - \tau_p}{K_s} \tag{27}$$

τ_n is the shear stress applied on fracture surface. τ_p is the shear strength described above. K_s is the fracture shear stiffness, can be expressed as:

$$K_s = \gamma \frac{G}{r} \tag{28}$$

γ is a geometric parameter which is used as $\frac{7\pi}{24}$ in this model (Eshelby, 1957). r is the penny shape fracture radius. G is the surrounding material shear modulus.

The change in aperture due to excessive shear stress can be calculated from shear displacement, as:

$$a_s = U_s \tan(\varphi_{dil}^{eff}) \tag{29}$$

When the fracture surfaces are in contact, the "in contact" fracture aperture is given by (Willis-Richards et al. 1996):

$$a = \frac{a_0}{1 + 9\sigma' / \sigma_{nref}} + a_s + a_{res} \tag{30}$$

where a_{res} represents the residual aperture at high effective stress, taken to be zero in this model. a_0 is the initial total compliant aperture of the fracture. And a_s is the aperture change due to shear slippage, as discussed above.

For fully open fractures, the opening aperture is the normal displacement multiplied by 2. For a circular shape fracture of radius *R* under normal stress σ_n, the normal displacement of any point of the crack surface is given by (Jaeger and Cook, 1969):

$$u(r) = \frac{2(1-\upsilon)}{\pi G} \sqrt{R^2 - r^2} \tag{31}$$

Resulting in the maximum width at the center:

$$a = \frac{4(1-\upsilon)R}{\pi G} \tag{32}$$

The volume of the penny shaped crack is obtained from:

$$V = \int_0^R 2\pi r \left(\frac{4(1-\upsilon)R}{\pi G}\right) dr = \frac{8(1-\upsilon)R^3 \sigma_n}{3G} \tag{33}$$

Indicating an average aperture of:

$$\bar{a} = V / \pi R^2 = \frac{8(1-\upsilon)R\sigma_n}{3\pi G} \tag{34}$$

The updated aperture due to new stress distribution will be input for the equivalent permeability calculation of next time step as described previously.

The magnitude of radiated elastic energy is calculated according to McGarr et al. 1979 and Hanks and Kanamori, 1979. The seismic moment due to slip "U_s" over the slip area, can be obtained from:

$$M_0 = \int_{\Sigma} G U_s dA \tag{35}$$

G is the shear modulus of the rock. The magnitude of a mini-earthquake generated by the slippage can then be estimated as:

$$M = (\frac{2}{3}) \log_{10} M_0 - 10.7 \tag{36}$$

2.6 Analysis of Near Wellbore Response

This simulation focuses on utilizing a stochastic fracture network and poroelasticity to simulate the thermal-hydro-mechanical response of near wellbore fractured zone during the fluid injection process, and to assess the permeability enhancement in the stimulated zone. The fractured geothermal reservoir is modeled using a system of rock blocks some of which contain stochastically-distributed fractures and fractured zones. The effect of the fractures on permeability is introduced into the model by using the equivalent permeability approach. The rock matrix is assumed to be poroelastic and the fractures are allowed to deform and to slip. Heat transport within the fractures and the associated thermal stress on the rock is also considered. A series of simulations are carried out to analyze the rock mechanical response and permeability evolution for a Newberry-type reservoir. In granitic fractured reservoirs, like Newberry-Tuff, the overall fluid flow pattern is dominated by flow within the interconnected natural fracture network, since the conductivity of fractures is much higher than intact rock. However, the heat energy is stored in the rock mass surrounding the fractures, and it takes time to heat-up the fracture fluid to a desirable temperature. Therefore, to engineer a geothermal system, one need to enhance the permeability/connectivity of the pre-existing natural fractures without creating massive hydraulic fractures.

2.5.1 Stochastic fracture network

In this work, a natural fracture network of 500 penny-shape cracks is introduced into the poroelastic model (Figure 20). The 3D hydraulically conductive fracture network is generated using stochastic descriptions of its characteristics: Poisson distribution for fracture location, log-normal distribution for fracture size, and Fisher von-Mises distribution for fracture orientation. The parameters of these distributions are usually found from field tests or experimental data. The fracture data can be complied in to form a network by defining location, size, and orientation of the fractures. One of such stochastic fracture network (Table 1) is shown in Figure 20. The parameters of the fracture distribution used herein are from fracture analysis of Newbery field (AltaRock 2011), and from empirical suggestions (Cacas et al. 1990). Fracture apertures are assigned following the relationship with the fracture size (Tezuka 20005):

$$a = \alpha \sqrt{r} \tag{39}$$

Table 1. Parameters of the probability functions of stochastic fractures in Figure 20.

Density [m^{-1}]	1.0
Mean of the log(radius) [radius in meters]	0
Standard deviation of the log(radius) [radius in meters]	0.7
Fisher von Mises distribution parameter	2.8
α	4.0 X10^{-3}
Number of fractures	500

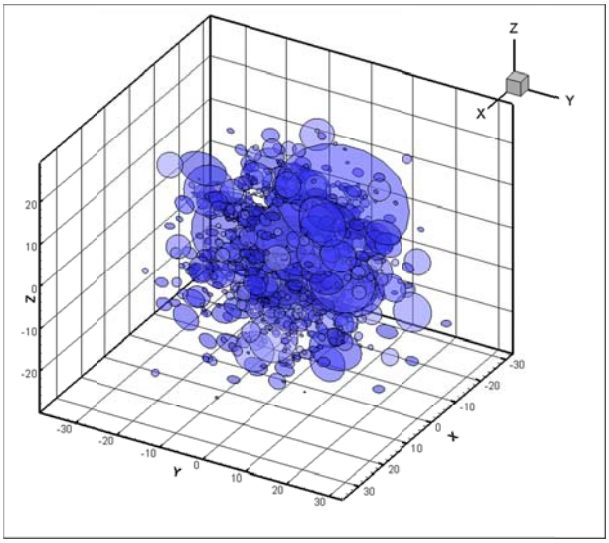

Figure 20. A stochastic fracture network.

2.5.2 Model set-up

In order to investigate the near wellbore reaction, a small scale reservoir model of size 40 m × 40 m × 20 m is considered. Figure 21 shows the simulation domain with selected finite element mesh, and Figure 22 shows the fractured zone that contains 500 stochastic fractures (half domain). Rock properties are from experiment conducted on Newbery Tuff core plugs (Li et al. 2012). A constant wellbore pressure increment is applied to this model. The outer boundary of the reservoir block is assumed to be a no flow boundary.

Table 2. Parameters used in near wellbore simulation.

Rock properties		**Fracture properties**	
Model size (m^3)	40 x 40 x 20	Fracture density(m^{-1})	1
Young's modulus(GPa)	27.24	Fisher parameter, κ	2.8
Poisson's ratio	0.4	Mean fracture radial (lognormal)	0
Skempton's coefficient	1	Standard deviation of fracture radial, s	0.7
Matrix permeability (md)	5		
Porosity	0.025	Fracture basic friction angle (°)	50.2

Fluid density (kg/m^3)	1000	**Stress State**	
Fluid bulk modulus (MPa)	3291	Vertical stress (MPa)	67
Fluid viscosity (Pa s)	1.0 x 10^{-4}	Maximum horizontal stress (MPa)	62
Fluid viscosity (Pa s)	1.0 x 10^{-4}	Minimum horizontal stress (MPa)	41
Shear dilation angle (˚)	3.0	In-situ pore pressure (MPa)	25
90% closure stress (MPa)	100	Injection pressure (MPa)	5

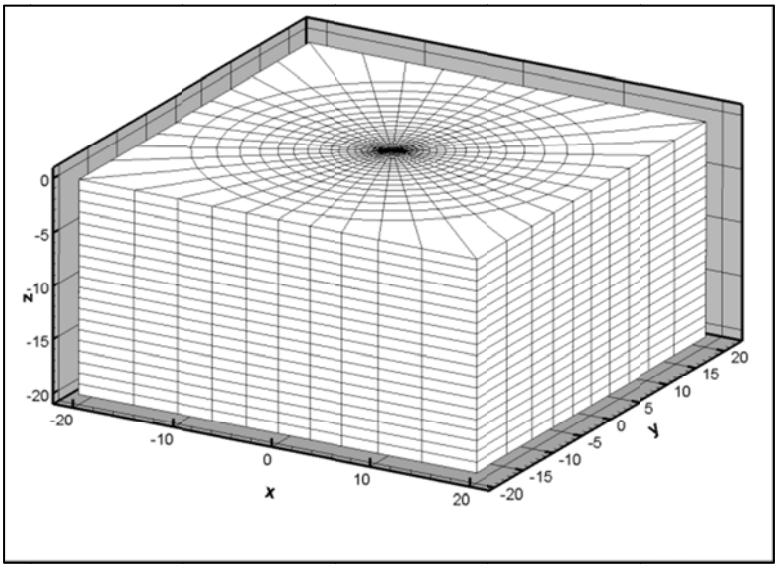

Figure 21. Finite Element mesh of a small scale reservoir model.

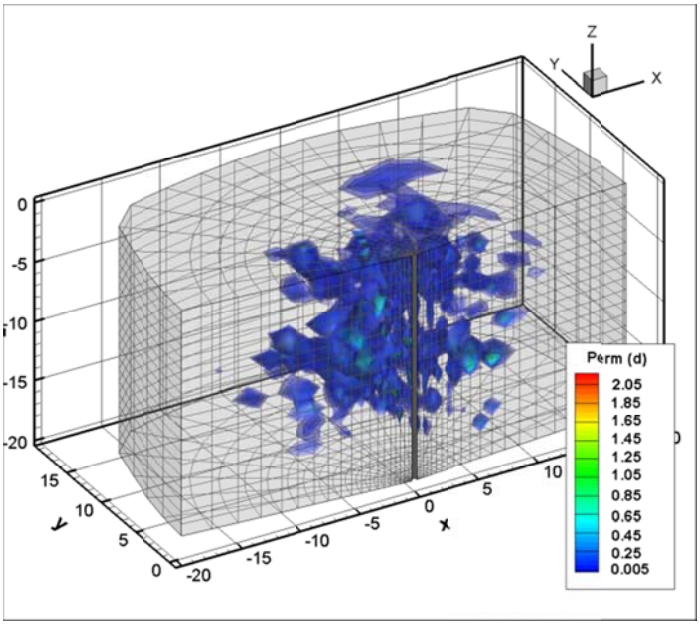

Figure 22. Fractured zones shown in half domain. Color bar shows the equivalent permeability of the fractured zone.

2.5.3 Simulations and results

Pore pressure developments after 2 hours of injection and the corresponding micro-seismic events are plotted in Figure 23 and Figure 24, respectively. Figure 23 shows the pore pressure distribution of three fracture networks with different stochastic parameters. In these figures, κ is the fracture orientation parameter and s is the fracture size parameter (Table 2). We can see from both the pore pressure and the seismic clouds that the fracture properties dramatically influence the stimulation results. The seismic events of the fracture network with fisher von Mises orientation distribution are limited near the injection well. The randomly distributed fracture network has a larger zone of micro-seismic events and higher pore pressure build up. The fracture size also has influence on the permeability improvement result (Figure 24B and C). The location of shear slippage is different from each case. This phenomenon indicates the important role of characterizing fracture properties for reservoir stimulation modeling and design.

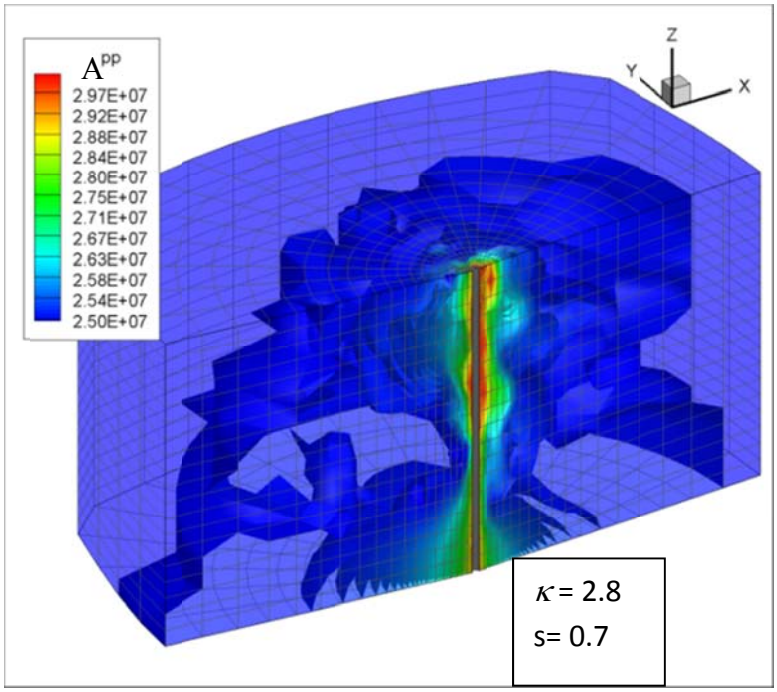

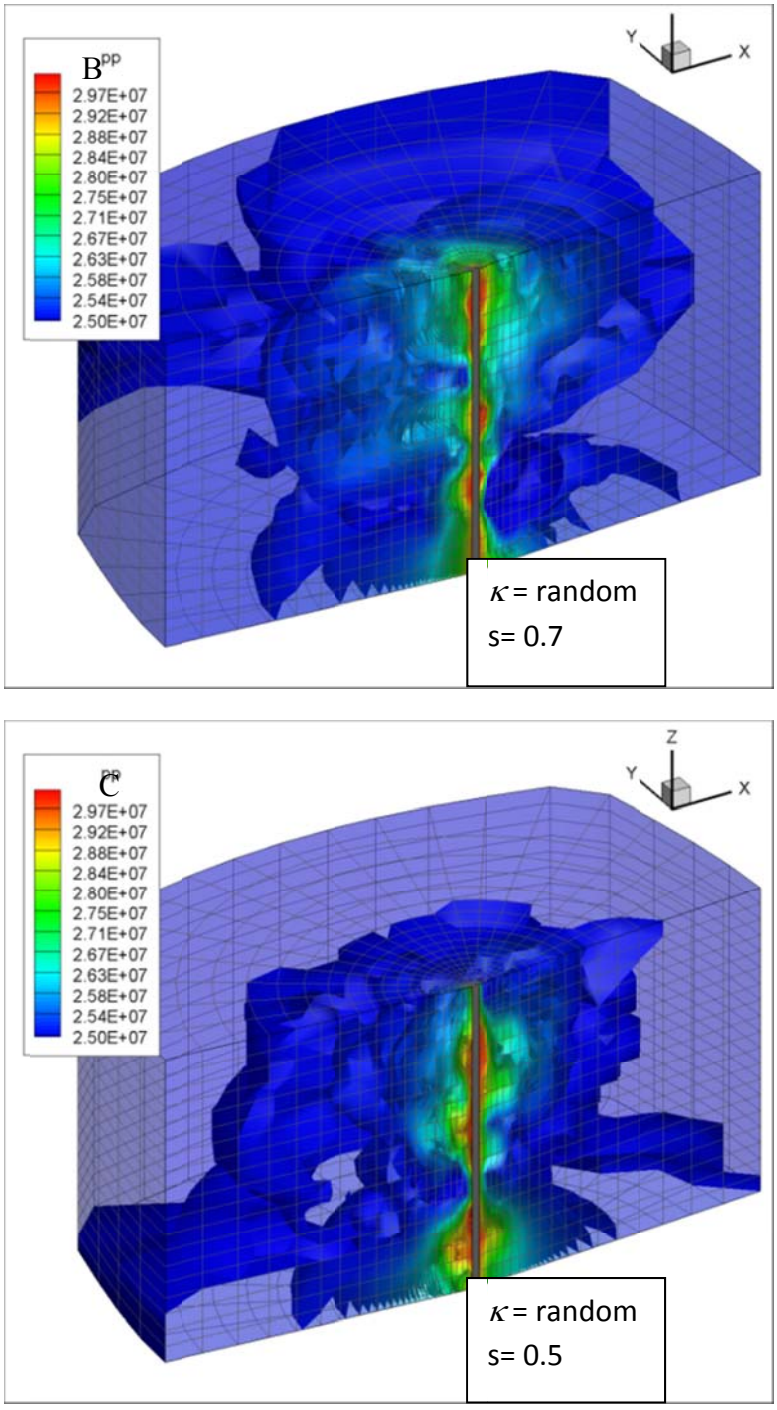

Figure 23. Pore pressure development at t = 2 hour in the fractured reservoir.

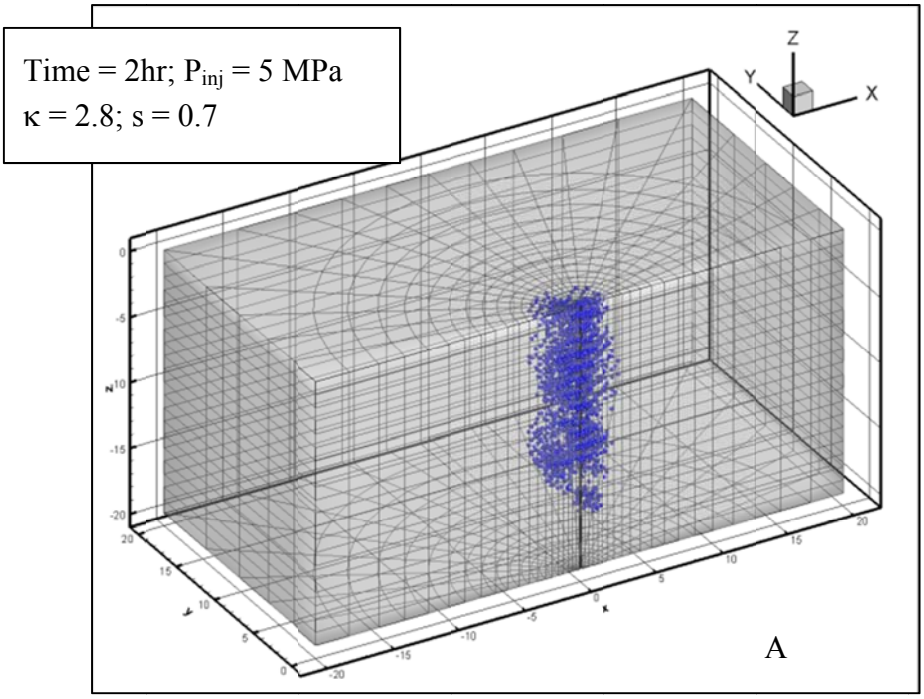
Time = 2hr; P_{inj} = 5 MPa
κ = 2.8; s = 0.7
Z
Y
X
A

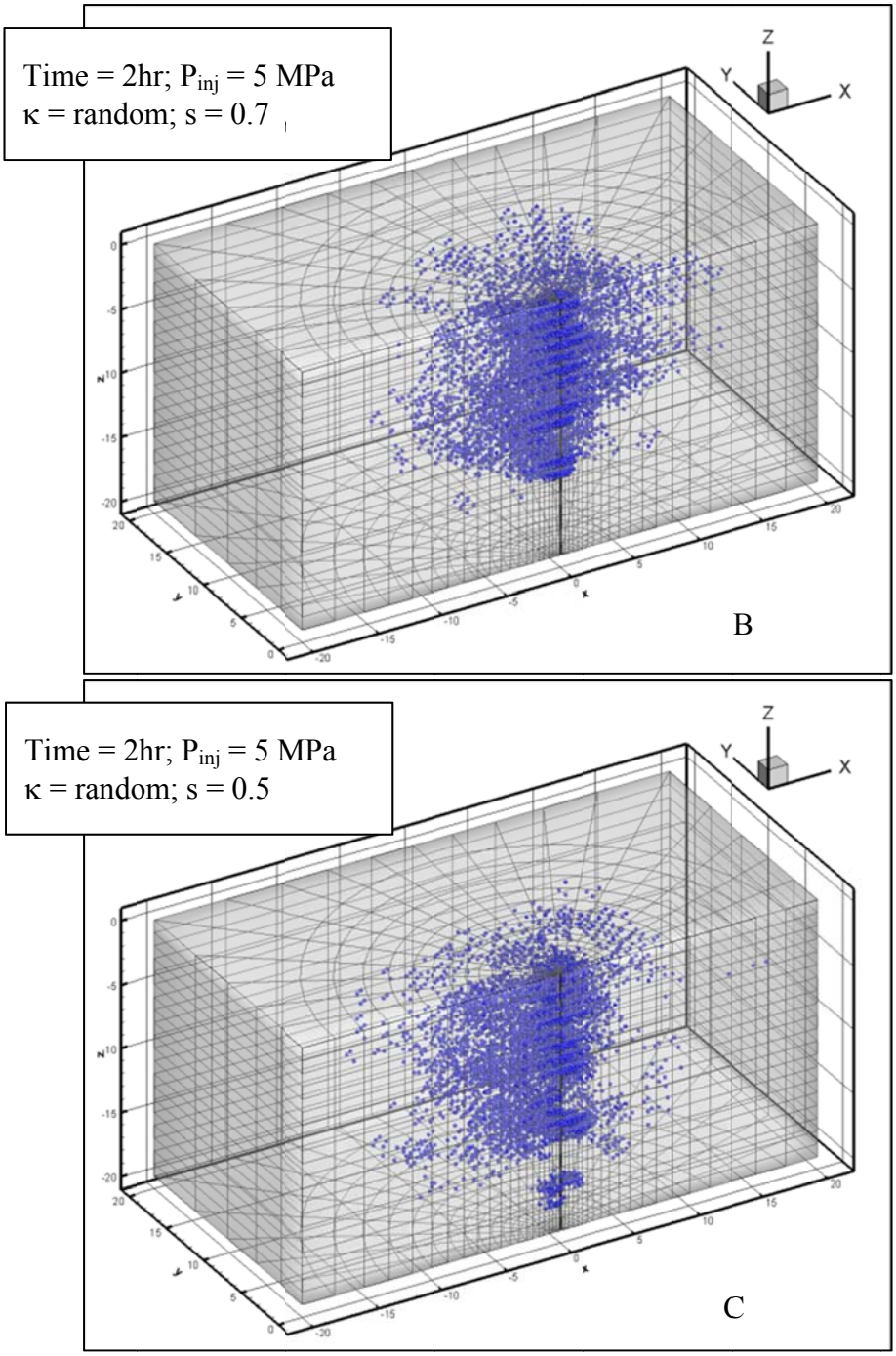

Figure 24. Micro-seismic events at t = 2 hour of three blocks with different fracture properties.

To illustrate the permeability improvement, Figure 25 shows the comparison of injection in two reservoirs have the same fracture networks, but with different rock type. One of them (group B) is assumed to have rigid rock which does not allow failure during the injection. The other one (group A) has the same rock type as tested before. We can see that before shear dilation happens, the pore pressure distributions are the same in both reservoirs. After shear dilation, the pore pressure distribution in rock A is affected by the updated permeability, and higher pore pressure is shown in the upper zone (Figure 25 A2). We can see

from Figure 25 A3 and B3, after 10 hours of injection, the pore pressure built-up in reservoir A has been delayed. Higher reservoir pressure is shown in Figure 25 B3. This observation resulted from the fracture opening and permeability increasing in reservoir A.

A1

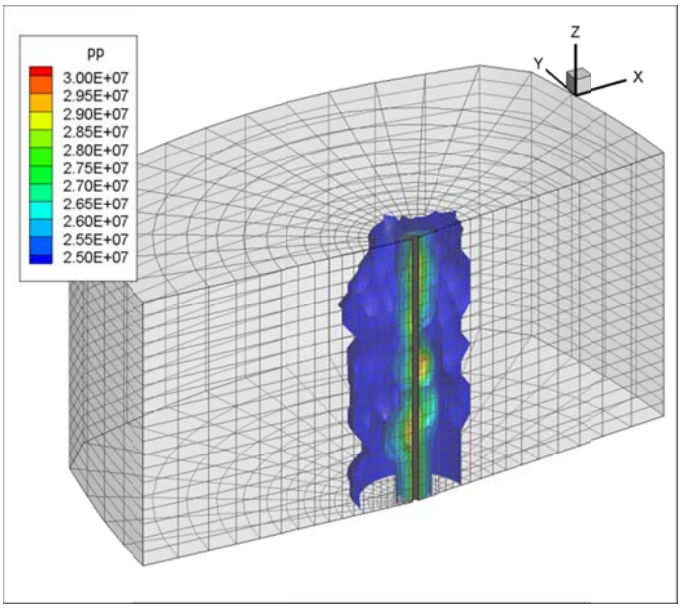

B1

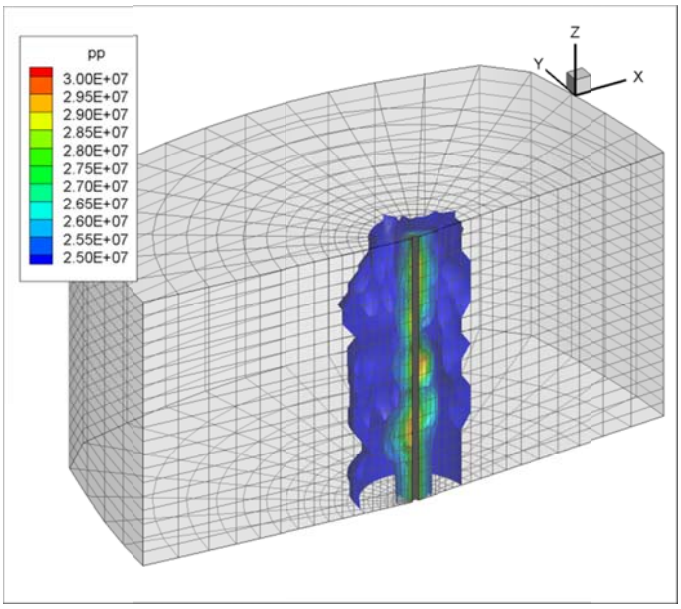

A2

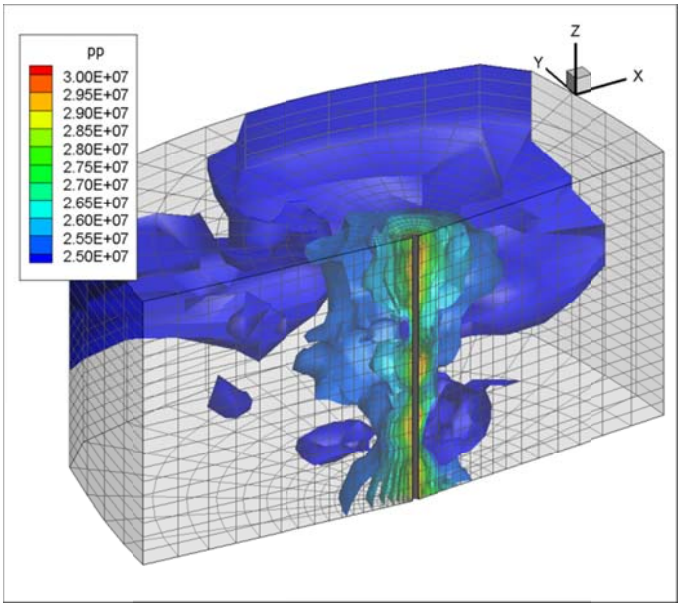
pp
3.00E+07
2.95E+07
2.90E+07
2.85E+07
2.80E+07
2.75E+07
2.70E+07
2.65E+07
2.60E+07
2.55E+07
2.50E+07
Z
Y
X

B2

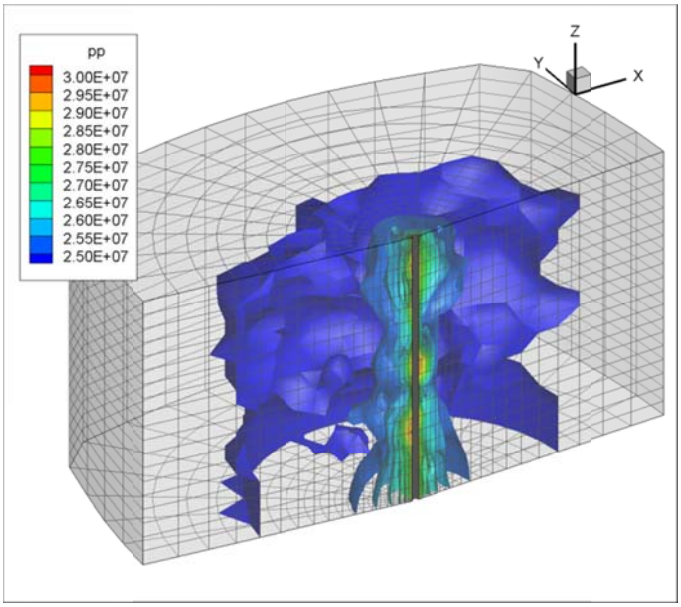
pp
3.00E+07
2.95E+07
2.90E+07
2.85E+07
2.80E+07
2.75E+07
2.70E+07
2.65E+07
2.60E+07
2.55E+07
2.50E+07
Z
Y
X

A3

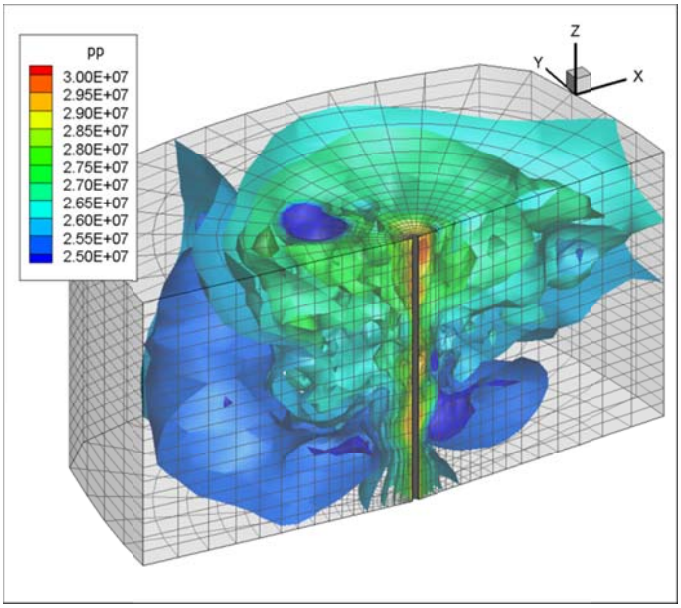

B3

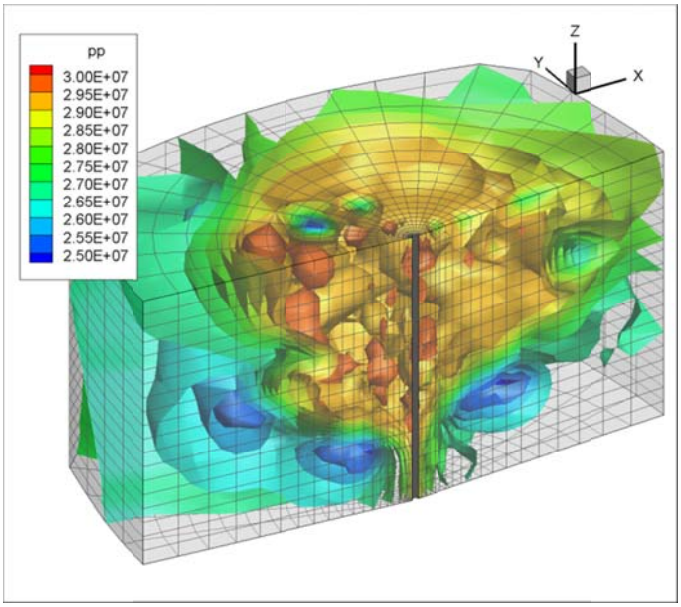

Figure 25. Iso-surfaces of pore pressure distribution for reservoirs with (A) and without (B) permeability improvement at (1) t = 0 hour, (2) t = 2 hour, and (3) t = 10 hour of injection.

The flow rate vs. time profile of the above two reservoirs is shown in Figure 26. The green line shows the flow rate profile of a permeability improved reservoir. Red line shows the flow rate profile of rigid rock reservoir. We can see that, in the stimulated reservoir, the flow rate increases quickly after the shear dilation. Figure 27 shows the seismic events at t = 5 hour, when a large of flow rate is observed in Figure 26. Large shear slippages are recorded, which is one of the reasons for the large increase of flow rate at t = 5 hour (the well pressure is maintained constant during injection). The flow rate will also increase when the injection fluid front reaches the higher permeability zones. Therefore, we can see periodic increase of flow rate from both curves. To show the permeability improvement, slices of permeability contours of the reservoir A at t = 4 hour and t = 5 hour are plotted in Figure 28. Permeability changes at all locations of

shear slippage shown in Figure 27. But, all the change cannot be shown in a single contour map because of the rather broad range of permeability values (5×10^{-16} m^2 to 6.2×10^{-8} m^2) with the simulation domain. Therefore, only the values in the range of 2.5×10^{-13} m^2 to 8.5×10^{-11} m^2 are plotted in Figure 28 for illustration purpose. The results show the correlations between seismic events, permeability improvement, and flow rate increase.

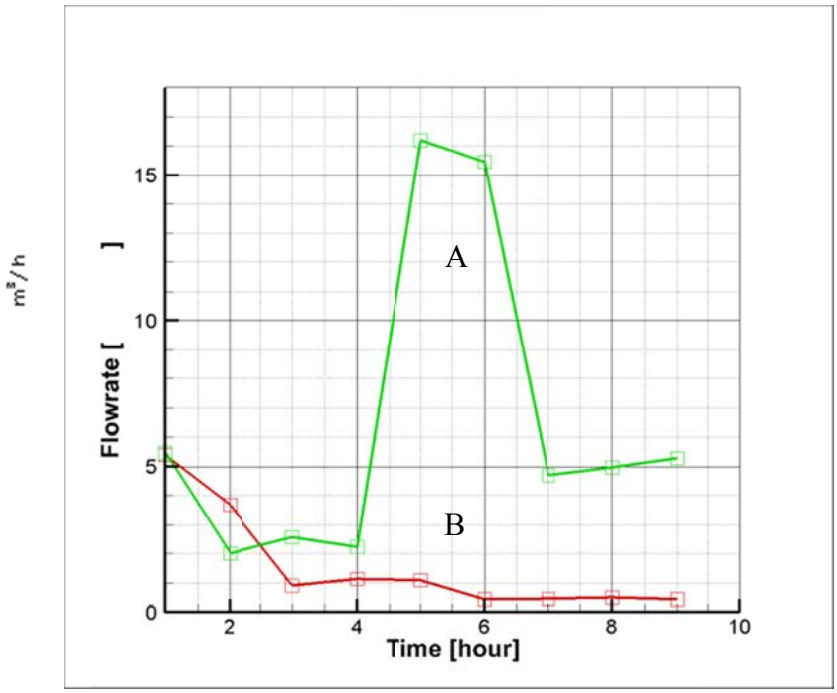

Figure 26. Wellbore flow rate profiles with time for reservoirs with (A) and without (B) permeability improvement.

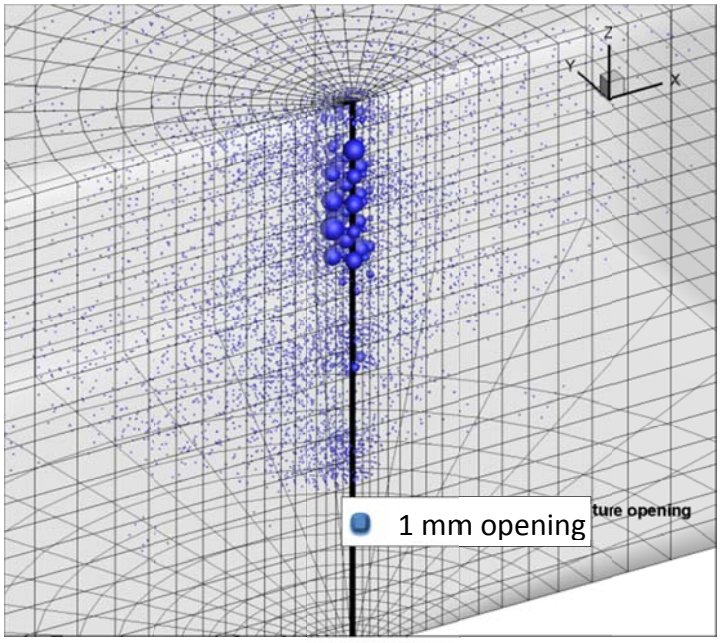

Figure 27. Micro-seismic events plot at t = 5 hours. Bubble size indicates the shear slippage value.

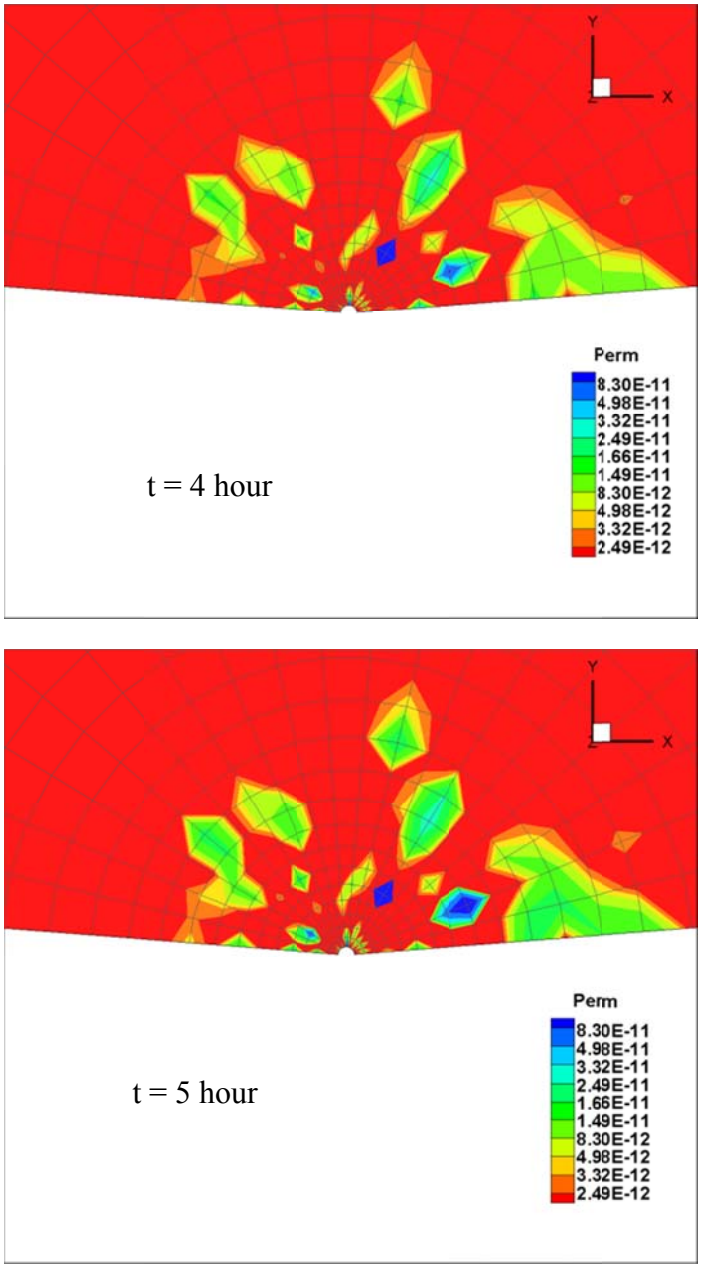

Figure 28. Near-well permeability showing the center layer at t = 4 hours and t = 5 hours. Only 25 Darcy to 850 Darcy permeability range is plotted for the best illustration.

2.5.4 Near-well response using a line injection source

Larger scale stimulation cases are also carried out to get a general view of stimulated zone. Considering the scale of the simulation domain and the computational cost, the injection well section is represented as three vertical injection elements served as a line source (15 m vertical interval) (Figure 29). Instead of using wellbore mesh, uniform grid mesh 50 × 50 ×50 is used. The reservoir domain is 100 m ×100 m ×100 m size. Far field boundary is set to be no flow, and traction specified boundary. The injection rate of

the line source is specified (per unit volume) and well pressure during the injection will be calculated. The far field tractions are equal to the in-situ stresses. The rock properties are the same as Table 2. The fracture properties are as Table 3. And one of the fracture geometry is shown in Figure 30. Figure 31 shows the resulting high permeability fractured zone.

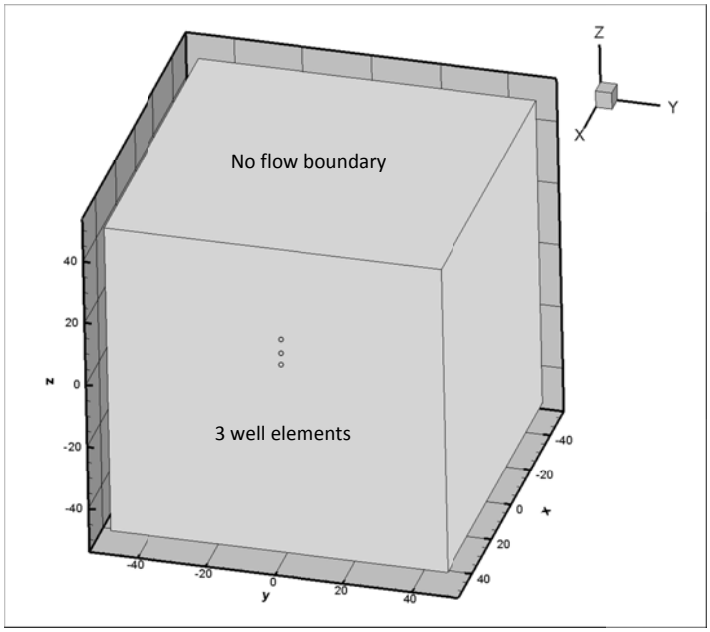

Figure 29. Model size and setup for large scale simulation test.

Table 3. Parameters used in line source simulation.

Fracture properties	
Fracture density(m^{-1})	1
Fisher parameter, κ	1.7
Mean fracture radial (lognormal)	0
Standard deviation of fracture radial, s	0.7

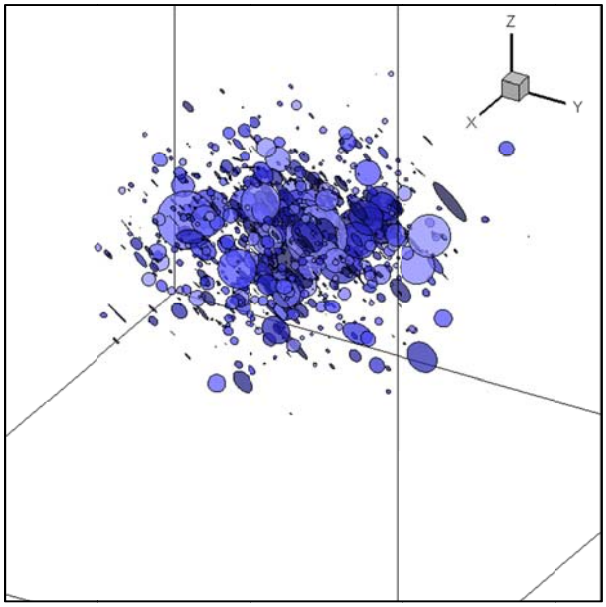

Figure 30. Fracture geometry of a fracture network with 1000 fractures.

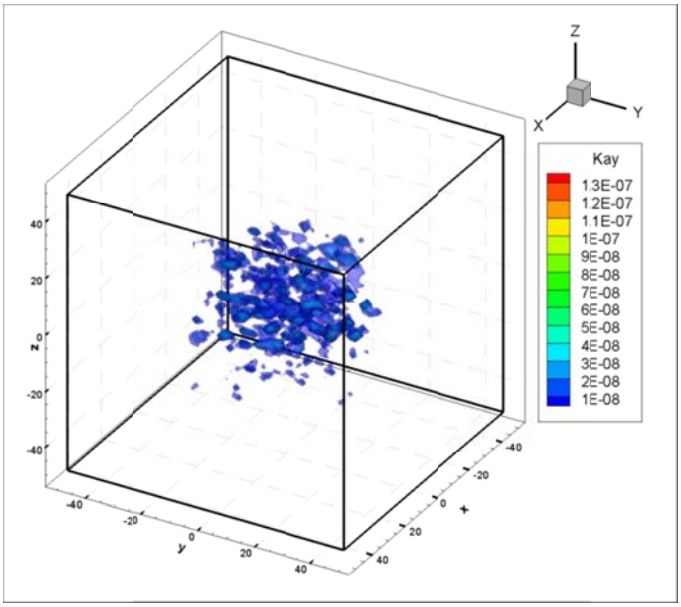

Figure 31. Fractured zone permeability heterogeneity due to the fracture network shown in Figure 40.

Figure 32 shows the pore pressure distribution development at 1 hr., 3 hr., 6 hr., and 9 hr. during the stimulation of 12 hours. Figure 33 shows the injection well pressure profile with prescribed injection rate. The results show that the shear failure of natural fractures do not have significant influence on the injection pressure vs. injection rate profile, considering the size disparity of reservoir and injection source, as well as highly fractured transport media. Figure 34 shoes the pressure distribution and shear slippage failure location at time = 9 hour on the center slice (z = 0). We can see that the stimulated zone indicated by micro-seismicity cloud shows similar shape as pore-pressure developed zone. In this model, the pore pressure is the only disturbance applied to initially balanced in-situ state. Therefore, the stress change of the rock and hence the displacement of the fracture can only happen where the induced pressure

developed. Figure 35 gives a 3D view of the potential micro-seismicity cloud at 9 hours, which indicates the stimulated zone volume at that time.

t = 1 hr.

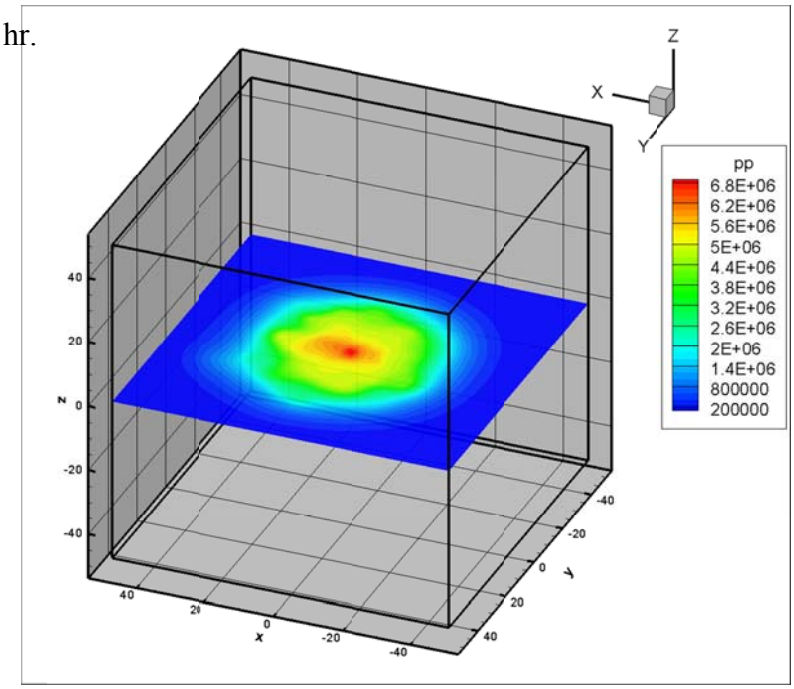

t = 3 hr.

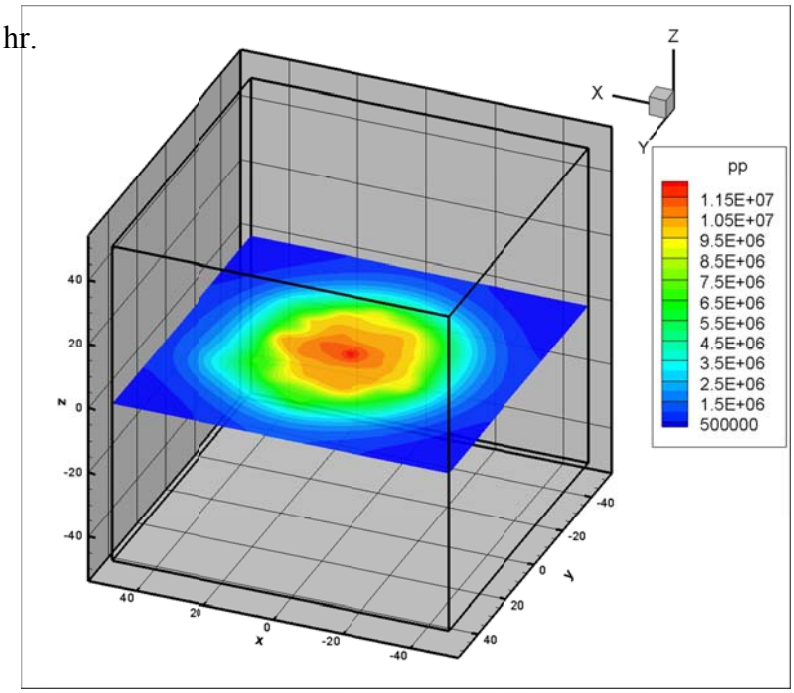

t = 6 hr.

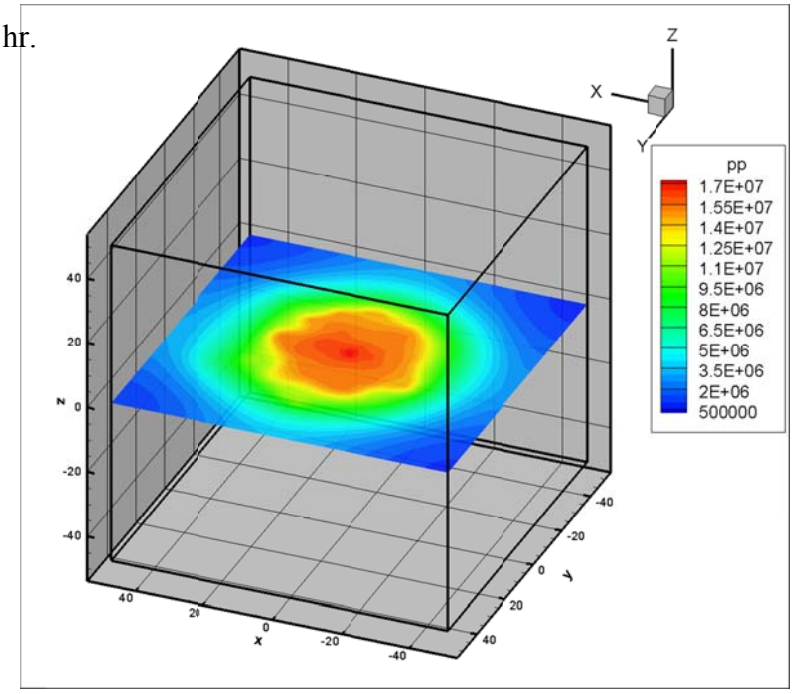

t = 9 hr.

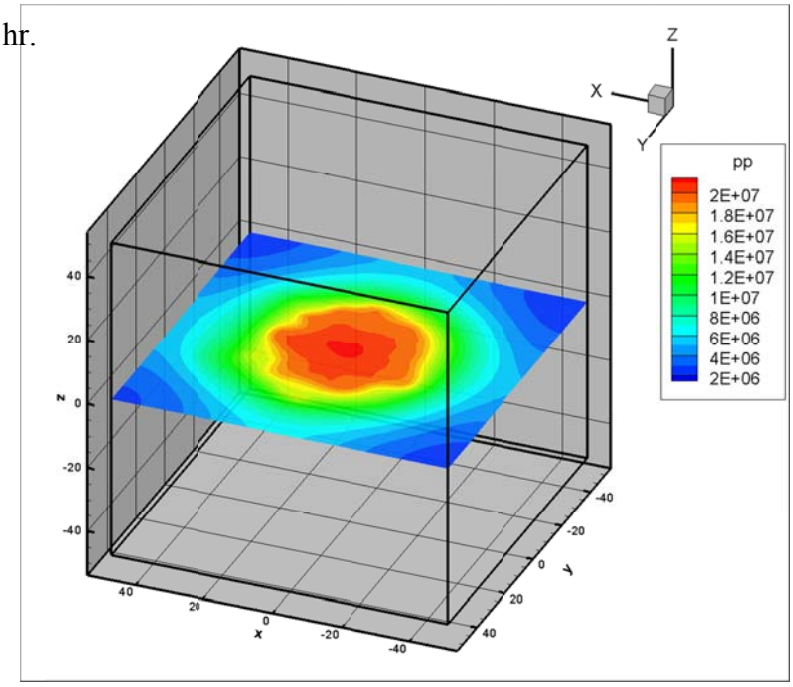

Figure 32. Excess pore pressure development due to stimulation.

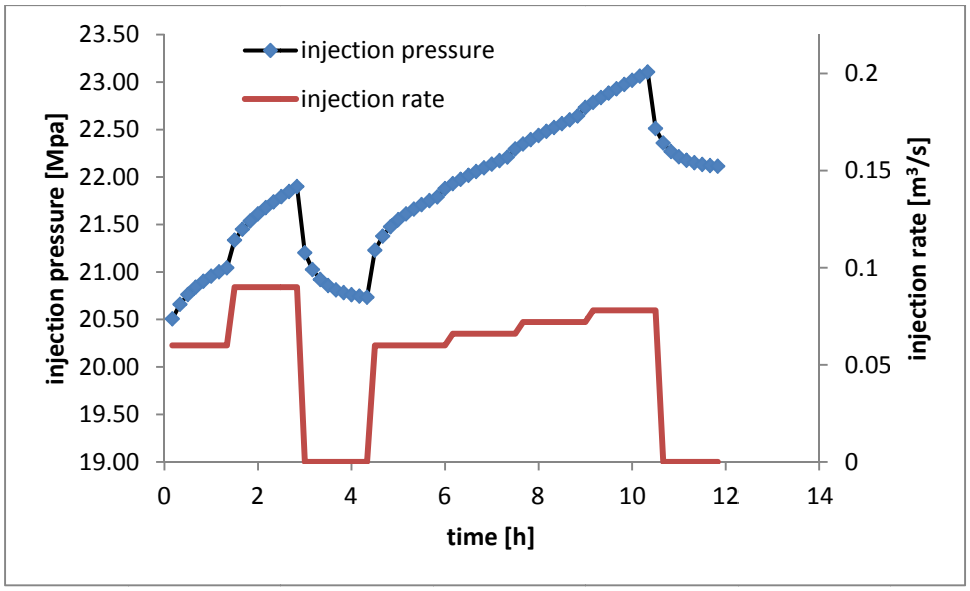

Figure 33. Injection pressure vs. injection rate profile.

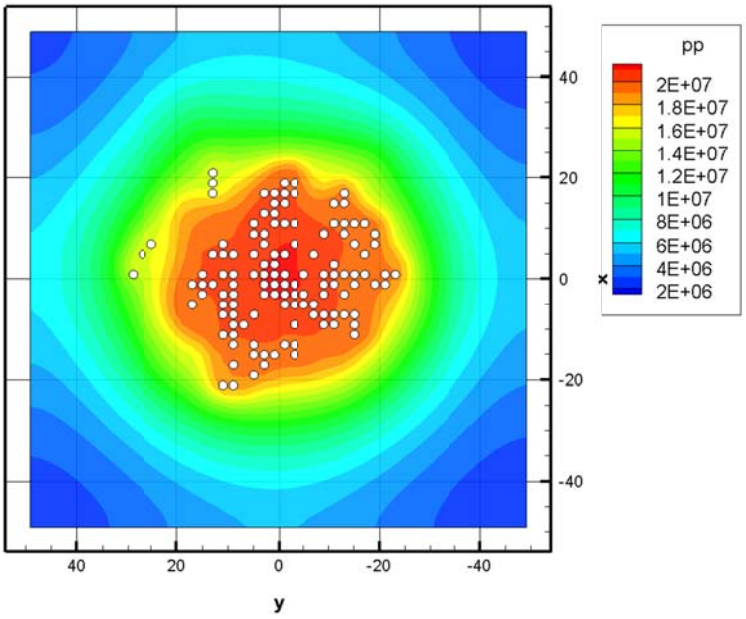

Figure 34. Pressure distribution and shear slip failure location at time = 9 hour on the center slice (z = 0).

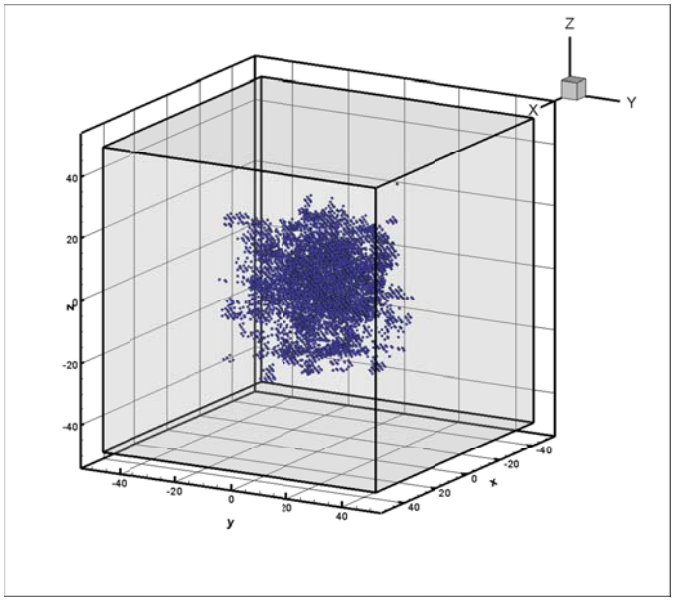

Figure 35. Shear slippage failure location (accumulative) at time = 9 hour at the center plane.

Mont Carlo tests are usually request for models using stochastic distributions, because different random data set can deliver varsity results. Stochastic data analysis is out of the scope of this study, but it is necessary to verify that the influence of data set selection on the simulation results. Figure 36 shows the pore pressure distributions at 9 hours of two models, in which the fracture networks are generated using same stochastic parameters but different random seeds. We can see that the overall results, such as induced pore pressure m pressurized zone shape and stimulated volume, show consistency. Local inconsistent can be caused by the different distribution of fractures in two networks. Figure 36 compares the well pressure profiles of two sets. The overall patterns of the profiles are similar. Set 1 shows smaller fracture conductivity compared to Set 2, which is indicated by the slight higher built-up well-pressure in set 1 than Set 2. However, the difference is with-in practical error tolerance.

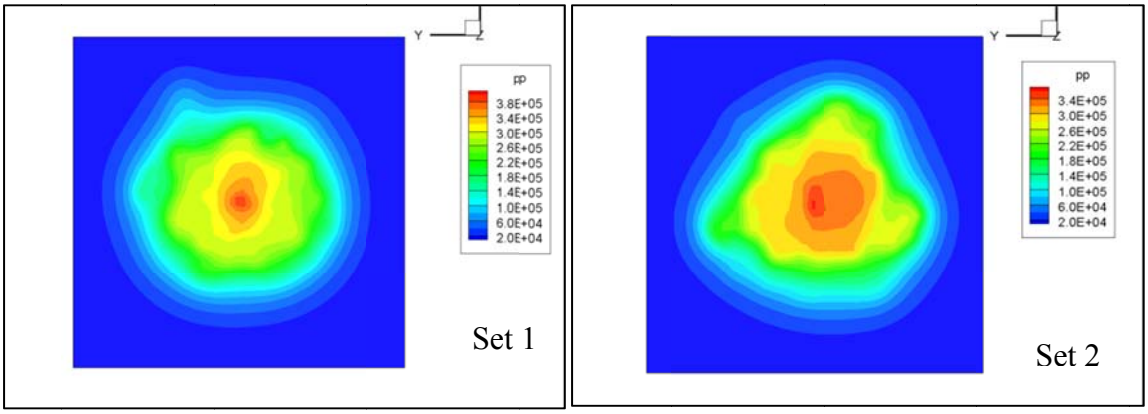

Figure 36. Pore pressure distributions of fractured reservoirs, in which natural fractures are generated from different random data sets with same stochastic parameters.

2.5.5 Case summary

This simulation example shows different aspects of permeability enhancement in EGS. The model is shown to be capable of analyzing the stress variations, pore pressure distributions, and potential injection induced micro-seismicity. From the results, we have seen the important role of fracture network properties (fracture distribution, orientation, and fracture network connectivity) in geothermal reservoir design and development. The fracture aperture changes with stress variations associated with injection and directly influence the reservoir permeability evolution. The orientation of the fractures in the reservoir dramatically influences the permeability development. In a fractured reservoir, properties of fracture network have a significant impact on pore pressure and seismic events distribution. Results also show a correlation between pore pressure increase, fractures slip and MEQs. A comparison with field/lab test needs to be conducted in the future work. Calibration of fracture distribution parameters and damage induced permeability change are being considered and will be reported in the following context.

2.6 Large Scale Reservoir Response Analysis

2.6.1 Model set up

This model is also applied to a fractured geothermal reservoir, in which the natural fracture network is connected to the injection well via a hydraulic fracture, as shown in Figure 37. A one-wing elliptical hydraulic fracture on x-z plane is centered at coordinates (670.0, 242.5, 250.0) with a major axis (x-direction) of 300 meters and s miner axis (z-direction) of 150 meters. The elliptical fracture has a uniform width of 5 mm. The modeled reservoir has a length of 1000 meters in x-direction, a width of 500s meter in y-direction, and a thickness of 500 meters in z-direction. The injection well is set vertically along the minor axis of hydraulic fracture, and the open-hole injection section is 160 m (140 m-300 m). The injection rate is held at 26.56 l/s for 40 hours. The injection water temperature is set to be 50°C and the reservoir temperature is 115°C. The whole domain is selected large enough to eliminate boundary effects. We assume fixed displacement and fixed pressure difference boundary condition at far field. This domain is discretized into 20,000 uniform finite element bricks and subject into the fully coupled FEM model. The in-situ stress state is indicated in Figure 37A also. The maximum horizontal stress is in x-direction, and this is a normal regime stress state where the largest in-situ stress is vertical. A cluster of natural fractures, 1000 count, is located in front of the hydraulic fracture. The coordinates of the center of natural fracture network is (450, 250.0, 250.0), and the fractured zone is 500 m X 500 m X 500 m. Figure 37B shows more details about natural fracture network and hydraulic fracture. Rock properties and fracture network parameters are listed in Table 4. Rock and fracture properties are from AltaRock (2011) on Newberry reservoir and Li et al. 2012.

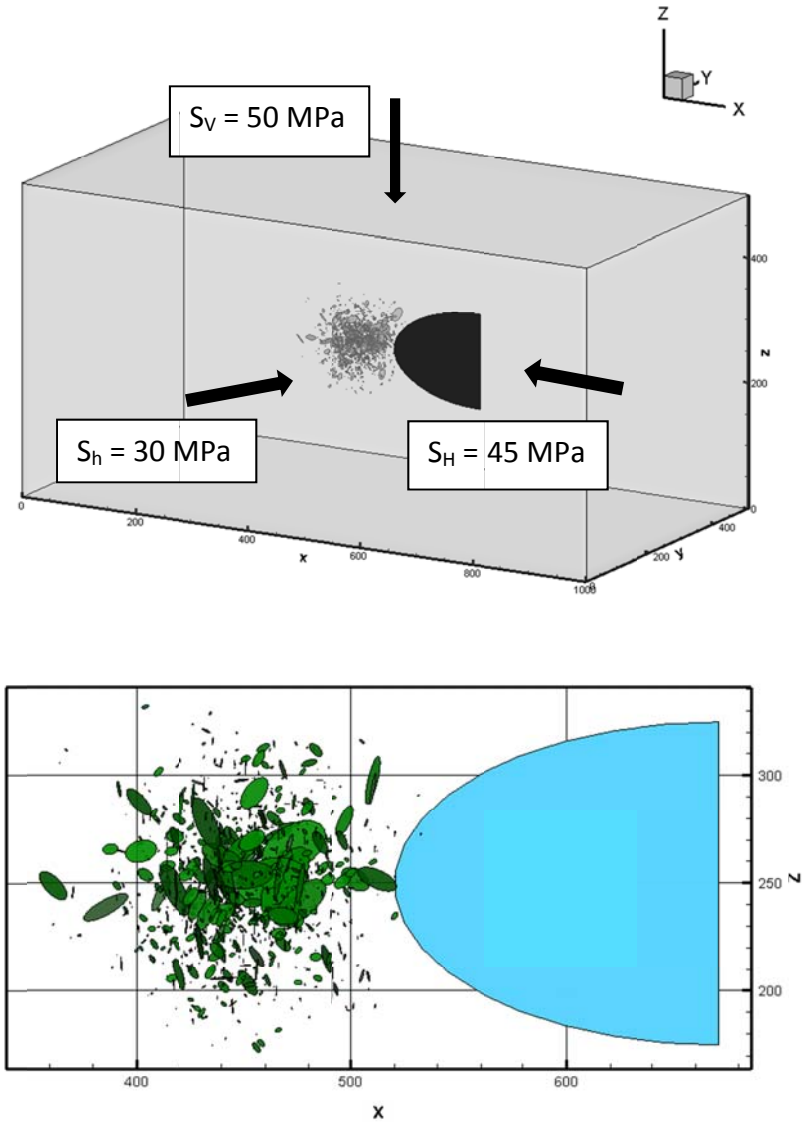

Figure 37. (a) Reservoir geometry and in-situ stress state. (b) Details on natural fracture network and hydraulic fracture.

Table 4. Rock and natural fracture properties used in large scale simulation.

Rock density	2700 kg/m^3
Fluid density	1000 kg/m^3
Rock permeability	3.24 X 10^{-12} m^2/s
Rock porosity	0.2989
Young's Modulus	10 GPa
Boit's coefficient	0.915
Poisson's ratio	0.219 (drain), 0.461(undrain)
Bulk Modulus (fluid)	3.291GPa
Number of fractures	1000
Fracture size (Log EX)	0.0

Fracture orientation, κ	2.8
Fluid viscosity	$3.0X10^{-4}$ Pa s
Basic friction angle	0.698
Dilation angle	0.052
90% closure stress	100 MPa
Thermal expansion coefficient (solid)	$1.8 X 10^{-5} K^{-1}$
Thermal expansion coefficient (fluid)	$3.0 X10^{-4} K^{-1}$
Thermal diffusivity	$6.0 X 10^{-12} m^2/s$
Fracture density	$1.5 m^{-1}$
Fracture size (Log SD)	1.0
size-aperture coefficient	$4.0 X 10^{-3}$

2.6.2 Simulations and results

The response of natural fracture network to injection is analyzed. At first, two sets of fractures are tested individually. These two sets of fractures have same distribution and orientations, different size and aperture. The resulting micro-seismic events location is the same for both sets. Results show the significant influence of fracture orientation on the occurrence of shear slippage. Figure 38 is a plot of the normal to the slipped fractures and their corresponding MEQ events at time = 10 hour. Gray circles represent all the fractures, while color rectangles are the slipped fractures. The color bar gives the magnitude of slippage induced micro-seismicity. It can be seen that shear slippage happens on fractures whose normal orientation falls into a certain range as indicated in the plot. The direction cosines of a fracture plane can be written in terms of its fracture dip and azimuth. From Figure 38, we can see that most fractures with azimuth between (-30°, 30°) slip after 10 hours of injection. Slipped fractures are sorted and plotted in Figure 39. Colors on fractures indicate the magnitude of MEQ events. It is evident from the figure that the event magnitudes are less related to the fracture orientation, size, or the distance to the injection source. We observe same magnitude of events on different size of fractures. We also observe higher magnitude of events on fracture far from injection source than the near ones. And from Figure 38, we can see the same magnitude events occur on fractures with large range of azimuth angles. However, due to our assumption of the dependency of fracture aperture and size (aperture is 10^{-4} of fracture size, Equation 13), the correlation between the fracture aperture and event magnitude is not evident. In order to characterize the sensitivity of fracture slip to injection, fluid gravity is ignored in this work, and we can see slippage occur on shallow fractures (Figure 39). By adding fluid gravity, the lower part of reservoir would be pressurized first, as discussed in Wang and Ghassemi, (2012b).

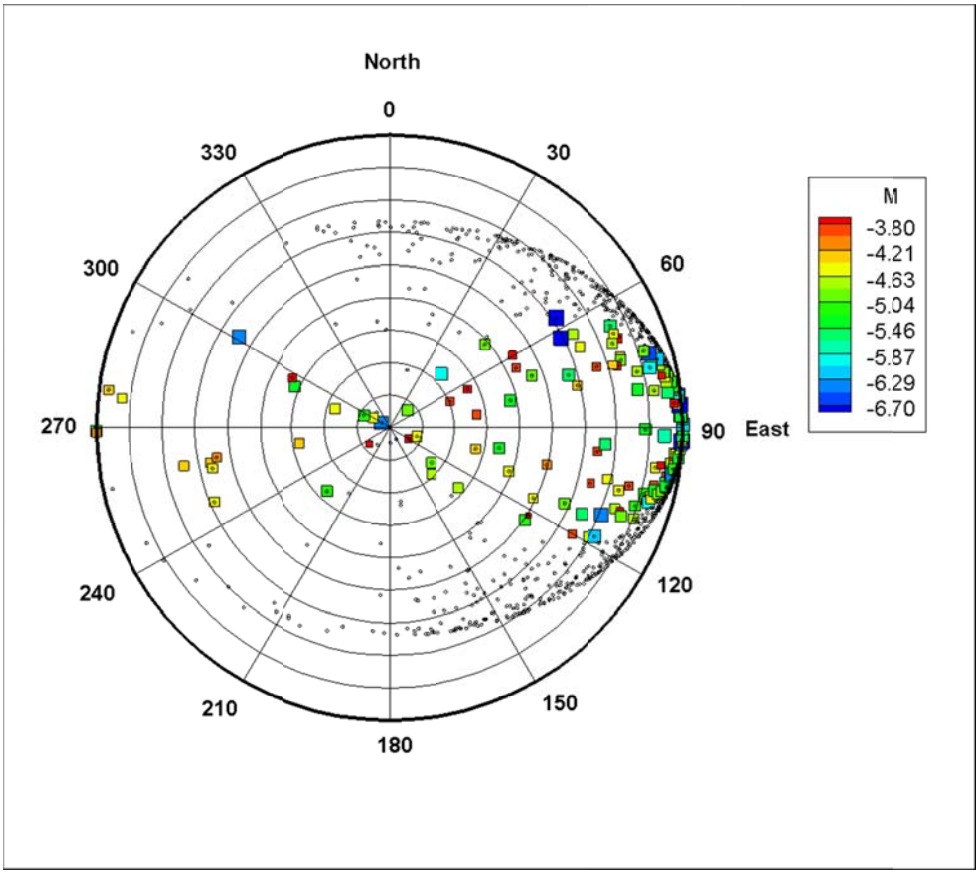

Figure 38. Slipped fractures' normal directions are plotted as colored squares. Gray circles show all the normal directions of natural fractures.

Pore pressure distributions within fracture network from time = 1 hour and time = 10 hour are shown in Figure 40. It can be seen that injection fluid mainly pressurizes interconnected fractures. This indicates small amount of fluid is transported through matrix and most of it occur within the interconnect fractures test. We can see from results that the pore pressure development is mostly controlled by the connectivity, and there is less pore pressure development in some isolated fractures near injection source (hydraulic fracture). This is reasonable because the rock permeability is much lower (two orders of magnitude) than fracture permeability, and injected fluid mostly goes into high permeable zones.

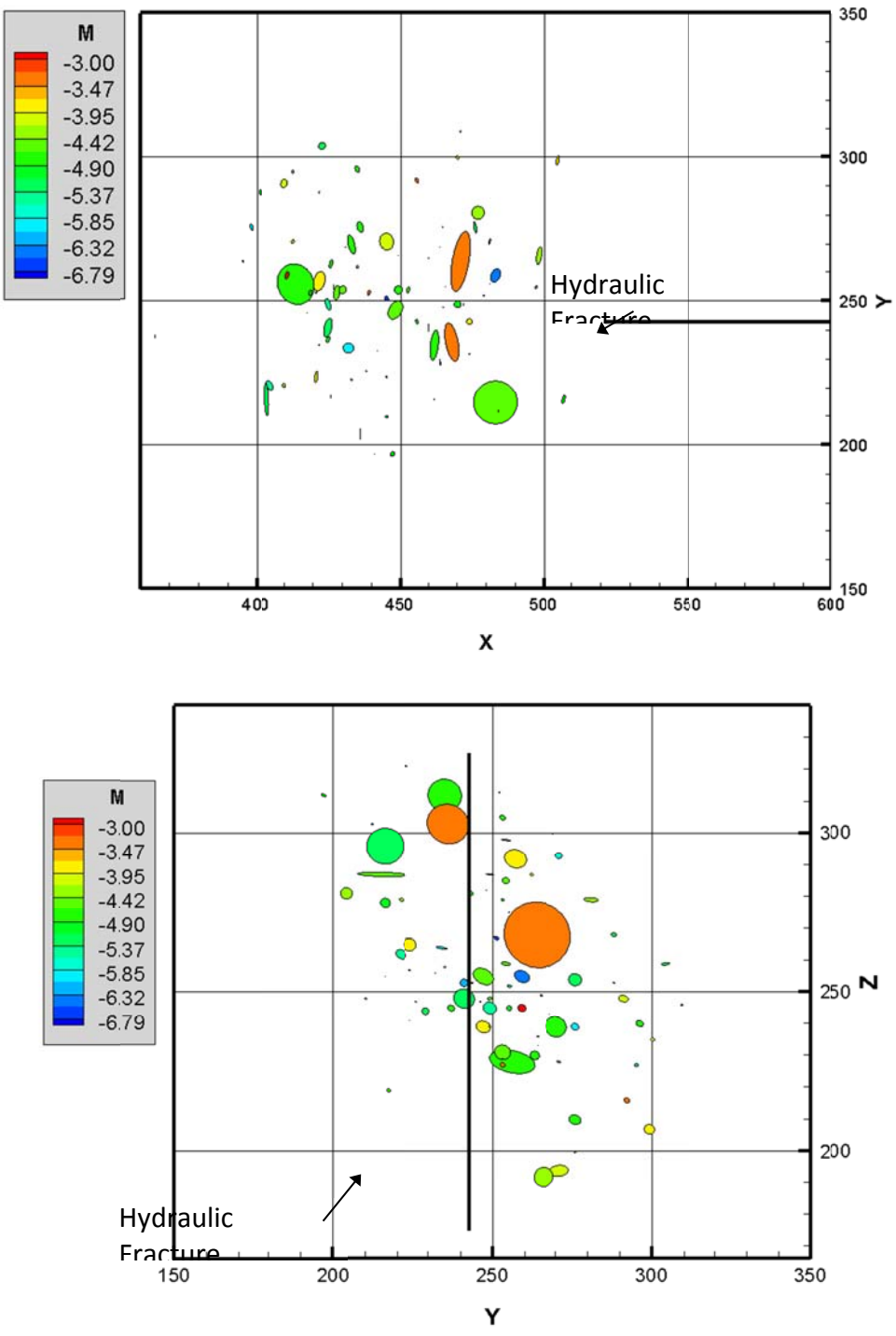

Figure 39. Slipped fractures and magnitude of the induced micro seismicity. (a) x-y plane view, (b) y-z plane view.

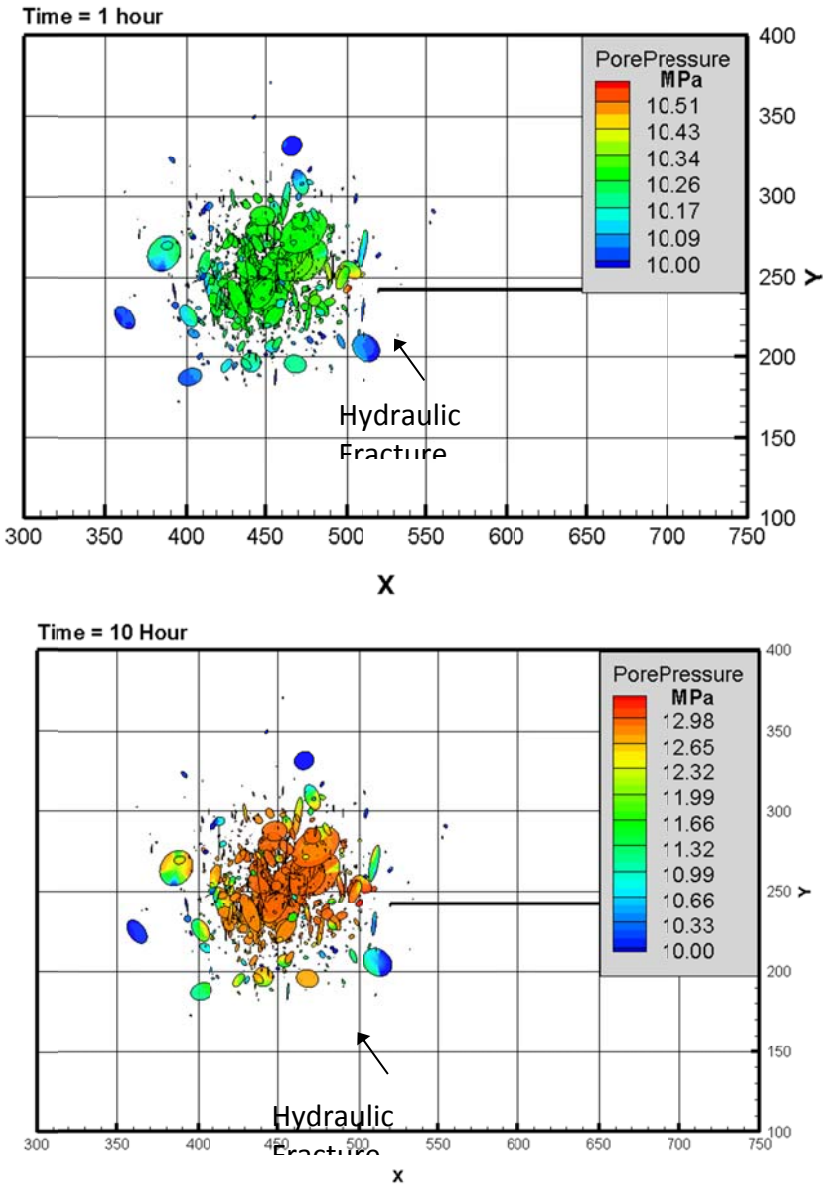

Figure 40. Pore pressure distributions in individual fractures at time = 1 hour and time=10 hour.

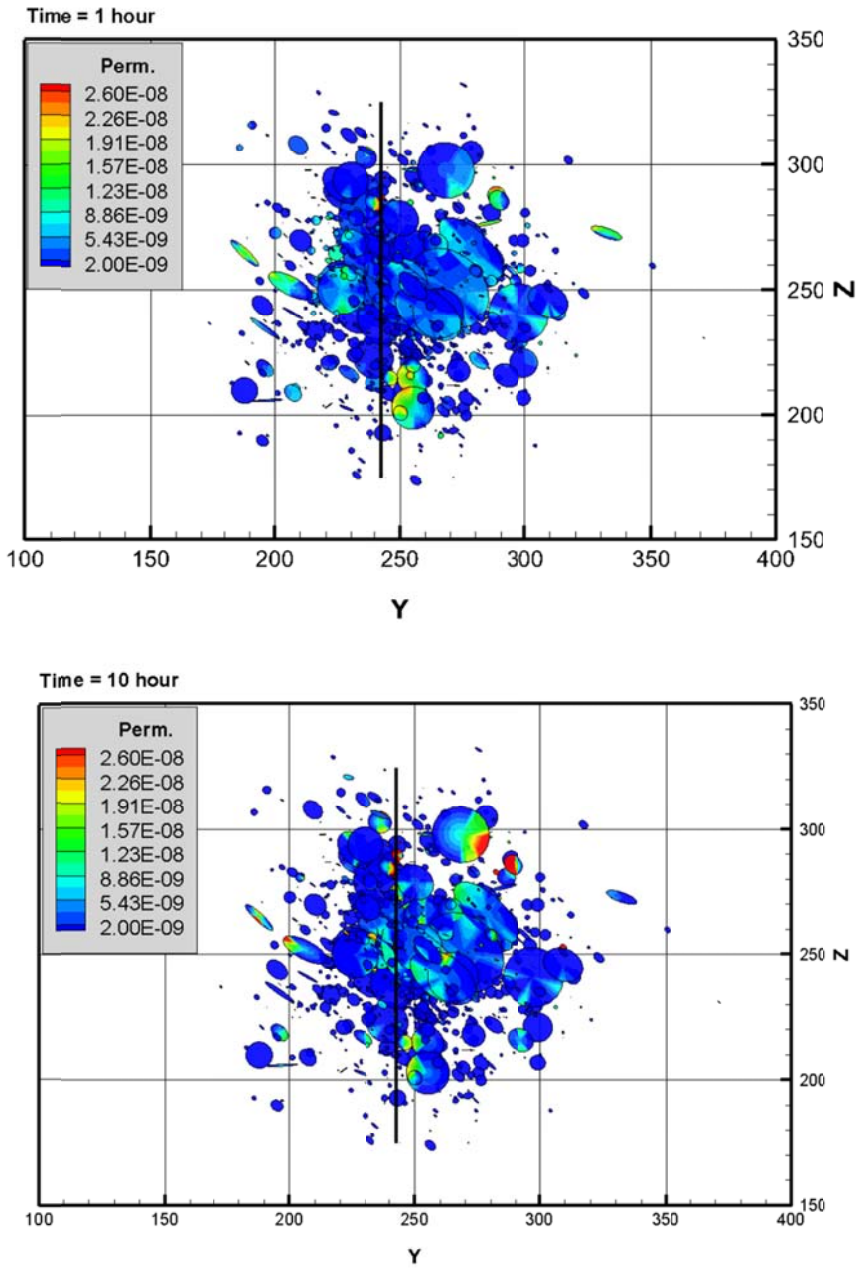

Figure 41. The permeability enhancement of fracture network. y-z plane view. Thick black line indicates location of the hydraulic fracture.

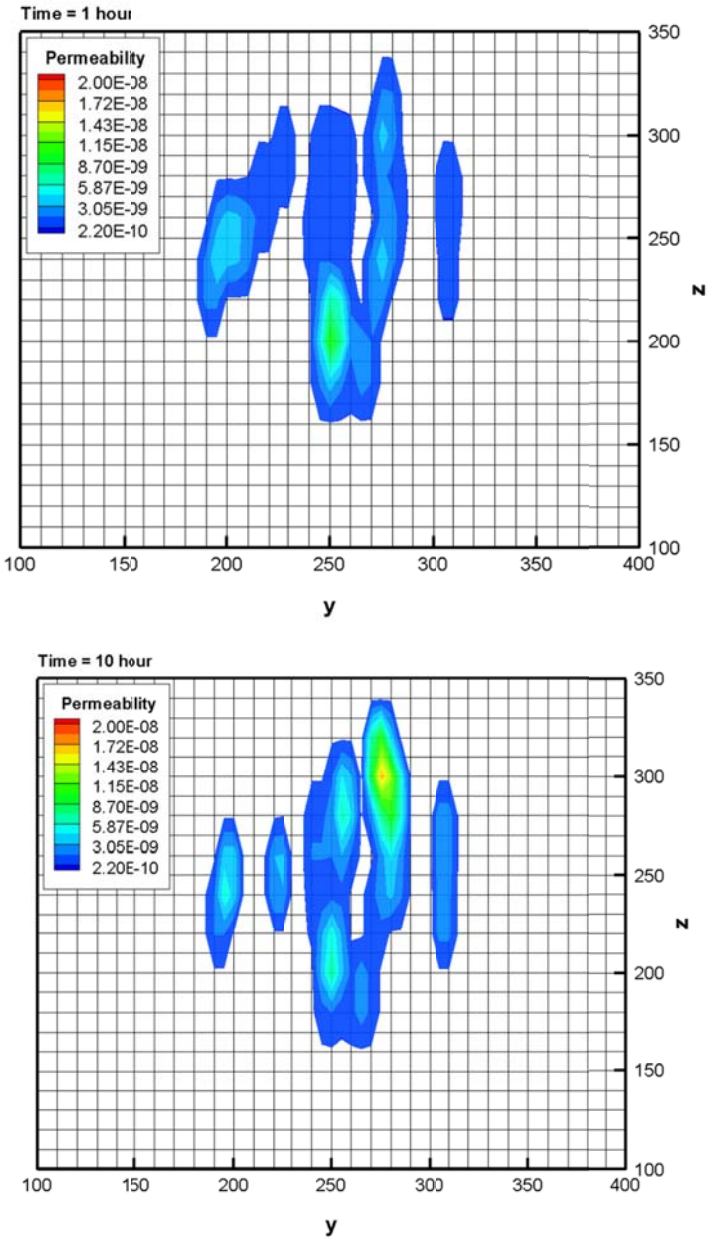

Figure 42. Improvement of averaged permeability of elements, low permeability zone (< 2.0×10^{-10} m^2/s) has been blank out. y-z plane slice at x = 450.0 m (center of fracture network).

In the fracture deformation mechanism, there are two sources of permeability improvement: fracture opening and shear dilation. By comparing slipped fractures in Figure 39 and fracture permeability enhancement n Figure 41, much of the large permeability increases happen where no slippage is observed. For example, the permeability of the fracture located on 270Y-300Z in Figure 41B, has been enhanced by approximately one order of magnitude. We do not observe any shear slippage event on this fracture in Figure 39B. Therefore we can conclude the permeability enhancement of this fracture is caused by fracture opening by pressurization (and thus eventual mode I propagation). There are also fractures where permeability decreases at lower part of near hydraulic fracture zone. This decrease can be caused by fracture closing or shear squeezing, which could lead to aperture reduction.

In this model, not all the natural fractures have been utilized in calculation (when small fractures are contained totally within one element their attribution of the permeability is not take into account). . As discussed previously, only fractures that intersect the finite element mesh faces are considered for permeability evaluation. Figure 42 shows the permeability improvement in terms of equivalent permeability of finite elements at time = 1 hour and time = 10 hour, respectively. We can see that there are zones where permeability is increased after injection. Also, there are zones where permeability is decreasing during injection. In this study, the fracture deformation is assumed to be elastic and reversible. As can be read from figures, the maximum accumulate permeability enhancement is approximately four folds.

We also examine the thermal effects during injection. The results show that during stimulation, the temperature variation is very little due to low thermal conductivity of the material, as can be seen from Figure 43. The reservoir temperature is 115°C, and the injection fluid temperature is 20°C.

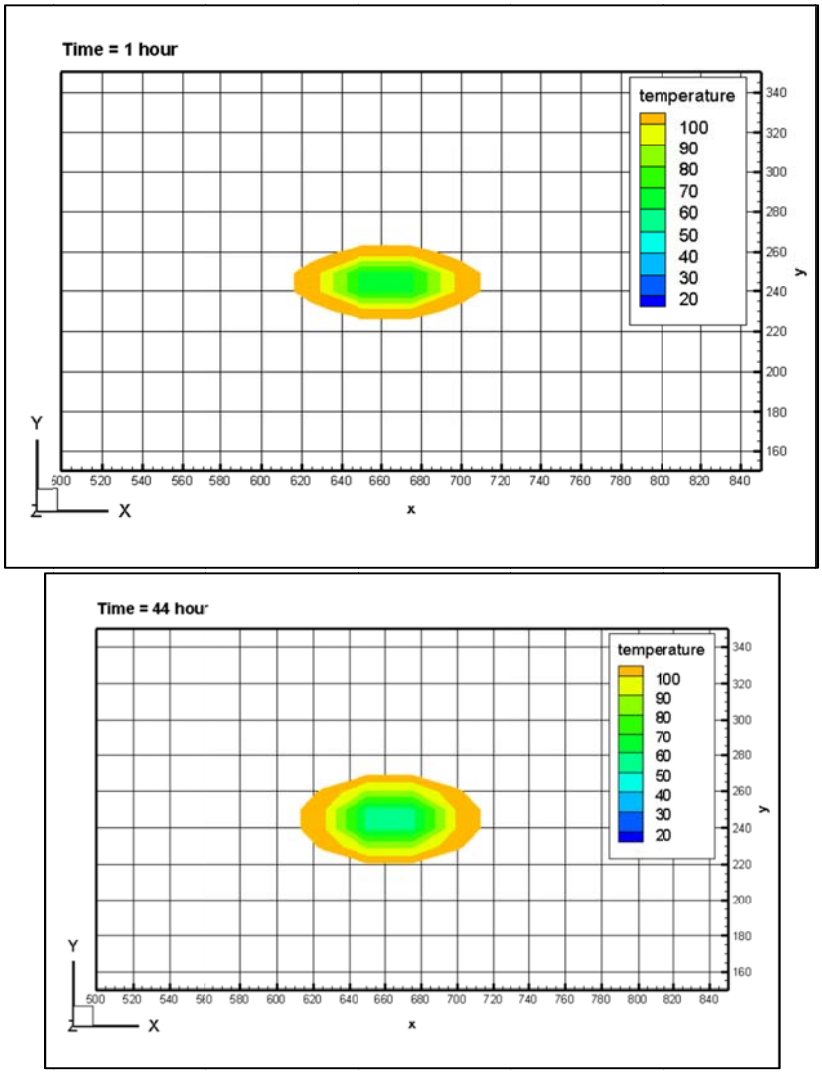

Figure 43. Temperature variation during injection at Time = 1 hour and Time = 44 hour.

2.6.3 Case summary

The 3D Thermal and Poroelastic model developed in this work calculates the performance of fractured reservoir during stimulation. The permeability enhancement of the natural fracture networks, and the corresponding slippage induced MEQ events have been analyzed. The result shows that the as one would expect, fractures orientations have a major influence on the initiation of shear slippage. From permeability improvement, we can conclude that as the pressure field changes during injection, fracture permeability can be enhanced. Also, stress change can also cause fracture closure, hence decrease the local permeability. Shear slippage does not necessary indicates permeability enhancement according to the simulation results. Some fractures' aperture decreases while shear slipping. Since the zone of temperature disturbance is so small (not even reach the fractured zone as shown in Figure 21), we do not observe cooling effect in this studying case.

This model is useful to analyze the geothermal reservoir response during stimulation. It can give assistance when design an injection schedule and to predict the effects of the stimulation. By comparing simulation result and field observations, this model can also be used to evaluate the fracture network models.

3. References

ALTAROCK. 2011. Newberry volcano EGS demonstration stimulation planning. *GRC Annual Meeting, San Diego, CA, October 25, 2011.*

Barton N., S. Bandis, K. and Bakhtar. 1985. Strength, deformation and conductivity coupling of rock joints. *International Journal of Rock Mechanics and Mining Sciences & Geomechanics, Abstracts* 22(3): 121-140.

Biot, M.A. 1941. General theory of three-dimensional consolidation. *Journal of Applied Physics* 12(2): 155-164.

Bruel, D. 2002. Impact of induced thermal stresses during circulation tests in an engineered fractured geothermal reservoir. *Oil & Gas Science and Technology* 57(5): 459-470.

Bruel, D., M.C. Cacas, E. Ledoux, and G. Marsily. 1994. Modeling storage behaviour in a fractured rock mass. *Journal of Hydrology* 162: 267-278.

Cacas M.C., E.Ledoux, G. De Marsily, and B. Tillie. 1990. Modeling fracture flow with a stochastic discrete fracture network: calibration and validation 1. The flow model. *Water Resources Research* 26(3): 479-489.

Carrera, J., J. Heredia, S. Vomvoris, and P. Hufschmied. 1990. Modeling of flow on a small fractured monzonitic gneiss block. *Selected Papers in Hydrogeology of Low Permeability Environments, International Association of Hydrogeologists, Hydrogeology:* 2: 115-167.

Carter, J.P. and J.R. Booker 1982. Elastic consolidation around a deep circular tunnel. *International Journal of Solids Structures*18(12): 1059-1074.

Chen, Z.H., L.G. Tham, M.R. Yeung, and H. Xie. 2006. Confinement effects for damage and failure of brittle rocks. *International Journal of Rock Mechanics and Mining Sciences* 43(8):1262-1269

Cheng, A.H.D. and E. Detournay. 1988. A direct boundary element method for plane strain poroelasticity. *International Journal for Numerical and Analytical Methods in Geomechanics* 12(5): 551-572.

Cladouhos, T.T., M. Clyne, M. Nichols, S. Petty, W. Osborn, and L. Nofziger. 2011. Newberry volcano EGS demonstration stimulation modeling. *GRC Transactions* 35: 317-322.

Dershowitz, W.S. 1984. Rock joint systems. Ph.D. thesis, Massachusetts Institute of Technology, Cambridge.

Detournay, E. and A. H-D. Cheng. 1988. Poroelastic response of a borehole in a non-hydrostatic stress field. *International Journal for Numerical and Analytical Methods in Geomechanics* 25(3): 171-182.

Ekbote, S. and Y. Abousleiman. 2006. Porochemoelastic solution for an inclined borehole in a transversely isotropic formation. *Journal of Engineering Mechanics* 132(7): 754-763.
Eshelby, J.D. 1957. The determination of the elastic field of an ellipsoidal inclusion, and related problems. *Proceddings of the Royal Society of London. Series A, Mathematical and Physical Sciences* 241(1226): 376-396.
Fujii, Y., Y. Ishijima and T. Kiyama. 1999. Confining pressure-dependency of coefficients in the simple constitutive equations for brittle rock. *Processing 1999 Japan-Korea Joint symposium on Rock Engineering*. 323-330.
Ghassemi, A. and A. Diek. 2003. Linear chemo-poroelasticity for swelling shales: theory and application. *Journal of Petroleum Science and Engineering* 38(3-4): 199-212.
Ghassemi, A. and G.S. Kurma. 2007. Changes in fracture aperture and fluid pressure due to thermal stress and silica dissolution/precipitation induced by heat extraction from subsurface rocks. *Geothermics* 36(2): 115-140.
Ghassemi, A., Q. Tao, and A. Diek. 2009. Influence of coupled chemo-poro-thermoelastic processes on pore pressure and stress distributions around a wellbore in swelling shale. *Journal of Petroleum Science and Engineering* 67(1-2): 57-64.
Griffiths, D.V. and I.M. Smith. 1991. Numerical methods for engineers. Oxford: Blackwell Scientific Publications Ltd.
Hallinan Jr., A. 1993. A review of the Weibull distribution. *Journal of Quality Technology* 25(2): 85-93.
Hanks, T.C. and H. Kanamori. 1979. A moment magnitude scale. *Journal of Geophysical Research: Solid Earth* 84(B5) 2248-2350.
Heidug, W.K. and S.W. Wong. 1996. Hydration swelling of water-absorbing rocks: a conostitutive model. *International Journal for Numerical and Analytical Methods in Geomechanics* 20(6): 403-430.
Hristopulos, D.T. and G. Christakos. 1999. Renormalization group analysis of permeability upscaling. *Stochastic Environmental Research and Risk Assessment* 13(1-2): 131-160.
Hudson, J.A. and P.R. La Pointe. 1980. Printed circuits for studying rock mass permeability. *International Journal of Rock Mechanics and Mining Science and Geomechanics Abstracts* 17(5): 297-301.
Jaeger, J.C. and N.G.W. Cook. 1969. Fundamentals of rock mechanics. New York: Chapman and Hall.
Jaeger, J.C., N.G.W. Cook, and R.W. Zimmerman. 2007. Foundamentals of rock mechanics.4th edn. Blackwell Publishing.
Johnson, N.L., S. Kotz, and N. Balakrishnan. 1994. Continuous univariate distributions, Vol. 1, 2nd Edn. New York: Wiley.
Kachanov, L.M. 1958. On the creep fracture time. *Izv Akad, Nauk USSR Otd. Tech.* 8: 26-31.
Kachanov, L.M. 1986. Introduction to continuum damage mechanics. The Netherlands: Martinus Nijhoff Publishers.
Kolditz, O. and C. Clauser. 1998. Numerical simulation of flow and heat transfer in fractured crystalline rocks: application to the hot dry rock site in rosemanowes (U.K.). *Geothermics* 27(1):1-23.
Krempl, E. 1977. On phenomenological failure laws for metals under repeated and sustained loading (fatigue and creep). Conf. on Environmental Degradation of Engineering Materials, Blaksburg, VA.
Kurashige, M. 1989. A thermaoelastic theory of fluid-filled porous materials. *International Journal of Solids Structures* 25(9): 1039-1052.
Lee, S-H, and A. Ghassemi. 2011. Three-dimensional thermo-poro-mechanical modeling of reservoir stimulation and induced microseismicity in geothermal reservoir. *Proceedings, Thirty-sixth Workshop on Geothermal Reservoir Engineering, Stanford University, Stanford, California, 31 January – 2 Feburary, 2011*.
Lemaitre, J. 1985. A continuous damage mechanics model for ductile fracture. *Journal of Engineering Materials and Technology* 107(1): 83-89.
Li, L.C., C.A. Tang, G. Li, S.Y. Wang, Z.Z. Liang, and Y.B. Zhang. 2012. Numerical simulation of 3D hydraulic fracturing based on an improved flow-stress-damage model and a parallel FEM technique. *Rock Mechanics and Rock Engineering* 45(5): 801-818.

Li, X., L. Cui, J-C. Roegiers. 1998. Thermoporoelastic modeling of wellbore stability in non-hydrostatic tress field. *International Journal of Rock Mechanics and Mining Sciences & Geomechanics, Abstracts* 35(4): 584-588.
Li, Y., J. Wong, and A. Ghassemi. 2012. Mechanical properties of intact and jointed welded tuff from Newberry volcano. *Proceedings of Thirty-Seventh Workshop on Geothermal Reservoir Engineering, Stanford University, Stanford, California, 30 January – 1 Feburary, 2012*.
Liang Z.Z. 2005. Three-dimensional numerical modelling of rock failure process. Ph.D. Thesis. Dalian University of Technology, Dalian, China.
Mandel, J. 1953. Consolidation des sols (etude mathematique). *Geotechnique* 3: 287-299.
Marin, E. 2010. Characteristic dimensions for heat transfer. Latin-American Journal of Physics Education 4(1): 56-60
Maury, V.M. and J-M. Sauzay. 1987. Borehole instability: case histories, rock mechanics approach, and results. *SPE/IADC Drilling Conference, New Orleans, LA, March 15-18, 1987*.
McGarr, A., A.M. Spottiswoode, N.C. Gay, and W.D. Ortlepp. 1979. Observations relevant to seismic driving stress, stress drop, and efficiency. *Journal of Geophysical Research: Solid Earth* 84(B5) 2251-2261.
McTigue, D. 1986. Thermoelastic response of fluid-saturated porous media. *Journal of Geophysical Research* 91(B9): 9533-9542.
Mody, F.K. and A.H. Hale. 1993. Borehole stability model to couple the mechanics and chemistry of drilling fluid shale interaction. *Proceedings, SPE/IADC Drilling Conference, Amsterdam, 23-25 Feburary 1993.*
Muller A.L., E.D.A. Vargas Jr., L.E. Vaz, and C.J. Goncalves. 2008. Borehole stability analysis considering spatial vairiability and poroelastoplasticity. *International Journal of Rock Mechanics and Mining Sciences* 46(1): 90-96.
Murakami, S. and N. Ohno. 1980. A continuum theory of creep and creep damage. *3rd IUTAM Symposium on Creep in Structures, Leicester.*
Murthy, D.N.P., M. Xie, and R, Jiang. 2003. Weibull models. New York: Wiley.
National Research Council. 1996. Rock fractures and fluid flow. Washington, D.C.: National Academy Press.
Noetinger, B. 1994. The effective permeability of a heterogeneous medium. *Transport in Porous Media* 15(2): 99-127.
Rahman, M.K., M.M. Hossain, and S.S. Rahman. 2002. A shear-dilation-based model for evaluation of hydraulically stimulated naturally fractured reservoirs. *International Journal for Numerical and Analytical Methods in Geomechanics* 26 (5): 469-497.
Rice, J.R. and M.P. Cleary. 1976. Some basic stress-diffusion solutions for fluid-saturated elastic porous media with compressible constituents. *Reviews of Geophysics and Space Physics* 14(2): 227-241.
Robinson, P. 1984. Connectivity, flow and transport in network models of fractured media. Ph.D. thesis. Oxford University, Oxford, UK.
Robotnov, Y.N. 1969. Creep problems in structural members. North-Holland.
Rosso, R.S. 1976. A comparison of joint stiffness measurements in direct shear, triaxial compression, and in situ. *International Journal of Rock Mechanics and Mining Sciences & Geomechanics, Abstracts* 13(6): 167-172.
Rubin, Y. 2003. Applied stochastic hydrogeology. Oxford: Oxiford University Press.
Safari, M.R. and A. Ghassemi. 2011. 3d analysis of huff and puff and injection tests in geothermal reservoirs. *Proceedings 36th Workshop on Geothermal Reservoir Engineering, Stanford University, Stanford, California, Jan. 31- Feb. 2, 2011.*
Schoenball, M. and T. Kohl. 2013. The peculiar shut-in behavior of the well GPK2 at Soultz-sous-Forets. *GRC Transactions* 37: 217-220.
Schoenball, M., T.M. Muller, B.I.R. Muller, and O. Heidbach. 2010. Fluid-induced microseismicity in pre-stressed rock masses. *Geophysical Journal International* 180(2): 813-819.

Shapiro, S.A., P. Audigane, and J.J. Royer. 1999. Large-scale in situ permeability tensor of rocks from induced microseismicity. *Geophysical Journal International* 137(2): 207-213.
Smith I.M. and D.V. Griffiths. 2004. Programming the finite element method, fourth ed. New York: John Wiley.
Smith, L. and F.W. Schwartz. 1984. An analysis of the influence of fracture geometry on mass transport in fractured media. *Water Resources Research* 20(9): 1241-1252.
Sneddon, I.N. 1946. The distribution of stress in the neighborhood of a crack in an elastic solid. *Proceedings of the Royal Society of London. Series A, Mathematical and Physical Sciences* 187: 229-260.
Tang, C.A., L.G. Tham, P.K.K. Lee, T.H. Yang, and L.C. Li. 2002. Coupled analysis of flow, stress and damage (FSD) in rock failure. *International Journal of Rock Mechanics and Mining Sciences* 39(4): 477-489.
Terzaghi, K. 1923. Die Berechnung des durchlassigkeitsziffer des tones aus dem verlauf der hydrodynamischen spannungserscheinungen. *Sitz. Akad. Wiss. Wien, Abt.IIa.* 132: 125– 38.
Tezuka, K. and K. Watanabe. 2000. Fracture network modeling of hijiori hot dry rock reservoir by deterministic crack network simulator (D/SC). *In proceedings of World Geothermal Congress, Kyushu-Tohoku, Japan, 28 May – 10 June, 2000.*
Tezuka, K., T. Tamagawa, and K. Watanabe. 2005. Numerical simulation of hydraulic shearing in fracture reservoir. *In proceedings of World Geothermal Congress, Antalya, Turkey, 24 –29 April 2005.*
Warren, J.E. and H.S. Price. 1961. Flow in heterogeneous porous media. *SPE Journal* 1(3): 153-169.
Weibull, W. 1939. A statistical theory of the strength of material. Ing. Betenskapa Acad. Handlingar. Stockholm. 151.
Weibull, W. 1951. A statistical distribution function of wide applicability. *Journal of Applied Mechanics* 18: 293-297.
Westmann, R.A. 1965. Asymmetric mixed boundary-value problems of the elastic half-space. *Journal of Applied Mechanics* 32(2): 411-417.
Willis-Richards, J., K. Watanabe, and H. Takahashi. 1996. Progress toward a stochastic rock mechanics model of engineered geothermal systems. *Journal of Geophysical Research* 101(B8): 481-496.
Zhou, X. and A. Ghassemi.2009, Finite element analysis of coupled chemo-poro-thermo-mechanical effects around a wellbore in swelling shale. *International Journal of Rock Mechanics and Mining Science* 46(4), 769-778.

Chapter 4: Geomechanics-Based Stochastic Analysis of Microseismicity Considering Fracture Networks

1. Introduction

Fractures which represent discontinuities in rock have a significant effect on the fluid transport capability of a reservoir. Fractures orientations, spacing, connectivity are important features that control network permeability. Table 1 summarizes common properties used for characterizing fractures and fracture networks. Table 2 summarizes the properties of a fracture set which could constitute a fracture network. Despite their essential role in reservoir development, there still are uncertainties regarding direct and indirect diagnostic technologies for characterizing fractures orientations in-situ. In the last several decades, many methods have been used to constrain the uncertainty in measuring the fractures orientations. Those methods are mainly geophysical in nature, ranging from simple extrapolation of field observations to high resolution seismic survey and transient electromagnetic method (see Table 3). Active geophysical methods can naturally be divide into three distinct scales: (1) large scales associated with surface geophysics, (2) intermediate scale associated with surface-borehole and borehole-borehole, and (3) small scales associated with measurements made on rocks immediately adjacent to a borehole or tunnel. In general, active geophysical methods that probe into the subsurface have a poor ability to spatially resolve the fracture geometry. Borehole logging and camera and outcrop mapping commonly suffer from lower dimensional limited exposures (Einstein and Baecher 1983; Williams and Johnson 2004; Li, Feng et al. 2013). Furthermore, the description of fracture geometries obtained from local field surveys has to be scaled up from the local scale to the entire reservoir which can cause loss of geometric characteristics of the fractures. The question of how to establish a reliable fracture pattern away from the borehole remains a challenging issue. Thus, fracture pattern in numerical analysis are commonly treated in a stochastic framework (Leung and Zimmerman 2012, Berrone, Pieraccini et al. 2015, Farmahini-Farahani and Ghassemi 2015, Ghassemi and Tao 2016). Thus, the numerical simulation results are uncertain and might not be reliable for optimizing completions design and production assessment.

Table 1. Properties commonly used to characterize a fracture.

Characteristic	Fracture property		SI unit	definition
Wall rock rheology	UCS		Pa	Uniaxial compressive strength
	JCS		Pa	Joint compressive strength
	JRC		-	Joint roughness coefficient
	κ_n		Pa/m	Fracture normal stiffness
	κ_s		Pa/m	Fracture shear stiffness
Geometry	Orientation	2D	o	Fracture strike
		3D	o	Fracture dip and dip direction

	Size	Length(l)	m	Length of a fracture trace on a surface
		Area	m^2	Area of the fracture surface
		Volume	m^3	Volume of fracture void
	Aperture	Mechanical(a_m)	m	Distance between two fracture walls
		Hydraulic (a_h)	m	Effective fluid transport relevant fracture aperture
	Displacement	Shear direction	m	Measure of shear displacement for fracture wall
		Normal direction		Measure of normal displacement for fracture wall
Filling			-	Description of the material inside the fracture void

Table 2. Properties commonly used to characterize fracture networks.

Fracture network property		SI unit	definition
Density(p)	Areal($P20$)	m^{-2}	Number of fractures per unit area
	Volumetric($P30$)	m^{-3}	Number of fractures per unit volume
	sets	-	Number of sets in this field
Intensity(I)	Linear($P10$)	m^{-1}	Number of fractures per unit length
	Areal($P21$)	$m \cdot m^{-2}$	Fracture length per unit area
	Volumetric($P32$)	$m^2 \cdot m^{-3}$	Fracture area per unit volume
Spacing(S)		m	Average distance between fractures
Mean length(l_m)		m	Average fracture length
Length distribution	Scanline sampling	-	Trace length of fractures intersecting with a scanline
	Window sampling	-	Trace length of fractures inside a sampling area

Table 3. Fracture detection methods.

Methods	Length scale of investigation and resolution	Remarks
Differential methods	$0.1 - 5000\ m$	
Elastic methods: seismic band $(10 - 100Hz)$	$100 - 5000\ m$	Zero shear modulus of fluids
Elastic methods: sonic band $(2 - 20Hz)$	$0.1 - 10\ m$	
Elastic methods: ultrasonic band $(200 - 2000Hz)$	$0.1 - 5\ m$	Fracture aperture is critical
Borehole televiewer	$10 - 30\ cm\ [0.3 - 5\ cm]$	Detects fractures in boreholes
Electrical methods	$10 - 300\ m$	Resistivity of fracture fluid
Electromagnetic methods	$[10 - 300\ m]$	
Radar methods	$3 - 100\ m$	
Conventional well logs	$0.1 - 10\ m$	Near-borehole environment
Geological observation	$0.1 - 500\ km$	Surface lineations
Tiltmeter methods	$100 - 2000\ m$	Expansion of fracture
flowmeters	$1 - 100\ m$	Directly detects fracture flow

A source of data on the nature of reservoir fracture network is micro-seismic data or micro-earthquakes (MEQs). Cold water injection perturbs the pore pressure and the in-situ stress state within the reservoir leading to fracture initiation and/or activation of discontinuities such as faults and fractures which is often manifested as multiple MEQs. Detection and interpretation of MEQs using downhole receiver arrays (Brady, Withers et al. 1994; Warpinski, Wright et al. 1999) can be analyzed to provide useful information on the stimulated zone, created reservoir permeability and fracture growth, and geometry of the geological structures and the in-situ stress state(Pine and Batchelor 1984; Gutierrez-Negrin and Quijano-Leon 2003; Warpinski, Wolhart et al. 2004; Gao and Ghassemi 2016) MEQs are believed to be associated with rock failure in shear, and shear slip on new or pre-existing fracture planes (Pearson 1981; Ye, Janis et al. 2017). The generated MEQs contain information about the sources of energy that can be used for understanding the hydraulic fracturing process (Talebi, Young et al. 1991; Shapiro, Huenges et al. 1997; Foulger, Julian et al. 2004) and the created reservoir properties. The growth of the fractured zone direction can be determined using inverse modeling of micro-seismic observations. This inverse modeling is commonly referred to as seismicity based reservoir characterization (SBRC) and can been used to estimate the rock mass permeability tensor resulting from stimulation without explicitly considering the fracture network and its mechanical characteristics and response (Shapiro, Patzig et al. 2003). In the work (Shapiro, Huenges et al. 1997), developed a diagnostic technique to estimate the reservoir permeability from MEQs. Pore pressure diffusion model was used to link MEQs to equivalent permeability at reservoir scale assuming the rock to be in the limiting state. Therefore, MEQs are assumed

to generate at the onset of injection. The hydraulic diffusivity can be determined using the diffusion length-time curve fit for the onset of seismicity. This approach is very simple and lacks quantitative analysis of the relation between the true MEQs (TMEQs) and the theoretically generated MEQs (GMEQs). This framework was further improved by combining a geomechanics model and ensemble Kalman filter (EnKF) to infer reservoir permeability and geomechanical property from MEQs as part of our DOE-funded research (Ghassemi 2012; Tarrahi and Jafarpour 2012; Ghassemi 2013; Tarrahi, Jafarpour et al. 2015). Figure 1 show that the workflow of EnKF.

A Kernel Density Estimation (KDE) was used to smooth the MEQs as continuous seismicity density since most inversion algorithms (e.g. EnKF) are designed to integrate continuous data. However, a noticeable limitation of KDE is that it cannot capture the discrete natural of MEQs and the value of discrete MEQs is compromised. There are also several limitations for the EnKF used as tool for interpreting MEQs, including (a) EnKF used in large data results in sever ensemble spread underestimation. (b) EnKF can only handle continuous data and MEQ data is a type of discrete data. (c) EnKF cannot handle a highly nonlinear relation between the flow data and unknown parameters so that it may not converged.

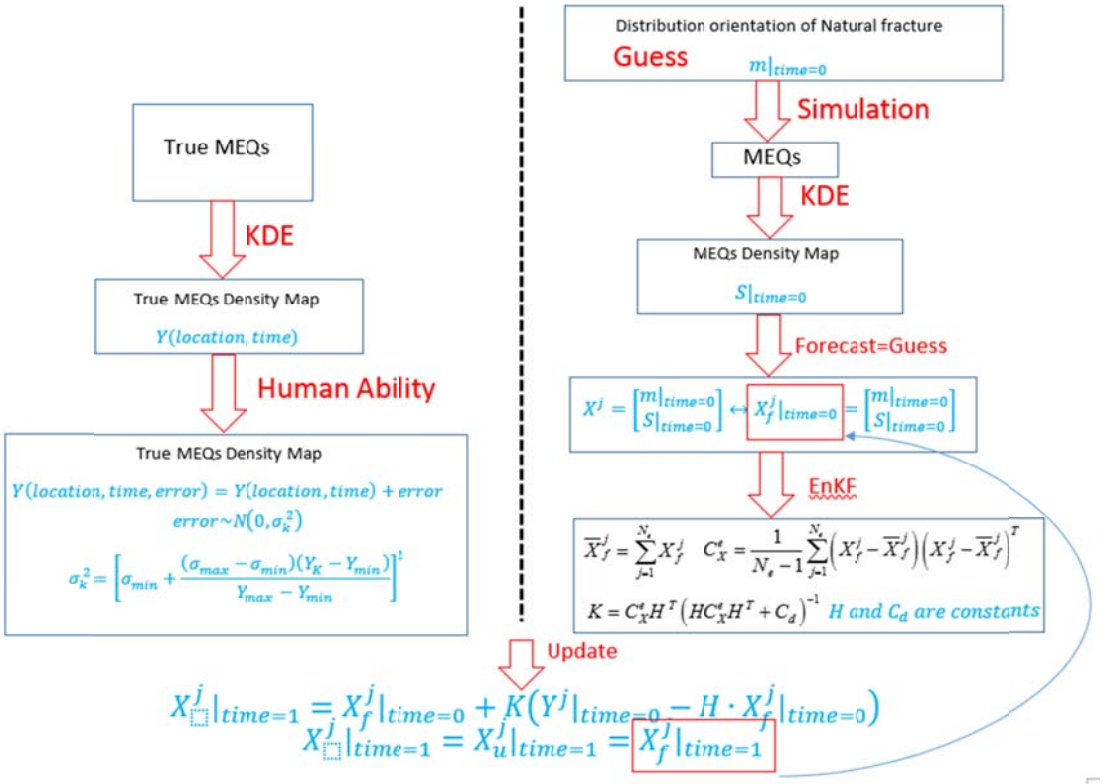

Figure 1. Overall workflow of EnKF with KDE.

Other traditional MEQs interpretations have relied on grouping MEQs based on the graph operations which rely on the locations of the MEQs hypocenters (Fehler, House et al. 1987; Fehler and Johnson 1989; Fehler 1990; Jones and Stewart 1997). Another type of approach is to first group the MEQs within similar waveforms (e.g., focal mechanisms, ratio of S wave to P wave amplitudes) and then search for self-similar MEQ clusters to define the fractures (Aster and Scott 1993; Roff, Phillips et al. 1996; Kuang, Zoback et al. 2017). So, sets of clusters are grouped into fault planes that can be defined as the best fit for

each cluster. An objective function depending on the ratio of S wave to P wave amplitudes and maximum separation distance is proposed to measure the matching level between different MEQs (Roff, Phillips et al. 1996). A further study suggests a four-term objective function that becomes much more complex(Kuang, Zoback et al. 2017). In these approaches, the focal mechanism solution with the largest value of the objective function is most likely to be the best. However, due to arbitrariness of the objective function and low magnitude of MEQs, this method seems to be poorly constrained and contains large errors. Furthermore, these methods suffers from three limitations: 1) the objective function is complex resulting in convergence difficulties; 2) waveform of MEQs is probably disorganized and amplitude is very low, so only very strong MEQs can be selected; 3) there is no general theoretical framework to quantitatively measure the matching level between the MEQs.

1.1 Objectives

The objective of this part of the research work was to develop an alternative method to help characterize fractures orientations in the reservoir. We first apply the concept of similarity measure which is a real-valued function which quantifies the similarity between two objects (Jarvis and Patrick 1973; Frey and Dueck 2007). The core of the similarity measure is to build the distance metrics between the two objects. For instance, the distance metrics is calculated from the center of one object to the center of another object. In this study, we use this approach to develop a stochastic framework called Geomechanics-Based Stochastic Analysis of Microseismicity (GBSAM) to integrate TMEQs as prior information to infer fractures orientations. GMEQs are generated when the shear stress at the center of fractures are larger than the shear strength according to the Mohr-Coulomb failure criterion. If one fracture slips, the stored shear strain energy is calculated and it is supposed that a certain part of the shear strain energy will be released as seismic energy. If the released seismic energy is larger than the threshold energy of MEQs, additional MEQs are generated on the fracture plane stochastically. The threshold energy of MEQs can be defined as the minimum detection capacity of sensors. Mahalanobis distance (Huberty 2005) is then applied to measure the similarity between TMEQs and GMEQs. The uniqueness and existential of solution from GBSAM also has been investigated. Finally, the GBSAM is applied to a data set of MEQs recorded during phase 2.2 of Newberry Volcano EGS demonstration project, Fenton Hill EGS and Mississippi Hydraulic fracturing.

2. Analytical and Numerical Procedures

2.1 Poroelastic Solution of Finite Duration Line Injection

Water injection will disturb the initial pore pressure and stress fields in the reservoir and fractures are reactivated and potentially induce MEQs. This problem can be approximated via a line injection source in permeable zone which is bounded by two semi-infinite impermeable zones (Figure 2). The line injection source ($r = 0$) extends over the thickness of the permeable layer and fluid is injected into the surrounding rock masses at a constant volumetric rate Q over the finite time interval $0 < t < T$. The shear modulus G and Poisson's ratio v and other poroelastic constants are assumed known. The fractures are stochastically distributed throughout the permeable zone which is assigned an effective permeability. The effective permeability of fractures is assumed as the same as the permeable zone. Poroelastic and thermal effects are neglected in this study. Initially ($t = 0$), all the hydraulic and mechanical fields are assumed to be in equilibrium state.

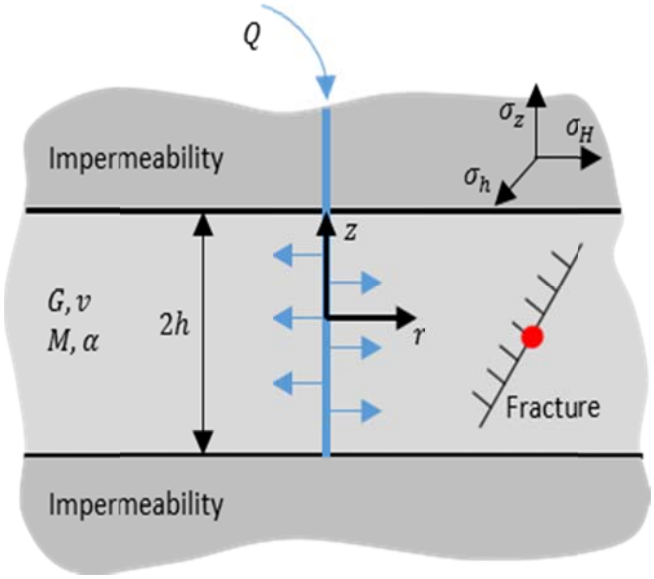

Figure 2. Geometry of the problem: a line injection source with fractures in permeability layer. The red point is the center of the fracture.

This problem can be transformed into a scaled form by introducing the following dimensionless variable

$$\rho = \frac{r}{h}, \quad \zeta = \frac{z}{h}, \quad \tau = \frac{t}{t^*}, \quad P = \frac{p}{p^*} \tag{1}$$

Where $p^* = Q/8\pi\kappa h$ is the characteristic pressure and κ is the permeability coefficient and p is the pore pressure, $t^* = h^2/4c$ is the characteristic time and c is the diffusivity coefficient. The pore pressure field $P(\rho, \tau, \zeta)$ in subsurface is given as

$$P(\rho, \tau, \zeta) = \begin{cases} P_r(\rho, \tau), & |\zeta| \le 1 \\ 0, & |\zeta| > 1 \end{cases} \tag{2}$$

$P_r(\rho, \tau)$ is the pore pressure field in reservoir. To drive the analytical solutions for pore pressure generated by a uniform line source density over the thickness of the reservoir, the diffusion equation is:

$$\frac{\partial p}{\partial t} = c\nabla^2 p \tag{3}$$

The diffusion equation (3) can be re-written as:

$$\frac{\partial P_r}{\partial \tau} - \frac{\partial^2 P_r}{\partial \rho^2} - \frac{1}{\rho}\frac{\partial P_r}{\partial \rho} = 0, \qquad \tau > 0 \tag{4}$$

Equation (4) can be solved together with the initial conditions and boundary conditions to get the pore pressure field $P_r(\rho, \tau)$.

In this work, we consider constant volumetric rate Q over the finite time interval $0 < \tau < T$. This is simply achieved by superimposing the solution for injection rate Q starting at $\tau = 0$ with the solution for withdrawal rate Q beginning at $\tau = T$:

$$P_r(\rho, \tau) = \begin{cases} E_1\left(\frac{\rho^2}{\tau}\right), & 0 < \tau < T \\ E_1\left(\frac{\rho^2}{\tau}\right) - E_1\left(\frac{\rho^2}{\tau - T}\right), & T \le \tau \end{cases} \tag{5}$$

Where E_1 is the exponential integral:

$$E_1(x) = \int_x^\infty \frac{e^{-t}}{t} \mathrm{d}t \tag{6}$$

Figure 3 shows a plot of the equation (5) with $T = 10$. After fluid injection stops (shut-in), the pore pressure continues to increase for some time and then declines. Equation (6) can be simplified using asymptotic expansions for small and large x. Thus equation (5) can be also approximated by the first term of its asymptotic expansions for small and large ρ^2/τ.

$$P_r(\rho,\tau) = \begin{cases} \ln\left(\frac{\rho^2}{\tau}\right) - \gamma, & 0 < \tau < T \\ \ln\left(\frac{\rho^2}{\tau}\right) - \ln\left(\frac{\rho^2}{\tau - T}\right), & T \le \tau \end{cases} \quad \text{for } \frac{\rho^2}{\tau} \lesssim x_s \qquad (7)$$

$$P_r(\rho,\tau) = \begin{cases} \frac{e^{-\frac{\rho^2}{\tau}}}{\frac{\rho^2}{\tau}}, & 0 < \tau < T \\ \frac{e^{-\frac{\rho^2}{\tau}}}{\frac{\rho^2}{\tau}} - \frac{e^{-\frac{\rho^2}{\tau - T}}}{\frac{\rho^2}{\tau - T}}, & T \le \tau \end{cases} \quad \text{for } \frac{\rho^2}{\tau} \gtrsim x_d = \frac{\rho^2}{\tau}(\tau = T) \qquad (8)$$

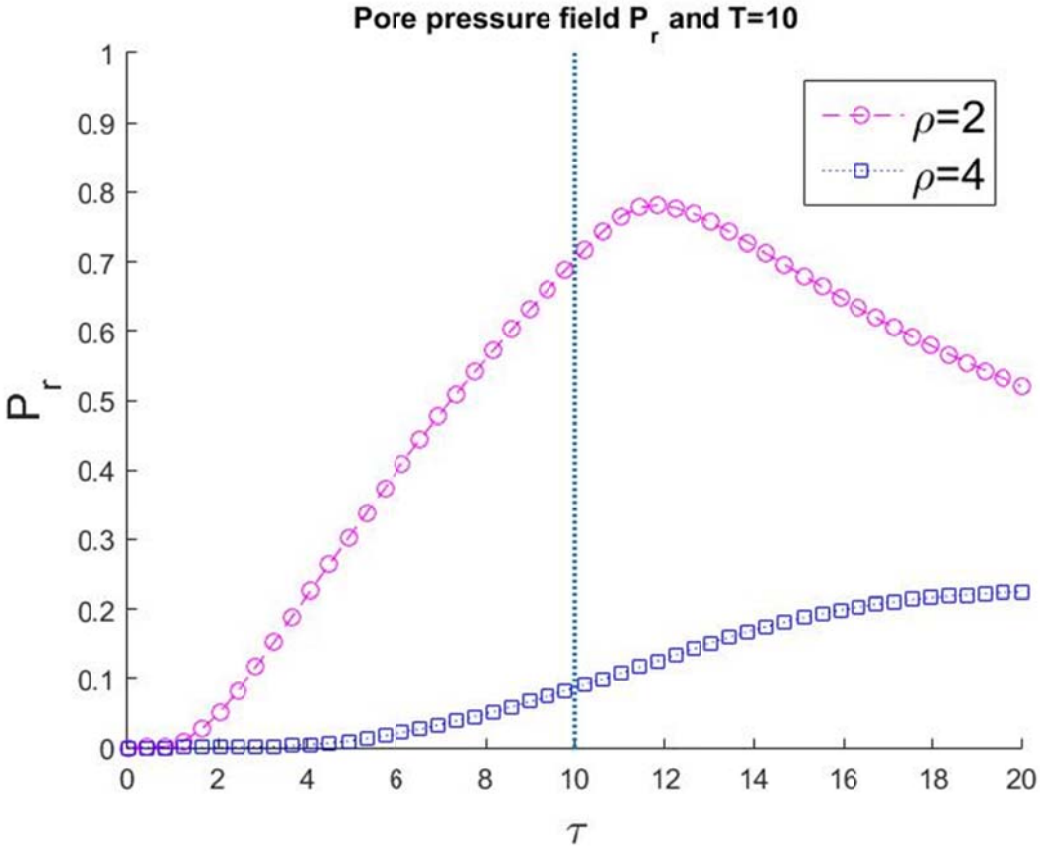

Figure 3. Pore pressure field in the reservoir during finite duration injection at a constant volumetric rate, at $\boldsymbol{\rho = 2}$ and $= \mathbf{4}$. Dotted vertical line indicates the shut-in time.

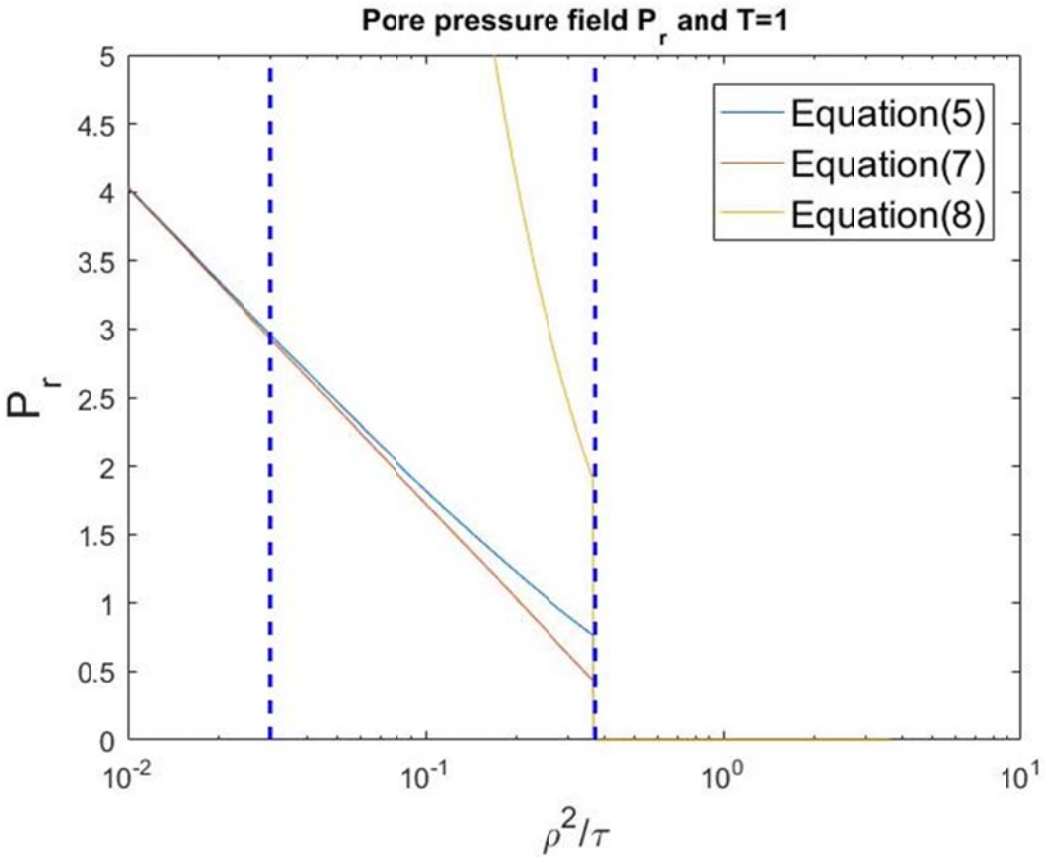

Figure 4. Three evolving regions defined by $\boldsymbol{x_s}$and $\boldsymbol{x_d}$ in the permeable zone.

In equation (7), γ is the Euler constant($\simeq 0.577$), $x_s \simeq 0.03$. In equation (8), x_d equate to $\frac{\rho^2}{\tau}(\tau = T)$. x_s corresponds to a relative error of about 1% between equation (5) and equation (7), while x_d corresponds to the shut in time T. Interpretation of these asymptotic bounds for the similarity variable ρ^2/τ in terms of a radius function of time leads to the introduction of the pseudo steady-state radius $\rho_s(\tau) = \sqrt{x_s \tau}$ and the diffusion radius $\rho_d(\tau) = \sqrt{x_d T}$. Those two radii divide the permeable zone into three evolving regions (Figure 4)(Marck, Savitski et al. 2015). In the inner region, the pore pressure field evolves uniformly with time and spatial gradient is time independent. In the intermediate region, the compressibility of fluid and porous media affects the pore pressure variations. In the outer region, the induced pore pressure is negligible due to the injection shut-in and its distance from the sources. Those three regions may indicate the generating mechanism of MEQs based on a purely diffusion conceptual model. For example, if the MEQs are located in inner region mean generated of MEQs are dominated by value of pore pressure. If MEQs are located in outer region mean that generated of MEQs are dominated by late in time diffusion processes.

2.2 Point Injection Source: The Distribution of Stress and Pore Pressure

The constitutive equations for an isotropic, poroelastic rock relate the strains ε_{ij} linearly to the stresses σ_{ij} and changes in pore pressure p. To drive the analytical stress and pore pressure solutions for

continuous fluid injection into an infinite homogeneous poroelastic rock, we use the poroelastic equation in the form proposed by Rice and Cleary (1976):

$$2\mu\varepsilon_{ij} = \sigma_{ij} - \frac{\nu}{1+\nu}\sigma_{kk}\delta_{ij} + \frac{(1-2\nu)\alpha}{1+\nu}p\delta_{ij} \quad (9)$$

Where μ is shear modulus, ν is the drained Poisson's ratio (that is for no change in pore pressure), and α is the Biot coefficient. A second constitutive equation relates the change in pore fluid mass per unit volume of solid (measured in the unstrained state) to the volumetric strain and pore pressure. Rudnicki (Rudnicki 1986) gives the solution for a point source of fluid mass injection at time $t = 0$ and $r = 0$, where $r = \|X\|_2$. From this, superposition yields the pore pressure and stress for a specified injection history $q(t)$:

$$p(X,t) = \frac{1}{(4\pi)\rho_w r^3}\frac{(\lambda_u-\lambda)(\lambda_u+2\mu)}{\alpha^2(\lambda_u+2\mu)}\int_0^t q(t')\,\xi^3 e^{-\frac{1}{4}\xi^2}\,dt' \quad (10)$$

$$\sigma_{ij}(X,t) = \frac{1}{2\pi\rho_w r^3}\frac{\mu(\lambda_u-\lambda)}{\alpha(\lambda_u+2\mu)}\int_0^t q(t')\left[\delta_{ij}(g-\xi g') + \frac{X_iX_j}{r^2}(\xi g' - 3g)\right]dt' \quad (11)$$

where the similarity variable ξ is

$$\xi(t') = \frac{r}{\sqrt{c(t-t')}} \quad (12)$$

The function g and g′ are defined as:

$$g(\xi) = \operatorname{erf}\left(\frac{1}{2}\xi\right) - \frac{\xi}{\sqrt{\pi}}e^{-\frac{1}{4}\xi^2} \quad (13)$$

$$g'(\xi) \stackrel{\text{def}}{=} \frac{d}{d\xi}g(\xi) = \frac{1}{2\sqrt{\pi}}\xi^2 e^{-\frac{1}{4}\xi^2} \quad (14)$$

We also defined the constant flux, $q(t) = q$ equation can be integrated exactly yielding:

$$p(X,t) = \frac{1}{4\pi\rho_w r}\frac{(\lambda_u-\lambda)(\lambda_u+2\mu)}{\alpha^2(\lambda_u+2\mu)}\operatorname{erfc}\left(\frac{1}{2}\xi\right) \quad (15)$$

$$\sigma_{ij}(X,t) = \frac{1}{2\pi\rho_w r^3}\frac{\mu(\lambda_u-\lambda)}{\alpha(\lambda_u+2\mu)}\left\{\delta_{ij}\left[\operatorname{erfc}\left(\frac{1}{2}\xi\right) - 2\xi^{-2}g(\xi)\right] + \frac{X_iX_j}{r^2}\left[\operatorname{erfc}\left(\frac{1}{2}\xi\right) + 6\xi^{-2}g(\xi)\right]\right\} \quad (16)$$

The variable ξ is now $\xi = \frac{r}{\sqrt{ct}}$. Figure 5 show the distribution of stress and pore pressure change with time at a partial location without in-situ stress with specially parameters.

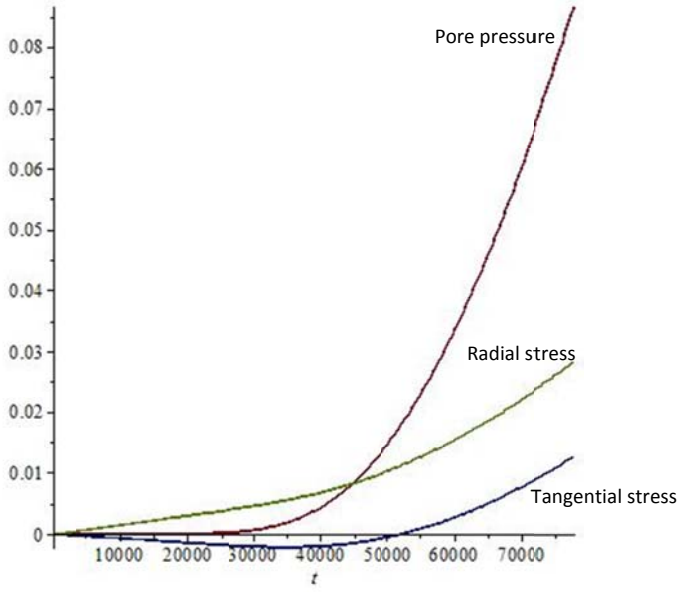

Figure 5. Stress and pore pressure change with time at a partial location without in-situ stress.

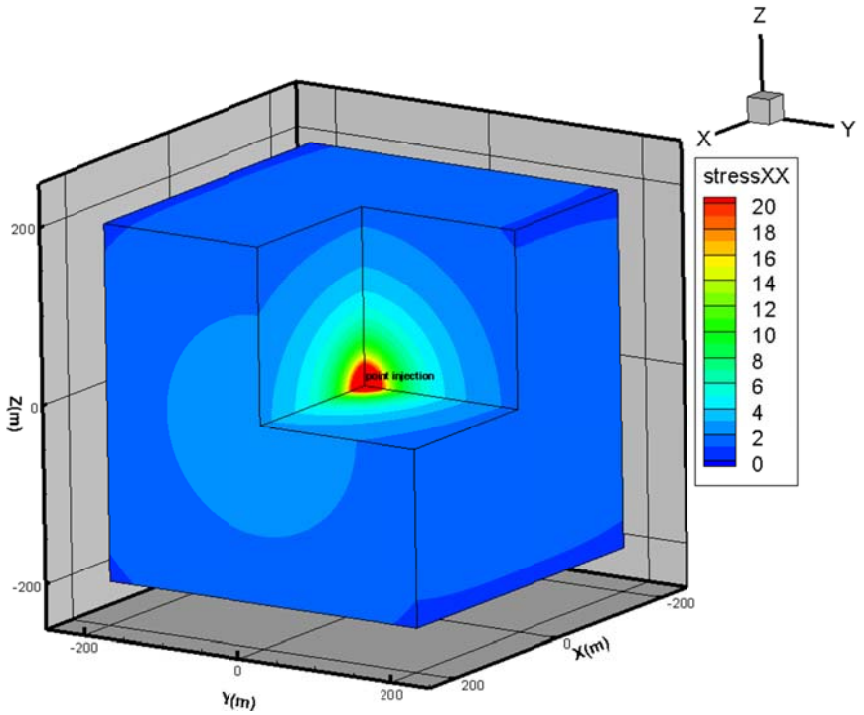

Figure 6. Induced σ_{XX} in MPa. Values of stress larger than 20 are set as 20.

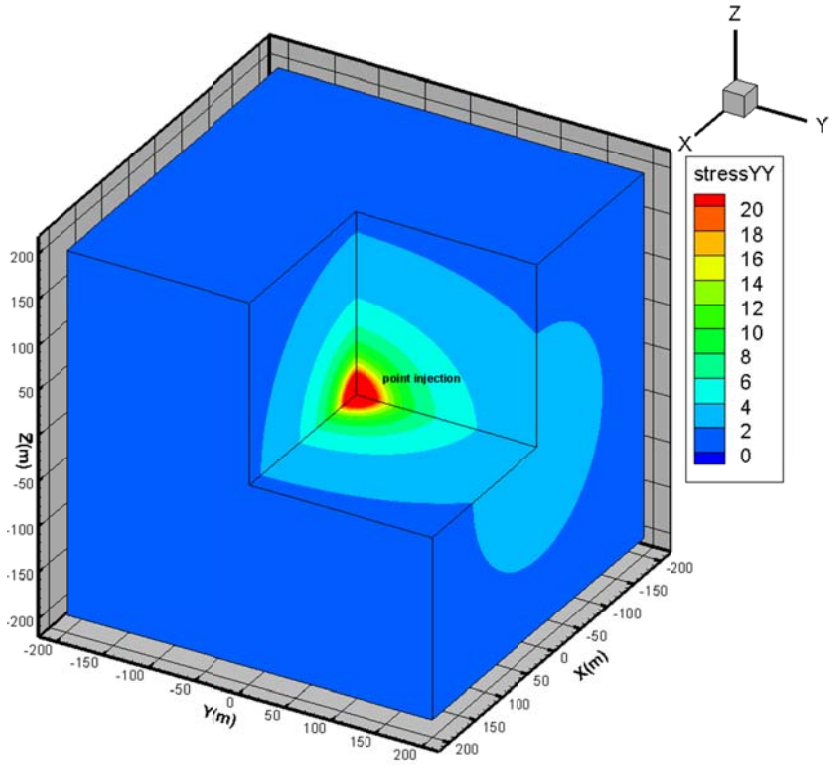

Figure 7. Induced σ_{YY} in MPa. Values of stress larger than 20 are set as 20.

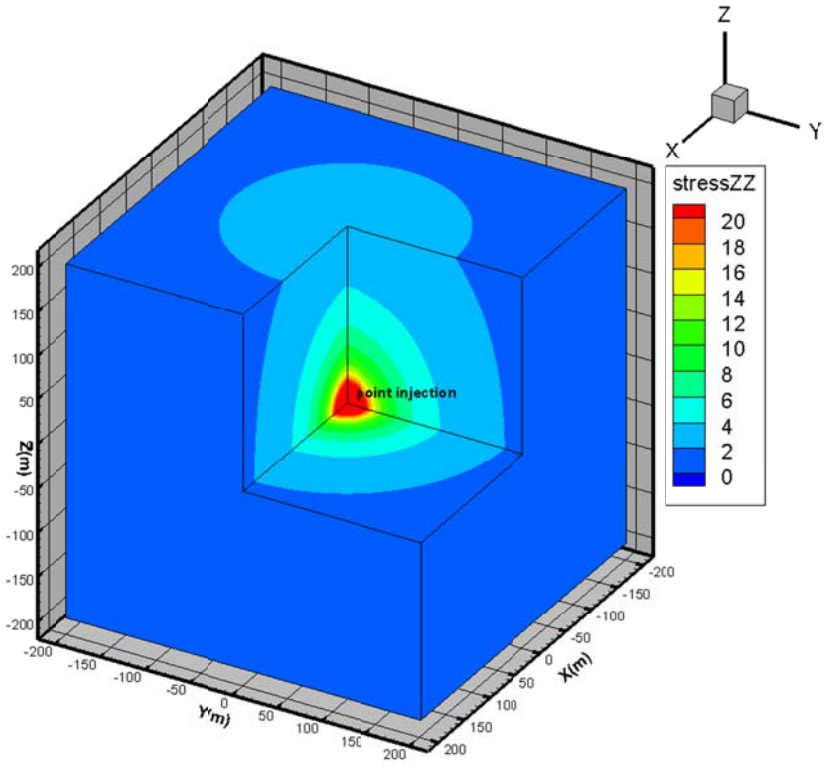

Figure 8. Induced σ_{ZZ} in MPa. Values of stress larger than 20 are set as 20.

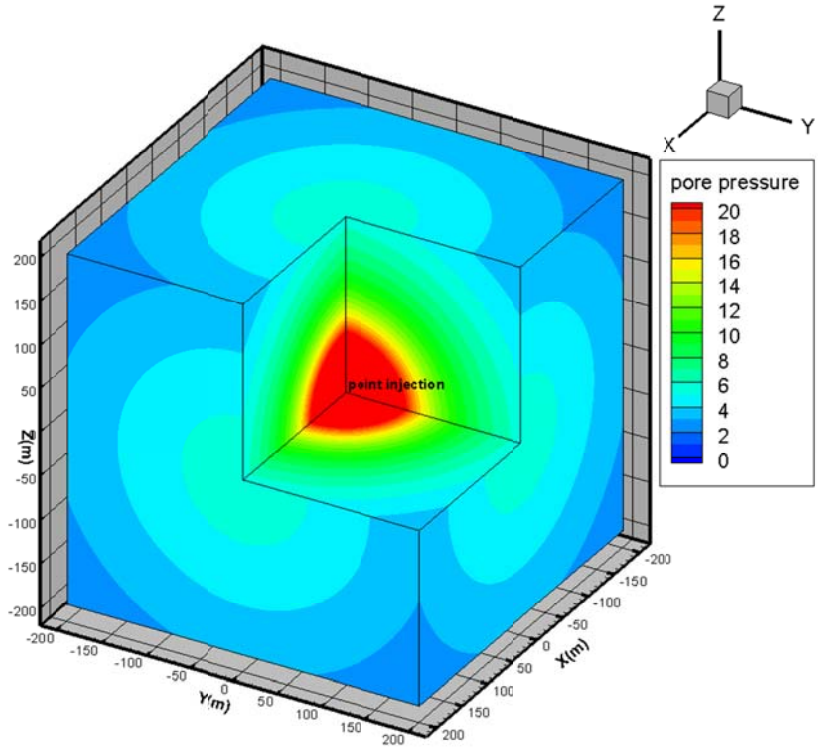

Figure 9. Induced pore pressure, p in MPa.

We use Equation (9) - (16) to calculate the pore pressure and stress induced by point injection source. Fig. 5 shows the radial and tangential stress changes for a particular representative case as a function of time since the beginning of injection to a fixed position (here 200m distance to the injection point). Figures 6 - 8 show the stresses induced by a point injection source. Figure 9 shows the pore pressure distribution due to point injection. There are considerable differences in radial and tangential stress changes created by the same pore pressure change. σ_{rad} is larger than $\sigma_{\tan}$ and only after some time has passed dose the pore pressure, p exceeds radial stress, σ_{rad} . This can be interpreted as indicating that the stress is transferred poro-elastically faster than the pore pressure diffuses through the medium. Also, note that in the same time interval $\sigma_{\tan}$ is negative. A similar analysis has been carried out by (Segall and Lu 2015).

2.3 MEQs Generation

Here MEQs is generated when the fractures fail in shear. To do so, the effective normal stress σ_n and shear stress σ_s acting on an arbitrary plane whose unit normal is $[n_x, n_y, n_z]$ at the center of fracture (red point in figure 11) are calculated. From the Cauchy's law, the traction vector $\boldsymbol{t}^n$ on fracture is $\sigma'_{ij}n_j$, with σ'_{ij} as the effective stress. The normal stress on the fracture is $\sigma_n = \boldsymbol{t}^n \cdot n$ and shear stress σ_s is $\sqrt{|\boldsymbol{t}^n|^2 - \sigma_n^2}$. The slip direction on the fracture S is $\left[\frac{\sigma_1-\sigma_n}{\sigma_s}n_x, \frac{\sigma_2-\sigma_n}{\sigma_s}n_y, \frac{\sigma_3-\sigma_n}{\sigma_s}n_z\right]$. Figure 10 shows the definition of each variable.

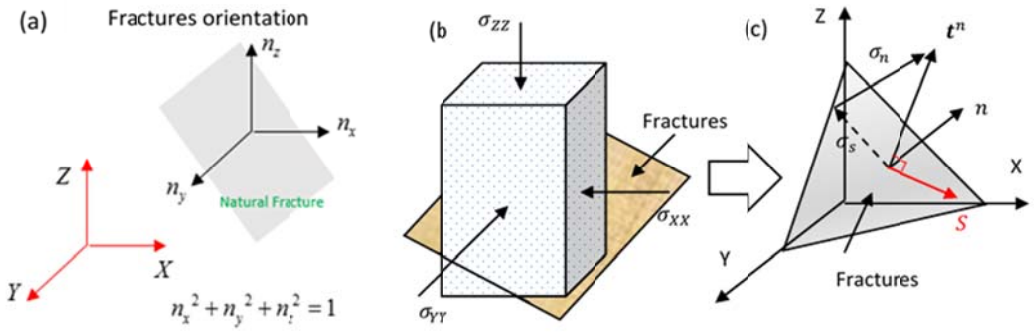

Figure 10. Geometry of the fracture: (a) fracture orientation and (b), (c) stress field on the fracture.

The Coulomb failure function (CFF) which describes the proximity of fracture to frictional slip is:

$$\mathrm{CFF}=\sigma_s - \mu\sigma_n - C \qquad (17)$$

Where μ is the friction coefficient and C is the cohesive strength. In this analytical study, the geometry of the fracture is treated as a mass point which is inherits all the geometrical and mechanical properties of the fracture (Figure 11(a)) and is located at the center of fracture (Figure 11(b)). So the mechanics of the mass point represents the mechanics state of entire fracture. Another essential assumption in the current formulation is that if any physical point (element) on the fracture fails, one GMEQ is generated. Thus the processes of generating MEQs have severe mesh-dependency issues. Recently, different numerical methods such as discrete element method (Zhao and Paul Young 2011; Khazaei, Hazzard et al. 2016), hybrid boundary element/finite element(Safari and Ghassemi 2016) are applied to simulate MEQs. A fracture plane can have multiple MEQs and usually some heuristics are used to control the number of

MEQs. From this aspect, numerical methods do not necessarily provide a significant advantage. Due to the scale mismatch between the physical point (element) and the fracture, we propose a new simple method to outline the location and the number of GMEQs that will be generated on a fracture plane. If CFF is large than zero and the fracture is slipping, one GMEQs will be occurred at the center of fracture. In this configuration, the stored shear strain energy of fracture is calculated. One third of stored shear strain energy in the contact surface is supposed to be released in the form of seismic wave during the fracture slipping processes. If the released seismic energy is larger than the pre-defined threshold energy of MEQs, additional MEQs will be generated (Figure 11(b)). Specially, the locations of additional MEQs are randomly distributed on the fracture plane.

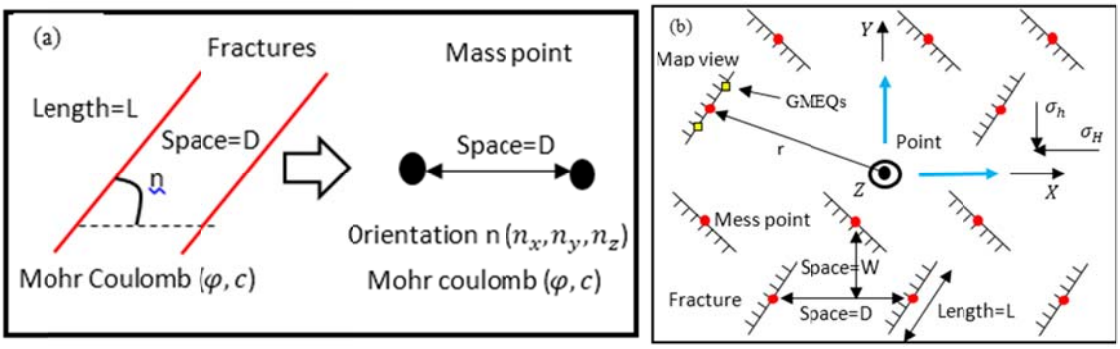

Figure 11. Assumptions nade in GBSAM: (a) mass point assumption and (b) generation of additional GMEQs.

2.4 Mahalanobis Distance and Similarity Measure

The concept of similarity is essential to the pattern recognition problems and is applied to the data classification and clustering in data sciences (Cha 2007). From the data scientist's perspective, similarity is defined as a quantitative degree of how far apart are two discrete or continuous objects. Hence, the concept of similarity is appropriate for measuring the matching level between the GMEQs and TMEQs.

The fracture orientation in the forward model with the smallest value of similarity is most likely to be the best and is considered to be the same as the true fracture orientation in the reservoir. Here, the Mahalanobis distance (MD), a concept of similarity, is used to quantify the matching level between GMEQs and TMEQs. MD is defined on both the mean and variance of the predictor variables and the covariance matrix of all the variables, and therefore it takes advantage of the covariance among variables. For instance, suppose we have two data groups of MEQs and they are all two dimensional. Data group 1 is $X(x_i^1, x_i^2)$ and Data group 2 is $Y(y_j^1, y_j^2)$. The number of MEQs in each group may not be the same $(i \neq j)$. The center of each data group can be calculated as $X - mean(X)$ and $Y - mean(Y)$ respectively. In the next step, we center these two data groups on the arithmetic mean of each variable as follow:

$$S_1 = \frac{1}{n_1}\bar{X}\bar{X}^T = \frac{1}{n_1}[x^1\ x^2\ ]\begin{bmatrix}x^1\\x^2\end{bmatrix} \quad (18)$$

$$S_2 = \frac{1}{n_2}\bar{Y}\bar{Y}^T = \frac{1}{n_2}[y^1\ y^2\ ]\begin{bmatrix}y^1\\y^2\end{bmatrix} \quad (19)$$

Where n_1 and n_2 is the number of data in group 1 and group 2, respectively. The covariance matrix of each group is computed using the centered data matrix. The pooled covariance matrix of two data groups is computed as weighted average of the covariance matrices as follow:

$$S = \frac{n_1}{n_1+n_2} S_1 + \frac{n_2}{n_1+n_2} S_2 \quad (20)$$

The value of MD is simply quadratic multiplication of the mean difference and inverse of pooled covariance matrix.

$$d(X,Y) = \sqrt{(\bar{X}-\bar{Y})^T S^{-1} (\bar{X}-\bar{Y})} \quad 21$$

Now, suppose a 3D reservoir an unknown fracture orientation $n = \{n_x, n_y, n_z\}$ or $\{dip, dip\ direction\}$ and the goal is to identify the unknown fracture orientation by performing inverse analysis. Since it is difficult to determine the components of fracture orientation from a highly complex reservoir system, some necessary assumptions are made. The locations of the fractures are assumed to be the same as the TMEQs. The fractures are assumed penny-shape and the radius is pre-defined. The parameters in the line source model are also assumed to be known (Cheng and Ghassemi 2016). Fracture population is equally divided into several sets in random form in every cycle. For instance, there are only one set in dip and three sets in dip direction. In each set, the fractures orientation are followed by normal distribution.

To interpret TMEQs for fracture orientation we propose a general inverse analysis named GBSAM. These assumptions preserve the GBSAM characteristics while optimizing the inverse analysis. Here we need to point out that GBSAM cannot predict the orientation of each individual fracture and it only provides the likely orientation of each set.

The procedures of the computational algorithm for extracting fractures orientation from TMEQs, plus an additional converged analysis are summarized as follows:

Step 1. Define the all parameters but fracture orientation. It is assumed that the reservoir has two sets of fractures. The location and number of fractures are the same as the TMEQs. The initial fracture orientation of each set is $\{n_x^1, n_y^1, n_z^1\} = \{0.1, 0.01, \sqrt{1-0.1^2-0.01^2}\}$ and $\{n_x^2, n_y^2, n_z^2\} = \{0.1, 0.01, \sqrt{1-0.1^2-0.01^2}\}$. In order to simplify the inverse analysis, n_x^1 and n_x^2 is constant and equated to 0.1.

Step 2. The members of each set are also different in every cycle because each set is randomly selected from the fractures population. The number of set 1 is equated to set 2 and properties are assigned to the reservoir and the fracture for execution of geomechanics model with boundary and initial conditions.

Step 3. Compute the distribution of induced stress and pore pressure and stored strain energy on the fractures planes.

Step 4. Check whether the CFF is larger than zero. If CFF is positive, frictional sliding occurs on a fracture and a GMEQs will be generated. Check whether the ratio of stored strain energy to threshold energy of MEQs is larger than one. If yes, the number of GMEQs which lower the ratio will be generated.

Step 5. Compare the TMEQs with GMEQs via MD.

Step 6. Store the value of MD w_i and the current properties of the reservoir, fracture orientations and the current number of cycles i. Calculate the average value of MD v_i. So $\frac{\sum w_i}{i}$ is equated to the average value of MD v_i.

Step 7. Repeat calculation from step 2 to step 6 until the number of cycles i equals the maximum number of cycles c. Check whether the $|v_i - v_{i-1}| \leq \varepsilon$ ($\varepsilon\ is\ a\ small\ number$) is satisfied. If yes, the inverse analysis in this cycle has converged.

Step 8. Update fracture orientations $\{n_x^1, n_y^1, n_z^1\} = \{0.1, 0.01, \sqrt{1-0.1^2-0.01^2}\}$ and $\{n_x^2, n_y^2, n_z^2\} = \{0.1, 0.02, \sqrt{1-0.1^2-0.02^2}\}$.
Step 9. Repeat calculating from step 1 to step 8 via tree traversal.
Step 10. The fracture orientation with the minimal average value of MD v_i is assumed as to represent the reservoir conditions.

One needs to check whether the GBSAM has converged during the solution process. For instance, Figure 6(a) show the evolution of the value of MD, w, with the number of cycles when $n_z^1 = 0.33$ and $n_z^2 = 0.61$. The orientation of individual fractures is randomly allocated and then fracture population are equally divided into two sets in random form in every cycle. Thus, Figure 12(a) also show that the value of MD seems disorganized, yet they still are distributed around a certain value. Figure 12(b) shows that, the average value of the MD becomes smooth and constant when number of the cycles is larger than 300. So in this configuration, the GBSAM has converged and the maximal cycle number is 300. Figure 12(c) is an error bar analysis which show that when n_z^2 is from 0 to 1, so that GBSAM has also converged.

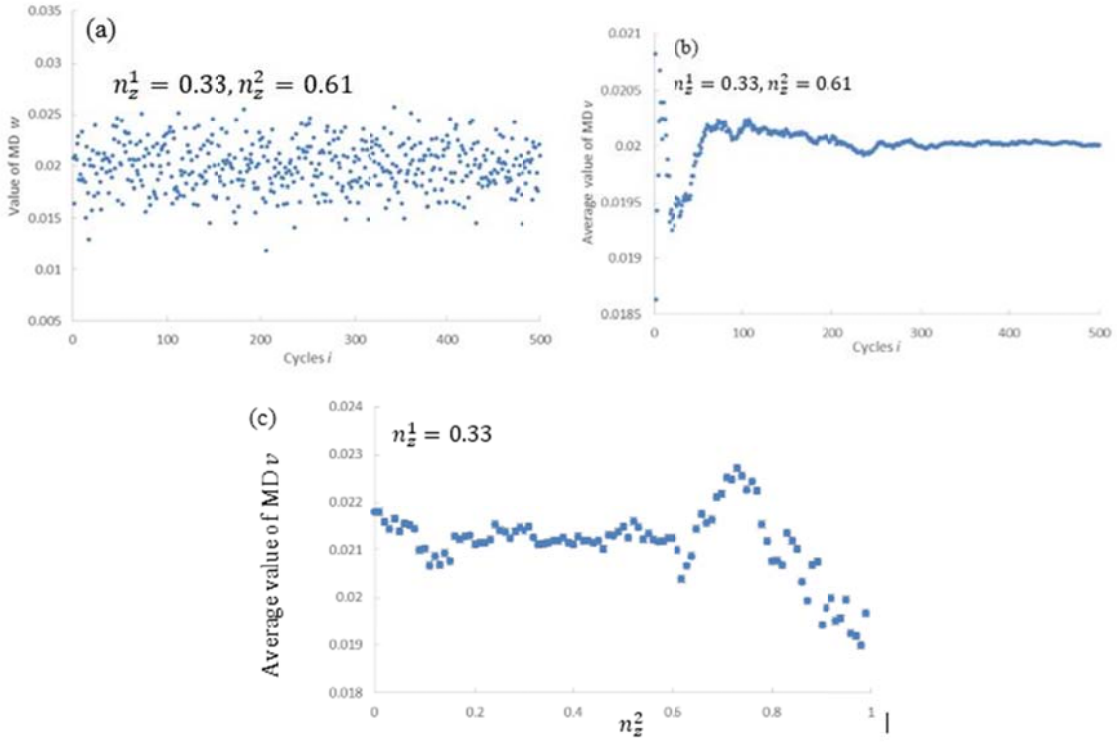

Figure 12. Convergence analysis of GBSAM: (a) the evolution of value of MD with cycles; (b) the evolution of average value of MD with cycles; (c) the error bar analysis for GBSAM.

From the above analysis, one needs to select an appropriate maximal cycle number to ensure GBSAM convergence during the process. For instance, when the maximal cycle number is set to 300, the GBSAM converges under the orientation combination $n_z^1 = 0.33$ and $n_z^2 = 0{\sim}1$. Another check has to be perform under different orientation combinations. In the current, the maximal cycle number of 300 is satisfactory for GBSAM convergence.

2.5 Newberry EGS Example

In this section, GBSAM is applied to estimate the fractures orientation of Newberry Volcano EGS demonstration, phase 2.2. Phase 2.2 of Newberry EGS stimulation began from September 23, 2014 to November 21, 2014. During this time period, about 2.5 million gallons (9464 m3) of water was injected. A fall-off test was carried out from October 15 to November 10. During phase 2.2 stimulation, 344 MEQs were located and recorded (Figure 13(a), (b) and (c)). Borehole tele viewer (BHTV) was installed to map the fractures and 399 fractures were recorded. In order to predicate the fracture orientation of Newberry EGS, further assumptions are needed. The orientation of fracture system are supposed to be followed a normal distribution. Specially, there is only one dip grouping of the fractures and two dip direction groupings. The standard deviation is kept constant while the mean varies the inversion analysis.

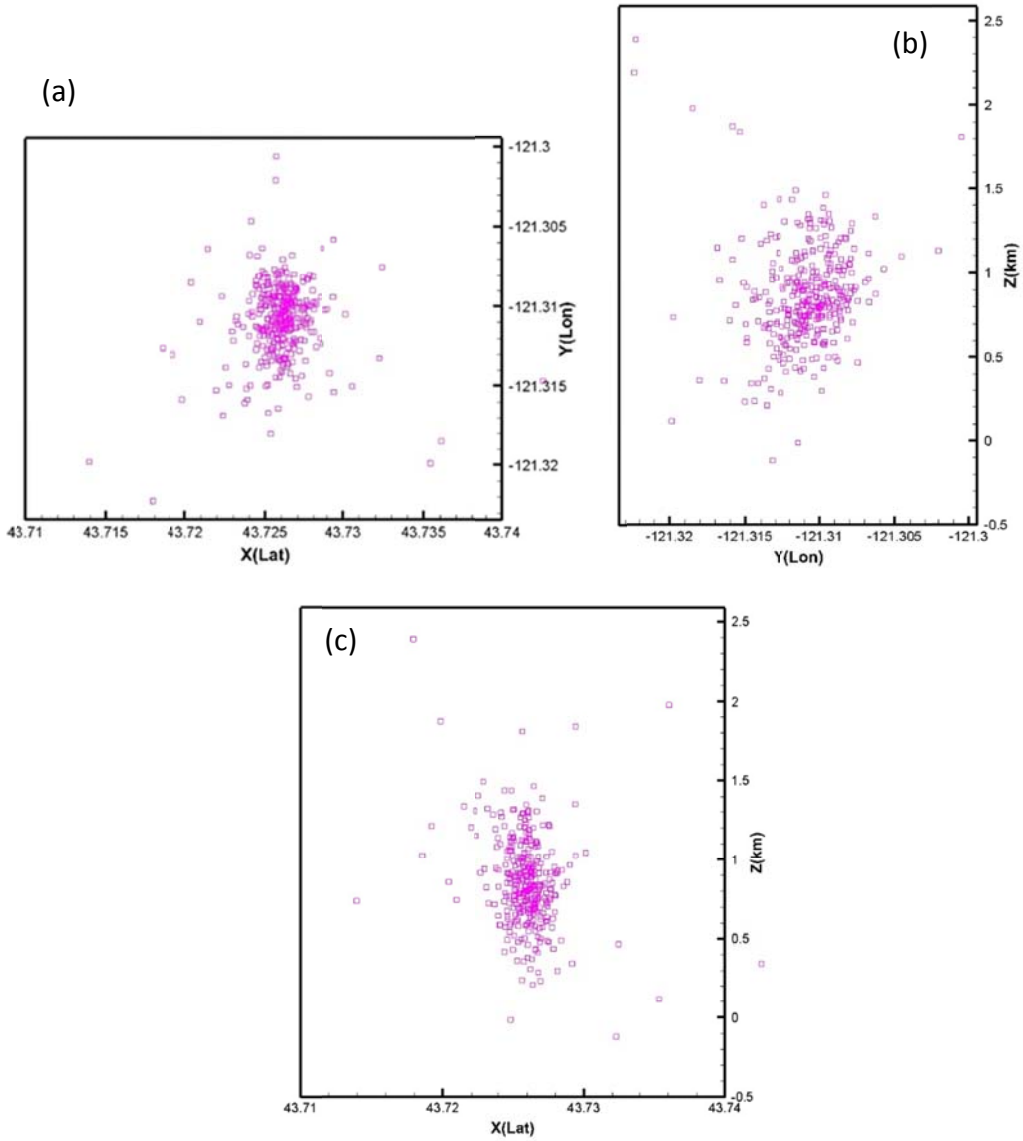

Figure 13. (a) the Lat-Lon view of TMEQs; (b) the Lon-depth (km below sea level) view of TMEQs and (c) Lat-depth (km below sea level) view of MEQs.

In this study, we use a line source of length almost equal to half the length of the open hole section of well NWG 55-29, having the same average inject rate $Q = \frac{0.063m^3}{s}$. The length of the open section of well NWG 55-29 is 906 m. The reservoir properties in GBSAM used are shown in Table 3. The permeability used is estimated value for the John Day formation(Cladouhos, Petty et al. 2015).

Table 3. Parameters used in this work for Newberry simulations.

Parameter	Variable	Value and unit
Vertical Stress (z direction)	σ_z	$67MPa$
Maximum Horizontal Stress(x direction)	σ_x	46 MPa
Minimum Horizontal Stress(y direction)	σ_y	30 MPa
Injection time	t	58 $days$
Injection rate	Q	$0.0063m^3/s$
Biot coefficient	α	0.65
Undrained Poisson's ratio	v_u	0.35
Shear modulus	μ	$10GPa$
Drained Poisson's ratio	v	0.3
Fluid Viscosity	η	$0.85 \cdot 10^{-4} Pa \cdot s$
Permeability	k	$0.01 \cdot 10^{-15}\ m^2$
Hydraulic diffusivity	c	$19.00 \cdot 10^{-2}\ m^2/s$
Cohesive strength	τ_0	0 Pa
Friction coefficient	mu	0.52
Total number of cycles		300
Permeability zone of thickness	$2h$	$200m$
Standard deviation for dip	degree	$\sqrt{80}$
Standard deviation for dip direction	degree	$\sqrt{160}$
Time of injection shut in	T	58 $days$

The results from the GBSAM show that the fractures dip are $\{\mu, \sigma\} = \left\{60^o, \sqrt{80}^o\right\}$ and the fracture dip direction are $\{\mu, \sigma\} = \left\{100^o, \sqrt{160}^o\right\}$ and $\{\mu, \sigma\} = \left\{270^o, \sqrt{160}^o\right\}$. Figure 13 shows the results from GBSAM and the results from BHTV. As can be observed from Figure 14(a), fracture dips from GBSAM are in good agreement with observations from BHTV. Figure 14(b) shows that the fracture dip direction from GBSAM are also in good agreement with observation from BHTV. The total number of GMEQs is 370. From Figure 14(c)-(e), GMEQs has a good match with TMEQs.

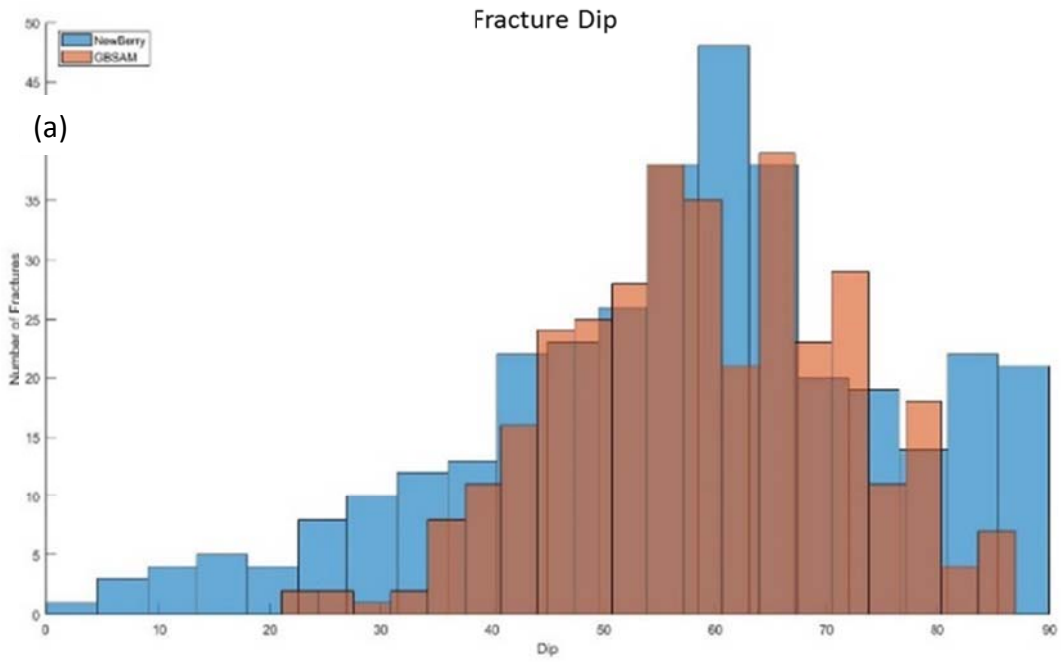
Fracture Dip
NewBerry
GRSAM
(a)
Number of Fractures
Dip
0
5
10
15
20
25
30
35
45
50
0
10
20
30
40
50
60
70
80
90

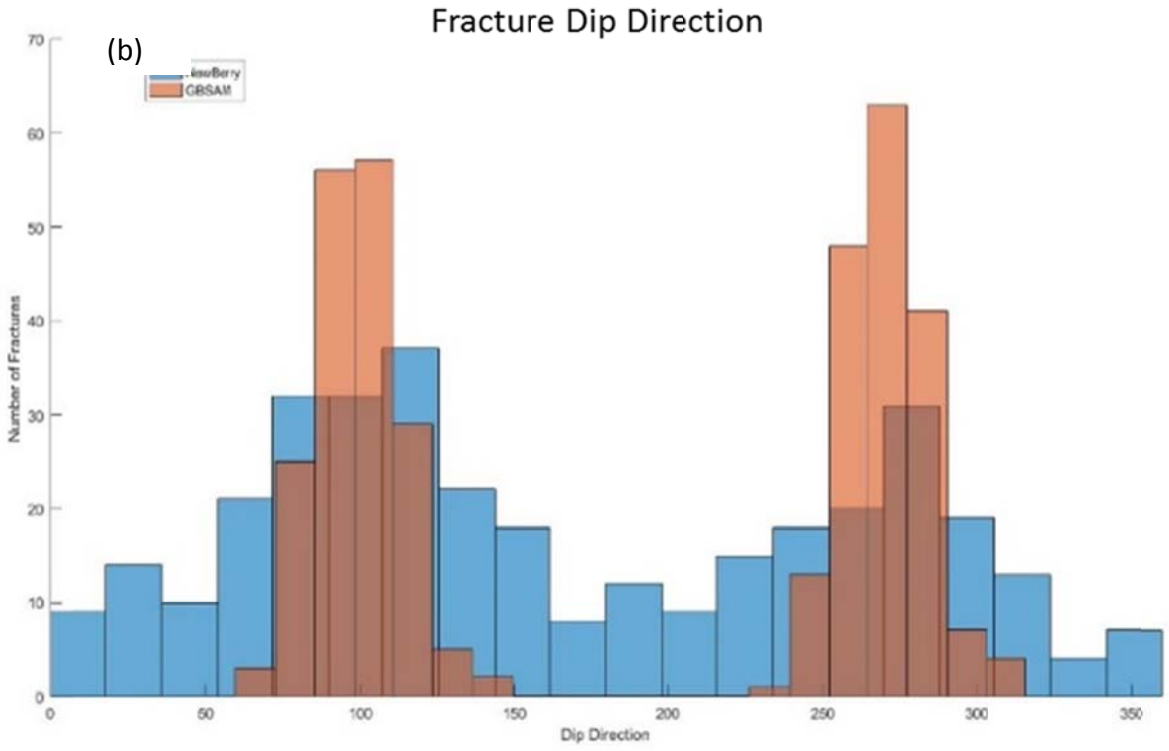
Fracture Dip Direction
(b)
GRSAM
Number of Fractures
Dip Direction
0
10
20
30
40
50
60
70
0
50
100
150
200
250
300
350

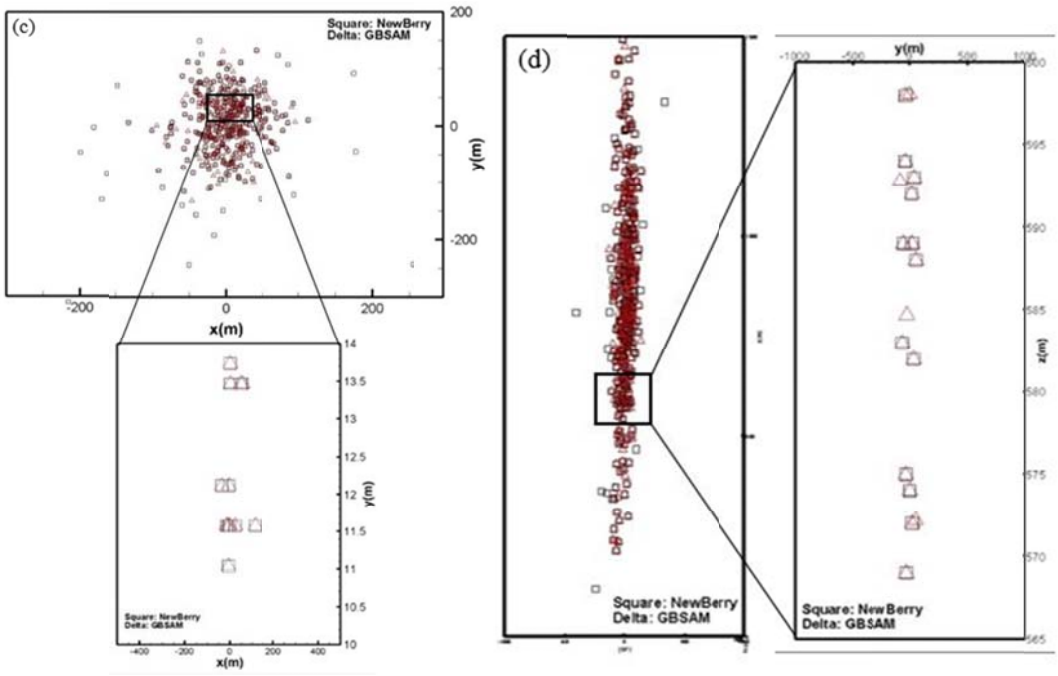

Figure 14. (a): Comparison between fracture dip from GBSAM and fracture orientation from BHTV; (b): Comparison between fracture dip direction from GBSAM and fracture orientation from BHTV. (c)~ (e) show the map view of GMEQ and TMEQs.

2.6 Fenton Hill HDR Example

The Fenton Hill HDR project was carried out from 1970 to 1995 at Fenton Hill, New Mexico. During this time period, the Los Alamos National Laboratory created and tested two reservoirs at depths in the range of 2.8-3.5 km. The first reservoir, named the Phase I reservoir, was created at a depth interval of 2800-2950m. The second reservoir, named the Phase II reservoir, was created at a depth of around 3500m. Figure 15 show the location map of Fenton Hill HDR and a simplified geological map of the Jemez volcanic field and the Espanola Basin of the Rio Grande Rift in north-central NewMexico. Figure 16 is a schematic showing the depth of Phase I and Phase II reservoirs with the geological formations and the geothermal gradient at Fenton Hill, NM, USA.

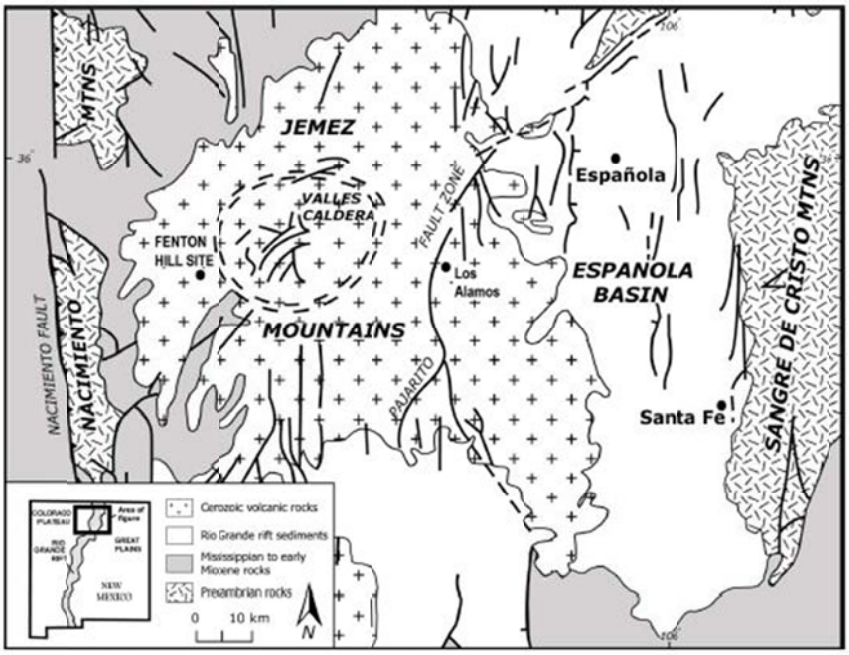

Figure 15. Location map of the Fenton Hill HDR site and simplified geological map of the Jemez volcanic field and the Espanola Basin of the Rio Grande Rift in north-central New Mexico (after Baldridge et al., 1995).

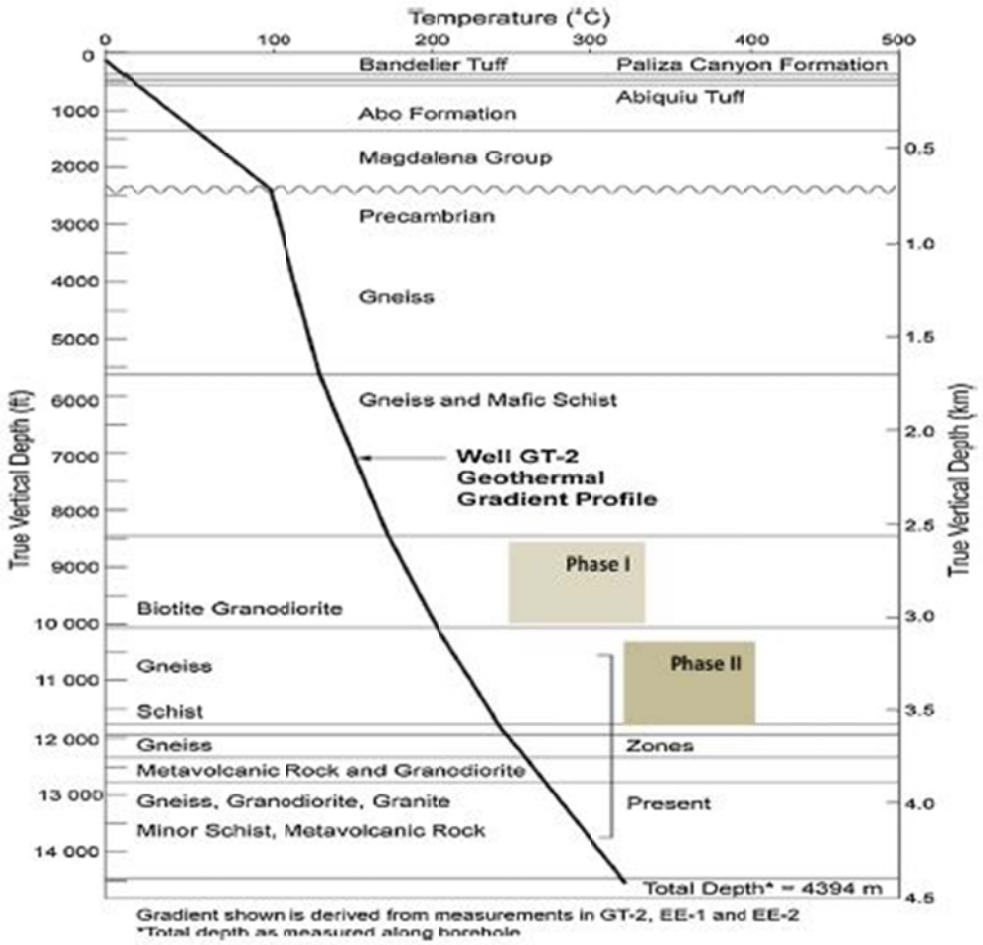

Figure 16. A schematic showing the depth of Phase I and Phase II reservoirs with the geological formations and the geothermal gradient at Fenton Hill, NM, USA.)Source: (Brown, Duchane et al. 2012).

Downhole and surface geophones were installed in the vicinity of the experimental site for seismic monitoring. An on-line system for recording and locating 3886 MEQs were developed and deployed. The distribution of MEQs for Phase II Expt2032-MHF is shown in Figure 17.

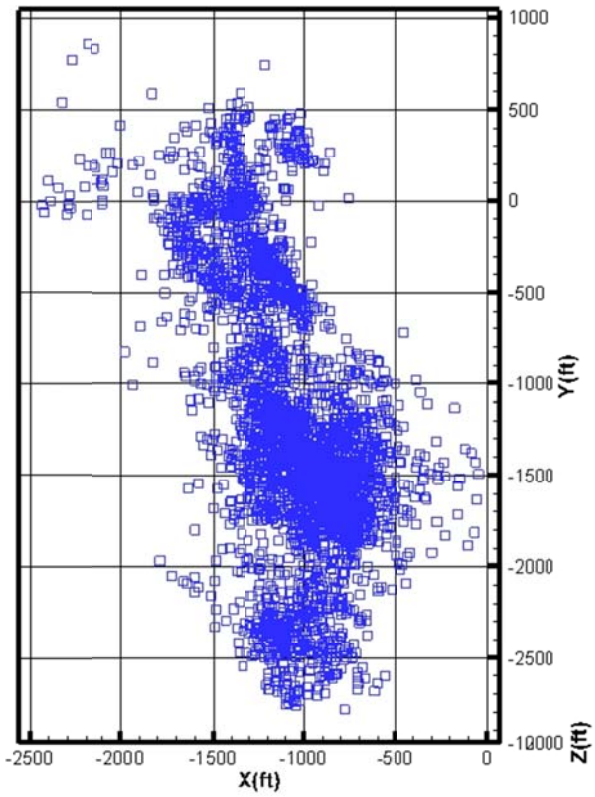
1000
500
0
-500
-1000
-1500
-2000
-2500
-10000
Y(ft)
Z(ft)
-2500
-2000
-1500
-1000
-500
0
X(ft)

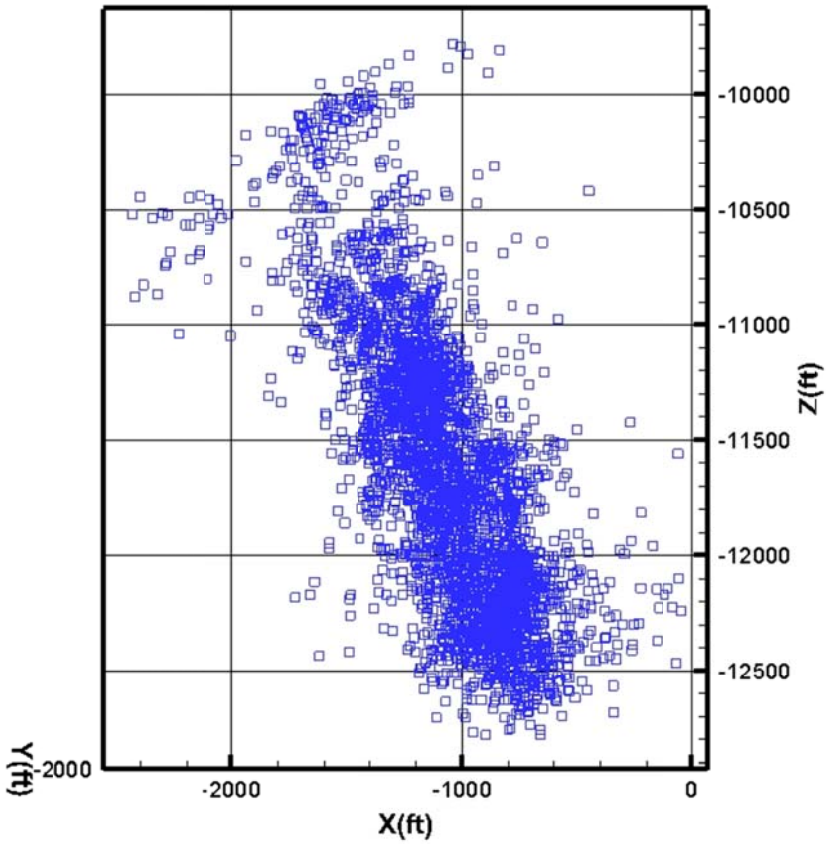
-10000
-10500
-11000
-11500
-12000
-12500
Z(ft)
-2000
Y(ft)
-2000
-1000
0
X(ft)

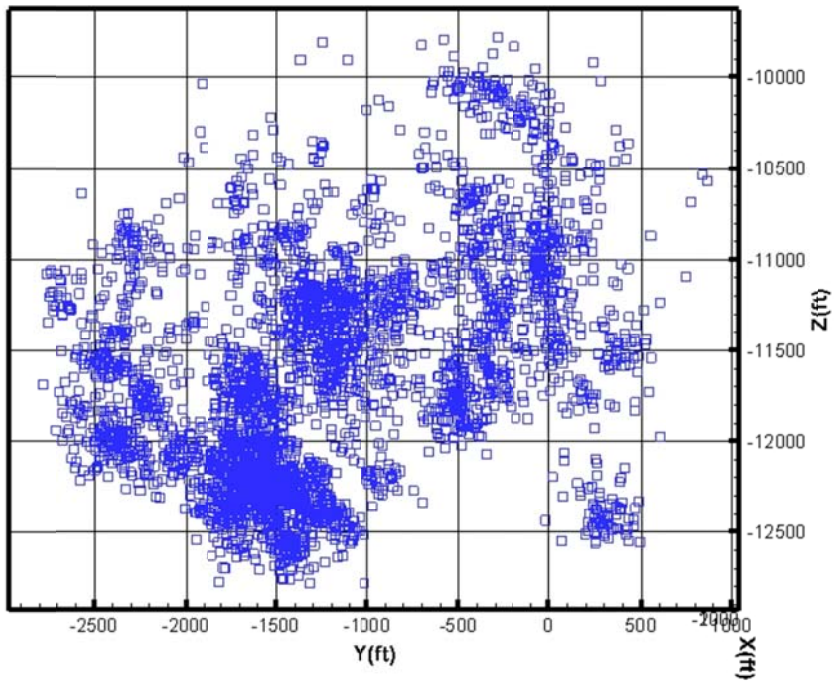

Figure 17. MEQs from Fenton Hill EGS: (a) is the x vs, y and (b) is the x vs Depth. (c) is the y vs depth. (Brown, Duchane et al. 2012).

The injection profile for Phase II is given in Figure 18. Table 4 list the input parameters for GBSAM.

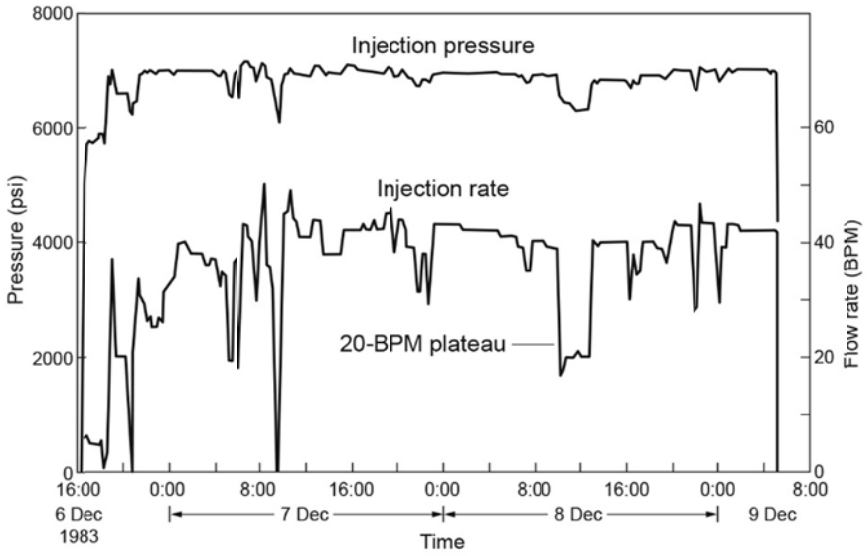

Figure 18. Injection profile of Well GT-2: well head pressure and flow rate in Phase 2. (Brown, Duchane et al. 2012).

Table 4. Parameters used in Fenton Hill HDR (Brown, Duchane et al. 2012)

Parameter	Variable	Value and unit
Vertical Stress (z direction)	σ_z	90 MPa
Maximum Horizontal Stress(x direction)	σ_x	45 MPa
Minimum Horizontal Stress(y direction)	σ_y	30 MPa
Injection time	t	2.5 $days$
Injection rate	Q	0.097 m^3/s
Biot coefficient	α	0.40
Undrained Poisson's ratio	v_u	0.25
Shear modulus	μ	21 GPa
Drained Poisson's ratio	v	0.2
Fluid Viscosity	η	$0.85 \cdot 10^{-4} Pa \cdot s$
Permeability	k	$0.5 \cdot 10^{-15}\ m^2$
Hydraulic diffusivity	c	$21.13 \cdot 10^{-2}\ m^2/s$
Cohesive strength	τ_0	1 MPa
Friction coefficient	mu	0.52
Total number of cycles		300
Permeability zone of thickness	$2h$	$200m$

The results of inversion analysis in comparison with field MEQs from Fenton Hill are shown in Figure 19-20.

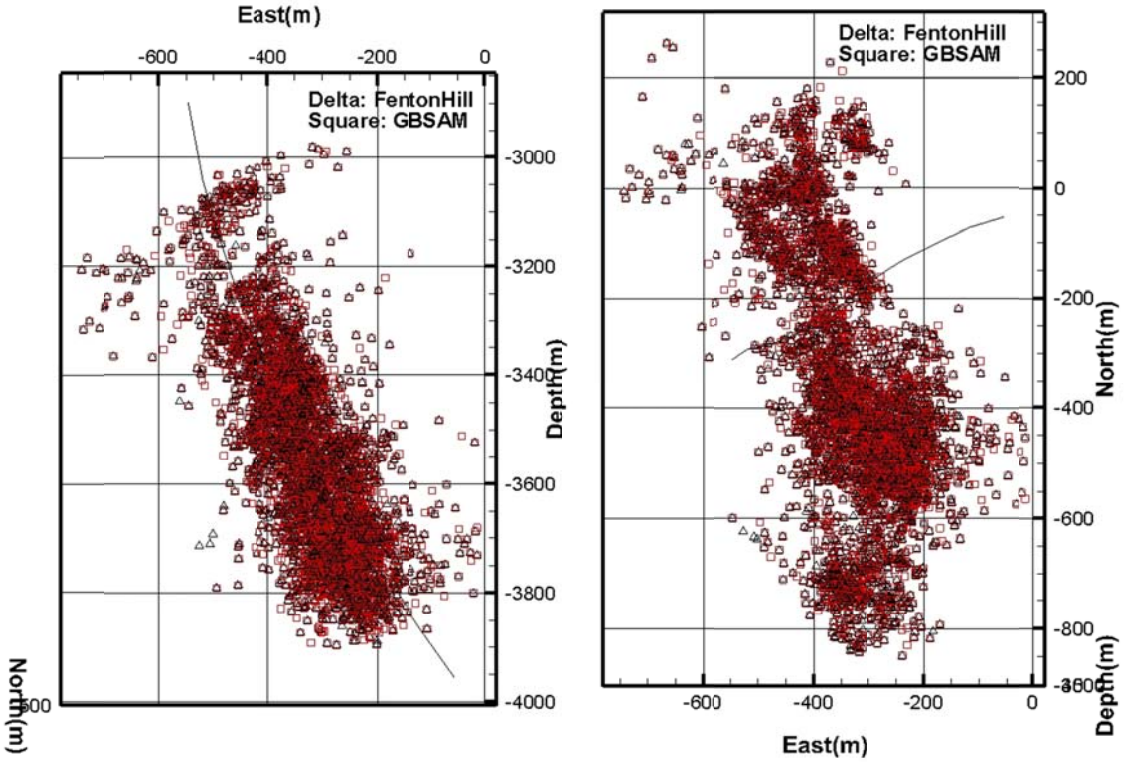

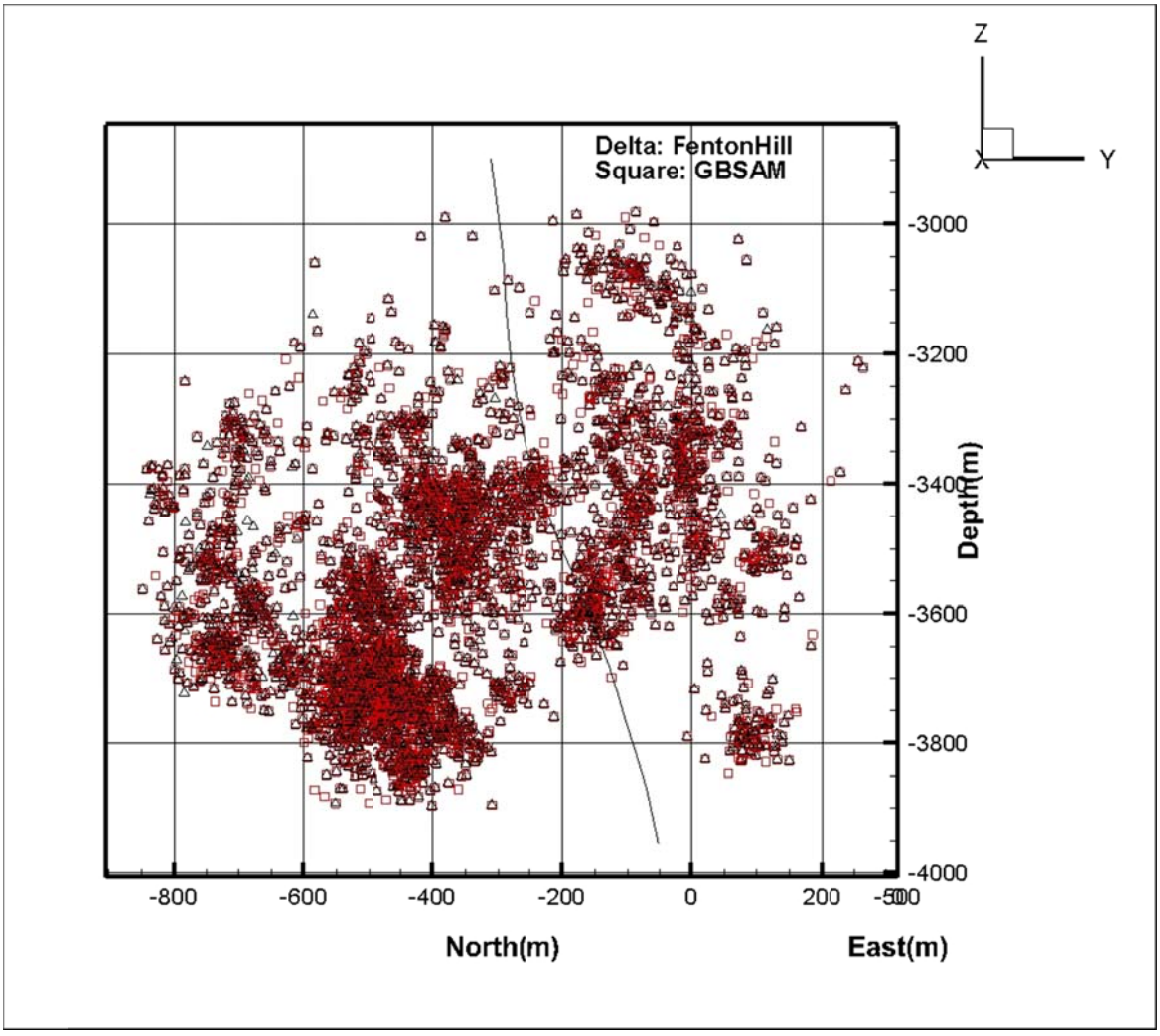

Figure 19. Comparison of MEQs from GBSAM and field observation.

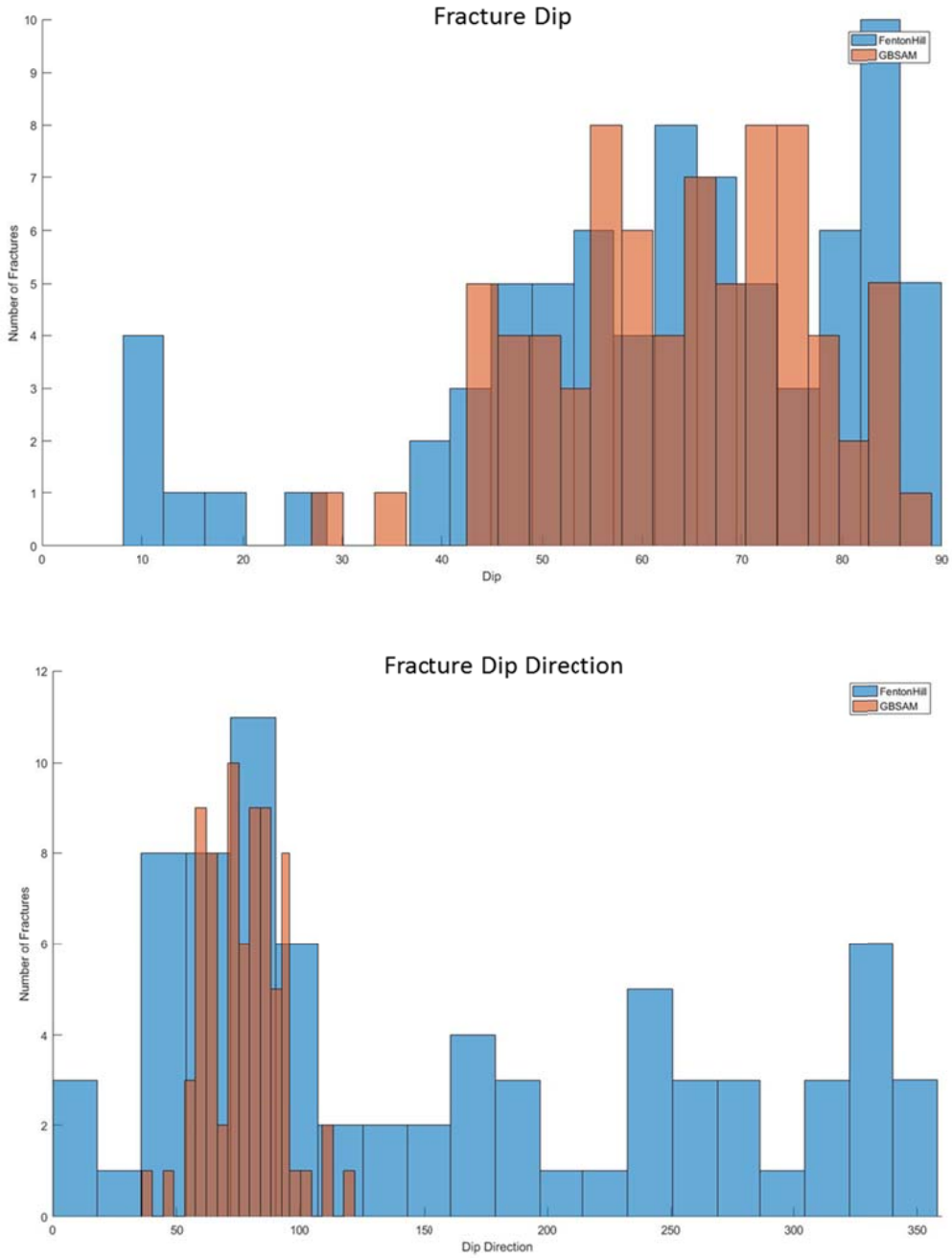

Figure 20. Predicted results for fracture dip and dip direction

The results from the GBSAM (Figure 20) show that the fractures dip is $\{\mu, \sigma\} = \left\{60^o, \sqrt{80}^o\right\}$ and fracture dip direction are $\{\mu, \sigma\} = \left\{80^o, \sqrt{160}^o\right\}$. Figure 20 also shows the results from GBSAM and from BHTV. From Figure 20(a) fracture dip from GBSAM are in good agreement with observations from Raff's results and from Figure 20(b) fracture dip direction from GBSAM are also in good agreement with observation from Raff's results. The total number of GMEQs is 3886. From Figure 19(a)-(c), GMEQs has a good match with TMEQs.

3. Conclusions

Constraining the fracture orientation in reservoir is the high interest to hydrocarbon industry. The fracture orientation (3D) or strike (2D) can be used to reconstruct the stress field, which led to the formation of the fracture. Fracture orientation are typically estimated from 1-D scan lines in outcrop and boreholes imaging log, or 2D circular sampling in outcrops. Recently, terrestrial laser scanner allow a comprehensive fracture analysis of an entire outcrop in 3D, which is therefore less subject to observation biases than scan lines or window samplings of limited sizes (Cecile Massiot 2017). In this work, we propose GBSAM to constrain the fracture orientation based on the microseismic data. The core steps in GBSAM are to handle with discrete MEQs data and measure similarity between field MEQs and stimulated MEQs. Here we apply Mahalanobis distance, a common tool from data sciences to measure similarity between field MEQs and stimulated MEQs and also handle with discrete data. The mechanism of generating MEQs is also improved which indicate one fracture may have multiple MEQs. The number of MEQs on a fracture is defined as the ratio of released seismic energy to threshold seismic energy. In order to verify model, GBSAM is applied to extract information of fracture orientation (dip and dip direction) in three examples, Newberry EGS and the Fenton Hill HDR. Results from GBSAM have good agreement with results from boreholes image logging or previous studies in those examples.

4. References

Aster, R. C. and J. Scott (1993). "Comprehensive characterization of waveform similarity in microearthquake data sets." BULLETIN-SEISMOLOGICAL SOCIETY OF AMERICA **83**: 1307-1307.

Brady, J. L., R. J. Withers, et al. (1994). Microseismic Monitoring of Hydraulic Fractures in Prudhoe Bay, Society of Petroleum Engineers.

Brown, D. W., D. V. Duchane, et al. (2012). Mining the earth's heat: hot dry rock geothermal energy, Springer Science & Business Media.

Cha, S.-H. (2007). "Comprehensive survey on distance/similarity measures between probability density functions." City **1**(2): 1.

Cheng, Q. and A. Ghassemi (2016). Numerical Modeling of Newberry Egs Stimulation, American Rock Mechanics Association.

Cladouhos, T. T., S. Petty, et al. (2015). Newberry EGS Demonstration: Phase 2.2 Report, ; AltaRock Energy, Seattle, WA (United States)**:** Medium: ED; Size: 138 p.

Einstein, H. H. and G. B. Baecher (1983). "Probabilistic and statistical methods in engineering geology." Rock Mechanics and Rock Engineering **16**(1): 39-72.

Fehler, M. (1990). "Identifying the plane of slip for a fault plane solution from clustering of locations of nearby earthquakes." Geophysical Research Letters **17**(7): 969-972.

Fehler, M., L. House, et al. (1987). "Determining planes along which earthquakes occur: Method and application to earthquakes accompanying hydraulic fracturing." Journal of Geophysical Research: Solid Earth **92**(B9): 9407-9414.

Fehler, M. and P. Johnson (1989). "Determination of fault planes at Coalinga, California, by analysis of patterns in aftershock locations." Journal of Geophysical Research: Solid Earth **94**(B6): 7496-7506.

Foulger, G. R., B. R. Julian, et al. (2004). "Non-double-couple microearthquakes at Long Valley caldera, California, provide evidence for hydraulic fracturing." Journal of Volcanology and Geothermal Research **132**(1): 45-71.

Frey, B. J. and D. Dueck (2007). "Clustering by passing messages between data points." science **315**(5814): 972-976.

Gao, Q. and A. Ghassemi (2016). 3D Thermo-Poromechanical Analysis of Reservoir Stimulation Using Damage Mechanics with Application to the Fenton Hill HDR Experiment, American Rock Mechanics Association.

Ghassemi, A. (2012). "Analysis of Geothermal Reservoir Stimulation using Geomechanics-Based Stochastic Analysis of Injection-Induced Seismicity." Retrieved 02/03, 2017.

Ghassemi, A. (2013). "Analysis of Geothermal Reservoir Stimulation using Geomechanics-Based Stochastic Analysis of Injection-Induced Seismicity." Retrieved 02/03, 2017.

Gutierrez-Negrin, L. C. and J. L. Quijano-Leon (2003). "Analysis of seismicity in the Los Humeros, Mexico, geothermal field." Geothermal Resources Council Transactions **28**: 467-472.

Huberty, C. J. (2005). Mahalanobis Distance. Encyclopedia of Statistics in Behavioral Science, John Wiley & Sons, Ltd.

Jarvis, R. A. and E. A. Patrick (1973). "Clustering using a similarity measure based on shared near neighbors." IEEE Transactions on computers **100**(11): 1025-1034.

Jones, R. H. and R. C. Stewart (1997). "A method for determining significant structures in a cloud of earthquakes." Journal of Geophysical Research: Solid Earth **102**(B4): 8245-8254.

Khazaei, C., J. Hazzard, et al. (2016). "Discrete Element Modeling of Stick-Slip Instability and Induced Microseismicity." Pure and Applied Geophysics **173**(3): 775-794.

Kuang, W., M. Zoback, et al. (2017). "Estimating geomechanical parameters from microseismic plane focal mechanisms recorded during multistage hydraulic fracturing." GEOPHYSICS **82**(1): KS1-KS11.

Li, S., X.-T. Feng, et al. (2013). "ISRM suggested method for rock fractures observations using a borehole digital optical televiewer." Rock mechanics and rock engineering **46**(3): 635-644.

Marck, J., A. A. Savitski, et al. (2015). "Line source in a poroelastic layer bounded by an elastic space." International Journal for Numerical and Analytical Methods in Geomechanics **39**(14): 1484-1505.

Pearson, C. (1981). "The relationship between microseismicity and high pore pressures during hydraulic stimulation experiments in low permeability granitic rocks." Journal of Geophysical Research: Solid Earth **86**(B9): 7855-7864.

Pine, R. J. and A. S. Batchelor (1984). "Downward migration of shearing in jointed rock during hydraulic injections." International Journal of Rock Mechanics and Mining Sciences & Geomechanics Abstracts **21**(5): 249-263.

Roff, A., W. S. Phillips, et al. (1996). "Joint structures determined by clustering microearthquakes using waveform amplitude ratios." International Journal of Rock Mechanics and Mining Sciences & Geomechanics Abstracts **33**(6): 627-639.

Rudnicki, J. W. (1986). "Fluid mass sources and point forces in linear elastic diffusive solids." Mechanics of Materials **5**(4): 383-393.

Safari, R. and A. Ghassemi (2016). "Three-dimensional poroelastic modeling of injection induced permeability enhancement and microseismicity." International Journal of Rock Mechanics and Mining Sciences **84**: 47-58.

Segall, P. and S. Lu (2015). "Injection-induced seismicity: Poroelastic and earthquake nucleation effects." Journal of Geophysical Research: Solid Earth **120**(7): 5082-5103.

Shapiro, S. A., E. Huenges, et al. (1997). "Estimating the crust permeability from fluid-injection-induced seismic emission at the KTB site." Geophysical Journal International **131**(2): F15-F18.

Shapiro, S. A., R. Patzig, et al. (2003). "Triggering of Seismicity by Pore-pressure Perturbations: Permeability-related Signatures of the Phenomenon." pure and applied geophysics **160**(5): 1051-1066.

Talebi, S., R. P. Young, et al. (1991). Microseismic Mapping of a Hydraulic Fracture, American Rock Mechanics Association.

Tarrahi, M. and B. Jafarpour (2012). "Inference of permeability distribution from injection-induced discrete microseismic events with kernel density estimation and ensemble Kalman filter." Water Resources Research **48**(10): n/a-n/a.

Tarrahi, M., B. Jafarpour, et al. (2015). "Integration of microseismic monitoring data into coupled flow and geomechanical models with ensemble Kalman filter." Water Resources Research **51**(7): 5177-5197.

Warpinski, N. R., S. L. Wolhart, et al. (2004). "Analysis and Prediction of Microseismicity Induced by Hydraulic Fracturing."

Warpinski, N. R., T. B. Wright, et al. (1999). "Microseismic Monitoring of the B-Sand Hydraulic-Fracture Experiment at the DOE/GRI Multisite Project."

Williams, J. H. and C. D. Johnson (2004). "Acoustic and optical borehole-wall imaging for fractured-rock aquifer studies." Journal of Applied Geophysics **55**(1–2): 151-159.

Ye, Z., M. Janis, et al. (2017). Experimental Investigation of Injection-driven Shear Slip and Permeability Evolution in Granite for EGS Stimulation. Proceedings of 42nd Workshop On Geothermal Reservoir Engineering, Stanford, CA, Stanford University.

Zhao, X. and R. Paul Young (2011). "Numerical modeling of seismicity induced by fluid injection in naturally fractured reservoirs." Geophysics **76**(6): WC167-WC180.

Chapter 5. PUBLICATIONS

1. Cheng, Q., Ghassemi, A., 2016. Numerical modeling of Newberry EGS stimulation. Proc. 50th US Rock Mechanics / Geomechanics Symposium held in Houston, TX.
2. Ghassemi, A., and Tao, Q. 2016. Thermo-poroelastic effects on reservoir seismicity and permeability change. Geothermics Special Issue on EGS. doi:10.1016/j.geothermics.2016.02.006.
3. Verde, A., Ghassemi, A. 2015. Modeling Injection/Extraction in a Fracture Network with Mechanically Interacting Fractures using an Efficient Displacement Discontinuity Method. Int. J. Rock Mech. (In press)
4. Safari, R., Ghassemi, A. 2016. Three-Dimensional poroelastic modeling of injection induced permeability enhancement and micro-seismicity. Int. J. Rock Mechanics. 84, 47–58.
5. Safari, R., Ghassemi, A. 2015. Three-dimensional Thermo-poroelastic Analysis of Fracture Network Deformation and Induced Micro-seismicity in Enhanced Geothermal Systems. Geothermics, 58, 1-14.
6. Verde, A., Ghassemi, A. 2015. Fast Multipole Displacement Discontinuity Method (FM-DDM) for Geomechanics Reservoir S Int. J. Num. and Anal. Methods in Geomech. (in Press)
7. Tarrahi M., Jafarpour B., Ghassemi A. (2015): Estimation of Rock Geomechanical Parameters From Micro-seismic Monitoring Data with Ensemble Kalman Filter. Water Resources Research, (in revision).
8. Ghassemi, A., and Rawal, A., Zhou, X. 2013. Rock failure and micro-seismicity around hydraulic fractures. J. Pet. Sci. and Engrg., 108, 118-127. DOI information: 10.1016/j.petrol.2013.06.005
9. Wang, X., Ghassemi, A., 2013. A three-dimensional poroelastic model for naturally fractured geothermal reservoir stimulation. GRC Annual Meeting. Las Vegas, Nevada.
10. Wang, X. and Ghassemi, A. 2012. A 3 D Thermal-poroelastic Model for Geothermal Reservoir Stimulation. Proc., 36th Workshop on Geothermal Reservoir Engineering, Stanford University.
11. Wang, X. and Ghassemi, A. 2011. A Three-Dimensional Stochastic Fracture Network Model for Geothermal Reservoir Stimulation. Proc., 36th Workshop on Geothermal Reservoir Engineering, Stanford University.
12. Lee S. H. and Ghassemi, A. 2011. Three-Dimensional Thermo-Poro-Mechanical Modeling of Reservoir Stimulation and Induced Microseismicity in Geothermal Reservoir. Proc. 36th Stanford Geothermal Workshop, Stanford, CA
13. Ghassemi, A., X. Zhou. .2011. A three-dimensional Thermo-poroelastic model for Fracture Response to Injection/Extraction in Enhanced Geothermal Systems. Geothermics, 40 (1), 39-49.
14. Lee S. H. and Ghassemi, A. 2010. A Three-Dimensional Thermo-Poro-Mechanical Finite Element Analysis of a Wellbore on Damage Evolution. Proc., 44nd US Rock Mechanics Symposium, Salt Lake City, UT

15. Lee S. H. and Ghassemi, A. 2010. Thermo-poroelastic Analysis of Injection-Induced Rock Deformation and Damage Evolution. Proc., 35th Stanford Geothermal Workshop, Stanford, CA

16. Lee S. H. and Ghassemi, A. 2009. Thermo-poroelastic Finite Element Analysis of Rock Deformation and Damage. Proc., 43rd US Rock Mechanics Symposium, Asheville, NC.

17. Tarrahi M., Jafarpour B. (2012): Inference of distribution from Injection Induced Discrete Micro-seismic Events. Water Resources Research, Vol. 48 (10), W10506, doi:10.1029/ 2012WR011920.

18. Jafarpour, B., and M. Tarrahi 2011. Assessing the Performance of the Ensemble Kalman Filter for Subsurface Flow Data Integration under Variogram Uncertainty, Water Resour. Res., 47, W05537, doi :10.1029/2010WR009090.

19. Tarrahi M., Jafarpour B. 2011. Inference of Geothermal Reservoir Properties from MicroSeismic Events with Ensemble Kalman Filter. American Geophysical Union Fall Meeting, December 2011, San Francisco, USA.

20. Tarrahi, M., and Jafarpour , B. 2011. Inference of Geothermal Reservoir Properties from Micro-Seismic Events with Ensemble Kalman Filter. In AGU Fall Meeting Abstracts (Vol. 1, p. 1163).

21. Tarrahi, M. and Jafarpour, B. 2012. Inference of Permeability Distribution from Injection-Induced Discrete Microseismic Events with Kernel Density Estimation and Ensemble Kalman Filter, Water Resour. Res., 48, W10506, doi:10.1029/2012WR011920.